Fall 2013

Spacecraft Orbit Design in the Circular Restricted Three-Body Problem Using Higher-Dimensional Poincaré Maps

Christopher D. Geisel
Purdue University

Graduate School ETD Form 9
(Revised 12/07)

PURDUE UNIVERSITY
GRADUATE SCHOOL
Thesis/Dissertation Acceptance

This is to certify that the thesis/dissertation prepared

By Christopher D. Geisel

Entitled
Spacecraft Orbit Design in the Circular Restricted Three-Body Problem Using Higher-Dimensional Poincaré Maps

For the degree of Doctor of Philosophy

Is approved by the final examining committee:

Kathleen C. Howell
Chair

James M. Longuski

William A. Crossley

Martin J. Corless

To the best of my knowledge and as understood by the student in the *Research Integrity and Copyright Disclaimer (Graduate School Form 20)*, this thesis/dissertation adheres to the provisions of Purdue University's "Policy on Integrity in Research" and the use of copyrighted material.

Approved by Major Professor(s): Kathleen C. Howell

Approved by: Weinong Chen 12/02/2013
Head of the Graduate Program Date

SPACECRAFT ORBIT DESIGN IN THE CIRCULAR RESTRICTED THREE-BODY PROBLEM USING HIGHER-DIMENSIONAL POINCARÉ MAPS

A Dissertation

Submitted to the Faculty

of

Purdue University

by

Christopher D. Geisel

In Partial Fulfillment of the

Requirements for the Degree

of

Doctor of Philosophy

December 2013

Purdue University

West Lafayette, Indiana

"Man's flight through life is sustained by the power of his knowledge."

Austin "Dusty" Miller

ACKNOWLEDGMENTS

I am grateful for all of the support I have received from my family and friends. I would also like to thank my advisor, Professor Howell, along with the other members of my advisory committee, Professors Longuski, Corless, and Crossley, for critical guidance during my research. Furthermore, it is a privilege to have been a member of the Purdue University Multi-Body Dynamics Research Group. Thank you to all of my fellow students in the group for your valuable advice and assistance during this effort, with special thanks to Cody Short for the initial idea that the "doughnut"-shaped structure in Figure 3.13 might involve a swapping of inside and outside surfaces.

My education program has been sponsored by the US Air Force and the Air Force Institute of Technology's Department of Aeronautics and Astronautics. *The views expressed in this dissertation are those of the author and do not reflect the official policy or position of the US Air Force, US Department of Defense, or US Government.*

This investigation has also benefited from the 3-D visualization resources in the Rune and Barbara Eliasen Visualization Laboratory at Purdue as well as the diligence and professionalism of the Purdue School of Aeronautics and Astronautics staff—most notably Ms. Flack and Ms. LaGuire.

TABLE OF CONTENTS

Page

Page

Page

LIST OF TABLES

LIST OF FIGURES

Figure Page

Figure Page

Figure Page

Figure Page

Figure Page

Figure Page

Figure Page

Figure Page

Figure Page

Figure Page

ABSTRACT

Geisel, Christopher D. Ph.D., Purdue University, December 2013. Spacecraft Orbit Design in the Circular Restricted Three-Body Problem Using Higher-Dimensional Poincaré Maps. Major Professor: Kathleen C. Howell.

Strategies for designing three-dimensional spacecraft trajectories in a multi-body dynamical environment are investigated using four-dimensional Poincaré maps. Unlike the planar circular restricted three-body problem, where a two-dimensional map provides a simplified view of a portion of the vast and often chaotic design space, the spatial problem requires a four-dimensional map to achieve an equivalent perspective. Such higher-dimensional maps present a visualization challenge. Furthermore, a spacecraft in the spatial problem can exhibit fundamentally more diverse and complex behavior than in the planar problem.

A novel approach to four-dimensional-map-based design in the spatial circular restricted three-body problem is developed and applied to practical examples with real-world spaceflight applications involving three-dimensional trajectories in the Earth-Moon, Sun-Earth, and Uranus-Titania systems. Included in the approach is a method for representing, interpreting, and manipulating four-dimensional Poincaré maps in an interactive, three-dimensional visual environment in which the fourth dimension is displayed using color. This "space-plus-color" method expands on the "color and rotation" method of Patsis and Zachilas (used for the study of motion in a galaxy) by applying additional tools and techniques enabling design in the circular restricted three-body problem. Design is often based on maps generated by many trajectories. Image manipulation in both spatial and color dimensions is accomplished iteratively using MATLAB® and Avizo®.

Four-dimensional-map-based design in the spatial circular restricted three-body problem is practical, and success is enabled by interactive tools and techniques in a visual environment. The design strategy is methodical and not restricted to any particular map formulation. Human insight is leveraged to determine reference solutions in a problem without a closed-form analytical solution. Estimates obtained through visual inspection of a map are fed into automated processes, leading to precise and/or locally-optimal solutions, including transfers to and between libration/Lagrange point orbits as well as capture, departure, and transit maneuvers near a planet or moon. Additionally, the long-term variations in instantaneous eccentricity of a high-altitude Earth orbit perturbed by lunar gravity are correlated with the shape and evolution of the surface of a deformed torus on a four-dimensional map.

1. INTRODUCTION

This investigation is motivated by a simple question: Given that two-dimensional (2-D) Poincaré maps have been demonstrated as useful tools for spacecraft (S/C) mission design in the 2-D, planar version of the multi-body dynamical problem known as the circular restricted three-body problem (CR3BP) [1], could 4-D Poincaré maps be exploited in a similar way in the 3-D, spatial version of that problem? Of course, from this question, two more immediately arise: How should a 4-D map be represented by an engineer living in a 3-D world, and is it practical—or even possible—to employ such a higher-dimensional (higher-D) representation to solve real-world S/C trajectory design problems?

Herein, a novel approach to higher-D-map-based analysis and design in the spatial CR3BP is developed and applied to a variety of S/C trajectory design scenarios using several different Poincaré map formulations. Distinguished from typical methods of representing 4-D Poincaré maps in the CR3BP, which involve adding some type of arrow or line segment to a point (e.g., Paskowitz and Scheeres [2] and Haapala and Howell [3, 4, 5]), the approach in the current effort includes a "space-plus-color" method for representing, interpreting, and manipulating a 4-D map of CR3BP trajectories in an interactive, 3-D visual environment in which the fourth dimension is displayed using color. This method expands on the "color and rotation" method proposed by Patsis and Zachilas [6, 7], which has been successfully employed in various studies related to stellar motion in a galaxy. In the present investigation, various tools and techniques that enable practical, 4-D-map-based design in the dynamical environment of the CR3BP are described, while highlighting the benefits and challenges inherent in utilizing information displayed on a higher-D map.

A recurring theme throughout this investigation is that map-based S/C mission design in a multi-body environment involves *contrasts*. The first contrast is inherent in the multi-body dynamical model itself: the modeling of three bodies rather than just two. The two-body problem (2BP) [8] of a satellite orbiting the Earth has a known, closed-form, analytical solution in terms of conics. However, the CR3BP modeling the motion of a S/C influenced by *both* the Earth's and the Moon's gravity does not have such a solution, even though the CR3BP models a simplified case in which the Moon travels in a perfectly planar, circular orbit about the Earth. In a 2BP-focused design procedure, conic arcs—i.e., portions of circles, ellipses, parabolas, hyperbolas, or straight lines—serve as reference solutions for the motion of a S/C in the vicinity of a central gravitational body treated as a point mass, assuming any additional forces can be modeled as *small* perturbations on the nominal, conic path. On the other hand, if the additional forces are more significant—e.g., for a S/C leaving the near-vicinity of the Earth and traveling to the Moon or beyond—a single, conic "guess" is no longer adequate to reasonably predict the S/C trajectory, or "orbit," for the entire path. This factor often motivates the use of the CR3BP, a simplified model for the behavior of a S/C under the influence of a *system* of two massive primary bodies such as: (1) the Moon revolving about the Earth or (2) the Earth revolving about the Sun. Yet, with no known, closed-form analytical solution to the CR3BP, it is far more difficult to obtain an appropriate reference solution for a given trajectory design objective. Moreover, there exist chaotic regions of the CR3BP phase space (i.e., the full space consisting of position and velocity coordinates), where the future state along a given trajectory/orbit is extremely sensitive to the initial condition—making the motion effectively unpredictable over more than a brief span of time. Despite these obstacles, modeling S/C motion in the CR3BP can often expand the design options available to include trajectories—and low-cost maneuvers transferring between trajectories—that are not predicted/possible based on a purely two-body analysis. In fact, although the sensitivities associated with dynamical chaos in the CR3BP make trajectory design more challenging, they can effectively increase the "maneuverability" of a S/C. This phenomenon is analogous to the difference between a civilian, light aircraft built to be naturally stable in flight and, on the other hand, a high-performance, computer-

controlled, military, fighter aircraft that is built naturally unstable—and is thereby much more maneuverable.

A second contrast related to map-based S/C mission design in a multi-body environment is the distinction between analytical and numerical methods. While analytical relationships exist to describe all possible motion in the 2BP, investigations of the vast design space in the CR3BP—with no known, closed-form analytical solution—rely on mostly numerical processes enabled by modern, high-speed computing. Even when analytical approximations are employed in the CR3BP, they are generally supported by follow-on, numerical procedures, which are needed to refine any approximation/prediction. In effect, algorithms based on numerical integrations, or propagations, make it feasible to test an initial state to determine the future states (the particular solution) over some span of time *to within some level of accuracy/tolerance*. In the definitive, 1967 treatise on the CR3BP, *Theory of Orbits: The Restricted Problem of Three Bodies* [1], Victor Szebehely described such numerical explorations: "One of the most important modern trends in dynamics is the extensive use of high speed electronic computers as experimental tools. It seems to be proper to refer to *experiments* because of the similarity of the processes of computational dynamics to experiments in the physical sciences" [emphasis in the original]. Yet, even when a particular solution based on an initial condition is calculated, it cannot provide a complete—or even partially adequate—picture of all possible solutions. This implies that insight regarding the design space as a whole is required for successful CR3BP trajectory design.

The third contrast evident in this investigation is the difference between visual and automated processes related to map-based trajectory design in a multi-body environment. Visual processes include those employed when displaying and interpreting a Poincaré map, which is basically a view of a single "slice" of the design space. Such processes leverage human cognitive capabilities; visual cues provide a map-based designer—i.e., a human engineer—with valuable insight used to obtain an estimate for a given problem and/or to compare various design options qualitatively. On the other hand, automated processes exploit the speed and numerical accuracy of computers to accomplish design tasks requiring quantitative precision and/or algorithmic repetition. Given the demands

of the CR3BP in terms of the numerical "experiments" described earlier, automated processes are critically important. However, due to the complex design space in the CR3BP, certain trajectory design steps *cannot be completely automated*. With no known, closed-form analytical solution, it is far more difficult to obtain an appropriate reference solution for a given design objective. Furthermore, a "brute-force" search of the design space would likely be computationally inefficient and, more importantly, would not likely result in sufficient understanding of that space. Understanding the "big picture" of a design space is critical when analyzing trade-offs between qualitatively different solutions and also in applying lessons learned from one design result to future design cases. Thus, map-based trajectory design in the present investigation involves both visual and automated processes. Successful design requires cooperation between uniquely-human intuition and the computational power of modern computers, with the appropriate balance between visual versus automated processes dependent on the specific application. This idea of determining the appropriate balance of cooperation between the human and the machine is reminiscent of debates over the relative utility of human versus robotic spaceflight or, alternatively, human-in-the-cockpit versus "unmanned" military aircraft.

A fourth contrast associated with map-based trajectory design in the CR3BP is the comparison of the 2-D, planar version of the problem with the 3-D, spatial version. The planar CR3BP assumes that the S/C motion begins in, and remains in, the plane of the primary bodies. That is, motion is possible only in the x and y directions. For example, in the Earth-Moon planar CR3BP, the S/C path remains in the same plane as the Moon's orbit about the Earth—more precisely, the orbit of both the Earth and Moon about their combined "center of mass," or barycenter. On the other hand, the Earth-Moon spatial CR3BP includes trajectories in which the S/C travels out of the plane of the massive primaries, in the z direction as well. Importantly, there is added complexity in the spatial CR3BP as compared to the planar CR3BP, a complexity which amounts to much more than simply the addition of a third direction of motion. Because of the differences between systems with two degrees of freedom (2-DOF) and three degrees of freedom (3-DOF), the spatial CR3BP exhibits dynamical behavior that is *fundamentally* more diverse and complex than in the planar CR3BP. Visual tools such as Poincaré maps, if they can

be represented and interpreted, have the potential to provide valuable insight needed to overcome these complexities by reducing the view of the design space to one "slice" at a time.

The fifth, final, and most important contrast relevant to this investigation arises from requirements on the dimension of a Poincaré map for the two different versions of the CR3BP. In the planar CR3BP, a traditional, 2-D Poincaré map allows a map-based designer to view a "slice" of the design space. Yet, in the spatial CR3BP, a 4-D map is required to achieve an analogous and equivalent view. Such a higher-D map obviously presents a visualization challenge because it exists in a space consisting of more dimensions than the 3-D "real world" with which a human being is intuitively familiar. The challenges associated with representing such a map—and then utilizing it for S/C mission design—provide the motivation for, and define the scope of, the present investigation.

1.1 Summary of Previous Contributions

This section highlights key contributions relevant to the current investigation into higher-D-map-based trajectory design in the spatial CR3BP. Additional details on these contributions, along with references to other important studies, are included in the context of various explanations throughout the remainder of this dissertation.

1.1.1 Trajectory Design in a Multi-Body Environment: From 2-D to 3-D

The CR3BP design space associated with the motion of a negligibly small mass, e.g., a S/C, attracted by the gravitational forces from two significantly larger primary masses, e.g., a planet and a moon, is of *fundamentally* greater complexity than the design space in the 2BP. This is true even though the CR3BP models a simplified case in which the two primaries orbit their barycenter in perfectly planar, circular orbits. Victor Szebehely's 1967 treatise [1] is arguably the most important resource for understanding the key elements of the CR3BP. Yet, this multi-body dynamical problem has been of considerable interest and has been studied by some of history's greatest minds for several centuries. Laying the groundwork, Isaac Newton's 1683 analytical solution (in terms of

conics) for the relative motion of just two bodies [9]—based on his laws of gravity and motion—exemplifies the Scientific Revolution philosophy that all natural phenomenon can be sufficiently explained and predicted through mathematical principles, simply by solving the correct equations. This belief has been subsequently applied to more complex dynamical models, and significant progress has been made in understanding the CR3BP. In the late eighteenth century, five stationary (equilibrium) points were determined to exist in the problem; they are frequently termed libration points, or Lagrange points, and are named L_1 through L_5. The first three (collinear) points were discovered by Leonhard Euler in 1765, and the last two (triangular) points were deduced by Joseph-Louis Lagrange in 1772 [10, 11]. In 1836, Carl Gustav Jacob Jacobi discovered that the problem admits one known integral of the motion, herein referred to as the Jacobi Constant (*JC*); it can be interpreted as the conserved "energy" value of a given trajectory even though it is not equal to the system mechanical energy [10]. Applying this constant of the motion in 1878, George William Hill identified regions of space that are inaccessible to any physical trajectory at a specified "energy" level; they are frequently termed "forbidden regions" [1, 12, 13]. By the late nineteenth century, it may have seemed as if a complete solution to the CR3BP would eventually be found. After all, the CR3BP models only *one* more body than the 2BP does. However, Henri Poincaré's studies in the 1890s represent a major turning point towards the modern understanding of chaos and the fact that some dynamical problems such as the CR3BP, though still driven by mathematical relationships, are effectively "unsolvable" [1, 10, 14]. Wiesel explains this subtlety: "It was Poincaré who first saw that the restricted problem was not simply unsolved, but actually unsolvable in closed form. Although the solution to this problem does exist, it is not an analytic, differentiable function of both the initial conditions and the time" [10].

Since an analytical solution to the CR3BP is unavailable, analytical methods including analytical approximations have serious limitations for exploring the problem. Fortunately, numerical studies offer an alternative strategy to explore the realm of this multi-body problem. Such numerical studies of *particular* solutions have yielded exciting new trajectory options that are not possible within the context of the 2BP. A

notable example of the early numerical investigations into the CR3BP is the series of studies conducted at the Copenhagen Observatory under the direction of Elis Strömgren in 1913-1939, primarily examining the CR3BP case of equal primary masses, now known as the Copenhagen problem [1]. To this day, a focus of similar investigations has been on the discovery of various types of periodic orbits, which offer important glimpses into the vast space of individual solutions. Further insight is gained by examining: (1) quasi-periodic orbits and (2) manifold trajectories that are asymptotic to periodic orbits. However, due to the complexity of the CR3BP, design of S/C trajectories is inherently challenging. Although the motion of the small mass in the vicinity of the two, larger primary masses is theoretically deterministic based on the laws of gravity and motion, the presence of chaos implies that prediction of long-term behavior may be, for all practical purposes, impossible in certain cases [12]. In fact, even with future advances in computing, the complexity of the CR3BP design space will demand innovative approaches.

Historically, the 2-D, planar version of the CR3BP, where S/C motion is restricted to the plane of the two primaries has received much greater attention than the 3-D, spatial version, not just because the former is *relatively* simpler and easier to visualize but also because planar trajectories are often adequate for modeling many problems in both astronomy and S/C mission design. A study by Deprit and Henrard [15], in the 1960s, offers an example of the type of numerical investigations that typically focused on the 2-D problem at the dawn of the modern age of high-speed computing. In more recent decades, the increased speed, precision, and graphical capabilities of computer simulations have allowed a serious exploration of the 3-D problem. The 1970s and 1980s saw an explosion of interest in 3-D libration point orbits (LPOs) such as the periodic "halo" orbits and neighboring quasi-periodic variants examined by Farquhar and Kamel [16]. This culminated in the ISEE-3 mission to the Sun-Earth L_1 point in 1978 [17, 18] and enabled later Sun-Earth LPO missions such as SOHO in 1995 [19].

Exploration of the spatial CR3BP, in particular, has been aided considerably in recent years by insight gained from dynamical systems theory. Pioneered by Poincaré and further developed by George David Birkhoff, this theory offers a *geometrical* approach to

understanding the dynamical "flow" in a nonlinear and chaotic system like the CR3BP [1, 14, 20, 21]. During the 1990s, advances in the graphical display capabilities of personal computers made it convenient for researchers like Howell, Mains, and Barden [22] (and others) to display and interpret complex, tube-like manifold structures associated with low-cost, theoretically zero-"delta-V" ($\left|\overrightarrow{\Delta V}\right|$) transfers to and from 3-D LPOs. A watershed event came in 2004 with the successful return of the Genesis spacecraft to Earth, after traveling along a series of 3-D trajectories determined by analyzing stable and unstable LPO manifolds in the Sun-Earth CR3BP [14, 23, 24]. A recent application of similar theory is the ARTEMIS extended mission to 3-D LPOs in the vicinity of the Earth-Moon L_1 and L_2 points, designed based on solutions from both the Sun-Earth and Earth-Moon CR3BPs [25, 26, 27]. Though more difficult to simulate and visualize, the spatial CR3BP offers a better understanding of the "real world" and many more options for design. Moreover, with ongoing advances in 3-D visualization technology, options for exploring this dynamical regime are expanding.

1.1.2 Poincaré-Map-Based Trajectory Design: From 2-D to 4-D

The current investigation relies heavily on a significant tool that has emerged within the last century for gaining insight into chaotic dynamical problems: the Poincaré surface of section, or Poincaré map [21]. It is named for Henri Poincaré, who developed the concept in 1881 [28] and, amazingly, envisioned a surface of section for a chaotic system in 1892, even though it would not be practical to numerically generate such a map until the mid-twentieth century [14]. Under this concept, a continuous-time system maps to a lower-dimensional (lower-D) discrete-time system by penetrating a surface called a hyperplane. The Poincaré map enables a simplification of the complex dynamics of a system like the CR3BP by reducing the dimension. By examining a map—which is a single "slice" of the design space—an engineer may gain significant insight for trajectory design.

A traditional, 2-D Poincaré map is all that is required to analyze a "slice" of the planar CR3BP at a specified "energy" level. Of course, it is straightforward to display a 2-D object on paper or on a computer screen. Not surprisingly, there are many examples

of map-based analysis and design in the planar CR3BP. In the 1960s, Hénon [29] analyzed quasi-periodic and chaotic regions of the phase space using Cartesian phase space maps for the Copenhagen [1] CR3BP case of equal primary masses. In the 1970s, Jefferys investigated orbits in the vicinity of the larger and smaller primaries in a variety of planar CR3BP systems by employing what have come to be known as periapsis/apoapsis maps [30, 31]. More recently, Koon et al. use maps of manifold intersections to design transfer trajectories between planar, "Lyapunov" LPOs in the Sun-Earth and Earth-Moon CR3BPs [32]. In addition, Villac and Scheeres [33] and Paskowitz and Scheeres [2] employ periapsis Poincaré maps to investigate escape and capture trajectories in the limiting case of the spatial CR3BP, frequently termed the Hill three-body problem [12]. Also, Craig Davis and Howell use periapsis Poincaré maps to design Titan capture maneuvers in the Saturn-Titan CR3BP [34, 35]. Some additional examples of map-based design in the planar CR3BP are provided by Craig Davis and Howell [36], Vaquero [37], Haapala [38], Haapala and Howell [39], Craig Davis [40], Vaquero and Howell [41], Craig Davis and Howell [42], and Howell, Craig Davis, and Haapala [43].

In contrast to the planar CR3BP, a 4-D Poincaré map is required to analyze a "slice" of the spatial CR3BP at a specified "energy" level. A higher-D map obviously presents a visualization challenge because it exists in a space consisting of more dimensions than the 3-D "real world" with which a human being is intuitively familiar. In fact, there is no universally-accepted method for displaying a 4-D object for practical applications. Furthermore, the actual dynamical behavior exhibited on the 4-D map representing motion in a 3-DOF system differs from that of a 2-DOF system in more ways than just the increased number of dimensions required to represent it. Due to the challenges inherent in representing and interpreting the information displayed on 4-D maps, there are fewer examples of map-based analysis and design in the spatial CR3BP, most of which employ some form of reduction or projection to fewer dimensions. In 1970, Froeschlé displayed 3-D projections of 4-D maps in the spatial version of the Copenhagen CR3BP using stereoscopic views [44]. In an example from 1998, Gómez, Masdemont, et al., while analyzing 3-D, quasi-periodic LPOs, depict a 2-D Poincaré map

of phase space surrounding the Earth-Moon L_2 point after completing a reduction of the full 6-D phase space to just the 4-D center manifold space [45]. Later, Gómez, Koon, et al. employ a series of 2-D projections of a 4-D map to design 3-D transit trajectories to and from the vicinity of Europa in the Jupiter-Europa CR3BP [46]. As a recent example, Craig Davis and Howell use 3-D projections of 4-D periapsis Poincaré maps to illuminate the design space near Saturn in the Sun-Saturn CR3BP [34]. Some additional examples of map-based design in the spatial CR3BP using 3-D projections are provided by Haapala [38], Haapala and Howell [39], Craig Davis [40], and Craig Davis and Howell [42].

Methods of representing *all four* dimensions associated with Poincaré maps for design in the spatial CR3BP are even rarer and typically involve adding some type of arrow or line segment to a point associated with a given map return. Paskowitz and Scheeres [2] demonstrate a method using arrows to represent a 4-D initial periapsis Poincaré map for analysis in the Hill three-body problem. During the period of the present investigation, Vaquero and Howell [47, 48] and Vaquero [49] employ a modification of the Paskowitz and Scheeres [2] arrow method to design low-$\left|\overrightarrow{\Delta V}\right|$ transfers between resonant orbits in the Earth-Moon and Saturn-Titan spatial CR3BPs. Also during the period of the present investigation, Haapala and Howell [3, 4, 5] apply a "glyph" representation of 4-D map coordinates using a planar visualization where points representing map returns are augmented with line segments or "stick-figures." Poincaré maps represented by this method are used to design low-$\left|\overrightarrow{\Delta V}\right|$ transfers in the Earth-Moon and Sun-Earth spatial CR3BPs. Moreover, this 4-D "glyph" method is extended to represent all six Cartesian coordinates associated with periapsis Poincaré maps, which are employed to locate periodic orbits and design a transfer in the Earth-Moon spatial CR3BP and also to analyze a comet capture in the Sun-Jupiter spatial CR3BP.

Because examples of 4-D-map-based analysis and design in the spatial CR3BP are sparse in the literature, studies involving 4-D mappings in other disciplines provide valuable insight and context. There is a richer history of examples of analysis using 4-D maps in the physics, astrophysics, and astronomy communities. Features on 4-D maps are most commonly displayed as black and white projections onto a lower-D space. For example, in 1972, Froeschlé projected 4-D maps onto 3-D space and then displayed the

3-D images using 2-D views from different perspectives in the study of an analytical mapping relevant to the motion of a star within an axisymmetric galaxy [50]. In 1995-1997, Vrahatis et al. [51, 52] and Vrahatis, Isliker, and Bountis [53] generated toroidal "islands" as well as larger "rotational invariant surfaces" as projections onto 3-D space for a 4-D, analytical mapping of perturbations on periodic trajectories related to magnetic focusing elements (for a particle accelerator). Thinner versions of similar tori in the neighborhood of "elliptic fixed lines" were displayed as projections onto 3-D space in 1994 by Todesco [54, 55] for a similar type of 4-D, analytical mapping as well as a 4-D, analytical, "twist" mapping—and in 1997 by Gemmi and Todesco [56] for a 4-D generalization of the analytical Hénon mapping. While such 3-D projections offer insight into various map features, one dimension of information is missing from any given view.

In a dramatic departure from the conventional, black and white projection approach, Patsis and Zachilas [6, 7] proposed a "color and rotation" method for displaying all four dimensions of a 4-D map in 1993-1994. Leveraging modern computer graphics capabilities, this method projects a 4-D map onto 3-D space and augments the image with color to represent the fourth dimension. The fourth coordinate associated with each map return, or "consequent," is interpreted based on color palette look-up tables (LUT). Patsis and Zachilas describe the benefits of their "empirical" method in a study of 4-D Poincaré maps related to stellar motion in a galaxy:

> *The representation of the 4th dimension as color variation in the 3D projections of the spaces of section helps in visualizing the distribution of the consequents in the four-dimensional space. Smooth variation of the colors in our figures, corresponding to the smooth succession of the colors in the LUT, indicates distribution of the points on a smooth 4D hypersurface. In contrast, mixing of colors characterizes chaotic regions. The range of variation of the colors also allows to estimate the areas that are close to each other in the 4D space. This method helps us reveal existing structures in cases where the consequents in the 3D projections seem to densely fill the space.*
>
> *The rotation helps in clearing up the geometry of the figures.* [7]

In 2011-2013, the color and rotation method is employed in several investigations of 4-D Poincaré maps related to motion in a galaxy by Katsanikas and Patsis [57], Katsanikas, Patsis, and Contopoulos (2011) [58], Katsanikas, Patsis, and Pinotsis [59], and Katsanikas, Patsis, and Contopoulos (2013) [60]. The method is also applied to a 4-D, analytical mapping related to motion in a galaxy by Zachilas, Katsanikas, and Patsis [61]. In each investigation, the focus is on visualizing and characterizing the behavior exhibited on maps that are generated by one trajectory at a time. One or more "tori" are often observed on the map. Overall, these studies indicate a relationship between the appearance of map features—in terms of both the 3-D shape and the color—and different types of dynamical behavior, especially the stability/instability of nearby fixed points generated by periodic orbits. The advantage of this type of color and rotation method for representing 4-D maps was also described, but not demonstrated, in a 1995 investigation by Contopoulos, Voglis, and Efthymiopoulos: "The advances in computers allow us to construct 4-D figures of the asymptotic curves. Namely, we have a good feeling of the 3rd dimension by rotation of the figure, while the 4rd [*sic*] dimension is represented by colors" [62]. In that study, 4-D Poincaré maps of a similar system as in Patsis and Zachilas [7] were investigated.

In 2012-2013, Richter [63] and Richter et al. [64] apply the color and rotation method to 4-D, analytical map visualization, mainly for the purpose of comparison, while describing the method as appropriate for viewing maps with "one or a few" trajectories at a time [64]. They contend that 3-D phase space slices/sections are more advantageous for viewing 4-D maps consisting of many trajectories, while the use of color to represent the fourth dimension "is only useful if one orbit is displayed. It is less useful if a whole regular domain should be visualized as then different orbits will overlap within the 3D section" [63]. To overcome the challenges of viewing multiple trajectories on 4-D maps, 3-D phase space sections—which are not the same as 3-D projections—are employed such that only trajectories with map returns having a particular value of the fourth coordinate, *to within a small tolerance*, are displayed on a space consisting of the remaining three coordinates. Different map features are then color-coded for clarity; however, color does not represent a fourth dimension in this case.

Finally, a somewhat relevant example of using color to represent the fourth dimension on mappings is given by Sprott in 1993 [65], where 4-D strange attractors are represented with *planar* visualizations and the third and fourth dimensions are represented by combinations of shadows, bands, color (or shades of a gray scale), stereoscopic pairs, or multiple slices. Sprott also demonstrates the color and shadow method in 2004 [66].

1.2 Contributions of the Present Investigation

In this investigation, a novel approach to 4-D-map-based analysis and design in the spatial CR3BP is developed and applied to practical examples with real-world spaceflight applications. Two-dimensional-map-based design strategies useful in the planar CR3BP are successfully extended to the higher dimensions required for the spatial CR3BP. This is demonstrated though a variety of S/C mission design cases involving 3-D trajectories in the Earth-Moon, Sun-Earth, and Uranus-Titania CR3BP systems while utilizing several different Poincaré map formulations. Reasonable design estimates obtained visually from a 4-D map are fed into follow-on, automated processes, leading to precise and/or locally-optimal solutions for S/C paths and transfer maneuvers. Thus, the design strategy leverages human insight to initiate automated processes.

Distinguished from typical methods of representing 4-D Poincaré maps in the CR3BP, which involve adding some type of arrow or line segment to a point (e.g., Paskowitz and Scheeres [2] and Haapala and Howell [3, 4, 5]), the design approach in the current effort includes a “space-plus-color” method for representing, interpreting, and manipulating 4-D Poincaré maps in an interactive, 3-D visual environment in which the fourth dimension is displayed using color. The method expands on the color and rotation method developed by Patsis and Zachilas [7] by applying additional tools and techniques that enable 4-D-map-based design in the dynamical environment of the CR3BP. The focus herein is on the practical techniques needed to overcome challenges inherent in utilizing information displayed on higher-D maps, especially in the case where a map is generated by *many different trajectories*. Thus, an ancillary contribution of the current investigation is the extensive demonstration of an effective, color-based method for

representing a 4-D Poincaré map in the context of *design*; the method seems well-suited to engineering applications in general.

Results of design examples considered in the present investigation include several preliminary S/C trajectory solutions of potential practical use, including: (1) a transfer between a geosynchronous-transfer-orbit-style trajectory and an LPO near the Moon, (2) transfers between LPOs in the vicinity of the Moon, and (3) a transfer into a capture orbit around Uranus's moon Titania. In the Titania example, the capture is also validated in a realistic, higher-fidelity model. Furthermore, the preliminary capture orbit design is considered in the context of a plausible mission scenario in which the designed path is the final phase of a Uranian system tour of the type designed by Heaton and Longuski [67]. Additionally, results of a design case involving a transfer between geosynchronous orbits with a large inclination difference—by means of a lunar flyby—indicate that the 4-D-map-based and CR3BP-focused design process can expand 3-D trajectory options available for consideration, with the potential to reveal lower-$\left|\overrightarrow{\Delta V}\right|$ solutions not predicted by 2BP-focused methods. Also relevant in the context of 2BP-focused methods is an analysis correlating the long-term variations in instantaneous eccentricity of a high-altitude Earth orbit perturbed by lunar gravity with the shape and evolution of the surface of a deformed 2-D torus on a 4-D map. This analysis suggests that the space-plus-color method—as applied to 4-D Poincaré maps displayed in a visual environment—could allow an intuitive means to explore relationships between Earth satellite perturbations and deformed Kolmogorov-Arnold-Moser (KAM) tori [68], a topic studied extensively by Wiesel [69, 70].

1.3 Dissertation Overview

The objective of this research is the investigation of strategies for trajectory analysis and mission design in the spatial CR3BP using 4-D Poincaré maps. Such maps are used to visualize and gain insight into the design space for a given astrodynamics problem in a multi-body environment. The effort entails developing and applying practical techniques for methodical, map-based analysis and design while addressing challenges inherent in representing and exploiting the information displayed on higher-D maps. Using a

MATLAB® [71] simulation with enhanced visualizations created in Avizo® [72], results are presented for several examples of design involving 3-D S/C trajectories. Lessons learned for effective, map-based design are noted. This dissertation is organized as follows:

- Chapter 2: Key concepts and methods related to S/C trajectory design in a multi-body environment are summarized, focusing on the CR3BP dynamical model along with the design of CR3BP trajectories based on a Poincaré map.

- Chapter 3: A novel approach to higher-D-map-based trajectory analysis and design in the spatial CR3BP is described. The space-plus-color method is introduced, along with various tools and techniques that enable 4-D-map-based design in a visual environment. Also included is a description of the procedure by which reasonable design estimates obtained visually from a 4-D Poincaré map can be fed into follow-on, automated processes. Finally, important 4-D map coordinate definitions are presented.

- Chapter 4: Four examples of basic, 3-D trajectory design are presented, which serve two distinct purposes. First, they demonstrate successful trajectory design results from applying the higher-D-map-based design approach. Second, each example offers an opportunity to highlight benefits, challenges, and lessons learned from this investigation into 4-D-map-based design. The focus is on the creation of appropriate 4-D Poincaré maps and the use of those maps in an interactive visual environment to obtain trajectory design solutions through what are mainly visual processes.

- Chapter 5: Four-dimensional-map-based design techniques are demonstrated for three, advanced, real-world astrodynamics problems involving 3-D S/C trajectories, thus providing a validation of the design approach presented in this investigation. The emphasis is on how reasonable guesses obtained visually from

the map are exploited in follow-on, automated processes to determine precise solutions that are of practical use for real-word trajectory design scenarios. These automated processes include targeting, optimization, and transitions to other dynamical models.

- Chapter 6: A summary and conclusions are presented along with recommendations for future work.

2. DESIGN IN A MULTI-BODY ENVIRONMENT

This chapter summarizes key concepts and methods related to S/C trajectory design in a multi-body environment, as applicable to the current investigation. The focus is on the dynamical model known as the circular restricted three-body problem (CR3BP) along with the design of CR3BP trajectories based on a Poincaré surface of section, or Poincaré map. This material establishes a foundation for the description—in Chapter 3—of a novel approach to higher-D-map-based trajectory design in the spatial CR3BP. Further details concerning previous analysis/design examples are provided as appropriate. Note that some additional descriptions of theory, methods, and previous studies are also referenced in the context of various explanations in Chapter 3 as well as in the presentation of 4-D-map-based design examples in Chapters 4 and 5.

2.1 The Circular Restricted Three-Body Problem (CR3BP)

The CR3BP [1, 12, 73] is a deceptively simple model for the motion of a negligibly small mass P_3 (e.g., a S/C) attracted by the gravitational forces from two significantly larger primary masses P_1 and P_2 (e.g., a planet and a moon). The model assumes that the primaries revolve in perfectly circular planar motion about their system barycenter B at a constant rate determined by solving only the two-body problem (2BP) [8, 9, 10, 74]. The CR3BP is nondimensionalized by defining certain characteristic quantities. The characteristic distance l^* is defined as the distance between the primaries, and the characteristic mass m^* is defined as the total system mass, where $m^* = m_1 + m_2$. Additionally, the characteristic time is defined as $t^* = 1/N = \sqrt{l^{*3}/Gm^*}$, where N is the mean motion and G is the universal gravitational constant. This definition of characteristic time renders the values of the nondimensional mean motion n and the

nondimensional gravitational constant G' to be equal to one. As illustrated in Figure 2.1, these definitions yield primaries at unit distance from each other and the nondimensional time τ that is equivalent to the number of radians swept by the rotation angle θ—through a barycentric inertial reference frame (X,Y,Z)—by a vector from the larger primary P_1 to the smaller primary P_2. The location of each of the two primaries is fixed along the x-axis of the rotating frame (x,y,z), with a distance from B given in terms of the mass ratio

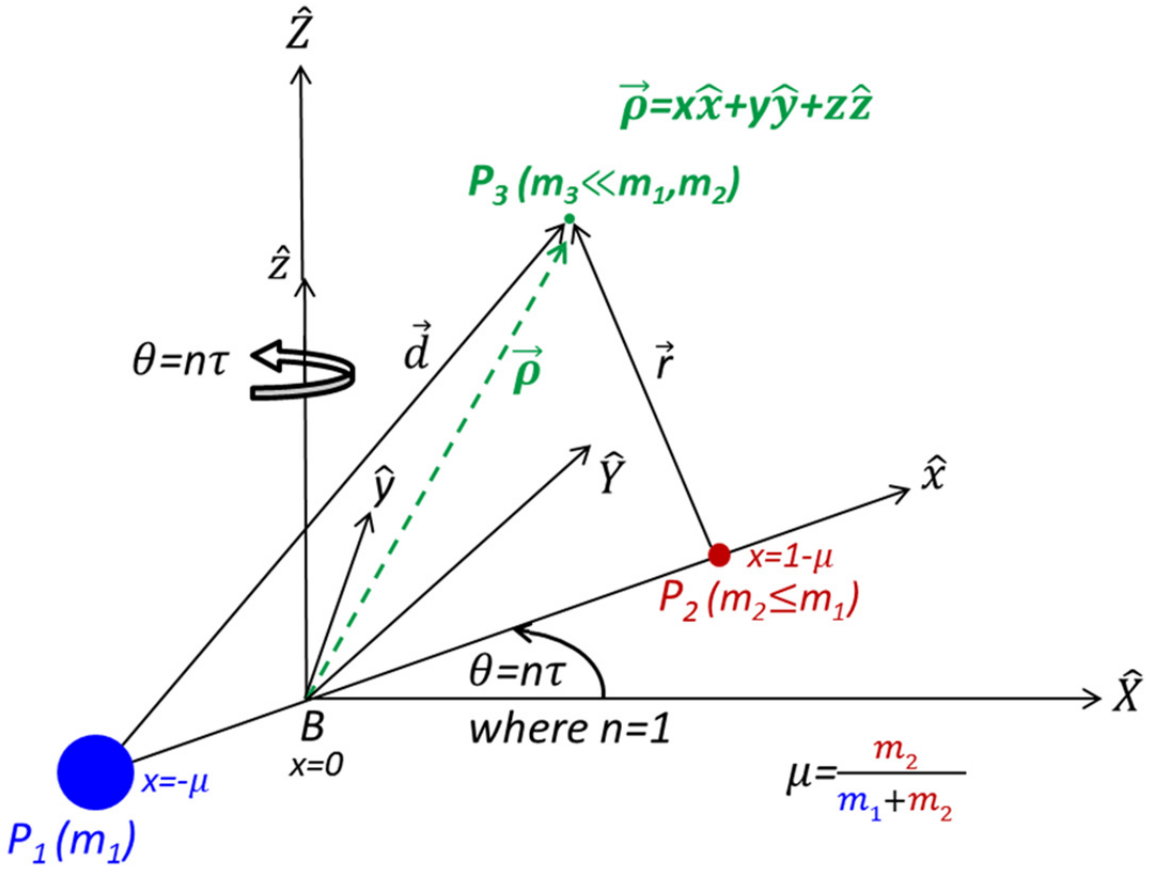

Figure 2.1. CR3BP (nondimensionalized)

$\mu = m_2/(m_1 + m_2)$. Note that $\hat{x}$ is a unit vector in the same direction as $\vec{x}$. Confirming that the primary system's motion is circular, its nondimensional angular rate $\dot{\theta} = d\theta/d\tau$ at any instant is simply the nondimensional time derivative $d(n\tau)/d\tau = n = 1$, which is also the mean motion.

The nondimensional equations of motion (with derivatives taken with respect to τ) for the vector $\vec{\rho} = x\hat{x} + y\hat{y} + z\hat{z}$ locating P_3 in the barycentric rotating frame are straightforward to derive [1, 12, 13]. In scalar, second-order form, the ordinary differential equations are,

$$\begin{aligned} \ddot{x} &= x + 2\dot{y} - \frac{(1-\mu)(x+\mu)}{d^3} - \frac{\mu(x-1+\mu)}{r^3} \\ \ddot{y} &= y - 2\dot{x} - \frac{(1-\mu)y}{d^3} - \frac{\mu y}{r^3} \\ \ddot{z} &= -\frac{(1-\mu)z}{d^3} - \frac{\mu z}{r^3} \end{aligned} \tag{2.1}$$

where $d = \sqrt{(x+\mu)^2 + y^2 + z^2}$ and $r = \sqrt{(x-1+\mu)^2 + y^2 + z^2}$. Unlike the 2BP, which possesses an analytical solution in terms of conics (circles, ellipses, parabolas, hyperbolas, straight lines, and, technically, a point), the CR3BP has no known, closed-form analytical solution. The behavior of P_3 in this problem is not only nonlinear but also sometimes chaotic, with a vast array of possible solutions that can be extremely sensitive to initial conditions. The presence of chaos (not encountered in the 2BP) implies that prediction of long-term behavior may be, for all practical purposes, impossible in certain cases. Due to the complexity of the problem, design of S/C trajectories in this multi-body environment is inherently challenging. In fact, even with future advances in computing, the complexity of the CR3BP design space will demand innovative approaches.

Since an analytical solution is unavailable, numerical simulations offer an alternative strategy to explore the realm of this multi-body problem, yielding exciting new trajectory options that are not possible within the context of the 2BP. In this investigation, the numerical simulations employed are created in MATLAB® [71]. Numerical integration of trajectories is normally accomplished using the built-in *ode113* function (an Adams-Bashforth-Moulton predictor-corrector [75]), with relative and absolute tolerance settings equal to 2.25×10^{-14}. A few key concepts support and aid in the interpretation of the numerical explorations. First, the CR3BP is autonomous (time-invariant), which implies that a solution for a given time interval is valid for any equivalent time interval. Second, there are five stationary (equilibrium) points, i.e., libration points L_1 through L_5. The first three (collinear) points were discovered by Euler in 1765, and the last two (triangular)

points were deduced by Lagrange in 1772 [10, 11]. Their nondimensional, barycentric rotating frame locations, which depend on the value of μ, are depicted in the x-y view in Figure 2.2 for the Earth-Moon system, with the Earth and the Moon shown to scale. The

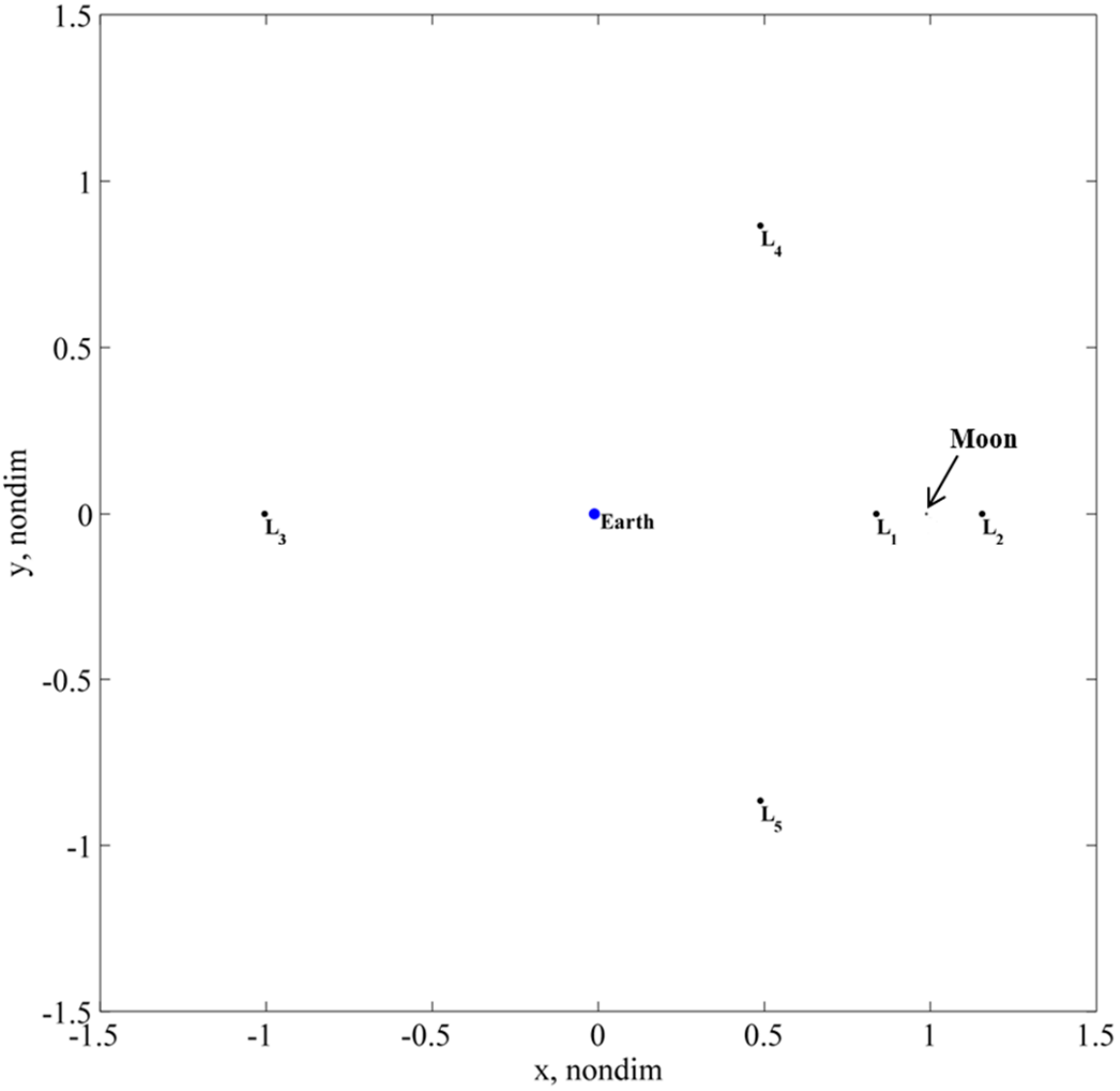

Figure 2.2. Earth-Moon CR3BP libration/Lagrange points

Earth-Moon barycenter, the origin of the plot, is located approximately 1,707 km beneath the surface of the Earth, or 4,671 km from the Earth's center. The mass ratio for this system is assumed to be equal to $\mu =$ 0.012150586550569. Note that the values of the coordinates for collinear Lagrange points L_1 through L_3 are determined numerically. Yet,

the locations of the triangular Lagrange points L_4 and L_5 are calculated based on an exact solution [76]. These two points are located at the corners of two equilateral triangles, with the other corners defined by the locations of the two primaries (the Earth and the Moon in this example). The nondimensional length of each leg of the triangles is equal to one—the distance between the two primaries—and the two triangles share a common leg formed by a line connecting the two primaries.

A third supporting concept is that the CR3BP admits one known integral of the motion, which was discovered by Jacobi in 1836 [10]. Besides offering insights into behavior, this Jacobi Constant (*JC*), which remains constant along any single trajectory, provides a means to evaluate the accuracy of a numerical integration of the equations of motion. It can be defined in terms of the CR3BP Hamiltonian H and the speed v relative to the rotating frame as [1, 12, 13, 77],

$$JC = -2H = x^2 + y^2 + \frac{2(1-\mu)}{d} + \frac{2\mu}{r} - V^2 \tag{2.2}$$

where $V = \sqrt{\dot{x}^2 + \dot{y}^2 + \dot{z}^2}$. *JC* is an energy-like quantity, with smaller *JC* values associated with higher "energy" trajectories, even though *JC* is not equal to the system mechanical energy [10]. The nondimensional and dimensional rotating frame coordinates (*x,y,z*) of each of the five libration points for the Earth-Moon system value of μ appear in Table 2.1 along with the value of *JC* associated with a stationary S/C located at each point of equilibrium. The dimensional coordinates are calculated based on the assumption that the Moon's orbit radius about the Earth is equal to l^* = 384,400 km; this value corresponds to unit distance in nondimensional units.

Table 2.1 Earth-Moon libration point rotating frame locations and "energy" values

Lagrange point	Barycentric rotating frame location (nondimensional units and km)	*JC* value
L_1	x = 0.836915121142417 (321,710.17 km) $y = 0$ $z = 0$	3.188341126426104
L_2	x = 1.155682169063842 (444,244.23 km) $y = 0$ $z = 0$	3.172160468395109
L_3	x = -1.005062646202315 (-386,346.08 km) $y = 0$ $z = 0$	3.012147151620889
L_4	$x = \frac{1}{2} - \mu$ = 0.487849413449431 (187,529.31 km) $y = \frac{\sqrt{3}}{2}$ = 0.866025403784439 (332,900.17 km) $z = 0$	2.987997050202954
L_5	$x = \frac{1}{2} - \mu$ = 0.487849413449431 (187,529.31 km) $y = -\frac{\sqrt{3}}{2}$ = -0.866025403784439 (-332,900.17 km) $z = 0$	2.987997050202954

A memory aid for guessing the *x,y,z* barycentric rotating frame locations and *JC* "energy" values of the five libration points L_i (based on approximate expansions in the case of the collinear points for small values of μ [12]) is given by the author of the present investigation as,

$$\begin{aligned} &x_{1,2} \cong 1 - \mu \mp h && \\ &x_3 \cong -1 - \tfrac{5}{12}\mu && JC_1 \cong 3 + 9h^2 - 10h^3 \\ &y_{1,2,3} = 0 && JC_2 \cong JC_1 - \tfrac{4}{3}\mu \\ &x_{4,5} = \tfrac{1}{2} - \mu && JC_3 \cong 3 + \mu \\ &y_{4,5} = \pm\tfrac{\sqrt{3}}{2} && JC_{4,5} = 3 - \mu + \mu^2 \\ &z_{1,2,3,4,5} = 0 && \end{aligned} \tag{2.3}$$

where the nondimensional Hill radius $h = (\mu/3)^{1/3}$ is a rough approximation for the distance between P_2 and either L_1 or L_2, although these distances are not exactly the same. Note that other authors often define the Hill radius differently, as $h = (m_2/3m_1)^{1/3}$ [10].

Applying the constant of the motion *JC* in 1878, Hill identified regions of space that are inaccessible to any physical trajectory at a specified "energy" level [1, 12, 13] because they correspond to imaginary values of S/C velocity magnitude V. At a given value of *JC*, zero velocity surfaces (ZVSs) are computed using $V = 0$ to identify the "forbidden regions" that no physical trajectory at that "energy" level can visit. These ZVSs, along with zero velocity curves (ZVCs)—the planar cross-sections of the ZVSs—are plotted in green in a four-perspective view of the rotating frame (dimensional units) in Figure 2.3 for a selected S/C trajectory in the Earth-Moon system propagated for ten days. Note that the trajectory itself is also plotted in green. Though not always the case, it is common in examples included in this dissertation for the ZVSs/ZVCs to be plotted with the same color as a trajectory at the associated "energy" level. This is especially useful for displaying trajectories at multiple "energy" levels—along with multiple sets of ZVSs/ZVCs—on the same plot. The "energy" value of the trajectory displayed in Figure 2.3 is equal to *JC* = 3.15. The ZVCs depicted in this example are the cross-sections of the ZVSs, where the origin of the cross-sections is the Earth with (*x,y,z*) = (-μ,0,0). The convention in the current investigation is to display ZVCs with the ZVS cross-section

origin located at the larger primary P_1 when the view is zoomed out to display the entire P_1 - P_2 system or when the view is zoomed in to the vicinity of P_1. On the other hand, when the view is zoomed in to the vicinity of the smaller primary P_2, the origin of the ZVS cross-section is P_2 instead.

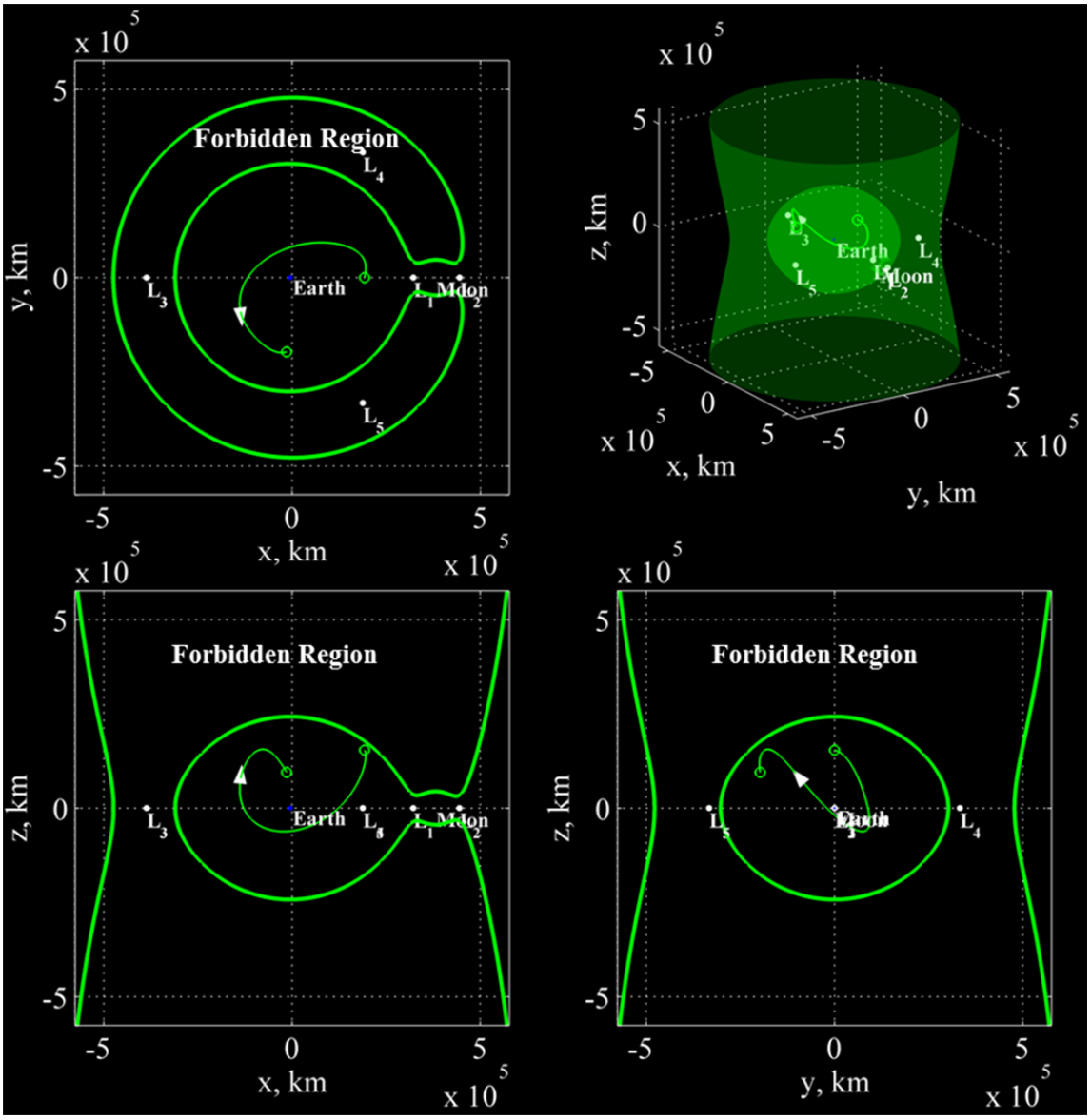

Figure 2.3. Four-perspective rotating view of 3-D, Earth-Moon trajectory (green) along with ZVSs/ZVCs (also green)

Also useful in the current investigation are two symmetry properties in the rotating frame of the CR3BP [78]. The first is symmetry with respect to the *x*-*y* plane of the primaries. If a S/C path specified by a series of row vectors [$x \;\; y \;\; z \;\; \dot{x} \;\; \dot{y} \;\; \dot{z}$] is a solution to the equations of motion (2.1), then reversing the sign of all z and $\dot{z}$ values produces another solution specified by [$x \;\; y \;\; -z \;\; \dot{x} \;\; \dot{y} \;\; -\dot{z}$]. This symmetry results in "northern" and "southern" orbits associated with each other. The second important symmetry is with respect to both the *x*-*z* plane and time. If [$x \;\; y \;\; z \;\; \dot{x} \;\; \dot{y} \;\; \dot{z}$] is a solution to the equations of motion in forward time, then [$x \;\; -y \;\; z \;\; -\dot{x} \;\; \dot{y} \;\; -\dot{z}$] is a solution *in negative time*. This second symmetry property motivates the search for symmetric, periodic orbits with two perpendicular crossings of the *x*-*z* plane (see next section).

While critical insight is gained by viewing S/C trajectories in the barycentric rotating frame of the CR3BP, it is also important to relate this perspective to a traditional, inertial view. In the current investigation, trajectories are often displayed in either the P_1–centric or the P_2–centric inertial frame, defined in *X,Y,Z* coordinates such that the *X*-*Y* plane is aligned with the *x*-*y* plane of the primaries and such that $\hat{x}$ is aligned with $\hat{X}$ at a nondimensional time τ equal to zero. Note that the origin is not the system barycenter, as for the *barycentric* inertial frame depicted in Figure 2.1. The transformation from the barycentric rotating frame to the P_i –centric inertial frame is,

$$\begin{aligned} X &= (x - k_i)\cos\tau - y\sin\tau \\ Y &= (x - k_i)\sin\tau + y\cos\tau \\ Z &= z \\ \dot{X} &= -(x - k_i)\sin\tau - y\cos\tau + \dot{x}\cos\tau - \dot{y}\sin\tau \\ \dot{Y} &= (x - k_i)\cos\tau - y\sin\tau + \dot{x}\sin\tau + \dot{y}\cos\tau \\ \dot{Z} &= \dot{z} \end{aligned} \tag{2.4}$$

where $k_1 = -\mu$ and $k_2 = 1 - \mu$. As an example of the transformation, the same Earth-Moon trajectory plotted in Figure 2.3 appears in both the 3-D, barycentric rotating view and the 3-D, Earth-centric inertial view in Figure 2.4 for ten days. Note that the path of the Moon also appears for the ten-day propagation, assuming the S/C initial condition is at nondimensional time $\tau = 0$.

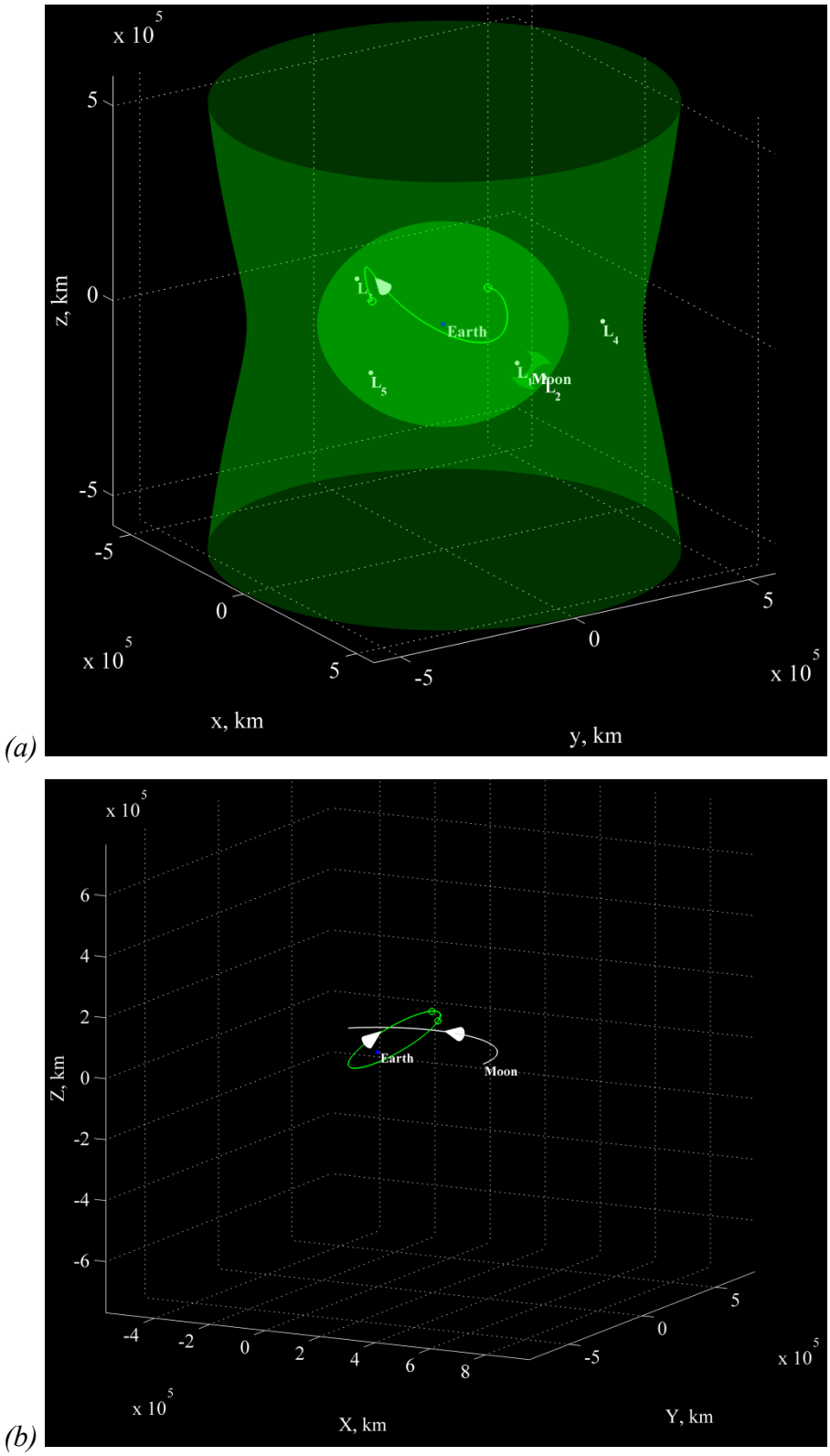

Figure 2.4. 3-D, Earth-Moon trajectory: barycentric rotating (*a*) and Earth-centric inertial (*b*) views

Displaying and interpreting a 3-D S/C trajectory on paper or with a single view on a computer screen is challenging. Much more insight is gained by examining a given trajectory by rotating and zooming the view in real time in a visual environment. In the current investigation, certain conventions aid in interpretation of the plots. All displays of S/C trajectories in the configuration space (i.e., *x,y,z* coordinates) of the CR3BP or in the associated inertial view (*X,Y,Z*) are plotted in MATLAB®. The MATLAB® script used to enlarge axes labels in these and all other plots in this dissertation is provided by Wawrzyniak [79], while the script used to export MATLAB® figures is created by Woodford [80]. The convention in this investigation is to plot views of trajectories (as opposed to Poincaré maps generated by trajectories) in dimensional units. The primary bodies are always plotted to scale, based on a simplified spherical model of the body size, when defined. The assumed body sizes of primaries are also used to define when a S/C path impacts the surface of a primary, often for the purpose of removing the portion of the trajectory after the impact. The origin of any P_i–centric inertial view is the center of P_i, while the origin of a barycentric rotating view is the system barycenter B, *unless an offset origin is defined*. An offset origin is indicated by an asterisk on the axes labels (e.g., x^*) and is typically employed to set the smaller primary P_2 as the origin of a rotating view for ease of interpretation when the view is zoomed in to the vicinity of P_2. Sometimes only one perspective (e.g., an *x-y* rotating view) of a S/C trajectory is sufficient to explain a step in the trajectory design process. In other cases, multiple views or even a four-perspective view (three different planar views and one 3-D view) is provided for greater clarity, as in Figure 2.3. Note that, in some 3-D views, axes are not included when the scale is either obvious and/or clear from previous plots. Also, ZVSs are sometimes omitted from 3-D views to avoid obscuring the view of one or more trajectories.

Finally, two important types of "icons" appearing in S/C trajectory plots in this dissertation require some explanation. First, arrows indicating the direction of motion of a S/C are attached to trajectories. In planar views of trajectories, these arrows are plotted as triangles. However, in 3-D views, they are plotted as *cones*, as is the case in Figure 2.4. The MATLAB® script used to generate these 3-D arrows is created by Lindner [81].

These cone-shaped arrows allow for greater clarity in visualizing the 3-D direction of a trajectory; yet, note that a cone appears as a circle when viewed along its axis of symmetry. While the exact location of arrows along a given trajectory may not necessarily be the same in different plots (e.g., inertial versus rotating views or zoomed-in versus zoomed-out views), the arrows are always in the same location in different views in the *four-perspective views* such as in Figure 2.3. This consistency can aid in determining the direction of motion of a 3-D trajectory by comparing the arrow location(s) and direction(s) across multiple views.

A second "icon" employed in this investigation is a circle at the beginning or ending of a leg of a trajectory, as plotted in Figure 2.3 and 2.4. While not always included, such circles are often useful for indicating the *link* between two different legs of a trajectory. For instance, if a S/C transfer maneuver is implemented at the ending position of one trajectory leg, indicated by a circle of a particular size, a new trajectory leg begins at that same position, as indicated by a circle of a different size. Such a link, which indicates a velocity discontinuity—i.e., a $\left|\overrightarrow{\Delta V}\right|$ maneuver is required at this position for the S/C to follow the path—is notionally depicted in Figure 2.5.

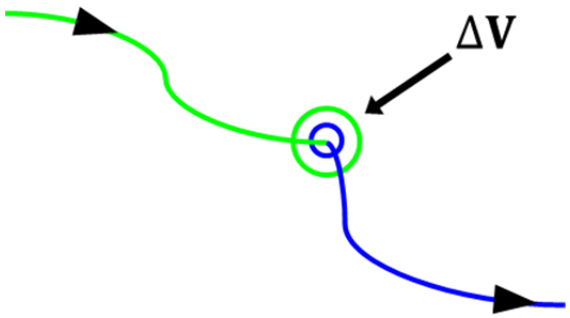

Figure 2.5. Notional link between two S/C trajectory legs

2.2 Trajectory Targeting

In this investigation, "targeting" refers to a differential corrections process by which a precise S/C trajectory solution is obtained to within a satisfactory convergence criterion/tolerance. This corrections process is based on the state transition matrix (STM). The STM is basically a linear approximation of the dynamical "flow" in the vicinity of a

nonlinear system trajectory. To obtain the STM, it is necessary to consider the linear variational equations of motion associated with a linear expansion about a reference condition in the CR3BP. Equations of motion (2.1) can be written in the form,

$$\begin{aligned} \ddot{x} &= 2\dot{y} + U_x^* \\ \ddot{y} &= -2\dot{x} + U_y^* \\ \ddot{z} &= U_z^* \end{aligned} \tag{2.5}$$

where pseudopotential $U^* = \frac{x^2+y^2}{2} + \frac{1-\mu}{d} + \frac{\mu}{r}$, and $[]_x = \frac{\partial []}{\partial x}$. As an aside, note that the definition of pseudopotential U^* also allows equation (2.2) to be written in the form,

$$JC = 2U^* - V^2 \tag{2.6}$$

A first-order, Taylor series expansion about a reference condition—where ξ, η, and ζ are small perturbations on that reference condition in x, y, and z, respectively—leads to the linear variational equations of motion,

$$\begin{aligned} \ddot{\xi} &= 2\dot{\eta} + U_{xx}^*\xi + U_{xy}^*\eta + U_{xz}^*\zeta \\ \ddot{\eta} &= -2\dot{\xi} + U_{xy}^*\xi + U_{yy}^*\eta + U_{yz}^*\zeta \\ \ddot{\zeta} &= U_{xz}^*\xi + U_{yz}^*\eta + U_{zz}^*\zeta \end{aligned} \tag{2.7}$$

where $[]_{xy} = \frac{\partial^2 []}{\partial x \partial y}$. It is important to emphasize that equations (2.7) constitute a linear approximation of the nonlinear "flow" in the vicinity of a reference condition; higher-order terms in the expansion (e.g., ξ^2, ξ^3, ξ^4, etc. terms) are ignored. Equations (2.7) can be written in the first-order differential form of a linear system as,

$$\dot{\delta\vec{x}} = A\delta\vec{x} \tag{2.8}$$

where column vector $\delta\vec{x} = [\ \delta x\ \ \delta y\ \ \delta z\ \ \delta\dot{x}\ \ \delta\dot{y}\ \ \delta\dot{z}\ ]^T = [\ \xi\ \ \eta\ \ \zeta\ \ \dot{\xi}\ \ \dot{\eta}\ \ \dot{\zeta}\ ]^T$ is a variation on a S/C state, and the matrix A is, in general, time-varying and given by,

$$A = \begin{bmatrix} 0_{3\times3} & I_{3\times3} \\ B & \Lambda \end{bmatrix} \tag{2.9}$$

where 0 is the null matrix, I is the identity matrix, and B and Λ are given by,

$$B = \begin{bmatrix} U_{xx}^* & U_{xy}^* & U_{xz}^* \\ U_{xy}^* & U_{yy}^* & U_{yz}^* \\ U_{xz}^* & U_{yz}^* & U_{zz}^* \end{bmatrix} \tag{2.10}$$

and,

$$\Lambda = \begin{bmatrix} 0 & 2 & 0 \\ -2 & 0 & 0 \\ 0 & 0 & 0 \end{bmatrix} \tag{2.11}$$

The general solution to equation (2.8) is,

$$\delta\vec{x}(\tau) = \Phi(\tau, \tau_0)\delta\vec{x}_0 \tag{2.12}$$

where $\delta\vec{x}_0 = \delta\vec{x}(\tau_0)$ is the initial condition for the variation, and $\Phi(\tau, \tau_0) = \frac{\partial\vec{x}(\tau)}{\partial\vec{x}_0}$ is the state transition matrix (STM) [14]. Note that $\Phi(\tau_0, \tau_0) = I_{6\times6}$. The STM Φ satisfies the differential equation,

$$\dot{\Phi}(\tau, \tau_0) = A(\tau)\Phi(\tau, \tau_0) \tag{2.13}$$

Equation (2.13) provides a means to obtain the STM as a function of time—and with respect to a given initial condition—by numerical integration of this equation (associated with the *linearized* system) in parallel with numerical integration of the true, nonlinear equations of motion (2.1)/(2.5) [14]. The STM consists of the elements of the Jacobian matrix,

$$\Phi = \frac{\partial\vec{x}}{\partial\vec{x}_0} = \begin{bmatrix} \frac{\partial x}{\partial x_0} & \frac{\partial x}{\partial y_0} & \frac{\partial x}{\partial z_0} & \frac{\partial x}{\partial \dot{x}_0} & \frac{\partial x}{\partial \dot{y}_0} & \frac{\partial x}{\partial \dot{z}_0} \\ \frac{\partial y}{\partial x_0} & \frac{\partial y}{\partial y_0} & \frac{\partial y}{\partial z_0} & \frac{\partial y}{\partial \dot{x}_0} & \frac{\partial y}{\partial \dot{y}_0} & \frac{\partial y}{\partial \dot{z}_0} \\ \frac{\partial z}{\partial x_0} & \frac{\partial z}{\partial y_0} & \frac{\partial z}{\partial z_0} & \frac{\partial z}{\partial \dot{x}_0} & \frac{\partial z}{\partial \dot{y}_0} & \frac{\partial z}{\partial \dot{z}_0} \\ \frac{\partial \dot{x}}{\partial x_0} & \frac{\partial \dot{x}}{\partial y_0} & \frac{\partial \dot{x}}{\partial z_0} & \frac{\partial \dot{x}}{\partial \dot{x}_0} & \frac{\partial \dot{x}}{\partial \dot{y}_0} & \frac{\partial \dot{x}}{\partial \dot{z}_0} \\ \frac{\partial \dot{y}}{\partial x_0} & \frac{\partial \dot{y}}{\partial y_0} & \frac{\partial \dot{y}}{\partial z_0} & \frac{\partial \dot{y}}{\partial \dot{x}_0} & \frac{\partial \dot{y}}{\partial \dot{y}_0} & \frac{\partial \dot{y}}{\partial \dot{z}_0} \\ \frac{\partial \dot{z}}{\partial x_0} & \frac{\partial \dot{z}}{\partial y_0} & \frac{\partial \dot{z}}{\partial z_0} & \frac{\partial \dot{z}}{\partial \dot{x}_0} & \frac{\partial \dot{z}}{\partial \dot{y}_0} & \frac{\partial \dot{z}}{\partial \dot{z}_0} \end{bmatrix} \tag{2.14}$$

Note that the determinant of the STM must be equal to one in the CR3BP, thus offering a means to evaluate the accuracy of the calculation of the STM. This unity determinant requirement is related to a fundamental property of Hamiltonian systems; the phase space "volume" visited by a given trajectory is preserved according to Liouville's theorem [82].

In the CR3BP, the values of many or all of the STM elements in equation (2.14) are required for any differential corrections (targeting) process based on a Newton-Raphson

iteration scheme. In the automated targeting scheme, a column vector of design (free) variables $\vec{X}$ is varied at each step of the iteration until a column vector of constraints $\vec{F}(\vec{X})$ is approximately equal to the zero vector $\vec{0}$ to within a satisfactorily small convergence tolerance. If the number of design variables is equal to the number of constraints, then vectors $\vec{X}$ and $\vec{F}$ are the same size, the Jacobian matrix $\frac{\partial \vec{F}(\vec{X})}{\partial \vec{X}}$ is square, and the update equation at the jth step of the iteration is,

$$\vec{X}^{j+1} = \vec{X}^{j} - \left[\frac{\partial \vec{F}(\vec{X}^{j})}{\partial \vec{X}}\right]^{-1} \vec{F}(\vec{X}^{j}) \tag{2.15}$$

A simple example of trajectory targeting employing update equation (2.15) is the "single shooting" process depicted in Figure 2.6. In this example, a single S/C path is assumed

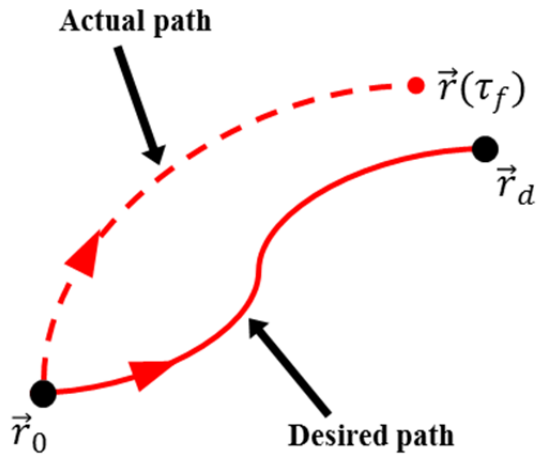

Figure 2.6. Notional single shooting targeting process; fixed initial and target positions; fixed time

to begin at a specified fixed position $\vec{r}_0 = [\, x_0 \;\; y_0 \;\; z_0 \,]^T$ at initial time τ_i. The targeting goal is for the S/C path to end at a different specified fixed position $\vec{r}_d = [\, x_d \;\; y_d \;\; z_d \,]^T$ at a specified fixed future time τ_f. The three design variables that may be modified to achieve this goal are the three components of the S/C initial velocity $\vec{V}_0$,

$$\vec{X} = \vec{V}_0 = \begin{bmatrix} \dot{x}_0 \\ \dot{y}_0 \\ \dot{z}_0 \end{bmatrix} \tag{2.16}$$

while the three targeting constraints are the three components of the desired final S/C position at time τ_f. Such constraints are defined using the following constraints vector $\vec{F}$,

$$\vec{F} = \vec{r}(\tau_f) - \vec{r}_d = \begin{bmatrix} x(\tau_f) - x_d \\ y(\tau_f) - y_d \\ z(\tau_f) - z_d \end{bmatrix} \tag{2.17}$$

where $\vec{F} = 0$ if the constraints are satisfied. The iterative targeting process is initiated using a *reasonable guess* for the values of $\vec{X}^1$ in equation (2.16). For the first iteration, the S/C initial state is propagated (numerically integrated) forward in time for a duration equal to $\Delta\tau = \tau_f - \tau_i$, and the values of $\vec{F}(\vec{X}^1)$ in equation (2.17) are calculated based on the final propagated S/C position. If the Euclidean norm of $\vec{F}(\vec{X}^1)$, i.e., $\left\|\vec{F}(\vec{X}^1)\right\|$, is less than a specified (small) convergence tolerance, then the targeting process is terminated, with the solution for the initial S/C velocity components given by $\vec{X}^1$. The resulting precise solution path (satisfying the constraints) is indicated by the solid red path in Figure 2.6. On the other hand, if the convergence criterion is not met, as represented by the dashed red path in Figure 2.6, the process repeats until the actual path satisfies the constraints associated with the desired path. Based on equation (2.15), the update equation to calculate the unique, revised estimate $\vec{X}^2$ is,

$$\begin{bmatrix} \dot{x}_0 \\ \dot{y}_0 \\ \dot{z}_0 \end{bmatrix}^{j=2} = \begin{bmatrix} \dot{x}_0 \\ \dot{y}_0 \\ \dot{z}_0 \end{bmatrix}^{j=1} - \left\{ \begin{bmatrix} \frac{\partial x}{\partial \dot{x}_0} & \frac{\partial x}{\partial \dot{y}_0} & \frac{\partial x}{\partial \dot{z}_0} \\ \frac{\partial y}{\partial \dot{x}_0} & \frac{\partial y}{\partial \dot{y}_0} & \frac{\partial y}{\partial \dot{z}_0} \\ \frac{\partial z}{\partial \dot{x}_0} & \frac{\partial z}{\partial \dot{y}_0} & \frac{\partial z}{\partial \dot{z}_0} \end{bmatrix}^{-1} \right\}^{j=1} \begin{bmatrix} x(\tau_f) - x_d \\ y(\tau_f) - y_d \\ z(\tau_f) - z_d \end{bmatrix}^{j=1} \tag{2.18}$$

Note that the inverted matrix $\frac{\partial \vec{F}(\vec{X})}{\partial \vec{X}} = \frac{\partial \vec{r}}{\partial \vec{V}_0}$ in this example consists of nine elements of the STM in equation (2.14)—specifically the upper right 3 × 3 block. To obtain these STM values, *revised at each step of the iterative process*, the STM Φ in equation (2.13) is propagated in parallel with the CR3BP equations of motion (2.1)/(2.5) on each step.

More complex variations of the "single shooting" targeting process depicted in Figure 2.6 can be constructed. A "multiple shooting" process is depicted in Figure 2.7. As in

the previous example, the S/C path begins at a specified fixed position $\vec{r}_0$ at initial time τ_i, and the targeting goal is for the path to end at a different specified fixed position $\vec{r}_d$ at a specified fixed future time τ_f. Yet, in this multiple shooting example, three different

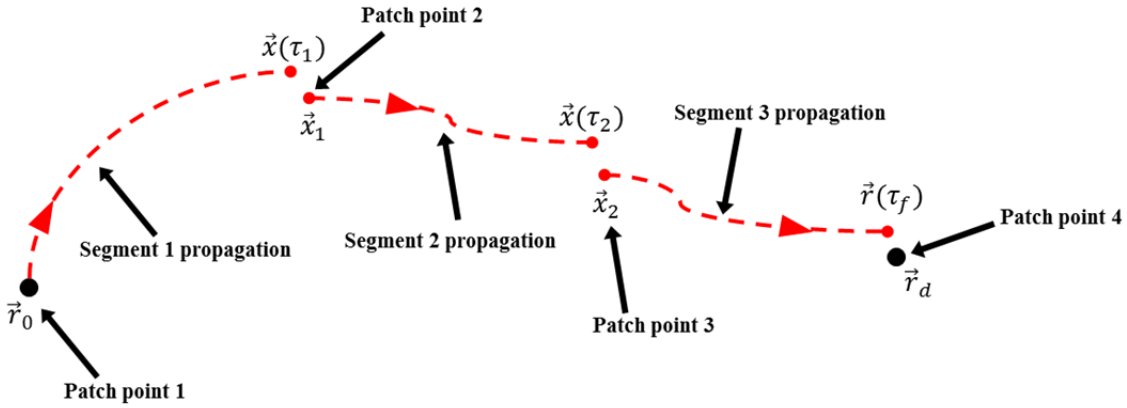

Figure 2.7. Notional multiple shooting targeting process; fixed initial and target positions; fixed total time; position and velocity continuity required at intermediate patch points

segments of the S/C path are considered separately. Each segment is constructed by propagating the S/C state at one of three "patch points" forward in time. The initial S/C state can be considered the first patch point, beginning the first segment, while the end state can be considered the fourth and last patch point. The second and third patch points are the intermediate patch points beginning the second and third segments, respectively; these patch points may be located at any positions. Thus, the design variables in this targeting example include the three components of the S/C initial velocity $\vec{V}_0$ (at the first patch point) along with both the position and velocity components of the states associated with the second and third patch points. The individual time spans for the three segments are also variables in this example; however it is desired that the *total* time-of-flight of the S/C trajectory between the first and last patch points be constrained to be equal to $\Delta\tau = \tau_f - \tau_i$. Furthermore, in this example, it is desired that the S/C path be continuous, in both position and velocity, at the intermediate patch points—to within a satisfactory convergence criterion/tolerance. This implies that the end state of the first segment $\vec{x}(\tau_1)$

must be equal to the state at the second patch point $\vec{x}_1$ —to within a satisfactory convergence criterion/tolerance. A similar requirement exists at the third patch point.

The iterative, multiple shooting targeting process depicted in Figure 2.7 is initiated using a reasonable guess for the values of the design variables $\vec{X}$. On each iteration, revised S/C paths for all three segments are generated by propagating the states at the appropriate patch points forward in time, and the values of the constraints vector $\vec{F}(\vec{X})$ are determined. The estimates for the variables in $\vec{X}$ are revised on each iteration until the desired convergence criterion is satisfied and a precise solution path is obtained. Note that the converged solution path between the first and last patch points is deemed "continuous." Even though discontinuities exist at the intermediate patch points, they are considered small enough (based on the convergence tolerance) to be ignored for preliminary S/C mission design.

An important difference between the two preceding targeting examples is the relationship between the number of design variables (the size of $\vec{X}$) and the number of constraints (the size of $\vec{F}$). For a revised estimate for $\vec{X}$ to be determined at each iterative step in the targeting process, the size of $\vec{X}$ must, in general, be greater than or equal to the size of $\vec{F}$. In the single shooting example depicted in Figure 2.6, $\vec{X}$ and $\vec{F}$ are the same size; therefore, the Jacobian matrix $\frac{\partial \vec{F}(\vec{X})}{\partial \vec{X}}$ is square (3×3). A square matrix is invertible unless it is singular; therefore, update equation (2.15) is valid, in general, for the case of a square $\frac{\partial \vec{F}(\vec{X})}{\partial \vec{X}}$ matrix, yielding a *unique* revised estimate for $\vec{X}$ on each iteration. However, in the multiple shooting example depicted in Figure 2.7, there are more design variables than constraints. There are eighteen design variables: three components of the S/C initial velocity; six position/velocity components at each of the two intermediate patch points; and three segment time spans. On the other hand, there are only sixteen constraints: six position/velocity continuity constraints at each of the two intermediate patch points; three fixed position coordinates at the last patch point; and the fixed total time-of-flight. In targeting cases where the design variables outnumber the constraints, there are, in general, infinitely many solutions associated with each update in the iterative process. This is

manifest in the fact that the matrix $\frac{\partial \vec{F}(\vec{X})}{\partial \vec{X}}$ has more columns than rows. Because a matrix must be square for it to be inverted in the traditional sense, a modification to the update equation (2.15) is required in this case. One possible choice (but not the only choice) for an update equation that yields a *unique* revised estimate for $\vec{X}$ is,

$$\vec{X}^{j+1} = \vec{X}^{j} - \left[\frac{\partial \vec{F}(\vec{X}^{j})}{\partial \vec{X}}\right]^{T} \left[\left[\frac{\partial \vec{F}(\vec{X}^{j})}{\partial \vec{X}}\right]\left[\frac{\partial \vec{F}(\vec{X}^{j})}{\partial \vec{X}}\right]^{T}\right]^{-1} \vec{F}(\vec{X}^{j}) \qquad (2.19)$$

which replaces the inverse of $\frac{\partial \vec{F}(\vec{X}^{j})}{\partial \vec{X}}$ in equation (2.15) with its pseudoinverse. In this case, the pseudoinverse of generic matrix K is defined as $K^{\dagger} = K^{T}[KK^{T}]^{-1}$. Update equation (2.19) is referred to as the minimum-norm solution and yields a revised estimate for $\vec{X}$ that is as close as possible to the previous estimate. Finally, note that the difference between the preceding targeting examples in terms of the relationship between the number of design variables and the number of constraints should *not* imply that single shooting always involves a square $\frac{\partial \vec{F}(\vec{X}^{j})}{\partial \vec{X}}$ matrix and multiple shooting does not. In fact, there are examples of single shooting where $\frac{\partial \vec{F}(\vec{X}^{j})}{\partial \vec{X}}$ is not square, just as there are examples of multiple shooting where that matrix is square.

In the present investigation, both single shooting and multiple shooting processes are employed for S/C trajectory targeting. While single shooting is sometimes sufficient to achieve a given targeting objective, multiple shooting is often utilized to improve the performance of a targeting scheme. Constructing a scheme with one or more intermediate patch points can increase the likelihood that the differential corrections process will successfully converge on a desirable solution. Since a particular targeting process requires an estimate for the S/C path(s) to initiate the process, the precise solution—if converged—resulting from the targeting process is often (but not always) qualitatively similar to the estimate. Therefore, certain qualitative characteristics of the precise solution (e.g., the shapes of various trajectory segments) may be prescribed more effectively by defining multiple intermediate patch points along an estimated S/C path. Schemes using several patch points can be especially useful for targeting S/C paths

through chaotic regions of the CR3BP phase space where future states are highly sensitive to initial conditions.

For any targeting scheme utilized for S/C trajectory design, convergence to a precise solution is not guaranteed. The corrections process could diverge away from what is deemed a reasonable estimate for the S/C path; if a precise solution is eventually obtained, that solution could be far from qualitatively similar to the original guess. The trajectory "solution" might be entirely undesirable for a particular S/C mission. Thus, the quality/accuracy of the initial estimate is arguably the most important factor in determining whether a targeting process leads to a successful outcome. On the other hand, in cases where the initial estimate is close enough to a desirable solution and where the algorithm does not diverge, even though the algorithm might appear (at first) to be in the process of converging on what would be a desirable targeted solution—through reduction of the norm $\left\|\vec{F}(\vec{X})\right\|$ on each successive iteration—a practical limit may be reached where that norm cannot be reduced any further. This limitation could be the result of the accuracy of the numerical integration and/or the inherent dynamical sensitivities in the CR3BP for a given design case. Furthermore, it must be recognized that the corrections process considered herein has an inherent limitation because it is based on the STM, which is only a *linear approximation* of the dynamical "flow" in what is actually a nonlinear system. If $\left\|\vec{F}(\vec{X})\right\|$ remains larger than the specified convergence tolerance, the targeting process is never terminated and a precise solution is never obtained. If this situation is encountered, it may be appropriate to redefine the targeting scheme, perhaps by adding or removing constraints. Because it is possible to construct a targeting scheme that is effectively "over-constrained"—even in cases where the number of constraints is less than or equal to the number of design variables—the careful choice of constraints is critically important to successful targeting for S/C trajectory design. Another option for improving targeting performance is to change the number and/or locations of various patch points in a multiple shooting scheme. Finally, it may be appropriate in certain cases to relax the convergence criterion, allowing a larger value of $\left\|\vec{F}(\vec{X})\right\|$ to be deemed sufficiently small so that a targeted solution can be obtained.

In the present investigation, targeting is accomplished for two main purposes: (1) targeting periodic trajectories and (2) targeting transfers to/from trajectories. For either purpose, the convergence tolerance specifying the value of norm $\left\|\vec{F}(\vec{X})\right\|$ that is deemed sufficiently small is generally between 10^{-11} and 10^{-13} in nondimensional units. Note that the vector $\vec{F}(\vec{X})$ typically consists of constraints involving nondimensional units of both distance and velocity and often other dimensionless quantities as well. A convergence criterion based on a value of $\left\|\vec{F}(\vec{X})\right\|$ between 10^{-11} and 10^{-13} usually corresponds to much better than sub-meter accuracy in S/C position and much better than sub-mm/s accuracy in S/C velocity for trajectory targeting in either the Earth-Moon CR3BP or the Uranus-Titania CR3BP, which are the systems in which targeting is accomplished in the mission design examples in the current effort (see Section 4.4 and Chapter 5). Note that targeting in this investigation is always performed using Cartesian, rotating frame coordinates, which are the variables used in equations of motion (2.1)/(2.5). For Poincaré-map-based design examples employing non-Cartesian systems (e.g., cylindrical or spherical), the appropriate coordinate transformations (see Section 3.4) are accomplished before and after targeting.

For targeting periodic trajectories in the current investigation, either single or multiple shooting is utilized to obtain an orbit that is continuous (to within a satisfactory convergence criterion/tolerance) at all patch points including the last patch point—which is defined to be the same as the first patch point. For either single or multiple shooting, the time span of each trajectory segment is a design variable; consequently, an initial guess for the period of a periodic trajectory is always required for this choice of targeting scheme. Furthermore, because the focus of this investigation is trajectory design based on Poincaré maps (see Section 2.4), periodicity targeting is initiated using estimates defined based on a particular map and constrained such that the resulting converged periodic orbit generates fixed point returns on the same map. Therefore, the initial condition for the periodic trajectory is also constrained (in the targeting process) to have the same hyperplane coordinate (e.g., $y = 0$) as the map as well as the same *JC* value, or "energy" level, as the map. Because *JC* is a constant of the motion along a given trajectory, it would effectively "over-constrain" a periodicity targeting scheme to enforce

continuity in all coordinates of the S/C state at the first/last patch point. Based on equation (2.2), it is sufficient to constrain all three position coordinates and only two of the three velocity coordinates at the first/last patch point, while also ensuring that the remaining velocity coordinate has the *same sign* at the initial and final S/C state in the converged solution. The *magnitude* of the remaining velocity coordinate is already *implicitly* constrained by the fact that *JC* is expected to be constant along the entire periodic S/C path—to the accuracy of the numerical integration. In the current investigation, the velocity coordinate not explicitly constrained at the first/last patch point is chosen to be the "missing" coordinate not explicitly represented on a given Poincaré map. For example, $\dot{y}$ is the "missing" coordinate associated with a return on a map defined by hyperplane $y = 0$. Finally, in multiple shooting schemes for targeting periodicity in the current investigation, the process of ensuring that the remaining velocity coordinate has the same sign at the initial and final S/C state in the converged solution is aided by the use of an additional design variable referred to as a slack variable. For example, by enforcing the constraint $\dot{y} = \beta^2$, where β is a free variable that can be equal to any real value, it is ensured that $\dot{y} \geq 0$.

While targeting of periodic orbits in the present investigation is mostly accomplished using the general periodicity constraints described in the preceding discussion, it also sometimes useful to target a special class of periodic trajectories possessing an important property: symmetry with respect to both the *x*-*z* plane (in the rotating frame) and time. As introduced in Section 2.1, if a series of row vectors [x y z $\dot{x}$ $\dot{y}$ $\dot{z}$] is a solution to the CR3BP equations of motion in forward time, then [x $-y$ z $-\dot{x}$ $\dot{y}$ $-\dot{z}$] is a solution *in negative time*. This symmetry property can be used to locate one-half of a periodic orbit by determining a S/C path that begins and ends at two different perpendicular crossings of the *x*-*z* plane: [x_1 0 z_1 0 $\dot{y}_1$ 0] and [x_2 0 z_2 0 $\dot{y}_2$ 0], with the time span between the two states equal to one-half of the period. One example of a targeting scheme involves fixing the value of x_1 at an initial perpendicular crossing ($y_1 = 0$ and $\dot{x}_1 = \dot{z}_1 = 0$) and determining the values of z_1 and $\dot{y}_1$ that lead to a future perpendicular crossing ($y_2 = 0$ and $\dot{x}_2 = \dot{z}_2 = 0$) after some variable time span $\Delta\tau$. The other half of the periodic orbit can then be obtained either by propagating the converged solution

initial state [x_1 0 z_1 0 $\dot{y}_1$ 0] backward in time or by propagating the converged solution final state [x_2 0 z_2 0 $\dot{y}_2$ 0] forward in time for one-half of the period.

After one periodic trajectory is determined through a targeting process, that converged solution may then be used as a reference to generate a *family* of periodic orbits with similar qualitative characteristics. A straightforward method of generating such a family is natural parameter continuation, where a S/C state along the known periodic orbit is modified to produce an estimate for a different periodic orbit, typically at a different "energy" level. The estimate is then used to initiate a new targeting process to determine a new periodic solution in the same orbit family. The process can then be repeated, using the new converged solution as a new reference to be modified to produce another new estimate for another periodic orbit. For example, the converged solution initial condition [x_1 0 z_1 0 $\dot{y}_1$ 0] associated with the symmetric periodic orbit in the preceding example could be perturbed slightly (by a small value ε) in the x_1 coordinate, which is a fixed coordinate in the targeting scheme. The estimate for the initial condition for a neighboring periodic orbit in the same family is then [$x_1 + \varepsilon$ 0 z_1 0 $\dot{y}_1$ 0]; this guess is used to initiate the new targeting process to determine the new values of z_1 and $\dot{y}_1$ that lead to a future perpendicular crossing.

In this investigation, targeting S/C orbit transfers to/from trajectories is accomplished through either single or multiple shooting. The originating and/or destination trajectories are often—but are not necessarily—periodic orbits. As with the schemes for periodicity targeting, the time span of each segment of the transfer path is a design variable. Yet, unlike periodicity schemes, the first and last patch points are not the same. Targeting a transfer to/from a particular trajectory is accomplished by constraining the S/C to be continuous *in position* at all patch points (to within a satisfactory convergence criterion/tolerance) and by enforcing continuity *in velocity* at all patch points except those patch points associated with S/C transfer maneuvers. Patch points where velocity continuity is not constrained are associated with positions along the S/C path where a $\left|\overrightarrow{\Delta V}\right|$ maneuver is required for the S/C to follow the desired path, as depicted previously in Figure 2.5. Furthermore, because the focus of this investigation is trajectory design based on Poincaré maps (see Section 2.4), orbit transfer targeting is initiated using

estimates defined based on a particular map, and it is assumed that either the first or last patch point along the resulting converged transfer path is at a fixed *position* on the same hyperplane as the original map. The state at this hyperplane patch point is sometimes—but not always—further constrained to possess the same "energy" value as the particular orbit that the S/C is to be transferred to/from. Such choices for the transfer targeting scheme are based on the specific design objective for a given mission design problem.

In the present investigation, the time required to perform a trajectory targeting process is anywhere from a few seconds to several minutes (elapsed time in MATLAB® Version: 7.14.0.739 (R2012a); benchmark: 0.0600, 0.0637, 0.0741, 0.1641, 0.2727, 0.7146).

2.2.1 Stability Assessment for Periodic Orbits

In the current investigation, trajectories converged to satisfactory periodicity through a targeting process are assessed based on a linear stability analysis. The stability assessment is based on the eigenvalues of the full-cycle STM, i.e., the STM Φ obtained by numerical integration of equation (2.13)—integrated in parallel with CR3BP equations of motion (2.1)/(2.5)—for one full period of the periodic orbit: $\Phi(\tau_0 + T, \tau_0)$ where T is the period. This full-cycle STM is referred to as the *monodromy matrix* [14]. Based on Floquet theory, the monodromy matrix can be written in terms of a periodic function of time $F(\tau)$ and a Jordan normal matrix J that is usually diagonal [14] such that,

$$\Phi(\tau_0 + T, \tau_0) = F(\tau_0)e^{JT}F^{-1}(\tau_0) \tag{2.20}$$

where $F(\tau_0) = F(\tau_0 + T)$ is the matrix of eigenvectors of the monodromy matrix. The diagonal elements ω_i of matrix J are termed the Poincaré exponents and are related to the monodromy matrix eigenvalues λ_i, termed the characteristic multipliers, by,

$$\lambda_i = e^{\omega_i T} \tag{2.21}$$

These characteristic multipliers λ_i, which can be complex numbers (in general), provide the information required for a *linear* stability analysis with respect to a given periodic trajectory, with the stability boundary in the linearized system defined by eigenvalues with unit magnitude.

In the spatial CR3BP, which is a 3-DOF, time-invariant, Hamiltonian system, the monodromy matrix possesses six eigenvalues consisting of reciprocal pairs [83]. Because the monodromy matrix is real-valued, any complex eigenvalues must exist in complex conjugate pairs. A commonly-observed (though by no means guaranteed) eigenstructure in the spatial CR3BP involves at least one complex conjugate pair of reciprocal eigenvalues on the unit circle of the complex plane. Furthermore, because any monodromy matrix is associated with a periodic orbit, one eigenvalue pair must always be equal to one; note that this pair not only has unit magnitude but it also is equal to the real value of one [83]. The pair of unity eigenvalues makes asymptotic stability in the linearized system impossible because that type of stability would require that all eigenvalues have magnitude less than one. At best, marginal linear stability is possible—if the remaining four eigenvalues have magnitudes equal to one. Unfortunately, unlike asymptotic stability, marginal stability in a linearized system does not guarantee local stability in the associated nonlinear system. On the other hand, if any of the four remaining eigenvalues have magnitude greater than unity, the periodic orbit can be considered unstable in both the linear and nonlinear sense; in this case, it is technically a *non-stable saddle* (see next section) because a CR3BP monodromy matrix eigenvalue having magnitude greater than unity requires a reciprocal eigenvalue having magnitude less than unity (and vice versa).

As a final note, by tracking changes in the eigenstructure of the monodromy matrices associated with periodic orbits, it is possible to characterize one or more families of periodic orbits in terms of changes in linear stability. Furthermore, changes in eigenstructure and/or stability are often associated with system bifurcations, which alter the qualitative characteristics of periodic orbits and the families to which they belong. An example investigation into bifurcations in the spatial CR3BP is that of Howell and Campbell [83].

2.3 Dynamical Systems Theory

Exploration of the spatial CR3BP, in particular, has been aided considerably in recent years by insight gained from dynamical systems theory. Pioneered by Poincaré and

further developed by Birkhoff, this theory offers a *geometrical* approach to understanding the dynamical "flow" in a nonlinear and chaotic system like the CR3BP [1, 14, 20, 21].

A geometrical interpretation of dynamical "flow" in the vicinity of a reference condition is applicable to both the CR3BP libration points as well as periodic CR3BP trajectories. First, a linear stability analysis of the linearized system in equation (2.8) evaluated at the five libration (equilibrium) points L_i leads to the characterization of the collinear libration points L_1 through L_3 as non-stable saddle-points (2-D saddle × 2-D center × 2-D center), while the characterization of the triangular points L_4 and L_5 depends on the value of mass ratio μ [73, 76]. For mass ratios up to a critical value equal to $\mu = (1 - \sqrt{23/27})/2 \cong 0.03852$ [84], which includes most systems of interest in the solar system except the Pluto-Charon CR3BP, the triangular points are generally characterized as marginally stable centers (2-D center × 2-D center × 2-D center). However, for mass ratios greater than the critical value, these libration points become unstable. The preceding linear stability conclusions are based on an examination of the eigenvalues associated with the system in equation (2.8), where the matrix A is a *constant matrix* in the special case considering the system equilibrium points [10]. Interestingly, for the linear stability assessment of the libration points, the in-plane (in the *x*-*y* plane of the massive primaries) motion and the out-of-plane (z) motion are decoupled and may be considered separately. For all five Lagrange points, the linearized out-of-plane motion is marginally stable (2-D center) regardless of the value of mass ratio μ.

Characterization of the CR3BP libration points in terms of marginally stable centers and non-stable saddles implies that there exist different modes to the local dynamical "flow" associated with these points. Each mode is associated with a subspace of a certain dimension, which is a subset of the full 6-D phase space "flow." Figure 2.8 notionally depicts the different modes of the "flow" associated with both a non-stable saddle equilibrium point and a center equilibrium point in phase space. The 2-D saddle behavior in Figure 2.8(a) is also associated with stable/unstable manifold trajectories that approach/depart the equilibrium point asymptotically as $\tau \to \infty$ in the true, nonlinear system. These manifold trajectories possess the same value of *JC* as that associated with

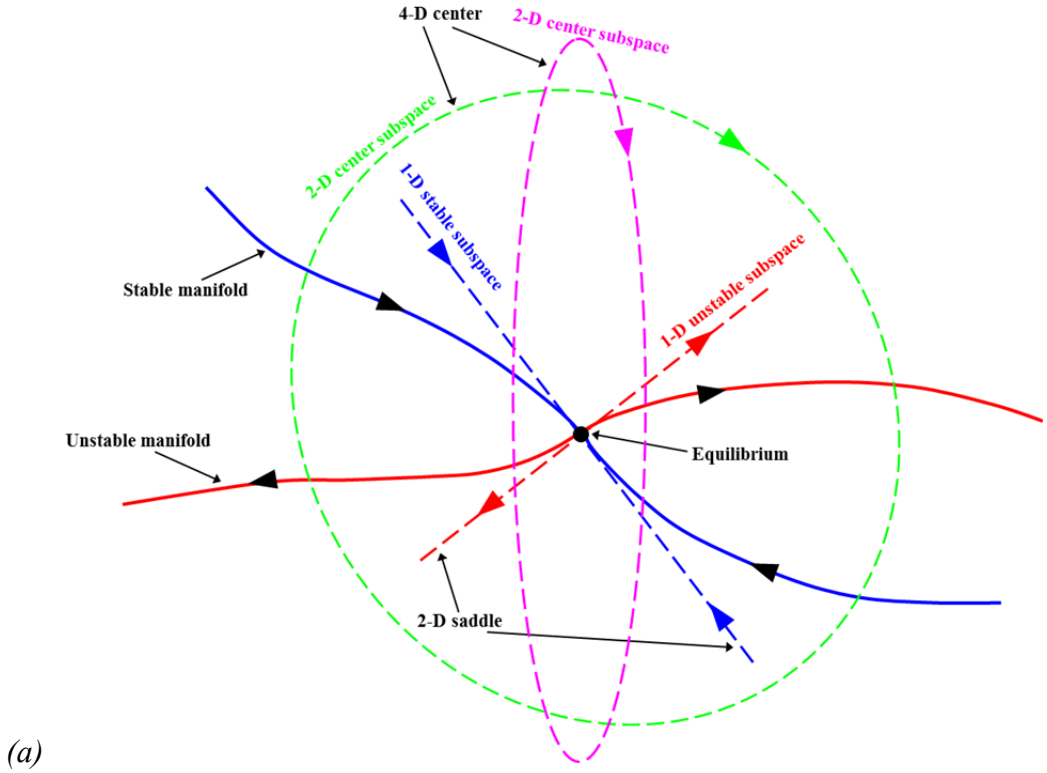

(a)

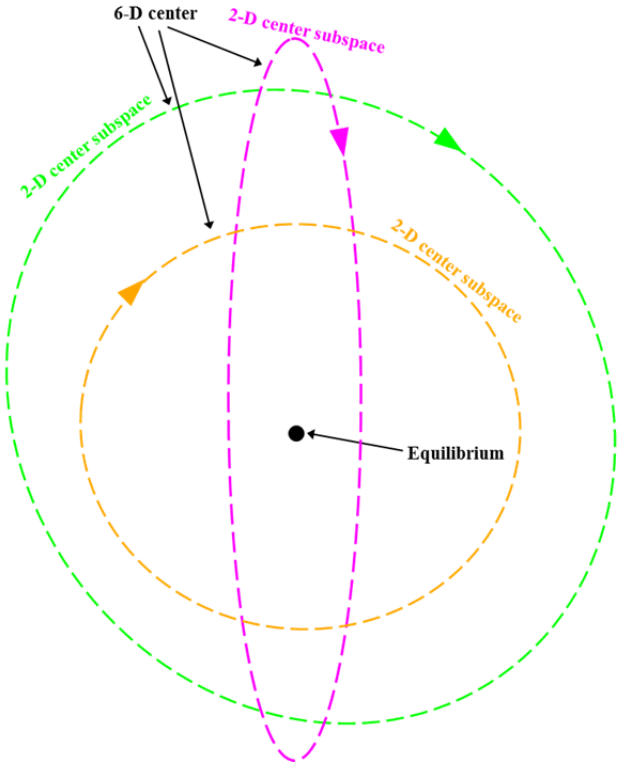

(b)

Figure 2.8. Notional "flow" in the vicinity of 2-D saddle × 2-D center × 2-D center (*a*) and 2-D center × 2-D center × 2-D center (*b*) equilibrium points

the equilibrium point and are tangent to the stable/unstable subspaces at the equilibrium point; the subspaces are defined by the eigenvectors of the constant matrix A corresponding to the pair of negative/positive real eigenvalues of A. Yet, note that the equilibrium point depicted in Figure 2.8(a) is also characterized by a 4-D center (2-D center × 2-D center) defined by *two* conjugate pairs of pure imaginary eigenvalues of matrix A. The center subspace is associated with a center manifold of all rotational motion—including all periodic and quasi-periodic trajectories at various "energy" levels—in the vicinity of the equilibrium point. The combined 2-D saddle × 2-D center × 2-D center behavior is representative of the non-stable "flow" associated with the collinear libration points. On the other hand, the 2-D center × 2-D center × 2-D center example depicted in Figure 2.8(b) is representative of the marginally stable "flow" associated with the triangular libration points for most CR3BP systems of interest in the solar system (having less than the critical value of mass ratio). In this example, there exists a 6-D center manifold of local rotational motion. There are no stable/unstable manifolds—at least none associated with the equilibrium point itself according to this linear stability analysis.

A geometrical interpretation is also possible for dynamical "flow" in the vicinity of periodic trajectories in the CR3BP. In this case, the *reference condition* for the linear stability analysis and the corresponding description of the linearized "flow" is *an entire periodic orbit* rather than simply an equilibrium (libration) point. Yet, the two types of reference conditions can be seen as somewhat equivalent considering that a fixed point return generated on a Poincaré map (see next section) by a periodic orbit behaves as an equilibrium point in the lower-D space on the map (defined based on a specified "energy" level). In fact, a given periodic trajectory is essentially a 1-D closed curve consisting of an infinite number of fixed points; each fixed point is an initial condition for a trajectory that repeats that initial state after a time span equal to one orbit period. A useful property is the fact that the eigenvalues of the monodromy matrix—which provide the key information needed for the linear stability assessment of the periodic orbit (see previous section)—are independent of the specific starting point along the orbit that is selected for

the analysis. Moreover, while the eigenvectors $\vec{\mathrm{v}}_i$ of the monodromy matrix are *not* independent of the starting point, they obey the following relationship,

$$\vec{\mathrm{v}}_i(\tau) = \Phi(\tau, \tau_0)\vec{\mathrm{v}}_i(\tau_0) \tag{2.22}$$

which states that the STM Φ transitions each monodromy matrix eigenvector from one possible starting point to the next in the same manner as $\delta\vec{x}$ is transitioned in equation (2.12).

Just as the characterization of a libration point in terms of its linear stability is associated with certain modes of the "flow" in the vicinity of that point, the linear stability assessment of a periodic trajectory allows for an analogous description of the "flow" in the vicinity of *all* possible fixed points on that orbit. For example, a periodic orbit with fixed points characterized as non-stable saddles—each of the type 2-D saddle × 2-D center × 2-D center—is associated with stable/unstable manifold *tubes* that approach/depart the periodic orbit asymptotically as $\tau \to \infty$ in the true, nonlinear system. A notional example of a stable manifold tube (blue) approaching a periodic orbit (violet) in phase space is depicted in Figure 2.9(a). Figure 2.9(b) is an analogous depiction of an unstable manifold tube (red) departing a periodic orbit (violet) in phase space. In either figure, the violet arrow indicates the direction of motion (in forward time) of each periodic orbit. The manifold tubes are 2-D surfaces existing in the full 6-D phase space of the spatial CR3BP; the surfaces are formed by an infinite number of individual (1-D) trajectories that are themselves asymptotic to/from the "unstable" periodic orbit and possess the same value of *JC* as that orbit. Like the single manifold trajectories asymptotic to the equilibrium point depicted in Figure 2.8(a), each stable/unstable manifold trajectory belonging to an entire stable/unstable manifold tube is tangent to the stable/unstable subspace at a particular fixed point along the periodic orbit. Naturally, these stable/unstable subspaces are defined by the monodromy matrix eigenvectors associated with a particular fixed point and correspond to the pair of negative/positive real monodromy matrix eigenvalues.

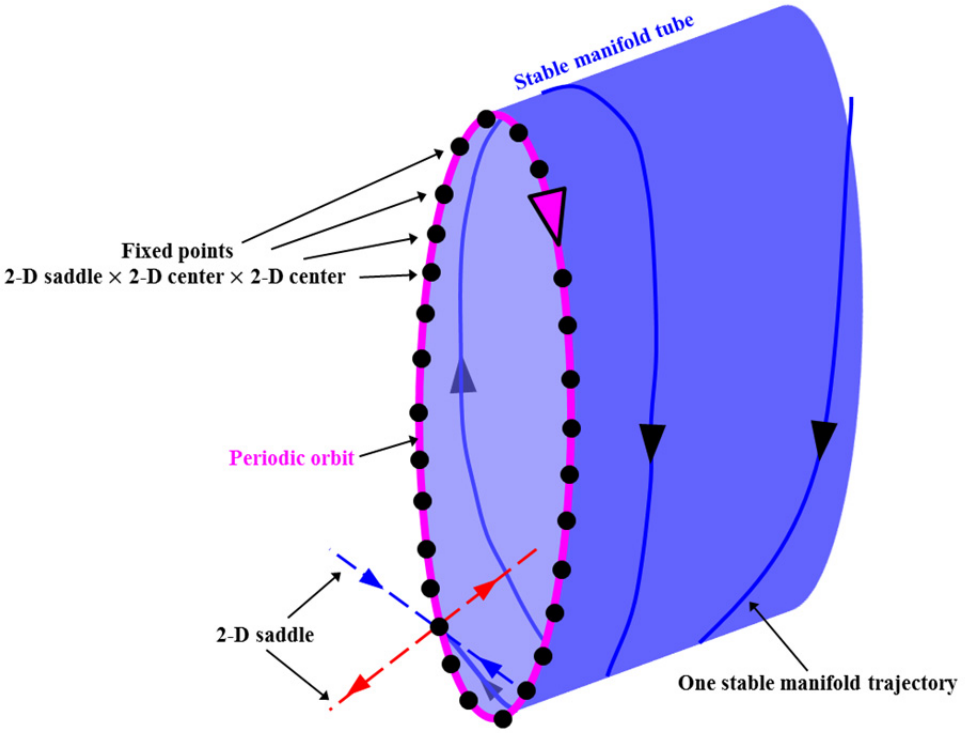

(a)

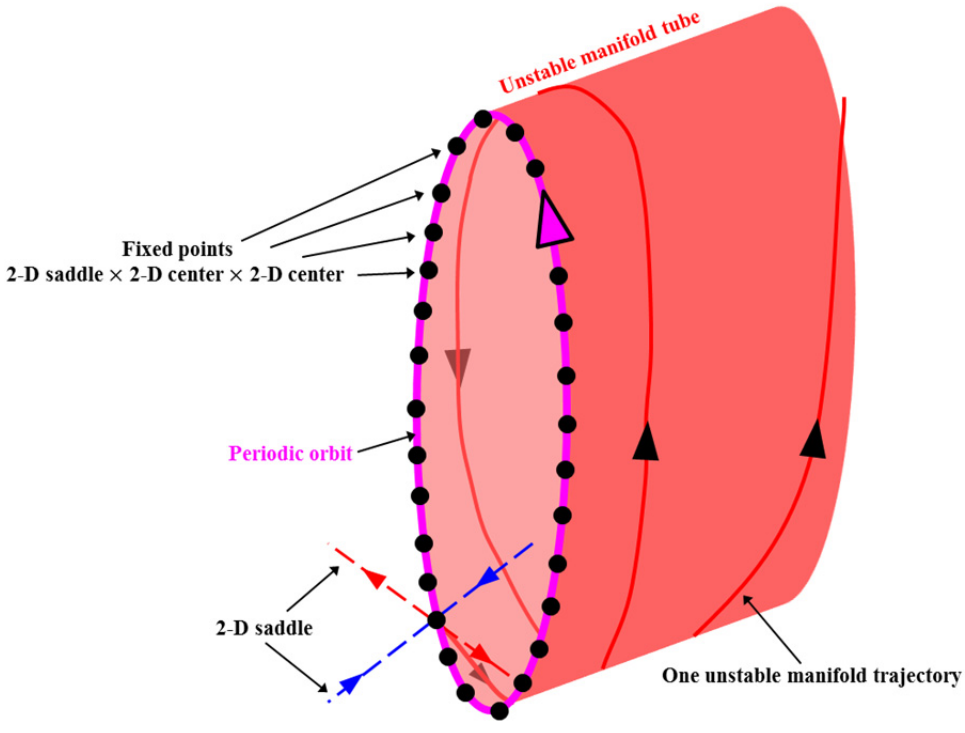

(b)

Figure 2.9. Notional 2-D stable (*a*) and unstable (*b*) manifold tubes asymptotic to/from unstable periodic orbits; fixed points of type 2-D saddle × 2-D center × 2-D center

Stable/unstable manifolds as well as center manifolds are invariant manifolds in the CR3BP; if a S/C trajectory exists along a given manifold at any given time, it must remain on that manifold for any finite time span, which also implies that a trajectory cannot cross an invariant manifold in finite time *in the full 6-D phase space*. The invariance property has special significance for mission design. In particular, the existence of stable/unstable manifolds associated with unstable periodic orbits motivates the search for low-cost, theoretically zero-$\left|\overrightarrow{\Delta V}\right|$ transfers to and from orbits such as unstable periodic LPOs. Moreover, intersections between stable and unstable manifold trajectories in the full 6-D phase space serve as zero-$\left|\overrightarrow{\Delta V}\right|$ connections for a S/C to follow between unstable periodic orbits. If an unstable manifold trajectory emanating in forward time from a periodic orbit perfectly intersects (in position and velocity) a stable manifold trajectory emanating in negative time from a *different* periodic orbit, the connection is termed heteroclinic. On the other hand, a connection is termed homoclinic if an unstable manifold trajectory and a stable manifold trajectory associated with the *same* periodic orbit intersect. In either case, because stable/unstable manifold trajectories associated with a given periodic orbit possess the same value of *JC* as the periodic orbit itself, connections exist only between orbits at the same "energy" level. In a typical orbit-to-orbit transfer design process, rather than determining a precise intersection between approximations of stable and unstable manifold trajectories, it is often much easier to locate an intersection *in position only*—with a reasonably small velocity discontinuity at that intersection. This process yields an approximately asymptotic S/C path between periodic orbits that requires a reasonably small $\left|\overrightarrow{\Delta V}\right|$ transfer maneuver somewhere along the path. Note that it is often useful to plot the *projections* of approximations of certain manifolds in the 3-D configuration (position) space. For example, the approximate *x,y,z* path of a S/C asymptotically approaching a periodic orbit along a stable manifold trajectory may be displayed along with the approximate *x,y,z* paths of various other possible stable manifold trajectories forming an entire stable manifold tube. Yet, it is imperative to recognize that such a plot explicitly contains only position information. The associated manifold tube is an invariant structure belonging to the full 6-D phase

space; there is no restriction on a trajectory crossing the projection of the tube in the configuration space.

It is important to distinguish between the planar CR3BP and the spatial CR3BP in terms of the topological significance of the invariance property of manifolds. Although it is impossible for a trajectory to cross an invariant manifold (in finite time) in either the full 4-D phase space of the planar problem or the full 6-D phase space of the spatial problem, this property alone does not necessarily imply that it is impossible to "go around" the manifold. In the planar CR3BP, a given S/C trajectory exists as a path through a 4-D phase space, which can be effectively reduced to a 3-D constant-*JC* space. Consequently, the 2-D surfaces of manifold tubes associated with periodic orbits in the planar problem can, in fact, divide the constant-*JC* space into separate regions because a 2-D tube has only one dimension less than the 3-D constant-*JC* space. On the other hand, a trajectory in the spatial CR3BP exists as a path through a 6-D phase space, which can be effectively reduced to a 5-D constant-*JC* space. Therefore, the 2-D surfaces of manifold tubes associated with periodic orbits in the spatial problem cannot divide the 5-D constant-*JC* space into separate regions because that space has three more dimensions than the tube. This is akin to the fact that a zero-dimensional point cannot divide a 3-D space. Interestingly, there do exist *higher-D* manifold tubes associated not with individual periodic orbits but with *entire center manifolds of trajectories*; these higher-D tubes can actually divide regions of the phase space in the spatial CR3BP in a manner relevant to S/C mission design (see Section 4.2 for more details).

To develop sets of initial conditions for trajectories that should—as a whole—closely approximate (upon numerical propagation) stable/unstable manifold tubes emanating from a particular unstable periodic orbit, the states associated with various fixed points along the orbit are perturbed in stable/unstable subspace directions in the phase space. As stated earlier, stable/unstable subspace directions at fixed points of the type 2-D saddle × 2-D center × 2-D center (the only type considered in the design examples in the current investigation) are defined by the monodromy matrix eigenvectors corresponding to the pair of negative/positive real monodromy matrix eigenvalues. Thus, if $\pm\vec{\mathrm{v}}_U = \pm[\, x_U \;\; y_U \;\; z_U \;\; \dot{x}_U \;\; \dot{y}_U \;\; \dot{z}_U \,]$ are the positive/negative eigenvector directions defining the

two directions associated with the 1-D unstable subspace at a given fixed point, then a small perturbation on the state at the fixed point in the $\pm\vec{\mathrm{v}}_U$ direction is expected to result in an approximation of initial conditions for two different unstable manifold trajectories emanating in forward time from the periodic orbit. In the current investigation, $\vec{\mathrm{v}}_U$ is normalized with respect to its *position* coordinates by,

$$\vec{\mathrm{v}}_U^P = \frac{\vec{\mathrm{v}}_U}{\sqrt{x_U^2 + y_U^2 + z_U^2}} \tag{2.23}$$

which allows for a perturbation on the state at the corresponding fixed point to be prescribed based on the resulting *position displacement* from the nominal state. The two initial conditions $\vec{x}_U$ resulting from the perturbation are given by,

$$\vec{x}_U = \vec{x}^* \pm d\vec{\mathrm{v}}_U^P \tag{2.24}$$

where $\vec{x}^*$ is the nominal state associated with periodicity, and d is a nondimensional distance. Such a perturbation is employed for multiple fixed points along an entire periodic orbit to generate multiple trajectories approximating two entire unstable manifold tubes. In the current investigation, a value of $d = 1.3 \times 10^{-4}$ is employed. This nondimensional distance corresponds to approximately 50 km in the Earth-Moon CR3BP, which is the only system for which manifold trajectories are considered in this dissertation (see Sections 4.4 and 5.1). The 50-km displacement for approximating manifold trajectories is based on a tradeoff: a smaller displacement results in a more accurate approximation of an initial condition associated with a "real" manifold trajectory; yet, if the displacement is too small, the associated trajectory requires an unreasonably long time span (of numerical integration) to depart the vicinity of the periodic orbit. Note that, while the perturbation expressed in equation (2.24) is defined in terms of its associated position displacement, this perturbation in the directions of the unstable subspace includes a perturbation in the nominal velocity as well. Thus, approximations for manifold trajectories emanating from periodic orbits in the current investigation involve a small discontinuity in *both position and velocity* between each manifold trajectory and the periodic orbit itself. Also note that, although equation (2.24) implies that the same value of d is used for *both* unstable manifold trajectories emanating from a fixed point, this does not necessarily have to be true. Finally, a similar process is used to

generate an approximation of initial conditions for two different *stable* manifold trajectories emanating in *negative time* from each selected fixed point along an unstable periodic orbit. Accordingly, perturbations on the states associated with multiple fixed points along an entire periodic orbit result in negative-time initial conditions for multiple trajectories approximating two entire *stable* manifold tubes.

The invariance of center manifolds in the CR3BP is important in the analysis of rotational motion associated with a particular reference periodic orbit possessing a particular value of *JC*. Such a center manifold is notionally depicted in Figure 2.10. Each S/C trajectory belonging to the center manifold *associated with the reference periodic orbit* exists along the surface of an invariant deformed torus in the full phase space and is at the same "energy" level as the reference orbit. In the planar CR3BP, either a 2-D or a 4-D center manifold in the vicinity of a reference periodic orbit is possible. A 2-D center manifold is associated with a 1-D constant-*JC* center manifold and corresponds to a deformed 1-D torus in the full 4-D phase space or the 3-D constant-*JC* phase space; this deformed 1-D torus is the reference periodic orbit itself. Yet, a 4-D center manifold is associated with a 3-D constant-*JC* center manifold and also includes deformed 2-D tori, or 2-tori, in the full 4-D phase space or the 3-D constant-*JC* phase space. A 1-D periodic orbit may exist along the surface of such a deformed 2-torus. In addition, a 1-D *quasi-periodic* trajectory can *fill out* the surface of a deformed 2-torus while theoretically remaining (bounded) in the vicinity of a reference periodic orbit for all finite time. In the spatial CR3BP, in addition to the types of motion discussed for the planar problem, a periodic or quasi-periodic trajectory may also exist along the surface of a deformed 3-D torus, or 3-torus—this motion is applicable to the case of a 6-D center manifold in the vicinity of a reference periodic orbit in the spatial problem. In particular, a quasi-periodic trajectory can fill out the surface of a deformed 3-torus. A 6-D center manifold is associated with a 5-D constant-*JC* center manifold and corresponds to deformed 3-tori in the full 6-D phase space or the 5-D constant-*JC* phase space.

The behavior of S/C trajectories in the center manifold associated with a reference periodic trajectory is explained by a fundamental property of *nearly*-integrable Hamiltonian systems like the CR3BP [85]. A *fully*-integrable Hamiltonian system is an

N-DOF system that can be expressed in terms of Hamilton's equations [82] and which also admits 2*N* constants of the motion that allow separability in those equations. That is, in addition to allowing the system to be "solvable," these constants of the motion must also be *isolating integrals*, which enable the motion to be separated into a system of *N*

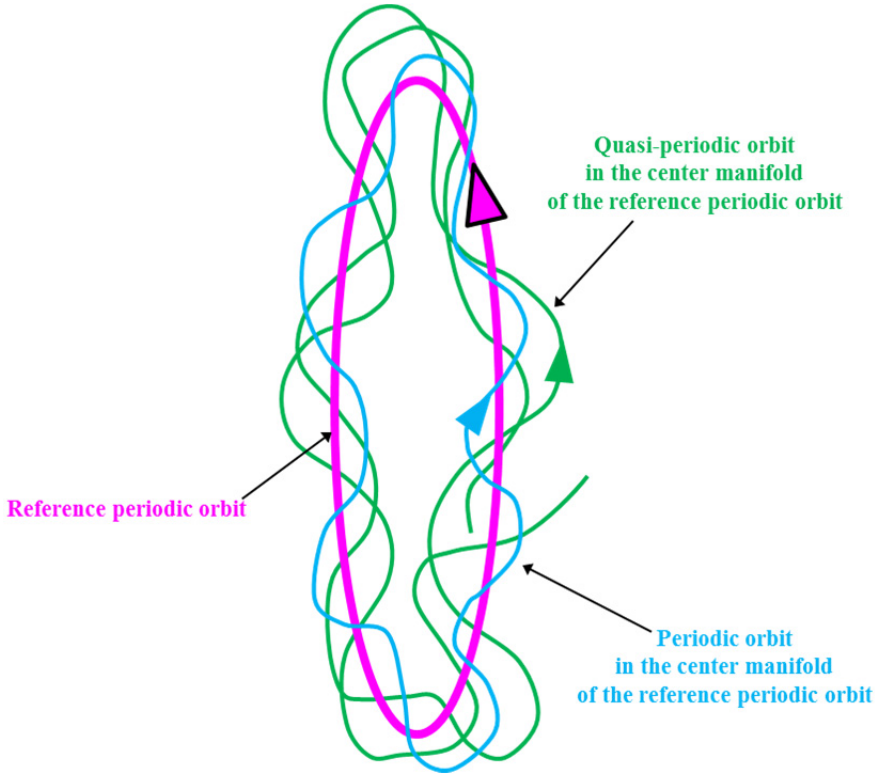

Figure 2.10. Notional center manifold of rotational motion in the vicinity of a reference periodic orbit at the same "energy" level

uncoupled harmonic oscillators in terms of some fundamental variables [85, 86]. Within this system of harmonic oscillators, the regular motion lies on the surfaces of *N*-dimensional invariant tori [21, 86]. Of course, the CR3BP as a Hamiltonian system is not fully integrable. Fortunately, this conservative, autonomous, phase-space-"volume"-preserving system is effectively a weak perturbation on a fully-integrable system and is therefore expected to contain both regular—i.e., periodic and quasi-periodic—and chaotic regions of its phase space. In the regular regions of the CR3BP, trajectories exist on the surface of deformed tori known as KAM tori, named for the Kolmogorov–Arnold–Moser (KAM) theory [68] that predicts their existence. Basically, *some* tori associated with a

fully-integrable system persist as invariant *deformed* tori in the nearly-integrable system under certain conditions. Thus, even though the Jacobi Constant is the only known constant of the motion in the CR3BP, the structure/order inherent in KAM tori implies that these tori are associated with trajectories that seem to behave *as if there were* an additional constant of the motion that is only applicable to certain phase space regions [14, 29].

2.4 Poincaré Maps

The current investigation relies heavily on a significant tool that has emerged within the last century for gaining insight into chaotic dynamical problems: the Poincaré surface of section, or Poincaré map [21], which is depicted in Figure 2.11. It is named for Henri Poincaré, who developed the concept in 1881 [28] and, amazingly, envisioned a surface of section for a chaotic system in 1892, even though it would not be practical to numerically generate such a map until the mid-twentieth century [14]. Under this concept, a continuous-time system maps to a lower-dimensional (lower-D) discrete-time

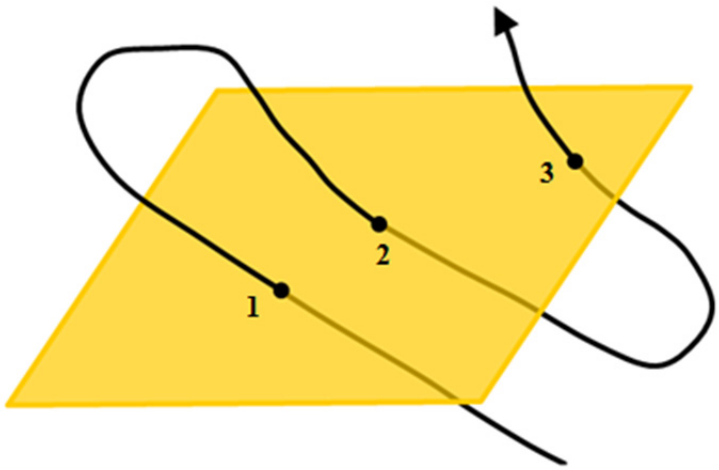

Figure 2.11. Notional Poincaré map

system by penetrating a surface called a hyperplane. The Poincaré map enables a simplification of the complex dynamics of a system like the CR3BP by reducing the dimension. By examining a map, an engineer may gain significant insight for trajectory

design by reducing the view of the design space to one "slice" at a time. According to Wiggins [21], the advantages of employing Poincaré maps to study systems expressed in terms of ordinary differential equations include: (1) "dimensional reduction" (at least one variable is eliminated); (2) "global dynamics" (Wiggins notes that the map display is "insightful and striking" in systems with less than or equal to four dimensions, which presumably means four phase space dimensions); and (3) "conceptual clarity" (concepts that are difficult to describe in the full-dimension system often translate to simpler terms in the reduced-dimension space of the Poincaré map).

A single trajectory in the planar CR3BP possesses two degrees of freedom (DOF) and a 4-D phase space, which is effectively reduced to a 3-D constant-*JC* space. A surface of section further reduces the dimension by one; thus, only a 2-D Poincaré map is required to analyze the planar CR3BP at a specified value of *JC*. It is straightforward to display a 2-D object on paper or on a computer screen. Not surprisingly, there are many examples of map-based analysis and design in the planar CR3BP (see Section 1.1.2).

In contrast to the planar CR3BP, a trajectory in the spatial CR3BP possesses three DOF and a 6-D phase space, which is similarly reduced to a 5-D constant-*JC* phase space. The surface of section still reduces this space by only one additional dimension; this implies that a 4-D Poincaré map is required to analyze the spatial CR3BP at a specified value of *JC*. A higher-D map obviously presents a visualization challenge because it exists in a space consisting of more dimensions than the 3-D "real world" with which a human being is intuitively familiar. In fact, there is no universally-accepted method for displaying a 4-D object for practical applications. Furthermore, the actual dynamical behavior exhibited on the 4-D map representing motion in a 3-DOF system differs from that of a 2-DOF system in more ways than just the increased number of dimensions required to represent it. Not only do maps that describe 3-DOF systems, e.g., the spatial CR3BP, contain more diverse and complex features than those of 2-DOF systems like the planar CR3BP but these higher-D maps also obey a *fundamentally* different topology [87, 88]. For example, in the spatial CR3BP, the deformed Kolmogorov–Arnold–Moser (KAM) tori [68] associated with quasi-periodic behavior (see Section 3.1.2 for further discussion) do *not* act as impenetrable boundaries that

divide the constant-*JC* phase space (and the map space) into separate regions, as such tori in the planar CR3BP [86, 89]. Consequently, intuition gained from 2-D maps can sometimes lead to conclusions that may be incorrect for 4-D maps.

Due to the challenges inherent in representing and interpreting the information displayed on 4-D maps, there are fewer examples of map-based analysis and design in the spatial CR3BP, most of which employ some form of reduction or projection to fewer dimensions (see again Section 1.1.2). As a recent example, Craig Davis and Howell use 3-D projections of 4-D periapsis Poincaré maps to illuminate the design space near Saturn in the Sun-Saturn CR3BP [34]. These 3-D plots depict the 3-D positions of successive periapses over a long-term propagation and are also color-coded based on the initial orientation of each trajectory with respect to Saturn.

Methods of representing *all four* dimensions associated with Poincaré maps for design in the spatial CR3BP are even rarer and typically involve adding some type of arrow or line segment to a point associated with a given map return. Paskowitz and Scheeres demonstrate a method using arrows to represent a 4-D initial periapsis Poincaré map for analysis in the limiting case of the spatial CR3BP, frequently termed the Hill three-body problem [2]. The base of each arrow indicates the 3-D position of the first periapsis along a particular trajectory, with the arrow length and orientation corresponding to the direction and magnitude of the velocity vector at that point. During the period of the present investigation, Vaquero and Howell [47, 48] and Vaquero [49] employ a modification of the Paskowitz and Scheeres [2] arrow method to design low-$\left|\overrightarrow{\Delta V}\right|$ transfers between resonant orbits in the Earth-Moon and Saturn-Titan spatial CR3BPs. The base of each arrow (on a 3-D grid) indicates three of the four dimensions on a Cartesian phase space Poincaré map (i.e., $x, \dot{x}, z$), while the orientation of the arrow in 3-D space represents the direction of the S/C velocity vector associated with a given map point. Furthermore, the length of the arrow completes the 4-D map representation by representing the fourth map coordinate (i.e., $\dot{z}$). Also during the period of the present investigation, Haapala and Howell [3, 4, 5] apply a "glyph" representation of 4-D map coordinates using a planar visualization where points representing map returns are augmented with line segments or "stick-figures." Under this method, two of the four

coordinates (e.g., x, z) of a Cartesian phase space 4-D Poincaré map are represented by a point on a 2-D grid, while the remaining two coordinates (e.g., $\dot{x}, \dot{z}$) are represented as vector components of a "stick-figure" originating from a given map point. Poincaré maps represented by this method are used to design low-$\left|\overrightarrow{\Delta V}\right|$ transfers in the Earth-Moon and Sun-Earth spatial CR3BPs. Moreover, this 4-D "glyph" method is extended to represent all six Cartesian coordinates (i.e., $x, y, z, \dot{x}, \dot{y}, \dot{z}$) associated with periapsis Poincaré maps by adding a second "stick-figure" attached to the first. These 6-D "stick-figures" are employed to locate periodic orbits and design a transfer in the Earth-Moon spatial CR3BP and also to analyze a comet capture in the Sun-Jupiter spatial CR3BP. In the Earth-Moon CR3BP analysis, the 6-D "stick-figures" are also color-coded based on the inclination of each periapse with respect to the Moon.

In the remainder of this section, key concepts related to 2-D-map-based trajectory analysis and mission design in the planar CR3BP are summarized. Of course, 4-D-map-based design in the spatial CR3BP, including a novel approach to such design, is the focus of the rest of this dissertation.

2.4.1 2-D-Map-Based Design in the Planar CR3BP

Traditional, 2-D Poincaré maps are effective for illuminating a "slice" of the phase space in the planar CR3BP in which it is assumed that the trajectories begin in, and remain in, the *x*-*y* plane of the primary bodies. The map display can provide visual cues that enable trajectory analysis/design. An example of such a 2-D Poincaré map is plotted in Figure 2.12 for the planar version of the Copenhagen CR3BP of equal primary masses (mass ratio μ = 0.5) [1, 29], which was investigated using maps by Hénon in the 1960s. The hyperplane for this map is defined in terms of Cartesian phase space coordinates such that $y = 0$ and $\dot{y} > 0$. Because the map points are generated by only the returns resulting from crossings from one particular side of the hyperplane to the other (i.e., $\dot{y} > 0$ crossings in this case), this map is a one-sided map. If the map were two-sided, it would include points generated by all returns (i.e., both $\dot{y} < 0$ and $\dot{y} > 0$ crossings). An advantage of displaying a one-sided, rather than a two-sided, map is that each 2-D map point uniquely represents a 4-D state in the full phase space of the planar problem

without sign ambiguity in the "missing" coordinate. This one-to-one mapping is based on the specified "energy" level of the map, which is the *JC* value equal to 3.5 in this

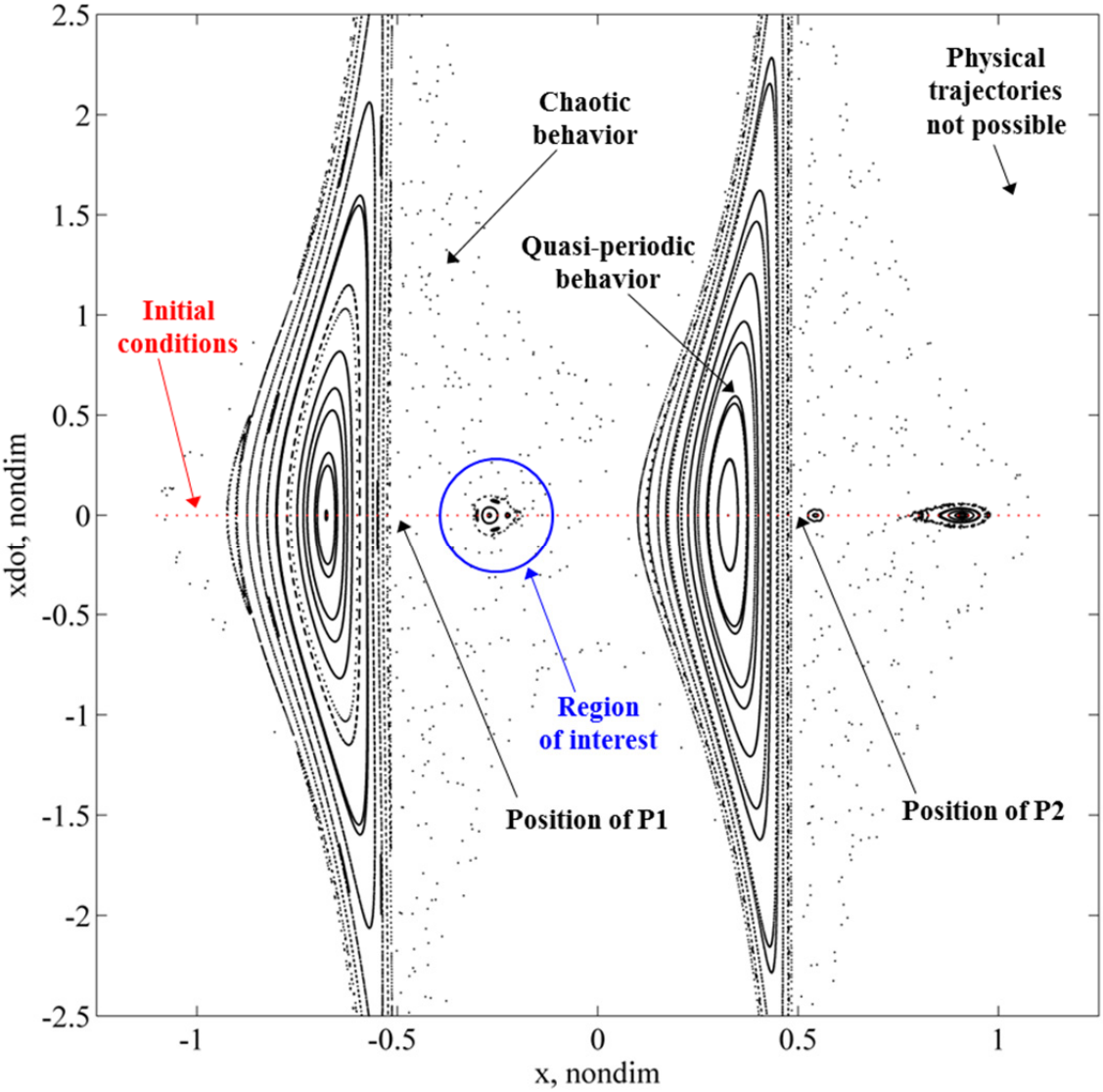

Figure 2.12. 2-D Poincaré map of returns generated by 87 planar Copenhagen problem trajectories over 159 primary revolutions; hyperplane $y = 0$, side $\dot{y} > 0$, $JC = 3.5$

example. Using equation (2.2), the phase space coordinates x and $\dot{x}$ of a particular map point on the hyperplane $y = 0$ can be associated with the "missing" $\dot{y}$ coordinate not explicitly represented. The *JC* value determines the *magnitude* of $\dot{y}$ at each x-$\dot{x}$ map point, while the *sign* of $\dot{y}$ must be positive based on the one-sided map definition in this

example. Note that the relative scaling of the two axes of this 2-D map is such that the difference between the values at the limits of velocity coordinate $\dot{x}$ is twice the difference between the values at the limits of position coordinate x. This scaling is employed in order to better display the qualitative shape of map features appearing on a reduced-dimension phase space measured by two different nondimensional units (position and velocity).

The 56,312 map returns plotted in Figure 2.12 are generated by eighty-seven different Copenhagen problem trajectories. The initial conditions for these trajectories are the map returns plotted in red on the map; they are seeded based on a 1-D grid of eight-seven points along the x-axis of the map, spaced by 0.025 nondimensional distance units. The only exception to this seeding criterion is the fact that two points are removed at the x-axis locations associated with the positions of the primaries P_1 and P_2, which are the locations of the singularities in the CR3BP. Since the x-axis of the map space is defined by values of $\dot{x}$ equal to zero, each initial condition (each first map return) is associated with a perpendicular crossing of the x-axis in the planar x-y configuration space. Sometimes, an initial condition map—i.e., a map of only initial conditions—is useful for trajectory design (see the design example in Section 4.3); however, most often a map generated by subsequent map returns is employed. It is important to emphasize that subsequent map returns are traceable to the chosen set of initial conditions. Certain restricted sets of initial conditions (like in this example) are useful for revealing *some* of the behavior on a given map; yet, they by no means reveal *all* of the possible behavior. In the present effort, map returns (crossings of a hyperplane by a numerically-integrated trajectory) are determined using the *event* property of the built-in *ode113* function in MATLAB®. In the example displayed in Figure 2.12, subsequent map returns are generated in forward time by the $y = 0$ and $\dot{y} > 0$ crossings of the eighty-seven trajectories for the following 1,000 nondimensional units of time, or approximately $159 \times 2\pi = 159$ primary system revolutions. There is a notable exception to this propagation time span: trajectories that pass closer than 1×10^{-3} nondimensional distance units from the location of either primary body are terminated when they reach that distance. The map returns associated with the trajectory leading up to the termination point are still

plotted. This trajectory termination method is a useful technique for excluding portions of trajectories possessing large numerical integration errors (evident by a large change in the calculated *JC* value along a trajectory) typically associated with paths very close to the primary body singularities. In realistic CR3BP systems considered for S/C mission design, the physical surface of the primary body frequently serves as an appropriate termination point, not only to avoid excessive numerical error but also because impacting a primary body is often an undesirable mission outcome in spaceflight.

It is evident upon visual inspection of the Poincaré map plotted in Figure 2.12 that this phase space "slice" associated with the specified hyperplane and "energy" level includes qualitatively different types of behavior. In the ordered regions on the "left" side of each primary body position, map returns appear along the shapes of "islands"—apparent closed "curves" in the phase space, many of which are concentric. These regions are associated with regular behavior. The apparent "curves" themselves are generated by quasi-periodic trajectories, with individual map points filling out the curved 1-D shapes over an infinite time span. Moreover, periodic behavior is expected to exist in the vicinity of these curves. As explained in the previous section, in the planar CR3BP, a 4-D center manifold in the vicinity of a reference periodic orbit is associated with a 3-D constant-*JC* center manifold. This 3-D manifold includes deformed 2-tori, and a quasi-periodic trajectory can fill out the surface of a deformed 2-torus while theoretically remaining (bounded) in the vicinity of a reference periodic orbit for all finite time. On the reduced-dimension map space, the cross-section of a 3-D constant-*JC* center manifold is a 2-D ordered region, an *area* containing apparent 1-D closed curves/contours. Each 1-D closed "curve" (or set of closed "curves") is the cross-section of a deformed 2-torus associated with a particular quasi-periodic trajectory. A strikingly different type of behavior is also apparent on the map displayed in Figure 2.12. On the "right" side of each primary, most returns fill out a "sea" in a seemingly random scattering. The appearance of this "sea" is the hallmark of chaos, where the future state along a given trajectory is extremely sensitive to the initial condition—making the motion effectively unpredictable over more than a brief span of time. Yet, within the mostly-chaotic regions, there are also small regions of regular behavior, such as the region of interest indicated by

the blue circle. Additionally, note that certain areas of the map display appear completely blank. No map returns exist in these areas because physical trajectories are not possible in these regions of the phase space. At the specified "energy" level of the map, there are certain position and velocity combinations that are not possible at this "energy" level; these restrictions in the 3-D constant-*JC* phase space are related to the restrictions in the 2-D position space that result in the ZVCs. In fact, the "energy" level examined in this example is higher than the "energy" level associated with the L_1 libration point and slightly lower than that of the L_2 point (see ahead to the ZVCs plotted in Figure 2.14(a)). As a result, any trajectory originating in the "interior" region of the primary system—which is the region associated with the map plotted in Figure 2.12—must remain in that region for all time.

The design objective in the current example is to obtain an estimate for a *linearly stable* periodic trajectory in the vicinity of P_1 that is *prograde* in the rotating frame of the CR3BP. That is, it is desired for the periodic trajectory in the full 4-D phase space to consist of marginally stable fixed points of the type 2-D center × 2-D center based on the method of assessing linear stability described in Section 2.2.1. In the 2-D Poincaré map space, such a periodic orbit is associated with one or more fixed points of the type 2-D center. Each fixed point behaves like a marginally stable equilibrium point in the reduced-dimension system associated with the map. Furthermore, a prograde trajectory about P_1 is defined to have the same direction of motion in the rotating frame as the prograde direction of P_2 in the P_1-centric inertial frame. Based on these design requirements, the region of interest circled in blue is identified. This small region of the phase space surrounded by a chaotic "sea" appears to contain regular behavior (associated with both quasi-periodic and periodic trajectories) formed by returns on the "left," P_1 "half" of the map. Moreover, because the one-sided map includes only returns with $\dot{y} > 0$, the region of interest circled in blue is associated with crossings of the hyperplane by trajectories that are prograde (in the rotating frame) with respect to P_1 at the time of the crossings.

A zoomed-in view of the region of interest for design appears in Figure 2.13 with areas associated with either quasi-periodic or chaotic behavior noted. Initial conditions

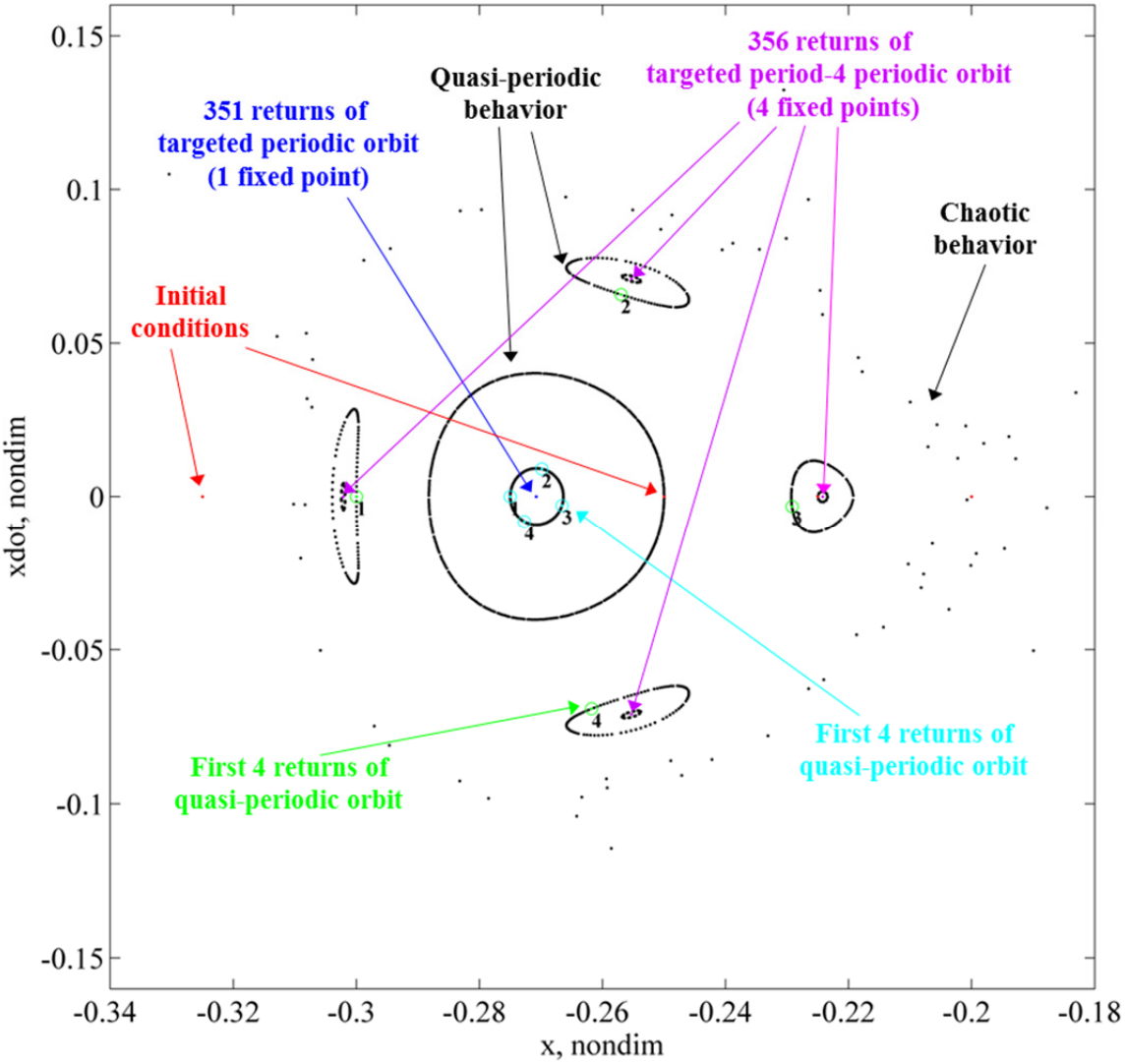

Figure 2.13. Zoomed-in view of 2-D Poincaré map region of interest

are again plotted in red except for two sets of initial conditions associated with two different quasi-periodic trajectories. For these two trajectories, the first four numbered map returns are plotted in cyan and green, respectively, and are also highlighted using small circles of the same color. The cyan returns are associated with a quasi-periodic trajectory generating points that appear to fill out the surface of a central "island." The

green returns are generated by a different quasi-periodic trajectory with returns filling out an "island chain" of four different "island" structures. All "island" structures plotted in Figure 2.13 belong to a constant-*JC* center manifold associated with a reference periodic orbit (in the rotating frame) generating a single linearly stable fixed point of type 2-D center located inside the concentric, central "island" contours. Also belonging to that constant-*JC* center manifold is a different periodic orbit possessing the same type of stability and which generates *four* fixed point map returns located at the "centers" of the "island chain" (of course, each of the four individual "island" structures in the chain can also be considered to belong to an individual constant-*JC* center manifold associated with each of the four fixed points). Not apparent in Figure 2.13 is the fact that four fixed points associated with an *unstable* periodic orbit are also expected to exist in the "chains" surrounding the central "island" region. Each of the four unstable fixed points is predicted to be located between two "island" structures associated with quasi-periodic and stable periodic behavior; thus, the four stable and four unstable fixed points alternate in the map space surrounding the central "island" region [14]. These unstable fixed points behave as 2-D saddle equilibrium points in the reduced-dimension map space; their precise locations are more difficult to visually estimate because they are not surrounded by concentric "islands." Note that, in the planar CR3BP—a nearly-integrable, 2-DOF Hamiltonian system (see previous section)—invariant deformed 2-tori divide the 3-D constant-*JC* phase space into separate regions. Accordingly, in the reduced-dimension phase space of the Poincaré map plotted in Figure 2.13, the 1-D cross-sections of those 2-tori divide the 2-D map area. This is an important property, which does *not* extend to the spatial CR3BP. In the planar problem, the fact that deformed 2-tori act as boundaries in the phase space implies that a trajectory generating a map return inside a closed "curve" on the map must remain inside that region for all time. Furthermore, if a regular region of the map space consists of multiple, concentric closed "curves," with each "curve" bounding a region inside it, then the smallest possible "curve" could bound an infinitesimally small region surrounding a single point on the 2-D map. This topological analysis predicts that stable fixed points associated with periodic orbits exist at the "center" of "island" structures. In fact, the concentric "curves" provide a

straightforward method for obtaining a visual estimate for a fixed point associated with a periodic orbit; in the current example, the approximate "center" of an "island" constitutes the estimate for the 2-D x-$\dot{x}$ map location of the fixed point map return, which can be uniquely associated with a state in the full 4-D phase space, as described earlier in this section. This visual estimate may then be used to initiate a differential corrections (targeting) process of the type described in Section 2.2 to obtain a precise periodic solution to within a satisfactory convergence criterion/tolerance.

As a reference for targeting the periodic orbit (in the rotating frame) associated with the fixed point at the "center" of the central "island" region appearing in Figure 2.13, the quasi-periodic trajectory generating the four cyan returns in that same figure is plotted in the barycentric rotating frame and the P_1-centric inertial frame in Figure 2.14 for the time span associated with the Poincaré map: approximately 159 primary revolutions. Note that the barycenter in the Copenhagen problem is collocated with the L_1 libration point. Also plotted in the rotating view in Figure 2.14(a) are the ZVCs associated with the JC value equal to 3.5 for the planar Copenhagen problem; these ZVCs are the x-y planar (z = 0) cross-section of the ZVSs. The hyperplane $y = 0$ is also displayed. In the P_1-centric inertial view, the motion of P_2 in its circular orbit (about P_1) is also plotted. Clearly, the trajectory plotted in cyan in Figure 2.14 is a prograde orbit about P_1 in both frames, yet it is not periodic in either frame. The estimate for the linearly stable periodic orbit associated with the fixed point at the "center" of the "island" contour appearing in Figure 2.13, which is formed by the quasi-periodic trajectory plotted in Figure 2.14, is obtained by guessing that the fixed point exists at a perpendicular crossing of the $y = 0$ hyperplane (with $\dot{x} = 0$) at the approximate "center" of the contour at $x = -0.27$. This location on the x-axis of the 2-D Poincaré map is associated with $\dot{y} = 1.489774273391047$ by equation (2.2). The 4-D estimated state is then used to initiate a single shooting periodicity targeting scheme (see Section 2.2), which is aided by an estimate for the time span of the periodic orbit. This time span estimate is obtained by noting the nondimensional time span between the first and second map returns plotted in cyan in Figure 2.13, which is roughly equal to 2.869. The differential corrections process yields a trajectory—at the

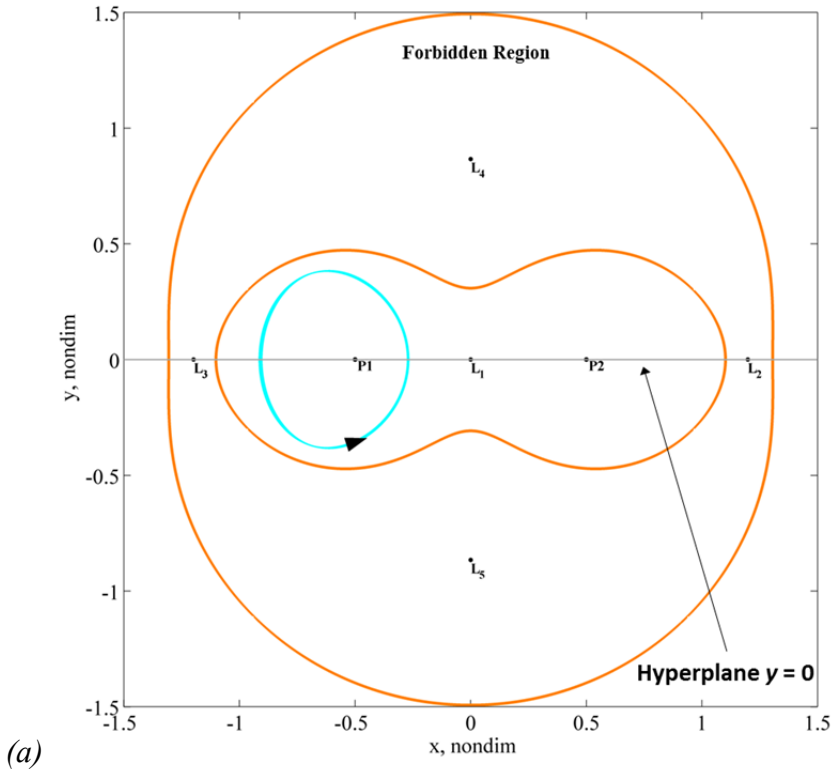

(a)

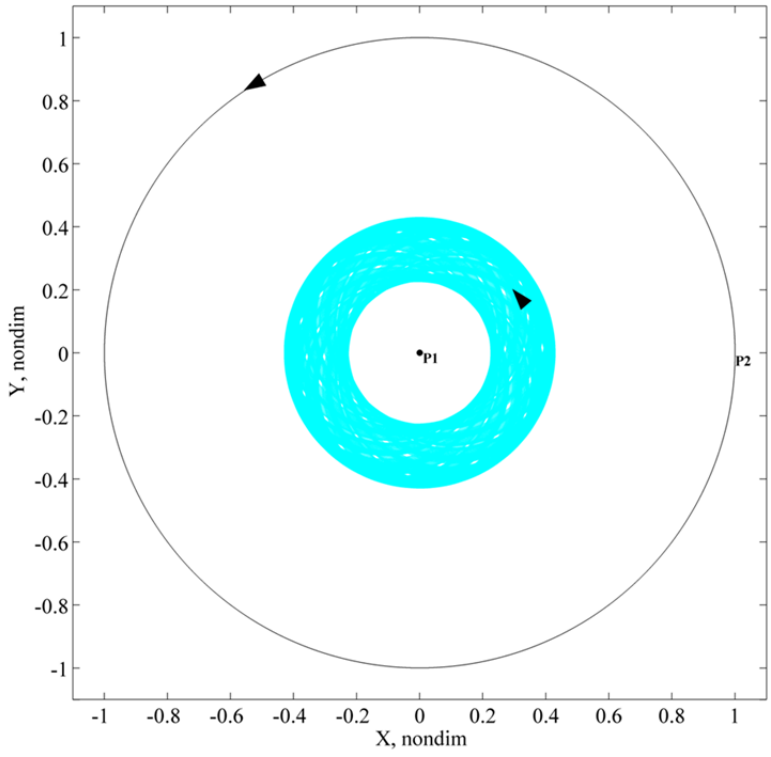

(b)

Figure 2.14. Quasi-periodic, planar Copenhagen problem trajectory over 159 primary revolutions: rotating (*a*) and P_1-centric inertial (*b*) views

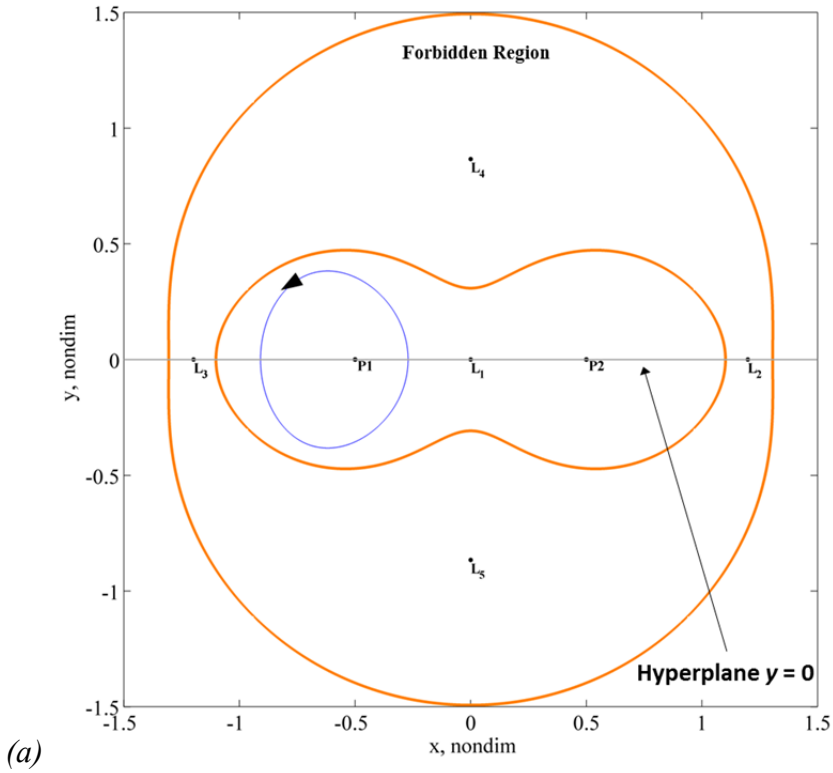

(a)

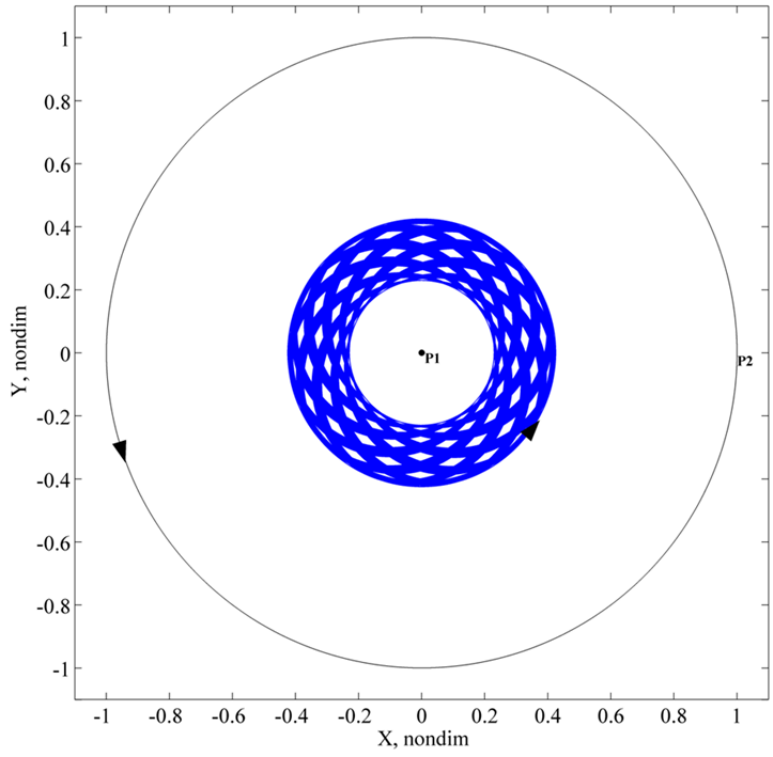

(b)

Figure 2.15. Targeted periodic, planar Copenhagen problem trajectory over 159 primary revolutions: rotating (*a*) and P_1-centric inertial (*b*) views

same "energy" level as the map and with an initial condition associated with a crossing of the map hyperplane—converged to satisfactory periodicity; it is plotted in blue in the barycentric rotating view and the P_1-centric inertial view in Figure 2.15 for 159 primary revolutions. A total of 351 map returns over 159 primary revolutions, associated with 350 orbit periods of the periodic orbit, are plotted in blue in Figure 2.13. As expected, the single fixed point associated with this period-one periodic orbit is located at what is apparently the "center" of the central "island" region. The targeting process actually converges on a solution over just one orbit period, equal to roughly 2.855 in nondimensional time, or 0.454 primary revolutions. The periodicity accuracy is such that the error after one orbit period is only 3.20×10^{-14} in nondimensional position and 1.75×10^{-13} in nondimensional velocity. After almost the full 159-primary-revolution time span associated with the Poincaré map in Figure 2.13, the error after 350 orbit periods is still quite small: 4.13×10^{-11} in nondimensional position and 2.64×10^{-10} in nondimensional velocity. Not surprisingly, the orbit plotted in Figure 2.15 appears periodic in the rotating frame even over the full 159-primary-revolution time span. Note that the trajectory is not periodic in the inertial frame—nor is it expected to be.

A similar single shooting targeted process is employed to satisfactorily converge on a period-four periodic orbit associated with four fixed points located at the "centers" of the "island chain" structures appearing in Figure 2.13. For insight, the quasi-periodic trajectory generating the four green returns filling out four contours in the "island chain" is plotted in the barycentric rotating view in Figure 2.16(a) for 159 primary revolutions. The rotating view of the converged solution for the associated period-four periodic orbit appears in Figure 2.16(b). Even though the targeting process converges on a solution over one orbit period, roughly equal to 11.236 in nondimensional time (1.79 primary revolutions), the orbit appears periodic in the rotating view over the full 159-primary-revolution time span. Corresponding to this fact, a total of 356 map returns over 159 primary revolutions, associated with 88.75 orbit periods of the period-four orbit, are plotted in purple in Figure 2.13. The returns appear as four fixed points. Note that the period of this period-four orbit is slightly less than four (3.94) times the period of the

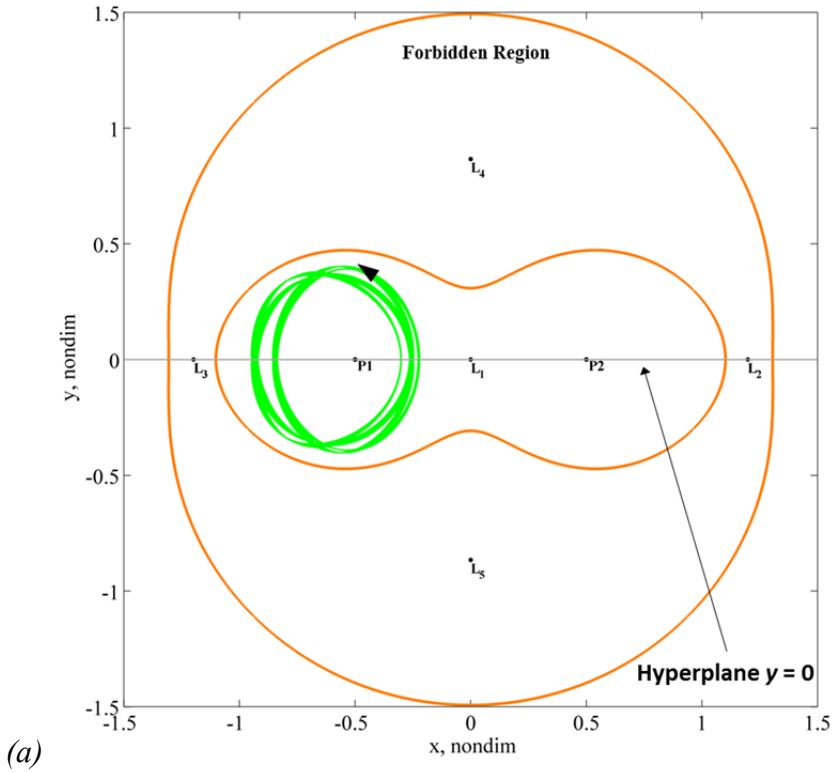

(a)

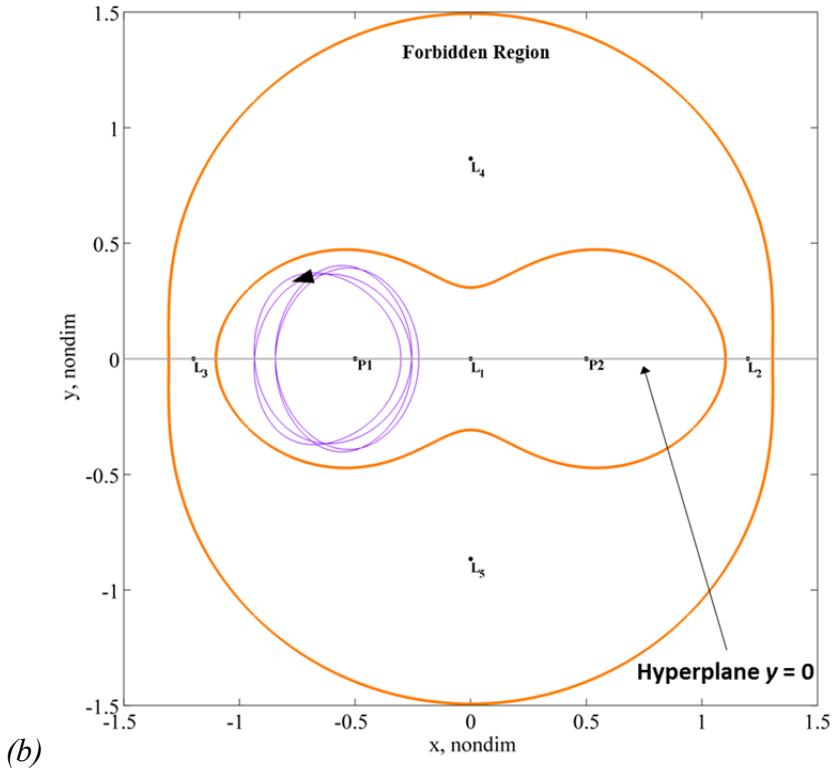

(b)

Figure 2.16. Rotating view of quasi-periodic (*a*) and targeted period-4 periodic (*b*) planar Copenhagen problem trajectories over 159 primary revolutions

period-one orbit plotted in Figure 2.15. Such an approximate ratio of the periods of these two periodic orbits is predictable based on the "island" structures observed on the Poincaré map in this design example. The central "island" region and the chain of four "island" structures in Figure 2.13 effectively "point" to each other. As an aside, such "island" structures on 2-D Poincaré maps can also, in some ways, "point" to the existence of different structures on maps associated with different "energy" values. For instance, structures of "island chains" on 2-D maps for the planar CR3BP often indicate the approximate map location of the bifurcation that formed such features at a different "energy" level.

Expanding on the concepts associated with the simplistic design objective in the preceding example, a 2-D-map-based trajectory design process typical requires that the map-based designer choose a reasonable "energy" level and map hyperplane that is expected to reveal a 2-D "slice" of the planar CR3BP phase space relevant to a particular mission design objective. After generating map returns based on a set of initial conditions, a region of interest is identified based on some type of visual cue(s). An estimate for desirable qualitative behavior is then obtained through visual inspection of the Poincaré map; the estimate may then be used to initiate an automated process such as a targeting scheme to achieve a precise solution to within a desired tolerance.

The mission objective in a particular map-based design process could require a map-based designer to locate periodic or quasi-periodic behavior on a map; yet, more complex types of design are also possible, most notably those involving various types of S/C transfer maneuvers. Figure 2.17 notionally depicts two examples of design spaces that can be utilized in transfer design based on 2-D Poincaré maps. The first, displayed in Figure 2.17(a), involves overlapping regions in the same 2-D map view. One possibility is that both regions are actually associated with the same Poincaré map. That is, the returns in both regions exist on the same hyperplane (e.g., $y = 0$ and $\dot{y} > 0$) as well as at the same "energy" level. Yet, these two regions could contain map returns that are generated based on different sets of initial conditions associated with different types of behavior relevant to a particular S/C mission. For instance, the returns in one region

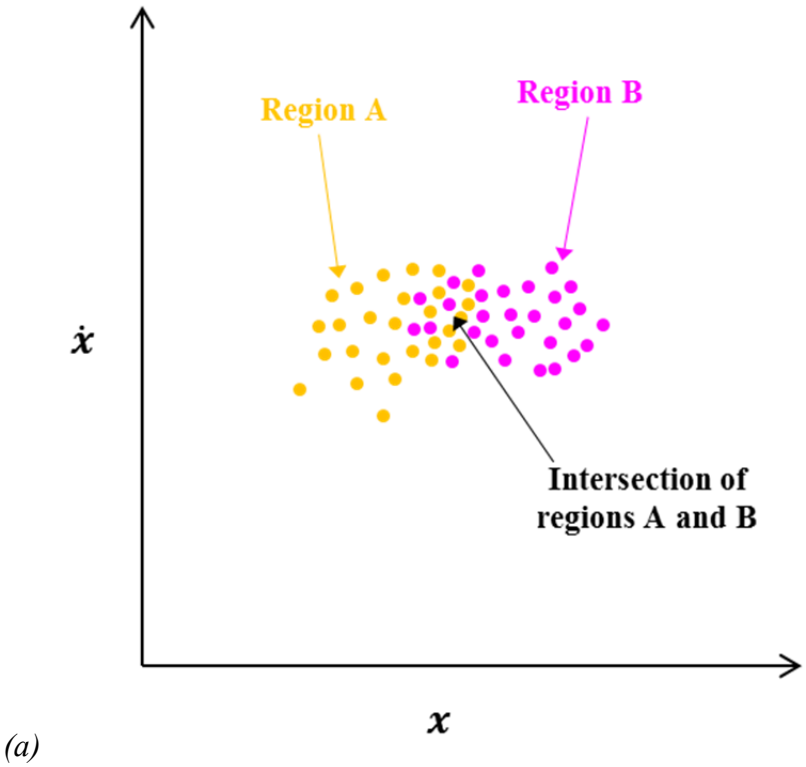

(a)

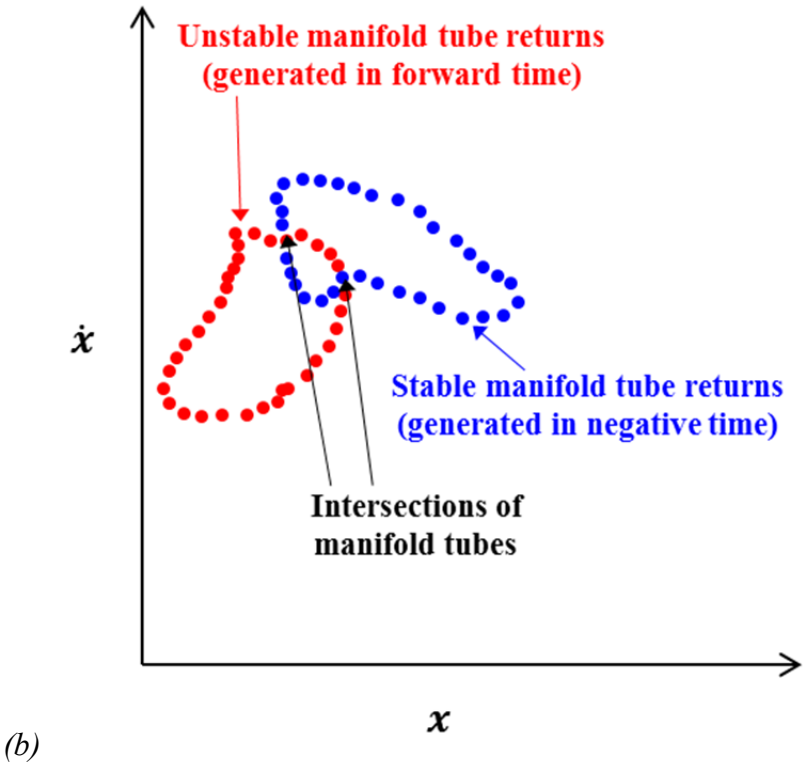

(b)

Figure 2.17. Notional 2-D-map-based design spaces involving intersecting regions (*a*) or intersecting manifold structures (*b*)

might be generated by trajectories propagated in forward time while the other region's returns could be generated in negative time. If both regions exist on the same hyperplane at the same "energy" level, then a map point selected from within the intersection of the two regions would be associated with a path that connects the two regions and their associated behaviors (in either forward or negative time). On the other hand, the generic example depicted in Figure 2.17(a) is also applicable to design spaces involving Poincaré maps at two different "energy" levels overlaid in the same map view associated with the same hyperplane. In cases involving maps at different values of *JC*, intersections between overlapping regions—or even between overlapping points from different regions—do not represent continuous S/C paths between the two regions/behaviors. For a S/C to actually follow a path between the two regions possessing an *apparent* intersection in the 2-D map view, an adjustment to the "energy" level is required. For instance, in the notional example displayed in Figure 2.17(a), assuming the map hyperplane is defined such that $y = 0$ and $\dot{y} > 0$, an "energy"-raising or "energy"-lowering $\left|\overrightarrow{\Delta V}\right|$ transfer maneuver would be required to adjust $\dot{y}$ (the "missing" coordinate) so as to achieve the correct value of *JC*—based on equation (2.2)—before and after the position along a path associated with the apparent intersection.

Another example of a design space utilized in map-based design in the CR3BP involves overlapping 1-D manifold structures, as depicted in Figure 2.17(b). A typical case involves one manifold structure generated in forward time and the other generated in negative time. The forward-time structure is the cross-section of the 2-D unstable manifold tube emanating from an unstable periodic orbit. The negative-time structure is the cross-section of the 2-D stable manifold emanating (in negative time) from another unstable periodic orbit. As with the case of overlapping regions displayed in Figure 2.17(a), the two manifold structures could be formed by returns generated on the same map hyperplane and at the same "energy" level. In that case, a visually-obtained estimate for an intersection between the manifold structures could be used to initiate a targeting process to determine a low-cost, perhaps even a theoretically zero-$\left|\overrightarrow{\Delta V}\right|$ path between two periodic orbits. On the other hand, intersections between manifold structures overlaid from two different "energy" levels in the same view could only provide a reasonable

guess for the negative-time and forward-time paths before and after a required transfer maneuver to achieve an orbit transfer between the two periodic orbits. Note that, similar to the properties of the "island" contours associated with a center manifold on a 2-D Poincaré map, the cross-section of a 2-D stable or unstable manifold tube is a 1-D structure that divides the 2-D area of the map into separate regions. This property, which does *not* extend to the spatial CR3BP, is useful for predicting the motion of trajectories that are carried by the dynamical "flow" associated with the inside of a manifold tube in the 4-D phase space (and 3-D constant-*JC* phase space).

As a final note, there are other types of design spaces utilized for 2-D-map-based trajectory design in the planar CR3BP. Variations on, or combinations of, the examples depicted in Figures 2.17(a) and 2.17(b) are commonly encountered. For instance, Poincaré maps involving a region overlapping/overlaid on a manifold structure—or some other type of 1-D structure (associated with a 2-D surface in the full-dimension space)—are often useful for mission design. Also, map returns associated with single trajectories generating one or more individual points are often overlaid on maps containing 2-D regions or 1-D structures relevant to the design objective. In general, the choice of map formulation, as well as the type of design space viewed on a map—or on overlaid maps—is problem dependent. There is no "one-size-fits-all" approach to S/C trajectory design, particularly in the complex design space of the CR3BP, even in the planar case.

2.5 Higher-Dimensional Realization

The challenges inherent in representing and exploiting information displayed on 4-D Poincaré maps in the present investigation can be considered in the context of multi-dimensional data analysis. Two broad categories of interest are (1) data visualization and (2) model reduction.

In the area of multi-dimensional data visualization, various methods seek to overcome the "information overload" associated with attempting to visualize systems or problems with many dimensions. The goal of such techniques is to support decision-making, often involving the optimization of many different cost/objective functions. Examples are provided by Eddy and Lewis (cloud visualization) [90], Wegman (parallel coordinates)

[91], Weaver (cross-filtered views) [92], Chiu and Bloebaum (hyper-radial visualization) [93], and Zhang, Simpson, et al. (interactive multi-scale visualization) [94].

Rather than attempting to visualize all the dimensions of a multi-dimensional problem, an alternative strategy is the reduction of the problem to fewer dimensions, essentially by projecting the higher-D data onto a lower-D model that is still representative of the design space relevant to decision-making. Examples of model reduction methods are given by Willcox and Peraire (proper orthogonal decomposition) [95] and Ribeiro, Sechi, and Biscaia (weighted residuals) [96].

In the current investigation, the full 6-D phase space of the spatial CR3BP is effectively *reduced* to a 4-D Poincaré map space representing a "slice" of the design space relevant to a particular S/C mission objective. Due to the challenges inherent in representing and interpreting the information displayed on 4-D maps, most examples of map-based analysis and design in the spatial CR3BP in the literature employ some form of *further reduction or projection* to fewer dimensions (see Sections 1.1.2 and 2.4). Methods of *visualizing all four dimensions* on 4-D maps for design in the spatial CR3BP are rare and typically involve adding some type of arrow or line segment to a point associated with a given map return. The strategy in this investigation is 4-D visualization—rather than further model reduction. The choice of the space-plus-color method (see Section 3.1) has the potential to maximize the ability of the human eye to discern all four dimensions on a 4-D map consisting of many points even when zoomed out.

2.6 Sampling

Sampling methods used in the current investigation for seeding S/C initial conditions to generate Poincaré map returns are relatively unsophisticated. Yet, the power of a Poincaré map as a visual tool is that a simple sampling process can illuminate a portion of the complex CR3BP that allows a designer to accomplish trajectory design through a methodical process. The sampling method in each design example is problem-dependent. The goal of the process is not necessarily a random sampling of all possible initial

conditions in a design space but rather an adequate sampling of the type of dynamical "flow" that may be relevant to a particular mission design objective.

Descriptions of various types of sampling strategies are given by Cochran [97] and Levy and Lemeshow [98]. In the current investigation, the sampling strategy for seeding initial conditions on a map can loosely be considered a type of systematic sampling, where S/C states are selected according to an evenly-spaced grid in one or more dimensions based on the first selected state. Although the first state is not *randomly* selected, it is selected somewhat arbitrarily based the edge(s) of a particular region of interest on a Poincaré map. For a 4-D map at a given "energy" value, the grid of states could be a 4-D grid filling the entire region of the map in all four dimensions—creating a kind of "full factorial" experiment [99]—or the grid could be formed by varying only some of the available dimensions. In many cases, all states on a grid are selected to be the initial conditions. However, in some examples, a smaller subset of the states is chosen based on a simple random sampling. For example, a specified grid could contain 100,000 states, but only 500 of those states are randomly selected to be initial conditions that are actually propagated to generate map returns. This method is useful when a fine grid is desired to ensure that "narrow" portions of the design space are represented in a sample yet it would not be computational efficient to propagate every state on the fine grid. The selection of the smaller subset of the grid of states is based on a pseudorandom sampling using the built-in *randi* function in MATLAB®.

In broader terms, various steps in the 4-D-Poincaré-map-based design process employed in this investigation (see Section 3.3) can be considered part of a "sampling" sequence, with the sampling strategy employed at each step heavily influencing what region of the design space is illuminated and under consideration in later steps. The selection of the Poincaré surface of section—e.g., the hyperplane location and the "energy" value—is the initial means by which the dynamical "flow" is sampled in order to isolate certain behavior of interest. Next, once the map is defined, a grid of initial conditions may be seeded, thus sampling within a subset of the design space relevant to the map. Finally, various visual map filtering processes are a type of human/visual sampling, with the goal of focusing on a particular region of the map from which a

reasonable design estimate may be obtained visually. Each step in the design process likely involves assumptions, subjective decisions, and various problem-dependent design preferences. Consequently, each design step "biases" the final result.

2.7 Trajectory Optimization

The optimization processes employed in this investigation seek *locally*-optimal results rather than global optima. The cost/objective function to be minimized is the total required $\left|\overrightarrow{\Delta V}\right|$ for a given S/C transfer maneuver sequence. During optimization, the S/C trajectory is constrained to have: (1) continuity in position at all patch points, (2) continuity in velocity at all patch points except those patch points associated with maneuvers, and (3) continuity in the direction of time, i.e., propagation time cannot change directions at any patch point. Additional requirements are problem-dependent. For instance, the trajectory may be required to have particular starting and ending reference states; in that case, the ending state is constrained explicitly in the optimization algorithm, while the starting state is prescribed implicitly using a fixed initial state. Furthermore, the total time-of-flight could be constrained to be no greater than, or perhaps equal to, a particular duration.

Methods for trajectory optimization can be divided into two classes: (1) parameter optimization, geared towards minimizing a cost function based on varying a finite number of parameters while obeying certain constraints and (2) functional optimization based on the calculus of variations [100] and optimal control theory. A comparison of the two methods, with a focus on optimal control, is provided by Longuski, Guzmán, and Prussing [101]. Optimization in the present investigation can be considered a type of parameter optimization.

The constrained, nonlinear optimization process in the current investigation is numerical and is accomplished using the *fmincon* function in the MATLAB® Optimization Toolbox, with continuity constraints incorporated by specifying a nonlinear constraint function based on the same numerical integration process employed for trajectory targeting (see Section 2.2). The gradient of the nonlinear constraints vector $\vec{F}$ with respect to the design variables $\vec{X}$ (e.g., the states associated with patch points) is

determined based on the elements of the STM used also for targeting. The gradient matrix of values supplied to *fmincon* is the transpose of the Jacobian matrix,

$$Grad\ \vec{F} = \left(\frac{\partial \vec{F}}{\partial \vec{X}}\right)^T \tag{2.25}$$

The transpose is required here based on how the inputs are defined in *fmincon*. Similarly, the supplied gradient of the scalar cost function C with respect to the design variables is the column vector,

$$Grad\ C\ = \left(\frac{\partial C}{\partial \vec{X}}\right)^T \tag{2.26}$$

where C is the total required $\left|\overrightarrow{\Delta V}\right|$ based on the velocity discontinuities at the appropriate patch points. Note that in the case of more complex nonlinear constraint functions, such as the requirement that a S/C trajectory pass no closer than a specified distance from a primary body, the gradient is estimated numerically by *fmincon.* Since this estimation process is computationally intensive, such constraints are not normally applied unless a trajectory resulting from optimization impacts a primary otherwise.

The specific nonlinear programming algorithm employed using *fmincon* is the "interior-point" algorithm [102, 103]. This choice is based on the recommendation in the MATLAB® documentation that this algorithm be used first, switching to other options if interior-point fails; the reason given is that it "handles large, sparse problems, as well as small dense problems" [71]. The tolerance for satisfying constraints is set equal to 10^{-11}, and the optimality tolerance (the function termination tolerance) is the default setting equal to 10^{-6}. Optimality is defined according to the Karush-Kuhn-Tucker (KKT) conditions; thus, *both the cost function and the constraints* are factors in determining what is considered a local optimum. In the current investigation, optimization is accomplished for S/C trajectories in the Earth-Moon and Uranus-Titania systems; it is observed that an optimality termination tolerance setting of 10^{-6} implies, roughly, that further reductions in $\left|\overrightarrow{\Delta V}\right|$ on the order of mm/s are considered negligible and thus a local minimum is considered reached. Note that the selected constraints tolerance is five orders of magnitude smaller than the selected optimality tolerance. Though not attempted in the current investigation, there may be some value in applying

scaling/weighting to the values in constraints vector $\vec{F}$ so as to allow the tolerance settings for both constraints and optimality to have the same order of magnitude.

In the present investigation, the time required to perform a trajectory optimization process is anywhere from roughly one minute to several hours (elapsed time in MATLAB® Version: 7.14.0.739 (R2012a); benchmark: 0.0600, 0.0637, 0.0741, 0.1641, 0.2727, 0.7146).

2.8 Transitions to Other Dynamical Models

In this investigation, a S/C trajectory in the CR3BP is often transitioned to another dynamical model. The other dynamical model could be a primary-centric 2BP for the purpose of interpreting a S/C state or an entire two-body path in terms of two-body orbital elements. On the other hand, the transition could be to a higher-fidelity, ephemeris-based model, which is a more accurate simulation of the "real world."

2.8.1 The Two-Body Model

One particular two-body problem that is relevant to the present investigation is that of the primary system in the CR3BP, in which the two primaries revolve in perfectly circular planar motion about their system barycenter at a constant mean motion $N = \sqrt{Gm^*/l^{*3}}$, where l^* is the distance between the primaries, m^* is the total system mass, and G is the universal gravitational constant (see Section 2.1). However, it is also useful to consider a *restricted* 2BP in which one body is the S/C, a negligibly small mass, and the other body is one of the two primaries having a significantly larger mass. The gravitational influence of the other primary is ignored. In this case, the nondimensional equations of motion, in scalar, second-order form, for the vector $\vec{s} = X\hat{X} + Y\hat{Y} + Z\hat{Z}$ locating spacecraft *S* in the P_i –centric inertial frame (*X,Y,Z*) for the P_i –centric 2BP are,

$$\ddot{X} = -\frac{X}{d^3}$$
$$\ddot{Y} = -\frac{Y}{d^3} \tag{2.27}$$
$$\ddot{Z} = -\frac{Z}{d^3}$$

where $d = \sqrt{X^2 + Y^2 + Z^2}$. However, it is critically important to clarify what type of nondimensionalization is applicable to equations (2.27). These equations can be defined such that the same characteristic length (l^*) as the CR3BP equations of motion (2.1) applies. This choice allows for nondimensional units of distance to be the same when transitioning between the CR3BP and a primary-centric 2BP. However, if that choice is made, the nondimensional units of time must be *different* than for the CR3BP. Using the same length scales, if the derivatives in equations (2.1) are taken with respect to nondimensional time τ_{CR3BP}, then derivatives in equations (2.27) must be taken with respect to nondimensional time τ_{2BP}, calculated by,

$$\tau_{2BP} = \tau_{CR3BP}(1-\mu)^{-1/2} \tag{2.28}$$

for the P_1–centric 2BP and,

$$\tau_{2BP} = \tau_{CR3BP}(\mu)^{-1/2} \tag{2.29}$$

for the P_2–centric 2BP, where $\mu = m_2/(m_1 + m_2)$ is the same CR3BP mass ratio defined earlier.

Interestingly, the form of equation (2.28) is similar to that for time dilation under the theory of Special Relativity [82, 104, 105]. Consider a clock that is factory-calibrated to tick once every period of time Δt. If that same clock is moving at velocity v, an observer at rest would perceive the clock to be ticking at a slower rate, with the longer *apparent* time between ticks dt' given by,

$$dt' = \Delta t(1-\beta^2)^{-1/2} \tag{2.30}$$

where velocity ratio $\beta = v/c$, and c is the speed of light—the maximum allowable value of velocity v. The relationship between the CR3BP and the P_1–centric 2BP time scales can be considered a type of "relativistic" effect caused not by velocity with respect to a rest frame but instead by the fact that the mass of the other primary P_2 is ignored. To understand this relationship, it is necessary to define $v = (GM_{reduced})^{1/2}$, where

$GM_{reduced}$ is the gravitational parameter associated with reduced mass $M_{reduced} = m_1 m_2/(m_1 + m_2)$. Of course, v is not a velocity in this case. The notation v is used for an analogy to Special Relativity. Next, if the mass m_2 of the ignored primary were free to be equal to any value between zero and infinity, the upper limit on the reduced mass is expressed as $M_{reduced} \leq m_1$. Therefore, if $v = (GM_{reduced})^{1/2}$ were to behave like a velocity in this analogy, the constant "speed limit" would be given by $c = (Gm_1)^{1/2}$. This implies that the "velocity" ratio β is,

$$\beta = v/c = (GM_{reduced}/\, Gm_1)^{1/2} = \{m_2/(m_1 + m_2)\}^{1/2} = \mu^{1/2} \tag{2.31}$$

Thus, based on equation (2.30), the time dilation associated with the P_1–centric 2BP as "observed" from the CR3BP is given by equation (2.28) because $\beta^2 = \mu$. Also, a similar analysis for the time dilation associated with the P_2–centric 2BP, with the maximum "velocity" defined as $c = (Gm_2)^{1/2}$, yields the relationship in equation (2.29).

The restricted 2BP for the motion of a S/C in the vicinity of either of the two primary bodies possesses an analytical solution in terms of conics [8, 9, 10, 74]. The dynamics of the 2BP, first solved by Newton in 1683, can be described geometrically based on the polar equation of a conic section (with the origin at one focus),

$$r = \frac{a(1 - e^2)}{1 + e\cos\nu} \tag{2.32}$$

where r is the distance of the S/C from the central gravitational body—a point mass located at a focus (e.g., of an ellipse)—and a, e, and ν are the classical orbital elements semimajor axis, eccentricity, and true anomaly, respectively [9, 10]. The complete S/C state in the 2BP is often defined based on the typical set of classical orbital elements $(a, e, i, \Omega, \omega, \nu)$ consisting of semimajor axis, eccentricity, inclination, longitude of ascending node, argument of periapsis, and true anomaly, respectively [8, 106]. Note that the orbital element Ω is undefined for an equatorial orbit, and the orbital elements ω and ν are undefined for a circular orbit. Therefore, alternate orbital elements are often used. For instance, longitude of periapsis Π is defined for equatorial orbits, except those that are also circular. On the other hand, argument of latitude u is defined for circular orbits, except those that are also equatorial. Finally, true longitude l is defined for orbits that are circular *and* equatorial [8, 106].

Another useful relationship in the 2BP is what is referred to as the "vis-viva" equation [9], relating S/C velocity magnitude V to the distance r from the central body by,

$$V = \sqrt{GM\left(\frac{2}{r} - \frac{1}{a}\right)} \tag{2.33}$$

where a is the semimajor axis of the orbit and GM is the gravitational parameter associated with the central body. As $r \to \infty$ for an orbit that is parabolic or hyperbolic, equation (2.33) becomes,

$$V_\infty = \sqrt{-\frac{GM}{a}} \tag{2.34}$$

where V_∞ is referred to as the hyperbolic excess velocity, which is the velocity of a S/C at infinite distance from the central body. For a parabolic orbit, with a infinitely large, $V_\infty = 0$. For a hyperbolic orbit, $a < 0$ and thus $V_\infty > 0$. The hyperbolic excess velocity of an orbit is relevant to trajectory design based on the patched-conic approximation [10] in which different segments of a S/C path are modeled using different 2BPs. For instance, to model an interplanetary trajectory between the Earth and Mars, the S/C motion can be approximated using the Earth-centric 2BP when in the vicinity of the Earth and using the Mars-centric 2BP when in the vicinity of Mars. For the intermediate segment of the trajectory, the motion is approximated using the Sun-centric 2BP in which the planets Earth and Mars are also in orbits about the Sun. The concept of hyperbolic excess velocity V_∞ allows the "patch" between two 2BPs. For instance, when transitioning from the Sun-centric 2BP to the Mars-centric 2BP, the *relative* velocity of the S/C with respect to Mars in the Sun-centric inertial frame determines the hyperbolic excess velocity V_∞ of the S/C as it enters Mars's "sphere of influence." The radius of the sphere of influence is calculated as $SOI = L(GM_{Mars}/GM_{Sun})^{2/5}$ where L is the distance between the Sun and Mars. The value of *SOI* serves as a rough approximation for the radius of the region in the vicinity of Mars where the Mars-centric 2BP may be considered a valid approximation in a patched-conic analysis [74]. When the S/C is outside of this sphere, the Sun-centric 2BP is considered valid instead.

In a 2BP-focused design procedure, conic arcs serve as reference solutions for the motion of a S/C in the vicinity of a central gravitational body treated as a point mass, assuming any additional forces can be modeled as *small* perturbations on the nominal, conic path. Examples of perturbations [14, 74, 107, 108, 109] on the nominally two-body orbit of an Earth satellite are: (1) Earth's non-spherical gravity field, i.e., the geopotential, (2) atmospheric drag, (3) third-body (lunar/solar) gravity, and (4) solar radiation pressure. In the current investigation, portions of S/C trajectories at or below geosynchronous orbit (GEO) altitude are modeled using the Earth-centric 2BP. GEO altitude is defined herein as 35,786 km above the surface of the Earth, the approximate altitude of a circular, GEO [107] with a period of one sidereal day. On the other hand, Earth-Moon system S/C trajectories above that altitude are modeled using the Earth-Moon CR3BP. Transitioning between the Earth-centric 2BP and the Earth-Moon CR3BP at GEO altitude is a reasonable choice because it is at this approximate altitude where perturbations due to lunar gravity become more significant than perturbations due to the geopotential. Below GEO altitude, it is the geopotential—most significantly the J_2 zonal harmonic term in the expansion, due to the Earth's oblateness—that is the dominant perturbation [107].

Finally, different types of S/C transfer maneuvers [9, 74, 106, 110] defined in the 2BP are useful in the current investigation. All $\left|\overrightarrow{\Delta V}\right|$ maneuvers are assumed to be instantaneous (impulsive burns). The first type of maneuver is the Hohmann transfer, which is the optimal two-maneuver transfer between two coplanar, circular orbits. The transfer is accomplished via an ellipse that is tangent to both orbits. Another option for transferring between two circular orbits (for example) is the bi-elliptic transfer, consisting of two transfer ellipses and requiring three maneuvers. Each of the two ellipses is tangent to one of the two orbits, and the two ellipses also intersect each other. Finally, a general method for determining transfer solutions in the 2BP is given by the solution to Lambert's problem, where a S/C path between two points in space is a single conic arc [9].

2.8.2 The Ephemeris-Based Model

A model of the "real world" incorporates ephemeris data obtained from the Jet Propulsion Laboratory (JPL) HORIZONS System web-interface [111]. Data files such as DE405 provide accurate predictions for the orbits of various astronomical bodies in the solar system over a specified time span and with respect to a selected coordinate system.

Ephemeris data is used for two purposes in this investigation. First, the real-world data allows a S/C state expressed in the coordinates of the rotating and inertial frames of the CR3BP to be transformed to a more useful reference frame associated with orbital elements in the 2BP. For example, to analyze an Earth-Moon CR3BP trajectory from a *two-body* dynamical perspective in the Earth-centric inertial frame, it is useful to calculate the instantaneous (osculating), Earth-centered, two-body orbital elements for the S/C at a particular time. Yet, it is appropriate to define such orbital elements with respect to the Earth's mean equatorial reference frame at a particular epoch (time) based on the ephemeris data. In this case, the calculation of the osculating orbital elements for a S/C is based on the Moon's own osculating elements at the selected epoch. Specifically, the inclination i, longitude of ascending node Ω, argument of perigee ω, and true anomaly ν of the Moon at the epoch provide the angles that define the transformation between the Earth-centric inertial frame of the CR3BP—based on the plane of the primaries, i.e., the plane of the Moon's orbit about the Earth—and the mean equatorial reference frame, defined in relation to the approximately "fixed" stars. The transformation from the Earth's mean equatorial reference frame to the Earth-centric inertial frame of the CR3BP is the body 3-1-3 Euler angle rotation sequence: $A_{313}(\Omega, i, \phi) = A_3(\phi)A_1(i)A_3(\Omega)$, where Ω is the first angle in the sequence, $\phi = \omega + \nu - \tau$, and τ is the nondimensional time (in the CR3BP) associated with the epoch. Of course, the reverse (inverse) of this sequence provides the transformation from the Earth-centric inertial frame of the CR3BP to the Earth's mean equatorial reference frame.

Ephemeris data is also used to define the locations of various astronomical bodies in a higher-fidelity dynamical model constructed in STK® [112]. Transitioning to a higher-fidelity model provides a mean of validating preliminary design accomplished in the CR3BP. The simplifying assumptions of the CR3BP are replaced with a more realistic

dynamical model for S/C motion. The two primaries P_1 and P_2 are still treated as point masses in the gravity model, however, their orbits are now modeled based on JPL ephemeris data; they are no longer assumed to be perfectly planar or perfectly circular. Furthermore, the orbits and the gravitational influence of additionally bodies—such as other planets and moons—are modeled, as is solar radiation pressure [74]. Note that, in this higher-fidelity model, the libration/Lagrange points of equilibrium cannot be precisely defined. Moreover, *JC* is no longer a constant of the motion, and therefore the ZVSs/ZVCs associated with an "energy" level cannot be precisely defined either. Nevertheless, if the simplifying assumptions of the CR3BP are *reasonable*—i.e., the orbits of the two primary bodies are roughly circular and additional forces can be modeled as small perturbations—the CR3BP enables useful preliminary design (often much more accurate than the 2BP) with results that can ultimately be transitioned to a higher-fidelity model to verify and/or refine the final mission design.

3. HIGHER-DIMENSIONAL-MAP-BASED DESIGN: A NOVEL APPROACH

Leveraging the concepts, methods, and previous contributions related to design in a multi-body environment—as summarized in Chapters 1 and 2—the present investigation develops and applies techniques for trajectory design using a "true" 4-D Poincaré map for the spatial CR3BP in a manner that is analogous to strategies already established for 2-D maps in the planar CR3BP. The basic premise of this effort is that twenty-first-century visualization technology has advanced sufficiently such that the task of representing and interpreting higher-D maps may only be difficult—but not impossible.

This chapter describes a novel approach to higher-D-map-based trajectory analysis and design in the spatial CR3BP. The approach includes a method for representing, interpreting, and manipulating a 4-D Poincaré map of CR3BP trajectories in an interactive, 3-D visual environment using color. What is referred to in this investigation as the space-plus-color method is introduced, along with various tools and techniques that enable 4-D-map-based design in a visual environment. The space-plus-color method is applied to an analysis correlating the long-term variations in instantaneous eccentricity of a high-altitude Earth orbit perturbed by lunar gravity with the shape and evolution of the surface of a deformed torus on a 4-D map. Also included is a description of the procedure by which reasonable design estimates obtained visually from a 4-D Poincaré map can be fed into follow-on, automated processes that lead to precise and/or locally-optimal solutions. Finally, important 4-D map coordinate definitions are presented.

3.1 The Space-Plus-Color Method

To illustrate as much as possible of the "true" shape of 4-D map features for the spatial CR3BP, all four map dimensions are represented in this analysis. This allows for a one-to-one mapping between a 6-D state in the phase space and a 4-D point on a map.

The goal in this investigation is full representation of higher-D map features and realization of some aspects of their form that might be lost when viewing merely their lower-D projections. Lichtenberg and Lieberman [85] supply theoretical support for this concept in their description of the properties of higher-D Poincaré maps. A surface of section for the spatial CR3BP (a 3-DOF, autonomous, Hamiltonian system) has a fundamental property that preserves the phase space "volume" visited by a given trajectory. Yet, on a 4-D map, a 4-D volume is actually preserved; unlike a 2-D map for a 2-DOF Hamiltonian system, 2-D projections of the 4-D map are not expected to possess an analogous, area-preserving property. Lichtenberg and Lieberman also state that—in contrast to a map for a 2-DOF system—an *arbitrary*, 2-D projection of a higher-D map of quasi-periodic features does not, in general, yield an area-preserving, 2-D map of smooth curves. In summary, the higher-D nature of a map for the spatial CR3BP is not completely represented by the sum of its lower-D parts.

To employ a 4-D Poincaré map for trajectory design, a key decision concerns how to represent the four dimensions. Since there is no universally-accepted method for displaying a 4-D object, there are a variety of reasonable methods that may be employed (see Sections 1.1.2 and 2.4). In the current investigation, the purpose of representing all four dimensions is to visualize—as much as is possible—the "true," higher-D shape of features on a map. Consequently, three of the four map dimensions are displayed in a 3-D space. That is, the location of a point plotted on a 3-D grid represents three map coordinates (not necessarily the S/C position); the points can be displayed in any 3-D visual environment using computer software. The use of 3-D space maximizes the number (three) of map coordinates that can be represented in a familiar and intuitive manner. Note that, because a point is theoretically zero-dimensional and thus invisible, it is always necessary to plot the location of a point using an object that is higher-than-"zero"-dimensional, e.g., a small circular area always facing the observer, which is basically a 2-D "dot."

The next critical decision is how to represent the fourth dimension. Since there are no more spatial dimensions available—either in the physical, everyday world or in a 3-D visual environment—the extra, fourth dimension must be represented by some other

characteristic associated with a given map point. The choice in the present investigation is the use of the plotted color of a dot to represent the value of the extra coordinate. In effect, the space-plus-color method is based on the idea that a clear ice cube represents a 3-D object while an image of a RUBIK'S CUBE® [113] could represent a 4-D object. Thus, 4-D Poincaré maps are represented with three spatial dimensions and one color dimension. Within this context, it is possible to distinguish the 4-D locations of each map point and also to define higher-D map regions. Moreover, patterns and symmetries are identified using a color scale—even amidst the clutter of many map points. This method expands on the color and rotation method developed by Patsis and Zachilas [7] (see Section 1.1.2) by applying additional tools and techniques that enable 4-D-map-based design in the dynamical environment of the CR3BP. The focus in the present investigation is on the practical techniques needed to overcome challenges inherent in utilizing information displayed on higher-D maps, especially in the case where a map is generated by *many different trajectories*. Yet, previous studies applying the color and rotation method [6, 7, 57, 58, 59, 60, 61] (see again Section 1.1.2) serve as valuable references for interpreting 4-D map features observed in the current investigation. Particular helpful are those studies' conclusions concerning the relationship between the appearance of map features—in terms of both the 3-D shape and the color—and different types of dynamical behavior, especially the stability/instability of nearby fixed points generated by periodic orbits.

The term "space-plus-color," rather than "color and rotation," is used in this investigation for two reasons. First, the representation of three dimensions in a 3-D visual environment is, by far, more intuitive familiar to a human than the concept of a fourth dimension represented by color. Accordingly, the interpretation of various shapes/structures on a 4-D map remains somewhat biased towards the appearance of the 3-D projection, even when color is added. Thus, it is appropriate to consider the color coordinate of a 4-D map as something *extra,* added to a nominally spatial representation. The second reason for not using the Patsis and Zachilas terminology is that the present investigation employs tools and techniques that go beyond just rotation of an image. To perform map-based trajectory design, often based on 4-D maps generated by many

different trajectories, further manipulation of the image is accomplished in an interactive visual environment. This additional manipulation (see Section 3.2 for details) is iterative in nature and includes: (1) interactively "zooming" in the color dimension in a manner similar to zooming in the spatial dimensions, (2) "filtering" out features that are obscuring the view based on the spatial and color coordinates as well as various other criteria, (3) exploring a map in stages with short versus long-term propagations, (4) associating and annotating map returns with information relevant to CR3BP trajectory design, and (5) interactively modifying the size(s) of plotted dots. Note that the "filtering" process employed is motivated by a similar principle as the 3-D phase space sections employed by Richter [63] and Richter et al. [64]. In those studies, in order to overcome the challenges of viewing multiple trajectories on 4-D maps, map returns having a particular value of the fourth coordinate—to within a small tolerance—are displayed on a space consisting of the remaining three coordinates. In the present investigation, the concept is generalized to include various other types of filtering criteria.

3.1.1 Justification for Using Color to Represent the Fourth Dimension

To understand a fundamental advantage of the space-plus-color method over other options, it is necessary to first consider several basic examples of representing extra coordinates associated with points in space. One straightforward option is to represent a fourth map coordinate by a text number, as depicted in Figure 3.1(a). In this figure, the depiction of "space" is simplified (for pedagogical purposes) as a 2-D plane with a point in that planar "space" defined by its location in Cartesian variables x and y. Thus, the 2-D space actually represents a 3-D space with text numbers representing an extra, fourth coordinate. The locations of nine points are represented by nine small circles; the center of each circle represents the x,y location of each point. The value of the extra coordinate, ranging from one to nine, is simply annotated directly beneath each circle. For instance, the point at the top left of the plot would have the smallest x value, the largest y value, and an extra coordinate value equal to one. The point at the bottom right would have the largest x value, the smallest y value, and an extra coordinate value equal to nine. To demonstrate a limitation of this method for representing the extra coordinate, a zoomed-

out view of the nine points in Figure 3.1(a) is displayed in Figure 3.1(b). This new view is of the same point locations, represented by the same size circles as well as the same size font for the text number. However, the *spatial* scale of the plot has changed. The points now appear closer together such that their surrounding circles actually touch one another. This is because the visible limits associated with the spatial coordinates *x,y* have increased while using the same size circles to represent each point. On the other hand, the scale associated with the extra coordinate represented by text numbers has not changed; the text numbers still range from one to nine, without any additional scale factor applied that would make them effectively closer together in value. However, since the text numbers are still plotted in a location in space directly beneath each circle with the same size font, the text numbers themselves do appear *physically* closer together. In fact, the numbers are barely readable, plotted on top of one another, even though the circles do not overlap one another. To alleviate the text number overlap problem, it is necessary to

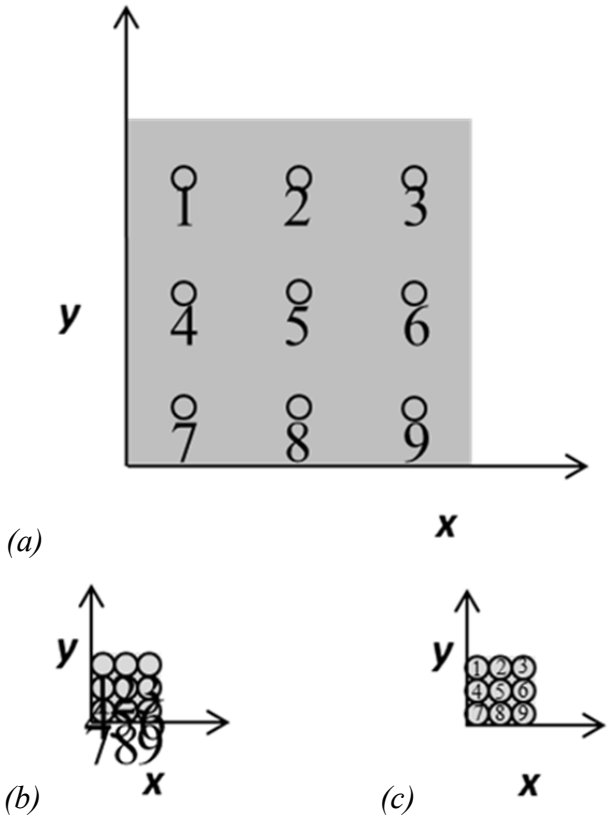

Figure 3.1. Text number method of representing an extra coordinate for a point in space

plot the numbers so that they are centered inside each circle and also change the font size of the text so that the numbers are no larger than the size of the circles, as depicted in Figure 3.1(c). Note, however, that this revised font size make the numbers more difficult to read. The key point in the example displayed in Figure 3.1 is that the *physical size* of the text numbers used to represent the extra coordinate is limited—in terms of readability—by the scale associated with the spatial dimensions of the plot. In other words, as the spatial view is zoomed out, the font size of the text numbers must be reduced so that they are not plotted on top of one another. This is a critically important observation because it implies that the text number method of representing the extra dimension associated with a point in space places an additional limit on the viewable spatial scale of a plot. Normally, the spatial scale of a plot of points in a space is limited only by the size of the dots used to represent the points. Smaller dots enable a finer plot resolution because a zoomed-out view can still distinguish between two point locations without the dots appearing on top of one another. However, in this case, even though the extra, non-spatial dimension of the plot should not be theoretically affected by the spatial dimensions, the practical truth is that the font size of the text numbers used to represent the extra coordinate also limits how far the view can be zoomed out before the values in the text are unreadable.

The problem with the spatial scale of a plot being limited by the physical size associated with some extra characteristic used to represent an extra dimension is not only encountered with the text number method. The issue actually applies to *all* methods of representing an extra dimension that involve augmenting a point with some type of higher-than-“zero”-dimensional object that occupies more space than is necessary simply to make the point itself visible. A certain dot size (e.g., a 2-D circular area) is necessary in any plot to make a point location visible. If a method of representing an extra coordinate requires an object that occupies more physical space on the plot than the dot itself, then the extra object become the limiting factor in determining how far the plot can be zoomed out. This is true even in the case where the object size is scaled along with the spatial view. If the plot is zoomed out while leaving the physical size of the extra object the same, then the value of the fourth coordinate can become unreadable due to

object overlap when points are plotted close to each other. On the other hand, if the object's physical size is reduced as the view is zoomed out (as with the text numbers in Figure 3.1(c)), there exists a size at which the extra characteristic is no longer visually discernible. That is, eventually the font size become so small that the human eye can detect the presence of a number but cannot discern whether the value is equal to three or four. Thus, even though a plotted dot may be visible, with its *x,y* location in space easily estimated, the extra characteristic associated with this dot may not be readable/discernible; the insight gained from the extra dimension is lost. For trajectory design applications of Poincaré maps for the spatial CR3BP, the more a plot of map returns can be zoomed out while still allowing insight into all four map dimensions, the more likely it is that a map-based designer can gain insight into the "global" view and the higher-D nature of the design space. While a particular method of representing an extra dimension on a map may allow visibility of all four dimensions when the view is sufficiently zoomed in to a region of interest, an important aspect of Poincaré map-based design is the ability of a fully-zoomed-out map to provide visual cues that indicate what region of interest should be zoomed into in the first place. In other words, the power of the 4-D Poincaré map is most realized when all map dimensions are visible in the "big picture" and features of interest for design can be located without prior knowledge of the appropriate region to zoom.

Figures 3.2 through 3.4 display three additional methods of representing an extra coordinate associated with points in a space. All involve augmenting a point with some type of higher-than-"zero"-dimensional object that occupies more space than is necessary to make the point itself visible as a small dot. Figure 3.2 depicts a method using the size of the dot itself (the 2-D circular area) to represent the extra dimension. The center of the circle locates a point in space, while circles with larger areas represent larger values of the extra coordinate. The sizes of the nine circles displayed in Figure 3.2(a) represent the same values (one through nine) as in the text number method displayed in Figure 3.1. The zoomed-out view using the circle size method in Figure 3.2(b) reveals a similar problem as that depicted in Figure 3.1(b) for the text number method. As just the spatial limits of the view are increased, the circle sizes are fixed because they still represent the

same values of the extra coordinate: one through nine. However, the circles are difficult to distinguish in the cases where they are plotted on top of one another. To remedy this, the scale of the extra coordinate must be modified, as depicted in Figure 3.2(c), so as to associate smaller differences in circle size with the differences between the values equal to one through nine. Note that the value of the extra coordinate at each spatial location has not changed, only the absolute scale of circle sizes used to represent the values. However, having smaller differences between the circle sizes in this zoomed-out view means that the differences between the values of the extra coordinate are less discernible. A similar process is depicted in Figure 3.3, where a line segment length method is now employed. In Figure 3.3(a), the lengths of the vertical lines attached to the centers of the circles represent the same extra coordinate values as before. Figure 3.3(b) indicates that, after zooming out the view, the line segments associated with the larger values of the extra coordinate (values seven, eight, and nine in the bottom row of points) cover up the line segments attached to the points in the rows above them. It is again necessary to

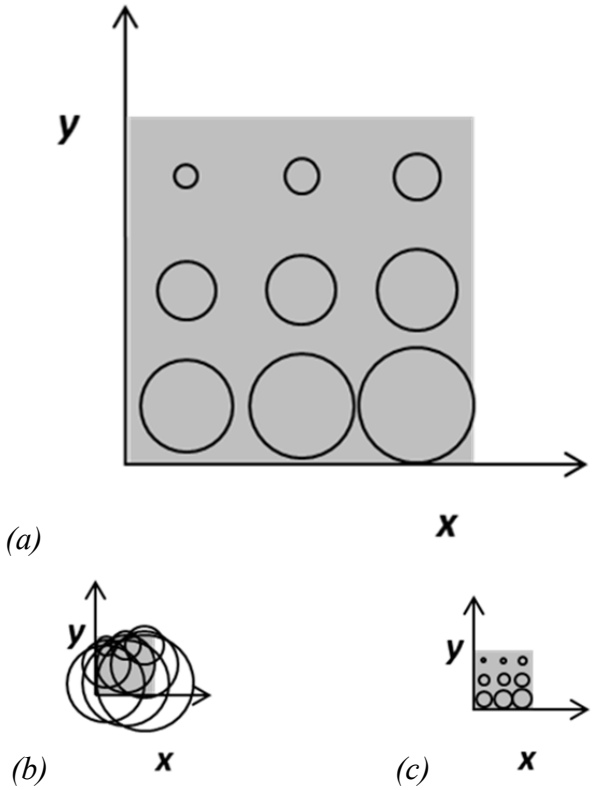

Figure 3.2. Circle size method of representing an extra coordinate for a point in space

redefine the scale for the extra coordinate in order to display each line segment without overlap, as depicted in Figure 3.3(c). However, the drawback now is that the segments associated with smaller values seem barely distinguishable from very small dots.

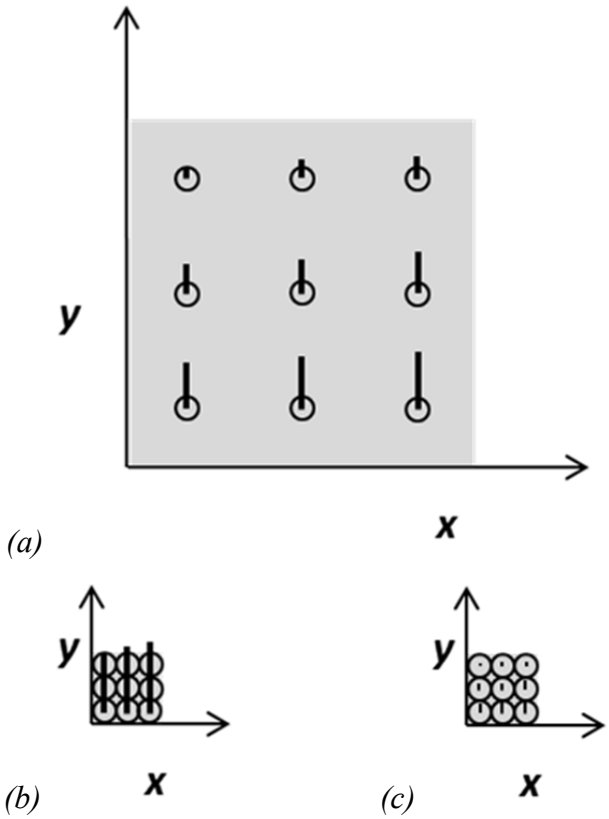

Figure 3.3. Line segment length method of representing an extra coordinate for a point in space

An additional example is depicted in Figure 3.4(a), where the direction of a line segment, with fixed length, represents the same values of the extra coordinate as before. The zoomed out view in Figure 3.4(b) causes various line segments to overlap, an issue that is resolved by readjusting the size of the line segments, while leaving the direction associated with each value of the extra coordinate unchanged, as depicted in Figure 3.4(c). Note that, because all line segments are free to be as large as the radius of the circles, it appears that the extra coordinate values associated with line segment direction are easier to discern at the smaller scale than in the case of the line segment length

method displayed in Figure 3.3, where the *largest* line segment length must be no greater than the circle radius. Also note, however, that an ambiguity exists using the line segment direction method because the "twelve o'clock" direction associated with the extra coordinate value equal to one for the top left point is the same direction used to represent the value equal to nine for the bottom right point. This ambiguity results from the cyclical nature of line segment direction; it could be avoided if the scale of the line segment direction is chosen such that the difference between the smallest and largest value of the extra coordinate is associated with less than 360° of angle.

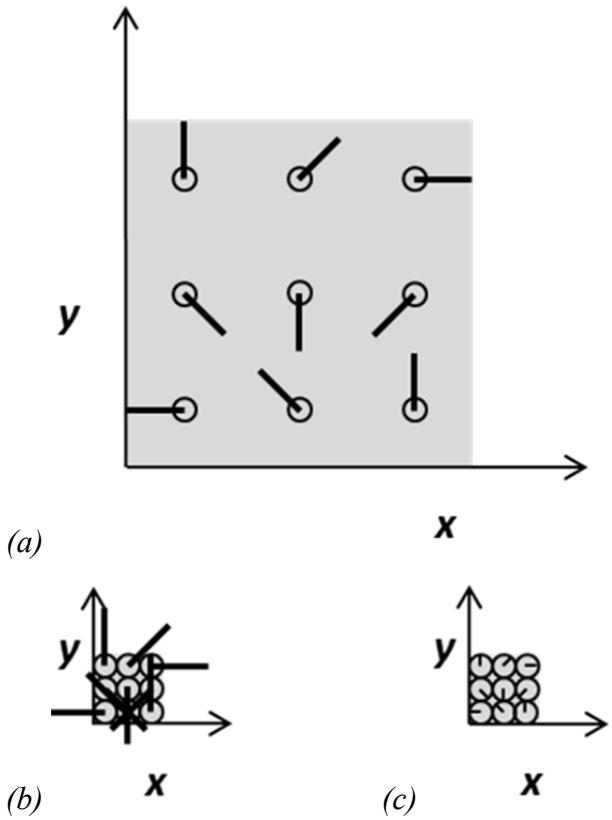

Figure 3.4. Line segment direction method of representing an extra coordinate for a point in space

The preceding basic examples of representing an extra dimension by augmenting a point in space with a higher-than-"zero"-dimensional object all suffer to various extents from the spatial scale limitation, as demonstrated in Figures 3.1 through 3.4. The line segment length method (Figure 3.3) and the line segment direction method (Figure 3.4)

are essentially fundamental descriptions of the methods typically employed to represent 4-D Poincaré maps in the spatial CR3BP (see Sections 1.1.2 and 2.4), where either the length or direction (or both) of one or more arrows or line segments represents the value of an extra map coordinate. To maximize the ability of a 4-D Poincaré map representation to provide insight into all four map dimensions—even when greatly zoomed out—it is desirable to choose a method for representing the extra dimension that suffers *the least* from the spatial scale limitation. The chosen method in the present investigation is what is referred to herein as the space-plus-color method, which is depicted in Figure 3.5. The same nine points with the same spatial locations and extra coordinate values as before are plotted in Figure 3.5(a). A color scale is provided to

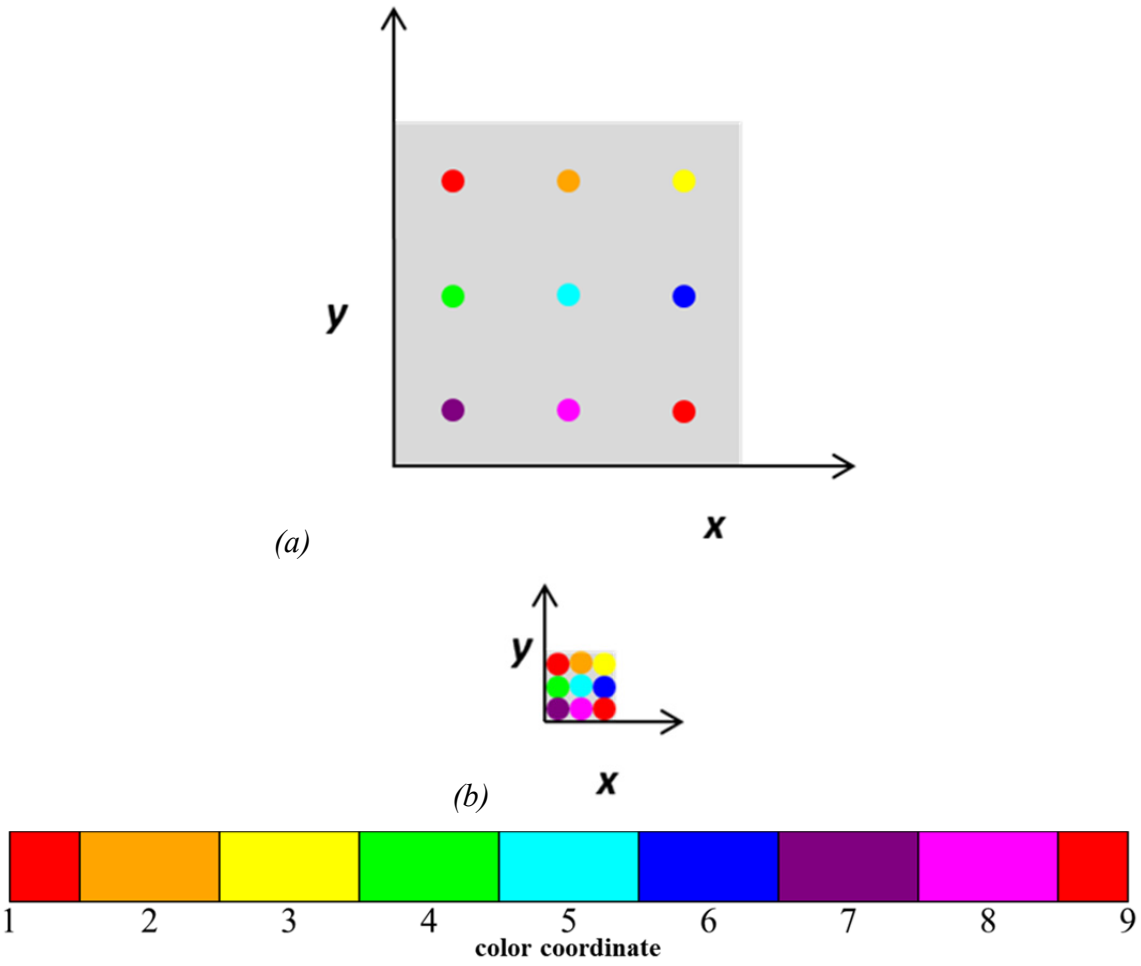

Figure 3.5. Space-plus-color method of representing an extra coordinate for a point in space

define a value associated with the color of each plotted dot. For pedagogical purposes, the color scale in this example is discretized to only 9 different colors; for design applications in the present investigation, 1,000 different colors are typically utilized. The color scale in Figure 3.5 is centered on the color cyan, indicating an extra coordinate value equal to five. Any value of the extra coordinate outside the color scale limits—less than one or greater than nine—could be plotted in black (or in white on a black background) or not at all. Setting limits to the color scale is analogous to setting the spatial limits of a zoomed spatial view. Note that the "spectrum" of colors constitutes one full period of a cycle in color, with the lower and upper limits of the scale both represented by the color red. This implies a similar type of ambiguity as that described for the line segment direction method depicted in Figure 3.4. To resolve the ambiguity between the color coordinate values equal to one and nine, the color scale values may be redefined such that the limits are large enough to have all possible extra coordinate values uniquely associated with the "inner" colors on the scale (i.e., orange though magenta).

A major advantage of the space-plus-color method is demonstrated when the view in Figure 3.5(a) is zoomed out in just the spatial dimensions. The view in Figure 3.5(b) displays a scale in which the dots appear to be just touching but not overlapping. Unlike in the previous basic examples, the extra coordinate values represented by the space-plus-color method are still just as easily discernible. There is effectively no "overlap" in the color dimension. The fundamental explanation for this is that this method employed to represent the extra dimension associated with each point does not require any additional physical space on the plot. In other words, the use of color to add an extra dimension to the plot does not appear to place any significant additional limit on the viewable spatial scale of a plot. In effect, the "zero"-dimensional nature of a point is preserved when encoding that point with color. Text annotation, increased dot size, or the addition of a line segment are all methods that destroy the "zero"-dimensional property of a point. Of course, from a theoretical standpoint, it is possible that, in the extreme, the ability for the human eye to resolve a small, plotted dot (a light source, in effect) is somewhat better than the ability to distinguish the color of that dot; this factor likely depends on the particular color of the dot relative to the background color of the plot. It is also possible

that the observed color of multiple neighboring points in space could be subject to some type of light mixing. Yet, from the practical standpoint of 4-D-map-based design in this investigation, any spatial scale limitation appears negligible when compared to other methods. That is *not* to say that the space-plus-color method is necessarily superior to other methods for all types of map-based design, nor is it free from its own unique limitations (see later in this section). What can be claimed is that the space-plus-color method, at a fundamental level, has the potential to maximize the ability of the human eye to discern *all four* dimensions on a 4-D Poincaré map consisting of many points *even when zoomed out*.

3.1.2 Applying the Space-Plus-Color Method to 4-D Maps in the Spatial CR3BP

Figure 3.6 depicts a notional 4-D Poincaré map of a single map return, plotted as a blue dot, generated by a trajectory crossing a given hyperplane. The four coordinates displayed on the map are the generic variables *a,b,c*—the spatial coordinates for the 3-D space of the map—along with the color coordinate, which is defined by the color of a dot according to the color scale. Estimates for the values of the spatial coordinates ($a = 1$, $b = 1$, $c = 2$) associated with the blue dot are determined by visually measuring the location of the dot along each of the three spatial axes. Furthermore, inspection of the color scale indicates that the blue dot represents a value equal to six for the fourth coordinate. Therefore, the 4-D map location of the point is: ($a = 1$, $b = 1$, $c = 2$, *color coordinate* = 6).

In this investigation, the specific formulation for a 4-D Poincaré map is selected based on the appropriate requirements for a given S/C mission design problem. The definition of the map hyperplane is not restricted to any particular coordinate system (i.e., Cartesian, cylindrical, or spherical), nor is it restricted to involve any particular coordinate (e.g., position x or velocity $\dot{x}$) or any particular value of the selected coordinate. Depending on the problem, it may be desirable to employ either a one-sided map, with map points generated by only the returns resulting from crossings from one particular side of the hyperplane to the other (e.g., $\dot{y} > 0$ crossings), or, alternatively, a two-sided map, with map points generated by all returns (e.g., both $\dot{y} < 0$ and $\dot{y} > 0$

crossings). The map coordinate to be represented with color is also problem-dependent. Finally, the convention in this investigation is to display 4-D Poincaré maps using nondimensional units, with an exception made for coordinates that are angles, which are

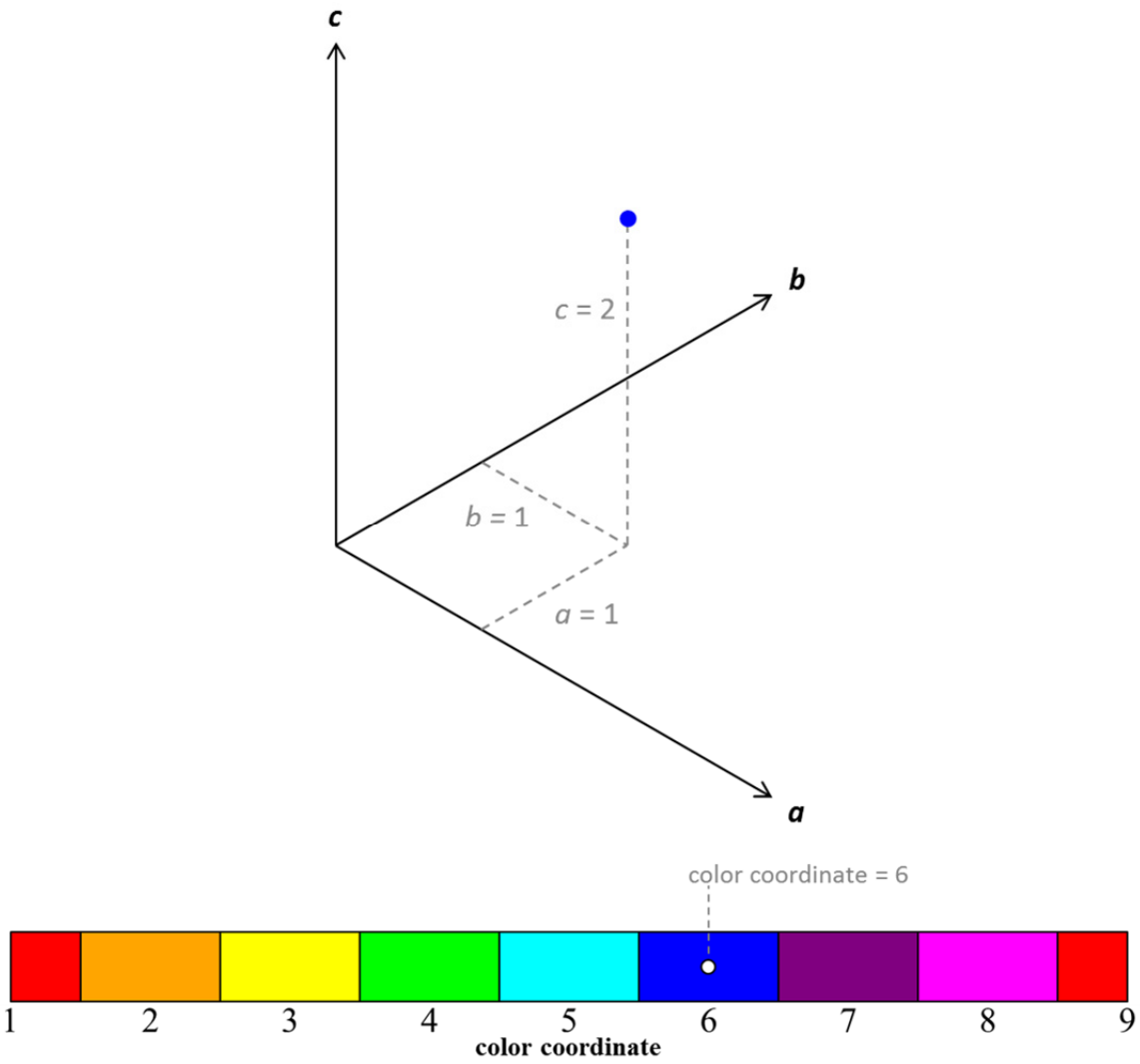

Figure 3.6. Notional 4-D map of a single map return

expressed in degrees. The relative scaling of the spatial axes of the map is generally chosen such that multiple axes displaying the same units (e.g., two position axes both displayed in nondimensional distance units) are appropriately "square," with the same difference between the values at their limits. Sometimes, however, a slightly less intuitive "stretched" scale may be employed in order to better display the qualitative

shape of a map feature. Furthermore, it is often useful to set the limits of the color scale without regard to the limits of the spatial scale. For instance, even though both a spatial dimension and the color dimension could display velocity in nondimensional units, the difference in the spatial axes limits might be equal to one, while the difference in the color scale limits might be equal to two.

A realistic example of a trajectory generating a 4-D Poincaré map is considered next. A 3-D trajectory in the vicinity of the Earth in the Earth-Moon spatial CR3BP is plotted in Figure 3.7 (dimensional units) in both the Earth-centric inertial frame (*X,Y,Z*) and the barycentric rotating frame (*x,y,z*) for three revolutions of the Moon, or roughly 81.85 days (three "months"). The mass ratio is assumed to be equal to μ = 0.012150586550569, and the Moon's orbit radius about the Earth is assumed to be equal to l^* = 384,400 km. Not shown in the rotating view are the ZVSs/ZVCs for the "energy" value of the orbit; these edges of the "forbidden region" are instead plotted (in orange) in the four-perspective, barycentric rotating view of the same trajectory in Figure 3.8. The ZVCs depicted are the cross-sections of the ZVSs (in the spatial problem), where the origin of the cross-sections is the Earth, with (*x,y,z*) = (-μ,0,0). At the "energy" level depicted, the L_1 libration point gateway between the interior region (i.e., the region of the Earth) and the vicinity of the Moon is slightly open. Yet, for this example, the 3-D trajectory remains in the vicinity of the Earth for the propagation time examined, with a retrograde direction in both the rotating and the inertial frame. That is, the motion of the 3-D trajectory in both frames—from a purely planar perspective—is opposite the prograde direction of the Moon in the Earth-centric inertial frame, as displayed in the four-perspective inertial view in Figure 3.9.

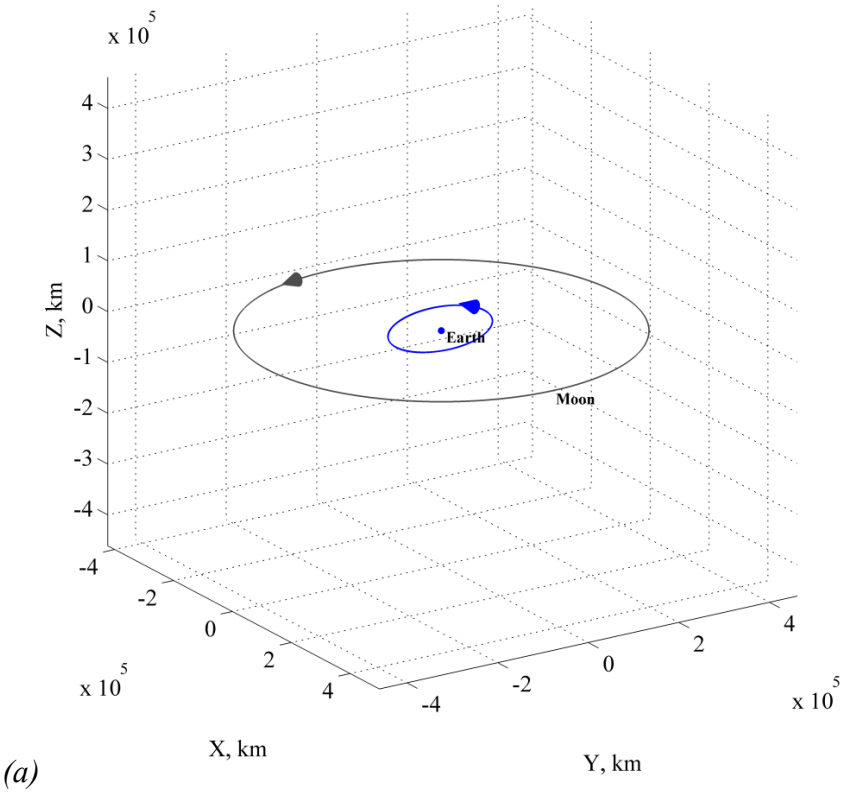

(a)

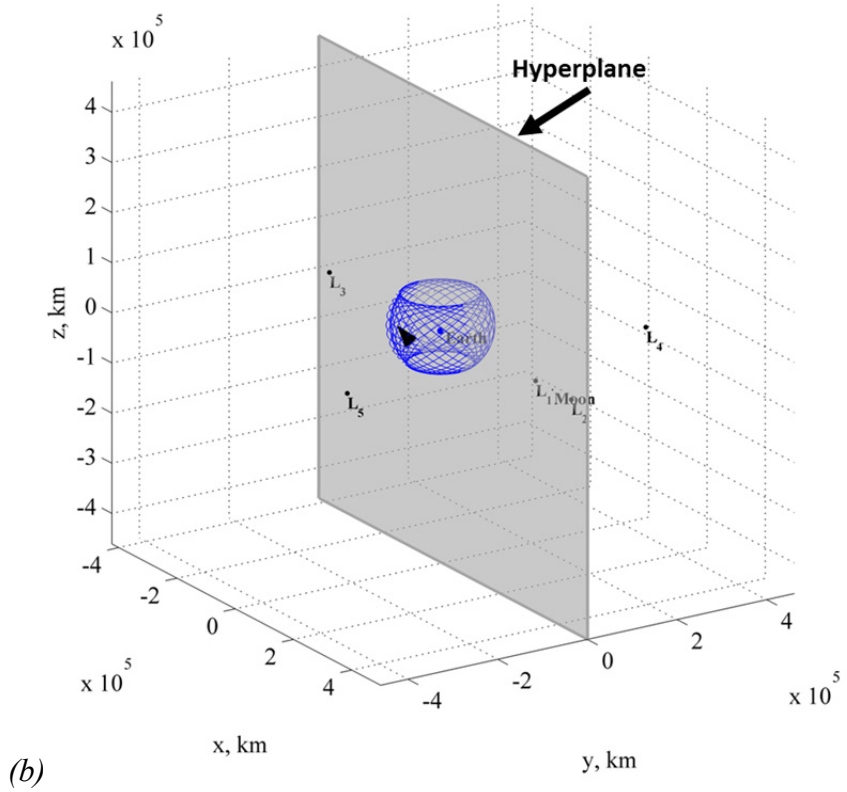

(b)

Figure 3.7. 3-D, Earth-Moon trajectory over 81.85 days: inertial (*a*) and rotating (*b*) views

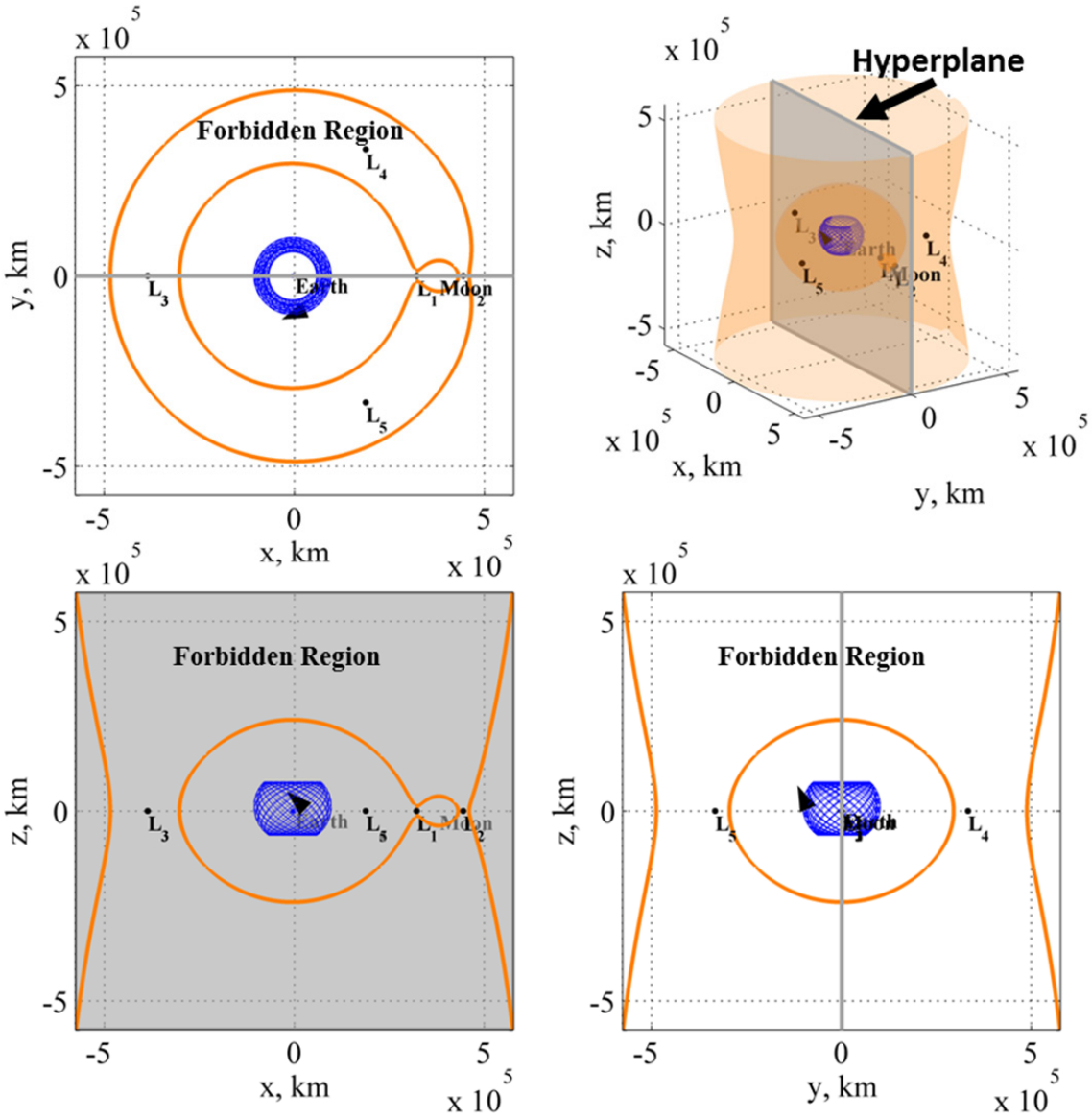

Figure 3.8. Four-perspective rotating view of 3-D, Earth-Moon trajectory over 81.85 days along with ZVSs/ZVCs (orange)

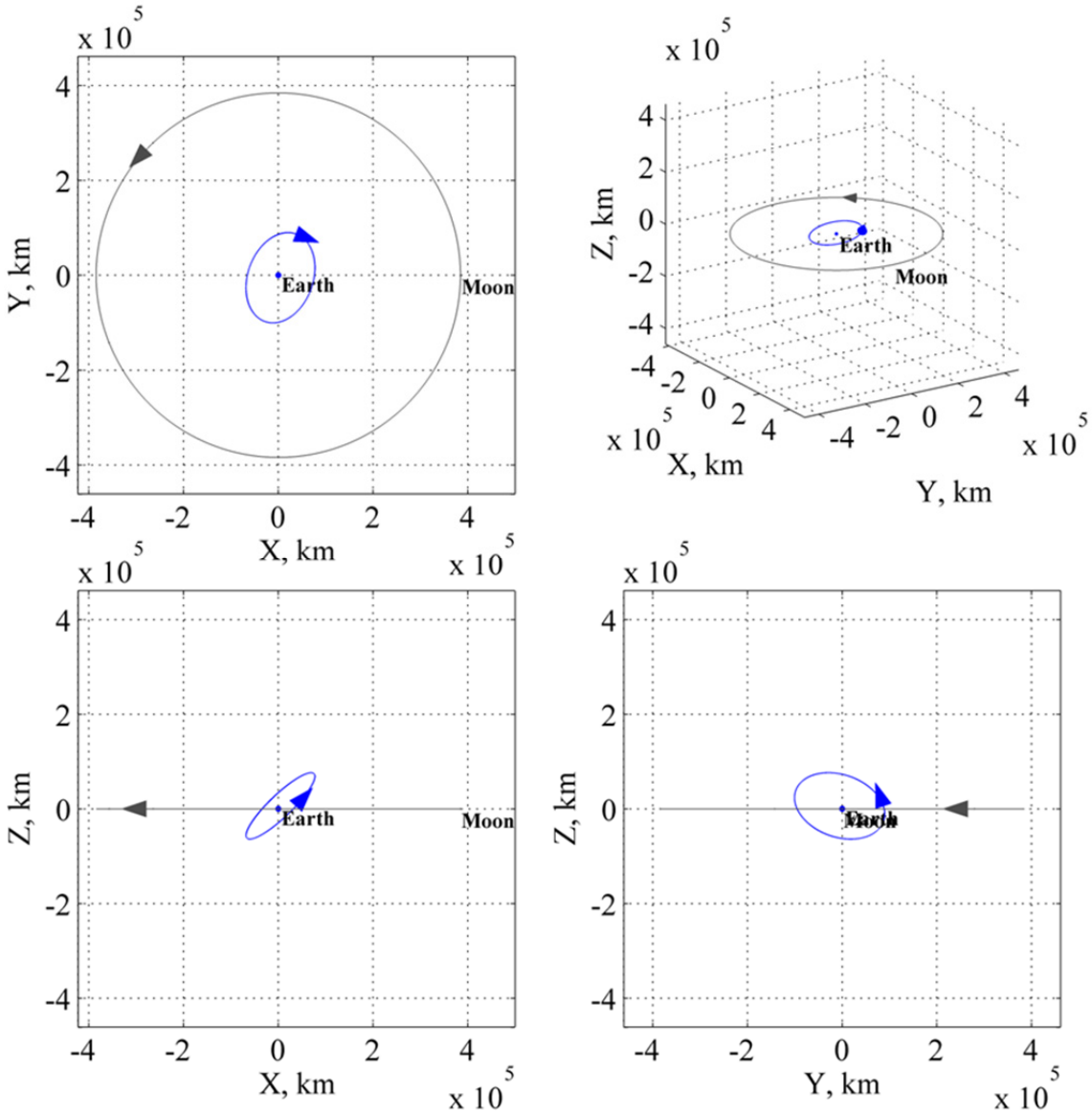

Figure 3.9. Four-perspective inertial view of 3-D, Earth-Moon trajectory over 81.85 days

Apparent in the rotating views displayed in Figures 3.7(b) and 3.8 is a hyperplane defined by $y = 0$, which is used to generate a one-sided, 4-D Poincaré map of returns with $\dot{y} > 0$ over the same time span using the space-plus-color method. That map appears in Figure 3.10 (nondimensional units) with rotating frame coordinates $x, \dot{x}$, and z plotted on the 3-D grid and $\dot{z}$ represented by color. In this investigation, the following compact notation is used to describe this Cartesian phase space map formulation: $(y = 0+;\ x,\ \dot{x},\ z,\ \dot{z}\_color)$; the plus sign indicates that the direction of returns to this one-sided map is

positive ($\dot{y} > 0$ crossings of $y = 0$). Note that the color scale displayed along with the 4-D map plotted in Figure 3.10 is plotted with a smoother spectrum of color than in the notional examples displayed in Figures 3.5 and 3.6. This scale is representative of those used throughout this investigation and contains a full range of colors based on the hue-saturation-value (HSV) color map in MATLAB® [71]. Rather than being automatically generated in MATLAB®, the color scale is actually created manually as a plot of columns of dots ranging in color along the horizontal axis. Such color scales in this investigation utilize 1,000 different colors, properly sequenced according to the HSV color "wheel" such that the color red is associated with both the upper and lower limits, with a red, green, blue (RGB) triplet of [1 0 0]. With the exception of that value, no other color repeats. Thus, for a 1,000-color scale, cyan (RGB = [0 1 1]) is the 501st (middle) color. Any map return with a $\dot{z}$ value less than -1.6 or greater than 1.6 would be plotted with a black dot; however, in this case, the color scale is defined so as to associate as much as possible of the full spectrum of color with the range of $\dot{z}$ values without having any map return outside the color scale limits. In addition, note that the return counter associated with each map return (numbers one through twenty-seven) is annotated below each dot, with the black arrow highlighting the fact that the twenty-seventh return is located fairly close to the first return—i.e., close in both the spatial and color dimensions of the map.

The structure on the 4-D map plotted in Figure 3.10 appears figure-8-shaped in the 3-D map space (i.e., the 3-D, spatial dimensions of the map) and consists of twenty-seven map returns forming an imaginary 1-D "curve" that involves a smooth progression in color coordinate value from one end of the "curve" to the other. During the trajectory propagation time equal to three primary system revolutions, consecutive map returns trace out the three complete cycles of the figure-8—without repeating a 4-D location—before returning to a 4-D location fairly close to the first return. Note that *all four coordinates* of a given map return must be considered when determining whether it is close to any other map return on the 4-D Poincaré map. The first and twenty-seventh returns, which appear near each other in the spatial dimensions of the map, are also both plotted with a greenish color. On the other hand, the apparent "intersection" of the

"curve" in the 3-D map space, which gives the structure in Figure 3.10 its figure-8 shape, is *not* a real intersection in the 4-D map space because the intersection occurs between portions of the figure-8 possessing different colors (magenta and orange) on opposite ends of the $\dot{z}$ color scale. That is, the seventh and twentieth map returns appear relatively close together in the spatial dimension of the map, but their colors correspond to a

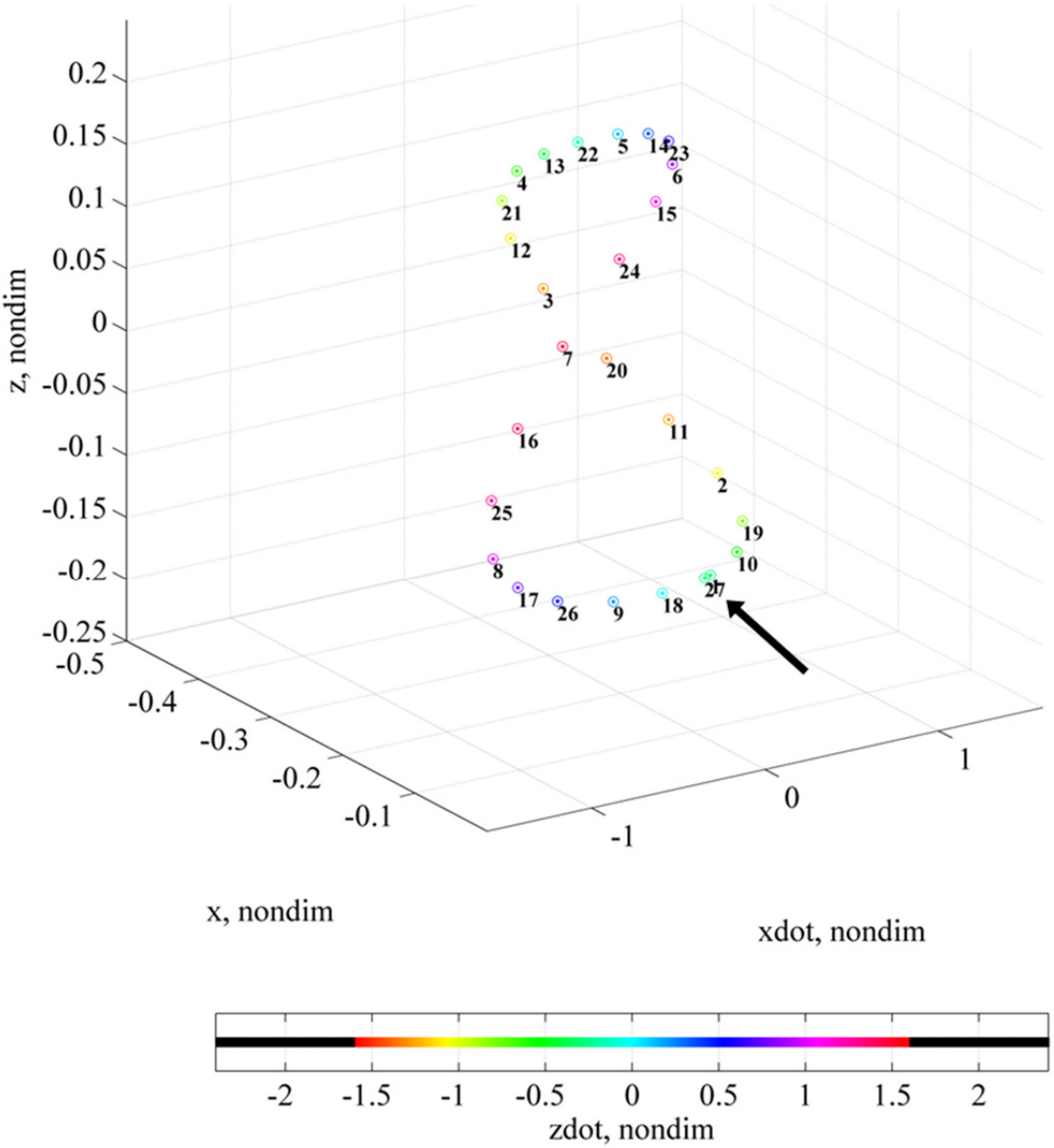

Figure 3.10. 4-D Poincaré map of 3-D, Earth-Moon trajectory; 27 returns over 81.85 days; $(y = 0+;\ x,\ \dot{x},\ z,\ \dot{z}\_color)$

relatively wide "gap" in the color dimension. In effect, if one could view this structure in a real 4-D world, it would appear more like a circle than a figure-8 (see Irons [114] for a generic example of interpreting color as a fourth dimension). As discussed later in this section, the 1-D, figure-8-shaped "curve" depicted in Figure 3.10 appears to be associated with motion that *approximates*—for a brief span of time—rotational (quasi-periodic) motion along the center manifold associated with an unstable periodic orbit

Interestingly, even though the seventh map return plotted in Figure 3.10 is reddish in color, which is associated with color coordinate values near *both* the lower and upper limits of the color scale, it is possible in this example to unambiguously determine the approximate $\dot{z}$ value associated with that color. The reason for this is that this 4-D map, like many other spatial CR3BP maps examined in this analysis, has structure not just in its spatial dimensions but also in its color dimension. As a consequence of the dynamics associated with the orbit generating the map returns, there is an obvious "rainbow" spectrum of color—ranging between a color close to red on the lower limit of the scale and a color close to red on the upper limit—which evolves along a figure-8-shaped structure in the 3-D map space. Thus, a reddish dot with a value near the lower limit of the color scale would be found near orange dots, while a reddish dot with a value near the upper limit of the color scale would be found near magenta dots. Based on this principle, the seventh map return, which is located between the magenta-colored sixteenth and twenty-fourth returns along the 1-D "curve," is clearly associated with a $\dot{z}$ value near 1.6 rather than -1.6.

A long-term propagation of the Earth-Moon CR3BP trajectory plotted in Figures 3.7 through 3.9 appears in Figure 3.11, again in both the Earth-centric inertial view and the barycentric rotating view. The time span is approximately 59.4 years—exactly 5,000 nondimensional time units (roughly 796 revolutions of the primaries). Moreover, the associated long-term 4-D Poincaré map, defined in the same manner as in Figure 3.10, is plotted in the four-perspective view in Figure 3.12. A comparison of the short-term and long-term Poincaré maps plotted using MATLAB® reveals that the apparent 1-D "curve" forming a figure-8 shape evolves into a more complex, higher-D structure that is best examined in a more sophisticated visual environment.

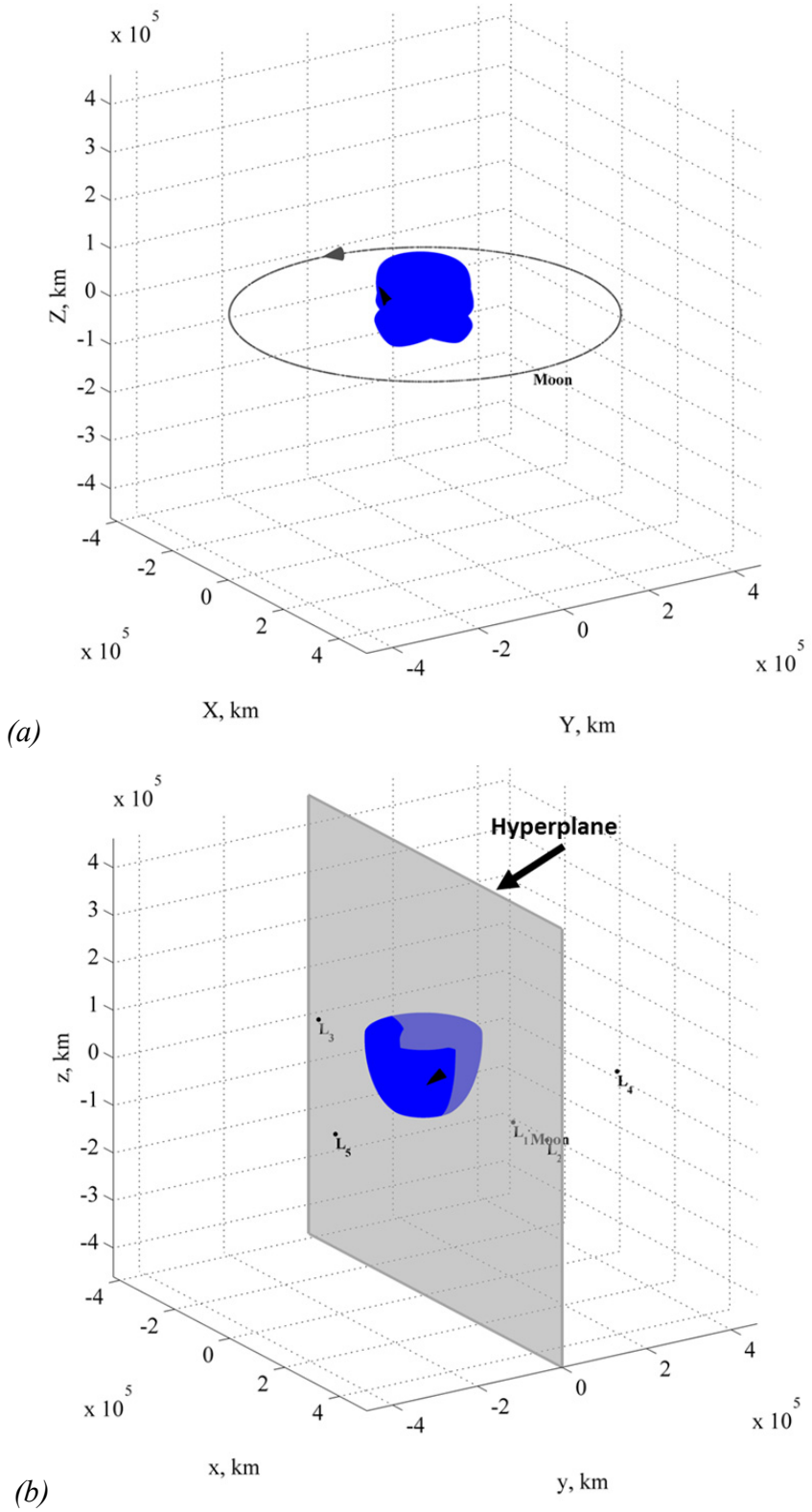

Figure 3.11. Long-term propagation of 3-D, Earth-Moon trajectory over 59.4 years: inertial (*a*) and rotating (*b*) views

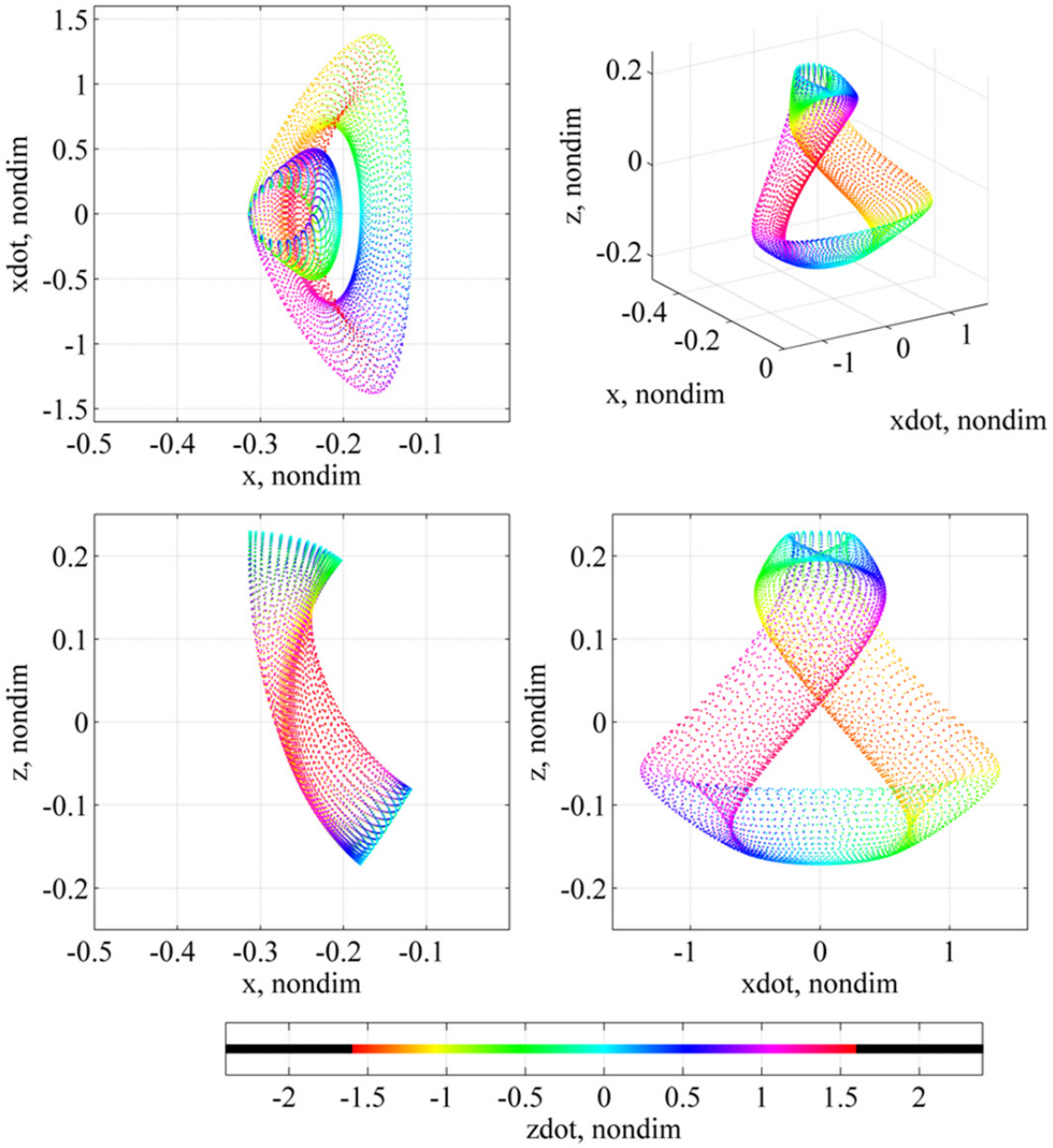

Figure 3.12. Four-perspective view of 4-D Poincaré map of 3-D, Earth-Moon trajectory; 6,903 returns over 59.4 years; ($y = 0+;\ x,\ \dot{x},\ z,\ \dot{z}\_color$)

Transitioning the 4-D map plotted in Figure 3.12 to the Avizo® [72] visual environment provides greater clarity in interpreting the shape of the image, which is displayed in Figure 3.13. Like all Avizo® images included in this dissertation, this view is a "perspective" view, as opposed to an orthographic view; the object displayed is stretched so as to give a realistic "depth perception" in 3-D space. Furthermore, dots

plotted with the same nominal size appear larger or smaller depending on whether they are closer or farther from the observer of the image. Since interpretation of map features in the Avizo® visual environment is mostly accomplished in terms of qualitative factors concerning the overall appearance of the features, the convention in this investigation is to display Avizo® images without spatial axes represented. A color scale is still included when necessary for explanation of various color coordinate values. Note that the same

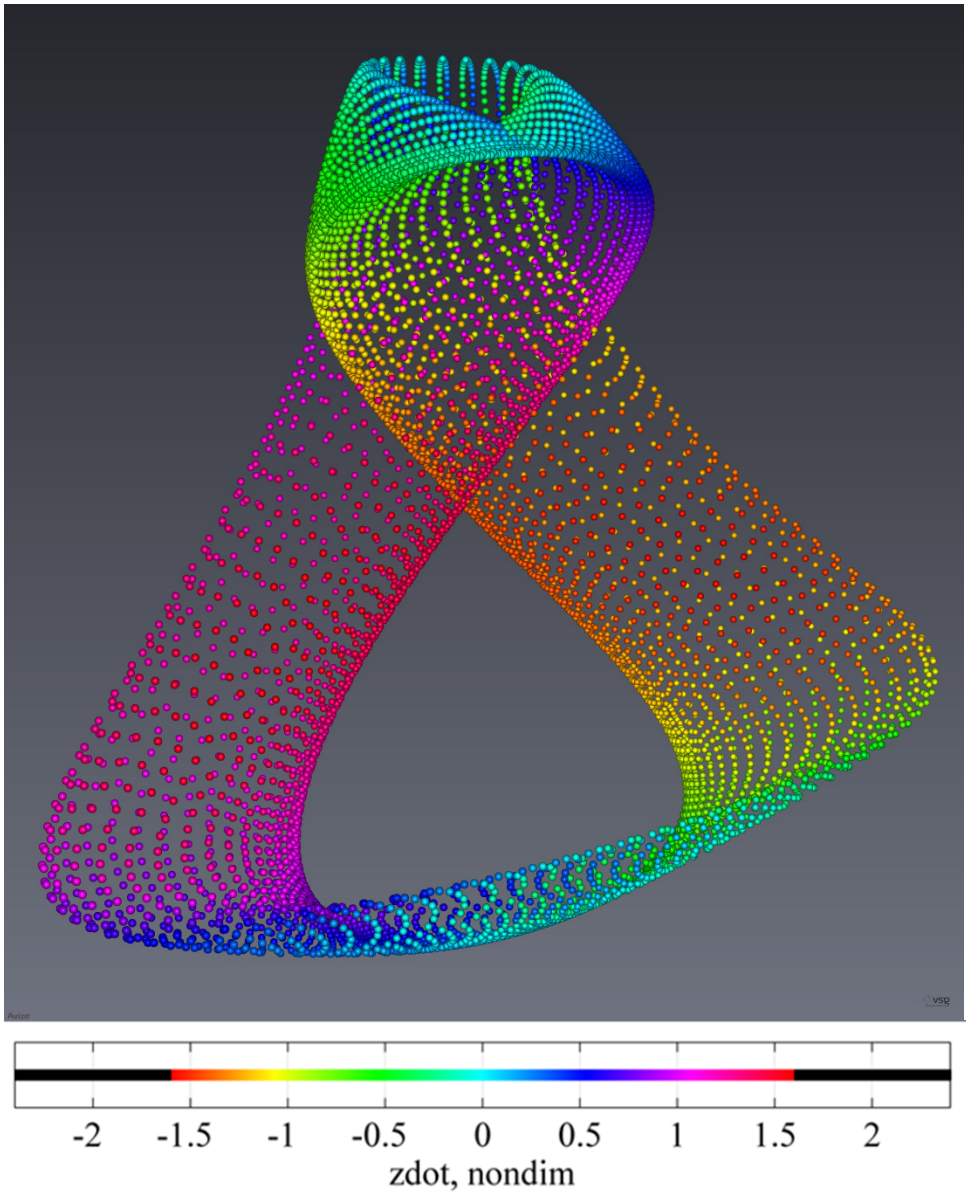

Figure 3.13. Avizo® view of 4-D Poincaré map of 3-D, Earth-Moon trajectory; 6,903 returns over 59.4 years; ($y = 0+;\ x,\ \dot{x},\ z,\ \dot{z}\_color$)

color can appear slightly different between the MATLAB® and Avizo® visual environments; for simplicity, the color scales produced using MATLAB® are included in Figure 3.13 and elsewhere in this dissertation. By examining the 4-D map structure displayed in Avizo® using 3-D glasses and a stereoscopic view, it appears—at least for returns generated during the specified propagation time—as an orientable, two-sided, 2-D surface that is topologically equivalent to a deformed 2-D torus, or 2-torus. This structure, formed by a total of 6,903 map returns, also appears to possess a prominent self-intersection in 3-D space. However, as is the case with the figure-8 structure plotted in Figure 3.10, this long-term map structure does not have a real intersection in the 4-D map space; the apparent intersection occurs between segments with different colors (magenta and orange) on opposite ends of the $\dot{z}$ color scale. This figure-8-shaped, "doughnut"-like object resembles the toroidal "islands" generated in 1995-1997 by Vrahatis et al. [51, 52] and Vrahatis, Isliker, and Bountis [53] as black and white projections onto 3-D space for a 4-D, analytical mapping of perturbations on periodic trajectories related to magnetic focusing elements. Thinner versions of similar tori in the neighborhood of "elliptic fixed lines" were displayed as projections onto 3-D space in 1994 by Todesco [54, 55] for a 4-D, analytical mapping related to magnetic focusing elements as well as a 4-D, analytical, "twist" mapping—and in 1997 by Gemmi and Todesco [56] for a 4-D generalization of the analytical Hénon mapping. Furthermore, the "doughnut" in the present investigation has a similar "rainbow" spectrum of color as various 4-D structures generated using the color and rotation method (e.g., Katsanikas, Patsis, and Contopoulos (2013) [60] and Zachilas, Katsanikas, and Patsis [61]).

To demonstrate various aspects of the space-plus-color method and to gain insight into features on the 4-D Poincaré map that may be useful for map-based trajectory design, the "doughnut"-shaped structure appearing in Figure 3.13 is considered in more detail. One interpretation of this apparent 2-D surface is that it is associated with a kind of quasi-periodic motion *over the long-term propagation*. As discussed later in this section, there is an alternative explanation that is more illuminating and relevant to S/C trajectory design, however, the long-term, quasi-periodic interpretation is explored first because it also leads to important insight. In the full 6-D phase space (or the 5-D

constant-*JC* phase space), a quasi-periodic Earth-Moon spatial CR3BP trajectory, in general, could theoretically fill out the surface of a deformed 3-D KAM torus (a 3-torus) associated with regular motion in nearly-integrable Hamiltonian systems like this one [85, 115]. Therefore, a Poincaré map associated with such a 3-D surface would likely reduce to a 2-D surface, while preserving a 4-D phase volume. Such a 2-D surface could possess the form of the "doughnut" shape in Figure 3.13, Not only do the visual attributes of this map structure imply that it may be associated with quasi-periodic motion but that idea is also supported by a cursory frequency analysis using the MATLAB® built-in *fft* function, which calculates the discrete Fourier transform (DFT) utilizing a fast Fourier transform (FFT) algorithm [71, 116]. The "signal' associated with the trajectory plotted in Figure 3.11 appears to possesses a frequency spectrum that contains several large-amplitude "spikes" that represent *approximately discrete* frequencies along with linear combinations (sums, differences, and multiples) of those frequencies. In fact, these "spikes" in the frequency domain correspond to behavior observed on the short-term 4-D map plotted in Figure 3.10. One approximate frequency is associated with the progression of consecutive map returns around the figure-8 structure, with a figure-8 shape traced out roughly three times every eighty-two days (approximately three revolutions of the primaries). Another approximate frequency correlates with the observation that map returns along this 1-D "curve" repeat a *similar* 4-D location as a previous return after every twenty-six returns to the map and after a similar eighty-two-day time span. Over the almost sixty-year time span of the long-term 4-D map plotted in Figure 3.13, these two cyclical behaviors persist. As the simple 1-D "curve" evolves into an apparent 2-D, toroidal surface, consecutive map returns continue to trace out one cycle in the poloidal axis direction along the deformed torus roughly every one revolution of the primaries. Meanwhile, consecutive map returns form apparent "wires" along the apparent 2-D surface, with map returns filling in the "wires" in a similar location to a previous return every twenty-six crossings of the map and roughly every three primary revolutions. Finally, a *very-long-duration* cycle (with a very low frequency) completes after approximately fifty-three years when the map return progression arrives back near the original 1-D, figure-8-shaped "curve"—after filling out the full 2-D, "doughnut"

surface. Upon completion of one such long-term cycle, the map returns begin to evolve along the apparent 2-D surface again, increasing the dot density of the "wires." Note that reasonable variations in the numerical integration tolerance for propagating the trajectory associated with the "doughnut" do not have a noticeable effect on the shape of this 2-D surface or the time required for it to be generated. Therefore, it does not appear that the 2-D surface in Figure 3.13 can be explained in terms of some sort of numerical error.

To aid in interpretation of the long-term progression of map returns on the "doughnut", modified versions of the view in Figure 3.13 are plotted in Figures 3.14 through 3.16, now with certain sets of map returns plotted with larger dots. The first twenty-seven (out of 6,903) map returns are highlighted in the view in Figure 3.14; these returns trace out the figure-8 shape originally plotted in Figure 3.10, which appears as the "inner edge" of the "doughnut" in this view. After the initial time span of 81.85 days required to form this 1-D, figure-8-shaped "curve," the map returns essentially progress further away from this figure-8 location on every three-primary-revolution cycle, not tracing out the original figure-8 location again for roughly fifty-three years. Note that the "wires" of the "doughnut" near the first twenty-seven map returns appear more "compressed" than on the other parts of the deformed torus, implying that the 2-D surface is not filled out in a uniform way. This observation is important for the alternative explanation of the "doughnut" later in this section. Next, returns 3,881 through 3,907, generated after approximately 33.5 years, are highlighted in Figure 3.15. In contrast to the figure-8 shape formed by the first twenty-seven returns, the structure formed by these subsequent returns traces out a 1-D "curve" that does not have an apparent intersection in the 3-D space. Moreover, these returns are generated during a later stage of the process of filling out the 2-D, "doughnut" surface, and they are located on a different portion of the "doughnut" than the original figure-8. They appear to trace out the "outer edge" of the "doughnut" as displayed in this view. Finally, returns 6,118 through 6,144, generated after approximately fifty-three years, are highlighted in Figure 3.16. These subsequent returns trace out a 1-D "curve" that is similar in shape and 4-D map location to the figure-8 traced out by the first twenty-seven returns, thus completing a long-term cycle that fills out the entire 2-D surface.

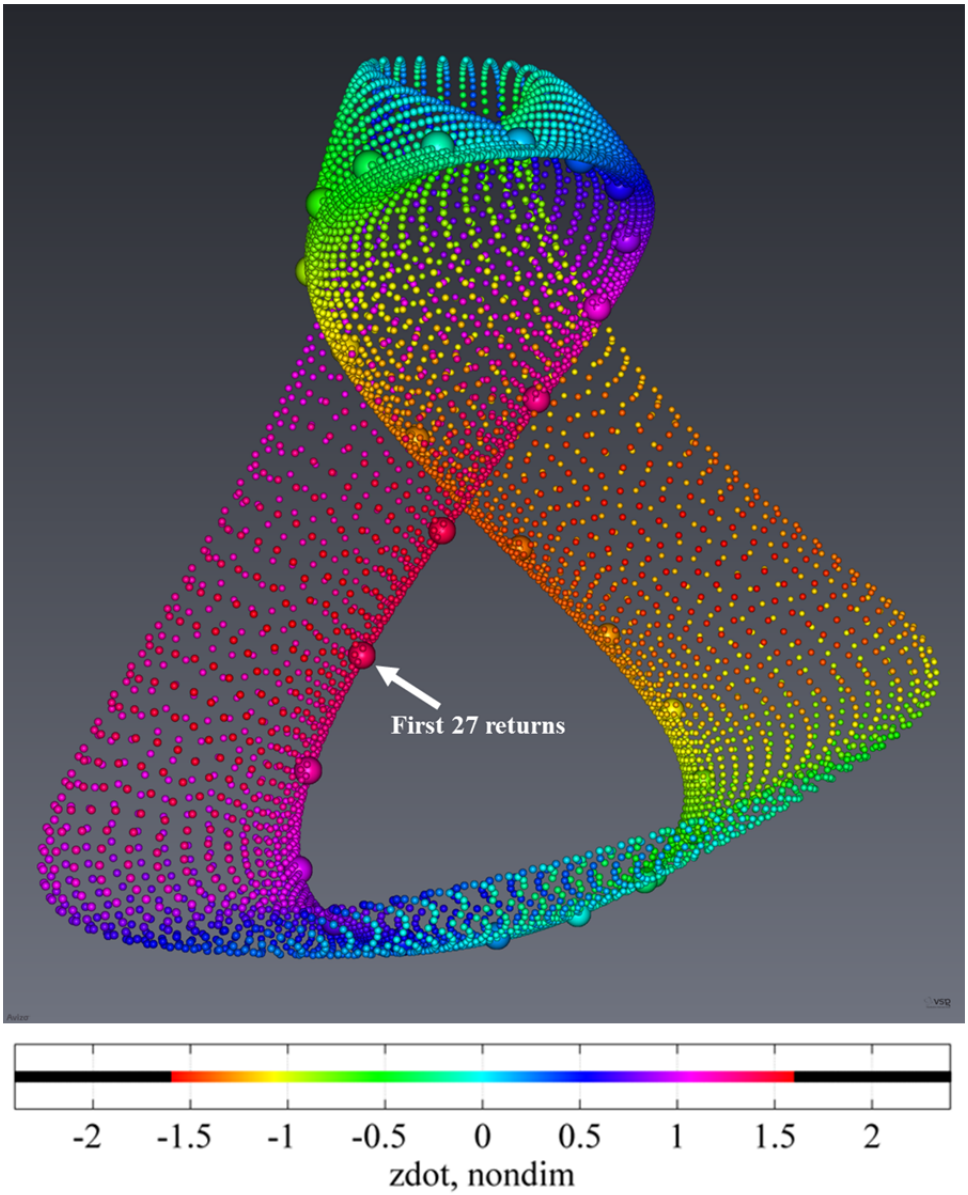

Figure 3.14. Modified Avizo® view of 4-D Poincaré map of 3-D, Earth-Moon trajectory; first 27 returns highlighted with larger dots; $(y = 0+;\ x,\ \dot{x},\ z,\ \dot{z}\_color)$

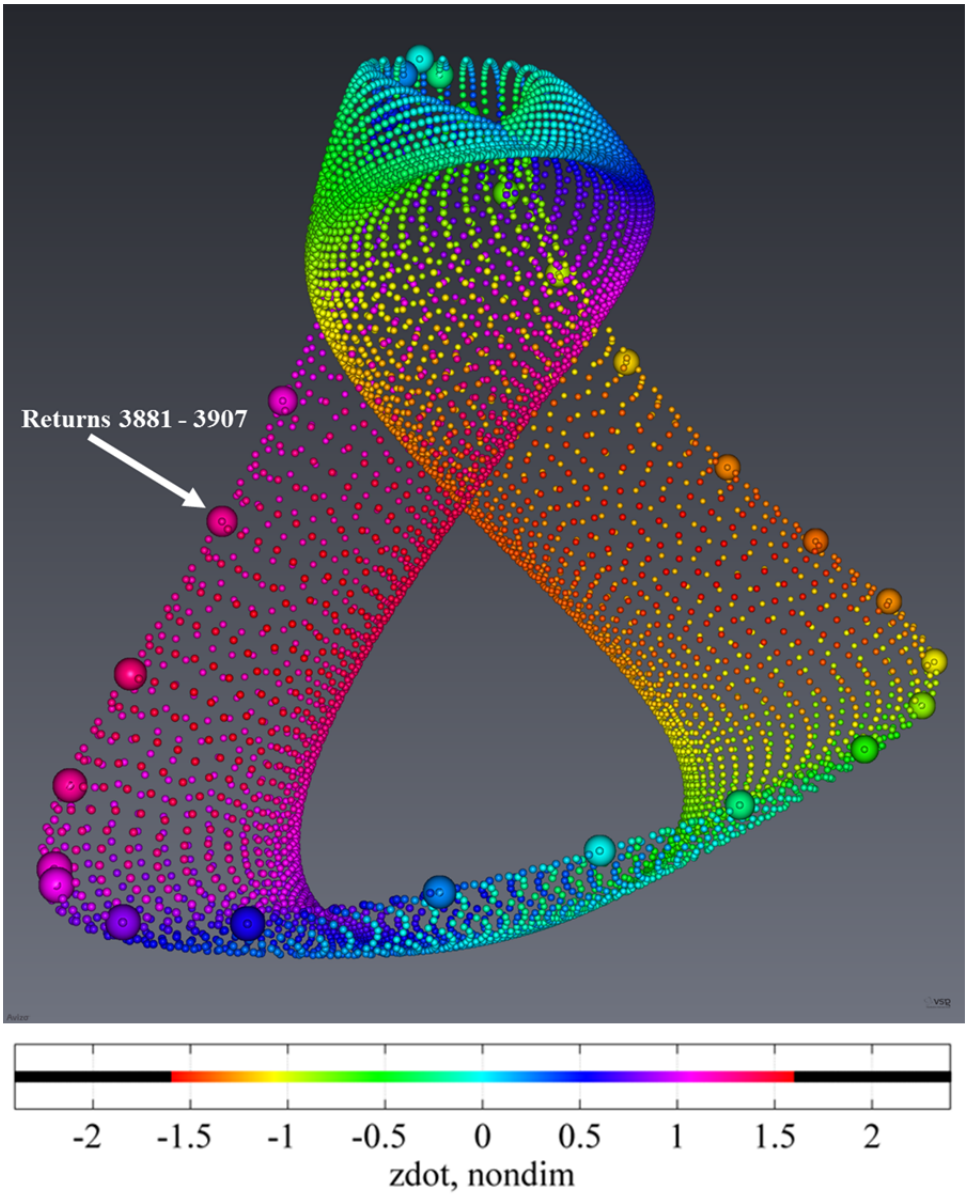

Figure 3.15. Modified Avizo® view of 4-D Poincaré map of 3-D, Earth-Moon trajectory; returns 3,881 through 3,907 highlighted with larger dots; $(y = 0+;\ x,\ \dot{x},\ z,\ \dot{z}\_color)$

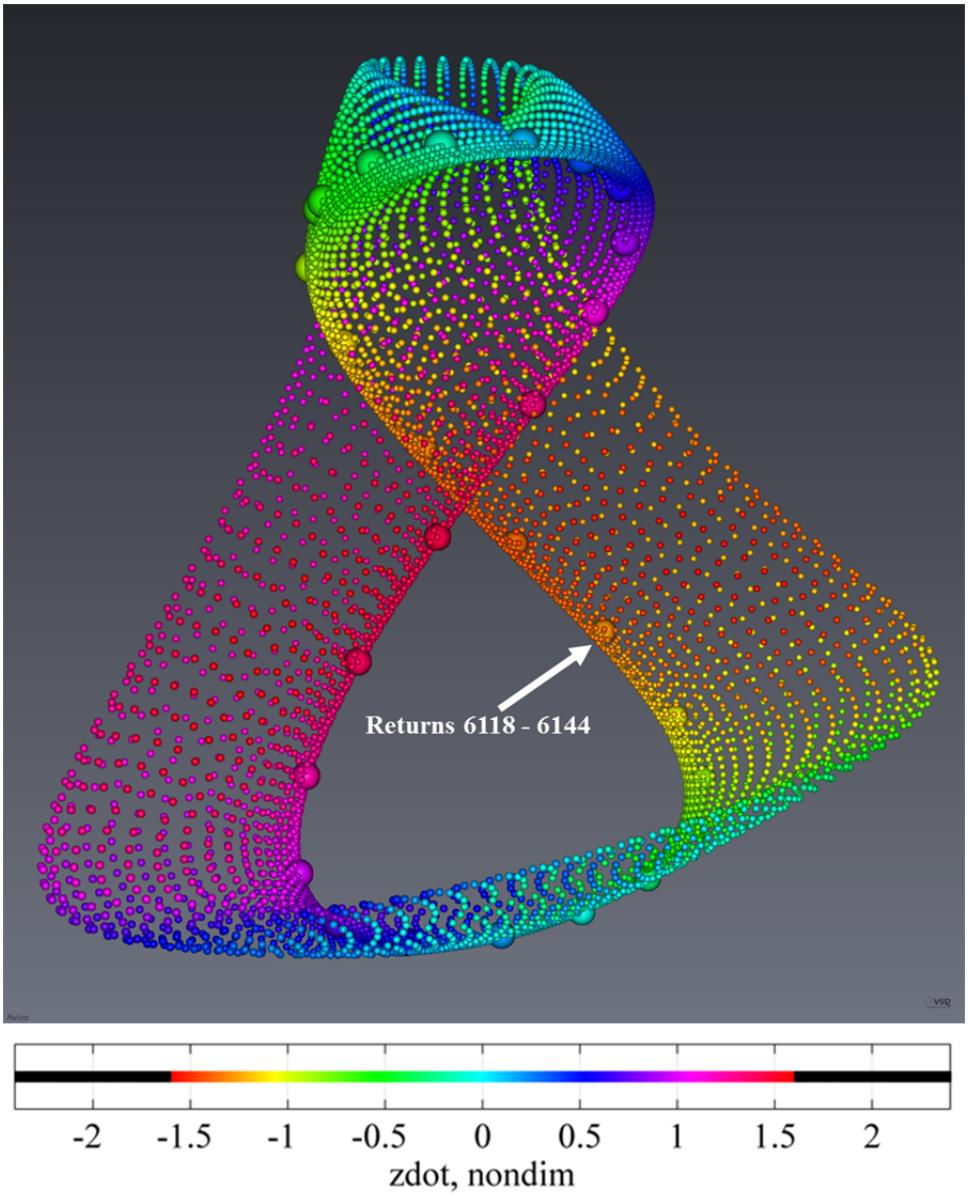

Figure 3.16. Modified Avizo® view of 4-D Poincaré map of 3-D, Earth-Moon trajectory; returns 6,118 through 6,144 highlighted with larger dots; $(y = 0+;\ x,\ \dot{x},\ z,\ \dot{z}\_color)$

The 2-D "doughnut" surface in Figure 3.16—represented using three spatial dimensions and one color dimension—possesses a remarkable topological property. It undergoes two inversions in 3-D space, near the maximum and minimum z values (the top and bottom of the figure), where the apparent outside surface of the yellow/orange segment becomes the apparent inside surface of the violet/magenta segment and vice versa. This even number of inversions guarantees that the "doughnut" does, in fact,

possess two distinct sides in the real 4-D space, making it topologically equivalent to a 2-torus. As an aside, if this structure were to undergo an odd number of inversions, it would be topologically equivalent to a Klein bottle [117]—a non-orientable, *one-sided*, 2-D surface—as opposed to a torus. At each of the two locations in Figure 3.16 where apparent inside and outside surfaces in the 3-D space swap places through inversion, a kind of *connection* is exposed between the apparent "interior" and "exterior" regions of the object. The most prominent of the two connections in this view is located at an apparent self-intersection at the top of the figure, where a large, "cup holder"-shaped indentation is visible in the 3-D map space; this connection, in the vicinity of cyan dots, allows an entry into the *apparent* "interior" region of the "doughnut." To clarify how this entry is possible, it is useful to imagine an ant walking along the apparent outside surface of the yellow/orange segment of the "doughnut." At the location of the inversion/connection at the top of the figure, the ant transitions from the apparent outside surface of the yellow/orange segment to the apparent inside surface of the violet/magenta segment. During this transition, the ant must cross what appears to be a physical obstruction in the 3-D space. However, the color of that obstruction is different from the color of the segment on which the ant is walking at the location of the obstruction. Therefore, the ant is free to cross because *the obstruction is not really there—from a 4-D perspective*. The second connection is present at an apparent self-intersection at the bottom of the figure, also in the vicinity of cyan dots. However, at the spatial scale utilized in this view, the "doughnut" appears extremely thin near the bottom connection, making the swapping of apparent inside and outside surfaces difficult to perceive unless viewed in the Avizo® visual environment. At this inversion/connection, the same ant transitions from the apparent inside surface of the violet/magenta segment back to the apparent outside surface of the yellow/orange segment where it began. Given that the "doughnut has two distinct sides in the real 4-D space, the ant walking along the apparent outside surface of the yellow/orange segment and the apparent inside surface of the violet/magenta segment never crosses paths with a different ant walking along the apparent inside surface of the yellow/orange segment and the apparent outside surface of the violet/magenta segment. Yet, both ants still visit both the apparent "interior" and

"exterior" regions of the "doughnut" due to the connections described. These connections may offer some intuitive confirmation that 3-D KAM surfaces, in this 3-DOF system, do not actually separate regions of the 5-D constant-*JC* phase space. As a result, the 2-D "doughnut" structure does not bound regions of the 4-D map space. This is a fundamental property of Hamiltonian systems with more than two DOF. Consequently, and in contrast to 2-DOF systems, chaotic trajectories are not contained by KAM tori but, rather, are allowed to visit the full range of the phase space. For an example of an inversion between surfaces of a deformed torus on a 4-D map depicted using the color and rotation method, see Fig. 12 of Katsanikas and Patsis [57].

The "doughnut" structure discussed thus far originates from a visual estimate of a 4-D state (and an associated 6-D spatial CR3BP trajectory) based on a prominent feature identified on a dense 4-D Poincaré map generated by seeding many initial conditions. Various 4-D map structures examined in this investigation also share this same "doughnut"-like property (see Section 5.3 for an example of 4-D-map-based S/C trajectory design exploiting similar structures). These "doughnut" structures *might,* loosely, be considered 4-D map analogs of the 2-D "island" structures appearing on 2-D maps, which are associated with quasi-periodic behavior in 2-DOF systems. Similar to the "islands" on 2-D maps that are often surrounded by a chaotic "sea," the "doughnuts" possess a definite structure—including an ordered "rainbow" spectrum of color—that produces a distinct appearance amidst a chaotic, mixed-colored "cloud" of other points on the 4-D map. However, it must be emphasized that, because the spatial CR3BP is a 3-DOF system, a 4-D Poincaré map generated for this system is expected to contain more diverse and complex features than those of 2-DOF systems like the planar CR3BP. Moreover, 4-D maps obey a *fundamentally* different topology [87, 88]. Therefore, associating a higher-D map feature in the spatial CR3BP with the "islands" on 2-D maps does *not* mean that they act as boundaries that divide the map space into separate regions, nor does it lead to a straightforward method of locating a stable periodic orbit at the "interior" of an "island" as in the planar CR3BP. Notably, *there is no "interior" of a 2-D surface on a 4-D map*, for the same reason that a 1-D line or circle cannot bound a region of a 3-D space.

Despite the complications inherent in classifying the "doughnut" (plotted in Figure 3.16) as a structure that is analogous to an "island" on a 2-D Poincaré map, it does appear that, like "islands" and "island chains" on maps for the planar CR3BP, these commonly-observed, higher-D map structures—as realized using the space-plus-color method in the spatial CR3BP—do "point" to various periodic behavior in their immediate vicinity. For example, in the 4-D map view appearing in Figure 3.17, a large cyan dot is plotted roughly beneath the apparent self-intersection (in 3-D map space) of the same "doughnut" as before. This cyan dot represents the single, fixed point map return associated with a linearly stable, period-one trajectory in the Earth-Moon CR3BP, converged to satisfactory periodicity, *in the rotating frame,* through a differential corrections (targeting) process as described in Section 2.2. In this case, the estimate for the targeting process is obtained visually by guessing that a fixed point associated with a periodic planar orbit exists at a perpendicular crossing of the $y = 0$ hyperplane (with $\dot{x} = \dot{z} = 0$) in the vicinity of the "doughnut" structure on the 4-D map. In fact, the fixed point represented by the cyan dot in Figure 3.17 is also located inside a true, 1-D "island" contour on a traditional, 2-D map for the planar CR3BP at the same "energy" level. This periodic orbit is a planar trajectory (in the *x*-*y* plane of the primaries) that is linearly stable in both the in-plane and out-of-plane directions; the 6-D, dynamical "flow" associated with the fixed point is of the type 2-D center × 2-D center × 2-D center. The orbit appears in Figure 3.18 in both the Earth-centric inertial view and the barycentric rotating view over a time span of 59.4 years. The period of the orbit in the rotating frame is approximately 2.87 days, slightly more than one-tenth the period of the primaries. The inertial view in Figure 3.18(a) indicates that this trajectory, although not periodic in the inertial frame, is almost circular. The minimum Earth altitude is roughly 85,536 km, and the variation in altitude along the path is only 60 km.

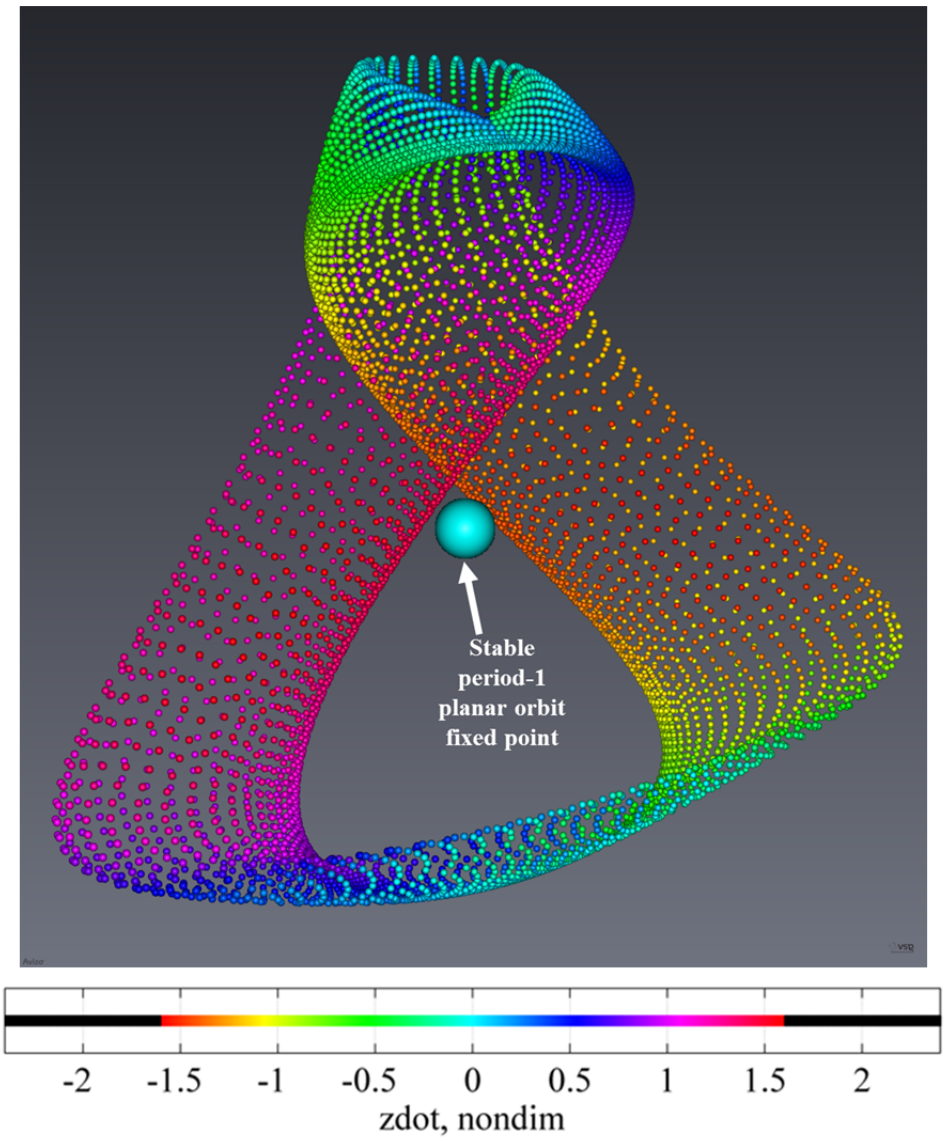

Figure 3.17. Avizo® view of 4-D Poincaré map of Earth-Moon trajectories; 6,903 returns of 3-D trajectory along with a period-1, planar trajectory fixed point; ($y = 0+;\ x,\ \dot{x},\ z,\ \dot{z}\_color$)

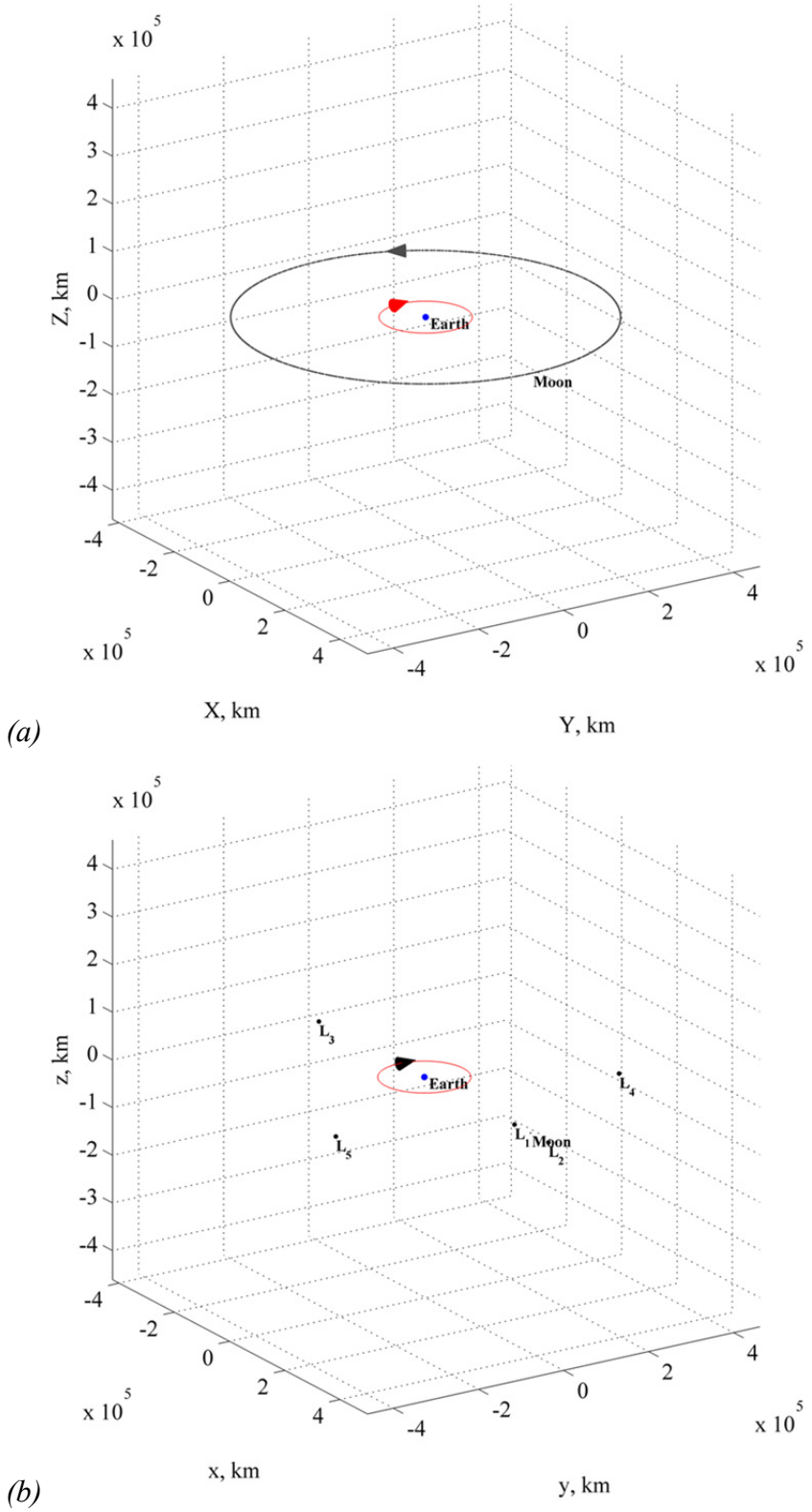

Figure 3.18. Long-term propagation of planar, period-l, Earth-Moon trajectory over 59.4 years: inertial (*a*) and rotating (*b*) views

While the preceding interpretation of the "doughnut" appearing in Figure 3.17 is valid according to the general principle that quasi-periodic motion in a nearly-integrable, 3-DOF, Hamiltonian system like the spatial CR3BP could theoretically fill out the surface of a deformed 3-torus, it has key weaknesses in two aspects. First, given the long time span (fifty-three years) required for the apparent 2-D surface to form, this form of quasi-periodicity may not be practically distinguishable from motion that—while roughly periodic for some brief time span and also bounded over a longer span—is essentially the result of an unstable evolution away from a nominal condition. Second, the interpretation of the "doughnut" as representative of quasi-periodic behavior in the spatial CR3BP is not consistent with knowledge of a broad class of quasi-periodic CR3BP trajectories, which are relevant for S/C mission design. A description of such orbits is important for an understanding of the complex behavior observed on the "doughnut" structure.

Various quasi-periodic variants of 3-D, periodic orbits in the vicinity of collinear libration points exist in families across a range of "energy" levels (*JC* values) [26, 27] These quasi-periodic orbits correspond to the more familiar, invariant deformed *2-tori* in the spatial CR3BP [118]. The topology associated with various quasi-halo and quasi-vertical ("Lissajous") orbits is explained by the fact that these 3-D, periodic orbits in the vicinity of L_1 and L_2 actually belong to a 4-D center manifold and thus a 3-D constant-*JC* center manifold of *all* rotational motion in the vicinity of the libration point at a particular "energy" level. Each quasi-periodic orbit, assuming it is *perfectly* on the center manifold surrounding the libration point, fills out a deformed 2-torus in a 5-D constant-*JC* phase space. Therefore, when examined on a 4-D surface of section for the spatial CR3BP, the quasi-periodic trajectory should appear as a 1-D "curve." In fact, these quasi-periodic orbits are often represented as 1-D "island" contours surrounding a 3-D, periodic orbit's fixed point on a 2-D Poincaré map generated after completing a *reduction* to the 4-D center manifold space [45]. However, a 2-D map representing such center manifold structure does not depict the unstable (saddle) dynamics in the vicinity of an unstable fixed point, and "islands" in a center manifold reduction do not behave the same way as "islands" on 2-D maps for the planar CR3BP. On the 4-D Poincaré map, which is required to properly represent the complete dynamics for any quasi-periodic, 3-D motion

in the spatial CR3BP, a 1-D "curve" generated by an invariant deformed 2-torus does *not* act as an impenetrable boundary that divides the 4-D space. Similarly, the deformed 2-torus itself cannot divide the 5-D constant-*JC* phase space.

Based on the understanding of quasi-periodic orbits existing along deformed 2-tori in the full phase space of the CR3BP, a more illuminating interpretation of the "doughnut" on the 4-D map plotted in Figure 3.17 is possible. This interpretation is also more relevant to S/C mission design. It appears that the "doughnut" is associated with a perturbation on unstable periodic behavior in the immediate vicinity of the structure. This is akin to both the "tori" as well as the larger, "rotational invariant surfaces" generated by Vrahatis et al. [51, 52], which "envelop" the map space surrounding unstable fixed points. In that study, the unstable fixed points—perturbed to produce the tori—are of the type 2-D center × 2-D saddle. Moreover, the 1-D, figure-8-shaped "curve" initially plotted in Figure 3.10—and also represented as the first twenty-seven map returns associated with the "doughnut" plotted in Figure 3.14—appears to be associated with motion that *approximates*—for a brief span of time—quasi-periodic motion along the center manifold associated with an unstable periodic orbit. Thus, it is the 1-D, figure-8-shaped structure—rather than the entire 2-D "doughnut" surface—that is best associated with practically relevant quasi-periodic behavior (for a brief time span). If the motion of the trajectory generating the returns on the 4-D map were truly quasi-periodic and perfectly associated with *only* a 4-D center manifold of an unstable periodic orbit, then the returns would form a 1-D "curve" such as the figure-8 shape generated initially; the "doughnut" would never form. However, because the trajectory also has a mode associated with the unstable (saddle) dynamics in the vicinity of the supposed unstable periodic orbit, the map returns gradually depart from the figure-8 location. To clearly demonstrate that the initial map returns on the "doughnut" form an *approximately* 1-D "curve" on the 4-D Poincaré map, the first 200 returns are plotted in Figure 3.19 over a time span equal to roughly 1.7 years. The figure-8 structure—while somewhat segmented due to the map returns beginning to fill out the 2-D "doughnut" surface—is associated with an *approximately* (for a brief span of time) quasi-periodic trajectory filling out an invariant deformed 2-torus in the 5-D constant-*JC* phase space. Note that

the figure-8 possesses a near-intersection (but not a perfect intersection) in the 3-D map space. Yet, because the apparent near-intersection occurs between segments with

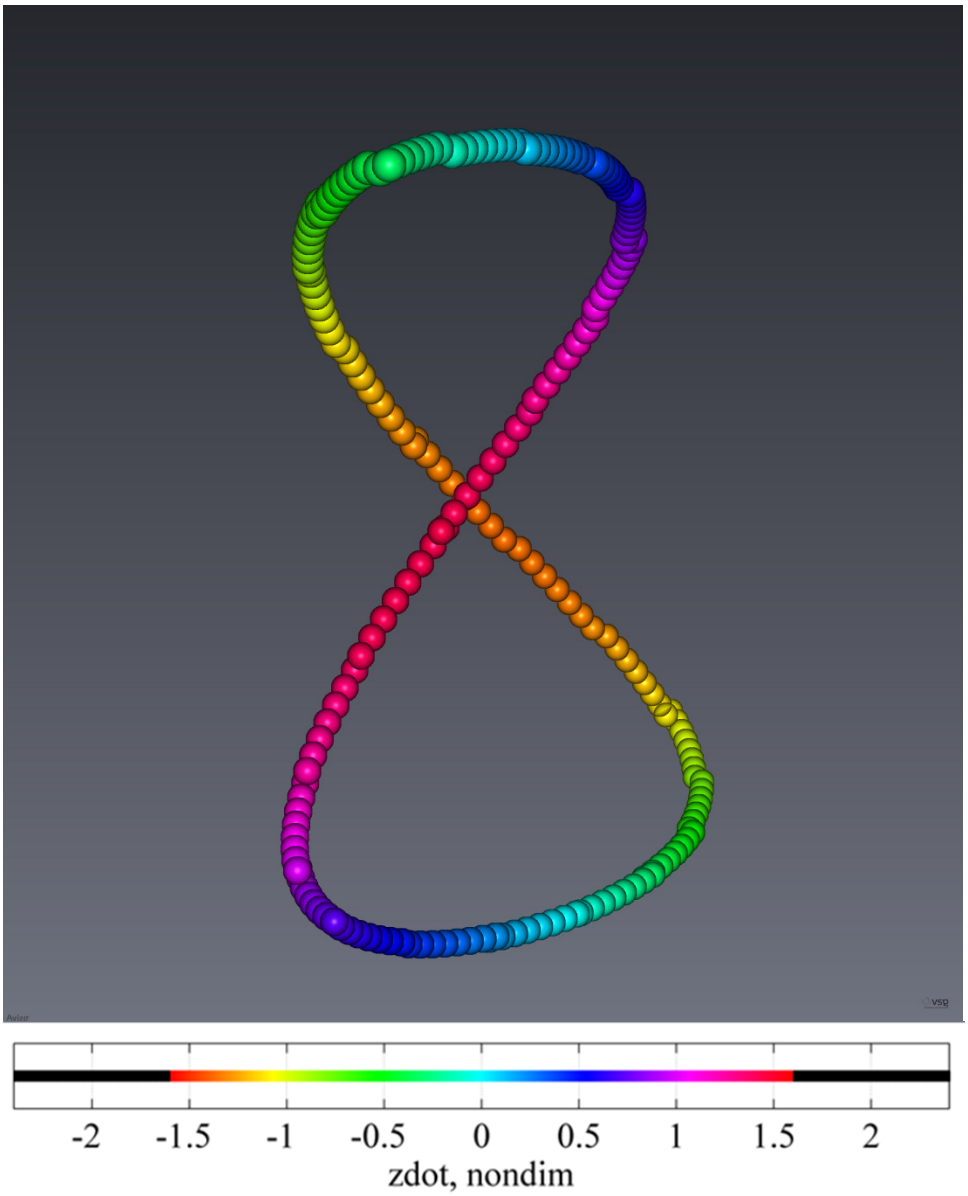

Figure 3.19. Avizo® view of 4-D Poincaré map of 3-D, Earth-Moon trajectory; first 200 returns over 1.7 years; $(y = 0+;\ x,\ \dot{x},\ z,\ \dot{z}\_color)$

different colors (magenta and orange) on opposite ends of the $\dot{z}$ color scale, it is not a near-intersection in the 4-D space. This "curve" would appear more like a circle than a figure-8 in a real 4-D world.

The fact that the map returns associated with the 3-D trajectory ultimately fill out a 2-D "doughnut" surface that eventually leads back to the original figure-8 location depicted in Figure 3.19 after roughly fifty-three years may be considered not only a type of long-term quasi-periodic motion but also, more important, a homoclinic-type behavior. A homoclinic trajectory that connect the unstable and stable "manifolds" associated with a quasi-periodic trajectory existing in the center manifold of an unstable periodic orbit would exhibit the type of behavior observed as the "doughnut" structure is formed. Based on this insight, the "doughnut" surfaces on a 4-D Poincaré map might be understood as analogs of the structure associated with "chains" of *unstable* fixed points on 2-D maps, rather than the "islands" associated with stable fixed points. Of course, the "doughnut" plotted in Figure 3.17 does not constitute a true homoclinic cycle, which would involve asymptotic behavior at each end of the cycle over infinite time. In fact, upon completion of one fifty-three-year cycle, the map returns begin to evolve along the apparent 2-D surface again, increasing the dot density of the "wires."

The interpretation of the "doughnut" structure plotted in Figure 3.17 as associated with a perturbation on unstable periodic behavior is supported by the existence of a figure-8 structure consisting of twenty-six *fixed-point* map returns in the immediate vicinity of the "doughnut." These fixed points, which are plotted with large dots along with the "doughnut" on the 4-D map view in Figure 3.20, are associated with an unstable periodic (in the rotating frame) trajectory in the Earth-Moon spatial CR3BP. The periodic orbit is converged to satisfactory periodicity through a differential corrections (targeting) process. The automated process is initiated by an estimate obtained through visual inspection of the 4-D map, by guessing that two fixed points exist at perpendicular crossings of the $y = 0$ hyperplane (with $\dot{x} = \dot{z} = 0$) near the top and bottom of the "doughnut" structure. The resulting period-twenty-six orbit is unstable; the 6-D, dynamical "flow" associated with each fixed point is of the type 2-D saddle × 2-D center × 2-D center, which is the same general type as the "flow" in the vicinity of the collinear libration points, where various quasi-periodic orbits belong to a 4-D center manifold. The periodic trajectory is plotted in Figure 3.21(a) in the Earth-centric inertial view for a time equal to one orbit period, which is approximately 81.92 days—slightly more than

three primary revolutions. A long-term inertial view over a time span equal to 59.4 years appears in Figure 3.21(b). Finally, the period-twenty-six orbit is plotted in the barycentric rotating view in Figure 3.22 over the same long-term time span.

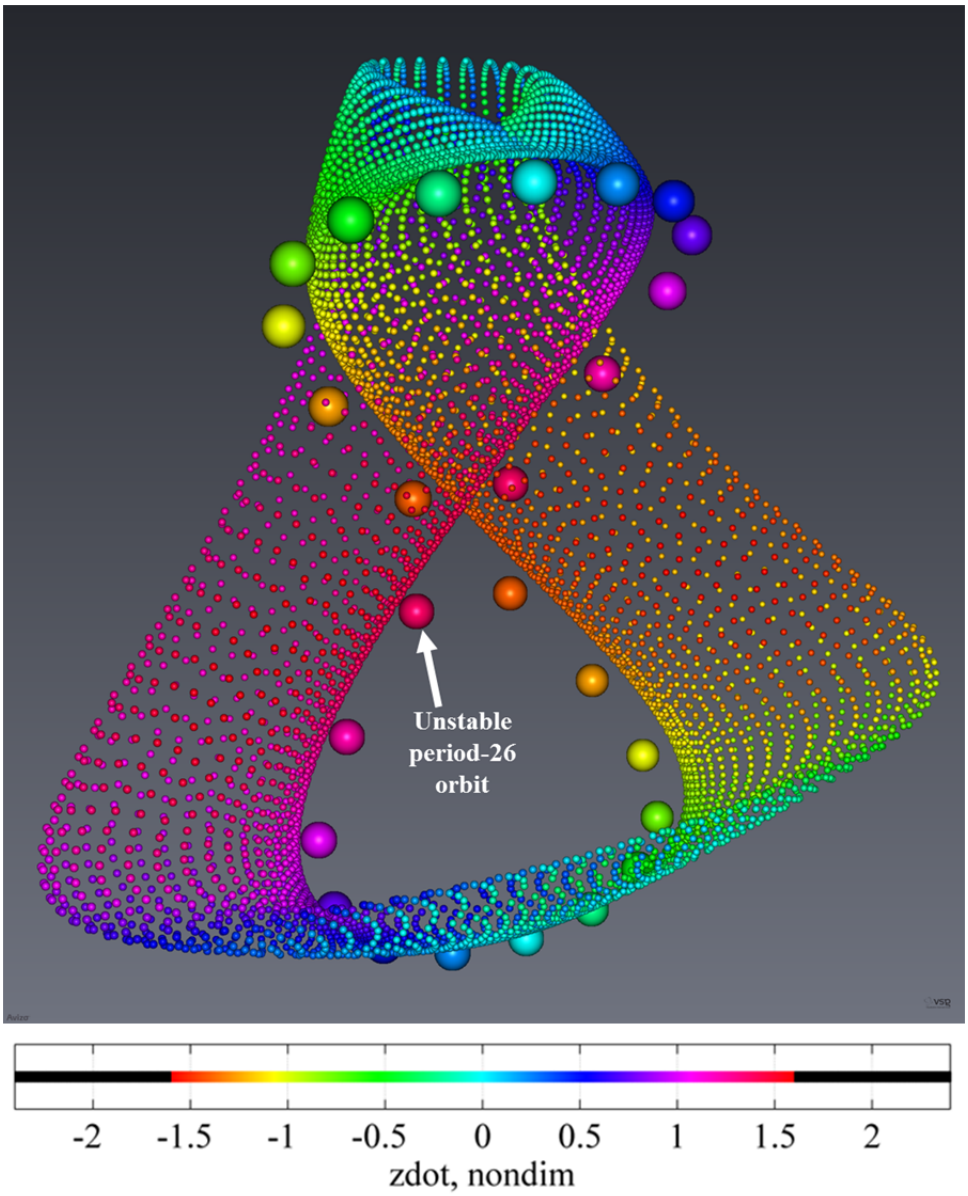

Figure 3.20. Avizo® view of 4-D Poincaré map of Earth-Moon trajectories; 6,903 returns of 3-D trajectory along with 3-D, period-26 trajectory fixed points; ($y = 0+;\ x,\ \dot{x},\ z,\ \dot{z}\_color$)

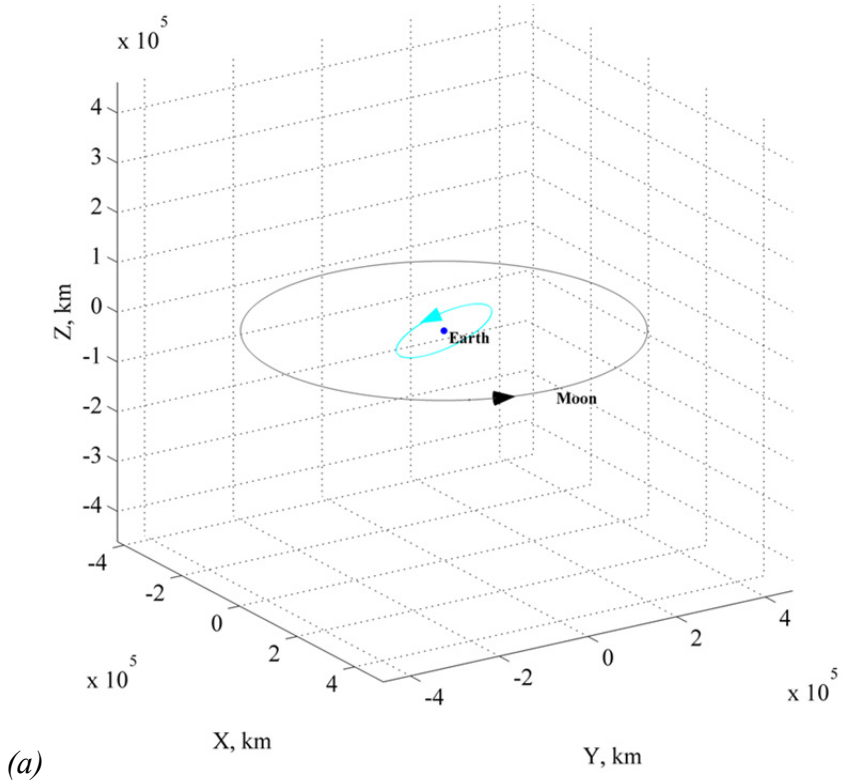

(a)

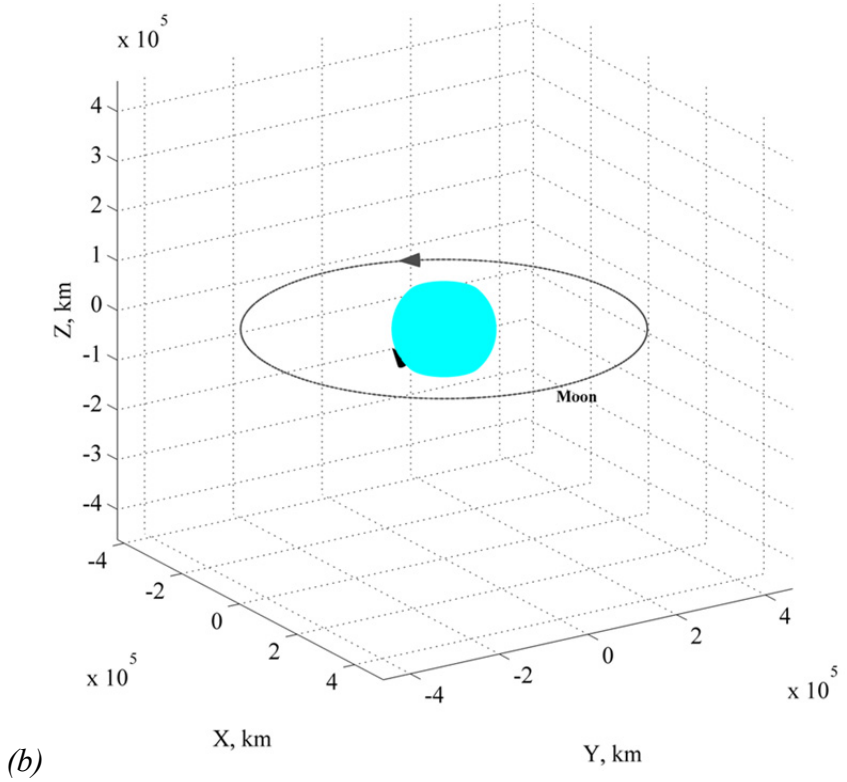

(b)

Figure 3.21. Inertial view of one-period (81.92 days) (*a*) and long-term (59.4 years) (*b*) propagations of 3-D, period-26, Earth-Moon trajectory

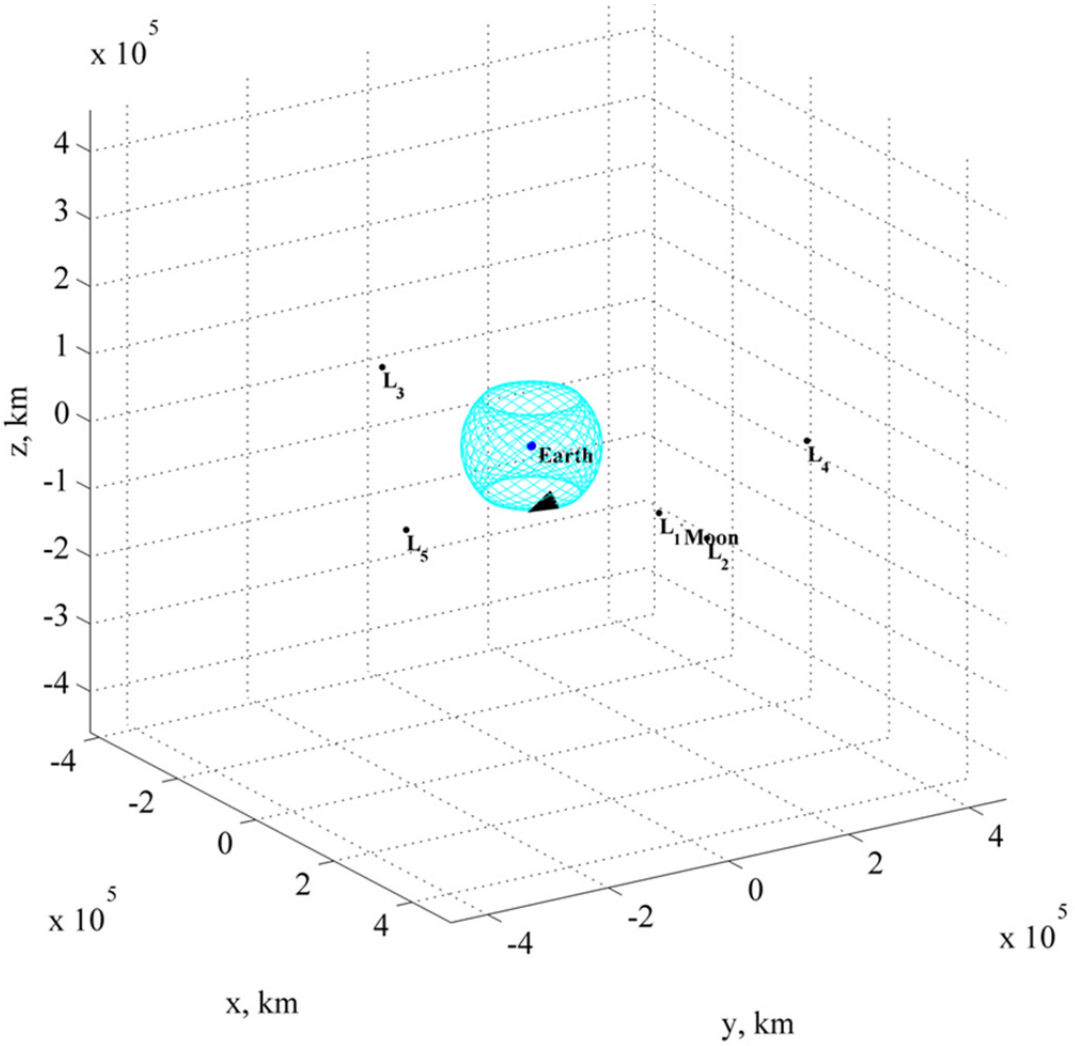

Figure 3.22. Rotating view of long-term propagation of 3-D, period-26, Earth-Moon trajectory over 59.4 years

In the characterization of the "doughnut" as the result of a perturbation on a nominal condition, it is further illuminating to examine the associated CR3BP trajectory from a *two-body* dynamical perspective in the Earth-centric inertial frame. The instantaneous (osculating), Earth-centered, two-body orbital elements for the initial condition of the 3-D trajectory plotted in Figures 3.7, 3.8, 3.9, and 3.11 are calculated and appear in Table 3.1. This calculation is based on the Moon's own osculating elements at an arbitrarily selected epoch, obtained from the JPL HORIZONS System web-interface (ephemeris data DE-0431LE-0431) [111] (see Section 2.8.2). The set $(a, e, i, \Omega, \omega, \nu)$ consists of semimajor axis, eccentricity, inclination, longitude of ascending node, argument of

perigee, and true anomaly, respectively. Note that the inclination of the 3-D trajectory is greater than 90°, indicating that this orbit, which is already determined to be retrograde with respect to the prograde motion of the Moon in the plane of the primaries, is also retrograde with respect to the Earth-centric mean equatorial reference frame. At the selected epoch, the osculating inclination of the Moon's orbit with respect to the Earth-centric mean equatorial reference frame is equal to 18.63° [111].

Table 3.1 3-D, Earth-Moon trajectory initial osculating orbital elements*

a	e	i	Ω	ω	ν
98,404.77 km	0.096021	122.39°	131.48°	310.74°	323.05°

* Earth-centric mean equatorial reference frame; equinox of reference epoch J2000.0; epoch: 1 January 2015 at "midnight"

The two-body orbit period—about the Earth in the Earth-centric 2BP—associated with an ellipse (eccentricity $e < 1$) with the value of semimajor axis a specified in Table 3.1 is approximately equal to 3.56 days. This period is close to 3/23 of the period of the Moon's orbit, equal to roughly 27.3 days, indicating that the 3-D trajectory begins in a nearly-23:3 orbital resonance with the Moon's orbit in the inertial frame. That is, in an Earth-centric two-body analysis, the 3-D trajectory completes twenty-three revolutions in almost the same time span that the Moon completes three orbits. In fact, this near-resonance is the fundamental explanation for the progression of consecutive map returns around the figure-8 structure plotted in Figure 3.10, with a figure-8 shape traced out roughly three times every approximately three revolutions of the primaries (three "months"). Moreover, the specific orbit period ratio of the near-resonance explains the observation that map returns along this 1-D "curve" repeat a similar 4-D location as a previous return after every *twenty-six* returns to the map and after a similar three-primary-revolution time span. The fact that there are twenty-six locations on the map—over each cycle—rather than twenty-three is due to the relationship between the rotating and inertial frames. In the inertial view, the 3-D trajectory generating the 1-D "curve" plotted in Figure 3.10 completes twenty-three revolutions in almost the same time span

that the Moon completes three orbits. Yet, the rotating frame itself is revolving in a prograde direction *opposite* the direction of the retrograde, 3-D trajectory. Therefore, over the three-primary-revolution time span, the 3-D trajectory crosses the *inertial X*-axis in a positive direction twenty-three times, while it crosses the *rotating x*-axis in a positive direction twenty-six times. The three revolutions of the rotating frame effectively add three "extra" returns (23 + 3 = 26) to the map, which is defined such that $y = 0$ and $\dot{y} > 0$.

To explain the evolution of map returns along the 2-D surface of the "doughnut" appearing in Figure 3.20, the osculating, Earth-centered, two-body orbital elements for the 3-D trajectory specified in Table 3.1 are calculated over an extremely-long-term time span equal to 594 years (50,000 nondimensional time units), as plotted in Figure 3.23. This time span is *ten times* that required to generate the "doughnut" plotted in Figure 3.20. It is important to emphasize that the instantaneous orbital elements are based on ephemeris data at a single epoch along with the simplifying assumption that the Moon's orbit about the Earth still obeys the dynamics of the CR3BP; the Moon's orbit is assumed to be perfectly circular. Furthermore, the variation in the Moon's orbit with respect to the Earth-centric mean equatorial reference frame is ignored; the inclination of the Moon's orbit is assumed to be equal to 18.63° for the entire 594 years. This is an unrealistic assumption, given that the Moon's inclination actually varies between approximately 18.4° and 28.6°, completing a cycle every 18.6 years [74]. However, for this analysis, it is not appropriate to realistically model the Moon's orbit in order to explain the evolution of the "doughnut" surface that is generated in the lower-fidelity model of the CR3BP. Accounting for variations in the Moon's orbit would actually introduce additional variables not relevant to the behavior observed on the 4-D Poincaré map in the CR3BP.

The extremely-long-term plot of osculating orbital elements in Figure 3.23 reveals that the amplitude of high-frequency variations in the instantaneous semimajor axis a is relatively small, equal to less than 100 km (peak-to-peak). This implies that the two-body orbit period—and the associated nearly-23:3 orbital resonance—remains fairly constant, explaining the long-term persistence of the frequencies associated with the tracing out of map returns in twenty-six locations similar to the previous twenty-six every

three primary revolutions as the surface of the "doughnut" is filled out. Also apparent in Figure 3.23 are significant, long-term variations in the values of instantaneous

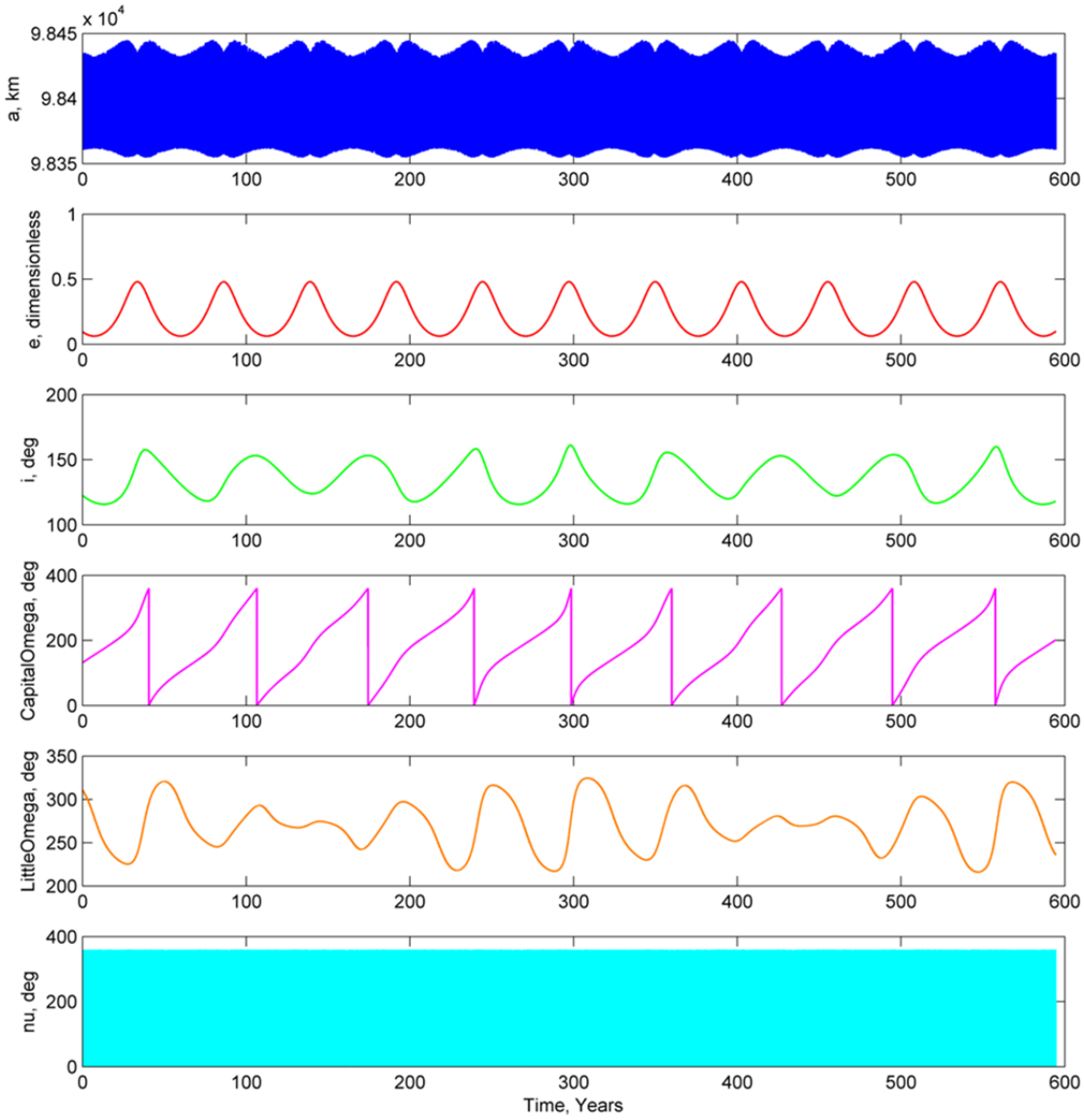

Figure 3.23. 3-D, Earth-Moon trajectory osculating orbital elements

eccentricity e, inclination i, longitude of ascending node Ω, and argument of perigee ω. The variation in eccentricity e appears nearly-periodic on each cycle, while the "cycles" in inclination i, longitude of ascending node Ω, and argument of perigee ω do not. Most

notably, the apparent period of the long-term variation in instantaneous eccentricity *e* is approximately fifty-three years, *the same time span over which the 4-D map returns fill out the entire 2-D surface of the "doughnut" once.* Furthermore, the initial eccentricity is fairly close to the value of the first minimum in eccentricity ($e = 0.06$), while the first maximum in eccentricity ($e = 0.48$) is reached after roughly 33.5 years, the same time span after which the map returns highlighted in Figure 3.15 appear to trace out the "outer edge" of the "doughnut." In addition, the troughs on the "sinusoidal" plot of eccentricity *e* are significantly wider than the crests. This asymmetry correlates with the "wires" on the "doughnut" near the "inner edge" (the original figure-8 shape) appearing more "compressed" than on the "outer edge," as mentioned earlier. Overall, these observations strongly indicate that the 2-D surface of the "doughnut" on the 4-D map plotted in Figure 3.20 is filled out as the result of long-term, periodic variations in the Earth-centered osculating eccentricity *e* of the 3-D trajectory, with the progression between the "inner edge" and the "outer edge" of the "doughnut" tied to the evolution between minimum and maximum values of eccentricity *e*, respectively. Because the eccentricity *e* of the 3-D trajectory generated by the "doughnut" would be constant under purely two-body dynamics, the 2-D surface of the "doughnut" formed on the 4-D Poincaré map appearing in Figure 3.20 essentially represents the result of the perturbation by the Moon's gravity on the nominal, Earth-centered, two-body eccentricity *e* of the orbit.

The indicated relationship between long-term, periodic variations in the Earth-centered, osculating eccentricity *e* of the 3-D orbit examined in this example and the shape/evolution of the "doughnut" generated on the 4-D map by that orbit leads to two important predictions. The first prediction is that, because the period-twenty-six orbit represented in Figure 3.20 does not generate map returns that evolve into a 2-D, "doughnut" surface, it is not expected to have a significant, long-term variation in its own instantaneous eccentricity *e*. The returns generated by the converged period-twenty-six orbit remain close to the twenty-six fixed point locations plotted in Figure 3.20 even after 59.4 years. Therefore, an analysis of the osculating orbital elements for that time span is expected to accurately represent the "true" periodic motion. The plot of the osculating, Earth-centered, two-body orbital elements for the period-twenty-six trajectory over the

59.4-year time span appears in Figure 3.24 (with a different scale from Figure 3.23 on several subplots). The prediction that the trajectory does not have significant, long-term variation in its instantaneous eccentricity *e* is confirmed. In fact, the maximum value

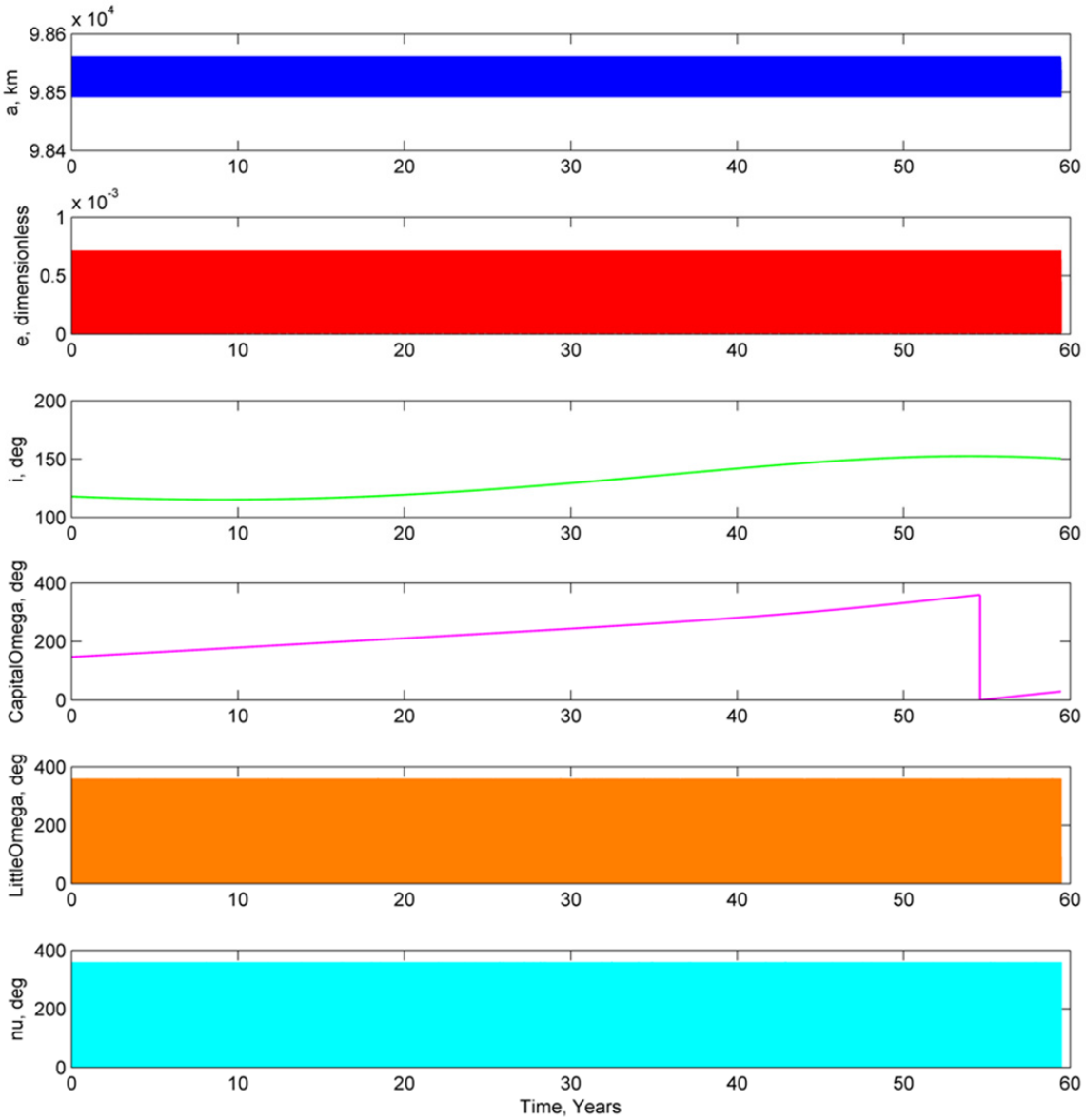

Figure 3.24. 3-D, period-26 trajectory osculating orbital elements

reached in the high-frequency variations in the value of the instantaneous eccentricity is less than $e = 0.0007$, indicating almost circular motion in the Earth-centric inertial frame

at any instant. Interestingly, the period-twenty-six orbit is similar to the trajectory generating the "doughnut" in that it also undergoes significant, long-term variations in the values of inclination i and longitude of ascending node Ω as well as relatively small (less than 100 km peak-to-peak) amplitude, high-frequency variations in the instantaneous semimajor axis a. Furthermore, the two-body orbit period—about the Earth in the Earth-centric 2BP—associated with an ellipse with the mean value of semimajor axis a displayed in Figure 3.24 is approximately equal to 3.56 days and only slightly longer than that of the trajectory generating the "doughnut." Accordingly, this orbit is also associated with a nearly-23:3 orbital resonance with the Moon's orbit in the inertial frame. However, unlike for the trajectory generating the "doughnut," the instantaneous argument of perigee ω varies across the full range between 0° and 360° at a high frequency; this is likely explained by the small value of eccentricity e, where argument of perigee ω is closer to being undefined.

A second prediction based on the relationship between long-term, periodic variations in the Earth-centered, osculating eccentricity e of the 3-D orbit examined in this example and the shape/evolution of the "doughnut" generated on the 4-D map by that orbit is that the overall shape of the "doughnut" should appear invariant over the extremely-long-term time span equal to 594 years. This prediction is based on the nearly-periodic, sinusoidal variation in eccentricity e displayed in Figure 3.23. To confirm the predicted invariance, the 4-D map associated with this 594-year propagation is plotted in Figure 3.25. The time span and total number of map returns are each *ten times* that associated with the "doughnut" plotted in Figure 3.20. In the extremely-long-term, 4-D map view, the overall shape of the "doughnut" remains essentially the same—as predicted—and it appears that the "wires" filling out the apparent 2-D surface of the "doughnut" are still well-defined. Yet, they are now slightly thicker, with successive map returns gradually drifting away from locations along perfect, 1-D "wires" and apparently beginning to fill out more of the 2-D surface of the "doughnut" in the gaps between "wires." This thickening of the wires does not seem to be purely the result of numerical error. It is further confirmation that this "doughnut" represents an invariant deformed 2-torus in the 4-D map space—at least over the time span examined (594 years). As described earlier,

such a surface is associated with a type of long-term quasi-periodic motion filling out a deformed 3-torus in the 5-D constant-*JC* phase space. Yet, given the preceding analysis, the theoretical explanation of such behavior is now also correlated with long-term variations in a practically-relevant osculating two-body orbital parameter: the eccentricity *e* of the 3-D trajectory.

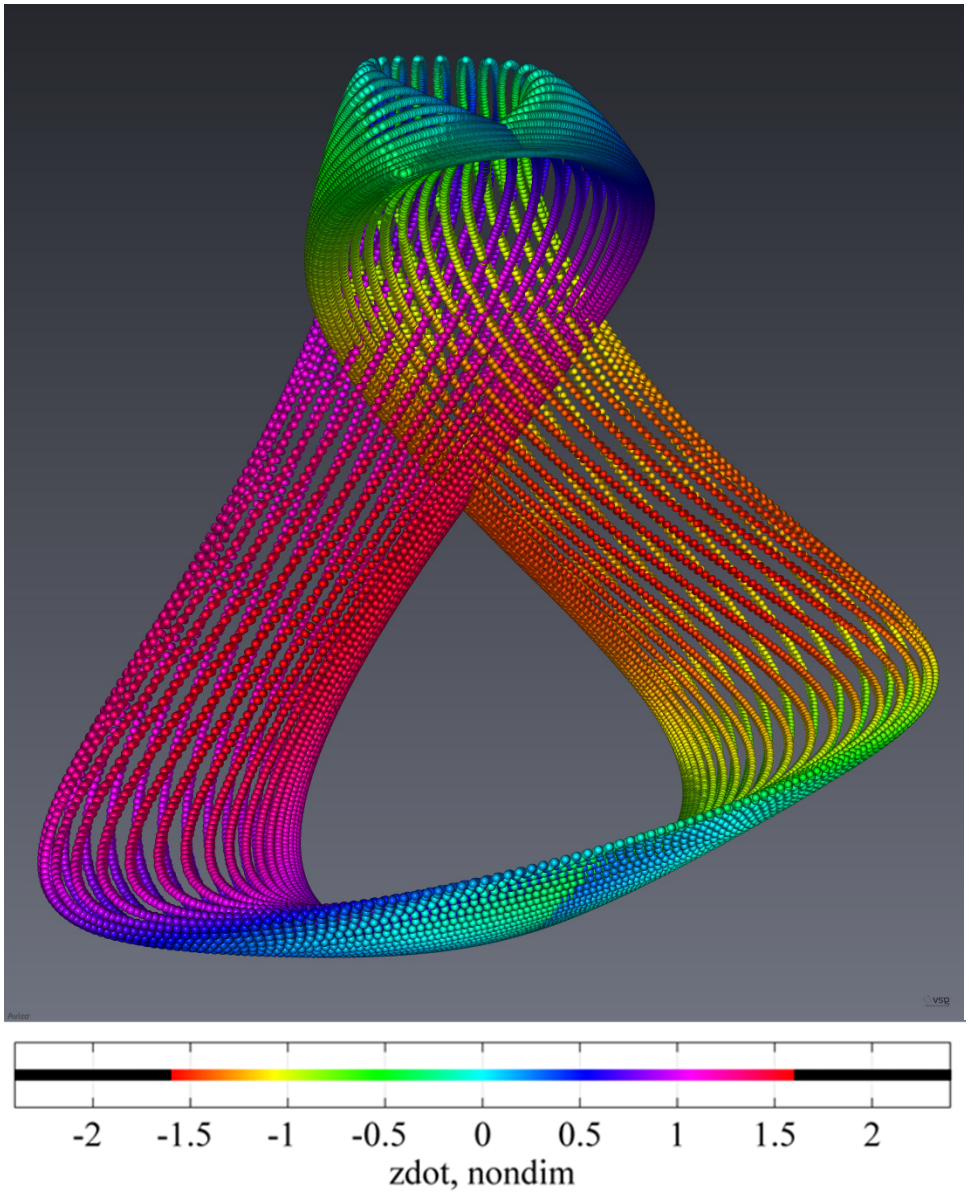

Figure 3.25. Avizo® view of 4-D Poincaré map of Earth-Moon trajectory; 69,030 returns over 594 years; $(y = 0+;\ x,\ \dot{x},\ z,\ \dot{z}\_color)$

Additional study is necessary to determine the extent to which the specific relationship, in this one example, between the osculating eccentricity *e* of a 3-D, high-altitude, Earth orbit perturbed by lunar gravity and the shape/evolution of an associated "doughnut" on a 4-D Poincaré map displayed using the space-plus-color method is applicable in other cases. Yet, the association of perturbed, nominally two-body, Earth orbits with KAM tori is evident from investigations by Wiesel [69, 70] of low-altitude orbits perturbed by the Earth's non-spherical gravity field, i.e., the geopotential. Also, based on analyses using reference KAM tori that ignore lunar gravity, Bordner [119] and Hagen [120] both indicate that there may be value in incorporating/fitting lunar gravity into a reference KAM torus for Earth satellite motion. Although this topic is not the focus of the present investigation, the space-plus-color method could allow an intuitive means to explore further relationships between Earth satellite perturbations and KAM tori using 4-D Poincaré maps displayed in a visual environment.

"Doughnut"-shaped structures—along with less-well-defined variations on those structures—appear frequently on dense 4-D Poincaré maps generated by seeding many initial conditions, often forming chains of multiple structures, perhaps analogous to the 2-D "island chains" on 2-D maps. For example, a five-"doughnut" "chain" formed by a single trajectory in the Copenhagen spatial CR3BP of equal primary masses (mass ratio μ = 0.5) [1, 29] is plotted in the four-perspective view of the 4-D Poincaré map in Figure 3.26. This Cartesian phase space 4-D map is defined using the same formulation as in the previous example: $(y = 0+;\ x,\ \dot{x},\ z,\ \dot{z}\_color)$. In this example, 3,845 returns are generated by a trajectory possessing a value of *JC* equal to 3.5, which defines the "energy" level of the map. The time span is equal to 1,592 primary revolutions. The same five-"doughnut" "chain" also appears in the Avizo® view in Figure 3.27. This type of apparent figure-8 shape (or multiple shapes) formed in the 3-D map space is a feature observed in many cases; however, "doughnuts" without an apparent intersection are also observed. In fact, the apparent shape of 4-D map structures generated by any given trajectory varies depending on the choice of map formulation. It should be noted that not all "doughnut"-shaped features examined in this investigation have an apparent invariance over the long term. Instead, many structures that appear "doughnut"-shaped

over a short-term plot eventually evolve into less well-defined structures over the long-term. This implies that structures appearing "doughnut"-like on the 4-D map may belong to a general form associated with perturbations on nominal, "quasi-periodic" motion

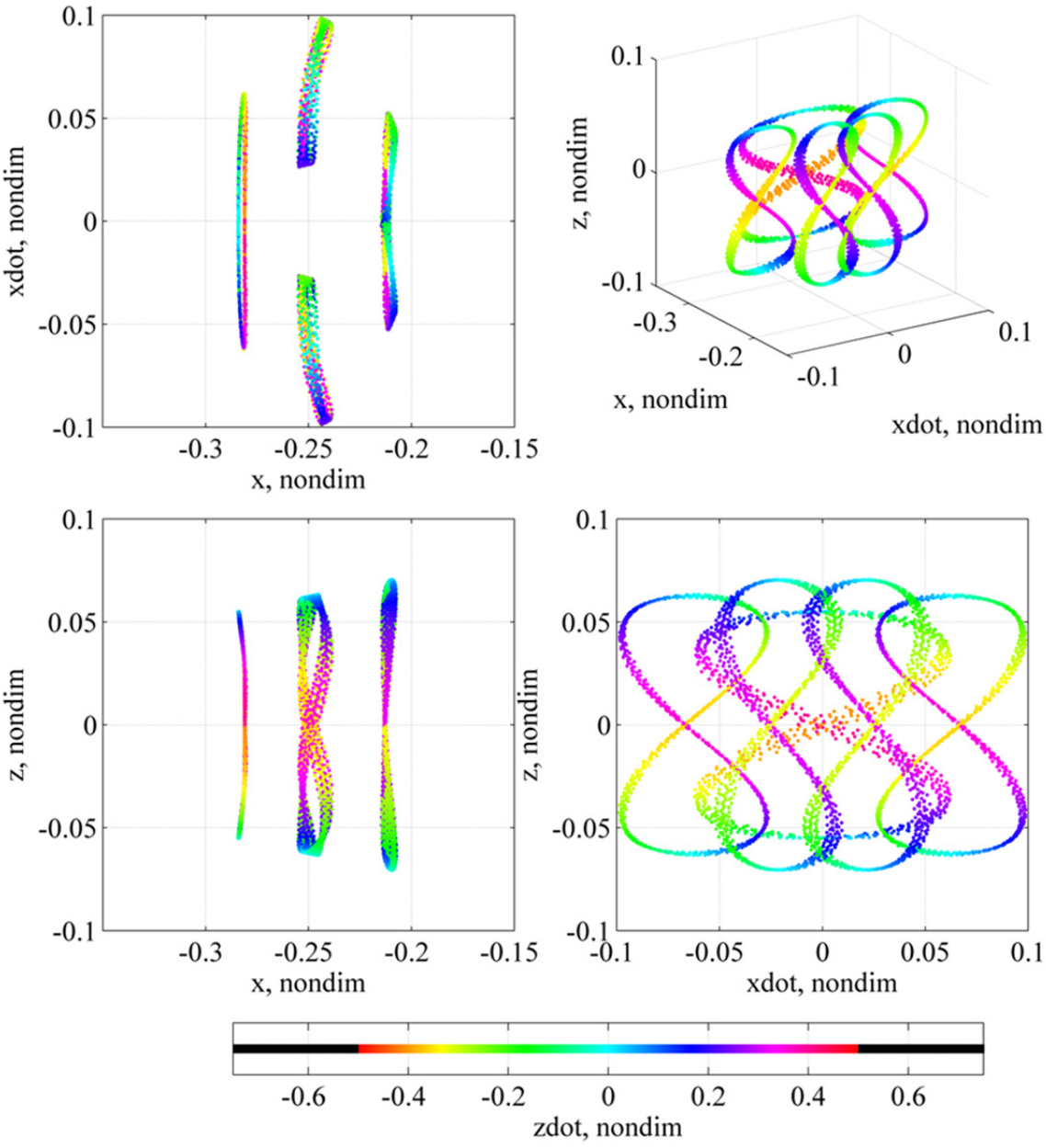

Figure 3.26. 4-D Poincaré map of 3-D, Copenhagen problem trajectory; 3,845 returns over 1,592 primary revolutions; $(y = 0+;\ x,\ \dot{x},\ z,\ \dot{z}\_color)$

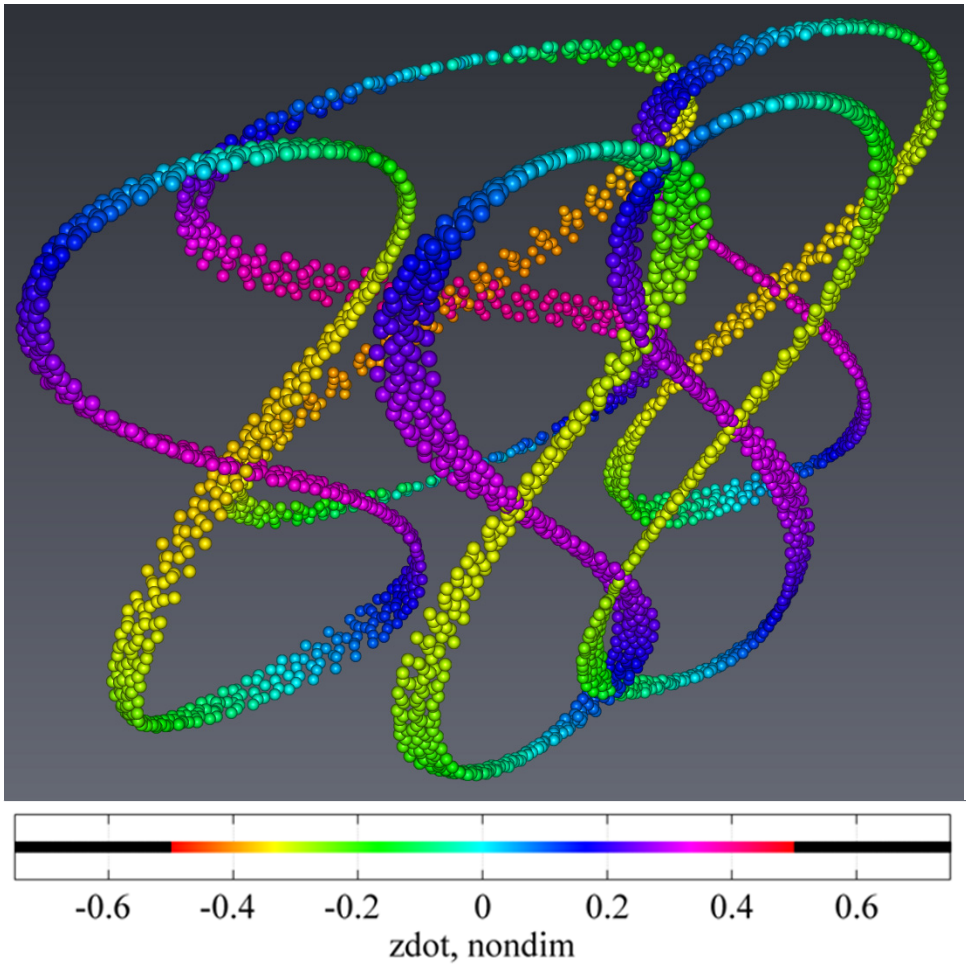

Figure 3.27. Avizo® view of 4-D Poincaré map of 3-D, Copenhagen problem trajectory; 3,845 returns over 1,592 primary revolutions; ($y = 0+;\ x,\ \dot{x},\ z,\ \dot{z}\_color$)

possessing different degrees of instability/stability. Future investigation of the higher-D "doughnut" structures generated in the spatial CR3BP—as realized using the space-plus-color method—is warranted. Further insight may be gained by correlating various "doughnut"-like features observed on the 4-D map with a rigorous numerical frequency analysis of the type accomplished by Bosanac [121] and Bosanac et al. [122] for 2-D maps generated in a modified version of the planar CR3BP. Moreover, greater clarity may be achieved through a more in-depth comparison between structures observed on 4-D maps for the CR3BP and the various features analyzed using the color and rotation method [6, 7, 57, 58, 59, 60, 61]. In those studies related to stellar motion in a galaxy, the appearance of various types of "tori" and "tubes" are rigorously correlated with

dynamical behavior, especially the stability/instability of nearby fixed points generated by periodic orbits.

To further demonstrate—and clarify the subtleties of—the space-plus-color method as applied to 4-D Poincaré maps for the spatial CR3BP, it is useful to examine the appearance of the returns associated with a nearly-periodic orbit, presumably in the vicinity of a fixed point associated with perfectly periodic motion. A notional view of a 4-D map is displayed in Figure 3.28 with a region of interest identified by the black circle. Inside this circle, there are seven map returns that appear to be relatively close together in *both* the spatial dimensions of the map *and* the color dimension of the map.

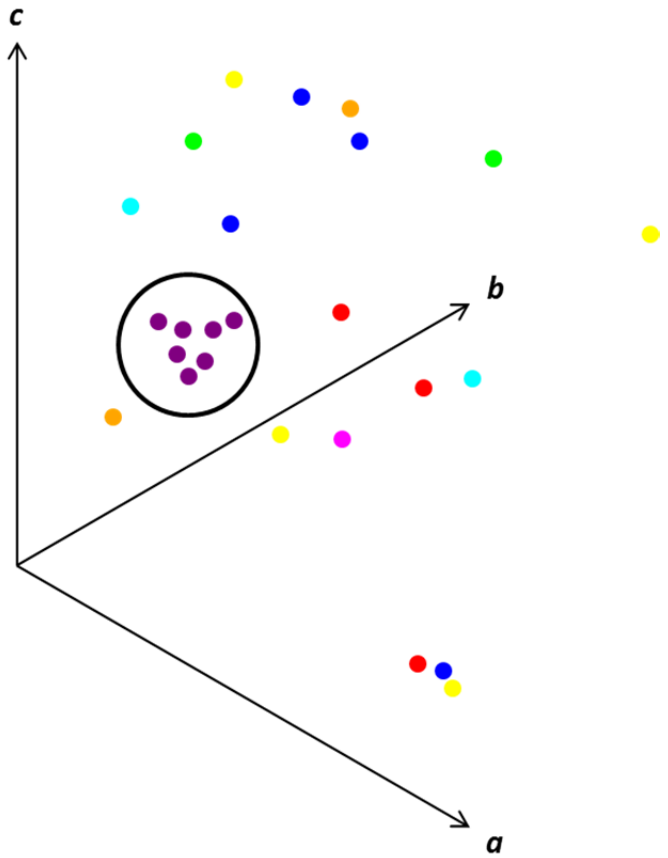

Figure 3.28. Notional 4-D map of a possible nearly-periodic orbit

For two points to be considered close together in this 4-D space, they must be at nearby locations on the 3-D grid and also plotted with colors that are "nearby" on the color scale.

Based on the clustering of purple dots, a reasonable 4-D estimate for a possible fixed point might be obtained by measuring the 3-D location of the "center of mass" of these points and by estimating an "average" color coordinate value. This presumes that the purple map returns are not just seven closely-seeded initial conditions but are, in fact, a natural consequence of dynamical "flow" and are generated by multiple crossing of the map by one or more nearly-periodic trajectories. The guess obtained visually from the map could be uniquely associated with a state in the full 6-D phase space and then fed into a follow-on, automated design process to target a periodic orbit to within a satisfactory convergence criterion/tolerance. Note that, if an orbit were perfectly periodic, it would generate map returns that repeat the same 3-D location(s) over and over again with the same color coordinate value(s) at each location.

For an example of 4-D map returns that may not represent near-periodicity, one can consider the three returns located towards the bottom of Figure 3.28 (near the *a*-axis). The red, blue, and yellow dots represent three returns that are relatively close together in the 3-D map space but which are not as relatively close together in color coordinate value, at least according to the current color scale. For the purposes of this notional example, it is assumed that the spatial axes and the color axis of the map are scaled in a similar way so that the values of the spatial and color limits are comparable. In general, it is possible that the limits of the color scale could be defined such that these three returns are actually closer in color coordinate value than they are in spatial values (for instance, if the color scale ranged from values equal to one to ten but the spatial limits of *a, b*, and *c* were each defined by values equal to zero and 100,000 in the same units). In any case, what is clear from this 4-D map is that the seven purple dots are clustered closer in color coordinate value than the cluster of red, blue, and yellow dots. This makes the purple cluster a better example of possible near-periodicity in this 4-D space.

3.1.3 Limitations of the Space-Plus-Color Method

As mentioned earlier, the space-plus-color method of representing 4-D Poincaré maps is not without its limitations. The most fundamental and significant limitation as compared to other methods happens to be a consequence of its greatest advantage over

those other methods. While the use of color to represent an extra coordinate associated with a point in a 3-D space effectively preserves the "zero"-dimensionality of a dot and thereby avoids the spatial scale limitation suffered by other methods (see again Figures 3.1 through 3.5), this same aspect of the space-plus-color method also leads to an ambiguity associated with plotting more than one point at the same location in the 3-D space but with different color coordinate values. Figure 3.29 depicts five different methods of representing the case of plotting two points at the same location in space (represented notionally as a 2-D, planar "space" as before) but with two different values of the extra coordinate. The specific values of the extra coordinate are equal to one and eight. The five methods depicted are the same methods examined in Figures 3.1 through 3.5: the text number method (top left), the circle size method (top middle), the line segment length method (top right), the line segment direction method (bottom left), and the space-plus-color method (bottom right as well as the color scale). A single location

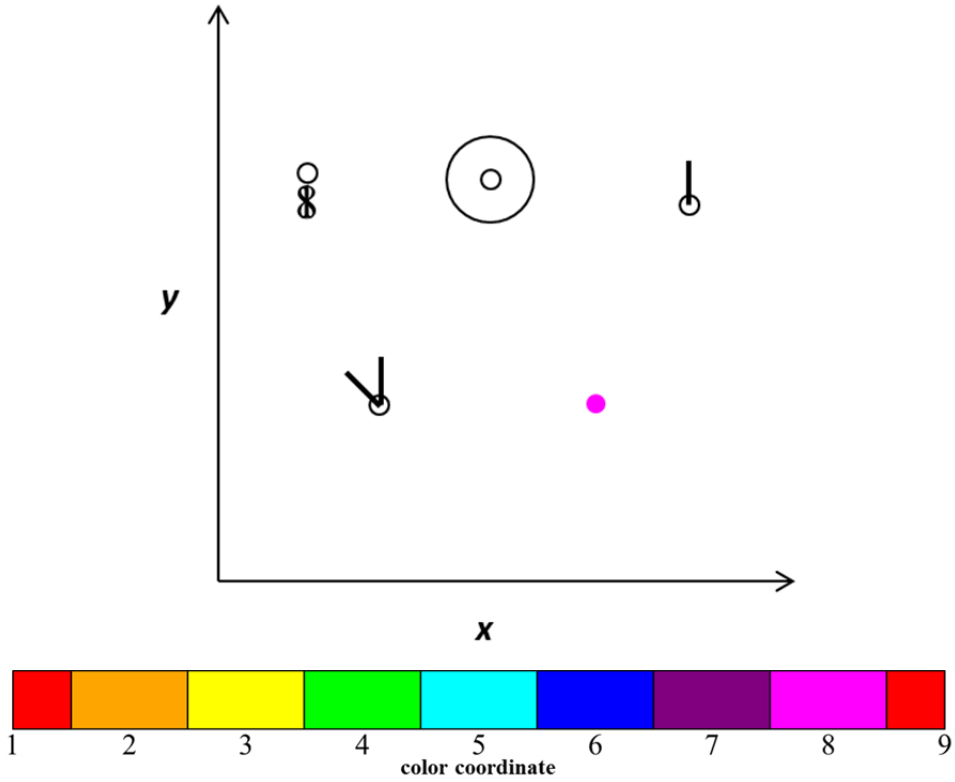

Figure 3.29. Five methods of representing the case of plotting two points at the same location in space but with two different values of the extra coordinate

ambiguity would exist if it is not possible to discern that two different dots—with two different extra coordinate values—are plotted at a given spatial location. Clearly, the circle size method and the line segment direction method do not suffer from the single location ambiguity. It is easy to recognize that two different circles with different sizes are associated with the same spatial location, as it is similarly easy to discern line segments with two different directions connected to the same dot. The text number method is not completely ambiguous since it is possible to discern that the "1" and the "8" are plotted on top of one another; however, this at least creates a readability problem. On the other hand, the line segment length method and the space-plus color method both suffer from the single location ambiguity. In the line segment length method, only the length of the longer line segment (associated with an extra coordinate value equal to eight) is visible; there is no indication that a shorter line segment connected to a second point (with an extra coordinate value equal to one) is also plotted at the *same* spatial location. In the space-plus-color method, the dot plotted first, a red dot associated with the extra coordinate value equal to one, is not visible because it is hidden "underneath" the magenta dot plotted second and associated with an extra coordinate value equal to eight. This single location ambiguity must be recognized when generating and interpreting 4-D Poincaré maps for the spatial CR3BP. In practical, map-based trajectory design applications, the ambiguity is most often encountered in the case of a seeded, 4-D grid of initial conditions, where multiple points with a range of different color coordinate values are selected to have the same exact location in the 3-D map space. Careful and problem-dependent interpretation of the initial condition map returns displayed (see Section 4.3) along with interactive filtering (see Section 5.3) assist a map-based designer in overcoming the challenges associated with this limitation of the space-plus-color method. Moreover, a unique example of a 4-D "map" representation useful for analysis in the spatial CR3BP that does not suffer from the single location ambiguity is presented in Section 5.1.1.

Other limitations of using color to represent an extra dimension are the result of the sensitivities associated with viewing color. For example, a point with the same specified color, defined based on an RGB triplet, can appear different on a computer screen when

displayed in different visual environments, depending on factors such as the background color used and the size and shape of the dot chosen to represent a point. Note that the Avizo® image displayed in Figure 3.13 (along with other Avizo® views in this investigation) employs dots created using small "plates" with black, shadowed outlines. This display choice gives each dot more definition in the case of overlapping dots; however, it can also make the color of any point appear darker than expected, especially in the case where many points are clustered near each other in the 3-D map space. Such discrepancies with color do not normally detract from the ability to interpret the Poincaré map and accurately estimate the value of the fourth (color) coordinate associated with a particular map point—as long as appropriate color scale limits are selected. Techniques for "zooming" and filtering in terms of the color dimension in order to properly estimate the value of the fourth coordinate are presented in the next section.

3.2 Tools and Techniques Enabling 4-D-Map-Based Design in a Visual Environment

This investigation employs a visual environment [123] created in MATLAB®. Six-dimensional trajectory data sets and 4-D Poincaré map data sets are processed in MATLAB®, and results are normally first displayed and interpreted using MATLAB® plots. Often, interpretation of Poincaré map images is then supported by transferring certain visualizations to the Avizo® visual environment, which greatly facilitates the interpretation of higher-D map features. The algorithm for transitioning point cloud data to the PSI file format (compatible with Avizo®) is a modified version of a MATLAB® script originally developed by Schlei [124]. Coloring points in a 3-D space to reflect four dimensions is effective in representing many points on the same 4-D Poincaré map while also adding insight into the overall structure. However, since points plotted in 3-D space often obscure other points when viewed at a particular angle, a 4-D map displayed using the space-plus-color method is well-suited to an interactive and iterative process, where a map-based designer utilizes various visual tools to modify the view in real time and gain insight into features on the map. Rather than analyzing one view of a single, dense map, it is more effective to work in a visual environment that can be manipulated, allowing not

only rotation and zooming of an image in 3-D space but also the capability to filter out features that are obscuring the view. In addition, it is frequently useful to explore a 4-D map in stages, using information gained from one short-term plot of a few map returns to narrow the focus to a particular feature, which is subsequently refined with more returns on a long-term plot. Furthermore, it is more intuitive if 4-D maps are displayed in a visual environment where information relevant to CR3BP trajectory design is associated with each map return and available for display. Such information associated with each map return—in addition to the four map coordinates—includes: (1) the trajectory number, (2) the return counter, (3) the trajectory propagation time since the initial condition, (4) the map/trajectory "energy" level, and (5) the value of the "missing" coordinate not explicitly represented on the map. For example, $\dot{y}$ is the "missing" coordinate associated with a return on a Poincaré map defined by $y = 0$. Overall, it should be emphasized that figures in this dissertation displaying the 4-D Poincaré maps generated as part of a map-based design process are only views—snapshots—of a visual environment that is best experienced on the screen of the computer on which the software is running. It is with that visual environment, rather than with a sheet of paper or a PDF file, that the actual higher-D-map-based trajectory design is accomplished.

In this analysis, 4-D-map-based trajectory design using the space-plus-color method is enabled by tools within the MATLAB® and Avizo® visual environments, which allow for map views to be interpreted and manipulated. Based on an initial view, the map-based designer decides how to modify the view for the next step of the interactive and iterative visual process. In both visual environments, the rotation and zooming of an image is accomplished interactively by the "point, click, and drag" of a mouse. A "point and click" also allows a map-based designer to identify the approximate, 3-D location of a plotted point. An interpolation in the empty space between map returns is enabled in the Avizo® visual environment using a measuring tool. Other tasks, such as redefining coordinates and units for the 4-D map display—perhaps based on visual cues from an initial plot—are accomplished by reprocessing/replotting the image in either visual environment. In the MATLAB® visual environment, the tasks of redefining the color scale, changing the size(s) of plotted dots, or annotating a return with information

relevant to design all require a reprocessing/replotting of the image—with the modified view selected based on visual cues from an initial plot. On the other hand, in the Avizo® visual environment, modifications to the color scale and dot size(s) can be implemented in real time using the built-in graphical user interface (GUI), while text annotation is not employed. Other visual tools utilized in this analysis allow for map returns to be filtered, often in terms of their spatial coordinate values *and* their color coordinate values. The term "filtering" herein refers to the process by which map returns associated with some value or characteristic—either on the 4-D map or in the full 6-D phase space—are either removed from or retained in the map view. That is, a 4-D map may be filtered to remove certain returns satisfying a particular removal criterion; equivalently, a 4-D map may be filtered to retain only those returns that meet a retention criterion. In the MATLAB® visual environment, such visual filtering processes are accomplished by reprocessing/replotting the image. On the other hand, in the Avizo® visual environment, filtering based on both the spatial and color coordinates of map returns, as well as the trajectory number, return counter, and propagation time associated with returns, is accomplished in real time using the GUI; other filtering tasks require reprocessing/replotting the image. To improve the interactivity of the visual processes employed in this investigation so that fewer of them require reprocessing/replotting of the image, software tools like those developed by Schlei [125, 126] may prove useful. Such tools interact directly with images in the Avizo® visual environment to initiate various numerical processes (and display their results); this capability could support more advanced implementations of the map-based design approach developed in this analysis.

A notional example employing map return filtering techniques is presented in Figures 3.30 through 3.35. In addition to demonstrating filtering in both the spatial and color dimensions of the map, this example also includes a process for "zooming" in terms of the color dimension in order to properly estimate the value of the fourth map coordinate. A 4-D map with sixteen returns—each defined by a 3-D location x,y,z and a color coordinate value—is presented in Figure 3.30. Also apparent is a 3-D "box" surrounding eight of the map returns. This "box," which is defined by upper and lower bounds on each of the spatial axes, represents a removal/retention criterion for a filtering process in

the spatial dimensions of the map. The returns inside the 3-D "box" represent a region of interest in terms of the spatial coordinates; to allow a map-based designer to view these returns with greater clarity (from all viewing angles in the visual environment), it is desired that all returns outside the "box" be removed from the plot. Utilizing tools in the visual environment, the filtering is accomplished and results in the revised map view in Figure 3.31. The eight map returns inside the specified "box" remain. Note that the color coordinate values associated with the returns have not changed, and filtering has so far been performed only in the map spatial dimensions.

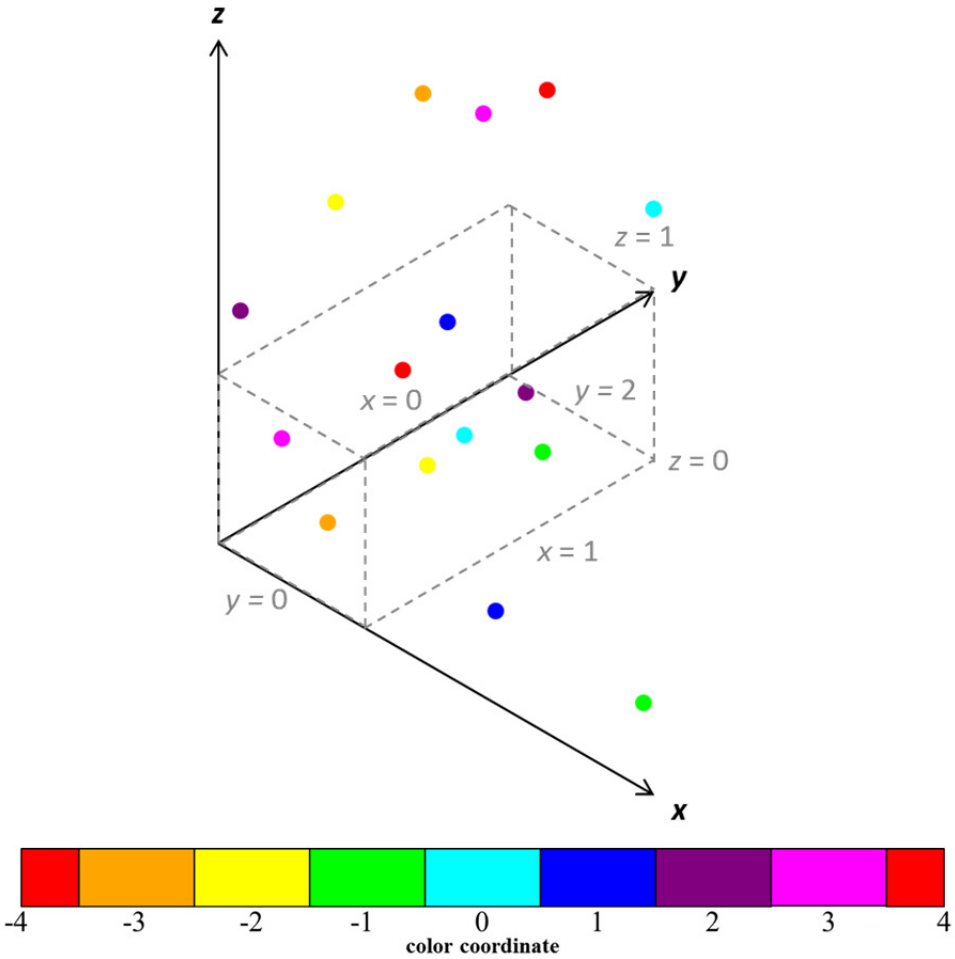

Figure 3.30. Notional 4-D map of sixteen returns; also represented: 3-D "box" criterion for planned filtering in spatial dimensions

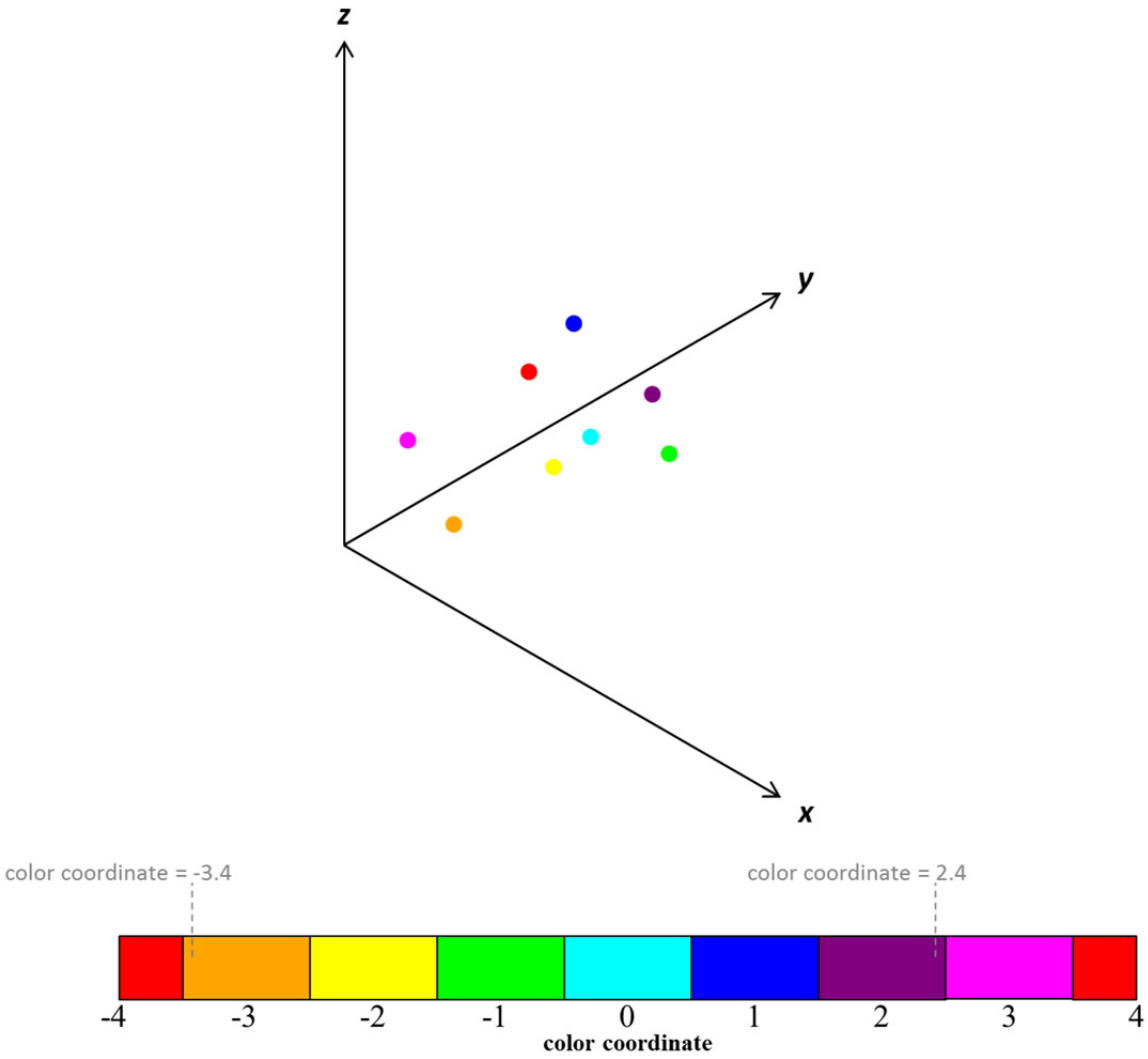

Figure 3.31. Notional 4-D map of eight remaining returns resulting from filtering in spatial dimensions; also represented: criterion for planned filtering in color dimension

The next step in the notional example is to filter the eight remaining map returns based on their color coordinate values according to the upper and lower filtering bounds indicated on the color scale in Figure 3.31. In this example, it is deemed desirable to display only those remaining points with a color coordinate value greater than or equal to -3.4 and less than or equal to 2.4. The result of this filtering in the color dimension appears in Figure 3.32, with the red and magenta dots now removed from the plot. The overall process depicted in Figures 3.30 through 3.32 has effectively filtered map returns based on a *4-D* "box" (a 4-D volume) with upper and lower bounds defined in terms of

the three spatial dimensions and the color dimension, leaving six returns remaining on the plot. Note that the upper and lower limits of the color scale itself have not changed. That is, the fourth coordinate value of each map return is still represented by the same color.

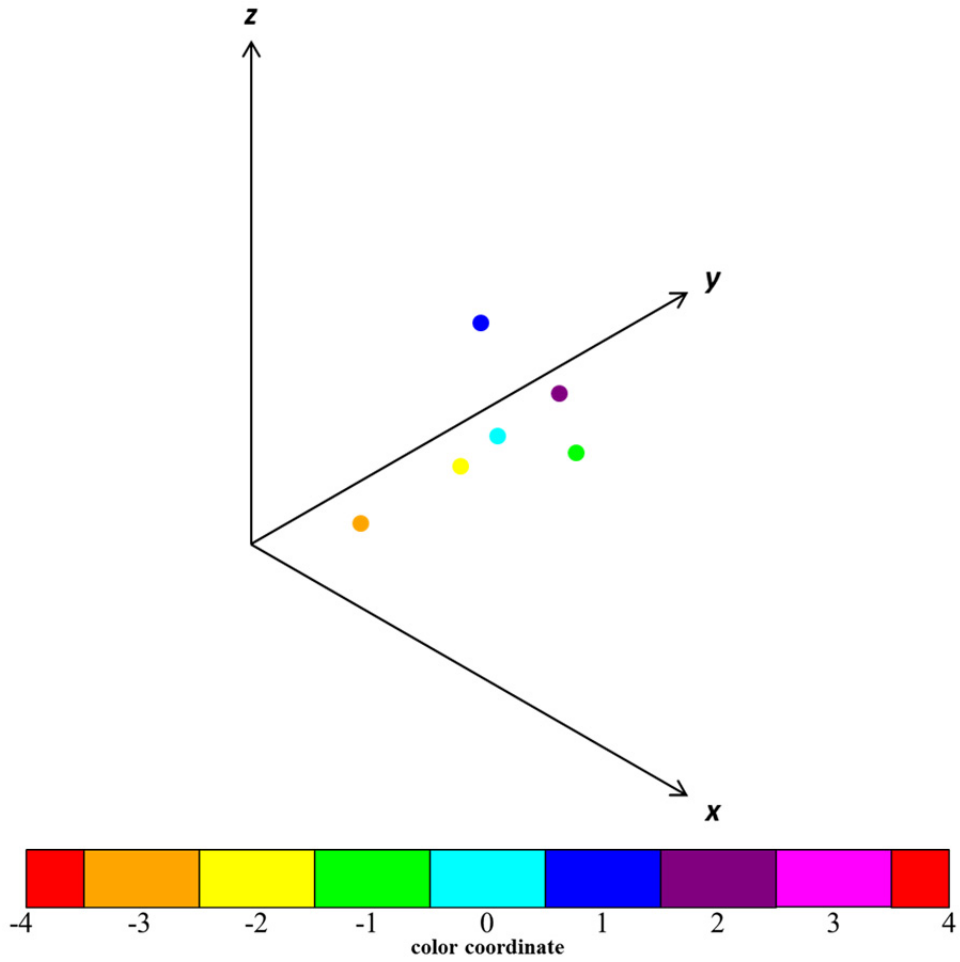

Figure 3.32. Notional 4-D map of six remaining returns resulting from filtering in color dimension

For instance, in the views displayed in Figures 3.30 through 3.32, it is clear that a cyan dot represents a color coordinate value somewhere between -0.5 and 0.5. Supposing that it is deemed desirable to obtain an estimate for the 4-D map coordinates associated with the cyan dot appearing in Figure 3.32, it is useful to "zoom" in the color dimension—in a manner that is analogous to zooming in spatial dimensions to obtain a more precise estimate for the 3-D location of a point. The revised 4-D map view after a "zoom" in the

color dimension is displayed in Figure 3.33. The new limits of the color scale are -2 and 2 instead of -4 and 4; this constitutes a "zoom" in the color dimension by a factor of two. As a result, most of the map returns—still at the same locations in the 3-D map space—

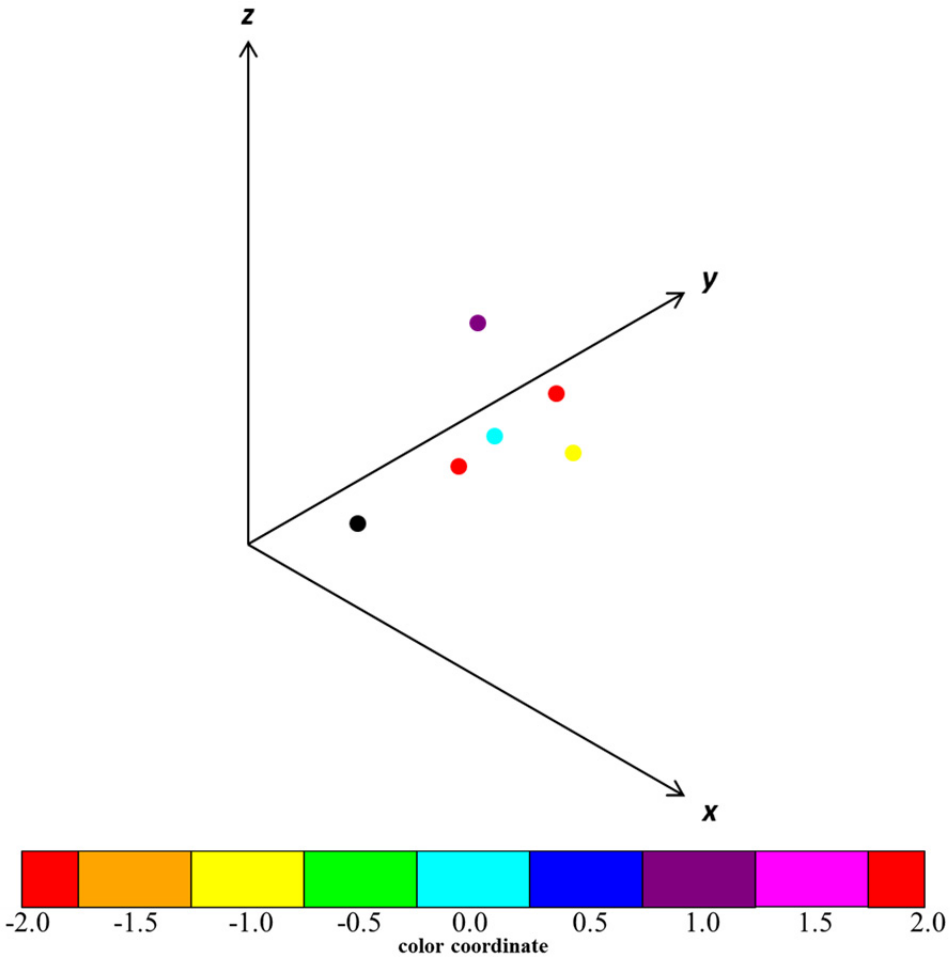

Figure 3.33. Notional 4-D map resulting from "zoom" in color dimension

are assigned different colors. It must be emphasized that the value of the fourth coordinate at each point has not changed, only the color that represents that value. For example, the dot colored green in Figure 3.32 is now colored yellow in Figure 3.33. According to the color scale in Figure 3.32, a green dot corresponds to a color value between -1.5 and -0.5. For this example, it is assumed that the actual data value associated with the green map return is equal to -1.0, at the middle of the green range. Therefore, after the color scale is "zoomed," a fourth coordinate value equal to -1.0 is

represented by the color yellow—instead of green—in Figure 3.33. As an aside, if the map return represented by the green dot in Figure 3.32 had a fourth coordinate value equal to -1.3, it would have turned orange after the "zoom" in color; if it had a value equal to -0.6, it would have remained green. Note that the orange map return in Figure 3.32, associated with a fourth coordinate value between -3.5 and -2.5, is represented by a black dot in Figure 3.33 because the "zoom" in the color dimension places the color coordinate value of this dot below the lower limit of the revised color scale. Interestingly, the color of the cyan dot appearing in Figure 3.32 has not changed after the zoom. Yet, a better (by a factor two) estimate for the fourth coordinate value associated with this point is now available in Figure 3.33. It is now evident that that the fourth coordinate value associated with the cyan dot is somewhere between -0.25 and 0.25.

To visually obtain an even more precise estimate for the fourth coordinate value of the map return represented by the cyan dot in Figure 3.33, a further "zoom" in the map color dimension is accomplished so that this map return is the only return with a fourth coordinate value within the limits of the revised color scale. The result of the further "zoom" in color, by an additional factor of five, appears in Figure 3.34. The previously cyan dot is now colored green, indicating that its fourth coordinate value is somewhere between the values -0.15 and -0.05 All other dots are colored black, indicating that their associated fourth coordinate values fall outside the limits of the color scale (-0.4 and 0.4). This highly-"zoomed" view of the color dimension is analogous to zooming in spatial dimensions until only a single point is visible within the view limits. Although the color "zoom" process could be continued to achieve greater precision, the process for this example is concluded at this step. A reasonable estimate for the four coordinate values associated with the green dot is: (x = 1.0, y = 0.6, z = 0.4, *color coordinate* = -0.1), as depicted in Figure 3.34. More precise estimates for the spatial coordinate values associated with this point could be obtained by simply zooming in the spatial dimensions of the 3-D visual environment. Note that, in this example, the five black dots associated with fourth coordinate values outside the limits of the color scale are retained on the map. As an option, these black dots could be removed from the plot by employing an additional filtering criterion. For Poincaré-map-based trajectory design in this

investigation, a "zoom" in color is often accompanied by a filtering based on the same color scale limits, thus completely removing any dots that would otherwise be colored black (or white when using a black background) according to the revised color scale.

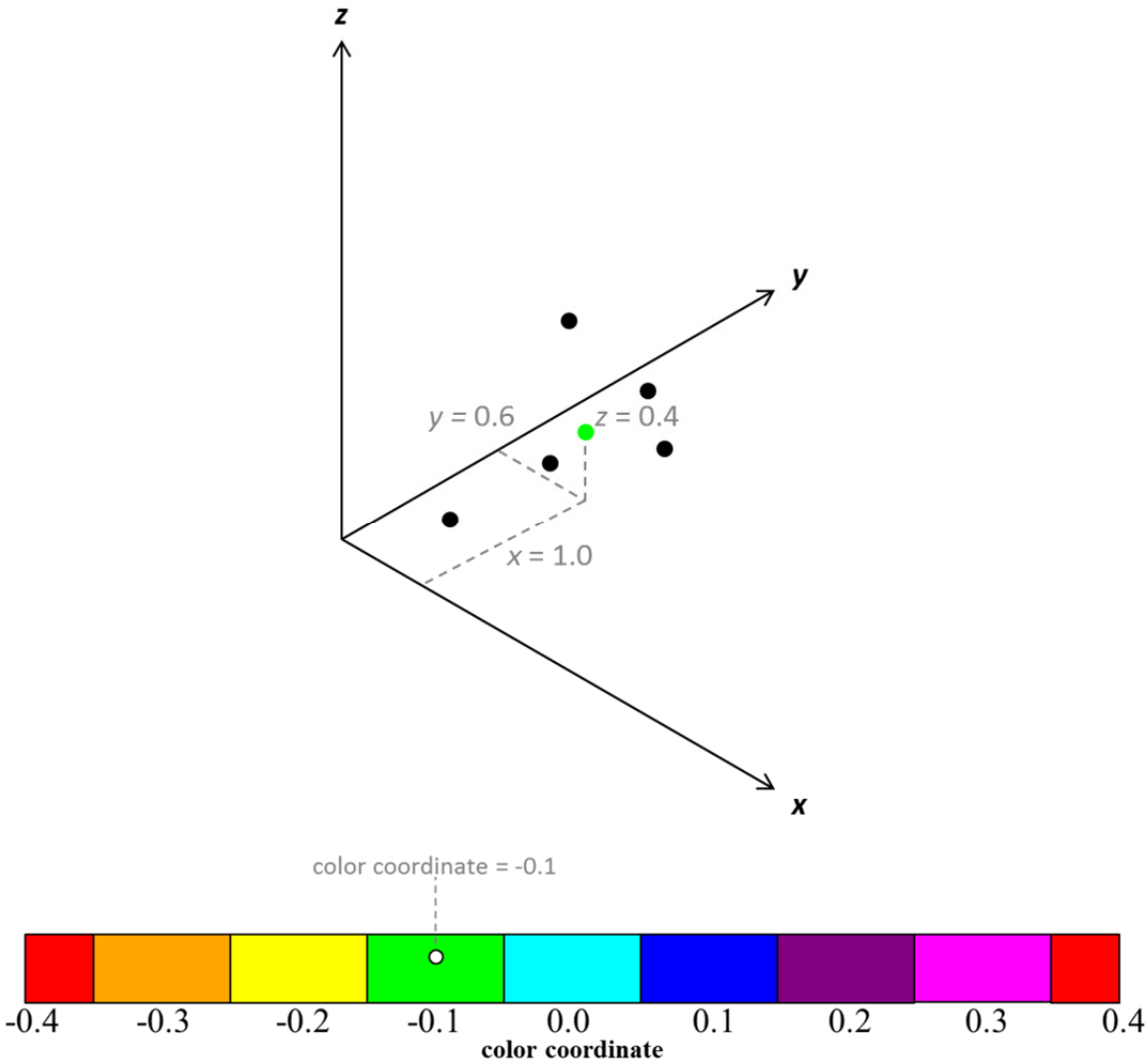

Figure 3.34. Notional 4-D map resulting from further "zoom" in color dimension

The final step in the notional example of map return filtering techniques is displayed in Figure 3.35, where the green dot representing the map return of interest is annotated with its associated trajectory number and return counter (in subscript). The notation indicates that this map return is generated by the eighth Poincaré map hyperplane

crossing of trajectory number seventy-three. Other useful information that could be annotated next to a plotted map return includes: (1) the trajectory propagation time since the initial condition, (2) the map/trajectory "energy" level, and (3) the value of the "missing" coordinate not explicitly represented on the 4-D map.

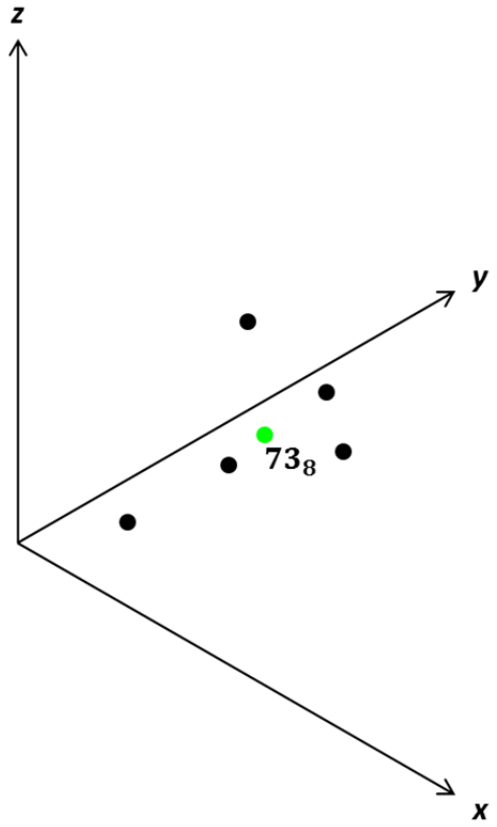

Figure 3.35. Notional 4-D map with return of interest annotated with trajectory number and return counter

In addition to the filtering techniques demonstrated in Figure 3.30 through 3.35, there are various other techniques employed in the visual environment to support 4-D-map-based trajectory design. First, while the focus of the preceding example is the use of filtering criteria based on the 4-D map coordinates of various returns, it is also useful in this investigation to filter map returns based on characteristics associated with the entire trajectory in the full 6-D phase space. For instance, a filtering criterion could be the removal of any map returns associated with any trajectory that reaches more than 100,000

km distance from the center of the Earth during the propagation time. Moreover, map returns can be associated with additional information (e.g., trajectory number, return counter, or propagation time) in the visual environment, allowing a map-based designer to filter the returns in terms of these values as well.

Another important technique used extensively in this investigation to highlight 4-D Poincaré map behavior of interest is the plotting of different-sized dots in the visual environment. An example appears in Figure 3.36, where the map returns associated with a single trajectory of interest are plotted with large dots while returns generated by all

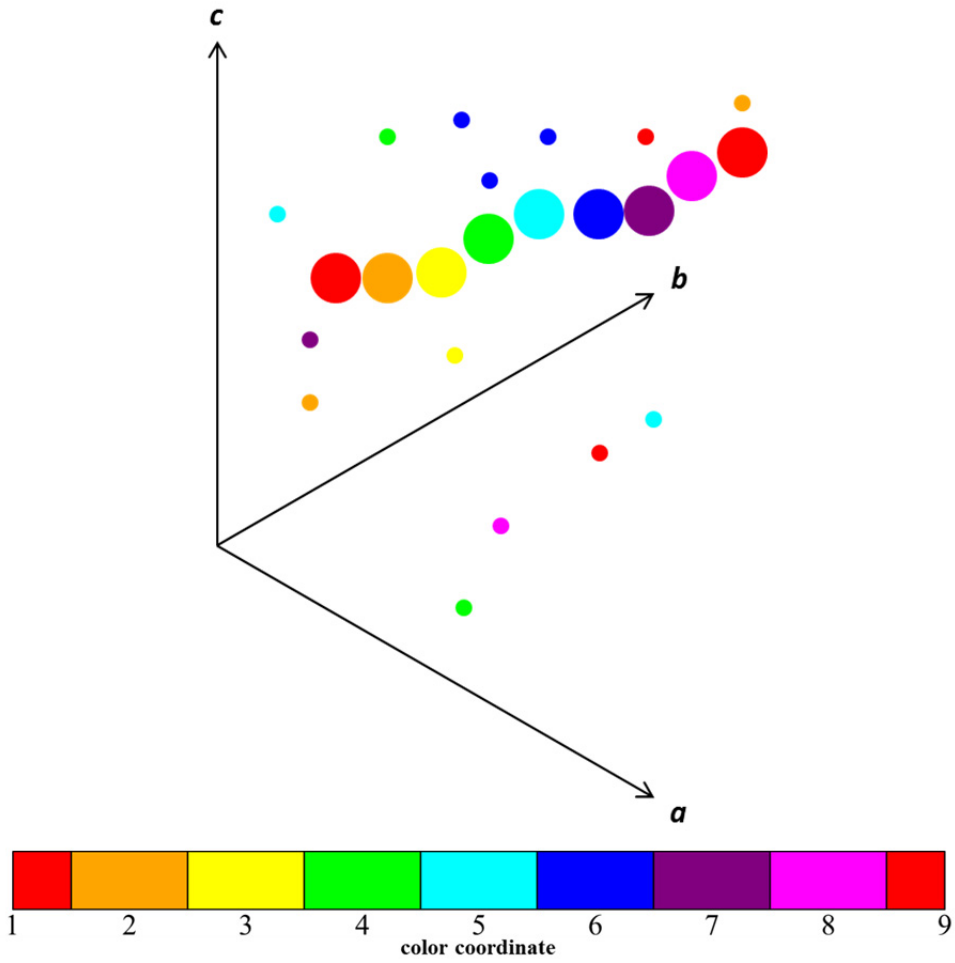

Figure 3.36. Notional 4-D map with returns from trajectory of interest plotted with larger dots

other trajectories are plotted with small dots. Note that the size of the dot in this case is chosen so that the returns generated by the trajectory of interest are clearly distinguishable from other returns on the map; thus, size is determined qualitatively and does not represent an exact quantity that is intended to be measured in the map view. The size of dots plotted on a map can also be used to highlight other differences between map returns. For instance, 4-D-map-based trajectory design often involves overlaying the returns generated on two different Poincaré maps in the same 4-D view. The two maps could be defined and plotted with two different dot sizes based on such characteristics as: (1) two different "energy" levels, (2) forward-time versus negative-time propagations, (3) opposite-side crossings, e.g., $\dot{y} < 0$ versus $\dot{y} > 0$ crossings, or (4) returns generated by two qualitatively different trajectories or sets of trajectories. In all cases, just as in Figure 3.36, dot size is determined qualitatively. Furthermore, the choice of which returns to plot with larger dots is problem dependent. In one design case, it may be desirable to plot map returns at a higher "energy" with larger dots; on the other hand, in a different case, the lower-"energy" returns could be represented by larger dots. Finally, the smallest and largest *absolute* sizes of plotted dots are limited by the issues examined in Section 3.1.1. The smallest dot size employed must be no smaller than is necessary to make a point location visible to the human eye. The largest possible dot size is limited by the spatial scale limitation: the larger the plotted dot, the less a map view may be zoomed out before dots overlap, making it difficult to discern their 3-D locations and color coordinates. In this investigation, the Avizo® visual environment allows a map-based designer to easily modify the dot size of some or all map returns while interpreting a 4-D map in real time. This technique is especially helpful when viewing maps consisting of a large number of returns (i.e., tens of thousands to hundreds of thousands of plotted points). Moreover, Avizo® views created in this analysis actually adjust the apparent size of dots based on how far they are from the observer of the image; therefore, even dots intended to have the same nominal size are plotted with different sizes, consistent with the "depth perception" of the "perspective" view in the visual environment.

In addition to demonstrating different-sized dots, the notional 4-D map depicted in Figure 3.36 also provides another example of how structure on the map may be used to

resolve the ambiguity due to the color red representing both the lower and upper limits of the color scale. Similar to the "rainbow" spectrum of color appearing on the "doughnut" plotted in Figure 3.13, the returns plotted with large dots in Figure 3.36 form a 1-D "curve" that involves a smooth progression in color coordinate value from one end of the "curve" to the other. Order/structure in both the spatial and color dimensions of a 4-D Poincaré map for the spatial CR3BP is often encountered—though not guaranteed—in practical examples of S/C trajectory design. Thus, while there is an apparent ambiguity in determining the color coordinate values of the two red returns plotted with small dots in Figure 3.36 (their values could be equal to either one or nine), the ambiguity seems to be resolved for the two red returns plotted with large dots. The two large red dots are located at the ends of this 1-D structure, and there is a smooth, "rainbow" progression along the color scale for the returns between these two end points. It is therefore probable that the large red dot on the left side of the figure has a color coordinate value equal to one, while the large red dot on the right side has a value equal to nine.

Utilizing the space-plus-color method of representing 4-D Poincaré maps in a visual environment can aid in understanding the higher-D "shape" of map features and can also resolve other ambiguities in interpretation. An example of a 1-D structure appearing on a notional 4-D map is depicted in Figure 3.37. Like the structure formed by the large dots in Figure 3.36, this structure is 1-D in the sense that it represents a "curve" in four dimensions, with a smooth progression in both the 3-D, spatial location (x,y,z) and the color coordinate value of each point from one end of the "curve" to the other. Rather than displaying the full 4-D view of this map feature, Figure 3.37 includes two "side views" of the map: an x-y view in Figure 3.37(a) and an x-z view in Figure 3.37(b). It is important to emphasize that these two views are not "2-D projections" of the 4-D map. The most obvious reason why they are not is that each "side view" actually represents *three* dimensions explicitly: two spatial dimensions *and* the color dimension. There is another more subtle, but just as important, reason why these "side views" are not even simple "projections" in the traditional sense. By inspection of the x-y view of the map return represented by the green dot, it is apparent that this dot has a smaller y value then the nearby (closest) yellow dot on the "curve." The appearance of the same green and

yellow map returns in the *x*-*z* view is fully consistent with this fact. Because the *y*-axis of the view in Figure 3.37(b) would be directed into the page by the right-hand rule, the

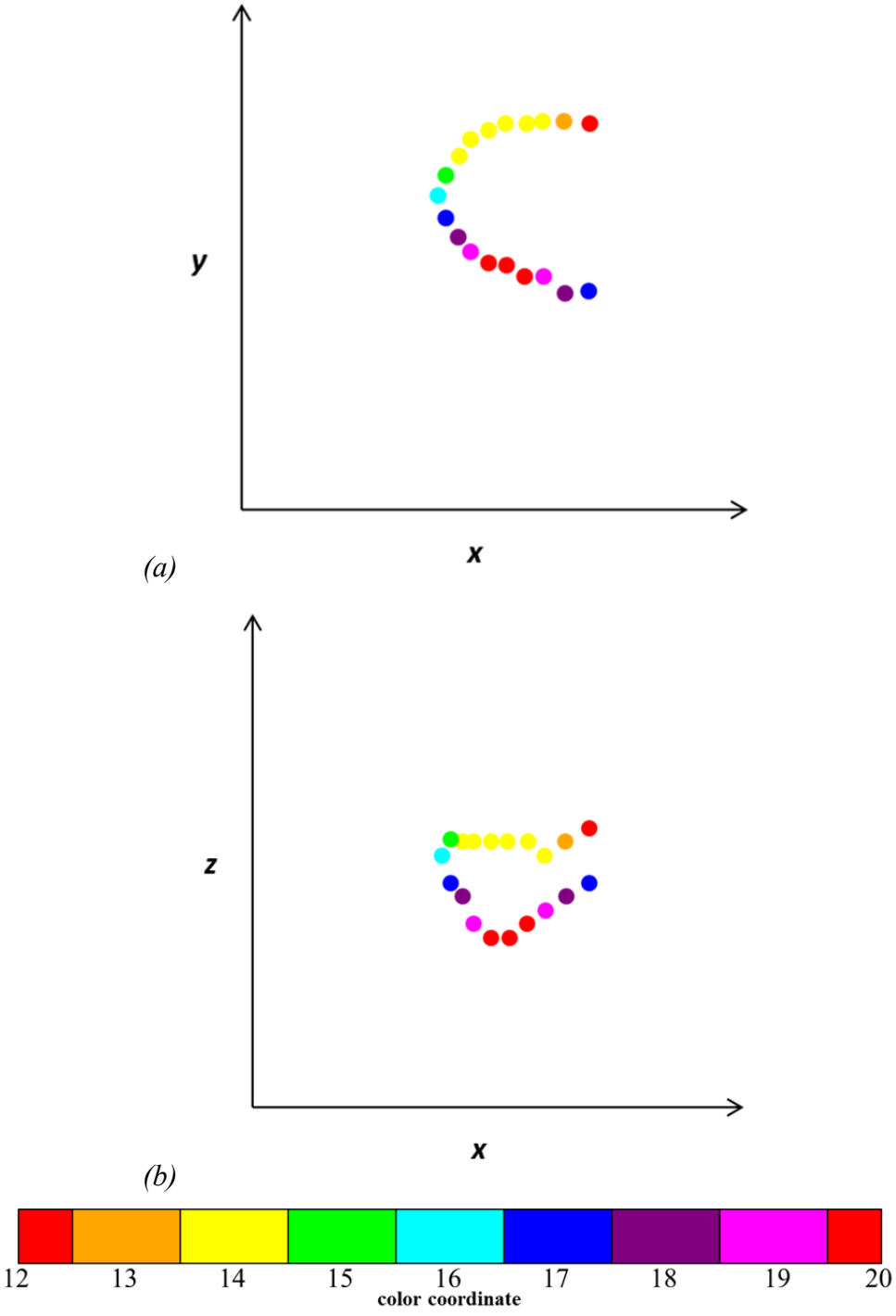

Figure 3.37. *x*-*y* (*a*) and *x*-*z* (*b*) "side views" of notional 4-D map structure

green dot appears partially on top of the nearby yellow dot (and not vice versa). The overlap results from the choice of dot size relative to the closeness of these two dots in *x* value. While a software-based "projection" of a higher-D image onto a lower-D space might *arbitrarily* decide the order in plotting one overlapping dot on top of the other, the specific ordering of the green and yellow dots in the "side view" in Figure 3.37(b) is generated so as to be consistent with what would be observed from that view of the 3-D (and 4-D) space. In the current investigation, this type of consistent ordering of plotted dots is employed for creating "side views" of 4-D Poincaré maps in a visual environment.

The notional example of two "side views" of a 1-D "curve" on the 4-D map displayed in Figure 3.37 also reveals another advantage of representing all four dimensions of a Poincaré map feature rather than only 2-D projections. It is evident from inspection of the *x*-*y* view in Figure 3.37(a) that the "upper" and "lower" halves of the "C" shape appearing in this view are formed by dots having the same values in the *x*-coordinate. For demonstration purposes, all *x* values are repeated, except for the cyan map return, which has the smallest *x* value. For example, the green and blue dots near the cyan dot each have different *y* values (and *z* values) but the same *x* values. Due to this symmetry, if the "curve" represented in Figure 3.37 were examined in black and white—with no color coordinates represented in either view—it would be impossible to determine which *z* values of dots in the *x*-*z* view are associated with which *y* values of dots in the *x*-*y* view. A third "side view," the *y*-*z* view, would be necessary to resolve the ambiguity. However, because there is a fourth dimension represented using color, the ambiguity described can be resolved in this case even with just these two "side views." It is clear from a comparison between Figures 3.37(a) and 3.37(b) that the "upper" half of the "C" shape in the *x*-*y* view is associated with larger *z* values than the lower half. This is because the "upper" half in the *x*-*y* view contains the same yellow dots that are displayed with larger *z* values in the *x*-*z* view. Equivalently, it is obvious that the yellow dots in the *x*-*z* view are associated with larger values of *y* than the magenta and purple dots on the other end of the "curve." This example implies that two "side views" (not just two "2-D projections") of a 4-D Poincaré map properly represented in a visual environment can display a total of four dimensions of information. In fact, even in the cases where more

than two "side views" of a map are displayed, the visual technique demonstrated in Figure 3.37 is still useful for interpreting the same map feature across multiple perspectives.

The preceding description of one advantage of representing all four dimensions of a Poincaré map (e.g., for the spatial CR3BP) rather than only the map's 2-D projections does not only apply, in principle, to 4-D maps represented using the space-plus-color method. It is a theoretical advantage of any method of representing all four map dimensions, subject to practical viewing limitations such as those examined in Section 3.1.1. In general, while the current effort represents three map dimensions by the location of a point in a 3-D space and the fourth dimension by color and focuses heavily on how tools and techniques in a visual environment enable that particular method, most of the basic concepts presented in this dissertation are relevant to 4-D-map-based design utilizing *any* representation method. Furthermore, many aspects of the trajectory design strategy in this analysis—from generic display methods and filtering processes to the specific design approaches for different 4-D-map-based design examples (see Chapters 4 and 5)—apply to higher-D-map-based design as a whole. Thus, this dissertation can be considered a report of an investigation into 4-D-map-based design (in the spatial CR3BP) accomplished using a visual environment, with many benefits, challenges, and lessons learned applicable to future investigations *no matter how the four map dimensions are represented*.

3.3 Feeding 4-D Map Visual Estimates into Automated Processes

Exploiting higher-D Poincaré surfaces of section for S/C orbit design in a multi-body environment requires a combination of visual and automated processes. Given the complex design space in the CR3BP—which is an effectively "unsolvable" dynamical problem [10, 14]—certain trajectory design steps cannot be completely automated. In a 2BP-focused design procedure, conic arcs serve as reference solutions for the motion of a S/C in the vicinity of a central body, assuming any additional forces can be modeled as *small* perturbations on the nominal, conic path. However, with no known, closed-form analytical solution to the CR3BP, which contains chaotic regions in its phase space, it is

far more difficult to obtain an appropriate reference solution for a given trajectory design objective. A "brute-force" search of the design space for a particular solution satisfying some criterion would not only be computationally inefficient but, more importantly, it would not likely result in sufficient understanding of the design space. This is particularly true in the chaotic regions of the CR3BP phase space, where the future state along a given trajectory is extremely sensitive to the initial condition. A small difference in either the position or velocity of a S/C could result in a *vastly* different future path. Understanding the "big picture" of a design space is critical when analyzing trade-offs between qualitatively different solutions and also in applying lessons learned from one design result to future design cases. The "big picture" view also provides an engineer the context to verify that a particular design result is valid and usable.

The Poincaré map itself is an effective visual tool for obtaining a reasonable initial guess for a design solution satisfying various qualitative criteria. Combined with other visual tools and techniques enabled by computer software (see previous section), a 4-D map generated by trajectories in the spatial CR3BP leverages human cognitive capabilities by providing an estimate that may then be used to initiate a more precise, automated process, e.g., targeting/corrections, optimization, or the transition to other dynamical models. Thus, the overall map-based design procedure involves cooperation between uniquely-human intuition and the computational power of modern computers. For trajectory design in the spatial CR3BP using 4-D Poincaré maps—as represented using the space-plus-color method in this investigation—interactive visual processes are most useful for obtaining initial guesses that meet certain qualitative criteria, while automated processes are normally better-suited for tasks requiring quantitative precision and/or algorithmic repetition.

A notional, eight-step description of the combined visual and automated processes employed in this analysis for 4-D-map-based trajectory design is depicted in Figure 3.38. The first five steps involve mainly qualitative analyses and visual processes (though supported by numerical trajectory propagations), while the final three steps are precise, mostly-automated processes. The first step of any design procedure is the definition of the objective, i.e., the statement of the problem. This is notionally represented in Figure

3.38 with the dashed arrow between regions *A* and *B*. This is meant to signify that the design objective is to determine a path (i.e., a spatial CR3BP trajectory solution) between two regions of the design space. For example, the two regions could represent two different positions, two different periodic orbits, or the vicinities of two different primary bodies.

The second step in the map-based design procedure is the definition of a 4-D Poincaré map, notionally represented in Figure 3.38 as a yellow surface. A map hyperplane must be defined in terms of appropriate coordinates, along with the "energy" level (the *JC* value) of the map. Other choices that must be made are: (1) whether the map is one-sided or two-sided, (2) what propagation time is used to generate the map returns, and (3) what coordinates and range of values for those coordinates are used to display the map. Overall, the selection of the map parameters is problem-dependent and based on what type of surface of section best captures the dynamical "flow" of interest and illuminates the design space associated with the design objective. As an aside, in more advanced design examples, two different Poincaré maps could be defined, e.g., at two different "energy" levels, and overlaid in the same 4-D map view.

Once the map is defined, the third step in the map-based design procedure is the seeding of initial conditions located on and/or off the map/hyperplane followed by numerical integration to generate map returns. The notional example in Figure 3.38 depicts (with blue dots) one set of initial conditions on the map and another set in region *A*. The set on the map is assumed to satisfy the map definition such that the initial conditions are themselves map returns. Additional returns (black dots) result from crossings of the red trajectories originating from all initial conditions. Note that color in this figure is employed to describe notional processes; the space-plus-color method for 4-D map representation is *not* depicted. For a grid of initial conditions, design choices include: (1) the number of initial conditions, (2) the criteria for seeding the initial conditions, e.g., the grid resolution and/or sampling strategy, and (3) any optional restrictions such as the removal of initial conditions within a certain distance from the center of a primary body.

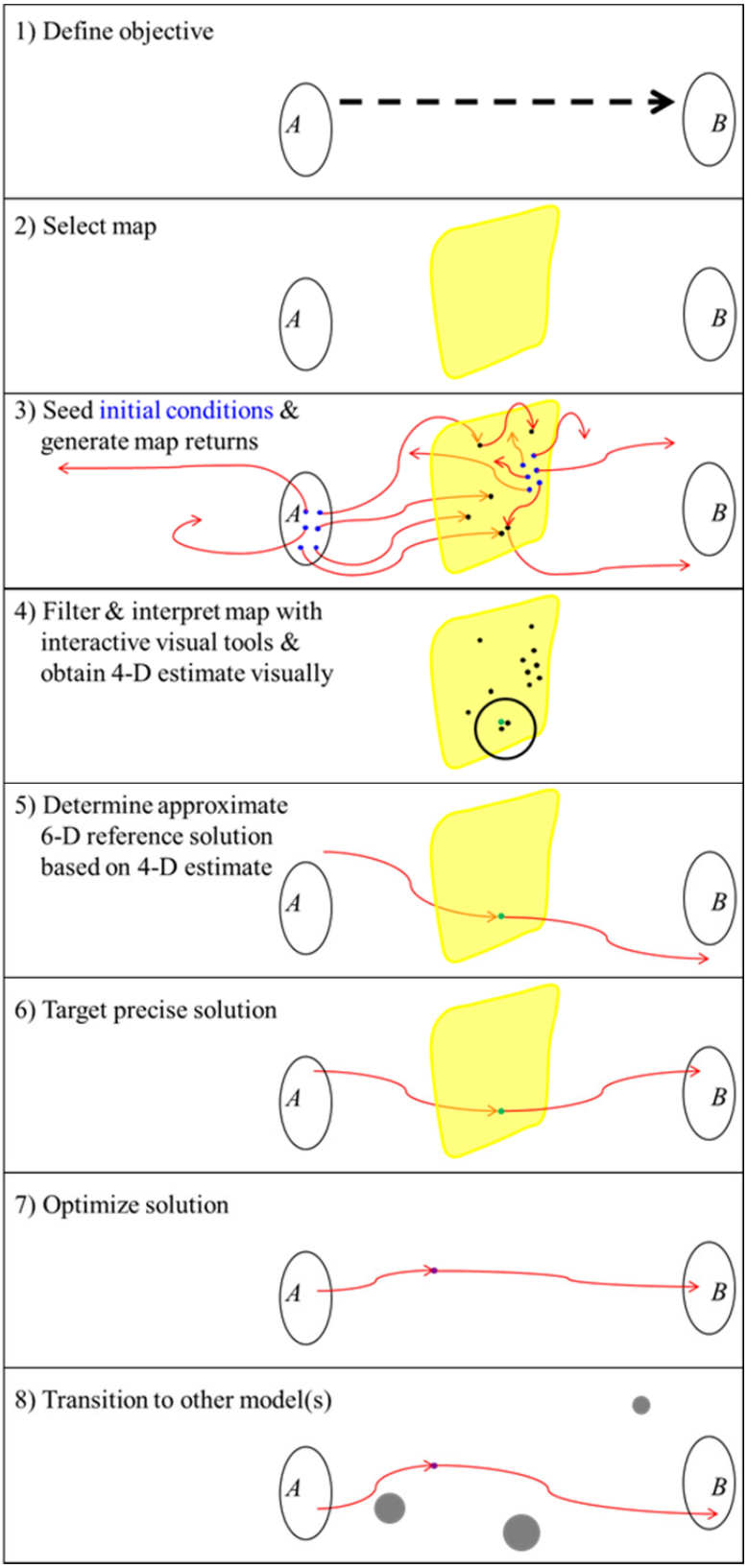

Figure 3.38. Notional 4-D-map-based trajectory design procedure

The fourth step in the notional map-based design procedure is accomplished using tools in the visual environment to filter map returns and properly interpret map features/structures. The end result of this visual process is a reasonable guess for a solution to the design objective that meets various qualitative criteria. Returns may be filtered in terms of: (1) 4-D map coordinates, (2) the characteristics of the associated trajectories in the full 6-D phase space, and/or (3) other parameters such as trajectory number or return counter. A region of interest is identified (represented by the black circle in Figure 3.38), from which a visual estimate is obtained. The estimate in this example is a single location on the 4-D map and is represented by a green dot; the location of this visual guess is *not* necessarily at the location of one of the original map returns generated from the trajectories originating from the initial conditions.

In the fifth design procedure step, the 4-D map estimate is associated with a state in the full 6-D phase space of the spatial CR3BP. The path notionally represented in Figure 3.38 could represent a path obtained by propagating states associated with the green dot in forward time with one initial velocity vector and also in negative time with a different initial velocity vector, thus requiring a $\left|\overrightarrow{\Delta V}\right|$ maneuver implemented at the position of the green dot on the map hyperplane. Note that the resulting path does not exactly satisfy the design objective in this example. However, the path resulting from the visual guess does originate close to region *A* and end close to region *B*. It is deemed a satisfactory guess—an *approximate* reference solution based on qualitative design criteria—that can be fed into follow-on, automated processes to obtain a precise and/or locally-optimal solution to the design problem. As an aside, depending on how the design objective is defined in other examples, an estimate obtained visually from the map could actually, in and of itself, be a valid—but not necessarily optimal—solution to the design problem. In that case, the targeting process described in the next step could be skipped.

The visual estimate—obtained through mainly qualitative analyses and visual processes (though supported by numerical trajectory propagations) in the first five steps of the notional map-based design procedure—is next fed into follow-on, automated processes. After human insight/intuition is leveraged to obtain an approximate reference solution, computer algorithms are next employed to obtain quantitatively precise

solutions. These automated processes begin with targeting in the sixth step of the procedure. In this investigation, "targeting" refers to a differential corrections process by which a precise, but not necessarily locally-optimal, solution is obtained to within a satisfactory convergence criterion/tolerance (see Section 2.2). The visual estimate supplies the initial guess to the targeting process. Figure 3.38 depicts the result of the targeting process, which is a precise solution to the design objective, i.e., a path originating from region *A* and ending in region *B*. Note that, even though the precise solution path is different from the path obtained from the visual estimate, the location on the 4-D map where the precise solution path crosses—represented by the same green dot—remains the same. This could signify that, at this stage of the design procedure for this notional example, the assumed maneuver (the velocity discontinuity) is required (in the targeting process) to be implemented at the same position on the hyperplane as that of the visual estimate.

The precise, targeted solution obtained in the sixth step of the design procedure is next fed into an additional follow-on process. This seventh step is an optimization process (see Section 2.7) designed to achieve a new path that satisfies the design objective and is also locally-optimal in terms of some quantitative cost function, e.g., a local minimum in maneuver $\left|\overrightarrow{\Delta V}\right|$. The optimization process might also apply various constraints, e.g., a maximum S/C time-of-flight. The result depicted in Figure 3.38 is a new, precise path between regions *A* and *B*, deemed superior to the targeted path in terms of the optimization criteria. Moreover, an important aspect of this new solution is that the maneuver position, now represented with a purple dot, is no longer at a position on the original hyperplane, perhaps not even at the same "energy" level as the original map. This signifies that, at this stage of the map-based design procedure, the original assumptions used to define the Poincaré map—along with an assumed maneuver position based on a visual estimate—are no longer necessary and are removed so that a locally-optimal solution can be determined with greater flexibility. In general, the fewer constraints that are enforced on a design space, the more flexibility there is in reducing a cost function through optimization of the design variables within that space.

In the eighth and final step of the notional 4-D-map-based design procedure displayed in Figure 3.38, the states associated with the maneuver position (represented with the purple dot) in the optimized solution are fed into another automated process whereby the resulting path in the CR3BP is transitioned to a different dynamical model. In this different model, the states immediately before and after the maneuver are the same, and the maneuver is implemented at the same position (represented with the same purple dot) as in the CR3BP model. Yet, due to the forces existing in the new dynamical model, the paths resulting from the transitioned states are different. However, it is verified that the new S/C path still originates in region *A* and ends in region *B*. Thus, the design objectives are still satisfied, even in the new model. The other dynamical model could be a higher-fidelity, ephemeris-based model, which is a more accurate simulation of the "real world." This option is notionally depicted by the gray circles in Figure 3.38, which could represent the force of gravity from other bodies. On the other hand, the optimized solution could also be transitioned to a lower-fidelity model; for example, a state from the CR3BP could be transitioned to a primary-centric 2BP to interpret that state or an entire two-body path in terms of two-body orbital elements. A combination of these two options is also possible. For instance, a CR3BP state could first be transitioned to a two-body model; the associated two-body orbital elements at that state could then be used as a convenient way to transition the solution to a higher-fidelity model.

The final result of the 4-D-map-based trajectory design procedure depicted in Figure 3.38 is not expected to be unique. Each step in the procedure likely involves assumptions, subjective decisions, and various problem-dependent design preferences. Consequently, each design step "biases" the final result. For the visual processes, the second, third, and fourth steps in the design procedure can be considered three tiers of a "sampling" sequence (see Section 2.6), with the sampling strategy employed at each step heavily influencing what region of the design space is illuminated and under consideration in later steps. The selection of the Poincaré surface of section—e.g., the hyperplane location and the "energy" value—is the initial means by which the dynamical "flow" is sampled in order to isolate certain behavior of interest. Next, once the map is defined, a grid of initial conditions may be seeded, thus sampling within a subset of the design

space relevant to the map. Finally, various visual map filtering processes are a type of human/visual sampling, with the goal of focusing on a particular region of the 4-D map from which a reasonable design estimate may be obtained visually. The follow-on, automated processes also involve choices that can lead to different possible solutions. Targeting strategies vary and—depending on the number of free variables versus the number of constraints in the corrections process—may not lead to a unique solution. In other words, different visual guesses used to initiate the targeting process would lead to different precise solutions. Furthermore, the optimization processes employed in this investigation seek *locally*-optimal results rather than global optima. This implies that the effectiveness of the optimization algorithm in reducing a cost function (such as maneuver $\left|\overrightarrow{\Delta V}\right|$) depends on which targeted solution is used to initiate the process. Finally, the choice of which forces to model when transitioning to another dynamical model influences the final S/C path and whether it satisfies the original design objective.

A given step in the 4-D-map-based design procedure will not always produce the expected or desired result, in which case it is necessary to return to one or more previous steps and consider a modification to the specific design approach. A result could be unfavorable either because: (1) it is not a feasible S/C path at all (e.g., a targeting process fails to converge) or (2) it is a precise path but it does not have desirable qualitative characteristics or perhaps it requires an unreasonably large maneuver $\left|\overrightarrow{\Delta V}\right|$ even at a local optimum. Thus, the eight steps depicted in Figure 3.38 are iterative, with the results of each step assessed in terms of the overall design objective. This is especially true for the fourth step, where interpretation of the 4-D map view may require a map-based designer to experiment with a variety of viewing techniques and filtering criteria to ultimately isolate a region on the map that is relevant to the design objective. It is also possible that the particular set of initial conditions and their associated trajectory propagation times do not generate enough returns on the 4-D map to properly illuminate a region of the design space relevant to the design objective. In such a situation, it may be that no feasible solution is available upon visual inspection; therefore, a new map must be generated based on different criteria. Moreover, a visual estimate obtained by inspection of the map may not always lead to a qualitatively desirable reference solution if features on the map

are not properly interpreted. There is a "learning curve" associated with any new type of map-based design problem. In addition, the targeting and/or optimization processes could fail to achieve a precise, feasible solution and/or a local optimum in terms of maneuver $\left|\overrightarrow{\Delta V}\right|$. It would then be necessary to re-evaluate whether the design variables and constraints are properly formulated based on the design objective and with careful consideration of the inherent dynamical sensitivities in the problem.

For each design example included in the present investigation (see Chapters 4 and 5), the total time required to successfully perform the entire design procedure depicted in Figure 3.38 is between several hours and roughly one day, depending on the complexity of the design objective and/or the associated design space. Note that this total time is actually spread out over a few days in the development of each design case in the current effort. Seeding initial conditions and generating 4-D Poincaré maps requires anywhere from several minutes to a few hours. Filtering/interpretation using tools in the visual environment also requires between minutes and a few hours. Trajectory targeting requires anywhere from a few seconds to several minutes, while trajectory optimization requires anywhere from roughly one minute to several hours. Finally, transitioning a CR3BP solution to another dynamical model requires roughly minutes for transitioning to the 2BP and several hours for transitioning to the higher-fidelity dynamical model constructed in STK®. The times required for automated tasks performed in MATLAB® are specified in elapsed time (MATLAB® Version: 7.14.0.739 (R2012a); benchmark: 0.0600, 0.0637, 0.0741, 0.1641, 0.2727, 0.7146).

As a final note, in this investigation, the follow-on, automated processes—i.e., targeting, optimization, and transitions to other dynamical models—are initiated (in MATLAB® scripts) outside the visual environment after obtaining a visual estimate from the 4-D Poincaré map. Moreover, displays of trajectories in the configuration space of the spatial CR3BP are separate from the map displays. The software tools utilized do not include any capability to "point and click" on a 4-D map return and immediately investigate the 6-D CR3BP trajectory associated with that return or initiate any follow-on, automated processes. As mentioned earlier, for future investigations, software tools like those developed by Schlei [125, 126], which interact directly with images in the Avizo®

visual environment to initiate various numerical processes (and display their results), may prove useful for more advanced implementations of the map-based design approach developed in this analysis.

3.4 4-D Map Coordinate Definitions

Any application of the higher-D Poincaré map display methods employed in this investigation requires the definition of some important quantities. The definitions of cylindrical (r, θ, z) and spherical (ρ, θ, φ) coordinates for non-Cartesian rotating frame formulations of the 4-D map for the spatial CR3BP are summarized in Figure 3.39. Point *O* is at a fixed location anywhere in the rotating frame. The in-plane angle θ is measured from the *x*-axis in the plane of the primaries and is positive in the direction corresponding to the motion of the primaries in the inertial frame. The out-of-plane angle φ is measured from the plane of the primaries and is positive in the $+z$ direction. Also useful in this analysis is the velocity angle α, sometimes employed as one coordinate on a 4-D map where the hyperplane involves a velocity coordinate. For example, on a 4-D periapsis map, with a hyperplane defined in terms of spherical coordinates such that $\dot{\rho} = 0$ and $\ddot{\rho} > 0$, the velocity angle α locates the S/C velocity vector $\vec{V}$, relative to the rotating frame, on the $\hat{\theta}$-$\hat{\varphi}$ plane, as demonstrated in Figure 3.40. Note that, in general, $\vec{V}$ is not restricted to the $\hat{\theta}$-$\hat{\varphi}$ plane; however, for a periapsis map, $\vec{V}$ has no $\hat{\rho}$ component. On the other hand, for a hyperplane defined such that $\dot{\rho} = c \neq 0$, α is *generalized* to be defined as locating the *projection* of $\vec{V}$ onto the $\hat{\theta}$-$\hat{\varphi}$ plane (but this generalization is not used for any design example in this dissertation).

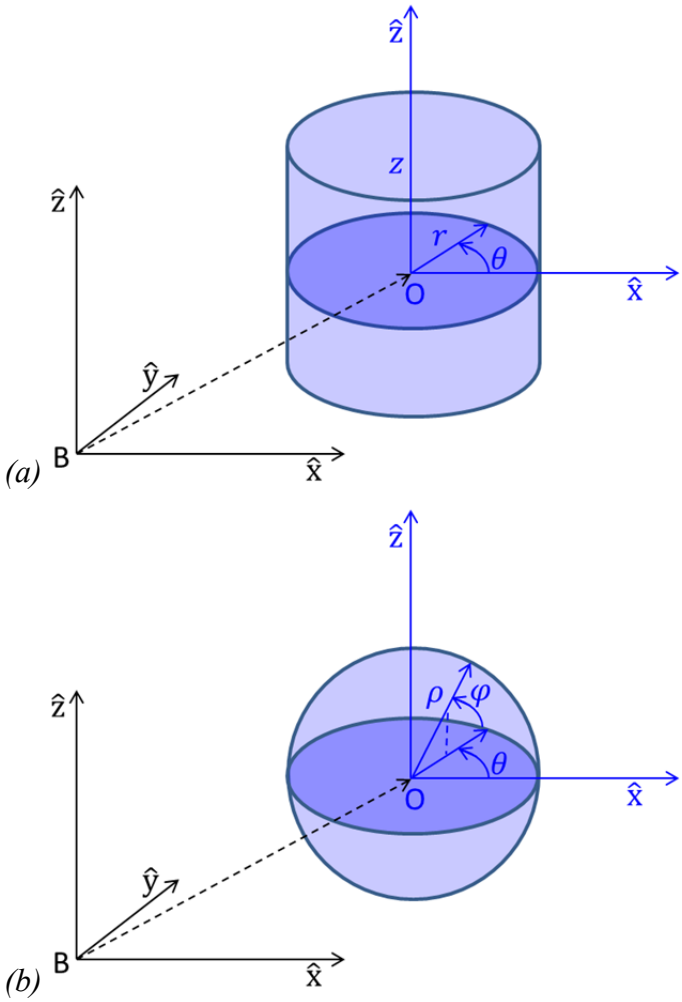

Figure 3.39. Definitions of cylindrical (*a*) and spherical (*b*) rotating frame coordinates

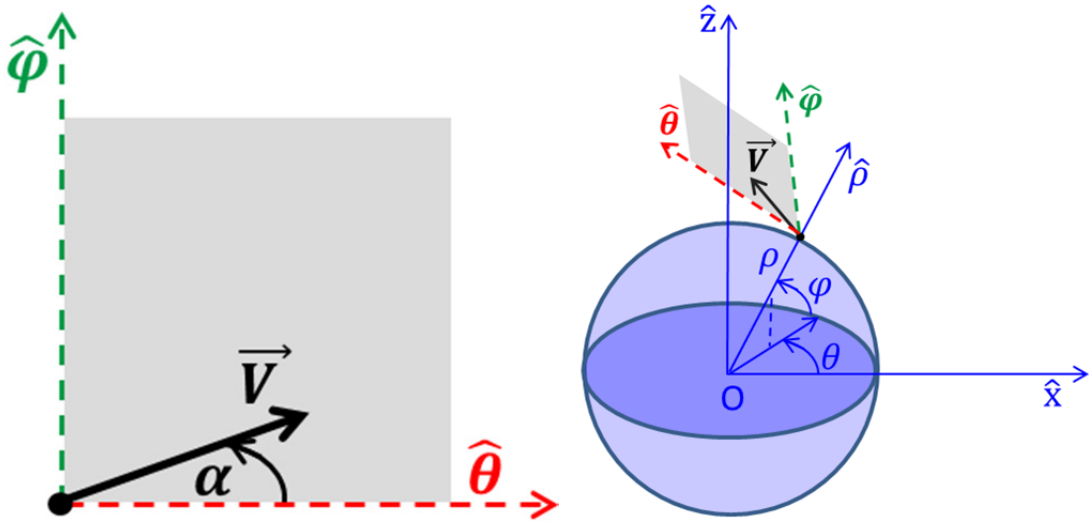

Figure 3.40. Definition of velocity angle α

4. BASIC 4-D-MAP-BASED DESIGN TECHNIQUES

This chapter includes four examples of basic, 3-D trajectory design, which serve two distinct purposes. First, these examples demonstrate successful trajectory design results from applying the higher-D-map-based design approach introduced in Chapter 3. Second, each example offers an opportunity to highlight different benefits, challenges, and lessons learned from this investigation into this type of 4-D-map-based design. Thus, this chapter is used both for documentation of design results and—more importantly—for pedagogical purposes to expand on the concepts in the previous chapter. Techniques employed for successful map-based trajectory design are problem-dependent. For each spatial CR3BP model, the mass ratio μ is noted, along with additional model parameters: P_2 orbit radius (l^*) about P_1; and P_1 and P_2 spherical body radii, defining the physical size of the real-world massive bodies [127]. When S/C transfer maneuvers are considered, all $\left|\overrightarrow{\Delta V}\right|$ maneuvers are assumed to be instantaneous (impulsive burns).

The focus of the basic design examples is on the creation of appropriate 4-D Poincaré maps and the use of those maps in an interactive visual environment to obtain trajectory design solutions through what are mainly visual processes. In Design Example #1, a process used by Craig Davis and Howell for S/C capture maneuver design in the planar CR3BP [34, 35] is extended to the spatial CR3BP. In Design Example #2, a transfer maneuver is implemented based on an adjustment to create a potential intersection in the full 4-D space of a map, with a reasonable guess for the required adjustment determined by visual inspection. Design Example #3 provides an example involving the single location ambiguity of the space-plus-color method as applied to 4-D maps along with a strategy for overcoming the challenge through careful interpretation of map returns. Finally, Design Example #4 demonstrates 3-D orbit transfer design based on 4-D manifold maps.

Follow-on, automated processes such as targeting, optimization, and/or transitions to other dynamical models are not the focus of this chapter but are instead emphasized as part of the advanced map-based design scenarios presented in Chapter 5. Note that the first three design examples in this chapter involve trajectory design in the context of different types of CR3BP libration point gateway dynamics in the vicinity of the smaller primary in various systems. In these three basic examples, the resulting visual guess obtained from the Poincaré map is, in and of itself, a valid—but not claimed to be optimal—solution to the qualitative objective of the problem (e.g., capture, departure, or transit). On the other hand, Design Example #4 is an orbit transfer problem between two periodic LPOs; the estimate obtained visually from the 4-D map must be fed into an automated targeting process to achieve a precise—but still not claimed to be optimal—solution to the problem. For completeness, a locally-optimal transfer solution to this orbit transfer problem is also presented.

4.1 Design Example #1: Extending 2-D-Map-Based Design Strategies to Higher Dimensions

An introductory example of 4-D-map-based mission design uses periapsis Poincaré maps to design a 3-D S/C capture maneuver in the vicinity of Titania in the Uranus-Titania spatial CR3BP, where the period of the primaries is roughly 8.7 days. The mass ratio μ, along with other assumed model parameters for this system, appears in Table 4.1 [127]. The periapsis map hyperplane is defined in Titania-centered spherical coordinates as $\dot{\rho} = 0$ and $\ddot{\rho} > 0$. This choice of hyperplane enables a methodical process to determine a capture maneuver by visual inspection of 4-D maps.

Table 4.1 Uranus-Titania CR3BP model parameters

μ (dimensionless)	l^* (km)	Uranus radius (km)	Titania radius (km)
$3.946029231723387 \times 10^{-5}$	435,910	25,559	788.9

The process to design the appropriate maneuver is an extension of the process used by Craig Davis and Howell for capture maneuver design in the planar CR3BP [34, 35]. In the previous analysis, desirable capture behavior near P_2 is identified on a long-term, forward-time periapsis Poincaré map of trajectories at a specified "energy" level where the L_1 and L_2 gateways are closed, thereby guaranteeing that all trajectories in the vicinity of P_2 remain captured for all time. This long-term map is then overlaid on a short-term, negative-time map of trajectories at a different "energy" level, one where the L_1 and L_2 gateways are open, thereby allowing trajectories to enter (or exit) the vicinity of P_2. By isolating a region of intersection—in 2-D space—on the overlaid maps, a maneuver point is identified that allows a capture maneuver between a gateway entry trajectory and a desirable capture trajectory. Note that the maneuver point is a periapsis and that the maneuver required is an "energy"-lowering, *tangential* burn in a direction opposite to the S/C velocity vector $\vec{V}$, *relative to the rotating frame*.

In Design Example #1, a similar process is applied to 3-D trajectories in the vicinity of Titania by employing 4-D Poincaré maps. In Figure 4.1, *x*-*z* rotating views (dimensional units) of ZVCs at the higher and lower "energy" levels are plotted in the vicinity of Titania. Following the convention described in Section 2.1, the ZVCs depicted represents the cross-section of the ZVSs, where the origin of the cross-section is Titania, with $y = 0$. The asterisk on each axis coordinate indicates that the plot origin is offset from the traditional barycentric origin of the rotating frame; in this case, the origin is Titania for ease of interpretation. The L_1 gateway is the opening in the ZVSs on the Uranus-facing side of Titania that makes it possible for certain trajectories to travel between the vicinity of Titania and the interior region, i.e., the region of Uranus. Likewise, The L_2 gateway is the opening in the ZVSs on the "far" side of Titania that makes it possible for certain trajectories to travel between the vicinity of Titania and the exterior region, i.e., outside Titania's orbit around Uranus.

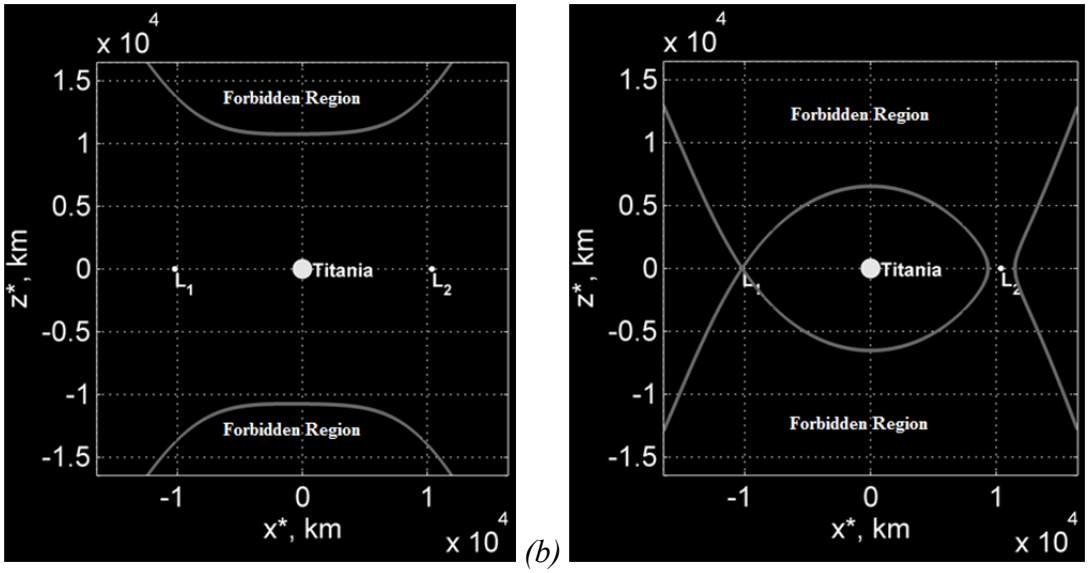

Figure 4.1. Rotating views of ZVCs in the vicinity of Titania at higher (*a*) and lower (*b*) "energies"

The first 4-D periapsis Poincaré map is generated in negative time at the higher "energy" level, where the L_1 and L_2 gateways are open. Employing the space-plus-color method, the 3-D periapse position of each trajectory return to the hyperplane is displayed in Cartesian coordinates, and the fourth—color—coordinate is selected to be the velocity angle α, as indicated in Figure 4.2(a) (nondimensional units of distance). A lesson learned from experimenting with various color schemes, with a range of observers [128, 129], for this 4-D map display method is the fact that the full spectrum of color is better resolved against a black (or gray) map background. Though dark colors (like blue and purple) are more difficult to view against a black background, lighter colors (like cyan and yellow) are even *more* difficult to view against a white background. Of course, larger dots do improve the viewing quality; but there exists a trade-off since dots that are too large can also obscure other points in the 3-D space. In Figure 4.2(a), a set of 643 initial conditions, selected based on a 4-D grid of x, y, z, α values, is propagated backward in time for the past month or until a negative-time primary impact, whichever is more recent. In Figure 4.2(b), with the same color scale, only those map returns from Figure 4.2(a) that are generated by trajectories that enter through either the L_1 or L_2 gateway during the past month appear; all other returns are filtered out. In other words,

Figure 4.2(a) includes trajectories that are already in the vicinity of Titania one month in the past, while Figure 4.2(b) excludes them. A comparison between the two maps offers

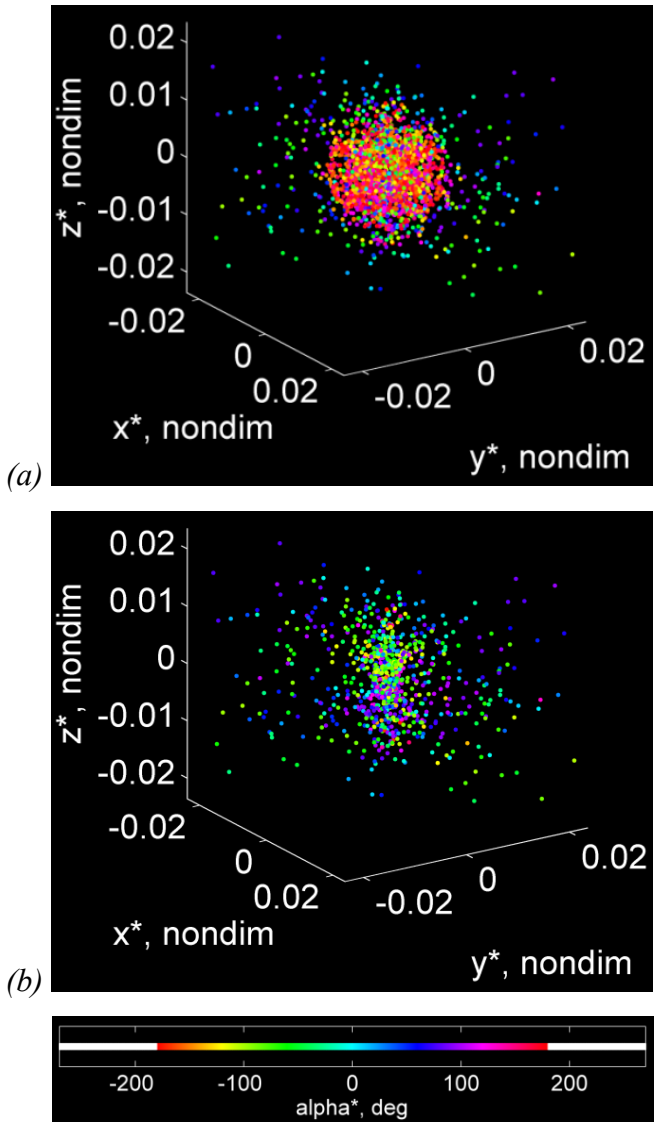

Figure 4.2. 4-D periapsis Poincaré maps (returns during previous month at higher "energy") in the vicinity of Titania with (*a*) and without (*b*) trajectories that are in the vicinity for the entire previous month; $(\dot{\rho} = 0+;\ x,\ y,\ z,\ \alpha\_color)$

a striking example of the potential insight by representing all four dimensions of the map, rather than simply a 3-D projection highlighting the 3-D periapse positions. The trajectories removed from Figure 4.2(a)—those that did not enter a gateway within the previous month—have map returns in a more isolated region around Titania and *also*

include velocity angles (colors) that are closer to $\alpha = \pm 180°$, indicating near-planar retrograde direction in the rotating frame. It is known that such 3-D, retrograde trajectories are more likely to be captured, at least over the time span of interest, as observed by Craig Davis and Howell [34]. The phenomenon is well-known in the case of purely planar trajectories, as observed by Jefferys [31] and Hamilton and Krivov [130]. Yet, note that the term "near-planar retrograde direction" used here within the context of the spatial CR3BP describes the instantaneous *direction* of the S/C velocity vector $\vec{V}$ with respect to the rotating frame at periapsis; this description does not necessarily imply that these 3-D trajectories, or the resulting 4-D periapsis map returns, are always close in *position* to the plane of the primaries.

In the next step of the analysis, a 4-D periapsis Poincaré map is generated in forward time at the lower "energy" level, where the L_1 and L_2 gateways are closed, as plotted in Figure 4.3(a). A set including 397 initial conditions, based on a 4-D grid, is propagated forward in time for the following year or until an impact, whichever occurs sooner. By transitioning the image in Figure 4.3(a) to Avizo®, it is possible to identify specific regions of the map associated with different types of orbit behavior in the vicinity of Titania. Yet, due to the obscuration difficulties in viewing a dense 4-D map using this display method, it is necessary to explore the space with interactive, visual tools and/or to examine the map in pieces, viewing the map returns associated with a dozen or so trajectories at a time. An effective technique is the encoding of the trajectory number and the return counter, associated with each map return, followed by the use of Avizo® to filter points based on these values. The result of such a process appears in Figure 4.3(b), where the periapsis map returns associated with a single trajectory are plotted (with large dots) among other points (small dots) on the map associated with other trajectories. This particular trajectory is selected based on a certain qualitative behavior that is desired for S/C capture in the vicinity of Titania. In this example, the desired behavior is defined as: (1) periapses that are not near the *x*-*y* plane (such a criterion guarantees a 3-D trajectory), and (2) periapses that are tightly grouped beneath Titania, i.e., with negative *z* values.

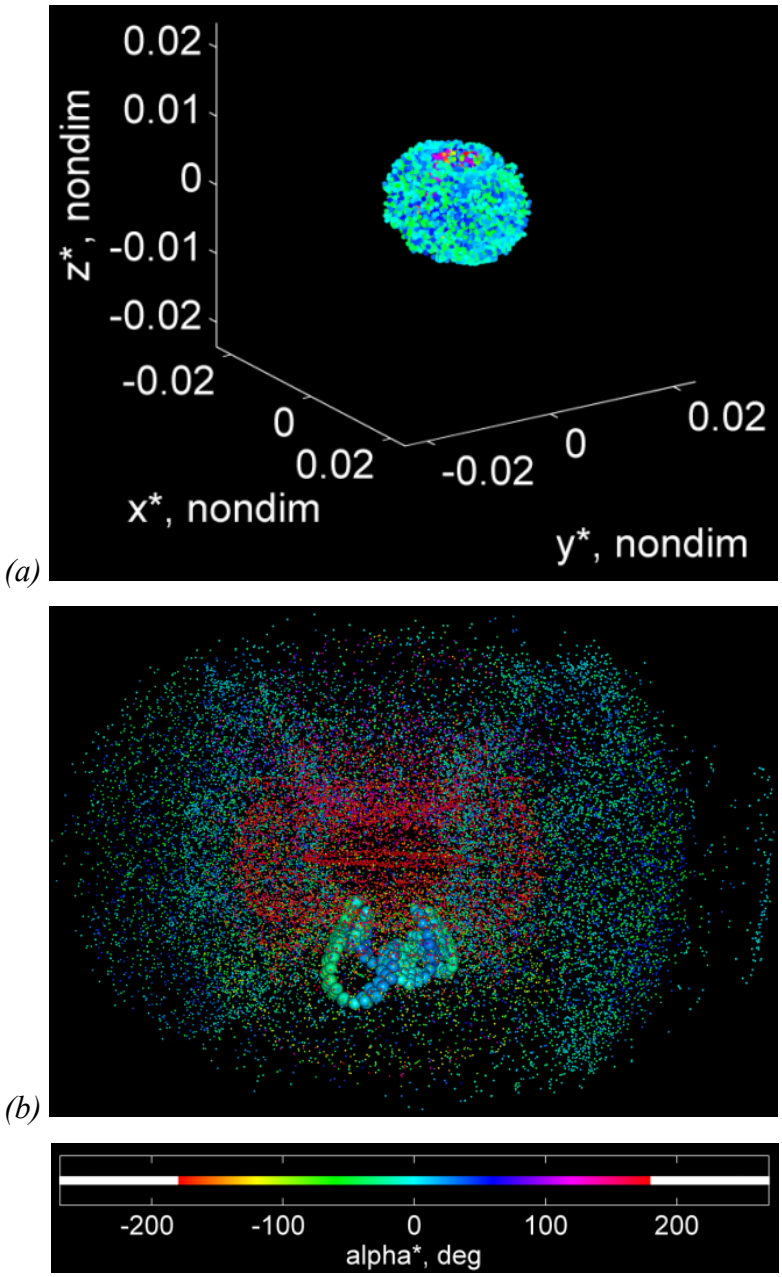

Figure 4.3. 4-D periapsis Poincaré map (returns during following year at lower "energy") in the vicinity of Titania; MATLAB® view (*a*) and Avizo® view with selected trajectory (*b*); ($\dot{\rho} = 0+;\ x,\ y,\ z,\ \alpha\_color$)

The trajectory selected from Figure 4.3(b), which eventually impacts Titania after 11.2 months, is now assumed to be representative of a region of the 4-D map in Figure 4.3(a) that can be targeted for the desired capture behavior. To design a capture maneuver after entry through the L_1 gateway, the negative-time map from Figure 4.2(b) is

filtered to isolate the returns associated with L_1 entry and then overlaid on the forward time map of *only* the selected trajectory from Figure 4.3(b). A zoom highlights the region of intersection in 3-D space; also adjusting the color scale—while filtering out points with α values outside of this new range of color—offers more resolution of the color dimension (essentially "zooming" in color) and results in the overlaid maps in Figure 4.4(a). Map returns corresponding to L_1 entry trajectories over the previous month at the higher "energy" level appear as large dots, while returns during the subsequent year along the representative capture trajectory at the lower "energy" level are plotted with small dots. As a useful technique for cross-referencing map points in this visual environment with actual map return data, the dots associated with L_1 entry are annotated with trajectory numbers and return counters.

The final step in the capture maneuver design process is an attempt to determine a potential region of intersection in the full 4-D space of the overlaid maps. After transitioning the overlaid maps in Figure 4.4(a) to Avizo® and rotating the view, a region of potential intersection (in both 3-D space *and* color) is located visually, as indicated in Figure 4.4(b). In this region, a large blue dot associated with a cross-referenced L_1 entry trajectory appears near other small blue dots associated with the selected trajectory representing the desired capture behavior. By implementing a tangential maneuver along the L_1 entry trajectory at the periapsis represented by the large blue dot, the "energy" value of that trajectory is immediately changed to the lower "energy" level in the capture region represented by the small dots. This maneuver is accomplished with $\left|\overrightarrow{\Delta V}\right|$ = 39.5 m/s and is directed exactly opposite to the S/C current velocity vector $\vec{V}$, with respect to the rotating frame, at a time equal to 22.6 hours after L_1 entry. This location is the very first periapsis after entry. The resulting capture maneuver is depicted in Figure 4.5(a) in the *x*-*z* rotating view for one month prior and one month following the maneuver. This view includes the overlaid ZVCs at the "energy" levels before (green) and after (blue) the maneuver. The view in the *X*-*Y* Uranus-centric inertial frame for one month ahead of the maneuver appears in Figure 4.5(b). Note that this maneuver is not claimed to be optimal; it simply yields a capture trajectory that is continuous in position and that can be used as an initial guess in an optimization process that attempts to reduce the $\left|\overrightarrow{\Delta V}\right|$.

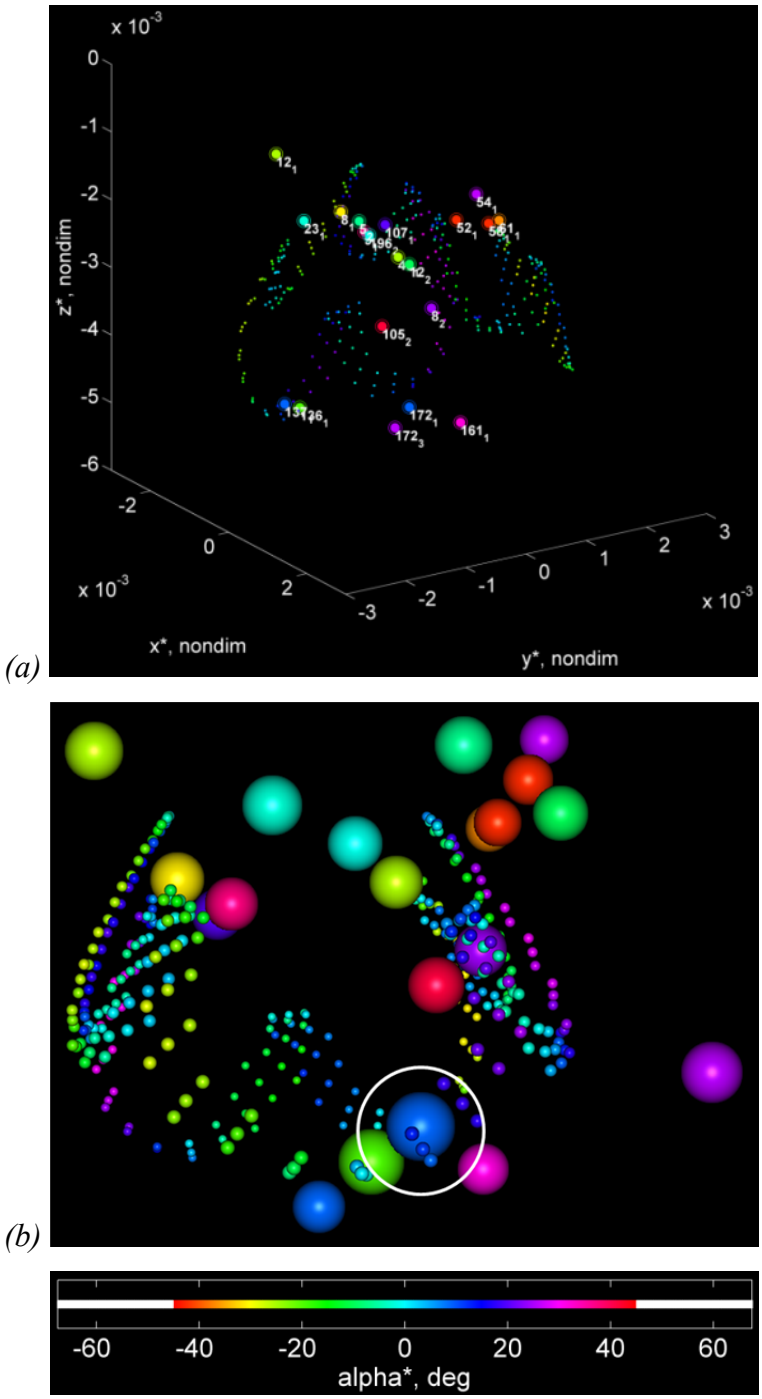

(a)

(b)

Figure 4.4. 4-D periapsis Poincaré maps (returns during previous month of L_1 entries at higher "energy" and following year at lower "energy") overlaid in the vicinity of Titania; MATLAB® view (*a*) and Avizo® view with region of potential intersection in 4-D space identified (*b*); $(\dot{\rho} = 0+;\ x,\ y,\ z,\ \alpha\_color)$

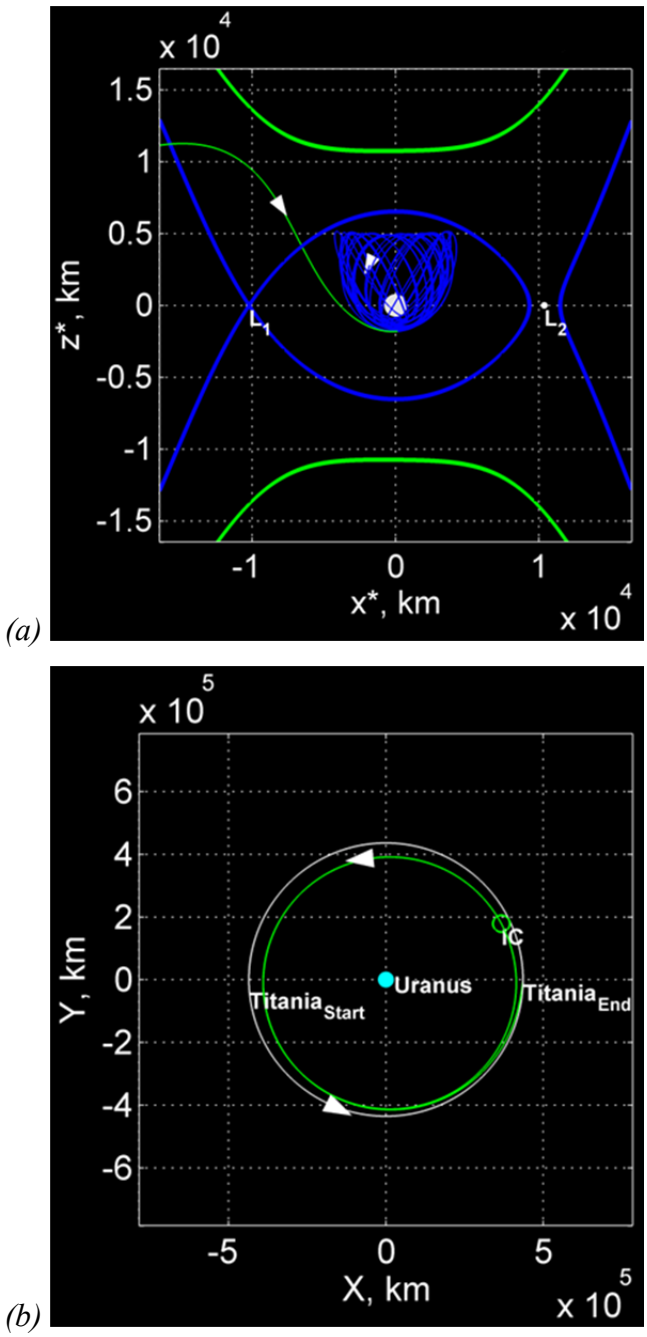

Figure 4.5. Rotating (*a*) and inertial (*b*) views of designed capture maneuver; before maneuver (green) and after maneuver (blue)

The final capture trajectory illustrated in Figure 4.5, which does not impact Titania within the following year, is not the same trajectory as the one originally selected from the 4-D map, but the new path is qualitatively similar to the original trajectory; it is a 3-D

trajectory with periapses tightly grouped beneath Titania. Thus, the original selected trajectory is, in fact, representative of a region of the 4-D map associated with the desired behavior. Furthermore, the visual environment of the overlaid 4-D periapsis Poincaré maps is successfully employed to visually locate an L_1 entry trajectory—as well as an exact point and time along the trajectory—that allows for a capture in the vicinity of Titania with only a tangential maneuver (in the rotating frame). Under this process, although the L_1 entry trajectory is necessarily one of the negative-time entry trajectories originally used to generate the negative-time Poincaré map, the final capture trajectory is not expected to be precisely one of the original trajectories used to generate the forward-time map. The capture trajectory solution is determined based on a visual inspection of potential intersecting regions in the space explored on the 4-D map.

For completeness, the instantaneous (osculating), Uranus-centered, two-body orbital elements for the L_1 entry trajectory are calculated one month prior to the capture maneuver (at the initial condition "IC" in Figure 4.5(b)) and appear in Table 4.2. This calculation is based on Titania's own osculating elements at the time of the maneuver,

Table 4.2 S/C osculating orbital elements one month prior to Titania capture maneuver*

a	e	i	Ω	ω	ν
402,692.63 km	0.040871	178.36°	311.05°	106.91°	248.64°

* Uranus-centric mean equatorial reference frame; node of 4 July 2030 at "midnight," the assumed epoch of the capture maneuver

obtained from the JPL HORIZONS System web-interface (ephemeris data URA083 and URA095) [111], with a Uranus-centric, two-body gravitational parameter assumed to be equal to $GM_U = 5.7941801464777915 \times 10^6$ km^3/s^2, associated with the entire Uranian system mass. The set $(a, e, i, \Omega, \omega, \nu)$ consists of semimajor axis, eccentricity, inclination, longitude of ascending node, argument of periapsis, and true anomaly, respectively. Note that the osculating inclination of the S/C is near-planar retrograde (almost 180°), also true for Titania's orbit in this reference frame, where, in fact, Uranus rotates in the retrograde direction as well. These osculating elements could be used as a target state in a two-body

Titania approach solution, perhaps as part of a Uranian system tour of the type designed by Heaton and Longuski [67] (see also Section 5.3).

4.2 Design Example #2: Adjustments on the 4-D Map

A second example of 4-D-map-based mission design uses cylindrical phase space Poincaré maps to design a 3-D S/C "return-to-Earth" maneuver in the Earth-Moon spatial CR3BP. This type of maneuver can be seen as a departure maneuver in the sense that the objective is to depart the vicinity of the Moon. The Earth-centric and Moon-centric two-body gravitational parameters are assumed to be equal to GM_E = 398,600.4418 km^3/s^2 and GM_M = 4,902.801076 km^3/s^2, respectively. The assumed model parameters for this system appear in Table 4.3 [127]. In this example, the hyperplane in the phase space is defined in terms of Moon-centered cylindrical coordinates such that θ = -45° and $\dot{\theta} > 0$; this hyperplane captures returns to the map in a prograde direction with respect to the Moon in the rotating frame.

Table 4.3 Earth-Moon CR3BP model parameters

μ (dimensionless)	l^* (km)	Earth radius (km)	Moon radius (km)
0.012150586550569	384,400	6,378.14	1,737.4

The solution process to design a return to the region of the Earth is motivated by invariant manifold conduits for the collinear libration points (like L_1 and L_2) in the CR3BP. As noted by Gómez et al. [46], in the planar CR3BP, there exist 2-D manifold tubes that carry 3-D constant-*JC* dynamical "flow" through a libration point gateway. These tubes are asymptotic to a 1-D constant-*JC* center manifold at a given "energy" level, i.e., just a *single orbit* in the vicinity of the libration point. This concept enables 2-D-map-based mission design methods that seek intersections between cross-sections of the manifold tubes on 2-D Poincaré maps. If such intersections are available numerically, they represent transit pathways, which ultimately carry a S/C through one or

more libration point gateways. Unfortunately, in the spatial CR3BP, as a consequence of the higher-D topology discussed in Sections 2.4 and 3.1, the manifold tubes asymptotic to a 3-D orbit in the vicinity of a libration point gateway do not act as simple conduits in precisely the same way. However, Gómez et al. demonstrate that the general concept does extend to higher dimensions by means of higher-D conduits [46]. Remarkably, there exist 4-D manifold tubes that carry 5-D constant-*JC* dynamical "flow" through a libration point gateway. These tubes are actually asymptotic to a 3-D constant-*JC* center manifold at a given "energy" level. It is critical to note that this 3-D center manifold structure consists of not just a single trajectory but of *all rotational motion* in the vicinity of a libration point gateway. Rather than attempting to compute the higher-D conduits, the design methodology in this investigation simply uses the fact that these structures *should* exist to motivate a search for regions on 4-D Poincaré maps that may be associated with passage through a particular libration point gateway. Attempts to interpret the behavior in such regions are successful in designing a maneuver that achieves a gateway passage.

The specific objective in this example is the use of 4-D maps in the vicinity of the Moon to design a maneuver that alters a selected S/C path to ensure its return to the region of the Earth (inside the Moon's orbit) within the subsequent year. A 3-D trajectory to initiate the process appears in Figure 4.6. The orbit is located in the vicinity of the Moon with an initial condition arbitrarily selected to be 3-D, to be prograde with respect to the Moon in the rotating frame, and, finally, to possess an "energy" value associated with the L_1 libration point. This trajectory, which impacts the Moon after 3.4 months, appears in Figure 4.6 in both the *Y*-*Z* Moon-centric inertial view and the *x*-*y* rotating view with the Moon as the offset origin. Figure 4.6(b) also illustrates an edge-on view of the cylindrical phase space map hyperplane introduced earlier, which is used to generate the 4-D Poincaré map corresponding to the originating trajectory.

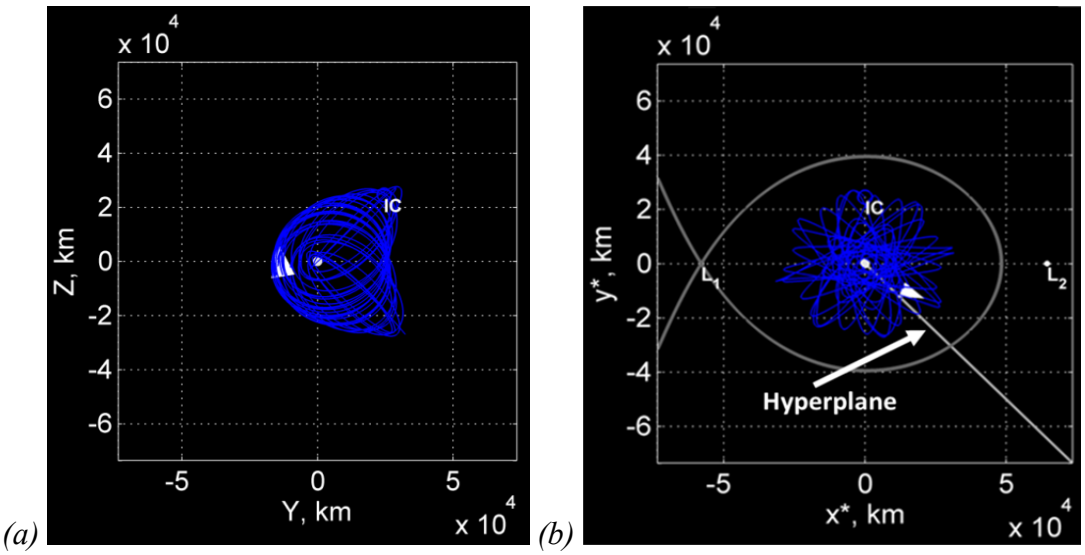

Figure 4.6. Inertial (*a*) and rotating (*b*) views of originating trajectory in the vicinity of the Moon

A map formulation that is practical for a given problem is a key element in a successful design strategy. The particular hyperplane employed in this example reveals 3-D trajectories with prograde motion with respect to the Moon in the rotating frame. Based on the same concept discussed in Design Example #1 (see previous section), such prograde trajectories are more likely than retrograde trajectories to leave the vicinity of the Moon whenever a libration point gateway is open. Thus, in the next step in the design process, a similar 4-D cylindrical phase space map is generated in forward time at a higher "energy" level where the L_1 gateway is now open but the L_2 gateway is just closed. Here, a set of 998 initial conditions is identified based on a 2-D grid of perpendicular crossings to the hyperplane; the trajectories are then propagated forward in time for the following year or until an impact, whichever occurs sooner. Using perpendicular crossings to seed the initial conditions is a technique to reduce the size of the initial conditions grid, which, for the 4-D map space in the spatial CR3BP, can easily push the current memory limits of most personal computers. A trade-off exists, of course, because a map created based on only a certain type of initial condition may not reveal all of the relevant dynamical behavior for a given problem.

To design a "return-to-Earth" S/C transfer maneuver that results in passage through the L_1 gateway within a given time interval—one year in this example—the forward-time

map corresponding to the higher "energy" level is filtered to illuminate only the returns associated with L_1 exit and is then overlaid on the forward-time map of the originating trajectory appearing in Figure 4.6 at the lower "energy" level. This process results in the overlaid maps plotted in Figure 4.7(a) (nondimensional units). Map returns corresponding to the originating trajectory (until impact) at the lower "energy" appear as large dots, while the returns over the following year on the higher-"energy" map are plotted with small dots.

In a process similar to that described in the Titania capture maneuver design process employed in Design Example #1, the final step is an attempt to locate a potential region of intersection in the full 4-D space via the overlaid maps. After transitioning the overlaid maps in Figure 4.7(a) to Avizo®, a region of potential intersection in *only 3-D space* (i.e., the 3-D, spatial dimensions of the map) is located visually, as noted in Figure 4.7(b). In this region, a large purple dot representing a point along the lower-"energy" originating trajectory *appears* to be inside a cluster of small dots representing a potential region associated with passage though the L_1 gateway over the following year. However, the small dots in the immediate vicinity of the large purple dot range in color from green to blue, a range on the $\dot{z}$ color scale that does not include purple. Thus, it is evident from a careful examination of the 4-D map that the purple dot is not really inside the region represented by the small green to blue dots. An adjustment in the map's color coordinate is necessary.

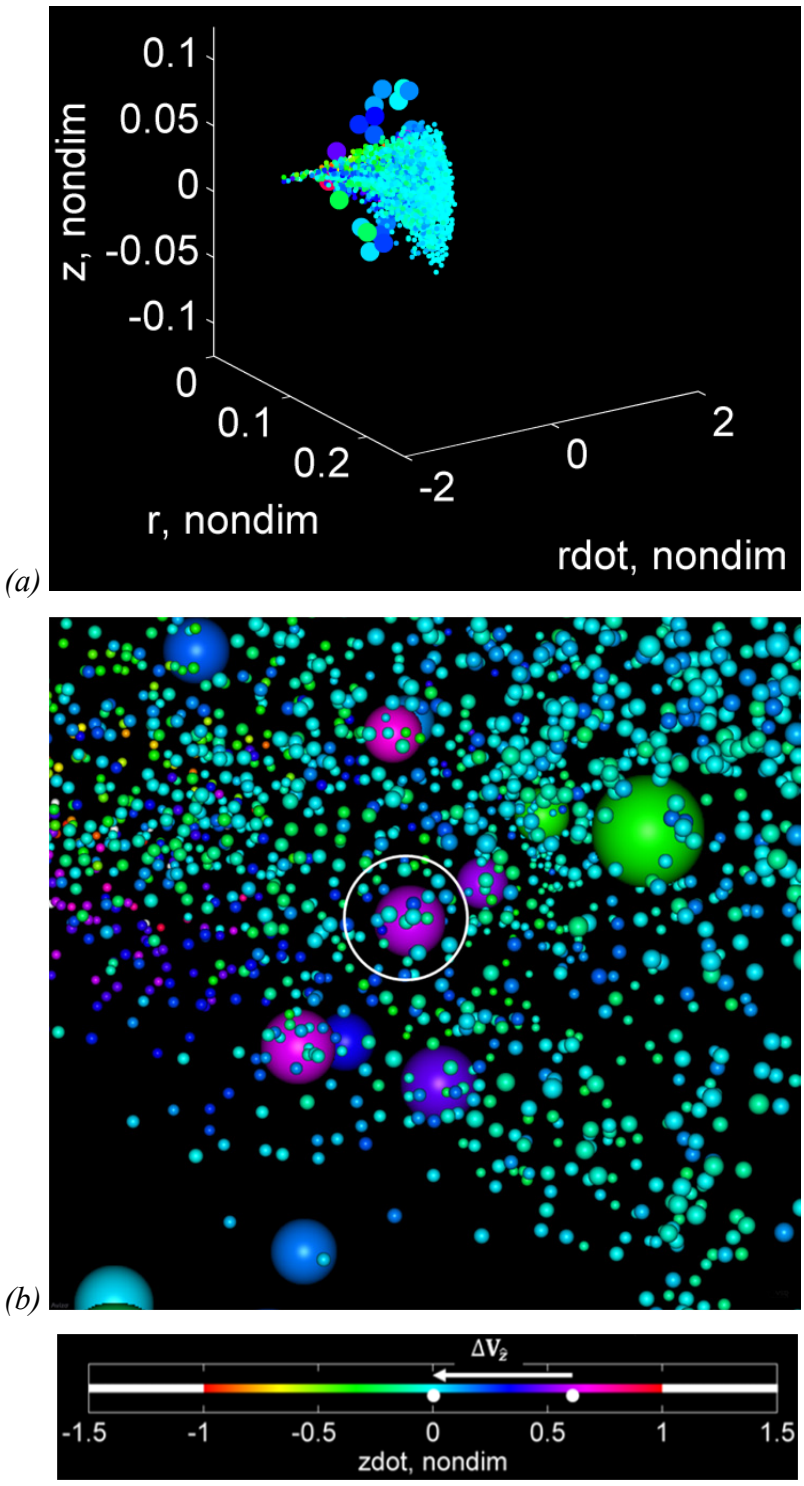

Figure 4.7. 4-D cylindrical phase space Poincaré maps (originating trajectory at lower "energy" and returns during subsequent year of L_1 exits at higher "energy") overlaid in the vicinity of the Moon; MATLAB® view (*a*) and Avizo® view with region of potential intersection in only 3-D space identified (*b*); maneuver depicted on color scale; ($\theta = -45°+;\ r,\ \dot{r},\ z,\ \dot{z}\_color$)

To design a "return-to-Earth" maneuver to be implemented at the point along the originating trajectory represented by the large purple dot in Figure 4.7(b), the $\hat{z}$ component of the S/C velocity vector $\vec{V}$ (in the rotating frame) is adjusted to create a potential intersection in the full 4-D map space. A reasonable guess for the required $\overrightarrow{\Delta V}$ adjustment in the $\hat{z}$ direction is determined by visual inspection noticing that a large cyan dot (corresponding to $\dot{z} = 0$), located at the same point in 3-D space as the large purple dot, would be well within the region represented by the small green to blue dots (which also includes cyan dots). This decrease in $\dot{z}$ is depicted on the color scale for Figure 4.7. In addition, it is necessary to increase the "energy" level to the level associated with the map of small dots. Because $\dot{r}$ is one of the three phase space coordinates represented in the spatial dimensions of the 4-D map employed in this example, and because it is desired that the same 3-D location in the phase space in Figure 4.7(a) be maintained, the design process requires that the $\hat{r}$ component of $\vec{V}$ be held constant during the maneuver; the potential intersection in the 4-D map space is then preserved. Therefore, the remaining velocity component $\hat{\theta}$, which is not explicitly represented on the 4-D map, is adjusted to increase the "energy" level to that associated with the map of small dots. The resulting maneuver, which decreases the $\hat{z}$ component of $\vec{V}$ by 620.2 m/s and also increases its $\hat{\theta}$ component by 427.2 m/s, is accomplished with a total $\left|\overrightarrow{\Delta V}\right|$ = 753.1 m/s at a time equal to 25.0 days after the initial condition of the originating trajectory appearing in Figure 4.6. The departure maneuver, which is not claimed to be optimal, is successful and results in passage through the L_1 gateway 22.6 days after the burn, as depicted in Figure 4.8(a) in the *x*-*y* rotating view. The *X*-*Y* Earth-centric inertial view is depicted in Figure 4.8(b) for one year following the maneuver. As in the previous design example, the rotating view includes the overlaid ZVCs at the "energy" levels before (blue) and after (green) the maneuver. The closest approach to the Moon before return to the region of the Earth is 897 km altitude, and the closest approach to the Earth over the following year is 77,013 km altitude.

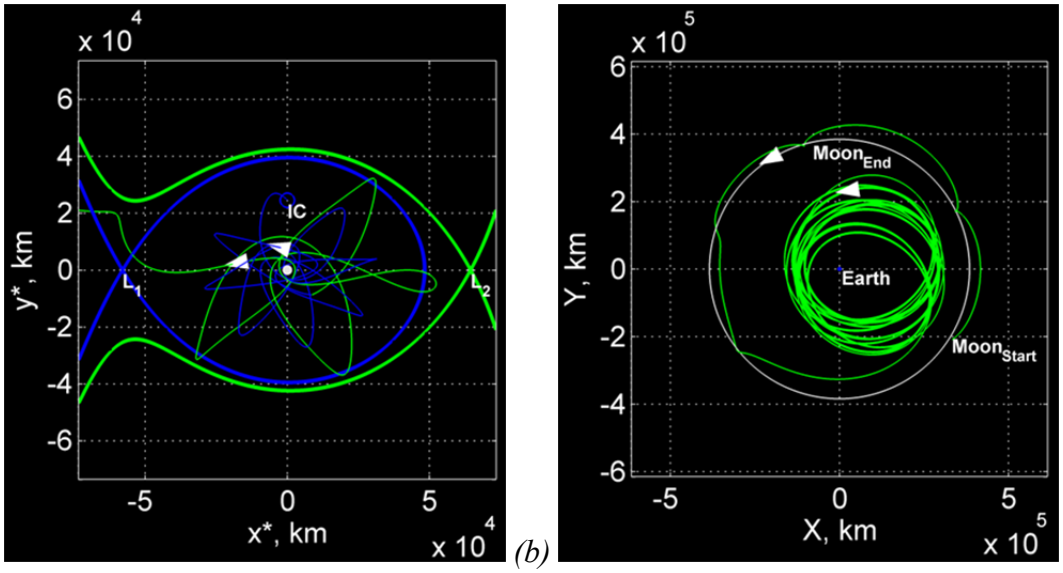

Figure 4.8. Rotating (*a*) and inertial (*b*) views of designed "return-to-Earth" maneuver; before maneuver (blue) and after maneuver (green)

Finally, the most noteworthy result of this design example is demonstrated by the case of a different S/C maneuver that is *not* successful. In this comparison case, the 3-D (only) intersection appearing on the overlaid Poincaré maps in Figure 4.7(b) is used to implement a maneuver as if it actually represents a true intersection of the overlaid map, thereby ignoring the information provided by the map's color dimension. Based on this, a maneuver to increase the "energy" level (as before) is implemented at the point along the originating trajectory represented by the large purple dot. This maneuver increases the $\hat{\theta}$ component of $\vec{V}$; both the $\hat{r}$ and $\hat{z}$ components are unchanged, therefore, the color of the dot remains purple. This maneuver is accomplished with a much smaller $\left|\overrightarrow{\Delta V}\right|$ = 31.2 m/s, however, it results in S/C impact with the Moon 52.1 days after the burn. Even if lunar impact is ignored, the resulting S/C path does not return to the region of the Earth over the following year, even though the L_1 gateway is open. This unsuccessful case highlights the benefit of using a "true" 4-D map—as is employed successfully earlier in this design example—rather than just a 3-D map projection that ignores the critical fourth dimension. Proper interpretation of all four dimensions on the Poincaré map allows a map-based designer to determine a solution possessing certain qualitative

characteristics—even without the aid of more precise processes such as targeting or optimization.

4.3 Design Example #3: The Challenges of the Space-Plus-Color Method

The third example of 4-D-map-based mission design uses Cartesian phase space Poincaré initial condition maps to design a 3-D S/C Earth transit maneuver in the Sun-Earth spatial CR3BP. The Sun-centric and Earth-centric two-body gravitational parameters are assumed to be equal to $GM_S = 1.327122 \times 10^{11}$ km^3/s^2 and $GM_E = 398{,}600.4418$ km^3/s^2, respectively. The assumed model parameters for this system appear in Table 4.4 [127]. In this example, the Cartesian phase space initial condition map hyperplane is defined such that $x = L_{2x}$ and $\dot{x} < 0$, where L_{2x} is the x value locating the L_2 libration point; this hyperplane captures initial conditions at entry into the vicinity of the Earth through the L_2 gateway.

Table 4.4 Sun-Earth CR3BP model parameters

μ (dimensionless)	l^* (km)	Sun radius (km)	Earth radius (km)
$3.003486074446236 \times 10^{-6}$	149,587,457	695,990	6,378.14

The solution process to design an Earth transit maneuver is again motivated by higher-D invariant manifold conduits for the collinear libration points, as discussed for Design Example #2 (see previous section). The specific objective in this example is the use of 4-D initial condition maps located at the L_2 gateway to design a maneuver that alters a selected S/C initial condition—while maintaining the same "energy" level—to ensure its transit from the exterior region, i.e., outside Earth's orbit around the Sun, past the Earth and then into the interior region, i.e., the region of the Sun. At the "energy" level examined, such a transit maneuver requires passage first through the L_2 gateway and then through the L_1 gateway. The *x*-*z* rotating view of the Cartesian phase space Poincaré initial condition map hyperplane appears in Figure 4.9(a); the hyperplane is located at the

Sun-Earth L_2 gateway at an "energy" level where both L_1 and L_2 gateways are open. The 4-D initial condition map is generated using a 4-D grid of 2000 initial conditions, as plotted in Figure 4.9(b). The origin of the map is effectively L_2.

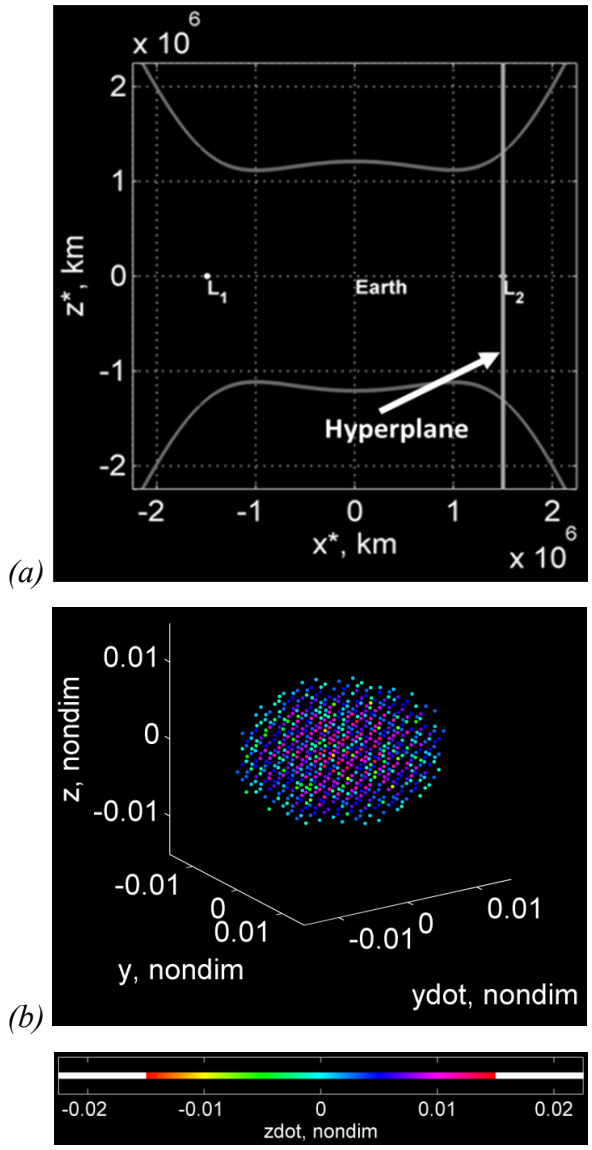

Figure 4.9. Rotating view of hyperplane (a) and Cartesian phase space Poincaré initial condition map (b) in the vicinity of the Earth; $(x = L_{2x}-;\ y,\ \dot{y},\ z,\ \dot{z}\_color)$

The 4-D initial condition map in Figure 4.9(b) reveals a significant difficulty in using the space-plus-color method to reflect the fourth dimension on a Poincaré map. This image is an attempt to represent 2000 grid points in a 4-D space; however, multiple

points with different colors are plotted directly on top of one another in 3-D space, thereby obscuring the full range of color (representing $\dot{z}$) existing at each 3-D location. This is an example of the single location ambiguity of the space-plus-color method as applied to 4-D Poincaré maps; it is difficult to associate a 3-D location in space with more than one color at a time (see Section 3.1.3). Fortunately, this approach to representing a 4-D initial condition map still enables successful interpretation and can support mission design if it is recognized which values of color are plotted last. In this case, for each point in 3-D space, the grid-generating algorithm plots the largest value of $\dot{z}$ last, which implies that each 3-D location includes the information about the maximum $\dot{z}$ value at that point. Not all 3-D grid locations have the same range of $\dot{z}$ values because some position and velocity combinations are not physically possible at the L_2 gateway at this "energy" level; these restrictions in the 5-D constant-*JC* phase space are related to the restrictions in the 3-D position space that result in the ZVSs. Note that, depending on the particular design problem, the algorithm could be reversed to plot the smallest $\dot{z}$ value last or to perhaps follow a more sophisticated order. For the specific case presented in this design example, an algorithm that plots the largest value of $\dot{z}$ last is effectively used to achieve the desired outcome.

To design an Earth transit maneuver that is implemented when the S/C passes through the L_2 gateway and that results in passage through the L_1 gateway within a given time interval—three months in this example—the initial condition map in Figure 4.9(b) is filtered to illuminate only the initial conditions associated with L_1 exit over the subsequent three months. To demonstrate the design process, a test trajectory initial condition located on the same 4-D map is arbitrarily selected to be inside the *position* region associated with L_1 exit over the following three months, but not inside the *velocity* region associated with the same behavior. In other words, the test trajectory is selected to be outside the region of the 4-D map associated with the desired transit behavior, but it is outside that region due only to its velocity coordinates ($\dot{y}$ and $\dot{z}$) on the map. It is effectively "on target" in terms of position but not in terms of velocity. Moreover, by propagating this initial condition in the configuration space, it is confirmed that this test trajectory does not pass through the L_1 gateway over the following three months. The

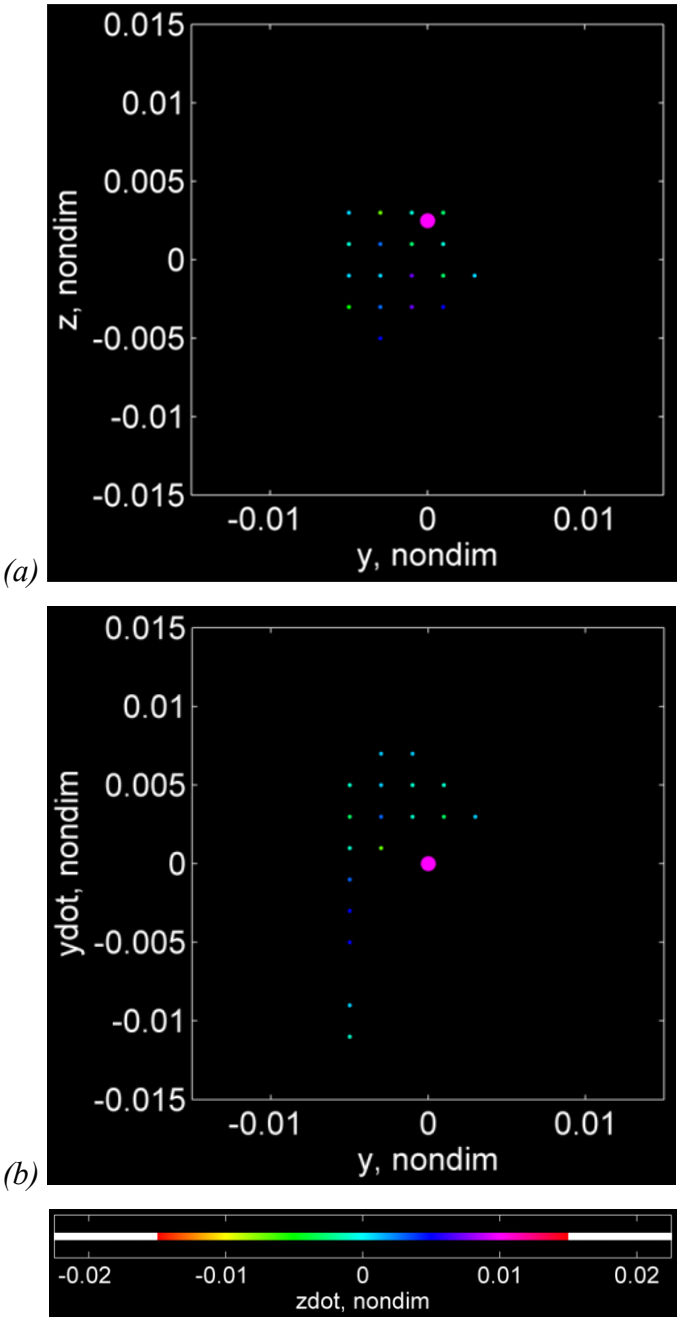

Figure 4.10. 4-D Cartesian phase space Poincaré initial condition map filtered to display only initial conditions associated with L_1 exit over subsequent three months: y-z (a) and y-$\dot{y}$ (b) views in the vicinity of the Earth; initial condition of test trajectory added; $(x = L_{2x}-;\ y,\ \dot{y},\ z,\ \dot{z}\_color)$

filtered initial condition map is plotted in Figure 4.10 with initial conditions on the grid plotted as small dots. The initial condition of the test trajectory appears as a large dot

added to the same 4-D map. While the *y*-*z* view of this 4-D map illustrates that the test trajectory initial condition (large dot) is inside the position target region (represented by the small dots), the *y*-$\dot{y}$ view reveals that it is outside the velocity target region in terms of its $\dot{y}$ value. It is not immediately clear from these views whether it is also outside the velocity target region in terms of its $\dot{z}$ color value. In other words, it remains to be seen whether just the $\hat{y}$ and $\hat{x}$ components of S/C velocity $\vec{V}$ must be adjusted at the L_2 gateway or whether the $\hat{z}$ component must also be adjusted to achieve the desired transit within three months. Figure 4.11(a) depicts (in Avizo®) a maneuver, determined by visual inspection of the map in Figure 4.10, designed to adjust only the $\hat{y}$ velocity component of the map—as well as the $\hat{x}$ component to maintain the same "energy" level of the map—at the test trajectory L_2 gateway position represented by the large magenta dot in Figure 4.10(a). This maneuver is implemented by increasing the $\hat{y}$ component of $\vec{V}$ by 119.1 m/s and also increasing its $\hat{x}$ component by 25.3 m/s. However, it is now possible to see that the selected $\dot{z}$ color value of the test trajectory must be adjusted as well. This adjustment to $\dot{z}$ is necessary because the magenta color of the large dot at its new location on the 4-D map is larger in value than the green and cyan colors of the small dots in its immediate vicinity. To draw this conclusion, it is essential to recognize that the grid-generating algorithm plots the largest value of $\dot{z}$ last. Therefore, because magenta is *higher* on the color scale than all of the colors in its immediate vicinity, this apparent intersection in 3-D space is not a true intersection in the 4-D space. Note that, as an aside, if the $\dot{z}$ color of the large dot were instead lower in value than the color of small dots in the immediate vicinity, it would be necessary to examine a 4-D grid that plots the smallest $\dot{z}$ value last to properly interpret the map.

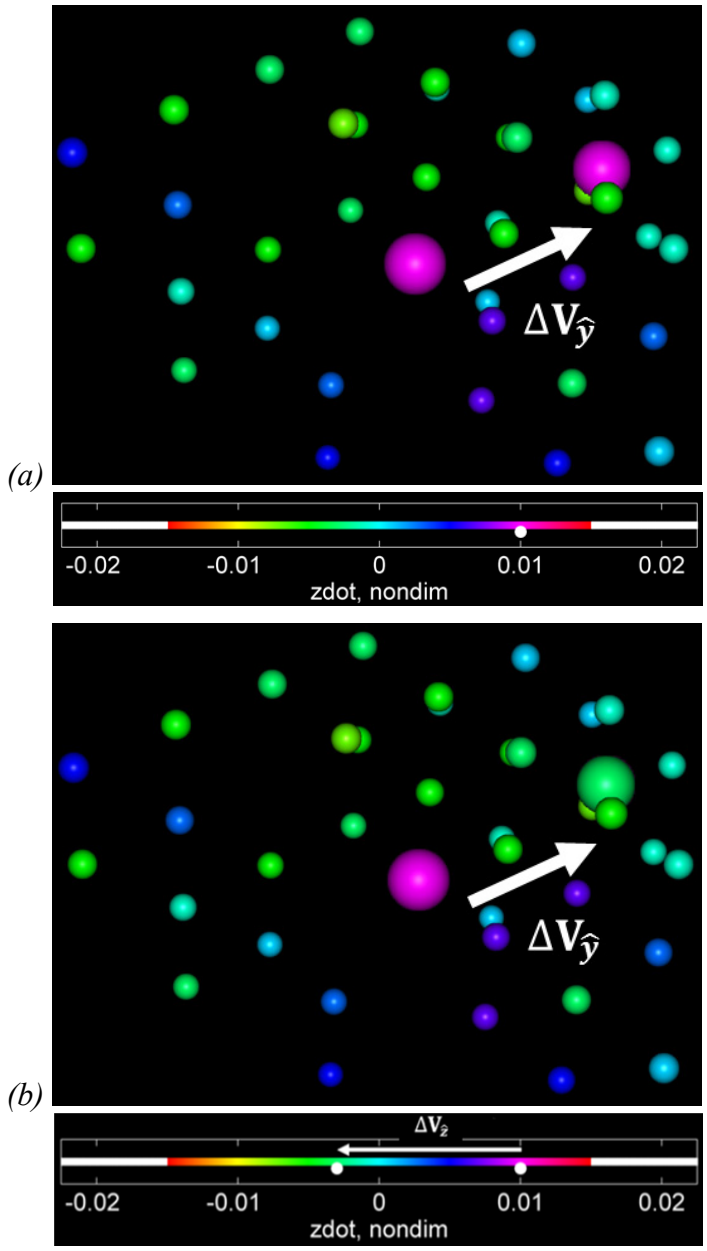

Figure 4.11. Unsuccessful (*a*) and successful (*b*) maneuvers depicted on 4-D Cartesian phase space Poincaré initial condition map (in Avizo®) in the vicinity of the Earth; initial condition of test trajectory modified; ($x = L_{2x}-$; $y,\ \dot{y},\ z,\ \dot{z}\_color$)

The value of employing a full 4-D map, as opposed to just a 3-D map projection, is demonstrated when the initial condition resulting from the maneuver depicted in Figure 4.11(a) (with total $\left|\overrightarrow{\Delta V}\right|$ = 121.8 m/s) is propagated in the configuration space. It is confirmed that the resulting trajectory still does not pass through the L_1 gateway over the

following three months. It is clearly necessary to rely on the insight gained from the color dimension of the 4-D map to accomplish the transit design goal. Figure 4.11(b) depicts a revised maneuver, determined by visual inspection of the maps in Figures 4.10 and 4.11(a), to adjust both the $\hat{y}$ and $\hat{z}$ velocity components of the map—as well as the $\hat{x}$ component to maintain the same "energy" level of the map—at the same test trajectory L_2 gateway position as before. This maneuver is designed to create a potential intersection between the large dot and the region represented by the small dots in the full 4-D space. The revised maneuver is implemented by increasing the $\hat{y}$ component of $\vec{V}$ by 119.1 m/s, decreasing its $\hat{z}$ component by 387.2 m/s, and also decreasing its $\hat{x}$ component by 97.2 m/s. The maneuver requires a total $\left|\overrightarrow{\Delta V}\right|$ = 416.6 m/s and is implemented when the S/C passes through the L_2 gateway. This maneuver is successful and results in a trajectory that passes through the L_1 gateway 77.3 days after passing through the L_2 gateway, as plotted in Figure 4.12(a) in the *x*-*z* rotating view and in Figure 4.12(b) in the *X*-*Y* Earth-centric inertial view for three months prior to (blue) and three months following (green) the burn. Also included for comparison with the green trajectory in the *x*-*y* rotating view in Figure 4.12(c) is the blue trajectory resulting from no maneuver as well as the red trajectory resulting from the unsuccessful maneuver ignoring the insight gained from the color dimension of the 4-D map, neither of which pass through the L_1 gateway over the following three months. Note that, because the "energy" (*JC*) value does not change during a transit maneuver in this example, the ZVCs are the same before and after the burn. Lastly, as in previous examples, this maneuver is not claimed to be optimal, but it does yield a transit trajectory—continuous in position—that can be used as an initial guess in an optimization process.

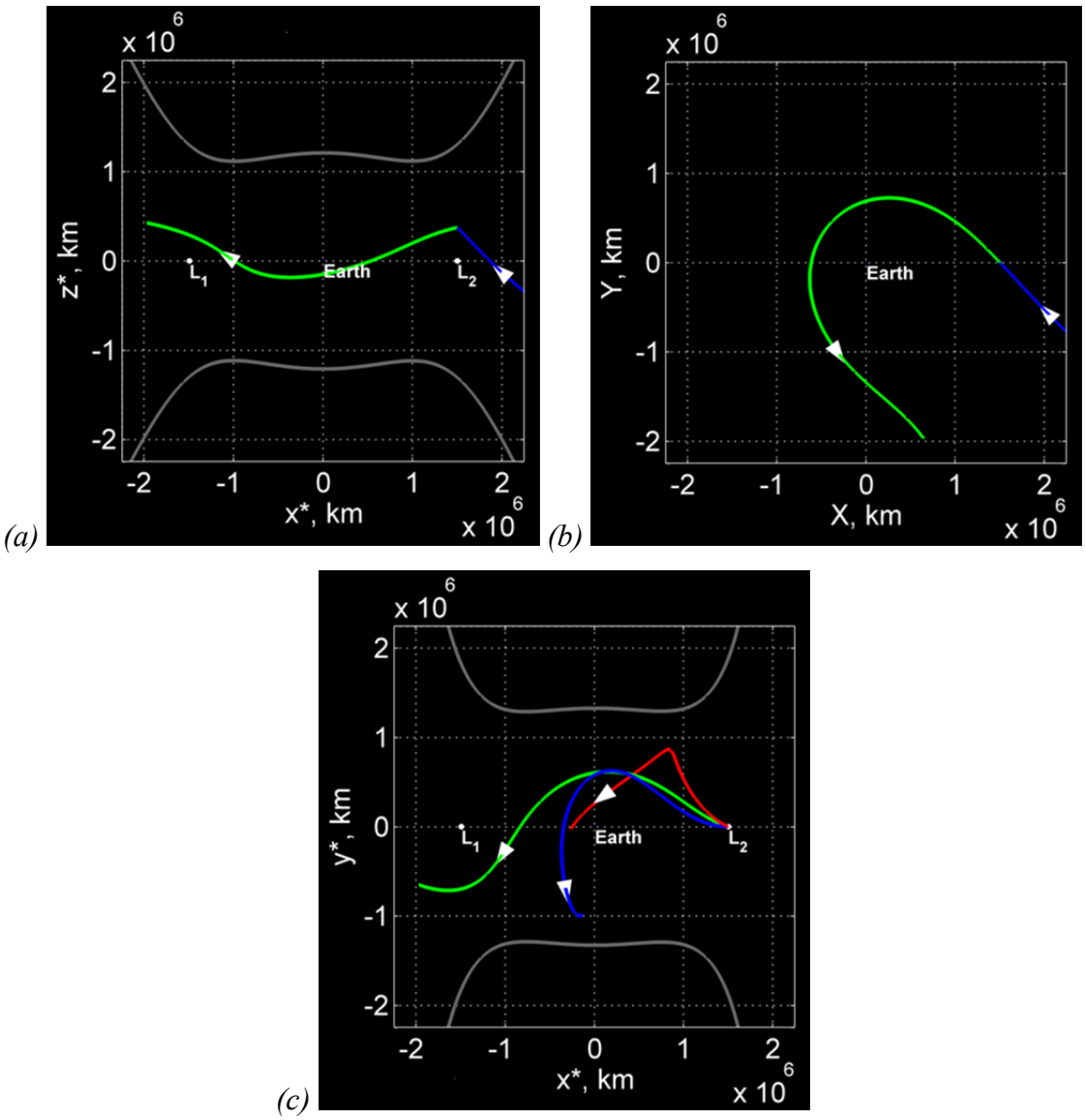

Figure 4.12. Rotating (*a*) and inertial (*b*) views of designed Earth transit maneuver in the vicinity of the Earth; before maneuver (blue) and after maneuver (green); comparison rotating view (*c*) of trajectories resulting from no maneuver (blue), unsuccessful maneuver (red), and successful maneuver (green)

4.4 Design Example #4: Orbit Transfers Based on 4-D Manifold Maps

The final basic example of 4-D-map-based mission design employs Cartesian phase space Poincaré manifold maps to design a 3-D S/C transfer maneuver between 3-D, unstable periodic LPOs in the Earth-Moon spatial CR3BP. As stated earlier, this system's mass ratio is assumed to be equal to $\mu = 0.012150586550569$ (see again Table

4.3 for other model parameters). In this example, the Cartesian phase space manifold map hyperplane is defined such that $x = L_{5x}$ and is two-sided to capture the complete first map returns of entire 2-D stable and unstable manifold tubes emanating from selected (1-D) periodic orbits.

Figure 4.13 depicts the four-perspective, barycentric rotating view of two 3-D, periodic LPOs: a "northern" axial orbit in the vicinity of L_5 and a vertical orbit in the vicinity of L_3. As indicated by the ZVSs illustrated, the L_3 orbit (green) is at the higher "energy" level, with its ZVSs even farther above and below the *x*-*y* plane than those of the L_5 orbit (cyan). Note that, following the convention described in Section 2.1, the ZVCs depicted are the cross-sections of the ZVSs, where the origin of the cross-sections is the Earth, with (*x,y,z*) = (-μ,0,0). The L_5 orbit has a period of 25.4 days, and the period of the L_3 orbit is 27.2 days; both periods are similar to that of the primary system (27.3 days). Both orbits are converged to satisfactory periodicity, in the rotating frame, through the differential corrections (targeting) process described in Section 2.2 using initial guesses from Grebow [131]. Following the process described in Section 2.3, initial conditions are developed that should closely approximate the stable and unstable manifold tubes emanating from a particular periodic orbit (represented by a fixed point on a map). An approximation for each manifold tube in this analysis is comprised of 500 individual trajectories asymptotic to (or from) a periodic orbit, as plotted in Figure 4.14 along with the hyperplane defined earlier. The blue tubes represent the stable manifold tubes asymptotic to the L_3 orbit in forward time, with the plot of each trajectory terminated in negative time at a $y = 0$ crossing on the L_1 side of the Earth; the red tubes represent the unstable manifold tubes asymptotic to the L_5 orbit in negative time, with the plot of each trajectory terminated in forward time at $x = 0$. The obvious complexity of visualizing these manifold structures in the 3-D configuration space (belonging to a 6-D

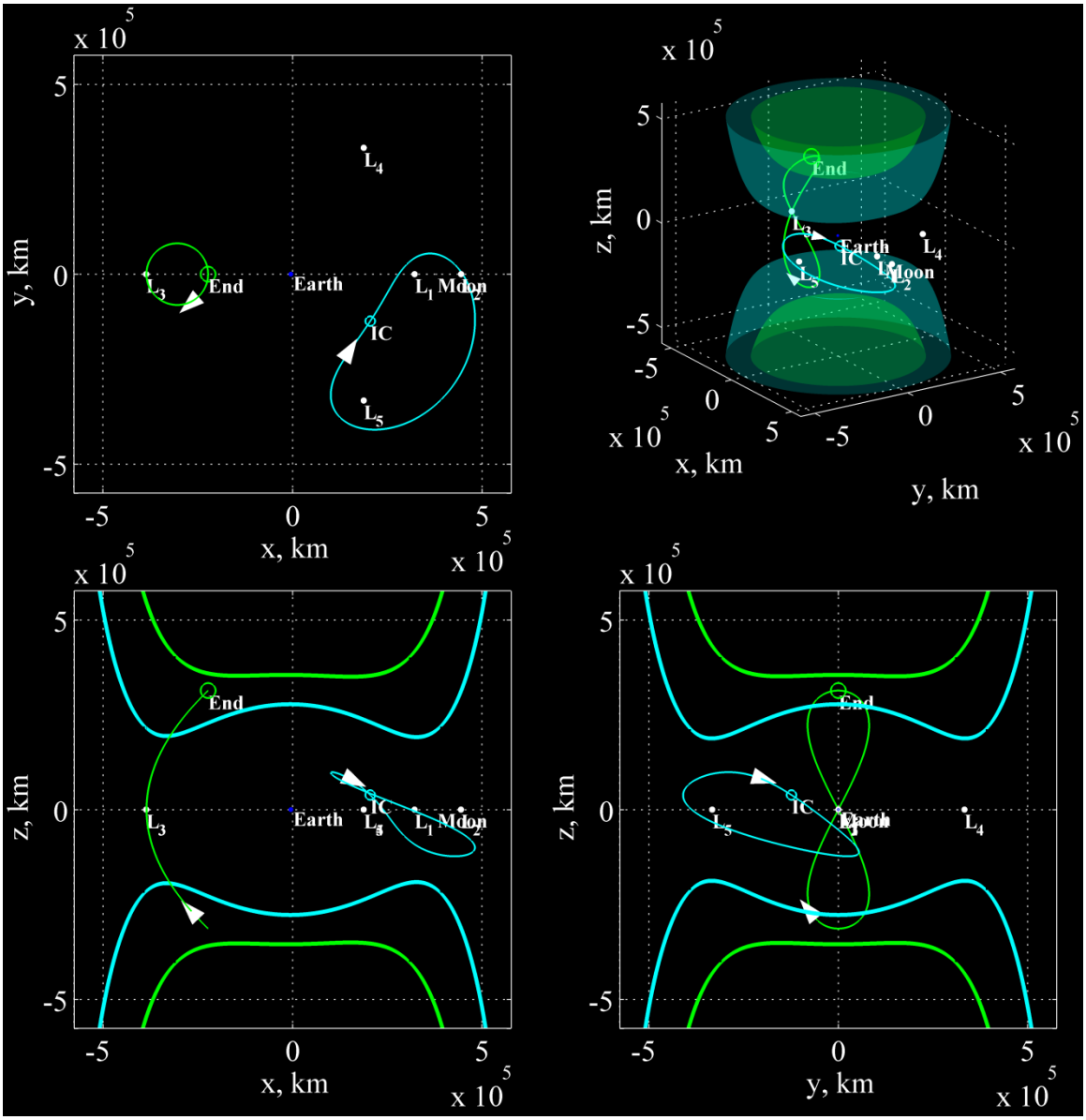

Figure 4.13. Four-perspective rotating view of 3-D, periodic L_3 and L_5 LPOs

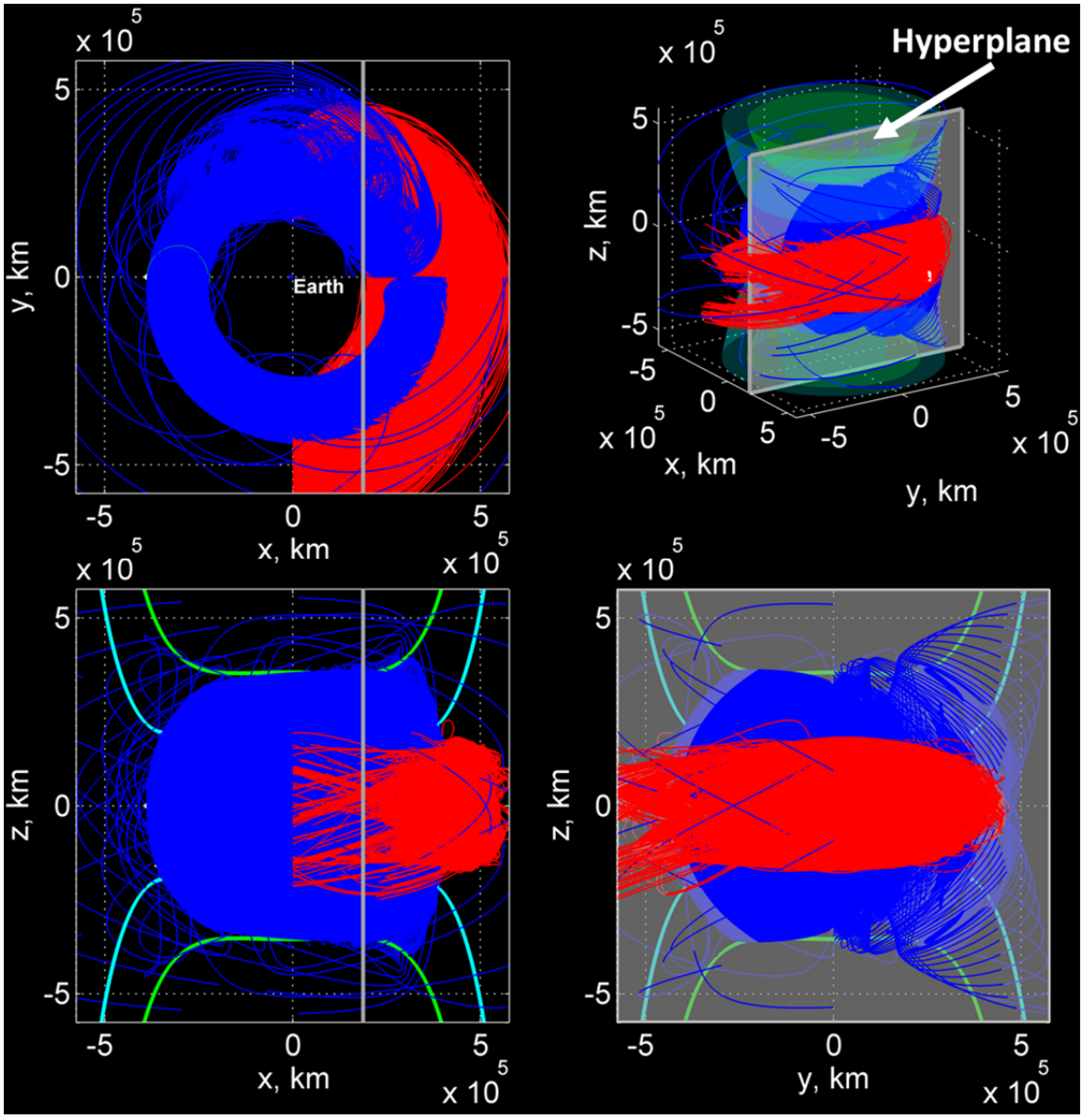

Figure 4.14. Four-perspective rotating view of 3-D, periodic L_3 and L_5 LPOs along with approximations for the L_3 stable (blue) and L_5 unstable (red) manifold tubes

phase space) motivates the use of a Poincaré map. A 4-D map offers the possibility of simplifying the problem by examining a lower-D design space.

The Cartesian phase space Poincaré manifold map hyperplane is used to generate 4-D manifold maps. The overlaid maps of the first returns of both stable and unstable manifold tubes are plotted in Figure 4.15. The origin of the map is effectively halfway between L_4 and L_5. The ring structure, ranging between green and blue, is the first map

return (in forward time) of an entire L_5 unstable manifold tube at the lower "energy" level. The figure-8 structure, ranging between yellow and magenta, is the first map return (in negative time) of an entire L_3 stable manifold tube at the higher "energy" level. To distinguish between the different sides of these two-sided Poincaré maps, returns with $\dot{x} < 0$ appear as small dots and returns with $\dot{x} > 0$ appear as large dots. These 1-D structures are revealed after a filtering process that is accomplished by visual inspection and then manipulation of the 4-D maps in the visual environment. The goal of the filtering is removal of map returns associated with subsequent returns of the manifold tubes; these subsequent returns obscure the structures of interest. Techniques for removing obscuration include: (1) only examining a certain range of map return counters associated with all or some trajectories, (2) removing any returns outside of a 4-D box containing a structure of interest, or (3) excluding returns occurring after a certain forward or negative time.

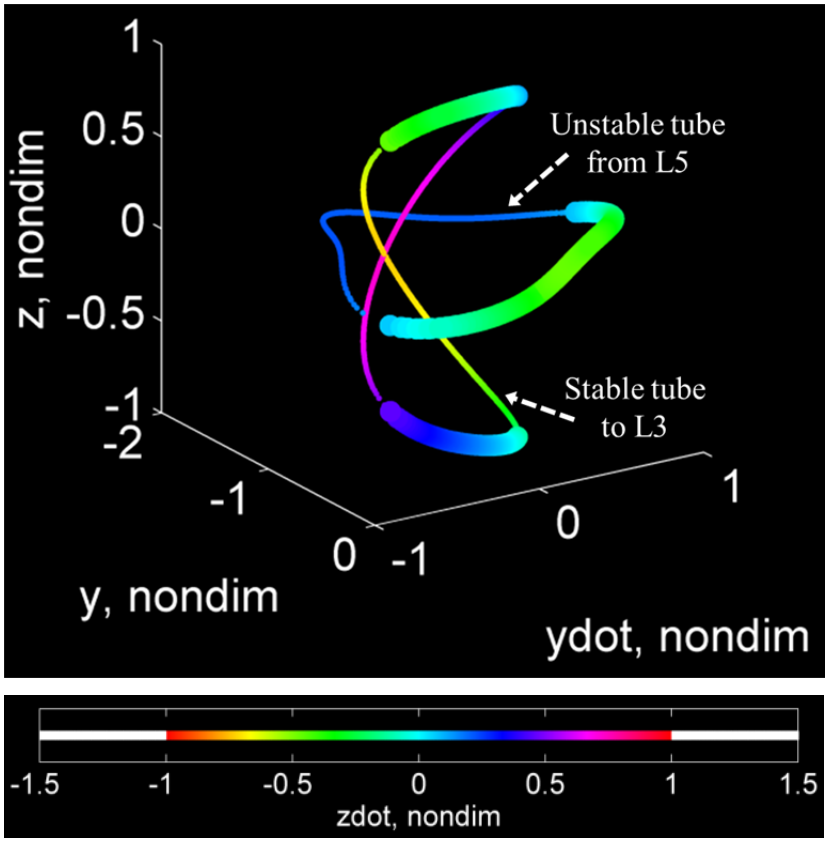

Figure 4.15. LPO-to-LPO transfer design space; Cartesian phase space Poincaré manifold maps; L_5 unstable manifold tube at lower "energy" and L_3 stable manifold tube at higher "energy" overlaid; $(x = L_{5x}\pm;\ y,\ \dot{y},\ z,\ \dot{z}\_color)$

An example of the visual filtering process necessary to produce the "clean" overlaid manifold map plotted in Figure 4.15 is depicted in Figure 4.16. The process for producing one of the two layers of the overlaid map, the layer associated with the L_3 stable manifold tube at the higher "energy" level, begins with the "dirty" map plotted in Figure 4.16(a). This map includes the first three returns (in negative time) associated with each of the 500 individual trajectories used to approximate one of the blue tubes plotted in Figure 4.14. A well-defined figure-8 structure, associated with the first map return of the entire tube, is visible amidst a cloud of "noise" associated with subsequent returns. In Figure 4.16(a), returns that are inside the spatial $(y, \dot{y}, z)$ grid limits but outside of the limits of the color $(\dot{z})$ scale are plotted with white dots. It is important to note that this first return of the *entire* tube is actually formed by *one or more* returns of the individual trajectories belonging to that tube. Next, the manifold map in Figure

4.16(a) is filtered to exclude any returns outside of a 4-D volume (3-D in space and 1-D in color) designed to fit tightly around the figure-8 structure of interest, resulting in the "cleaner" map plotted in Figure 4.16(b). By examining the return counters associated with the remaining "noise" on this manifold map, it is revealed that those points are all associated with the third returns of certain trajectory numbers. The final step of the filtering process is to remove the third returns of only those trajectory numbers associated with the "noise" on the map plotted in Figure 4.16(b), resulting in the "clean" manifold map plotted in Figure 4.16(c). A similar filtering process is employed to generate a "clean" version of the other layer of the overlaid manifold map used for this design example. Specifically, the "clean" ring structure in Figure 4.15, associated with the L_5 unstable manifold tube at the lower "energy" level, is obtained without "noise" by isolating manifold map returns with a return counter less than thirteen while also excluding any of those returns occurring more than 164 days subsequent to the time of the initial condition used to generate the L_5 periodic orbit.

To design a S/C transfer maneuver (implemented at $x = L_{5x}$) between the two 3-D libration point orbits plotted in Figure 4.13, it is necessary to estimate the *y*-*z* positions of intersections between the ring structure and the figure-8 structure on the 4-D maps overlaid in Figure 4.15. These maps are plotted with four perspectives in Figure 4.17. A position intersection estimate is obtained by a visual inspection of the map and an interpolation in the empty spaces between map returns. In the next step of the design process, an estimated position intersection is used to estimate, also through interpolation, the components of S/C velocity $\vec{V}$ that exist for each 1-D structure at that position. This visual process ultimately yields a *reasonable guess* for both a forward and a negative time solution that, if it were a perfect guess, would allow for a transfer between the L_5 unstable manifold tube at the lower "energy" level and the L_3 stable manifold tube at the higher "energy" level, creating a pathway between the two periodic LPOs that is continuous in position but that requires a single "energy"-raising maneuver to transfer between the two asymptotic trajectories. However, because the guess is not perfect—and

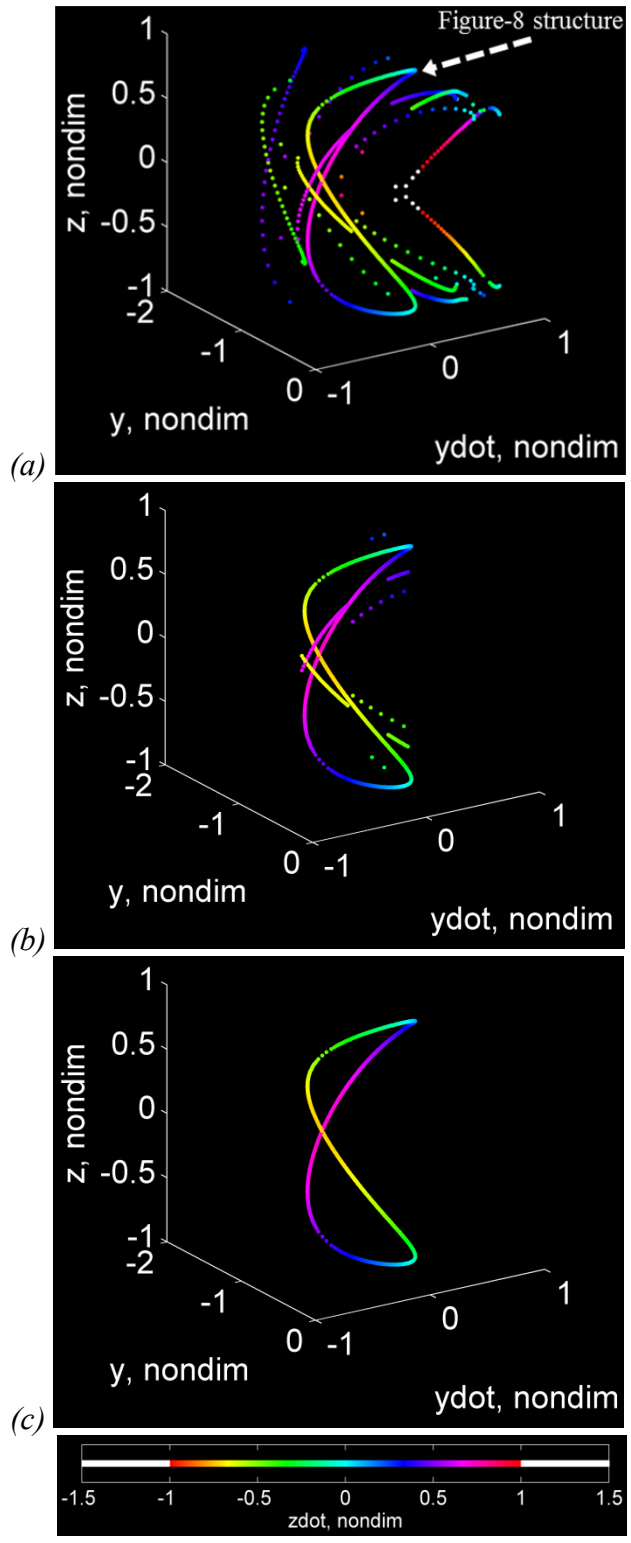

Figure 4.16. Manifold map filtering process: "dirty" (a), "cleaner" (b), and "clean" (c); Cartesian phase space Poincaré manifold map; L_3 stable manifold tube at higher "energy;" $(x = L_{5x}\pm;\ y,\ \dot{y},\ z,\ \dot{z}\_color)$

because approximations for manifolds are used as the nominal behavior—this process actually yields a similar pathway (and associated maneuver) between approximate "orbits" that remain in the vicinity of their respective libration points for a few revolutions. It is important to note that the overlaid maps actually reveal a total of four orbit transfer maneuver options. The least-costly option in terms of $\left|\overrightarrow{\Delta V}\right|$ is depicted in Figure 4.17. To determine the $\left|\overrightarrow{\Delta V}\right|$ of a given transfer option, it is possible to visually obtain estimates for the velocity discontinuities (in $\dot{y}$ and $\dot{z}$) at each position intersection, while the remaining velocity discontinuity (in $\dot{x}$) associated with the estimate, which is not explicitly represented on the 4-D map, is simply calculated based on the two "energy" levels associated with the two manifold tube structures (the "energy" levels of the two periodic LPOs). The result of the least costly of four transfer option guesses successfully designed using the overlaid 4-D manifold maps is plotted in the barycentric rotating view in Figure 4.18. The 3-D S/C path consists of roughly four orbits in the vicinity of L_5 followed by an "energy"-raising maneuver at $x = L_{5x}$, with a total $\left|\overrightarrow{\Delta V}\right|$ = 595.1 m/s, at a time equal to 136 days subsequent to the initial condition. This maneuver is implemented by decreasing the $\hat{x}$ and $\hat{y}$ components of $\vec{V}$ by 90.7 m/s and 268.3 m/s, respectively, and by increasing its $\hat{z}$ component by 523.4 m/s. The result is a transfer to the vicinity of L_3 for roughly six orbits, completed 273 days following the burn. The approximate "orbits" in the vicinity of the libration points resemble the original periodic orbits plotted in Figure 4.13. Yet, they are not, in and of themselves, valid solutions to the transfer problem.

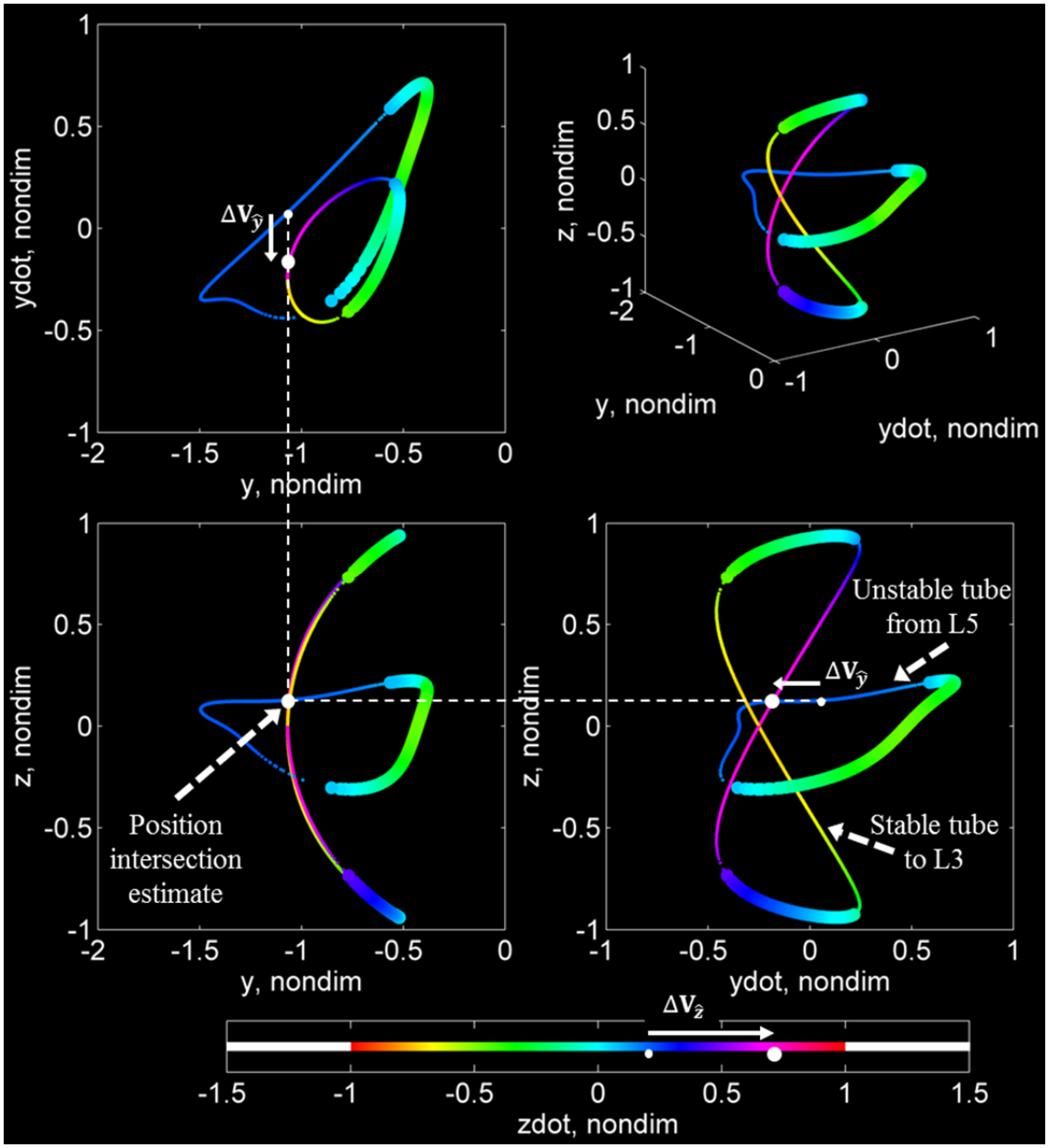

Figure 4.17. Four-perspective view of LPO-to-LPO transfer guess; Cartesian phase space Poincaré manifold maps; L_5 unstable manifold tube at lower "energy" and L_3 stable manifold tube at higher "energy" overlaid; $(x = L_{5x}\pm;\ y,\ \dot{y},\ z,\ \dot{z}\_color)$

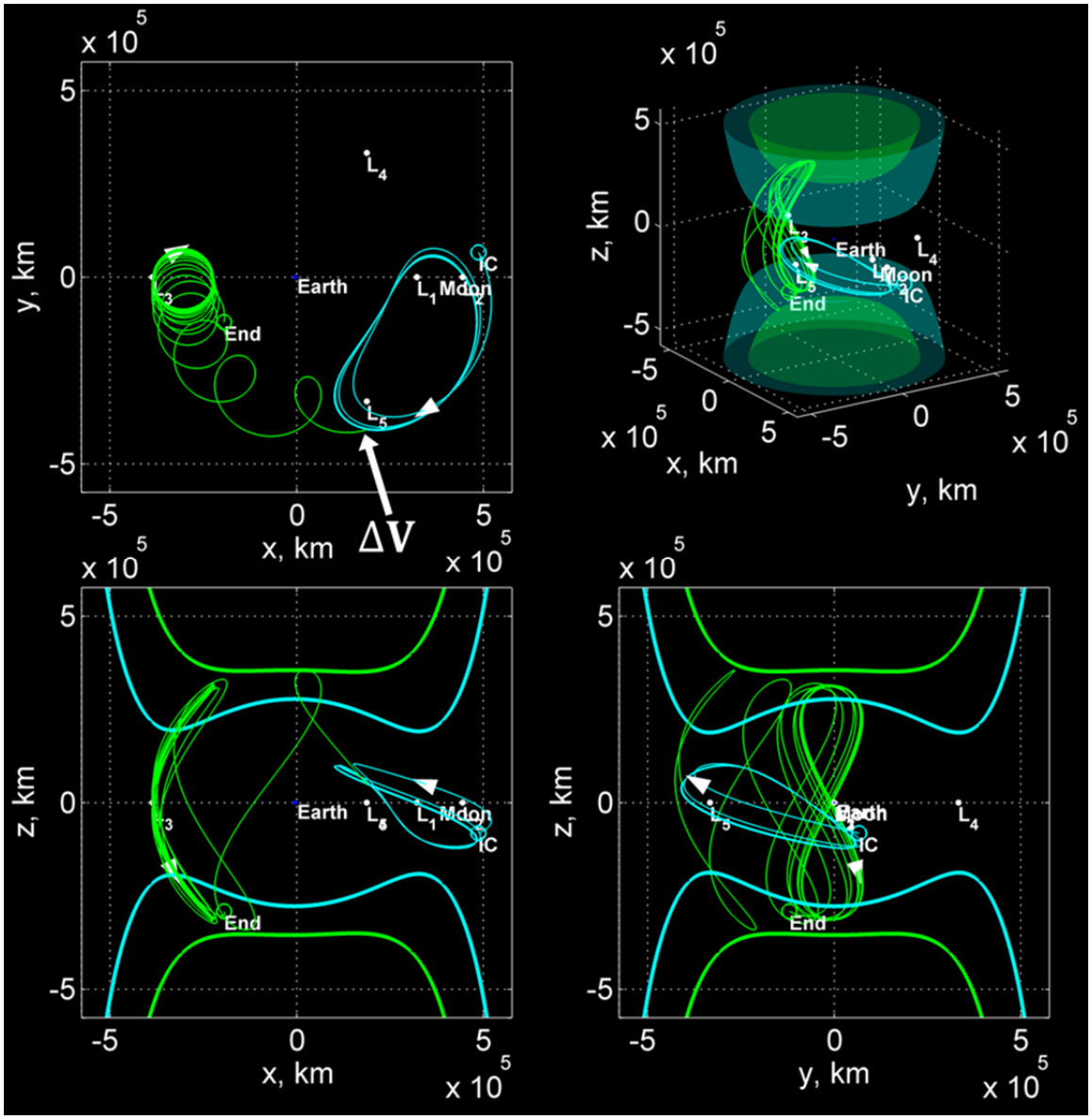

Figure 4.18. Four-perspective rotating view of LPO-to-LPO transfer guess; designed transfer maneuver between approximate 3-D libration point "orbits"

To obtain a precise solution for the desired orbit transfer, it is necessary to feed the transfer guess (depicted in Figure 4.18)—which is visually obtained from the Poincaré map—into an automated targeting process of the type described in Section 2.2. The goal of this corrections process is to obtain a three-maneuver transfer between reference states along the two periodic LPOs. The first and third maneuvers are implemented at positions along the two LPOs. The second (middle) maneuver is still assumed to be implemented

at the selected position on the original hyperplane $x = L_{5x}$, and this maneuver also involves a change between the same two "energy" levels as the transfer guess. Therefore, each path between the hyperplane maneuver and each LPO is constrained to possess the same "energy" value as the LPO. Each half of the transfer (i.e., the transfer path between the hyperplane maneuver and each periodic orbit) is targeted independently. For each transfer half, targeting is accomplished using multiple shooting with ten patch points between the hyperplane maneuver and the reference state along the periodic LPO. The tenth patch point is chosen to be along the LPO and is at the assumed position of the "energy"-maintaining maneuver that completes the transfer into the orbit. This patch point is at a fixed position chosen based on a criterion for closeness to the transfer guess. In this example, a successful technique is to weight distance and velocity equally (in nondimensional units) for the purpose of determining which state on the periodic LPO is closest to the transfer guess. The remaining nine patch points are selected somewhat arbitrarily; they are evenly spaced in trajectory data index (not time) between the hyperplane maneuver and the patch point along the periodic orbit.

The targeted three-maneuver transfer—using the LPO-to-LPO transfer guess in Figure 4.18 to initiate the targeting process—is plotted in the four-perspective, barycentric rotating view in Figure 4.19. The new 3-D S/C path begins at the initial condition ("IC") reference state along the L_5 LPO and is followed by an "energy"-maintaining maneuver, with $\left|\overrightarrow{\Delta V}\right|$ = 31 cm/s, to begin the orbit transfer 2.4 days subsequent to the initial condition. The "energy"-raising second maneuver at $x = L_{5x}$, with $\left|\overrightarrow{\Delta V}\right|$ = 595.9 m/s, is implemented at a time equal to 40.8 days subsequent to the first maneuver. Finally, the "energy"-maintaining third maneuver, with $\left|\overrightarrow{\Delta V}\right|$ = 5.7 m/s, completes the transfer into the L_3 LPO and is implemented at a time equal to 164.2 days subsequent to the second maneuver and 14.0 days prior to the final ("End") reference state. Thus, the transfer between periodic LPOs is accomplished with a total $\left|\overrightarrow{\Delta V}\right|$ = 601.9 m/s and a total time-of-flight (between the first and third maneuvers) of 205.1 days. The $\left|\overrightarrow{\Delta V}\right|$ required for the first and third maneuvers is relatively small compared to that

required for the second (middle) maneuver; this is a consequence of the fact that manifolds are used as the nominal behavior for designing the transfer.

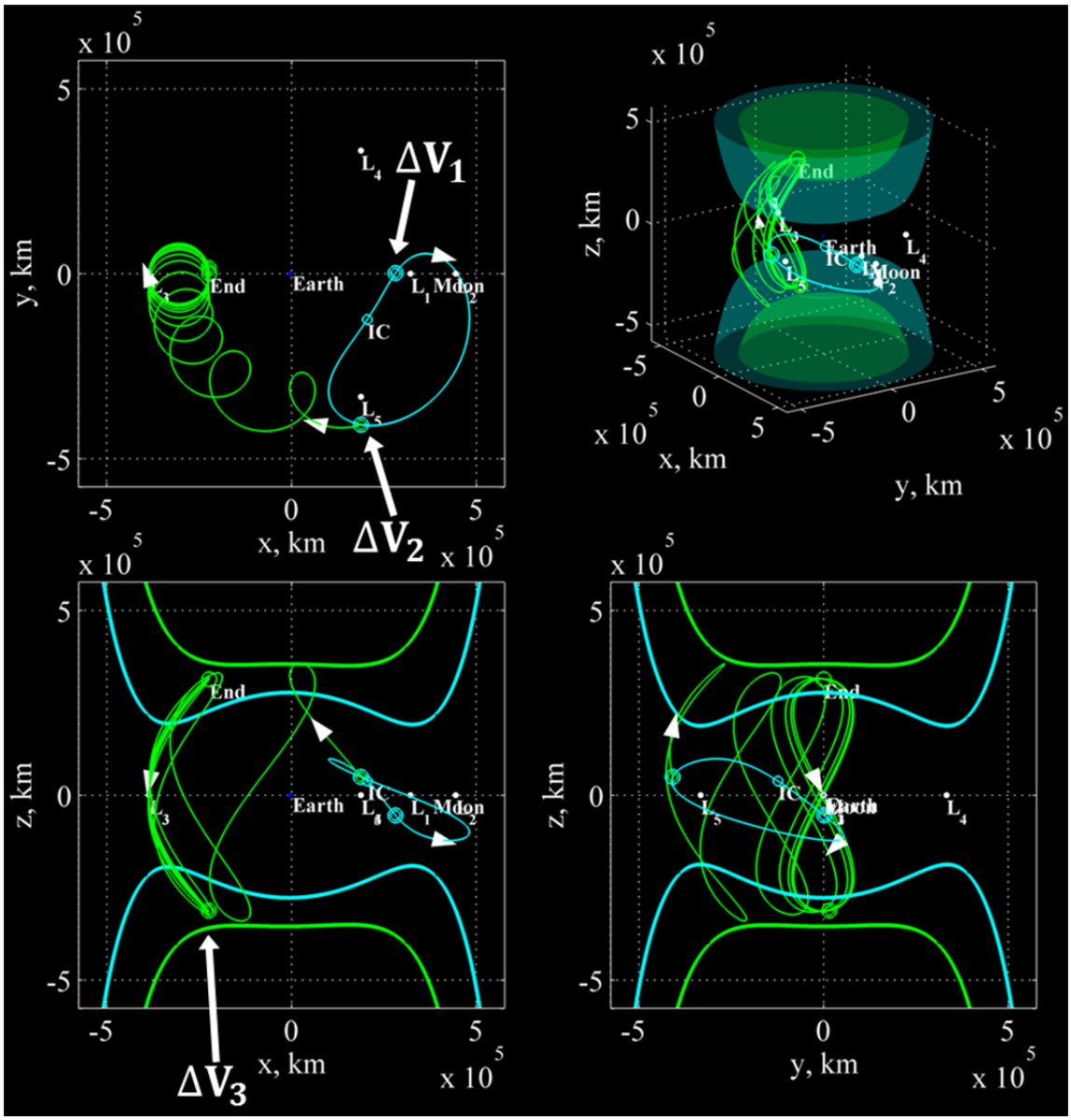

Figure 4.19. Four-perspective rotating view of precise LPO-to-LPO transfer solution; targeted three-maneuver transfer between 3-D, periodic LPOs; before middle maneuver at lower "energy" (cyan) and after middle maneuver at higher "energy" (green)

Finally, for completeness, the targeted three-maneuver transfer plotted in Figure 4.19 is fed into an automated optimization process of the type described in Section 2.7. The

cost function to be minimized is the total $\left|\overrightarrow{\Delta V}\right|$ of the transfer. The S/C path is constrained to have: (1) continuity in position, using the same patch points as in the targeting process, (2) continuity in velocity at all patch points except the three patch points associated with the three maneuvers, and (3) continuity in the direction of time, i.e., propagation time cannot change directions at any patch point. The path is also required to have the same starting and ending reference states (on the periodic LPOs) as in the targeting process. Yet, notably, the optimization process does remove some other key assumptions/requirements used in the previous visual and automated processes. First, the second (middle) maneuver is no longer assumed to be implemented at the original hyperplane $x = L_{5x}$. Second, the first and third maneuvers are now free to be implemented anywhere along the paths of each periodic LPO (the periodic path leading to the respective reference state). Third, each path between the middle maneuver and each LPO is no longer constrained to possess the same "energy" value as the LPO. The consequence of this is that the transfer path between periodic LPOs is no longer restricted to the original two "energy" levels used previously, and the first and third maneuvers are no longer required to be "energy"-maintaining.

The optimized three-maneuver transfer—using the targeted LPO-to-LPO transfer solution plotted in Figure 4.19 to initiate the optimization process—is plotted in the barycentric rotating view in Figure 4.20, with the L_3 LPO in the foreground for clarity. The resulting 3-D S/C path between reference states is locally optimal in total $\left|\overrightarrow{\Delta V}\right|$, with the optimality tolerance (based on the KKT conditions) set so as to consider further reductions in $\left|\overrightarrow{\Delta V}\right|$ on the order of mm/s to be negligible. The transfer between periodic LPOs is accomplished with a total $\left|\overrightarrow{\Delta V}\right|$ = 559.3 m/s, a modest 7% reduction from the targeted solution. The total time-of-flight (between the first and third maneuvers) is now 175 days, approximately one month shorter than for the targeted solution.

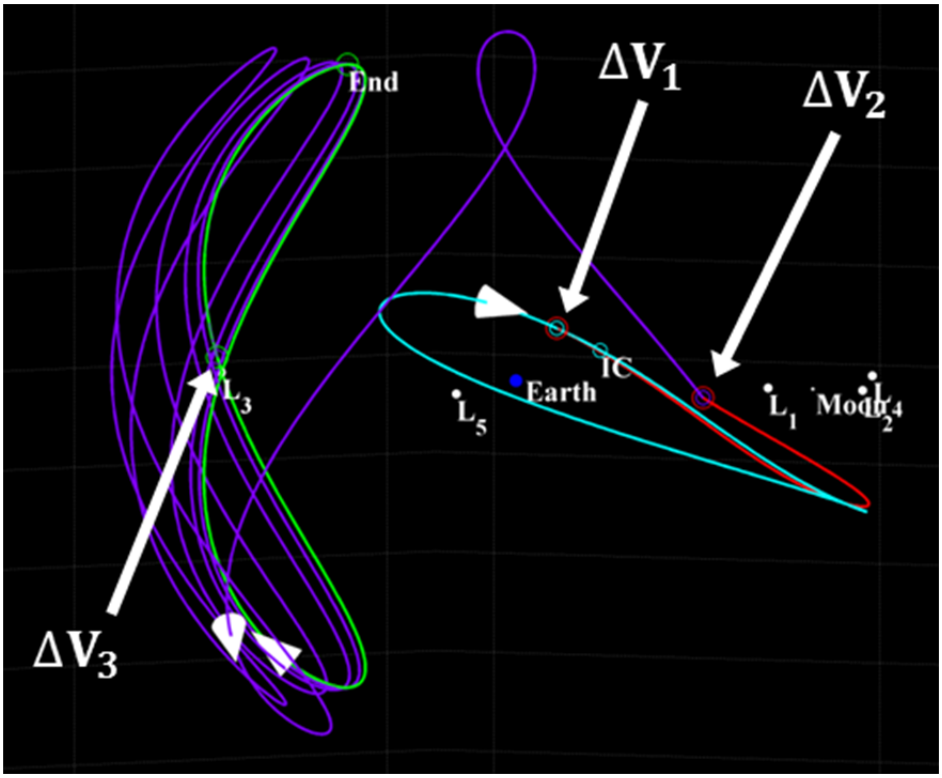

Figure 4.20. Rotating view of optimized LPO-to-LPO transfer solution; locally-optimal three-maneuver transfer between 3-D, periodic LPOs; before first maneuver (cyan), after first maneuver (red), after second maneuver (purple), and after third maneuver (green)

5. ADVANCED 4-D-MAP-BASED DESIGN SCENARIOS

In this chapter, 4-D-map-based design techniques are demonstrated for three, real-world astrodynamics problems involving 3-D S/C trajectories, thus providing a validation of the design approach presented in this investigation. In contrast to Chapter 4, where the pedagogical emphasis is on Poincaré map creation and the visual processes used to obtain solutions, the focus of this chapter is on how reasonable guesses obtained visually from the map are exploited in follow-on, automated processes to determine precise solutions that are of practical use for real-word trajectory design scenarios. These automated processes include targeting, optimization, and transitions to other dynamical models. A key theme is that the 4-D Poincaré map and its associated interactive visual processes are most useful for obtaining initial guesses that meet certain qualitative criteria, while the automated processes are normally better-suited for tasks requiring quantitative precision and/or algorithmic repetition.

In addition to showcasing more follow-on, automated processes, the three advanced design examples also involve more complex trajectory design tasks than the four basic examples of the previous chapter. In the first advanced example, Design Example #5, different 4-D maps are used for different phases of analysis/design for an orbit transfer problem consisting of multiple trajectory legs. In Design Example #6, a 4-D map is exploited to design a CR3BP transfer path between two orbits (at two epochs) defined based on both a lower-fidelity (two-body) model as well as two higher-fidelity (ephemeris) reference states. Finally, in Design Example #7, a 4-D map is used to locate a stable periodic orbit in the vicinity of Uranus's moon Titania; that orbit is then used as the basis for designing a Titania orbiter mission—with multiple contingencies—as the final phase of a plausible tour of the Uranian system.

As in Chapter 4, when S/C transfer maneuvers are considered, all $\left|\overrightarrow{\Delta V}\right|$ maneuvers are assumed to be instantaneous (impulsive burns). Model parameters are noted mostly by reference to earlier tables.

5.1 Design Example #5: Transfer from Earth Orbit to Earth-Moon LPOs

The first advanced, 4-D-map-based mission design scenario involves 3-D S/C transfer maneuvers between a high-Earth orbit (HEO) modeled in the Earth-centric spatial 2BP and an unstable periodic LPO in the vicinity of L_1 modeled in the Earth-Moon spatial CR3BP. The Earth-centric and Moon-centric two-body gravitational parameters are assumed to be equal to GM_E = 398,600.4418 km^3/s^2 and GM_M = 4,902.801076 km^3/s^2, respectively, and the Earth-Moon CR3BP model parameters are as before (see again Table 4.3). In this case, the desired HEO is assumed to be a highly-elliptical orbit similar in size and shape to a geosynchronous transfer orbit (GTO), with an apogee at 35,786 km altitude—the approximate altitude of a circular, geosynchronous orbit (GEO) [107] with a period of one sidereal day—and a low-Earth orbit (LEO) perigee altitude of 300 km. This first phase of the mission is followed by a second phase, consisting of a transfer from the L_1 LPO to a different LPO that is associated with L_2 and closer to the Moon.

5.1.1 Design Phase 1: Transfer from Earth Orbit to L_1 LPO

The specific objective of the first design phase of this mission scenario is the use of a 4-D Cartesian phase space Poincaré map to design a series of maneuvers to accomplish a transfer between a 3-D HEO at its GEO-altitude apogee and a 3-D, periodic LPO in the vicinity of L_1. The HEO is chosen through the map-based design process, while the LPO is arbitrarily selected from the family of "northern" L_1 halo orbits. Using an initial guess from Grebow [131], an unstable LPO in this family is targeted and converged to satisfactory periodicity. The periodic LPO appears in Figure 5.1 in the *x*-*y* rotating view, both zoomed out (with the Earth-Moon barycenter as the origin) and zoomed in to the vicinity of the Moon (with the Moon as the offset origin). The period of the halo orbit is 12.1 days, and it possesses an "energy" value where both L_1 and L_2 gateways are open.

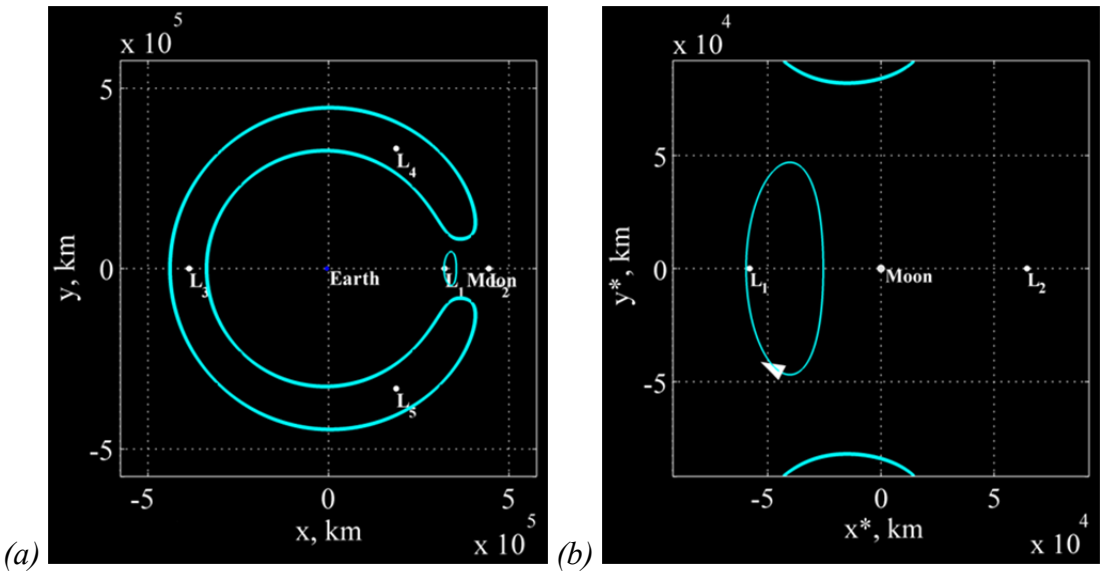

Figure 5.1. Zoomed-out (*a*) and zoomed-in (*b*) rotating views of 3-D, periodic L_1 LPO

As depicted in Figure 5.2, the Cartesian phase space manifold map hyperplane is defined such that $y = 0$ and $\dot{y} < 0$, so as to capture the first map returns on the L_3 side of the Earth of an entire 2-D stable manifold tube emanating (in negative time) from the (1-D) periodic LPO plotted in Figure 5.1. An approximation for each stable (blue) manifold tube is comprised of 500 individual trajectories asymptotic to the LPO. However, for clarity in representing the stable manifold tube of interest for this design example (i.e., the tube leading from the L_3 side of the Earth), any trajectories that belong to the other stable manifold tube that is mostly leading from the exterior region but that happen to visit the interior region are removed from Figure 5.2.

To design a transfer between a HEO with a GEO-altitude apogee and the periodic LPO, the Cartesian phase space Poincaré map hyperplane in Figure 5.2 is used to generate a 4-D manifold map at a single "energy" level. The first returns (in negative time) of the stable tube on the L_3 side of the Earth are plotted in Figure 5.3 with large dots as a ring structure. The origin of the map is effectively the Earth-Moon barycenter.

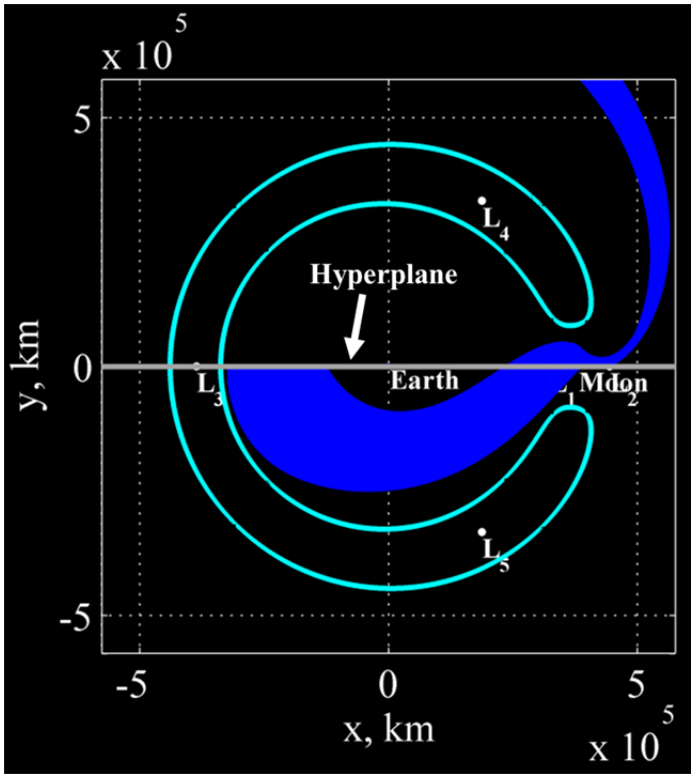

Figure 5.2. Rotating view of 3-D, periodic L_1 LPO along with approximations for the stable (blue) manifold tubes

Also plotted in Figure 5.3, with small dots, are the returns over one month (or until an impact, whichever occurs sooner) associated with trajectories originating from 6,924 initial conditions with a GEO-altitude *perigee* at the same "energy" level as the periodic LPO. The set of initial conditions is identified based on a 3-D grid of periapses ($\dot{\rho} = 0$ and $\ddot{\rho} > 0$.), defined in Earth-centered spherical coordinates on a "shell" surrounding the Earth at GEO altitude. Note that, even though the ultimate objective is the design of a S/C path originating from the apogee of a HEO, the apses at GEO altitude at the relatively high "energy" level of the L_1 LPO are, in fact, perigees. With spherical radius ρ fixed, the three dimensions of the seeding grid are the remaining spherical position coordinates θ and φ along with the full range of possible velocity angles -180°$< \alpha <$ 180°. By equation (2.2), since the *JC* of all initial conditions is fixed at the same "energy" level as the periodic LPO, the magnitude of the velocity vector V_{mag} in

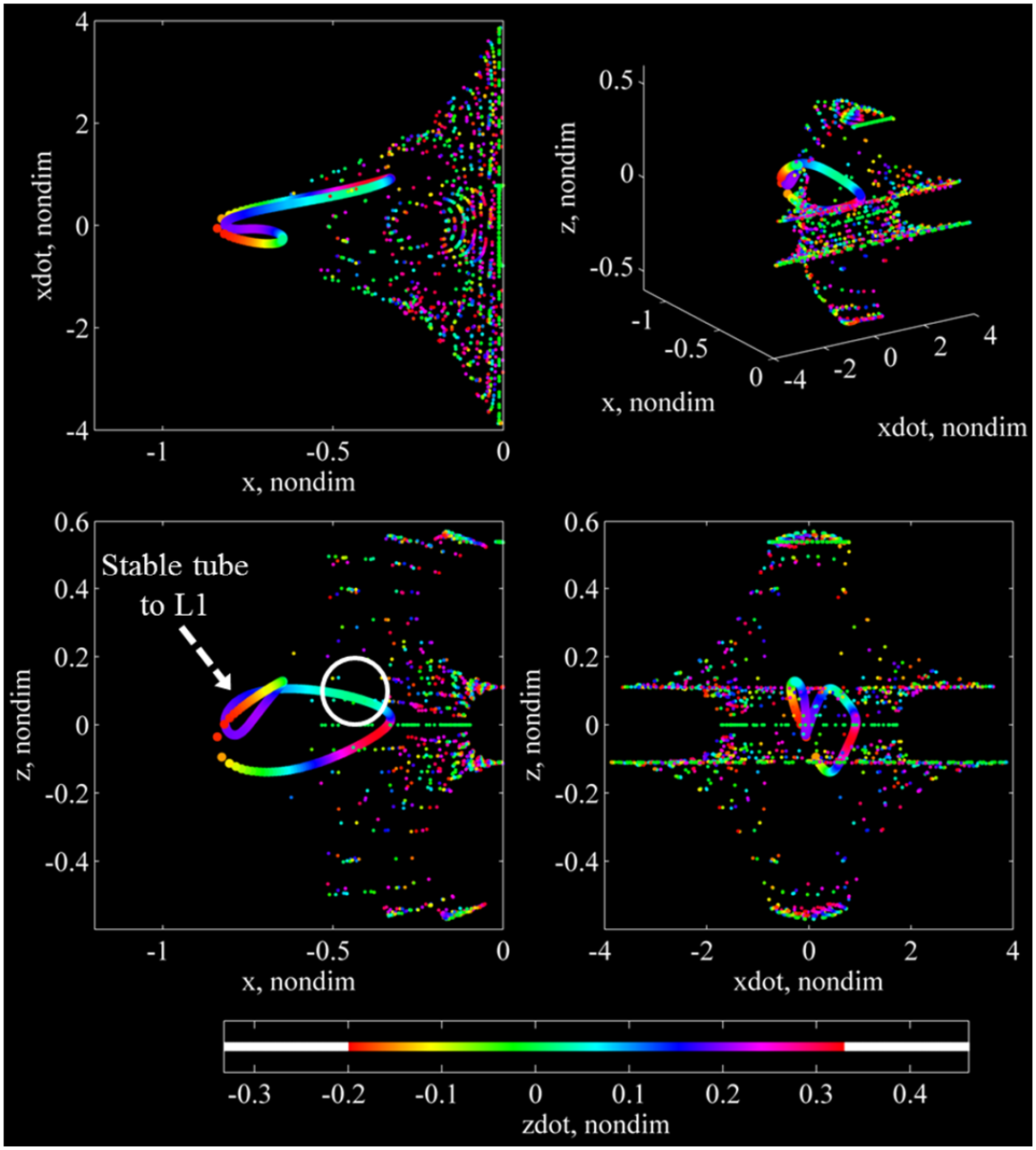

Figure 5.3. Four-perspective view of HEO-to-LPO transfer design space; Cartesian phase space Poincaré map in the vicinity of the Earth; L_1 stable manifold tube and following month of returns from GEO-perigee initial conditions at same "energy;" $(y = 0-;\ x,\ \dot{x},\ z,\ \dot{z}\_color)$

the CR3BP is a function only of position, regardless of velocity angle α. Therefore, a convenient way to visualize the grid of initial conditions is the 4-D periapsis initial condition "map" plotted in Figure 5.4, with the Earth-Moon barycenter as the map origin.

The 3-D periapse position of each trajectory initial condition is displayed in Cartesian coordinates in 3-D map space, while the color coordinate is selected to be V_{mag} instead of the velocity angle α used as the fourth map coordinate in Design Example #1 (see Section

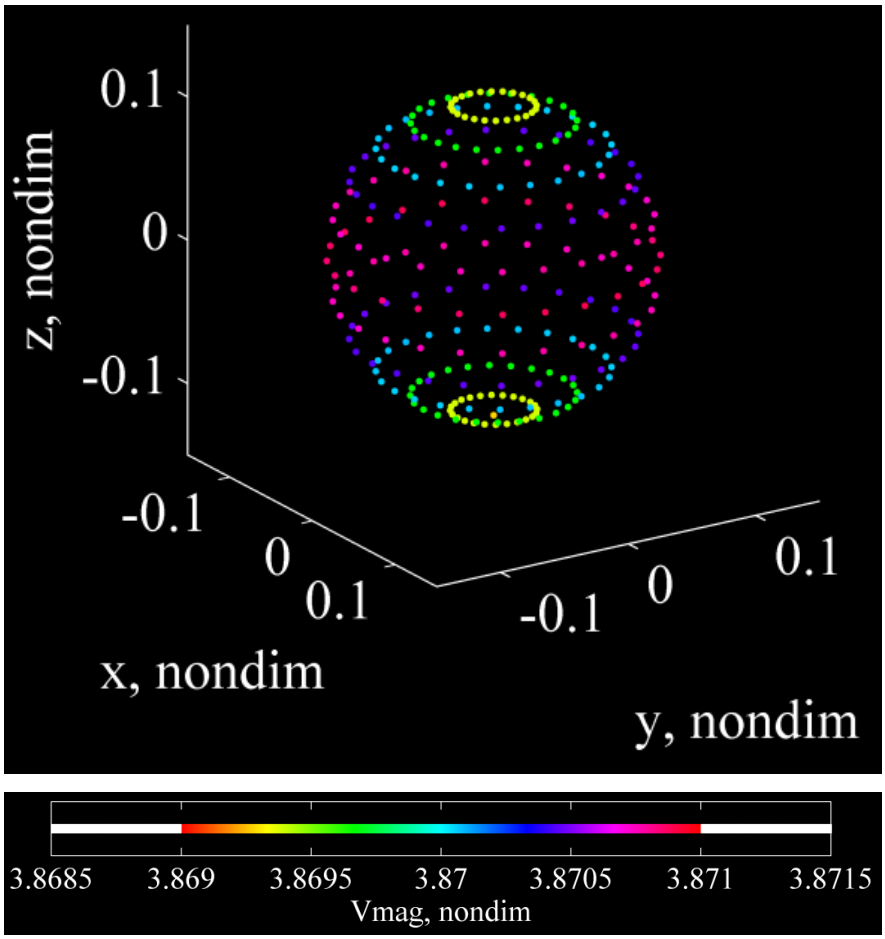

Figure 5.4. 4-D periapsis Poincaré initial condition "map" in the vicinity of the Earth; $(\dot{\rho} = 0+;\ x,\ y,\ z,\ V_{mag}\_color)$

4.1). Note that this 4-D representation is not a true Poincaré map because V_{mag} (the color coordinate on the map) is just a function of position (the spatial coordinates on the map); because of this redundancy, a point displayed in the 4-D visual environment does not fully define a 6-D state in the phase space of the CR3BP. Yet, the representation plotted in Figure 5.4 is useful for analysis because it does not suffer from the single location ambiguity normally associated with plotting different 4-D values at the same location in

3-D space using the space-plus-color method (see Sections 3.1 and 4.3). That is, no matter how many different velocity angles are seeded at a given position, only one velocity magnitude (only one color) is needed to define that point.

The next step in the process of designing a transfer between a GEO-altitude-apogee HEO and the periodic LPO plotted in Figure 5.1 is to obtain a reasonable guess for a S/C transfer maneuver (implemented at $y = 0$) between one of the trajectories originating from the grid of GEO-altitude perigee initial conditions and the stable manifold tube leading to the LPO. To accomplish this task, it is necessary to estimate the *x*-*z* position of an *approximate* intersection between the ring structure (large dots) associated with the stable manifold tube and one of the returns (small dots) associated with GEO-altitude perigees on the 4-D map plotted in Figure 5.3. Such an estimate is obtained by a visual inspection of the map, first by zooming in to the region of potential (approximate) intersection identified by the circle in Figure 5.3. In this region, there appears to be several small dots in the *x*-*z* vicinity of the ring structure that also share a similar color ($\dot{z}$) value as the ring structure near those points. It is not immediately apparent whether any of these small dots also share similar $\dot{x}$ values as the ring structure near those dots, however, the *x*-$\dot{x}$ and $\dot{x}$-*z* views in Figure 5.3 indicates that there are at least several small dots that are close to the ring structure in $\dot{x}$ value. A zoomed-in view of the region of potential intersection is plotted in Figure 5.5; the zoom is in the spatial map coordinates while the limits of the color scale are the same as in Figure 5.3. Returns outside the limits of the zoom are filtered from view. By annotating the small dots with trajectory numbers and return counters (in subscript), it is evident that not all small dot returns that appear close to the ring structure in *x*-*z* and $\dot{z}$ are similarly close in $\dot{x}$. For example, the small dot returns labeled "4778_1" and "1595_2" seem as close to the ring structure in *x*-*z* and $\dot{z}$ as return "6792_3." Yet, return "6792_3," i.e., the third return of trajectory number 6792, is clearly much closer to the ring structure in the value of $\dot{x}$.

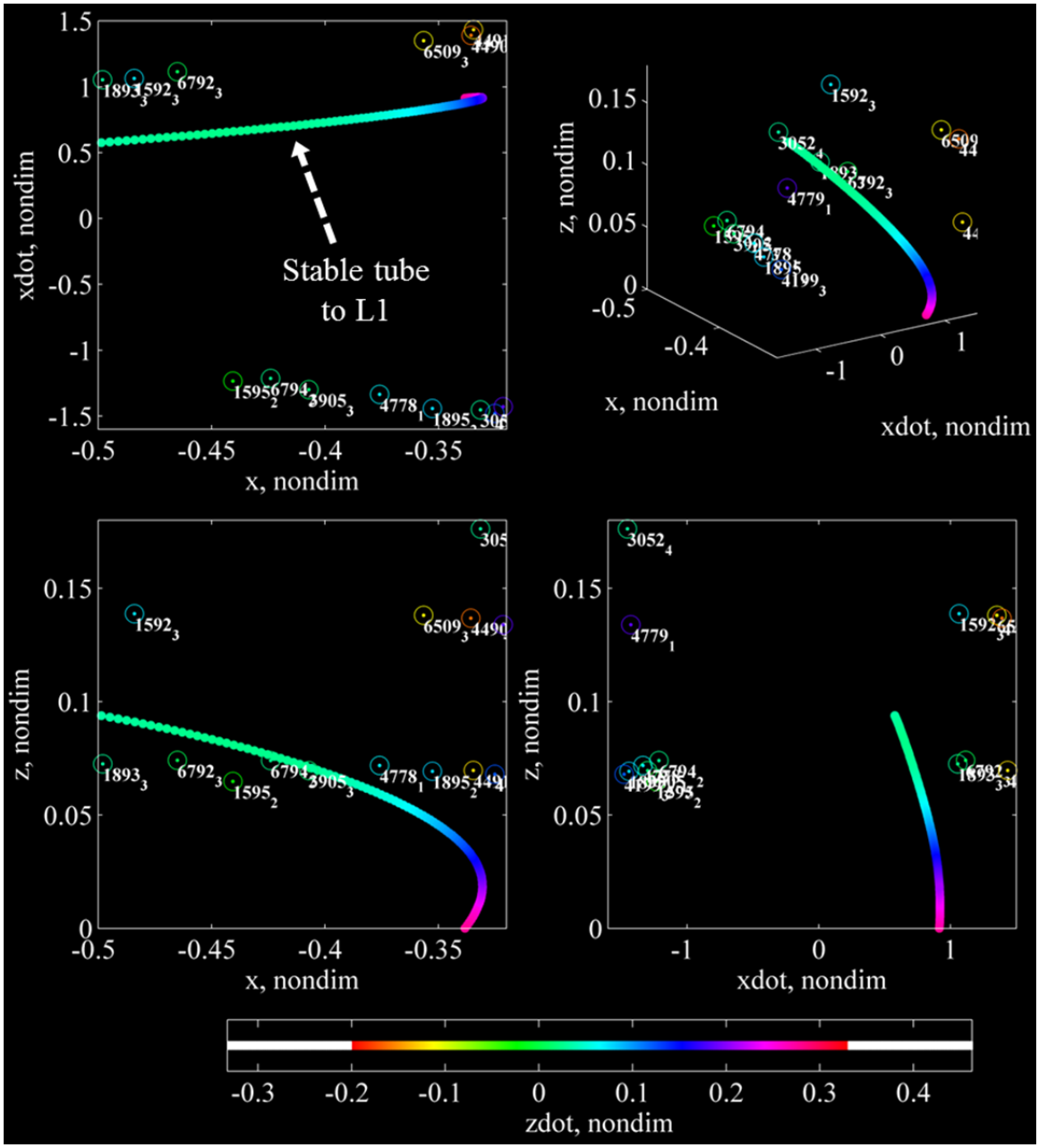

Figure 5.5. Four-perspective view of HEO-to-LPO transfer design space (zoomed in); Cartesian phase space Poincaré map in the vicinity of the Earth; L_1 stable manifold tube and following month of returns from GEO-perigee initial conditions at same "energy;" $(y = 0-;\ x,\ \dot{x},\ z,\ \dot{z}\_color)$

Based on the approximate intersection between return "6792_3" and the ring structure on the 4-D map plotted in Figures 5.3 and 5.5, trajectory 6792 is selected as the S/C path—originating at a GEO-altitude perigee—on which to implement a maneuver to

transfer to the vicinity of the L_1 LPO. Note that, because this 4-D map is a one-sided map plotted at a single "energy" level, a true intersection in 4-D map space represents an intersection in the full 6-D phase space. Thus, if return "6792_3" perfectly intersected the ring structure (in space and color), it would imply that a zero-$\left|\overrightarrow{\Delta V}\right|$ transfer exists between the trajectory originating at a GEO-altitude perigee and the approximation for the stable manifold tube leading to the periodic LPO. However, because return "6792_3" represents only an approximate intersection on the map, is necessary to implement a maneuver to adjust the S/C velocity vector $\vec{V}$ while maintaining the same "energy" level. This transfer maneuver is implemented at $y = 0$ (on the hyperplane) and at the exact *x*-*z* position of return "6792_3." Moreover, an estimate for the necessary adjustment to the S/C velocity vector $\vec{V}$ is obtained by visual inspection as well as by interpolation in the empty spaces between map returns, as depicted in Figure 5.6, which is a further zoomed-in view (in terms of both space and color) of the approximate intersection associated with return "6792_3." Returns are again filtered according to the zoom limits. The velocity adjustment is based on the assumption that a 4-D map return with the same *x*-*z* position value as return "6792_3" and with the same $\dot{x}$-$\dot{z}$ velocity value as a nearby portion of the stable manifold tube represents a reasonable guess for a 6-D state that leads to vicinity of the L_1 LPO. Estimates for the velocity adjustments in $\dot{x}$ and $\dot{z}$ are obtained visually, while the associated velocity adjustment in $\dot{y}$ is simply calculated based on the "energy" level of the map. This mainly visual process ultimately yields a reasonable guess for both a forward and a negative time solution that form a S/C path between a GEO-altitude perigee initial condition and the periodic LPO in the vicinity of L_1.

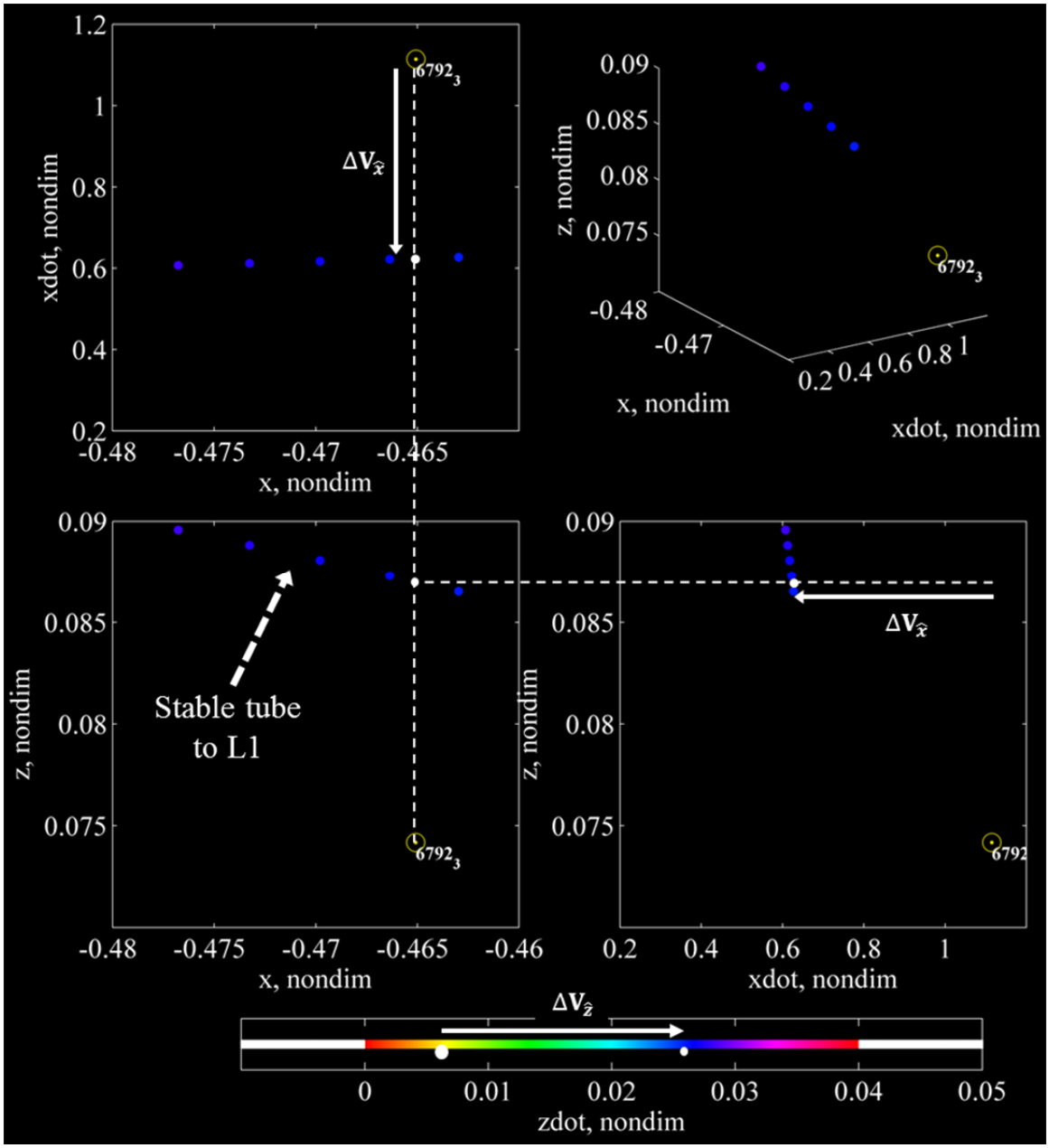

Figure 5.6. Four-perspective view of HEO-to-LPO transfer design space (zoomed in further); Cartesian phase space Poincaré map in the vicinity of the Earth; L_1 stable manifold tube and following month of returns from GEO-perigee initial conditions at same "energy;" ($y = 0-;\ x,\ \dot{x},\ z,\ \dot{z}\_color$)

To obtain a precise solution for the desired orbit transfer, it is first necessary to feed the transfer guess visually obtained from the Poincaré map plotted in Figure 5.6 into an automated targeting process, which determines a two-maneuver transfer between

trajectory 6792 and the periodic LPO. Note that both maneuvers are required to maintain the same "energy" level. The first maneuver in the targeted two-maneuver sequence is implemented along trajectory 6792, at the third return to the original hyperplane ($y = 0$ and $\dot{y} < 0$). The second maneuver in the sequence is implemented at a position along the periodic LPO. Targeting is accomplished using multiple shooting with forty-eight patch points between the hyperplane maneuver and a reference state along the periodic LPO. The final patch point is chosen to be along the LPO and is at the assumed position of the maneuver that completes the transfer into the orbit. This patch point is at a fixed position chosen based on a criterion for closeness to the transfer guess. As in Design Example #4 (see Section 4.4), a successful technique in this example is to weight distance and velocity equally (in nondimensional units) for the purpose of determining which state on the periodic LPO is closest to the transfer guess. The remaining patch points are selected to be evenly spaced in trajectory data index between the hyperplane maneuver and the patch point along the periodic orbit.

It is also necessary to determine the maneuver required to transfer from the GEO-altitude apogee of a HEO in the Earth-centric 2BP to the perigee initial condition of trajectory 6792 in the Earth-Moon CR3BP. This step in the transfer design process is essentially a transition of the initial condition for trajectory 6792 to the 2BP while also adjusting the "energy" level of that particular state. The initial transfer maneuver at the HEO apogee is an "energy"-raising maneuver from the standpoint of the CR3BP. It also constitutes an increase in S/C specific mechanical energy from the perspective of the 2BP. Is this case, the GEO-altitude maneuver is assumed to be tangential to the S/C velocity $\vec{V}$ *with respect to the Earth-centric inertial frame* and determined based on the apogee velocity required for a 2BP elliptical orbit with an apogee at GEO altitude and a perigee at 300 km altitude. The two-body period of the elliptical orbit (in the Earth-centric inertial frame) is 10.6 hours.

The 3-D S/C path of the targeted three-maneuver transfer between the HEO and the LPO is plotted in Figure 5.7 in the *x*-*y* rotating view, zoomed out as well as zoomed in to both the vicinity of the Earth and the vicinity of the Moon. Note that, even though *JC* is not a constant of the motion in the 2BP, Figures 5.7(a) and 5.7(b) include green ZVCs

associated with the single apogee state of the HEO, which is propagated (in green) in the 2BP for one orbit period before the first transfer maneuver. The first, "energy"-raising

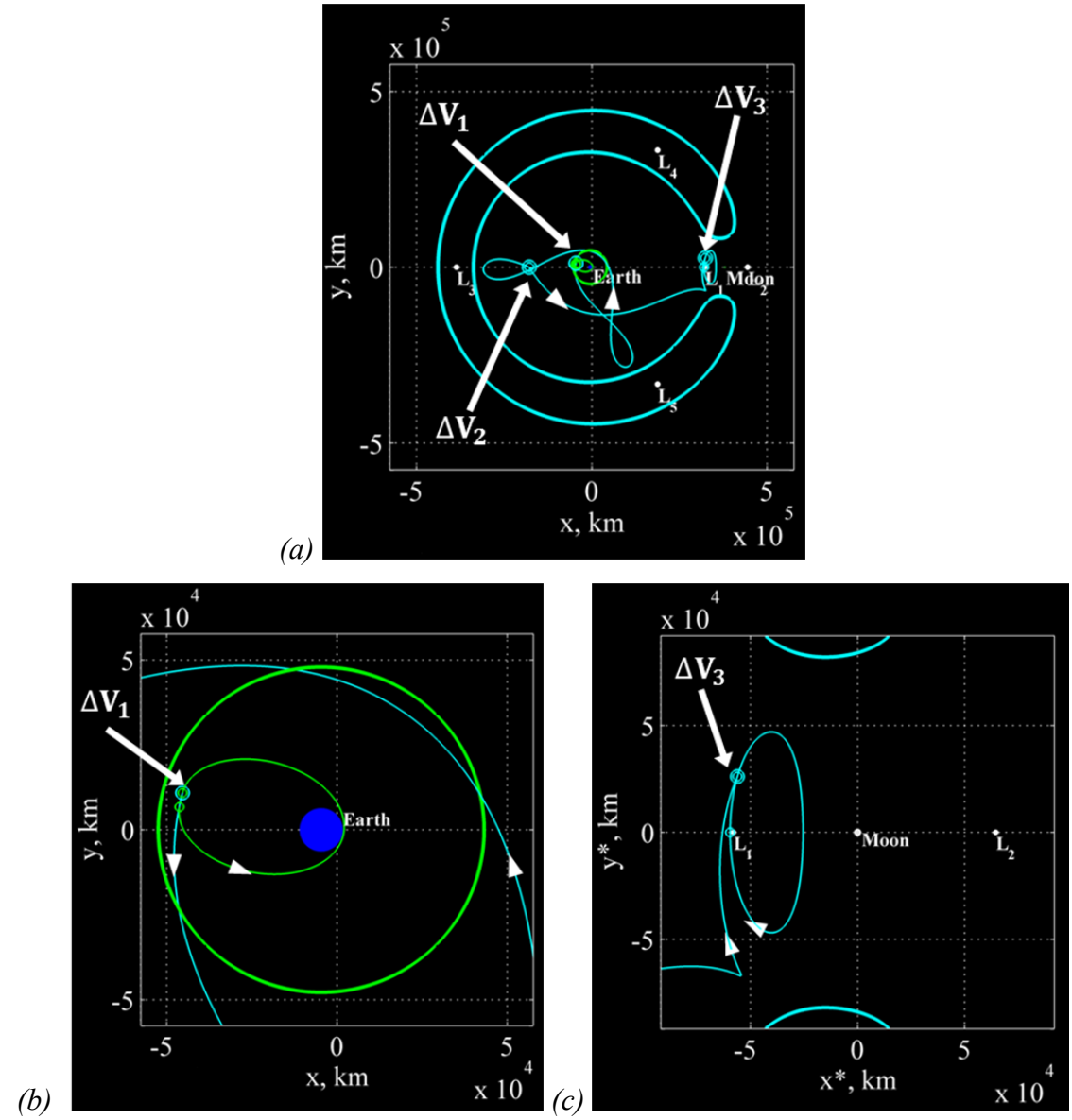

Figure 5.7. Zoomed out (*a*), zoomed in to Earth vicinity (*b*), and zoomed in to Moon vicinity (c) rotating views of precise HEO-to-LPO transfer solution; targeted three-maneuver transfer between apogee of HEO in 2BP and periodic L_1 LPO in CR3BP; before first maneuver at lower "energy" (green) and after first maneuver at higher "energy" (cyan)

maneuver in the three-maneuver sequence begins at the GEO-altitude apogee of the HEO, with a sizeable $\left|\overrightarrow{\Delta V}\right|$ = 2.47 km/s. The "energy"-maintaining second maneuver at $y = 0$, with $\left|\overrightarrow{\Delta V}\right|$ = 752 m/s, is implemented at a time equal to 15.5 days subsequent to the first maneuver. Finally, the "energy"-maintaining third maneuver, with $\left|\overrightarrow{\Delta V}\right|$ = 37.7 m/s, completes the transfer into the L_1 LPO and is implemented at a time equal to 14.6 days subsequent to the second maneuver. Thus, the entire transfer maneuver sequence is accomplished with a total $\left|\overrightarrow{\Delta V}\right|$ = 3.26 km/s and a total time-of-flight of 30.1 days.

The HEO plotted in green in Figure 5.7(b)—which is chosen through the map-based design process—appears in Figure 5.8 in the *X*-*Y* Earth-centric inertial view in the vicinity of the Earth. For an arbitrarily selected epoch of 1 January 2020 at "midnight" (00:00:00.0000 coordinate time) for the first (GEO-altitude) transfer maneuver, the two-body orbital elements for the HEO trajectory (propagated in the Earth-centric 2BP) are

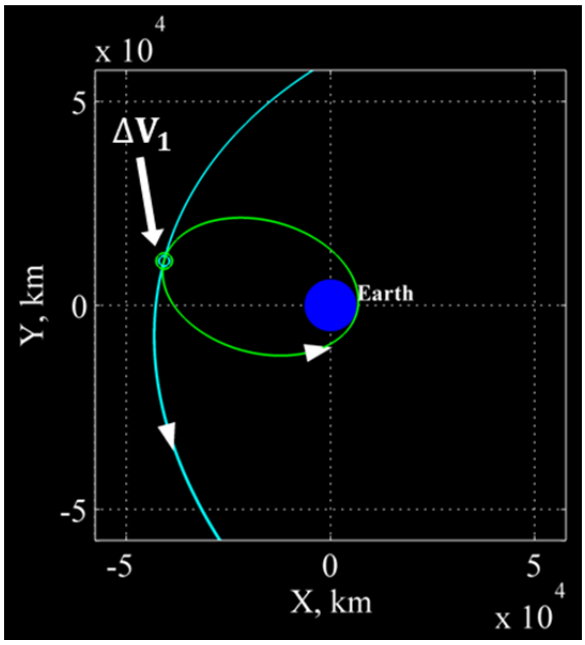

Figure 5.8. Inertial view of precise HEO-to-LPO transfer solution in the vicinity of the Earth; targeted three-maneuver transfer between apogee of HEO in 2BP and periodic L_1 LPO in CR3BP; before first maneuver at lower "energy" (green) and after first maneuver at higher "energy" (cyan)

calculated at apogee and appear in Table 5.1. The coordinate transformation required for this calculation is based on the Moon's own osculating elements at the time of the maneuver, obtained from the JPL HORIZONS System web-interface (ephemeris data

Table 5.1 S/C orbital elements at HEO apogee*

a	e	i	Ω	ω	ν
24,421.14 km	0.726543	35.50°	356.80°	333.25°	180.00°

* Earth-centric mean equatorial reference frame; equinox of reference epoch J2000.0; apogee maneuver epoch: 1 January 2020 at "midnight"

DE405) [111]. Even though a practical Earth-centric orientation for the HEO is not a consideration in the HEO-to-LPO transfer design process, the inclination of 35.50° for the solution chosen from the map is roughly representative of that of a real-world GTO. For example, a typical GTO inclination based on the latitude of the Kennedy Space Center (KSC) launch site is 28°. Furthermore, a launch into an inclination of 35.50° is well within the allowable limits of a KSC launch based on launch azimuth constraints [107].

The final step in the Poincaré-map-based process for designing a series of transfer maneuvers between a HEO and an LPO is to feed the targeted three-maneuver transfer plotted in Figure 5.7 into an automated optimization process similar to that used in Design Example #4 (see Section 4.4). The cost function to be minimized is the total $\left|\overrightarrow{\Delta V}\right|$ of the three-maneuver transfer between the apogee of the HEO plotted in Figure 5.8 and a reference state along the periodic LPO plotted in Figure 5.7(c). It is noteworthy that, because a precise (targeted) solution is available to initiate the optimization process, many of the assumptions that prove useful up until this step in the design process are no longer necessary and are removed so that a locally-optimal solution can be determined with greater flexibility. In other words, while various simplifying assumptions such as the location of the second maneuver (on the hyperplane) and the "energy" levels of the S/C path are useful for obtaining an initial estimate as well as a targeted solution using the 4-D map, these assumptions should not be requirements on the final solution. In

general, the fewer constraints that are enforced on a design space, the more flexibility there is in reducing a cost function through optimization of the design variables within that space. For optimization in this example, although the maneuver along the HEO is still required to be implemented at apogee, which is the same position as in the targeted transfer solution, the maneuver is no longer assumed to be tangential to the S/C velocity $\vec{V}$ with respect to the Earth-centric inertial frame. Moreover, the second (middle) maneuver is no longer assumed to be implemented at the original hyperplane $y = 0$, and the third maneuver is free to be implemented anywhere along the path of the periodic LPO (the periodic path leading to a reference state). Also, the path between the first and third maneuvers is no longer constrained to possess the same "energy" value as the LPO. The consequence of this is that the second and third maneuvers are no longer required to be "energy"-maintaining.

The optimized three-maneuver transfer—using the targeted HEO-to-LPO transfer solution plotted in Figure 5.7 to initiate the optimization process—is plotted in the barycentric rotating view in Figure 5.9. Figure 5.9(a) depicts the *x*-*y* view, while Figure 5.9(b) depicts a 3-D view with the L_1 LPO in the foreground for clarity. The resulting 3-D S/C path between reference states is locally optimal in total $\left|\overrightarrow{\Delta V}\right|$, with the optimality tolerance (based on the KKT conditions) set so as to consider further reductions in $\left|\overrightarrow{\Delta V}\right|$ on the order of mm/s to be negligible. The transfer maneuver sequence is accomplished with a total $\left|\overrightarrow{\Delta V}\right|$ = 2.82 km/s, a 13.5% reduction from the targeted solution. The total time-of-flight (between the first and third maneuvers) is now 42.4 days, approximately twelve days longer than for the targeted solution. Interestingly, the S/C transfer leg (plotted in red) between the first and second maneuvers is at a higher "energy" level such that there are no ZVCs on the *x*-*y* plane. Additionally, the "energy" level of the leg (plotted in purple) between the second and third maneuvers is just so slightly lower in "energy" than the L_1 LPO that the purple plot of the ZVCs associated with that leg covers up the cyan plot of the ZVCs associated with the LPO.

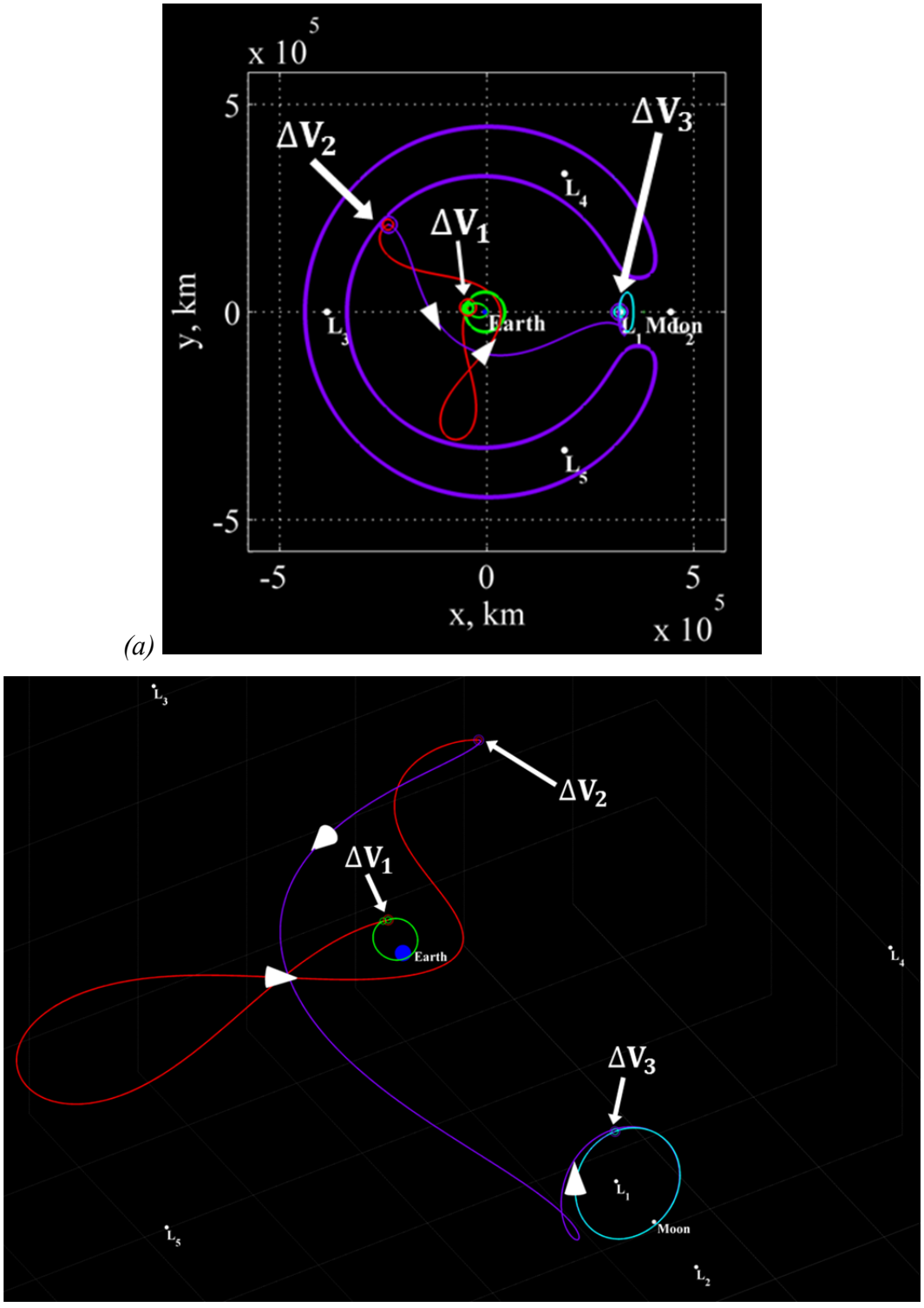

Figure 5.9. *x-y* (*a*) and 3-D (*b*) rotating views of optimized HEO-to-LPO transfer solution; locally-optimal three-maneuver transfer between apogee of HEO in 2BP and periodic L_1 LPO in CR3BP; before first maneuver (green), after first maneuver (red), after second maneuver (purple), and after third maneuver (cyan)

5.1.2 Design Phase 2: Transfer from L_1 LPO to L_2 LPO

The specific objective of the second design phase for Design Example #5 is the use of a different 4-D Cartesian phase space Poincaré map to design a series of maneuvers to accomplish a transfer between two 3-D, periodic LPOs. The S/C originates at the L_1 "northern" halo LPO used for the destination of the HEO-to-LPO transfer determined in the first design phase of the mission scenario (see previous section). The LPO-to-LPO transfer path designed in the second phase ends at a different LPO that is associated with L_2 and closer to the Moon. Two options for the L_2 LPO are selected from the "northern" and "southern" families of L_2 butterfly orbits. Using an initial guess from Grebow [131], an unstable LPO in the "northern" L_2 butterfly family is targeted and converged to satisfactory periodicity *at the same "energy" value* as the L_1 LPO. The "northern" butterfly LPO appears in Figure 5.10(a) in the *x*-*z* rotating view, zoomed in to the vicinity of the Moon (with the Moon as the offset origin), along with the L_1 halo LPO. The period of the butterfly orbit is 12.3 days, slightly longer than the 12.1-day period of the halo orbit. The "southern" L_2 butterfly orbit associated with the "northern" L_2 butterfly

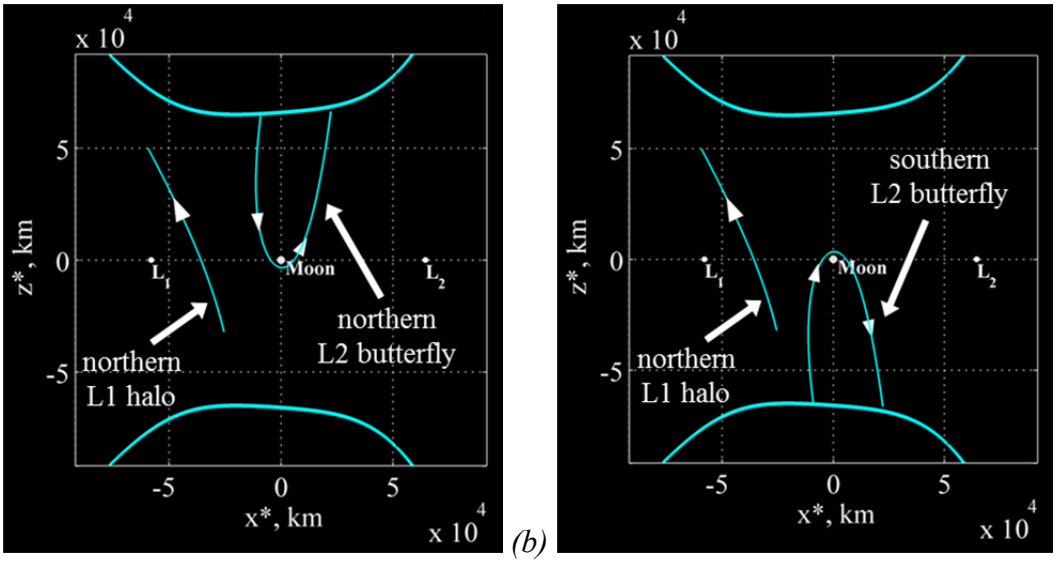

Figure 5.10. Rotating views of 3-D, periodic "northern" (*a*) and "southern" (*b*) L_2 butterfly LPOs along with L_1 "northern" halo LPO

orbit plotted in Figure 5.10(a) appears in Figure 5.10(b) in the same view. Both "northern" and "southern" butterfly orbits are unstable and possess identical periods and "energy" values. The two LPOs are related by the CR3BP symmetry in which reversing the sign of z and $\dot{z}$ values of a solution produces another solution. The minimum lunar altitude of either butterfly orbit is 1,677 km.

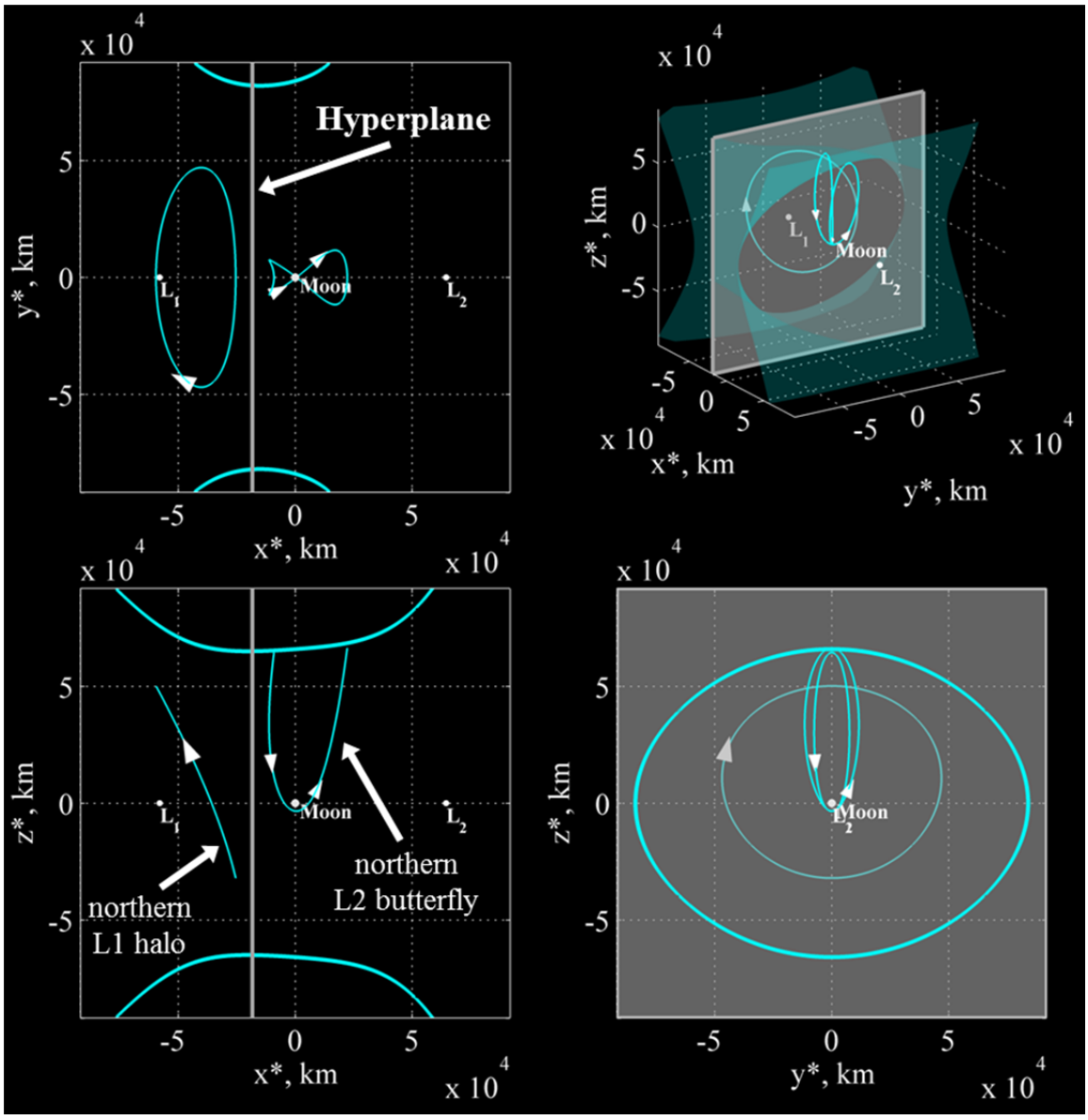

Figure 5.11. Four-perspective rotating view of 3-D, periodic, "northern" L_1 halo LPO and "northern" L_2 butterfly LPO

In a process similar to the LPO-to-LPO design process employed in Design Example #4 (see Section 4.4), a Cartesian phase space Poincaré map hyperplane is used to generate 4-D manifold maps. As depicted in the four-perspective rotating view in Figure 5.11, a one-sided Cartesian phase space manifold map hyperplane is defined such that $x = 0.94$ and $\dot{x} > 0$. The hyperplane is located between the two LPOs; its intersection with the *x*-axis is approximately 18,393 km away from the Moon. The maps of the first returns of a stable manifold tube associated with the "northern" L_2 butterfly LPO and the first returns of an unstable manifold tube associated with the L_1 halo LPO are plotted at a single "energy" level in Figure 5.12. As before, an approximation for each manifold tube in this analysis is comprised of 500 individual trajectories asymptotic to (or from) a periodic orbit. The ring structure plotted with small dots, ranging between green and blue, is the first map return (in forward time) of an entire L_1 halo LPO unstable manifold tube. The figure-8 structure (in the *y*-*z* view) plotted with large dots, ranging between orange and magenta, is the first map return (in negative time) of an entire L_2 "northern" butterfly stable manifold tube. An estimate for the LPO-to-LPO transfer path, with a maneuver implemented on the hyperplane at $x = 0.94$, is obtained by visual inspection of the map returns in Figure 5.12. First, an estimate for the *y*-*z* position of an intersection between the ring structure and the figure-8 structure is obtained. Next, the estimated position intersection is used to estimate the components of S/C velocity $\vec{V}$ that exist for each 1-D structure at that position. Estimates for the velocity adjustments in $\dot{y}$ and $\dot{z}$ are obtained visually, while the associated velocity adjustment in $\dot{x}$ is simply calculated based on the "energy" level of the map. The color coordinate of the 4-D map, in addition to defining the $\dot{z}$ value of structures on the map, also aids in the interpretation of the relationship between the structures in terms of the remaining (spatial) coordinates of the map. This process yields a reasonable guess for both a forward and a negative time solution that form a S/C path between the L_1 halo LPO and the "northern" L_2 butterfly LPO. A significant aspect of the velocity adjustment estimate obtained from the map plotted in Figure 5.12 is the fact that the required maneuver (with total $\left|\overrightarrow{\Delta V}\right|$ = 344.4 m/s) involves a reversing of the signs of both $\dot{y}$ and $\dot{z}$. This qualitative factor corresponds to the *y*-*z* rotating view in Figure 5.11, where the direction of motion of the "northern" L_1 halo LPO

is clockwise, while the direction of motion of the "northern" L_2 butterfly LPO is counterclockwise. Therefore, this transfer estimate yields a S/C path that is somewhat inconsistent with the natural dynamics of the two LPOs (as a whole).

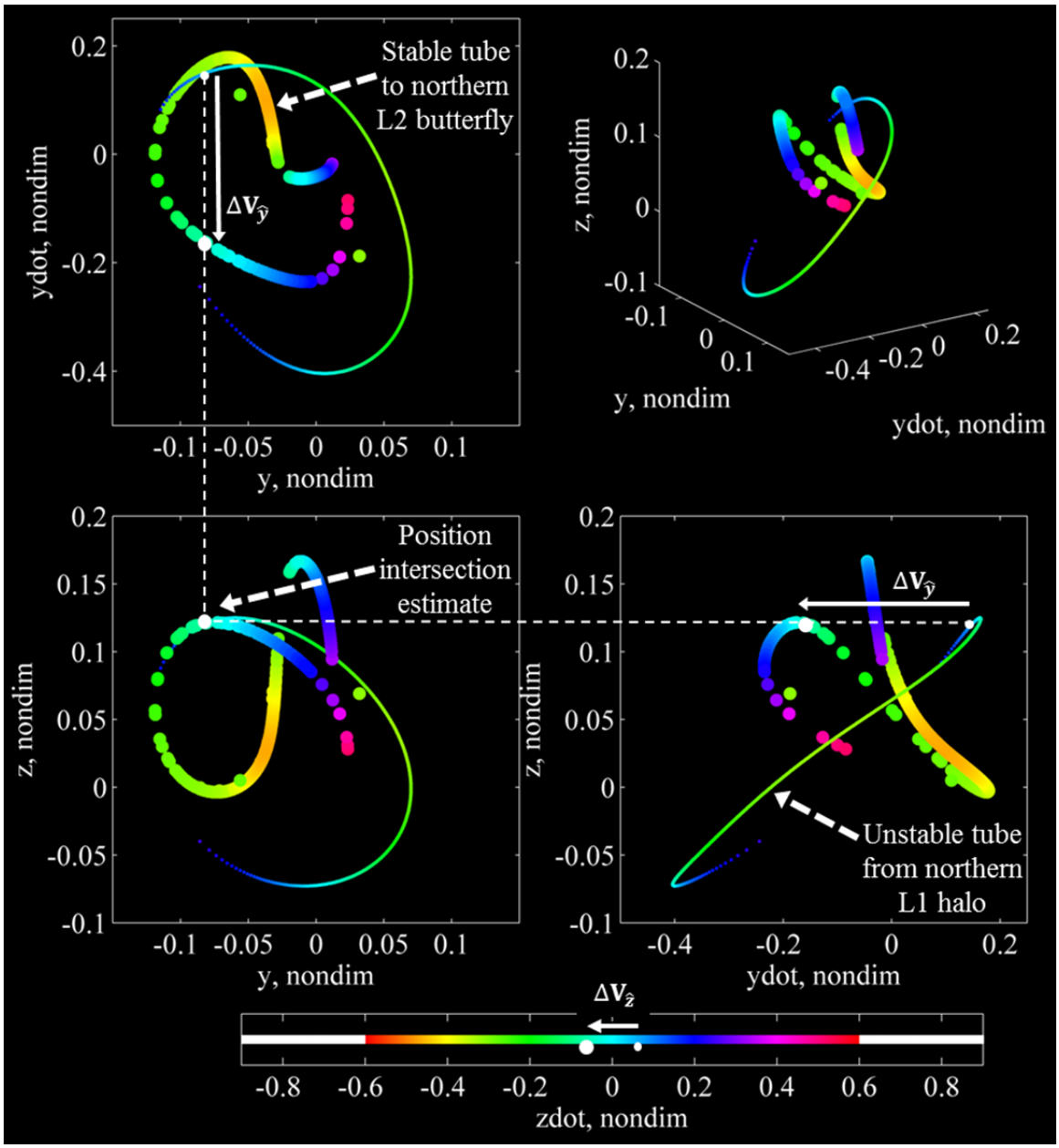

Figure 5.12. Four-perspective view of "northern"-halo-to-"northern"-butterfly transfer design space; Cartesian phase space Poincaré manifold map in the vicinity of the Moon; "northern" L_1 halo LPO unstable manifold tube and "northern" L_2 butterfly LPO stable manifold tube at same "energy;" $(x = 0.94+;\ y,\ \dot{y},\ z,\ \dot{z}\_color)$

To design an LPO-to-LPO transfer path that is more consistent with the natural dynamics of the two LPOs, the "southern" L_2 butterfly LPO, which has a clockwise direction of motion in the *y-z* rotating view, as plotted in Figure 5.13, is

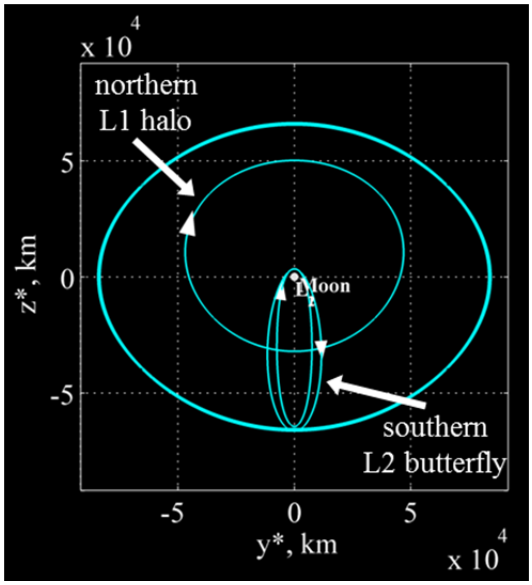

Figure 5.13. Rotating view of 3-D, periodic "southern" L_2 butterfly LPO along with L_1 "northern" halo LPO

alternatively considered as the destination of the S/C transfer path. Just as the "northern" L_2 butterfly orbit is associated—through symmetry by reversing the sign of z and $\dot{z}$ values—with the "southern" L_2 butterfly orbit, so too is the "northern" L_2 butterfly LPO stable manifold tube figure-8 structure plotted in Figure 5.12 associated with a "southern" figure-8 structure. By reversing the sign of z and $\dot{z}$ values for the figure-8 structure in Figure 5.12 (while leaving the ring structure unchanged), the alternative design space for a transfer between the "northern" L_1 halo LPO and the "southern" L_2 butterfly LPO is plotted in Figure 5.14. The figure-8 structure plotted in Figure 5.14 is the result of reflecting the figure-8 structure plotted in Figure 5.12 through both the spatial axis $z = 0$ and the color axis $\dot{z} = 0$ of the map. It is noteworthy that this reflection is accomplished entirely in the visual environment of the 4-D Poincaré map, *without having to calculate either the S/C trajectory or the stable manifold tube associated with the "southern"* L_2 *butterfly LPO*. An estimate for the alternative LPO-to-LPO transfer path between the L_1

halo LPO and the "southern" L_2 butterfly LPO, with a maneuver implemented at a different *y*-*z* position on the $x = 0.94$ hyperplane, is obtained by visual inspection as well as by interpolation in the empty spaces between map returns in Figure 5.14. Note that the

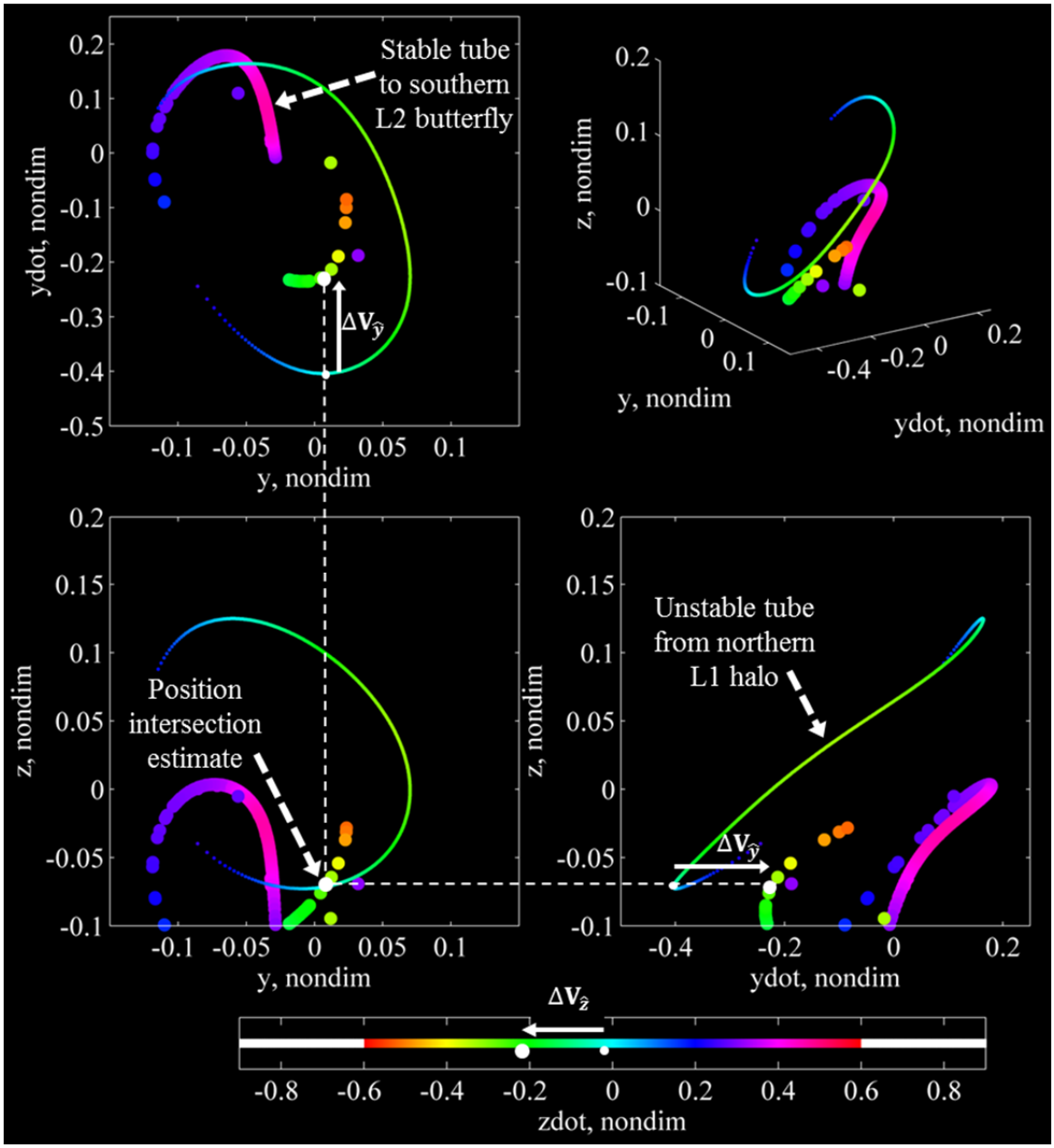

Figure 5.14. Four-perspective view of "northern"-halo-to-"southern"-butterfly transfer design space; Cartesian phase space Poincaré manifold map in the vicinity of the Moon; "northern" L_1 halo LPO unstable manifold tube and "southern" L_2 butterfly LPO stable manifold tube at same "energy;" ($x = 0.94+;\ y,\ \dot{y},\ z,\ \dot{z}\_color$)

required maneuver associated with the estimate obtained from the map plotted in Figure 5.14 (with total $\left|\overrightarrow{\Delta V}\right|$ = 355.6 m/s) does *not* involve a reversing of the sign of either $\dot{y}$ or $\dot{z}$. This qualitative factor corresponds to the *y-z* view in Figure 5.13, where the direction of motion of both the "northern" L_1 halo LPO and the "southern" L_2 butterfly LPO is clockwise.

A precise solution for the desired LPO-to-LPO orbit transfer between the "northern" L_1 halo LPO and the "southern" L_2 butterfly LPO is obtained by feeding the transfer guess visually obtained from the Poincaré map plotted in Figure 5.14 into an automated targeting process similar to the multiple shooting processes employed in Design Example #4 as well as in the first design phase of Design Example #5 (see Sections 4.4 and 5.1.1, respectively). The result of the targeting process is a three-maneuver transfer between the two periodic LPOs, with the second (middle) maneuver implemented at the selected position on the original hyperplane ($x = 0.94$). In this case, each path between the hyperplane maneuver and each LPO is constrained to possess the same "energy" value as both LPOs. For the portion of the targeting process dealing with the butterfly LPO, the design of a precise transfer into the periodic LPO is accomplished in two steps. First, multiple shooting using a revolution "stacking" process is employed to converge on a solution for a S/C path originating at the hyperplane maneuver and ending after completing multiple revolutions in the vicinity of the butterfly orbit. The *initial guesses* for the patch points along these multiple revolutions are selected to be states along the actual periodic orbit, with the same points used repeatedly on consecutive revolutions of the guessed path. Next, the converged "stacked" solution is used as an initial guess for a second multiple shooting process that converges on a solution to an actual transfer into the periodic butterfly LPO. The targeted three-maneuver transfer sequence is accomplished with a total $\left|\overrightarrow{\Delta V}\right|$ = 359.4 m/s and a total time-of-flight of 43.1 days.

The next step in the second design phase for Design Example #5 is to feed the targeted three-maneuver transfer into an automated optimization process similar to that used in Design Example #4 as well as in the first design phase of Design Example #5. The cost function to be minimized is the total $\left|\overrightarrow{\Delta V}\right|$ of the three-maneuver transfer between reference states along the "northern" L_1 halo LPO and the "southern" L_2

butterfly LPO plotted in Figure 5.13. Key assumptions useful in earlier steps in the map-based design process are now removed to achieve greater flexibility in the automated process of reducing the total $\left|\overrightarrow{\Delta V}\right|$. The second (middle) maneuver is no longer assumed to be implemented at the original hyperplane, and the first and third maneuvers are free to be implemented anywhere along the path of the periodic LPOs (the periodic path leading to each reference state). Furthermore, the path between the first and third maneuvers is no longer constrained to possess the same "energy" value as both LPOs. The consequence of this is that the three maneuvers are no longer required to be "energy"-maintaining. The optimized three-maneuver transfer is plotted in the four-perspective rotating view in Figure 5.15. The resulting 3-D S/C path between reference states is locally optimal in total $\left|\overrightarrow{\Delta V}\right|$, with the optimality tolerance (based on the KKT conditions) set so as to consider further reductions in $\left|\overrightarrow{\Delta V}\right|$ on the order of mm/s to be negligible. The optimized S/C transfer sequence begins with an "energy"-raising maneuver, with $\left|\overrightarrow{\Delta V}\right|$ = 17.3 m/s, to depart the L_1 halo LPO. The "energy"-lowering second maneuver, with $\left|\overrightarrow{\Delta V}\right|$ = 29.1 m/s, is implemented at a time equal to 11.5 days subsequent to the first maneuver. The "energy"-raising third maneuver, with $\left|\overrightarrow{\Delta V}\right|$ = 64.1 m/s, completes the transfer into the "southern" L_2 butterfly LPO and is implemented at a time equal to 34.9 days subsequent to the second maneuver. Thus, the transfer maneuver sequence is accomplished with a total $\left|\overrightarrow{\Delta V}\right|$ = 110.6 m/s, an impressive 69% reduction from the targeted solution. The total time-of-flight (between the first and third maneuvers) is 46.4 days, slightly longer than for the targeted solution.

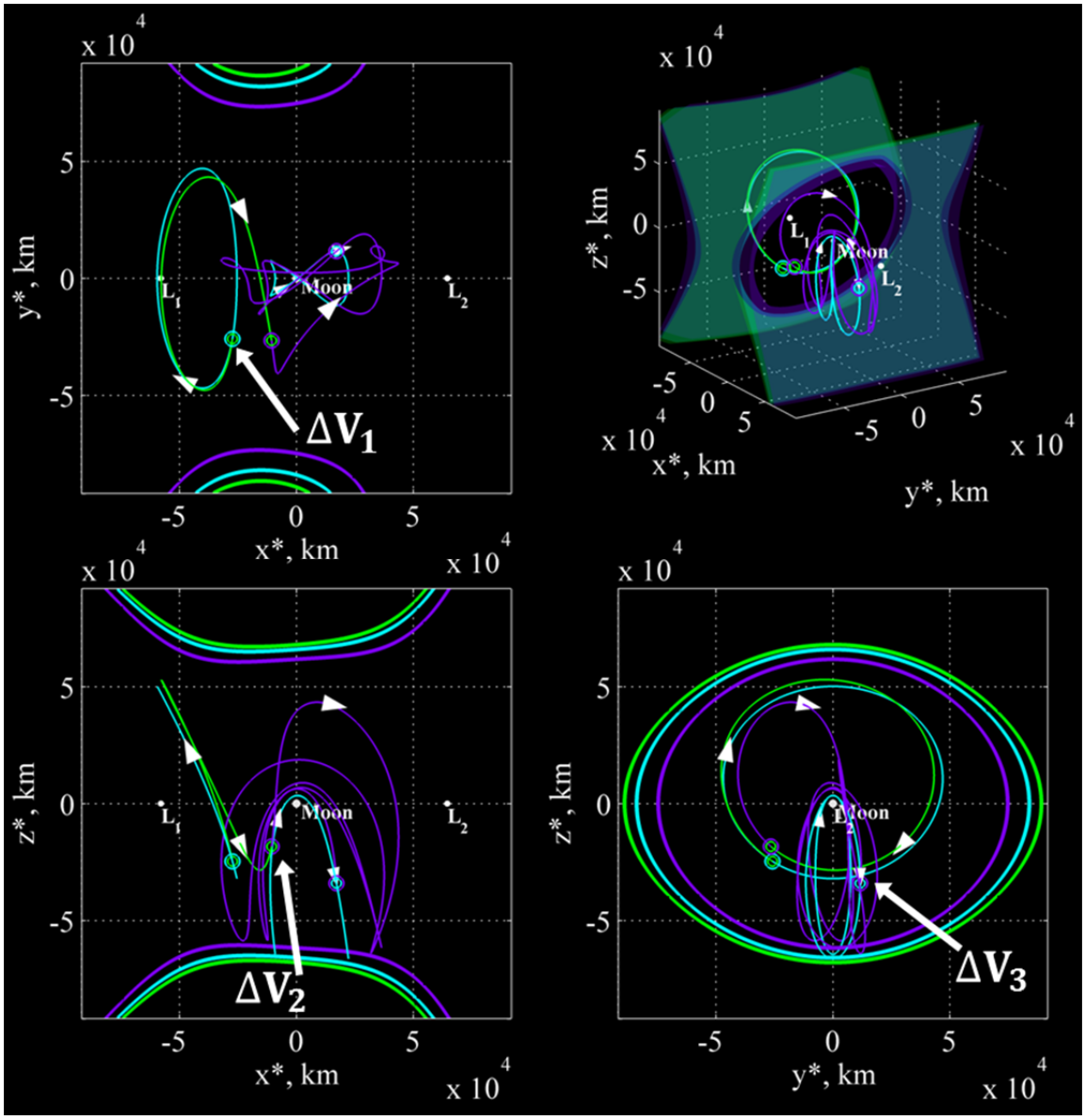

Figure 5.15. Four-perspective rotating view of optimized LPO-to-LPO transfer solution; locally-optimal three-maneuver transfer between "northern" L_1 halo LPO and "southern" L_2 butterfly LPO; before first maneuver (cyan), after first maneuver (green), after second maneuver (purple), and after third maneuver (cyan)

The choice of using the "southern" butterfly orbit instead of the "northern" butterfly orbit as the destination for the LPO-to-LPO transfer sequence—based on the idea that the "southern" option is more consistent with the natural dynamics of the LPOs—is vindicated by comparing the total $\left|\overrightarrow{\Delta V}\right|$ of the optimized solutions associated with each option. As indicated in Table 5.2, although the visually-obtained estimates and the

targeted solutions for the two transfer options yield similar values of total $\left|\overrightarrow{\Delta V}\right|$, the associated optimized solution for the "northern" butterfly option is more than twice as costly in terms of total $\left|\overrightarrow{\Delta V}\right|$ as the "southern" butterfly option. The comparison in Table

Table 5.2 Comparison of halo-to-butterfly transfer option total $\left|\overrightarrow{\Delta V}\right|$

Destination LPO	4-D map estimate	Targeted solution	Optimized solution
"Northern" L_2 butterfly	344.3 m/s	358.7 m/s	244.6 m/s*
"Southern" L_2 butterfly	355.6 m/s	359.4 m/s	110.6 m/s

* Path with "local minimum possible" in *fmincon,* constrained to 100 km minimum lunar altitude; removing constraint reduces value to 234.9 m/s with locally-optimal path ("local minimum found" in *fmincon)* reaching 980 km below Moon's surface

5.2 offers a striking example of the theme that the 4-D Poincaré map and its associated interactive visual processes are most useful for obtaining initial guesses that meet certain qualitative criteria rather than for assessing quantitative metrics such as total $\left|\overrightarrow{\Delta V}\right|$. If the visually-obtained transfer options are compared based on the quantitative criterion of the total $\left|\overrightarrow{\Delta V}\right|$ of the estimate—while ignoring the qualitative information from the 4-D map concerning the natural dynamics of the LPOs—it seems as if the "northern" butterfly option is at least equal to, and even slightly superior to, the "southern" butterfly option. However, because the "southern" option involves a S/C path with the same clockwise direction of motion (in the *y-z* view) as both the halo orbit and the "southern" butterfly orbit, it is not surprising than an automated optimization process yields a local optimum that is vastly superior to that of the "northern" option, which requires a reversing of the direction of motion from clockwise to counterclockwise. The preceding comparison also demonstrates how optimization can play a critical role in the overall Poincaré-map-based design strategy.

The second (middle) maneuver in the optimized halo-to-butterfly transfer sequence plotted in Figure 5.15 seems quite small, with $\left|\overrightarrow{\Delta V}\right|$ = 29.1 m/s, indicating the possibility of determining a reasonable *two-maneuver* transfer sequence. In general, a S/C path with

fewer transfer maneuvers offers the benefit of operational simplicity. Accordingly, the final step in the second design phase for Design Example #5 (and for the scenario as a whole) is to feed the targeted three-maneuver transfer between the "northern" L_1 halo LPO and the "southern" L_2 butterfly LPO into a new optimization process, where the new cost function to be minimized is the total $\left|\overrightarrow{\Delta V}\right|$ of a two-maneuver transfer. The second (middle) maneuver is removed by enforcing velocity continuity at the patch point previously associated with that maneuver, while all other constraints/assumptions are identical to those used to obtain the optimized three-maneuver transfer. The result of this new optimization process appears in Figure 5.16 in the rotating view and in the Moon-centric inertial view. Also included in this view is the arrival path to the L_1 halo orbit, as designed for the HEO-to-LPO transfer (see Section 5.1.1) along with the third maneuver (ΔV_3) in that transfer sequence. Therefore, the locally-optimal, two-maneuver halo-to-butterfly transfer sequence begins with the *fourth* maneuver in the overall transfer sequence, which is an "energy"-lowering maneuver, with $\left|\overrightarrow{\Delta V}\right|$ = 63.6 m/s, to depart the L_1 halo LPO at a time equal to 9.9 days after the third maneuver. The second and final halo-to-butterfly transfer maneuver—the fifth and final in the overall HEO-to-halo-to-butterfly transfer sequence—is "energy"-raising, with $\left|\overrightarrow{\Delta V}\right|$ = 66.5 m/s, and is implemented at a time equal to 44 days subsequent to the halo orbit departure maneuver. Thus, the optimized two maneuver sequence is accomplished with a total $\left|\overrightarrow{\Delta V}\right|$ = 130.1 m/s, an 18% increase over the optimized three-maneuver sequence, and a total time-of-flight of 44 days, slightly shorter than the optimized three-maneuver sequence.

In summary, the two-maneuver halo-to-butterfly transfer sequence (plotted in Figure 5.16) determined in the second design phase of Design Example #5 completes the Poincaré-map-based design of a five-maneuver transfer sequence in the Earth-Moon CR3BP. The sequence originates from a HEO (modeled in the 2BP), transitions through a periodic, "northern" L_1 halo LPO, and ends with a transfer into a periodic, "southern" L_2 butterfly LPO. The overall $\left|\overrightarrow{\Delta V}\right|$ = 2.95 km/s and the overall time-of-flight is 86.4 days. Of course, because the L_1 halo LPO is periodic, with a period of 12.1 days, a delay

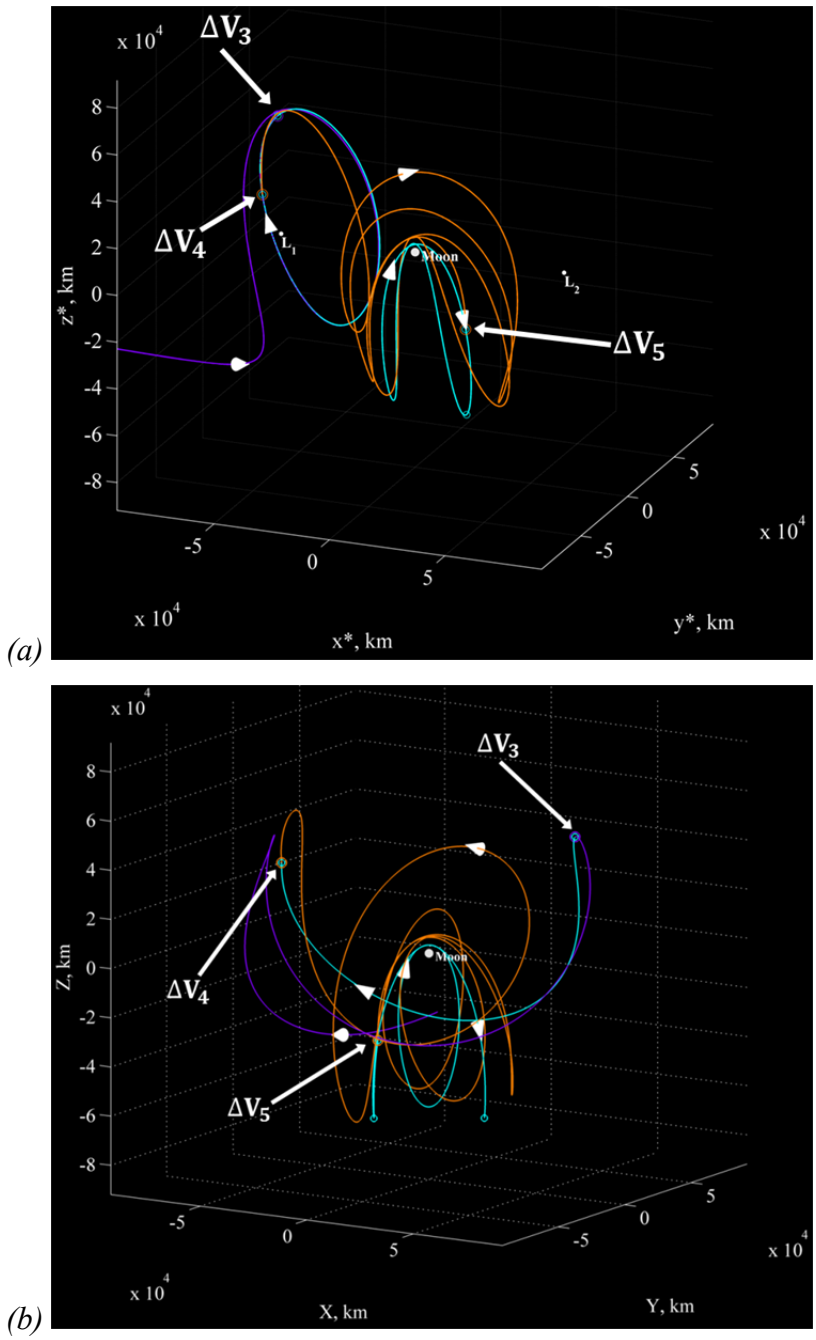

Figure 5.16. Rotating (*a*) and inertial (*b*) views of optimized LPO-to-LPO transfer solution; locally-optimal two-maneuver transfer between "northern" L_1 halo LPO and "southern" L_2 butterfly LPO (last two maneuvers in five-maneuver HEO-to-halo-to-butterfly sequence); before third maneuver (purple), after third maneuver (cyan), after fourth maneuver (orange), and after fifth maneuver (cyan)

of 12.1N days (where N is a positive integer) may be added to the overall transfer sequence between the third and fourth maneuvers. Thus, the use of the L_1 halo LPO as an intermediate destination between the HEO and the L_2 butterfly LPO provides some operational flexibility for this mission scenario.

5.2 Design Example #6: Transfer Between Earth Orbits Using Lunar Gravity

In the next advanced, 4-D-map-based design scenario, a map is exploited to design a CR3BP transfer path between two orbits (at two epochs) defined based on both a lower-fidelity (two-body) model as well as two higher-fidelity (ephemeris) reference states. The context for this example is the investigation of the possible uses of 4-D-map-based design approaches for determining 3-D trajectory solutions for repositioning Earth-orbiting satellites. Spherical phase space Poincaré maps are employed to explore higher-altitude paths in the Earth-Moon CR3BP that allow for a practical transfer between two 3-D, geosynchronous orbits (GEO) modeled in the Earth-centric 2BP. Such higher-altitude paths exploit multi-body effects to reduce the $\left|\overrightarrow{\Delta V}\right|$ required by the transfer. Finally, the results of the higher-D-map-based and CR3BP-focused design method are compared to results obtained through more traditional, 2BP-focused design methods.

The assumed scenario involves a satellite in geostationary orbit in the year 2025. The satellite, which is currently in a geosynchronous, circular, equatorial orbit about the Earth, receives an urgent tasking for a new mission in which it must be transferred into a geosynchronous, circular, *polar* orbit. It is assumed that fuel reserves and/or a futuristic on-orbit refueling capability such as that envisioned by the Robotic Refueling Mission [132, 133] is available to support the new tasking. However, the $\left|\overrightarrow{\Delta V}\right|$ required for a simple plane change accomplished at GEO altitude is deemed prohibitive. As a lower-$\left|\overrightarrow{\Delta V}\right|$ alternative, higher-altitude paths—involving multiple transfer maneuvers—are considered. The Earth-centric and Moon-centric two-body gravitational parameters are assumed to be equal to GM_E = 398,600.4418 km^3/s^2 and GM_M = 4,902.801076 km^3/s^2, respectively, and the Earth-Moon CR3BP model parameters are as before (see again Table 4.3).

Both the originating, equatorial GEO and the destination, polar GEO, which are propagated in the 2BP, appear in Figure 5.17 in the Earth-centric inertial view in the vicinity of the Earth. The two-body period of each orbit is one sidereal day, i.e., 23.934 hours. Also depicted is a simple, inclination-only, plane change maneuver [74] between the two orbits, with $\left|\overrightarrow{\Delta V}\right|$ = 4.35 km/s. The initial epoch for the 90° plane change maneuver, which is assumed to be instantaneous, is arbitrarily selected to be 1 January 2025 at "midnight." Note that the *X*-*Y* plane of the inertial view in Figure 5.17 is the plane of the primaries, not the Earth's equator. In fact, at the maneuver epoch, the osculating inclination of the Moon's orbit with respect to the Earth-centric mean equatorial reference frame is 28.44° [111].

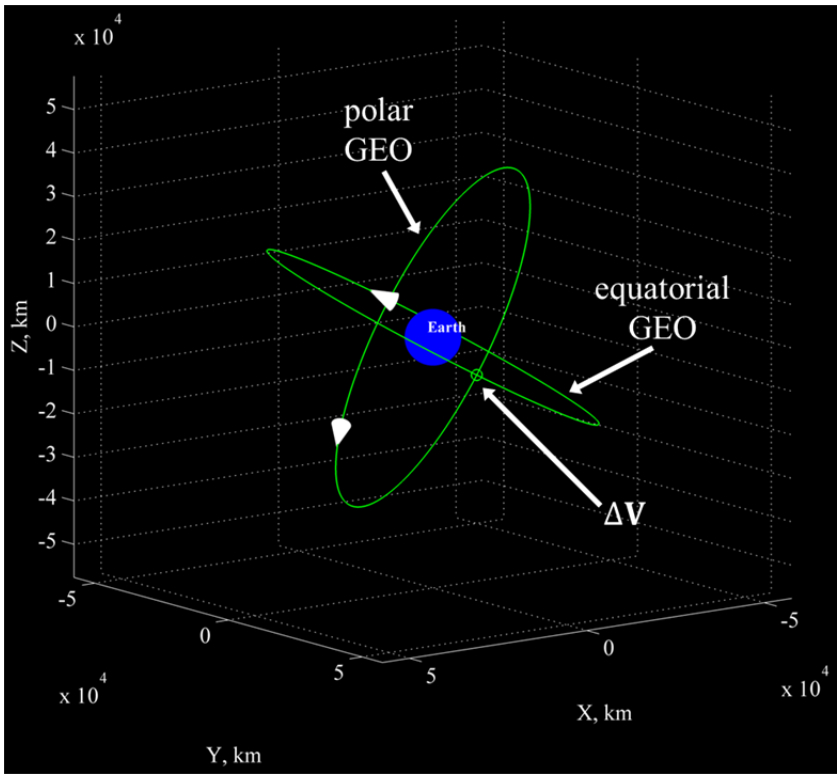

Figure 5.17. Inertial view of simple plane change maneuver between equatorial GEO and polar GEO in the vicinity of the Earth

The Earth-centered, two-body orbital elements for each GEO plotted in Figure 5.17 appear in Table 5.3. The sets of orbital elements are selected arbitrarily to create a

scenario involving an inclination-only, 90° plane change between two GEOs. The coordinate transformation required to transition these 2BP orbits into the inertial frame of the CR3BP is based on the Moon's own osculating elements at the time of the maneuver, obtained from the JPL HORIZONS System web-interface (ephemeris data DE405) [111]. The orbital element Ω is undefined for an equatorial orbit, and the orbital elements ω and ν are undefined for a circular orbit. Therefore, the alternate orbital elements argument of latitude u and true longitude l are used where appropriate [8].

Table 5.3 GEO orbital elements*

Orbit	a	e	i	Ω	u	l
Equatorial	42,164.14 km	0	0°	N/A	N/A	0°
Polar	42,164.14 km	0	90°	0°	0°	N/A

* Earth-centric mean equatorial reference frame; equinox of reference epoch J2000.0; initial epoch: 1 January 2025 at "midnight"

The use of higher-altitude paths for the transfer between the two GEOs plotted in Figure 5.17 is motivated by the reduced $\left|\overrightarrow{\Delta V}\right|$ of the Earth-centric 2BP bi-elliptic transfer [9] plotted in Figure 5.18 in the Earth-centric inertial view. Rather than changing the inclination of the equatorial GEO with a single (massive) maneuver at GEO altitude, the bi-elliptic transfer requires three maneuvers with a total $\left|\overrightarrow{\Delta V}\right| = 2.75$ km/s, 37% less than the cost of the simple plane change. The first maneuver, with $\left|\overrightarrow{\Delta V}\right| = 1.053$ km/s, is implemented along the equatorial GEO at the initial epoch. This maneuver is tangential to the S/C velocity $\vec{V}$ with respect to the Earth-centric inertial frame, inserting the S/C into an equatorial transfer ellipse with a perigee at GEO altitude and an apogee at the altitude of the Moon's (circular) orbit about the Earth. The path of the Moon also appears in Figure 5.8 for the duration of the transfer, however, for this Earth-centric, two-body propagation, lunar gravity does *not* affect the S/C path. The second maneuver is a 90° plane change maneuver implemented at the lunar-orbit-altitude apogee of the transfer ellipse (but not actually near the Moon in this case) at a time equal to 5.67 days

subsequent to the first maneuver, with $\left|\overrightarrow{\Delta V}\right| = 640.3$ m/s, resulting in a new transfer ellipse that is now in the same orbit plane as the polar GEO. Based on the symmetry inherent in the two-body dynamics, the third and final maneuver is implemented at the exact same position as the first maneuver, at a time equal to 5.67 days subsequent to the second maneuver, with $\left|\overrightarrow{\Delta V}\right| = 1.053$ km/s. This final maneuver is tangential to the S/C velocity $\vec{V}$ with respect to the Earth-centric inertial frame and inserts the S/C into the polar GEO after a total time-of-flight of 11.3 days.

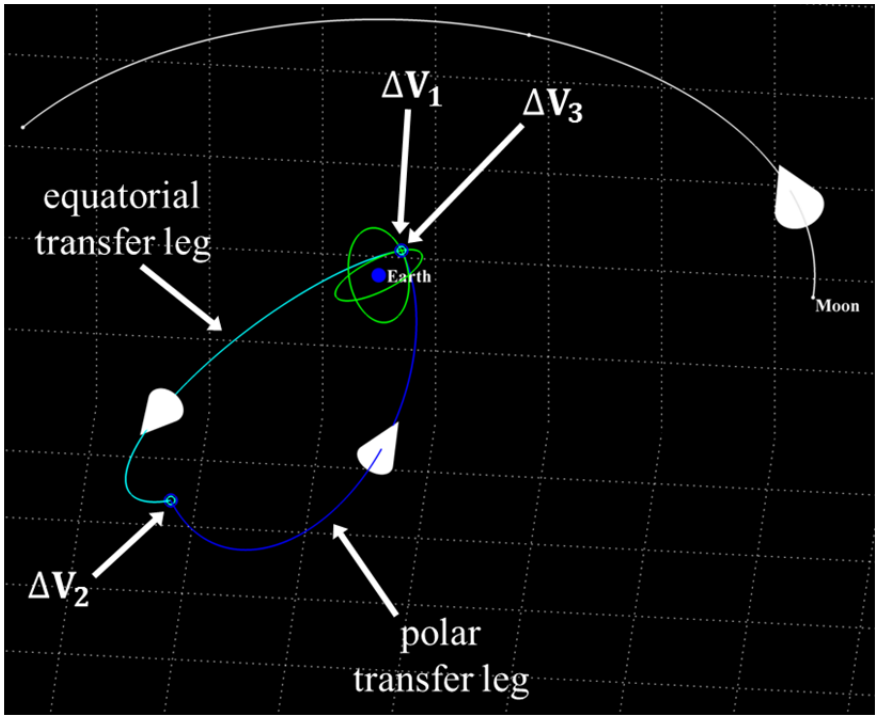

Figure 5.18. Inertial view of bi-elliptic transfer between equatorial GEO and polar GEO; before first maneuver (green), after first maneuver (cyan), after second maneuver (blue), and after third maneuver (green)

Based on the advantage of the bi-elliptic transfer plotted in Figure 5.18—in terms of $\left|\overrightarrow{\Delta V}\right|$ compared to the simple plane change plotted in Figure 5.17—the specific objective for Design Example #6 is the design of a series of maneuvers to accomplish a higher-altitude transfer between the GEOs defined by the orbital elements in Table 5.3. Most of the required plane change for the transfer is performed at approximately lunar orbit

altitude. Although the two GEOs are modeled in the Earth-centric 2BP, the transfer path between GEOs is modeled in the Earth-Moon CR3BP. The true longitude $l = 0°$ along the equatorial GEO defines the starting reference state, and the argument of latitude $u = 0°$ along the polar GEO defines the ending reference state. Each reference state is defined based on a higher-fidelity model, i.e., the JPL HORIZONS ephemeris data [111], at two different epochs. Given the bi-elliptic transfer total time-of-flight of 11.3 days, the final epoch used in the map-based design process is assumed to be exactly twelve days following the initial epoch. In other words, the S/C path begins at the starting reference state at the initial epoch of 1 January 2025 at "midnight" and ends at the ending reference state at the final epoch of 13 January 2025 at "midnight." Yet, the actual locations (i.e., the true longitude or argument of latitude) of the GEO departure and arrival maneuvers

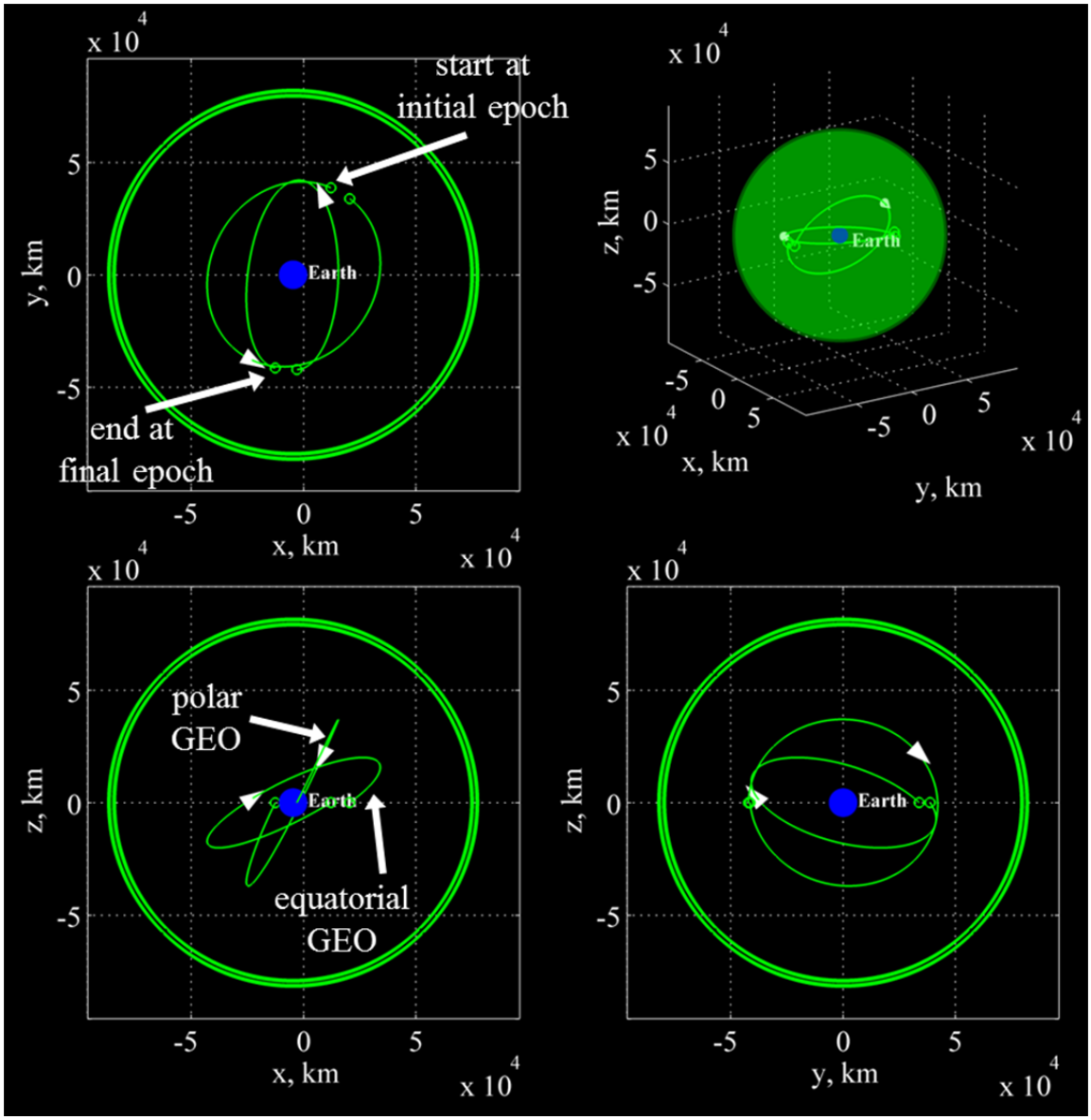

Figure 5.19. Four-perspective rotating view of equatorial GEO (one period following initial epoch) and polar GEO (one period before final epoch)

are chosen through the 4-D-map-based design process. The 2BP propagations for one period following the equatorial GEO starting reference state and one period before the polar GEO ending reference state appear in the four-perspective rotating view in the vicinity of the Earth in Figure 5.19. Thus, the goal of the GEO-to-GEO transfer design process is the determination of a S/C path between starting and ending reference states; these states along the GEOs are, in effect, "anchored" in a higher-fidelity, ephemeris-

based model, allowing for each GEO to be defined in terms of orbital elements with respect to the Earth-centric mean equatorial reference frame. The path along the GEOs is modeled in the Earth-centric 2BP, while the path between GEO departure and arrival maneuvers is modeled in the Earth-Moon CR3BP. Note that, even though *JC* is not a constant of the motion in the 2BP, Figure 5.19 includes green ZVSs (and ZVCs) associated with the single reference state along each GEO. The ending reference state (along the polar GEO) is at a slightly higher "energy" level than the starting reference state (along the equatorial GEO); therefore, the green sphere associated with the polar GEO is slightly larger.

To obtain an estimate for the GEO-to-GEO transfer path—with a plane change maneuver implemented at approximately lunar orbit altitude—a hypersurface is defined in Earth-centered spherical coordinates as $\rho = 1$ and $\dot{\rho} > 0$ so as to capture returns associated with trajectories crossing (outward) a sphere surrounding the Earth at a radius equal to the distance between the Earth and the Moon. This spherical hypersurface is used to generate a one-sided, spherical phase space Poincaré map at an "energy" value where the ZVSs are far enough above and below the *x*-*y* plane to permit trajectories crossing any position along the hypersurface, as depicted in Figure 5.20. Also plotted (in green, as in Figure 5.19) are the GEOs and their associated lower-"energy" ZVSs, for comparison with the higher-"energy" ZVSs (cyan) associated with the 4-D map. The higher "energy" level value is $(2/3)JC_{L4}$, where JC_{L4} is the *JC* associated with the equilibrium points L_4 and L_5. Because a smaller value of *JC* correspond to a higher "energy" level, the cyan ZVSs in Figure 5.20 are associated with trajectories that are more "energetic" than L_4 and L_5.

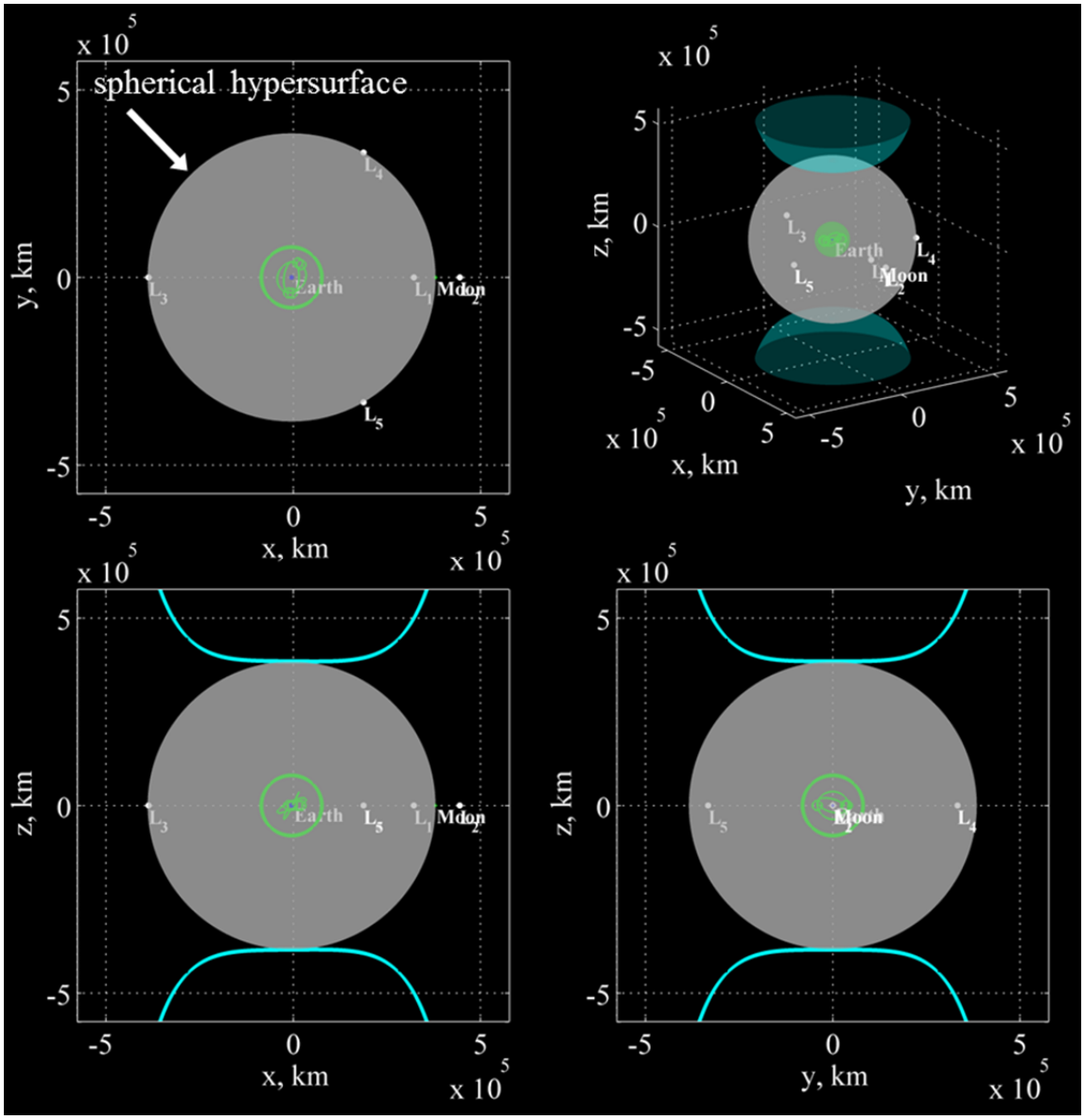

Figure 5.20. Four-perspective rotating view of spherical hypersurface (gray), higher-"energy" ZVSs (cyan), and lower-"energy" GEOs and ZVSs (green)

To determine an estimate for a S/C transfer path between the equatorial GEO and the polar GEO, with a maneuver implemented on the hypersurface depicted in Figure 5.20, a 4-D spherical phase space Poincaré map is generated at the higher "energy" level. The three spatial coordinates of the map are θ, $\dot{\theta}$, and φ, while the color coordinate is selected to be $\dot{\varphi}$. The origin of the map is effectively the Moon. The maps of the first returns of 360 trajectories originating from positions along the equatorial GEO in forward time and

the first returns of 360 trajectories originating from positions along the polar GEO in negative time are plotted at a single "energy" level in Figure 5.21. The 1-D "wave" plotted with large dots is formed by the trajectories departing from the equatorial GEO,

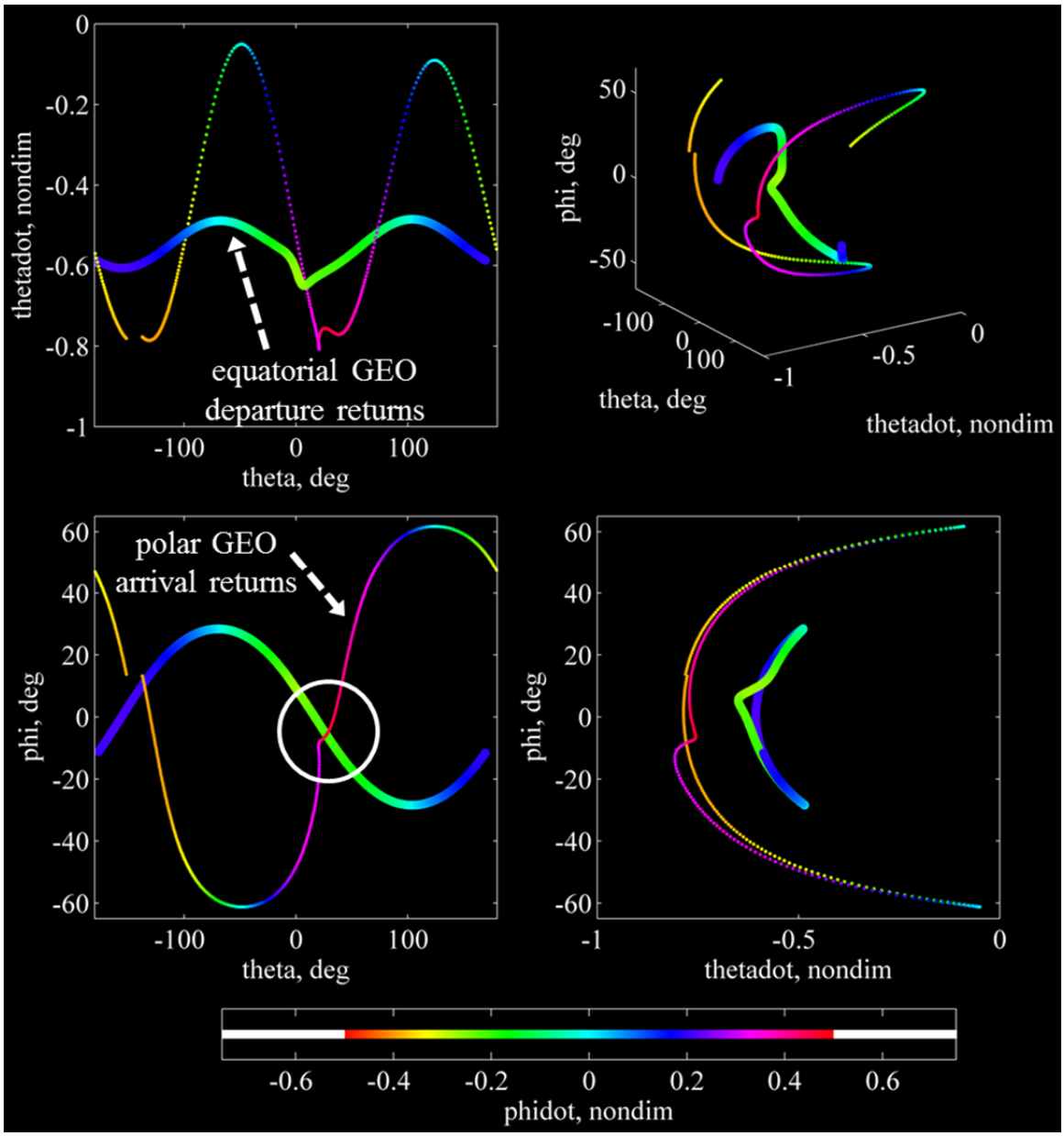

Figure 5.21. Four-perspective view of GEO-to-GEO transfer design space; spherical phase space Poincaré map; equatorial GEO departure forward time returns and polar GEO arrival negative time returns at same "energy;" ($\rho = 1+;\ \theta,\ \dot{\theta},\ \varphi,\ \dot{\varphi}\_color$)

with the initial conditions spaced in 1° increments of true longitude l during the following one period after the initial epoch. Similarly, the "wave" plotted with small dots is formed by the trajectories arriving to the polar GEO, with the initial conditions spaced in 1° increments of argument of latitude u during the one period before the final epoch. Each initial condition is generated based on a departure or arrival maneuver that is tangential to the S/C velocity $\vec{V}$ with respect to the Earth-centric inertial frame and such that the departure or arrival path is at the higher "energy" level.

Similar to the design process employed for 4-D manifold maps (see Sections 4.4 and 5.1.2), an estimate for the GEO-to-GEO transfer path is obtained by visual inspection of the map returns in Figure 5.21 through analysis of the region of intersection identified by the circle in the θ-φ view. First, an estimate for the θ-φ position of an intersection between the two "wave" structures is obtained. Next, the estimated position intersection is used to estimate the components of S/C velocity $\vec{V}$ that exist for each 1-D structure at that position. Estimates for the velocity adjustments in $\dot{\theta}$ and $\dot{\varphi}$ are obtained visually, while the associated velocity adjustment in $\dot{\rho}$ is simply calculated based on the "energy" level of the one-sided map. This process (with further details not depicted) yields a reasonable guess for both a forward and a negative time solution that form a S/C path between the equatorial GEO and the polar GEO. The region of intersection identified by the circle in Figure 5.21 actually represents one of two such intersections between the "wave" structures in the θ-φ view. The circled region is selected (as opposed to the other option) based on the "kink" that is visible in both wave structures near this position intersection. The "kink" in polar arrival returns is evident in all three side views. Although the "kink" in equatorial departure returns is not noticeable in the θ-φ view, it is prominent in the θ-$\dot{\theta}$ and $\dot{\theta}$-φ views, providing another reminder of the importance of realizing these higher-D map structures as full 4-D objects. This "kink" provides a unique visual indication that the effect of the CR3BP dynamics—namely, the addition of the Moon's gravity—is to warp the flat orbit plane geometry of what are nominally equatorial and polar-inclination trajectories with respect to the Earth-centric 2BP. Moreover, this significant warping effect provides a visual cue that the GEO-to-GEO transfer $\left|\overrightarrow{\Delta V}\right|$ might be reduced by exploiting lunar gravity. Given that the circled

position intersection in Figure 5.21 is relatively close to the origin of the map, which is the location of the Moon (with $\theta = \varphi = 0$ and $\rho = 1$), it is clear that this lunar-orbit-altitude intersection between the warped orbit planes actually occurs near the Moon itself. Thus, the arbitrarily selected epochs and GEO orbital elements—along with the assumed departure and arrival maneuvers that are tangential to the S/C velocity $\vec{V}$ with respect to the Earth-centric inertial frame—happen to allow for the possibility of a close lunar flyby in this example.

Further visual inspection of the 4-D map plotted in Figure 5.21, by zooming in spatial and color dimensions and annotating returns with trajectory numbers and return counters, reveals that the intersection identified by the circle is associated with an equatorial GEO departure at true longitude $l = 216°$ (at a time equal to 14.4 hours after the initial epoch) and a polar GEO arrival at argument of latitude $u =$ -172° (at a time equal to 11.4 hours before the final epoch). To ultimately obtain a precise, locally-optimal solution for the GEO-to-GEO transfer between these specified arrival and departure locations, it is first necessary to feed the transfer guess visually obtained from the Poincaré map into an automated targeting process. This corrections process is accomplished using single shooting (see Section 2.2) for each half of the transfer (i.e., the transfer path between the hypersurface maneuver and each GEO), with the goal of obtaining a three-maneuver transfer between the selected equatorial GEO departure ($l = 216°$) and polar GEO arrival ($u =$ -172°) locations. Although these targeted departure and arrival maneuvers along the GEOs are constrained to be implemented at the selected locations, they are not constrained to be tangential to the S/C velocity $\vec{V}$ with respect to the Earth-centric inertial frame as is the original assumption used to generate the various departure and arrival trajectories associated with the Poincaré map. The second (middle) maneuver is assumed to be implemented at the selected position on the original hypersurface ($\rho = 1$) and constrained to maintain the same "energy" level as the map. The targeted three-maneuver transfer sequence is accomplished with a total $\left|\overrightarrow{\Delta V}\right|$ = 2.99 km/s and a transfer time-of-flight of 12.5 days, however this solution is still *not*, in and of itself, a feasible solution for the GEO-to-GEO transfer required in this design scenario. Even though the targeted solution is a precise S/C path between the GEO departure and arrival locations as

expressed in the rotating frame of the CR3BP, the time-of-flight between the departure and arrival maneuvers is not consistent with the required twelve-day time-of flight between starting and ending GEO reference states, which are defined based on initial and final epochs spaced twelve days apart in time. Because the equatorial GEO departure occurs roughly 14.4 hours after the initial epoch and the polar GEO arrival occurs roughly 11.4 hours before the final epoch, the S/C time-of-flight between departure and arrival maneuvers must be equal to 10.9 days (precisely 10.925166156091864 days) so that the GEO-to-GEO transfer solution in the CR3BP is properly "anchored" in the higher-fidelity, ephemeris-based model.

To obtain a feasible and locally-optimal solution for a transfer between the equatorial and polar GEOs, the targeted three-maneuver transfer is fed into an automated optimization process where the cost function to be minimized is the total $\left|\overrightarrow{\Delta V}\right|$ of the three-maneuver transfer between the selected GEO departure and arrival locations. As in the optimization processes employed in other examples, key assumptions useful in the earlier steps in the map-based design process are now removed to achieve greater flexibility in the automated process of reducing the total $\left|\overrightarrow{\Delta V}\right|$. The second (middle) maneuver is no longer assumed to be implemented at the original hypersurface ($\rho = 1$), nor is it constrained to be "energy"-maintaining. However, most critically, an additional constraint is added to require that the time-of-flight between the (first) departure and (third) arrival maneuvers is precisely 10.925166156091864 days, so as to yield a feasible solution with a total time-of-flight of twelve days between the starting and ending GEO reference states.

The optimized three-maneuver transfer is plotted in the 3-D rotating view in Figure 5.22. The 3-D Earth-centric inertial view appears in Figure 5.23, which also includes the path of the Moon during each leg of the transfer. The resulting 3-D S/C path between the selected GEO departure and arrival locations is locally optimal in total $\left|\overrightarrow{\Delta V}\right|$, with the optimality tolerance (based on the KKT conditions) set so as to consider further reductions in $\left|\overrightarrow{\Delta V}\right|$ on the order of mm/s to be negligible. The optimized S/C transfer sequence begins with an "energy"-raising maneuver, with $\left|\overrightarrow{\Delta V}\right|$ = 1.37 km/s, to depart the

equatorial GEO at true longitude $l = 216°$. An "energy"-raising second maneuver, with $|\overrightarrow{\Delta V}|$ = 120.82 m/s, is implemented 3,958 km above lunar orbit altitude at a time equal to 3.8 days subsequent to the first maneuver. The closest S/C approach to the Moon is only 9,569 km altitude. The "energy"-lowering third maneuver, with $|\overrightarrow{\Delta V}|$ = 1.07 km/s, completes the transfer into the polar GEO, arriving at argument of latitude $u = -172°$, and is implemented at a time equal to 7.1 days subsequent to the second maneuver. Thus, the time-of-flight between the first and third maneuvers is 10.9 days as required by the constraint, making the total time-of-flight between starting and ending GEO reference

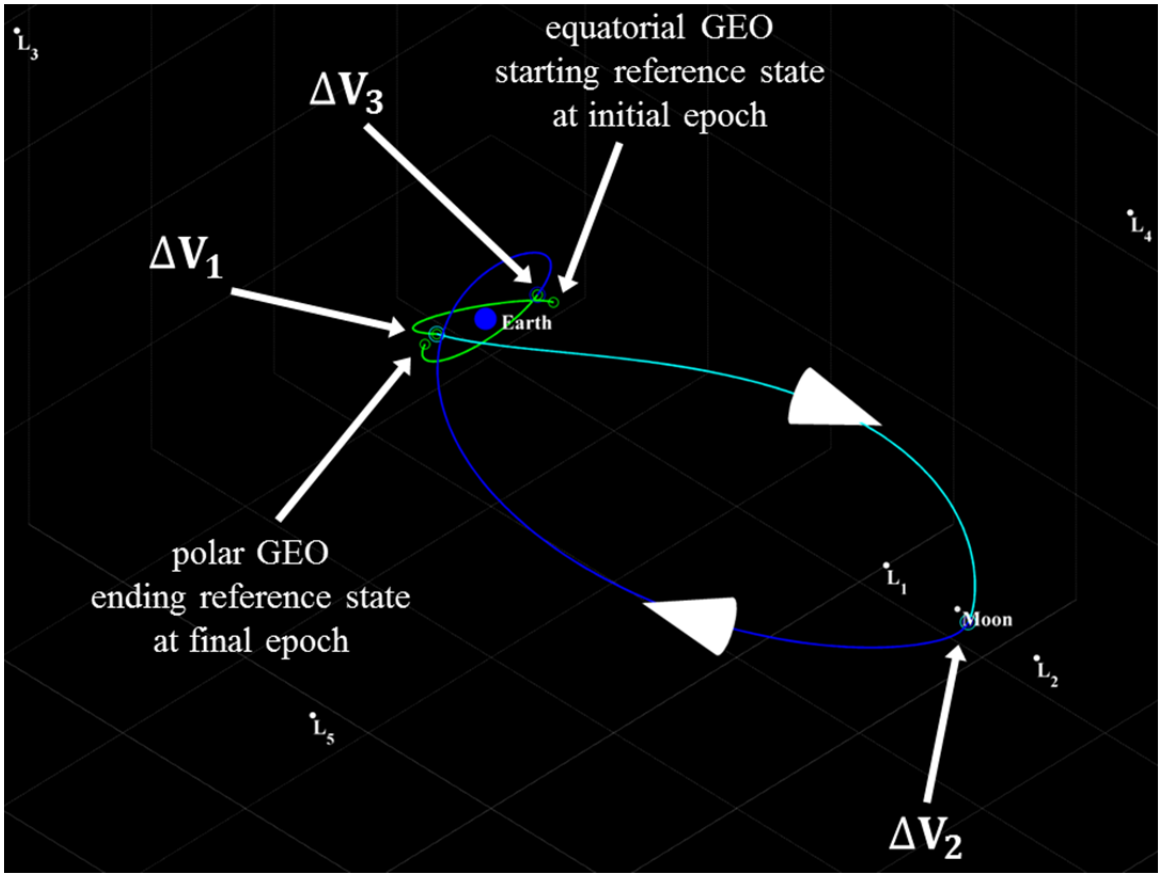

Figure 5.22. Rotating view of optimized GEO-to-GEO transfer solution; locally-optimal three-maneuver transfer between equatorial GEO and polar GEO; before first maneuver (green), after first maneuver (cyan), after second maneuver (blue), and after third maneuver (green)

states equal to twelve days. Note that the starting and ending GEO reference states do not share the same exact position in the inertial view in Figure 5.23. The reason for this is that these states are defined based on the equatorial and polar GEO orbital elements listed in Table 5.3 as applied to two different ephemeris data epochs. These different positions in the simplified CR3BP inertial frame actually represent the *same* position in the Earth-centric mean equatorial reference frame.

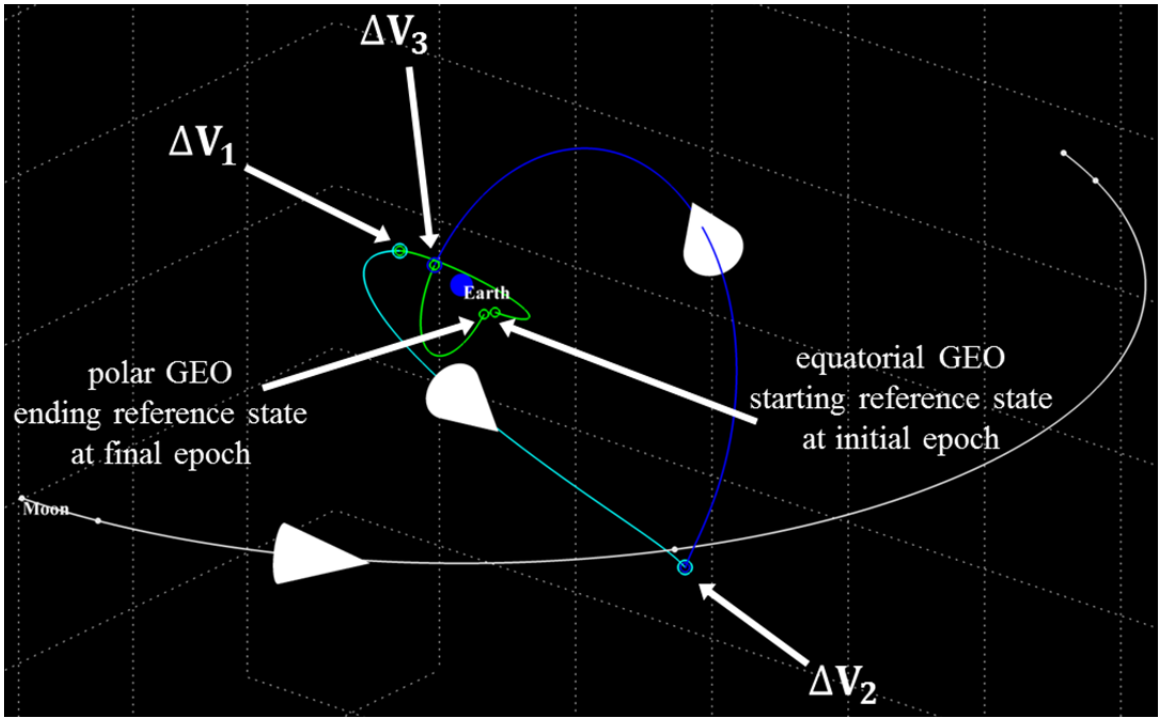

Figure 5.23. Earth-centric inertial view of optimized GEO-to-GEO transfer solution; locally-optimal three-maneuver transfer between equatorial GEO and polar GEO; before first maneuver (green), after first maneuver (cyan), after second maneuver (blue), and after third maneuver (green)

The CR3BP transfer maneuver sequence plotted in Figure 5.23 is accomplished with a total $\left|\overrightarrow{\Delta V}\right|$ = 2.56 km/s. For comparison, the $\left|\overrightarrow{\Delta V}\right|$ required is 7% less than that of the 2BP bi-elliptic-transfer ($\left|\overrightarrow{\Delta V}\right|$ = 2.75 km/s) depicted in Figure 5.18. As an additional point of comparison, it is possible to design a variation on the bi-elliptic transfer involving a powered lunar flyby, which is modeled in the Earth-centric 2BP except when the S/C is in the vicinity of the Moon, where the Moon-centric 2BP is used instead.

Based on the patched-conic approximation [10], the GEO-to-GEO transfer path in the Earth-centric inertial frame is the same as for the bi-elliptic transfer in Figure 5.18. However, it is assumed that the apogee of the equatorial transfer ellipse perfectly intersects the position of the Moon at the ascending node of the Moon's orbit. In that case, instead of performing a 90° plane change at the altitude of the Moon's orbit (with $\left|\overrightarrow{\Delta V}\right| = 640.3$ m/s), a smaller maneuver—modeled in the Moon-centric 2BP—can be implemented along the Moon-centric hyperbolic flyby trajectory at a perilune altitude of 11,671 km. In this idealized scenario, which serves only to approximate maneuver costs, the powered flyby maneuver requires $\left|\overrightarrow{\Delta V}\right| = 160.4$ m/s, making the overall transfer require only $\left|\overrightarrow{\Delta V}\right| = 2.27$ km/s. It is interesting to note that the required $\left|\overrightarrow{\Delta V}\right|$ for the CR3BP transfer maneuver sequence (plotted in Figures 5.22 and 5.23) is only 13% larger than that required for the powered lunar flyby. Moreover, the second (middle burn) for the CR3BP transfer, which is implemented at 11,822 km lunar altitude, actually requires 25% less $\left|\overrightarrow{\Delta V}\right|$ than the powered flyby.

The second (middle) maneuver in the optimized GEO-to-GEO transfer sequence plotted in Figure 5.23 requires a relatively small $\left|\overrightarrow{\Delta V}\right|$ = 120.82 m/s (compared to the total transfer $\left|\overrightarrow{\Delta V}\right|$ = 2.56 km/s), indicating the possibility of determining a reasonable *two-maneuver* transfer sequence. Therefore, the optimized three-maneuver transfer result is next used as an initial guess to initiate a new optimization process, where the new cost function to be minimized is the total $\left|\overrightarrow{\Delta V}\right|$ of a two-maneuver transfer. The second (middle) maneuver in the vicinity of the Moon is removed by enforcing velocity continuity at the patch point previously associated with that maneuver, while all other constraints/assumptions are identical to those used to obtain the optimized three-maneuver transfer. The result of this new optimization process appears in Figure 5.24 in the 3-D rotating view and in Figure 5.25 in the 3-D Earth-centric inertial view. The equatorial GEO departure maneuver (departing at the same location as before) is "energy"-raising, with $\left|\overrightarrow{\Delta V}\right|$ = 1.44 km/s, and the polar GEO arrival maneuver (arriving at the same location as before) is "energy"-lowering, with $\left|\overrightarrow{\Delta V}\right|$ = 1.49 km/s. Thus, the

optimized two maneuver sequence is accomplished with a total $\left|\overrightarrow{\Delta V}\right|$ = 2.93 km/s, a 14% increase over the optimized three-maneuver sequence. The time-of-flight between the two maneuvers is still 10.9 days as required by the constraint; therefore, the total time-of-

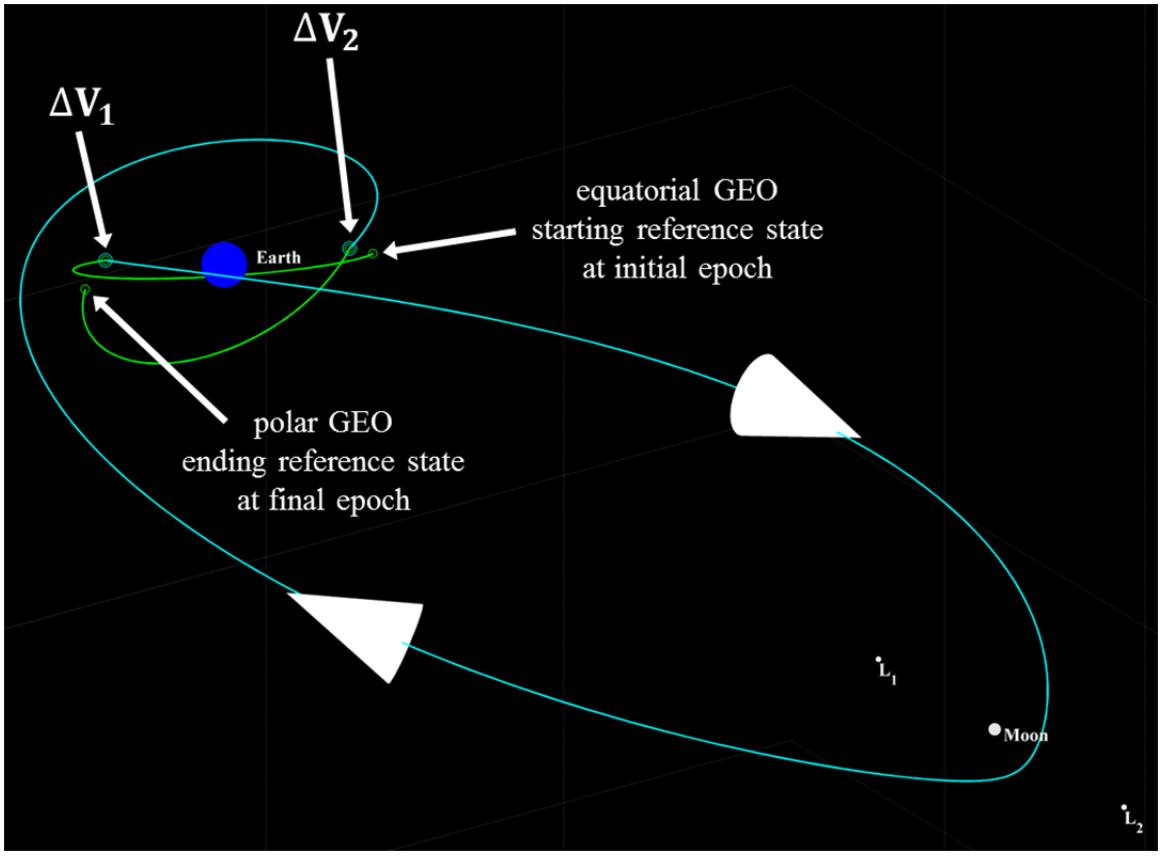

Figure 5.24. Rotating view of optimized GEO-to-GEO transfer solution; locally-optimal two-maneuver transfer between equatorial GEO and polar GEO; before first maneuver (green), after first maneuver (cyan), and after second maneuver (green)

flight between starting and ending GEO reference states remains equal to twelve days. With a closest S/C approach to the Moon of only 11,544 km altitude, the Moon's gravity is heavily exploited in reducing transfer $\left|\overrightarrow{\Delta V}\right|$ without the need for a lunar-orbit-altitude maneuver; the natural CR3BP dynamics of the lunar flyby "performs" most of the 90° plane change required in this GEO-to-GEO transfer scenario. A comparison of the two-maneuver transfer depicted in Figures 5.24 and 5.25 with the result of a similar map-based design process for a transfer that is *not* a close lunar flyby demonstrates the benefit

of a close flyby in terms of transfer $\left|\overrightarrow{\Delta V}\right|$. For instance, if the other region of "wave" structure intersection apparent in the θ-φ view of the 4-D map plotted in Figure 5.21 is

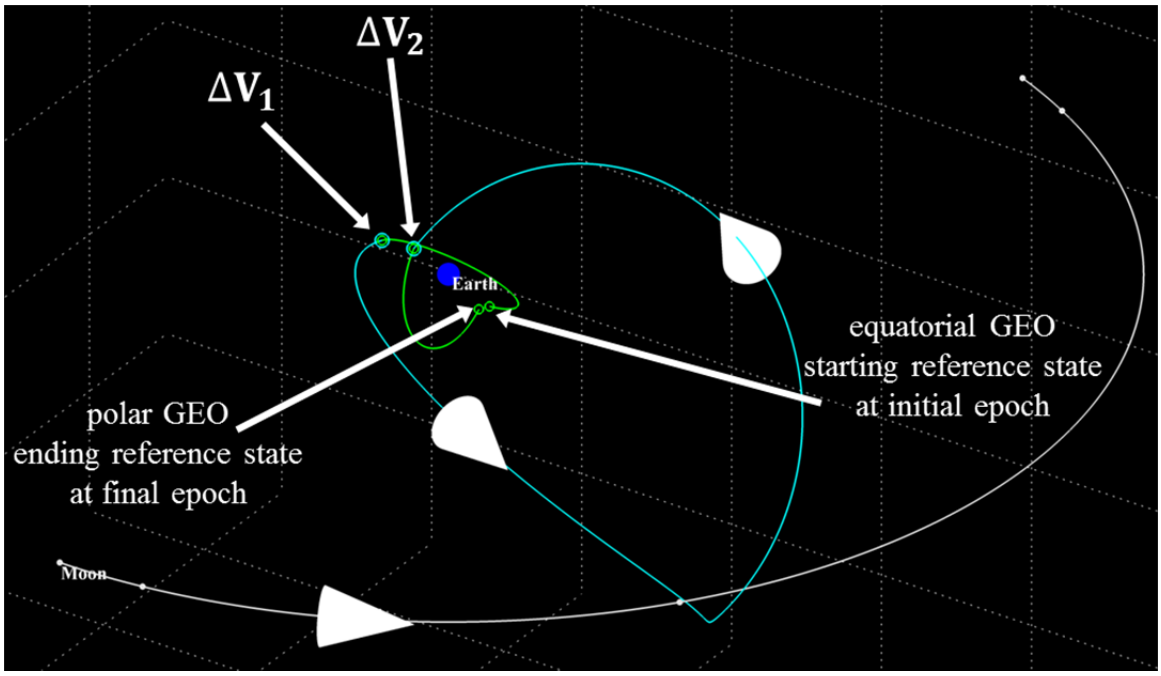

Figure 5.25. Earth-centric inertial view of optimized GEO-to-GEO transfer solution; locally-optimal two-maneuver transfer between equatorial GEO and polar GEO; before first maneuver (green), after first maneuver (cyan), and after second maneuver (green)

used to obtain an estimate for a GEO-to-GEO transfer, similar targeting and optimization processes ultimately yield a two-maneuver transfer solution that reaches almost to (7,576 km below) lunar orbit altitude but which does not involve a close lunar flyby. This two-maneuver transfer requires a prohibitive $\left|\overrightarrow{\Delta V}\right|$ = 6.37 km/s.

The three-maneuver and two-maneuver GEO-to-GEO transfer sequences (plotted in Figures 5.22 through 5.25) complete the Poincaré-map-based design process for Design Example #6. The map-based method for obtaining an initial estimate for the S/C transfer path is both numerical and visual. The numerical component is the trajectory propagation required to generate the map, while the visual component is the human interpretation of the 4-D map in the visual environment. Of course, follow-on, automated processes (i.e., targeting, optimization, and transitions to other dynamical models) are also numerical in

nature. Another aspect of this 4-D-map-based design method for obtaining an estimate is that it is focused on the CR3BP from the outset. Although the GEOs are modeled in the Earth-centric 2BP, the Earth-Moon CR3BP is used as the basis for obtaining a reasonable guess for the S/C path between GEOs, which is then fed into automated processes to determine a precision solution also in the CR3BP.

The three-maneuver ($\left|\overrightarrow{\Delta V}\right|$ = 2.56 km/s) and two-maneuver ($\left|\overrightarrow{\Delta V}\right|$ = 2.93 km/s) GEO-to-GEO transfer solutions in this example, although currently impractical, may be possible in a futuristic scenario involving an urgent tasking and the availability of fuel reserves and/or an on-orbit refueling capability. Considering the following: (1) injection into a geostationary orbit from a typical, 28°-inclination GTO requires an apogee "kick" of roughly $\left|\overrightarrow{\Delta V}\right|$ = 1.8 km/s, and (2) that the approximate orbit-maintenance requirements of a S/C in geostationary orbit is $\left|\overrightarrow{\Delta V}\right|$ = 50 m/s per year [134], it is not unreasonable to imagine a futuristic GEO satellite retaining a large empty fuel tank capable of being refueled to allow a new $\left|\overrightarrow{\Delta V}\right| \cong$ 2-3 km/s. Obviously, the 90° plane change assumed in this scenario represents an extreme case; smaller plane changes in a similar mission scenario would likely be accomplished with significantly less $\left|\overrightarrow{\Delta V}\right|$. As a point of reference, in 1998, the commercial communications satellite AsiaSat-3/HGS-1 was rescued from a highly-eccentric, 51°-inclination orbit (after a failed GTO apogee "kick" maneuver) by means of two lunar flybys, which placed the satellite into an 8°-inclination GEO for a total transfer of almost $\left|\overrightarrow{\Delta V}\right|$ = 2 km/s [135].

For additional perspective on the value of the map-based and CR3BP-focused method, the results for Design Example #6 are compared with those obtained through more traditional, 2BP-focused design methods. The comparison is in the time required to obtain solutions as well as in the transfer $\left|\overrightarrow{\Delta V}\right|$ for the final, optimized results. To allow for an "apples-to-apples" comparison between a 2BP-focused method and the CR3BP-focused method, bi-elliptic transfers (of the type depicted in Figure 5.18) are considered. Two bi-elliptic transfer options, propagated in the Earth-centric 2BP, are determined analytically based on the principle that the lunar-orbit-altitude apogee maneuver is implemented along the line of intersection between the equatorial and polar GEO orbit

planes at the initial epoch. Note that this is the basic principle underlying the search for position intersections between the "wave" structures on the 4-D map plotted in Figure 5.21. However, on the map, the effect of the CR3BP dynamics is to warp the flat orbit plane geometry of what are nominally equatorial and polar-inclination trajectories with respect to the Earth-centric 2BP. The two transfer options available based on the map are associated with the two position intersections between "waves" in the θ-φ view. In the 2BP-focused analysis, the two bi-elliptic transfer options in the scenario are associated with equatorial GEO departures at true longitudes $l = 0°$ or $l = 180°$. These two-body transfer ellipse options are then used as guesses to initiate the same type of targeting and optimization processes—still modeled in the CR3BP—employed for the CR3BP-focused analysis.

A comparison of the human analysis time and MATLAB® computational times required to determine three-maneuver and two-maneuver transfer solutions appears in Table 5.4. Overall, the 4-D-map-based process is accomplished in roughly 2.5 hours, while the traditional, 2BP-focused process requires only one quarter of that time. An initial impression of this time comparison is that the 2BP-focused process is more efficient. However, the efficiency of a design method must be considered in the context of the quality of the solutions computed. As indicated in Table 5.4, almost half of time required for the map-based process is devoted to optimizing the three-maneuver solution for transfer "Option #1" (72.4 minutes), which is the close lunar flyby option (with minimum lunar altitude of 9,569 km) associated with the circled region in Figure 5.21 and plotted in Figures 5.22 and 5.23. This locally-optimal transfer result requires a total $\left|\overrightarrow{\Delta V}\right|$ = 2.56 km/s. On the other hand, the optimization task for the 2BP-focused design process for "Option #1" requires only 0.4 minutes but results in a locally-optimal solution in the CR3BP with a total $\left|\overrightarrow{\Delta V}\right|$ = 2.88 km/s and a S/C path with a much larger minimum lunar altitude of 86,728 km. Thus, in this case, the fact that the optimization task for the map-based process takes longer is actually evidence of its *superiority* over the 2BP-focused method. The automated process of reducing total transfer $\left|\overrightarrow{\Delta V}\right|$ requires more time in the map-based process because that CR3BP-focused process yields what is essentially a better guess, i.e., a guess that can be used to determine a lower-$\left|\overrightarrow{\Delta V}\right|$ local

minimum after more lengthy calculations. The "kinked" position intersection between the "wave" structures on the 4-D map plotted in Figure 5.21 provides an estimate for a close lunar flyby where the Moon's gravity is heavily exploited to reduce $\left|\overrightarrow{\Delta V}\right|$ by 11% as

Table 5.4 Comparison of human and computation* times for Design Example #6

Design task	Time using guesses from 2BP bi-elliptic transfers (minutes)	Time using guesses from CR3BP & 4-D Poincaré map (minutes)
Generate map	N/A	5.8
Obtain guesses analytically (human)	~15	N/A
Obtain guesses visually (human)	N/A	~64
Target in CR3BP	1.8	1.2
Optimize Option #1, 3 burns	0.4	72.4
Optimize Option #1, 2 burns	2.9	0.4
Optimize Option #2, 3 burns	6.8	0.9
Optimize Option #2, 2 burns	2.0	1.4
Miscellaneous (some human)	~10	~10
Total	~39	~156

* Elapsed time in MATLAB® Version: 7.14.0.739 (R2012a);
benchmark: 0.0600, 0.0637, 0.0741, 0.1641, 0.2727, 0.7146

compared to the traditional method. In other words, the map-based process yields a guess that is sufficiently close to a preferred local minimum in the optimization design space (associated with a close lunar flyby), while the traditional process does not. An even more significant benefit of the 72.4-minute process used to determine a locally-optimal three-maneuver result in the map-based process is realized when that three-maneuver result is fed into the optimization process that yields a two-maneuver solution. The

locally-optimal two-maneuver result (plotted in Figures 5.24 and 5.25) requires a total $\left|\overrightarrow{\Delta V}\right|$ = 2.93 km/s. On the other hand, the 2BP-focused design process results in a locally-optimal transfer solution in the CR3BP requiring a prohibitive $\left|\overrightarrow{\Delta V}\right|$ = 6.23 km/s, more than twice that required for the result of the CR3BP-focused process. The $\left|\overrightarrow{\Delta V}\right|$ requirements for the lowest-cost three-maneuver option and lowest-cost two-maneuver option resulting from the two design processes are summarized in Table 5.5 along with the cost of the original estimates used in each process.

Table 5.5 Comparison of total transfer maneuver $\left|\overrightarrow{\Delta V}\right|$ for Design Example #6

Guess based on	Guess 3-burn $\left\|\overrightarrow{\Delta V}\right\|$ (km/s)	Optimized 3-burn / 2-burn CR3BP $\left\|\overrightarrow{\Delta V}\right\|$ (km/s)
CR3BP & 4-D Poincaré map	2.99	2.56 / 2.93
2BP bi-elliptic transfer	2.75	2.88 / 6.23

The comparison values included in Tables 5.4 and 5.5 indicate that the 4-D-map-based and CR3BP-focused design process, though requiring more time, achieves GEO-to-GEO transfer results (in this example) that are superior to those determined through a more traditional, 2BP-focused design process. The map-based process not only yields lower-$\left|\overrightarrow{\Delta V}\right|$ solutions for both a three-maneuver and a two-maneuver transfer, but it also is the only process that leads to a practical two-maneuver option. In fact, even when an additional 2BP-focused method is considered, the map-based process still compares favorably. Another 2BP-focused method for determining a two-maneuver GEO-to-GEO transfer is the solution to Lambert's problem [9], where the S/C path between the departure and arrival locations along each GEO is assumed to be a single conic arc. By solving for the Lambert transfer arc between various combinations of possible departure and arrival locations on the two GEOs—while also requiring that each particular transfer time-of-flight be consistent with the twelve-day duration between starting and ending GEO reference states in this scenario—a search over 260,632 Lambert arcs yields a

minimum two-maneuver $\left|\overrightarrow{\Delta V}\right|$ = 5.83 km/s for a transfer modeled entirely in the Earth-centric 2BP. Interestingly, when this two-body Lambert solution is used as a guess to initiate targeting and optimization processes in the CR3BP, the locally-optimal two-maneuver result is identical (to within the optimality tolerance) to that obtained using the bi-elliptic transfer "Option #1" as the initial guess, with $\left|\overrightarrow{\Delta V}\right|$ = 6.23 km/s. Yet, the Lambert transfer design process, which is both analytical and numerical, takes twenty-one minutes longer than the bi-elliptic transfer process.

Although the 4-D-map-based design process yields significantly lower-$\left|\overrightarrow{\Delta V}\right|$ GEO-to-GEO solutions than traditional, 2BP-focused processes in this particular example, it can certainly not be claimed that such benefits would be achieved in all problems. The benefits of any design method are problem-dependent and sensitive to the assumptions made in each design scenario. In this scenario, the arbitrarily-selected GEO reference states and epochs result in a certain "warped" orbit plane geometry in the CR3BP such that one option for a lunar-orbit-altitude plane change maneuver can occur close to the Moon itself. The "kink" in the 4-D map provides a visual cue that the Moon's gravity may be exploited to significantly reduce $\left|\overrightarrow{\Delta V}\right|$ required for a transfer. Furthermore, the CR3BP-focused design process yields a more accurate guess to feed into an automated process to achieve a superior locally-optimal solution in the CR3BP. Yet, in general, what is clear from this design example is that the map-based process can expand the design options available for consideration. This expanded design space has the potential in other design scenarios, just as in this particular scenario, to reveal lower-$\left|\overrightarrow{\Delta V}\right|$ solutions not predicted by 2BP-focused design methods. Moreover, since the CR3BP is used from the outset in the map-based design process, the estimates obtained from the Poincaré map are expected to be more accurate and more qualitatively similar to the precise CR3BP solutions than estimates based on the 2BP (a lower-fidelity model).

As a final note for Design Example #6, in the future, more advanced implementations of the map-based design approaches employed in this design scenario might involve a more sophisticated visual environment that allows for a map-based designer to quickly survey a wider variety of available GEO-to-GEO transfer options based on multiple 4-D

maps defined over a range of hypersurface locations and "energy" levels. Furthermore, more interactive software tools of the type developed by Schlei [125, 126] could greatly reduce the time required for a map-based designer to visually obtain estimates from the higher-D Poincaré map.

5.3 Design Example #7: Capture/Transit/Departure Near Uranus's Moon Titania

In the final advanced, 4-D-map-based design scenario, a periapsis Poincaré map is used to locate a stable periodic orbit in the vicinity of Titania in the Uranus-Titania CR3BP (where the period of the primaries is roughly 8.7 days). This periodic orbit is then used as the basis for designing a capture maneuver for a Titania orbiter during the final phase of a plausible tour of the Uranian system. Contingency options for (1) transit without capture or (2) departure after capture are also incorporated into the mission design. The Uranus-centric and the Titania-centric two-body gravitational parameters are assumed to be equal to $GM_U = 5.793965663939 \times 10^6$ km^3/s^2 and $GM_T = 228.640601$ km^3/s^2, respectively. The Uranus-Titania CR3BP model parameters are as before (see again Table 4.1). For validation purposes, the results of the designed capture and transit paths are also transitioned to a higher-fidelity, ephemeris-based model.

The periapsis map hyperplane for Design Example #7 is defined in Titania-centered spherical coordinates as $\dot{\rho} = 0$ and $\ddot{\rho} > 0$. Following a process similar to that employed for Design Example #1 (see Section 4.1), to determine a S/C capture orbit in the vicinity of Titania, a 4-D periapsis Poincaré map is generated in forward time at a lower "energy" level associated with L_1, where the L_1 and L_2 gateways are closed. Next, to determine available S/C L_2 entry trajectories (entering the region of Titania though the L_2 gateway), another 4-D periapsis Poincaré map is generated in negative time at a higher "energy" level, where the L_1 and L_2 gateways are open. The ZVSs (and ZVCs) at the lower and higher "energy" levels are plotted in the four-perspective rotating view in the vicinity of Titania in Figures 5.26 and 5.27, respectively.

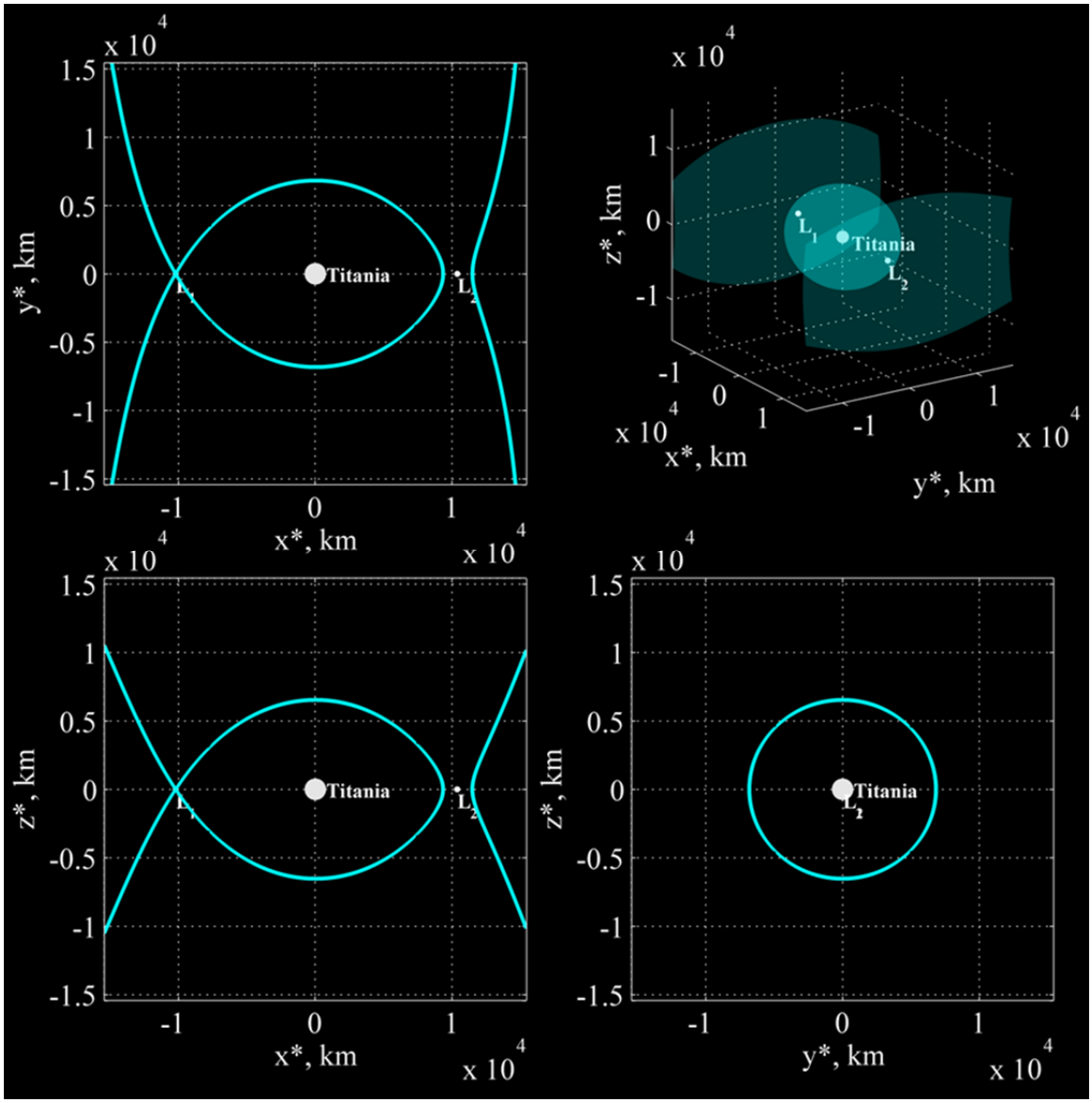

Figure 5.26. Four-perspective rotating view of ZVSs in the vicinity of Titania at lower "energy"

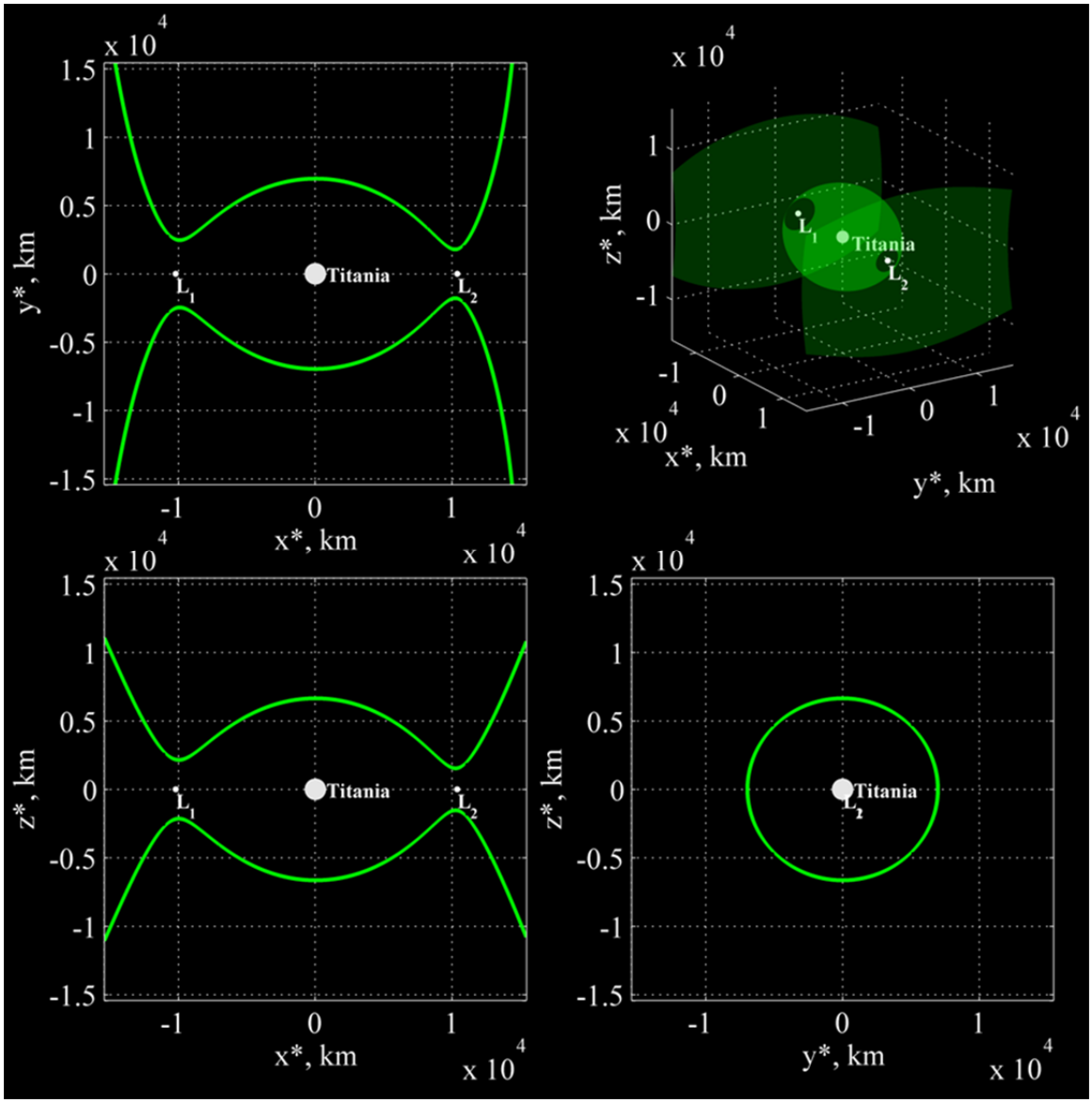

Figure 5.27. Four-perspective rotating view of ZVSs in the vicinity of Titania at higher "energy"

To begin the capture maneuver design process, a forward-time 4-D periapsis map is generated at the lower "energy" level associated with L_1, where all trajectories in the vicinity of Titania remain captured for all time. A set including 1,296 initial conditions is propagated forward in time for the following ten years or until an impact, whichever occurs sooner. The initial conditions are selected to be periapses at spherical radius $\rho = 0.12h$, where dimensional $h = l^*(\mu/3)^{1/3}$ =10,290 km is the approximate Hill

radius, which serves as a rough approximation for the radius of the accessible region in the vicinity of P_2 (Titania) at the lower "energy" level. These periapses are seeded based on a grid with 5° spacing in θ and φ along the surface of a hemisphere (on the positive y side of Titania) at the selected value of ρ, which translates to 446 km altitude above Titania. This method is an extension of the method employed by Craig Davis and Howell [34, 35] for 2-D periapsis maps where initial conditions are selected along a semicircle with cylindrical radius $r = 0.12h$ in the x-y plane. For a 4-D periapsis map, it is necessary to also select the velocity angle α for each initial condition. In this case, all initial conditions are seeded with velocity angle $\alpha = 0°$ so as to have planar prograde direction with respect to Titania in the rotating frame. Based on the concept discussed in Design Examples #1 and #2 (see Sections 4.1 and 4.2), near-planar prograde trajectories are expected to be more likely to enter or depart the vicinity of Titania if a libration point gateway is open. Yet, at the lower "energy" level associated with L_1, both gateways are closed; an increase in "energy" level is required to allow for entry or departure. The hemispherical grid of initial conditions is plotted on the 4-D periapsis map in Figure 5.28. The three spatial coordinates of the map display the 3-D periapse position (Cartesian x, y, z centered at Titania) of each initial condition on the hyperplane, while the color coordinate is selected to be velocity angle α. All initial conditions are plotted in cyan ($\alpha = 0°$) based on the seeding criteria. The Poincaré map of 543,816 returns generated by propagating the set of 1,296 initial conditions forward in time for ten years is plotted in Figure 5.29 after transitioning the image to Avizo®. Most map returns in Figure 5.29

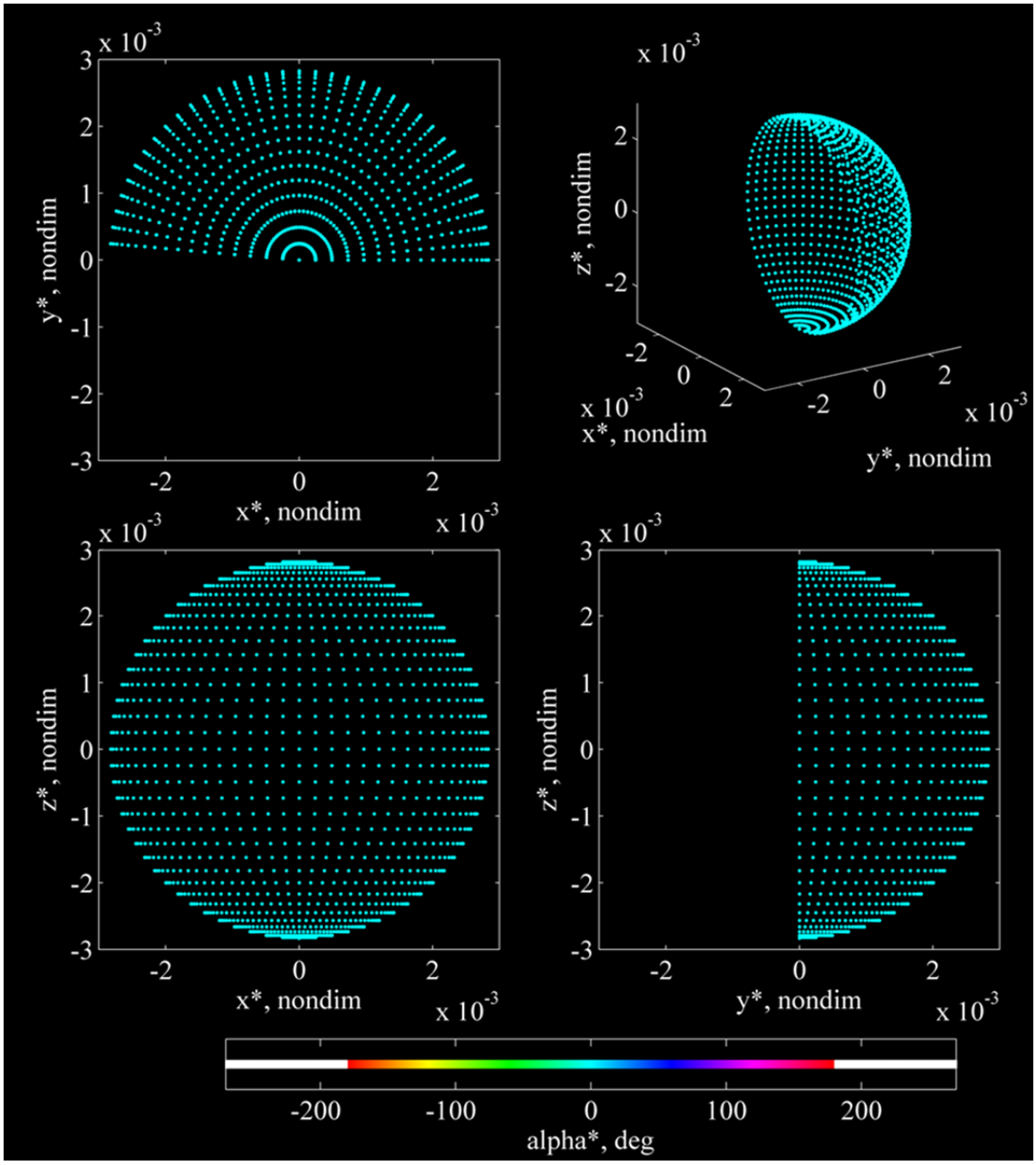

Figure 5.28. Periapsis Poincaré initial condition map in the vicinity of Titania; ($\dot{\rho} = 0+;\ x,\ y,\ z,\ \alpha\_color$)

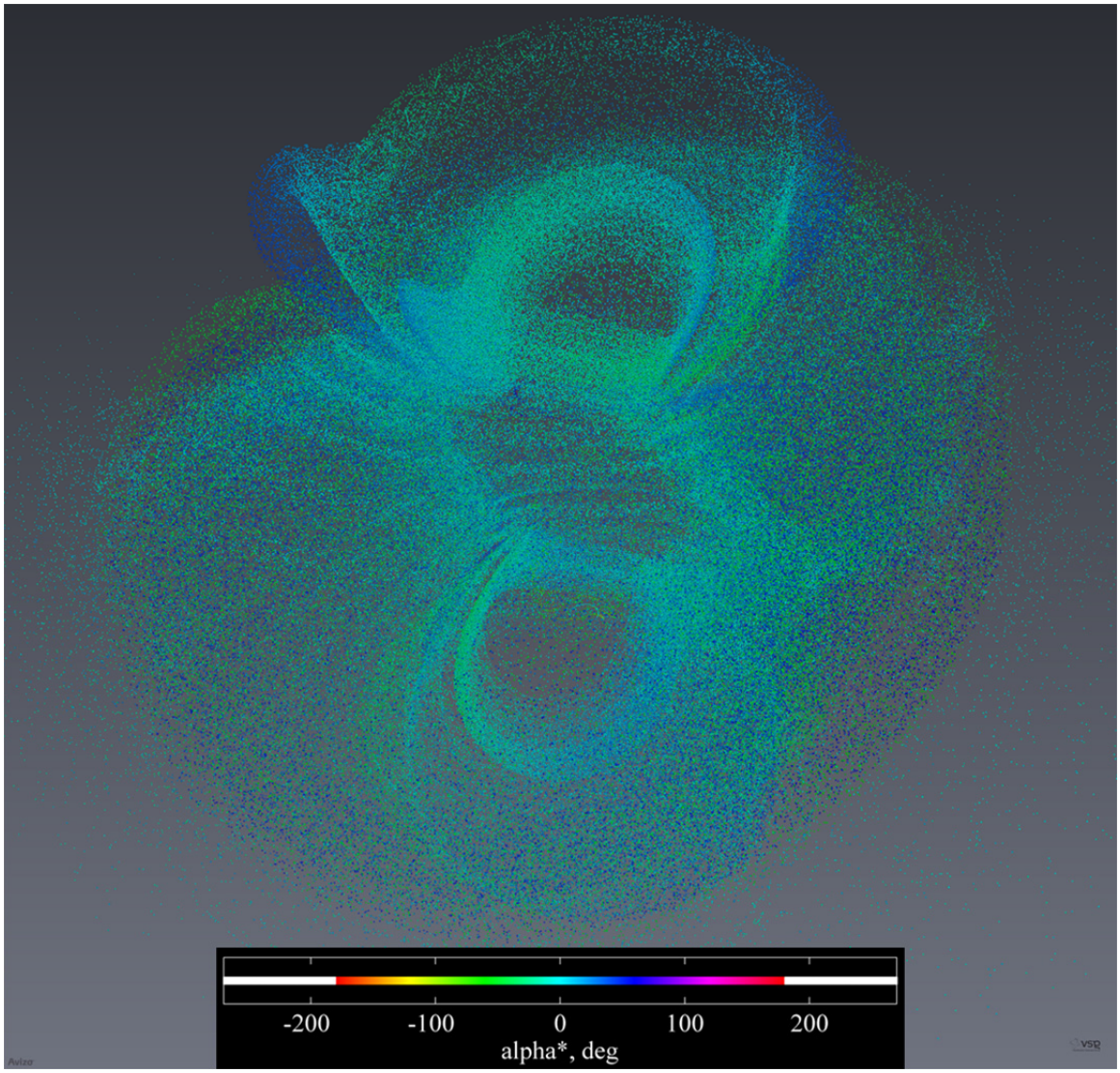

Figure 5.29. Avizo® view of 4-D periapsis Poincaré map (returns during following ten years at lower "energy") in the vicinity of Titania; ($\dot{\rho} = 0+;\ x,\ y,\ z,\ \alpha\_color$)

have prograde direction in the rotating frame, with the range of color between green and blue indicating velocity angles that are roughly in the range -90°$< \alpha <$ 90°. For the next step, to isolate map returns having near-planar prograde direction, a zoom in the map color coordinate restricts the limits of the color scale to the range -25°$< \alpha <$ 25°, with returns outside those limits filtered from view. The result of applying this new color scale—to the 4-D map plotted in Figure 5.29—appears in Figure 5.30.

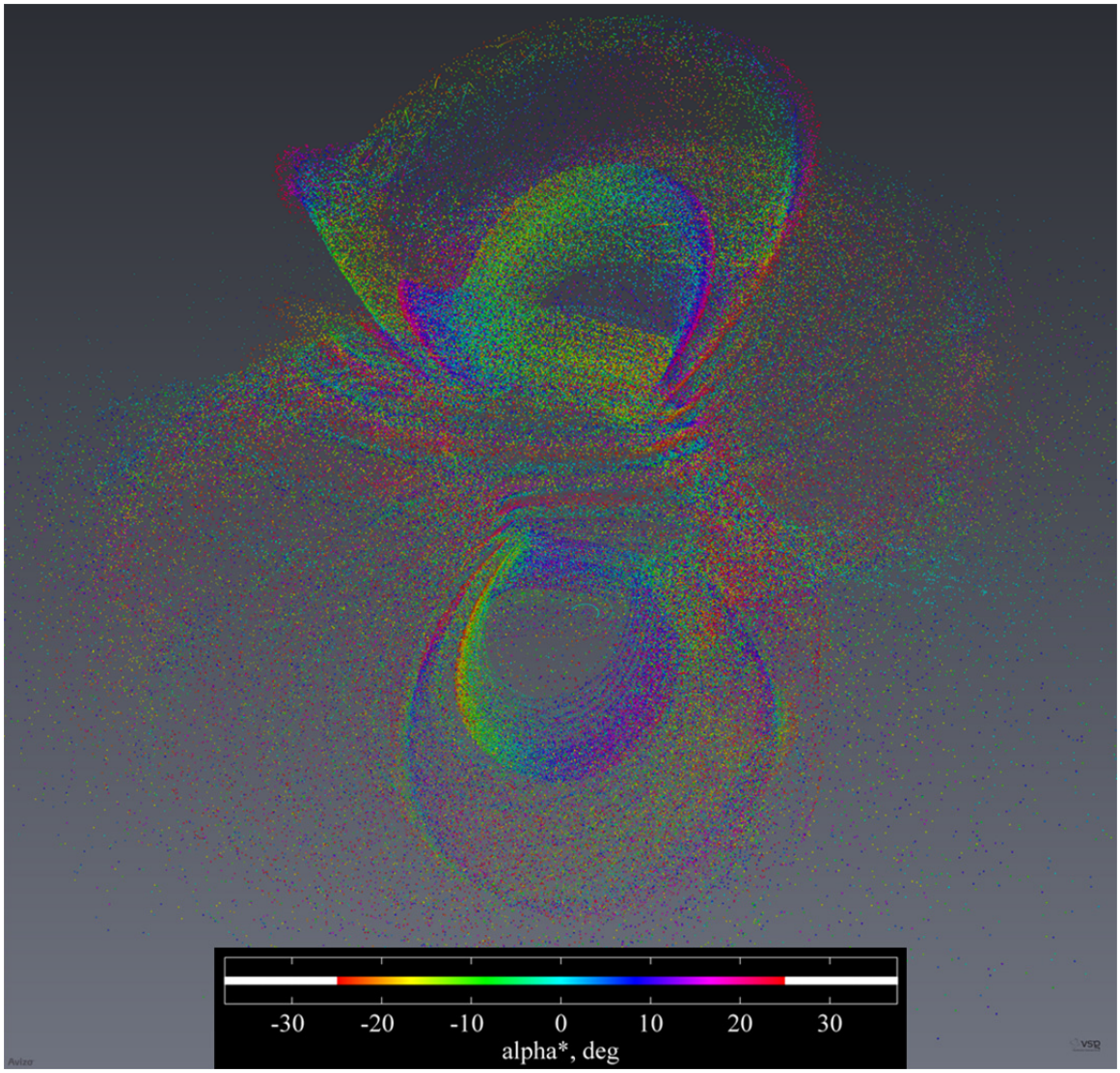

Figure 5.30. Avizo® view of 4-D periapsis Poincaré map (returns during following ten years at lower "energy") in the vicinity of Titania (zoomed and filtered in color); $(\dot{\rho} = 0+;\ x,\ y,\ z,\ \alpha\_color)$

The next step in the capture maneuver design process is to exploit tools within the visual environment to locate ""island"/"doughnut" structures associated with quasi-periodic motion (see Section 3.1.2) for the purpose of obtaining a reasonable guess for a periodic orbit, which can then be targeted precisely in an automated process. Through interactive filtering in the Avizo® visual environment, map structures formed by certain trajectories are identified visually from the 4-D map plotted in Figure 5.30. Techniques employed to locate these structures, which appear in Figure 5.31, include: (1) rotating

the map image; (2) zooming in spatial and/or color dimensions of the map, with the additional option of filtering any returns outside of the zoomed limits; (3) filtering returns by trajectory number so as to display only a few trajectories at a time; and (4) filtering returns by return counter or by time so as to control the number of returns displayed for any given trajectory. The eight regions containing the roughly figure-8-shaped, "rainbow"-patterned structures visible in Figure 5.31 form a 4-D map analog of a period-eight "island chain" on a 2-D Poincaré map. Also prominent is a cyan loop associated

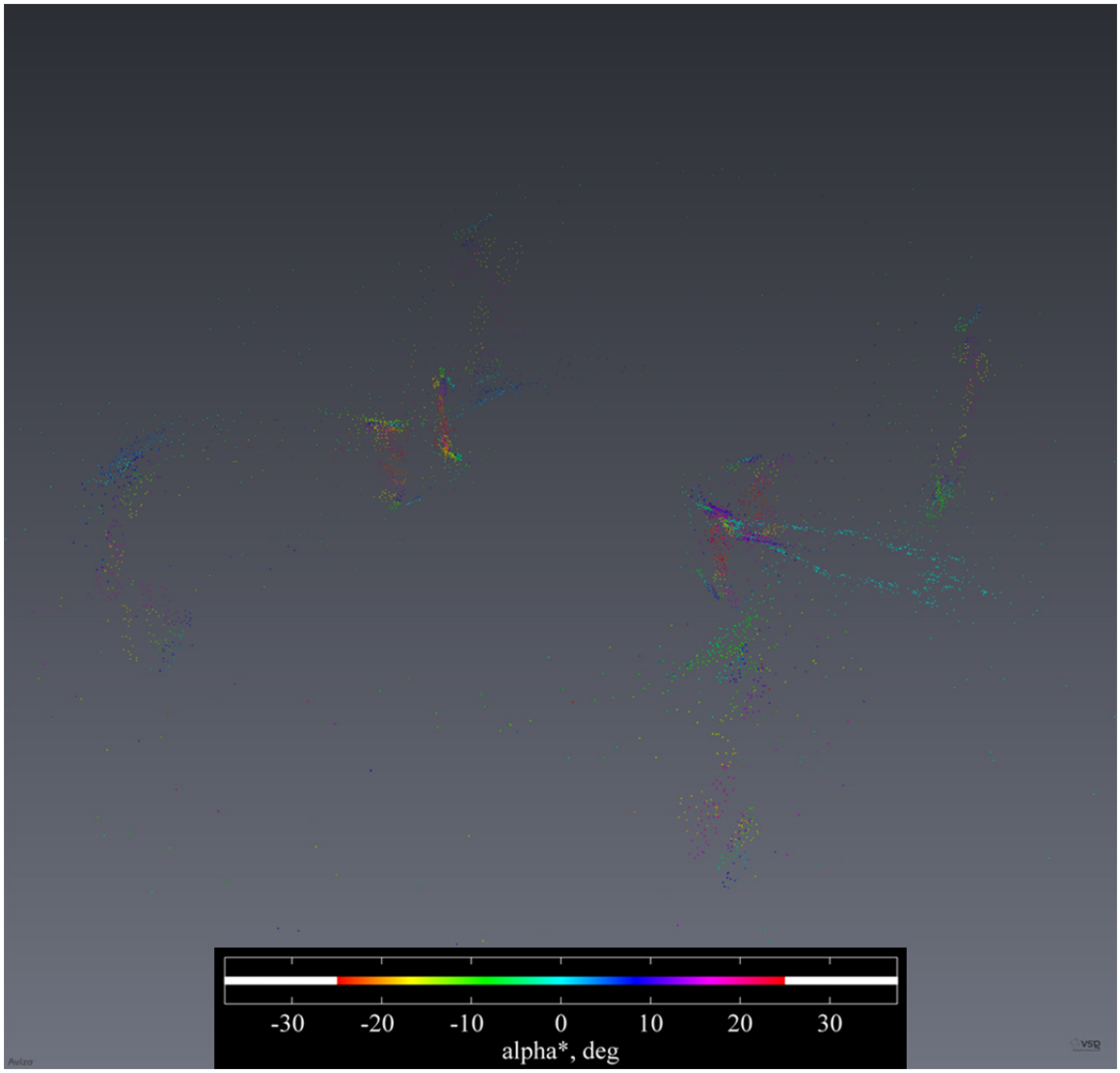

Figure 5.31. Avizo® view of 4-D periapsis Poincaré map structures identified through interactive filtering; ($\dot{\rho} = 0+;\ x,\ y,\ z,\ \alpha\_color$)

with quasi-periodic, planar motion (on the *x*-*y* plane). Reasonable guesses for periodic orbits associated with these structures are obtained by visual inspection (in the Avizo® visual environment) of the map along with interpolation in the empty spaces between map returns. This visual process results in an estimate for the x, y, z position and color value (representing velocity angle α) of a periapsis in the vicinity of a structure of interest. In addition, a guess for the period of a periodic trajectory associated with that periapse estimate is obtained by filtering in time to reveal the duration required for a trajectory associated with a structure to repeatedly generate map returns near a particular 4-D map location. That is, the time required for a nearly-period-one trajectory to generate a second map return close to a first map return offers an estimate for the period of the associated period-one trajectory. In general, for a nearly-period-*N* orbit, where integer $N \geq 1$, the time difference between the first and the (*N*+1)th map returns provides the estimate for the period.

To target various periodic trajectories, visual estimates based on the map structures plotted in Figure 5.31 are fed into a multiple shooting process, which results in the periodic solutions represented by the 4-D map returns in Figure 5.32. The returns associated with periodic trajectories are plotted with larger dots, while the original structures plotted in Figure 5.31 are also included with the same small dots as before. Different size larger dots are associated with different periodic trajectories, which are classified according to the labels and legend appearing in Figure 5.33. For instance, the medium-sized blue dot labeled "8N" is one of eight map returns associated with a 3-D, linearly stable, period-8 orbit around Titania. The other seven returns associated with this particular periodic orbit are the same size; note, however, that this Avizo® visual environment adjusts the apparent size of objects somewhat based on how far they are from the observer of the image.

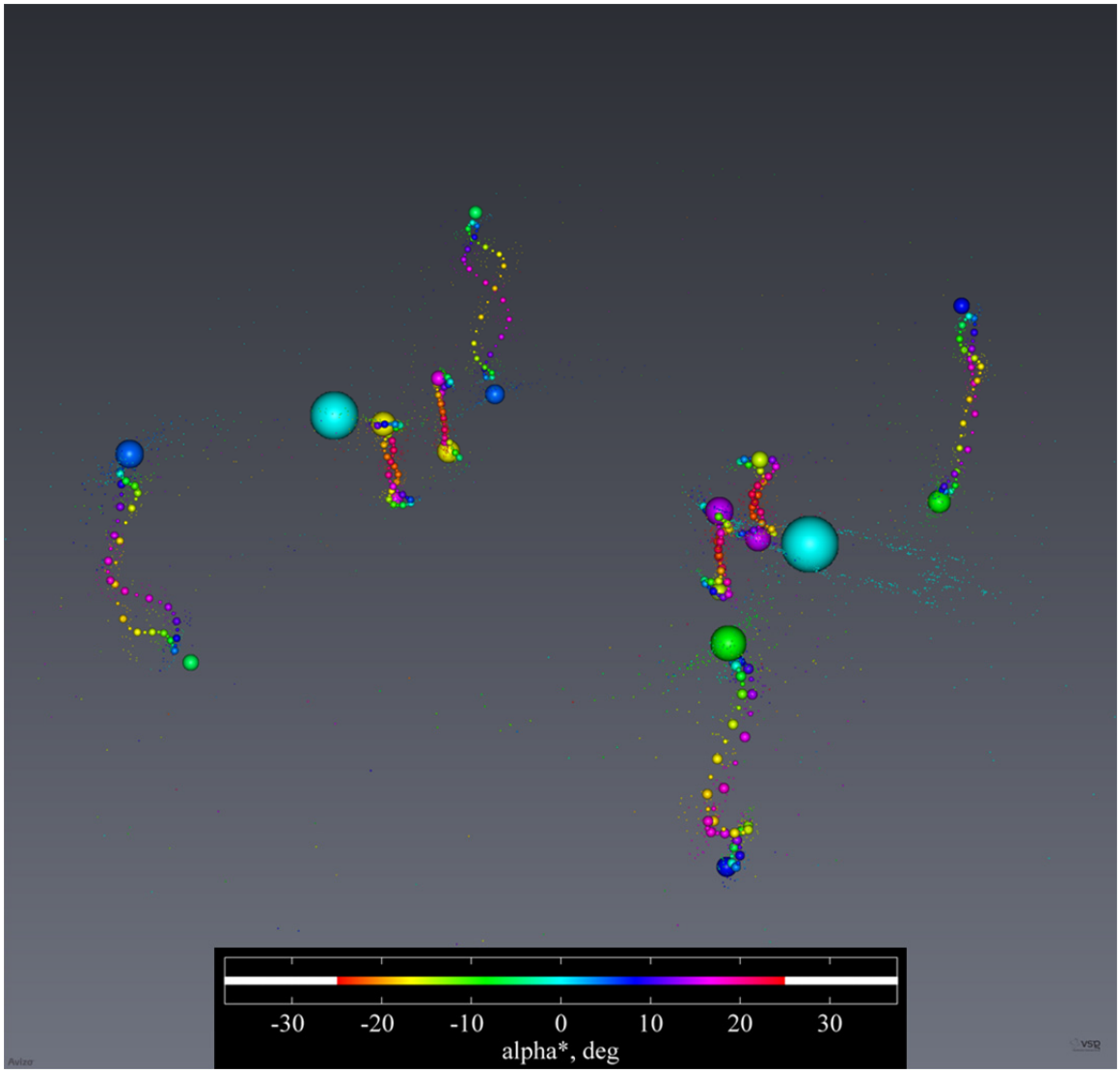

Figure 5.32. Avizo® view of 4-D periapsis Poincaré map periodic trajectory returns along with original structures used for targeting; ($\dot{\rho} = 0+;\ x,\ y,\ z,\ \alpha\_color$)

As indicated in the legend in Figure 5.33, the eight returns associated with the "northern," periodic trajectory "8N" include the four dots above the figure-8 structures in the foreground (on the -y side of Titania) as well as the four dots below the figure-8 structures in the background (on the +y side of Titania). The "southern," stable periodic orbit labeled "8S" is obtained not through targeting but instead though application of the "northern/southern" symmetry by reversing the sign of z and $\dot{z}$ (color) map return values associated with the "8N" trajectory. Both period-eight orbits possess a period of 13.6 days. The "southern," unstable, period-200 trajectory labeled "200S" is obtained using

the same symmetry based on the "northern," unstable, period-200 trajectory labeled "200N." These unstable, period-200 orbits, with a period of 350.1 days, each consist of 200 fixed points belonging to an "island chain" consisting of eight figure-8s. The figure-

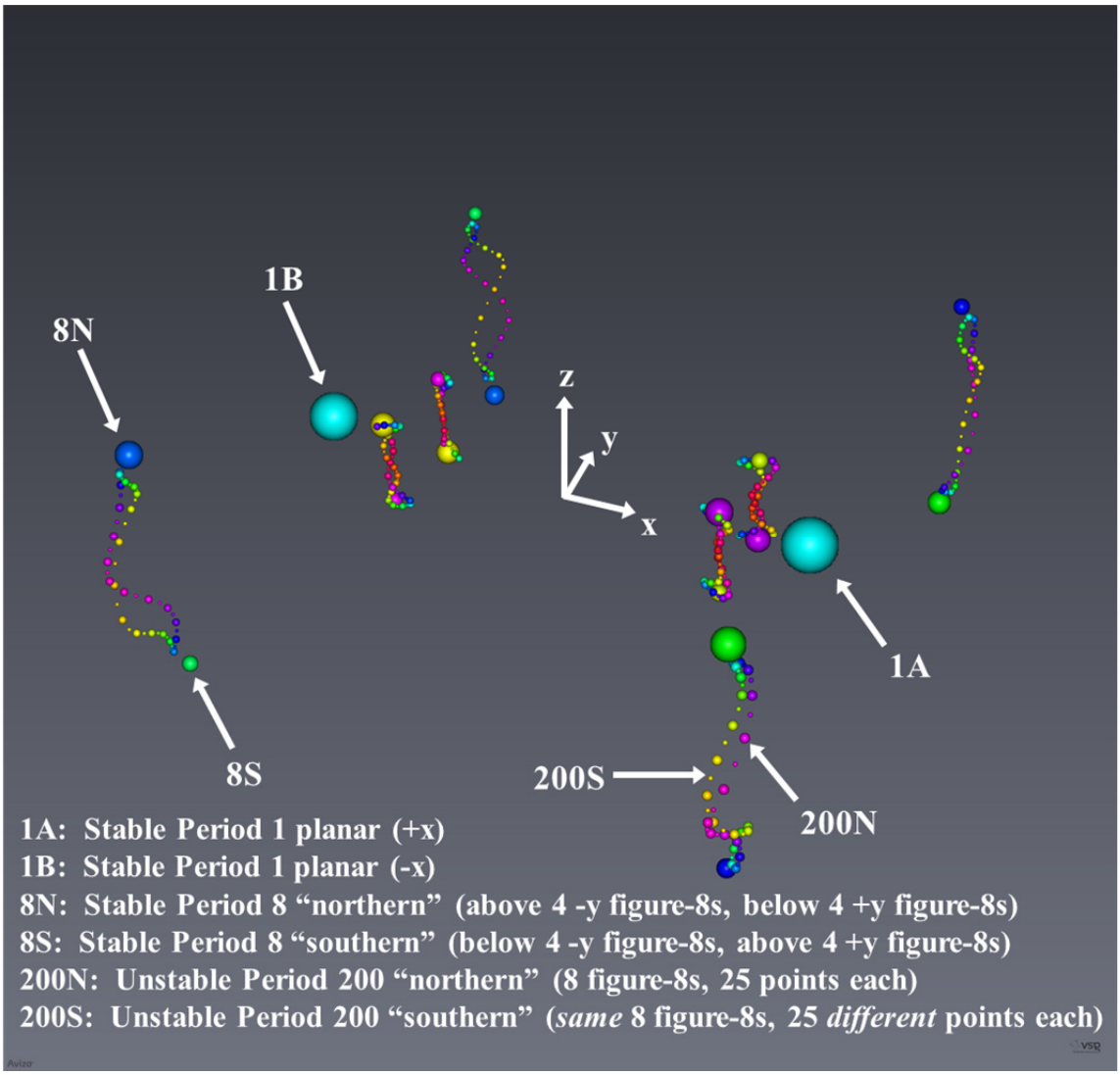

Figure 5.33. Avizo® view of 4-D periapsis Poincaré map periodic trajectory returns along with classification; $(\dot{\rho} = 0+;\ x,\ y,\ z,\ \alpha\_color)$

8s themselves each contain a type of twenty-five-fixed-point "island chain" associated with the "northern" orbit and another twenty-five fixed points associated with the "southern" orbit. Remarkably, these "northern" and "southern" fixed points appear to belong to the *same* 1-D structures in the 4-D map space, as represented using the space-

plus-color method. As indicated by the alternating size of the fifty small dots on each figure-8, each "northern" fixed point is between two associated "southern" fixed points and vice versa. Both the "northern" and "southern" fixed points appear to be "in line" with one another. Moreover, and even more remarkably, each 1-D figure-8, which each contains a total of fifty unstable fixed points, seems to exist as the poloidal axis inside a region containing various quasi-periodic "doughnut"-like structures similar to the examples discussed in Section 3.1.2. In fact, the eight roughly-figure-8-shaped structures plotted in Figure 5.31—which are used to target the period-200 orbits—are an example of such "doughnut" structures surrounding the unstable fixed points. Confirming the analysis in Section 3.1.2, it appears that the "doughnuts" are associated with the perturbations on the unstable periodic behavior in their immediate vicinity. Another important observation is the close relationship between the period-200 orbits and the period-eight orbits in terms of the locations of their respective map returns. Just as various "island" contours on 2-D Poincaré maps are often related in some way to similar structures in their vicinity, it is also clear from this 4-D map representation that the figure-8 structures "point" to the period-eight fixed points directly above and below them. It should be noted that the unstable, period-200 orbits appear to be only *slightly* unstable; propagating the converged "200N" initial condition results in map returns that remain close to the 200 fixed point locations plotted in Figure 5.33 even after 100 years. Finally, the two large cyan dots labeled "1A" and "1B" are the single fixed points associated with two different stable, *planar* period-one orbits—with periods of 7.0 and 6.4 days respectively—which are included as a reference. They are linearly stable in both the in-plane and out-of-plane directions.

For this design example, the period-eight orbit labeled "8N" in Figure 5.33 is selected to be the destination orbit for a Titania orbiter mission. This linearly stable orbit, which appears in the four-perspective rotating view in Figure 5.34, has a period of 13.6 days and an "energy" value associated with L_1. The orbit appears symmetric about the x-axis and also *roughly* symmetric about the plane defined by $x^* = 0$, which is the x value of Titania in this offset-origin plot. As an aside, note that the period number of a given orbit must always be specified with respect to a particular hyperplane. In this case, the periodic

orbit is period-eight with respect to the periapsis definition $\dot{\rho} = 0$ and $\ddot{\rho} > 0$, meaning that the S/C experiences eight unique periapses before returning to the first periapse. In general, a different hyperplane definition would assign a different period number to this or any other periodic orbit.

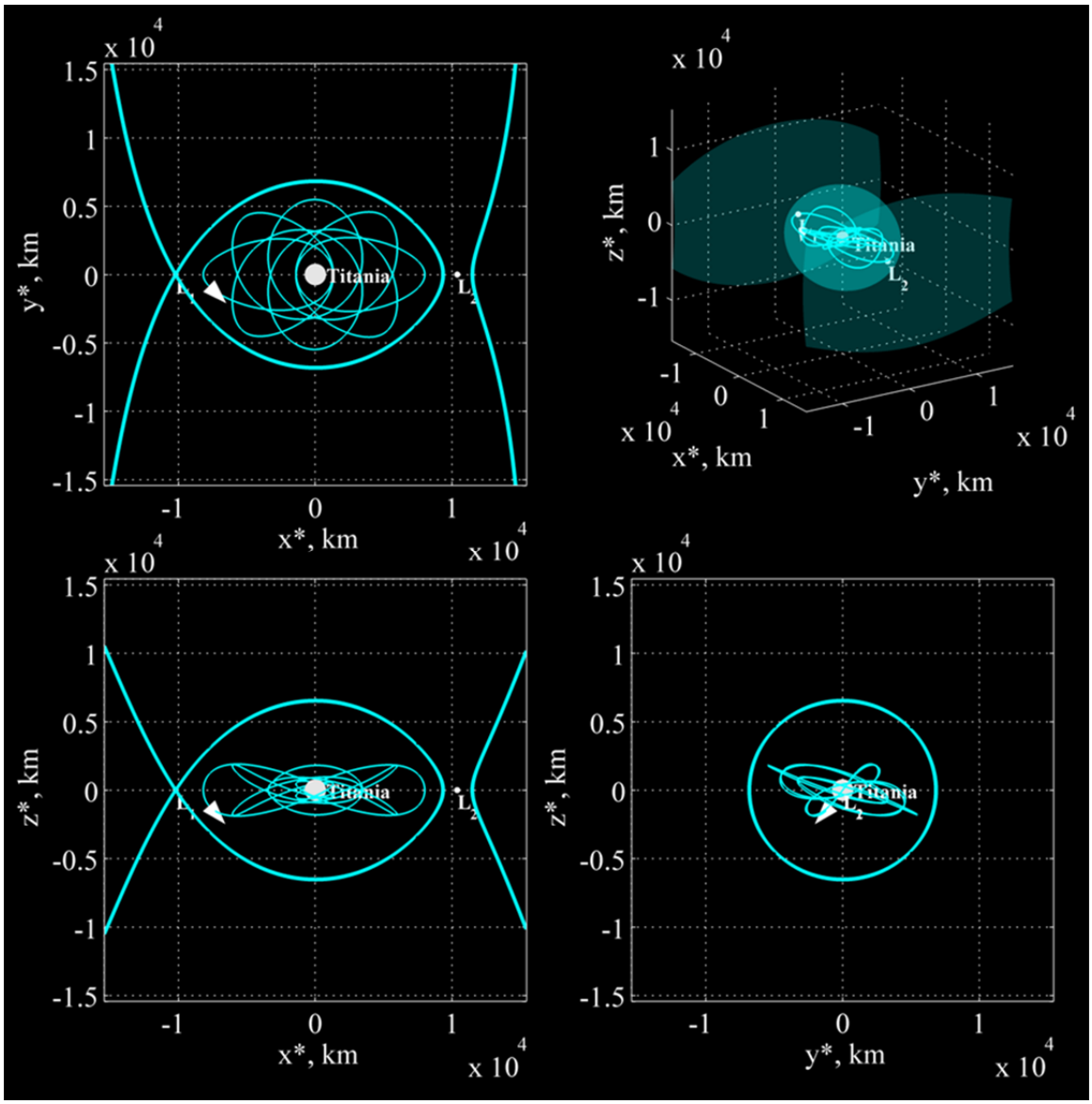

Figure 5.34. Four-perspective rotating view of 3-D, stable periodic orbit at lower "energy"

With the desired periodic capture orbit already chosen, the next step in the capture maneuver design process is to obtain a reasonable guess for a S/C entry trajectory

(entering the region of Titania though one of the libration point gateways), which can then be used to target a precise path leading to the capture orbit. In this design example, it is assumed that the S/C originates from outside Titania's orbit about Uranus and therefore must enter though the L_2 gateway. To create the design space for such a path, another 4-D periapsis Poincaré map is generated in negative time at the higher "energy" level (depicted in Figure 5.27), where the L_1 and L_2 gateways are open. A set of 93,354 initial conditions, selected based on a 4-D grid of x, y, z, α values, is propagated backward in time for the past two weeks or until a negative-time impact, whichever is more recent. The 4-D grid of initial conditions is seeded with the same periapse positions along the hemisphere displayed in Figure 5.28 for the forward-time map. However, unlike the grid for the forward-time map, the full range of possible velocity angles (colors) $-180° < \alpha < 180°$ is now included and seeded with 5° spacing. The resulting Poincaré map contains 714,705 map returns. Next, to isolate the available L_2 entry trajectories, the negative-time map is filtered to allow only returns generated by trajectories that enter through the L_2 gateway (during the past two weeks); all other returns are filtered out, which leaves 146 remaining returns. These L_2 entry returns at the higher "energy" are then overlaid on the forward-time map of the desired (period-eight) capture orbit at the lower "energy." A zoom to a region of approximate intersection (between the higher and lower "energy" returns) in 3-D space appears in Figure 5.35(a). Capture orbit returns are plotted with large dots, while L_2 entry returns are plotted with small dots. The large yellow dot identified by the circle is one of the eight periapsis returns associated with the capture orbit; as a reference, it is the yellow dot associated with trajectory "8N" in Figure 5.33 that is located beneath a figure-8 structure in the $-x$ and $+y$ region near Titania. Its approximate color value is α = -16.5°. The small blue dot (also inside the circle) near the large yellow dot is associated with an L_2 entry trajectory and is actually one of the negative-time initial conditions seeded based on the 4-D grid. The visual estimate for the 3-D periapse position of the small blue dot is selected as a reasonable guess for the position of a periapse on an L_2 entry trajectory (at the higher "energy" level) that intersects the capture orbit periapse represented by the large yellow dot (at the lower "energy"). It is also necessary to obtain a visual guess for the velocity angle α (color) of

an approximately-intersecting periapse at the higher "energy." Choosing the color value associated with the small blue dot (α = 5°) would seem to be an appropriate choice, although this would represent a difference of 21.5° in velocity angle between the periapse for the L_2 entry trajectory and the periapse of the capture orbit. In fact, there is a better guess available. Because of the single location ambiguity associated with plotting

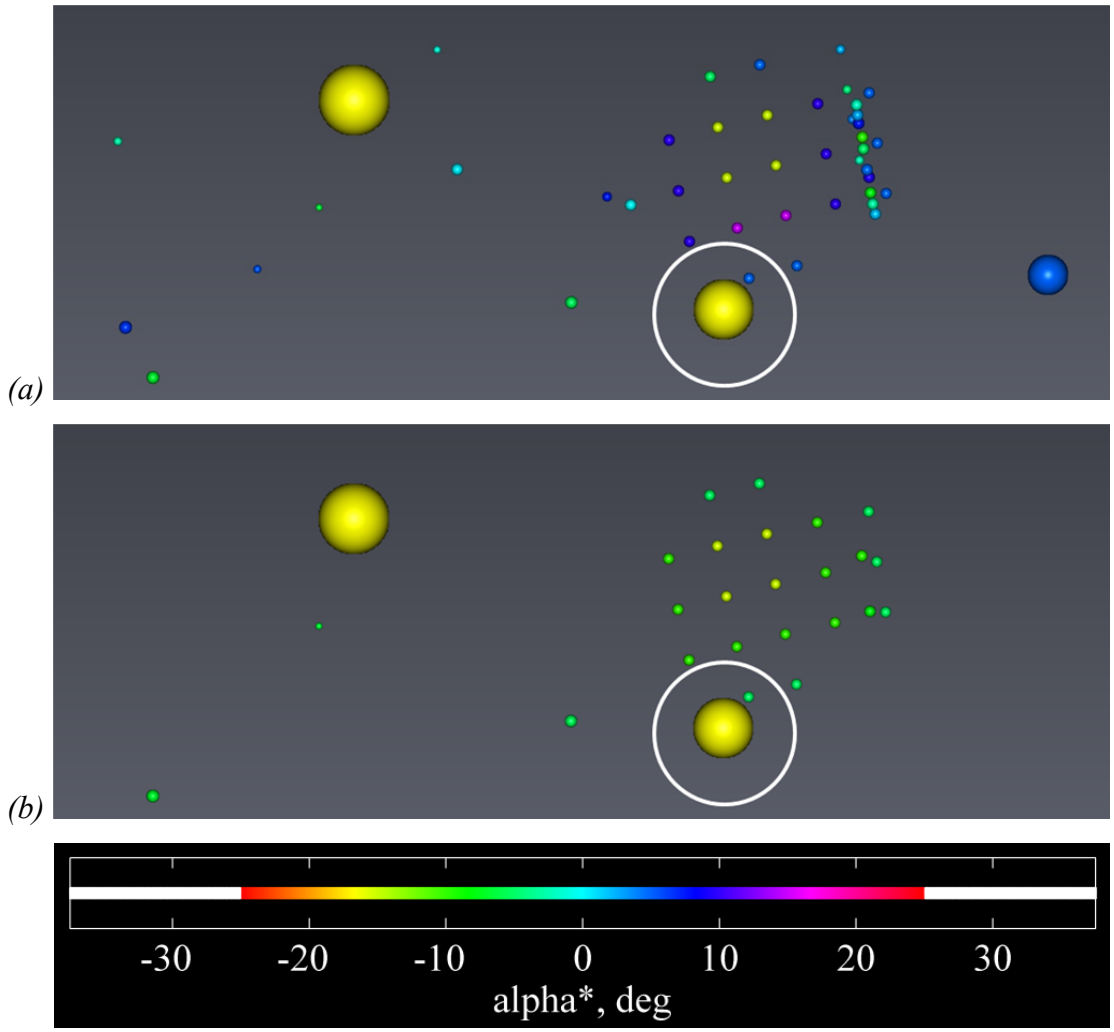

Figure 5.35. Avizo® view before (*a*) and after (*b*) filtering out α >-5° on 4-D periapsis Poincaré maps; returns during previous two weeks of L_2 entries at higher "energy" along with periodic capture orbit forward-time returns at lower "energy" overlaid in the vicinity of Titania; ($\dot{\rho} = 0+;\ x,\ y,\ z,\ \alpha\_color$)

different 4-D values at the same location in 3-D space using the space-plus-color method (see Section 3.1.3), there is actually another return—also one of the seeded initial

conditions—hidden "underneath" the small blue dot. By filtering the Poincaré map plotted in Figure 5.35(a) so as to remove velocity angles (color values) $\alpha > -5°$, a small green dot at the same 3-D position as the small blue dot is revealed, as plotted in Figure 5.35(b). The color value associated with the small green dot is $\alpha = -5°$, which is closer in value to that of the periapse of the capture orbit. The difference is now only 11.5°. Accordingly, the color value of the small green dot is selected as the reasonable guess for the velocity angle α of the approximately-intersecting periapse at the higher "energy."

To determine a precise L_2 entry trajectory leading to an "energy"-lowering capture maneuver along the chosen periodic capture orbit, the 4-D visual estimate for a periapse associated with the small green dot identified by the circle in Figure 5.35(b) is propagated in negative time for two weeks. The end state of that propagation, with a position in the exterior region (outside of the L_2 gateway) is then used as the initial condition for a forward time path (at the higher "energy" level) used in a capture maneuver targeting process. Targeting is accomplished using multiple shooting with ten patch points between the initial position in the exterior region and a reference state along the periodic capture orbit at the lower "energy." The final patch point—which is the assumed position of the maneuver that completes the transfer into the orbit—is at a fixed position chosen to be the periapse position associated with the large yellow dot circled in Figure 5.35. The targeted capture maneuver, implemented slightly prior to (2.7 minutes before) the first periapse after L_2 entry, is accomplished with a total $\left|\overrightarrow{\Delta V}\right| = 99.4$ m/s to insert the S/C into the period-eight capture orbit at the periapse associated with the large yellow dot circled in Figure 5.35. To reduce the $\left|\overrightarrow{\Delta V}\right|$ of this capture maneuver, the targeted transfer path is then fed into an automated optimization process where the cost function to be minimized is the total $\left|\overrightarrow{\Delta V}\right|$ of a *two-maneuver* transfer between the initial position in the exterior region and the reference state along the periodic capture orbit at the lower "energy." The patch point for the first maneuver is at the initial position in the exterior region and is initially assumed to have $\left|\overrightarrow{\Delta V}\right| = 0$. The addition of this exterior region maneuver is an effective technique to determine an L_2 entry path leading to a lower-$\left|\overrightarrow{\Delta V}\right|$ capture in the vicinity of Titania. The exterior maneuver itself is an artificial construction

that is not retained after the optimization process. Instead, the path occurring *after* the first maneuver determined by the optimization process is assumed to be the new baseline for a S/C entry path. The second maneuver is the capture maneuver itself, which is now free to be implemented anywhere on the periodic path leading to the capture orbit reference state. The *fmincon* optimization process does not technically result in a local minimum (to within the prescribed optimality constraints) but only a "possible" local minimum that satisfies the constraints. However, the process still reduces the capture maneuver cost to a relatively small $\left|\overrightarrow{\Delta V}\right|$ = 11.6 m/s. The new capture maneuver is implemented roughly 2.5 days after L_2 entry and only 2.65 minutes after (and 79.5 km away from) the first periapse after L_2 entry. This maneuver is very close to being tangential to the S/C velocity $\vec{V}$ with respect to the rotating frame (only 1.3° change). Interestingly, the S/C is inserted into the periodic capture orbit at a state that occurs only 5.1 seconds later than (and 2.5 km away from) the periapse state associated with the large yellow dot circled in Figure 5.35.

The optimized entry and capture path is plotted in the four-perspective rotating view in the vicinity of Titania in Figure 5.36. Note that the resulting 3-D S/C trajectory entering through the L_2 gateway is at a slightly higher "energy" level—with the gateways slightly larger—than the original higher "energy" level depicted by the ZVSs in Figure 5.27. The closest S/C approach to Titania is along the capture orbit (at the lower "energy" level originally plotted in Figure 5.26) at 562 km altitude. Next, to establish a contingency option for a transit without capture, the L_2 entry trajectory is propagated forward in time (at the higher "energy" level) for two weeks following the capture maneuver opportunity. Without implementing the "energy"-lowering capture maneuver, it is revealed that the S/C exits through the L_1 gateway roughly 7.7 after the capture maneuver opportunity and a total of 10.2 days after L_2 entry, as plotted in the 3-D rotating view in Figure 5.37. The closest approach to Titania is now only 96 km altitude. Thus, there is an alternative path for the S/C: a transit path from the exterior region, i.e., outside Titania's orbit around Uranus, past Titania and then into the interior region, i.e., the region of Uranus. This option is not a consequence of any *explicit* design requirement. However, it is not surprising given that this trajectory has prograde

direction in the rotating frame once it enters through the L_2 gateway. As discussed earlier, the prograde direction of motion which makes a libration point entry likely also makes a libration point exit likely (as long as the appropriate gateways are open). Moreover, the original forward-time 4-D periapsis Poincaré map (see Figure 5.29) used to located the capture orbit contains returns with mostly prograde direction, with velocity angles roughly in the range $-90° < \alpha < 90°$. Also, the eight periapsis returns associated with the chosen capture orbit have velocity angles well within the near-planar prograde direction range $-25° < \alpha < 25°$ (see Figure 5.32). These design choices increase the likelihood of determining a low-$\left|\overrightarrow{\Delta V}\right|$ capture maneuver along a gateway entry/exit trajectory because both the capture and entry/exit trajectories are expected to have near-planar prograde direction.

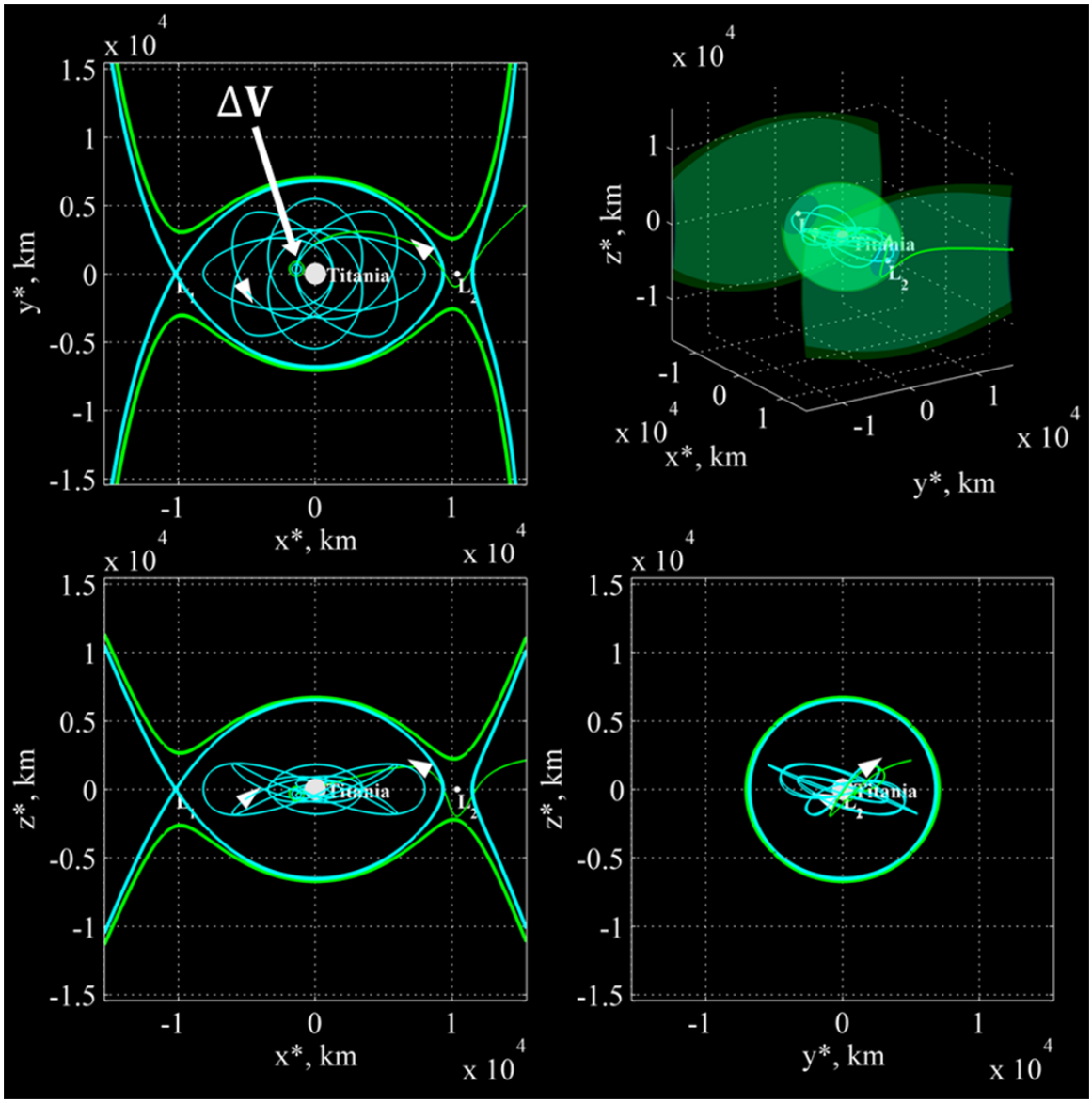

Figure 5.36. Four-perspective rotating view of "optimized" capture maneuver for Titania orbiter; before maneuver (green) and after maneuver (cyan)

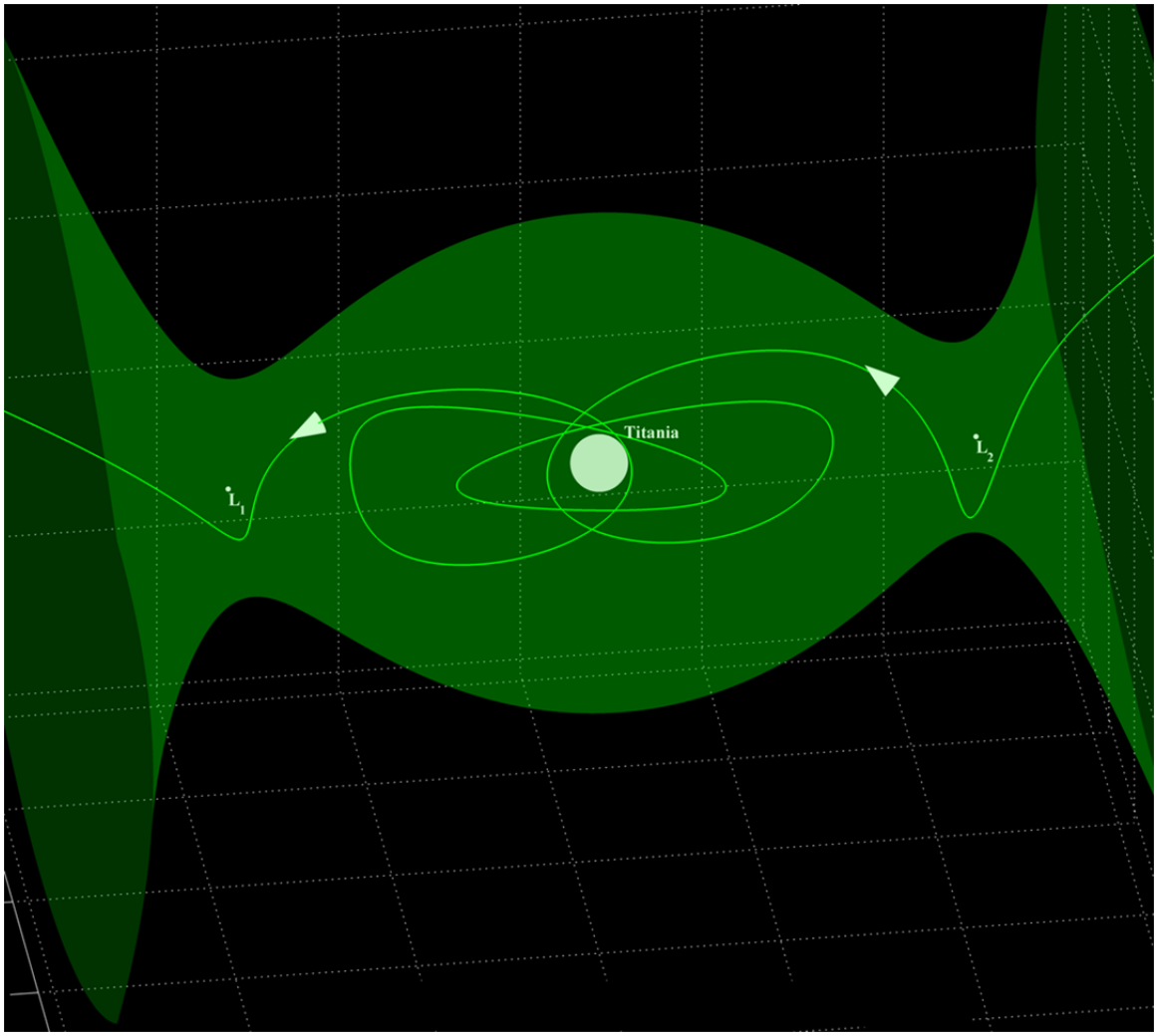

Figure 5.37. Rotating view of Titania transit contingency option

Because the capture orbit plotted in Figure 5.36 is periodic, the transit path appearing in Figure 5.37 is used to establish another contingency option, one where the S/C is captured and then departs the vicinity of Titania at a later time. The two-maneuver capture and departure sequence appears in Figure 5.38 in the 3-D rotating view and in Figure 5.39 in the 3-D Titania-centric inertial view. The first maneuver is the designed capture maneuver, with $\left|\overrightarrow{\Delta V}\right|$ = 11.6 m/s, implemented at a time equal to roughly 2.5 days after L_2 entry. The second maneuver is implemented exactly one period of the capture orbit (13.6 days) subsequent to the first maneuver and essentially reverses the capture process, returning the S/C to the original state (before the capture maneuver)

along the transit path in the rotating frame. This "energy"-raising departure maneuver is in a direction opposite to the capture maneuver (in the rotating frame) and with the same magnitude. Thus, it is implemented with $\left|\overrightarrow{\Delta V}\right|$ = 11.6 m/s, resulting in L_1 exit 7.7 days after the maneuver and a total of 23.8 days subsequent to L_2 entry. This contingency option is effectively a transit with a delay equal to one period of the capture orbit, requiring a total $\left|\overrightarrow{\Delta V}\right|$ = 23.2 m/s. Furthermore, it is possible to add additional delay—between the two maneuvers—equal to a positive integer multiple of the capture orbit

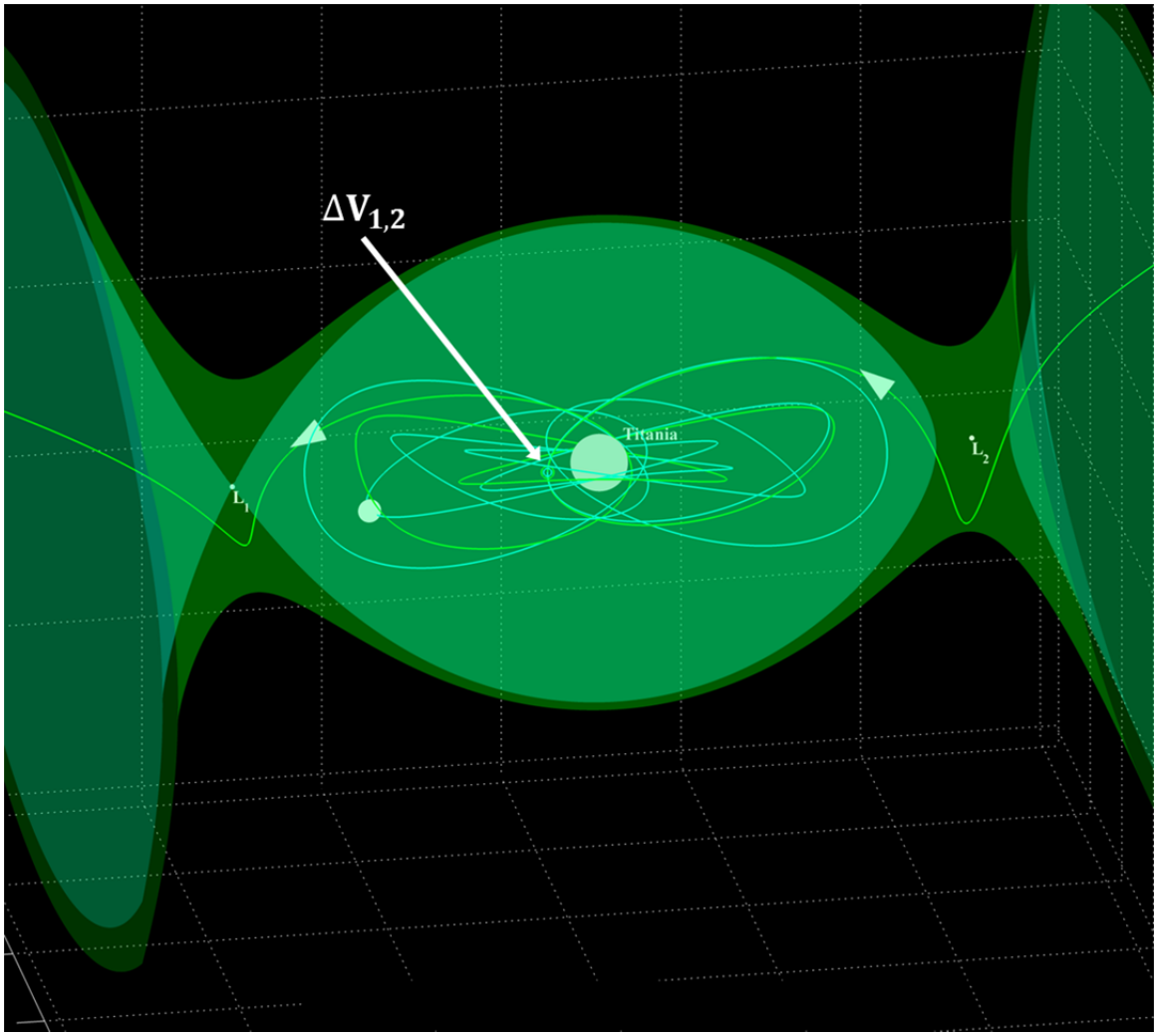

Figure 5.38. Rotating view of Titania capture and departure contingency option; before capture maneuver (green), after capture maneuver (cyan), and after departure maneuver (green)

period. Thus, the overall time-of-flight for the delayed transit path is (10.2 + 13.6*N*) days, where *N* is a positive integer. These contingency options provide some operational flexibility for the Titania orbiter mission scenario.

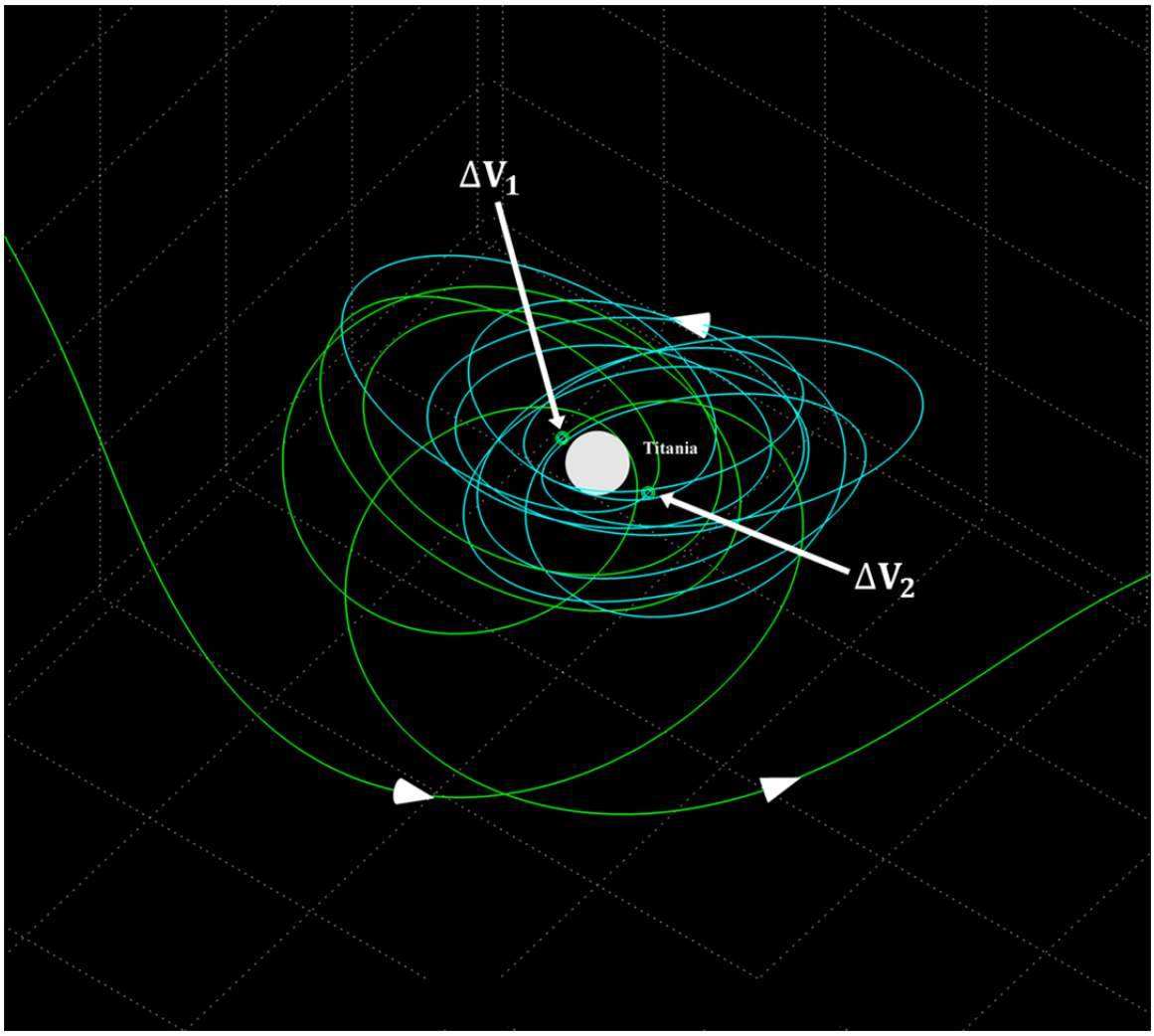

Figure 5.39. Inertial view of Titania capture and departure contingency option; before capture maneuver (green), after capture maneuver (cyan), and after departure maneuver (green)

To provide a convenient way to transition the transit and capture states—i.e., the two states at the instant before and after the capture maneuver depicted in Figure 5.36—to a higher-fidelity model, the instantaneous (osculating), Titania-centered, two-body orbital elements for these two states are calculated. These orbital elements appear in Table 5.6

for the assumed capture maneuver epoch of 29 June 2035 at "midnight." The values are calculated based on Uranus's own *apparent* orbital motion about Titania at the time of the capture maneuver, obtained from the JPL HORIZONS System web-interface (ephemeris data URA083 and URA095) [111]. Both sets of osculating orbital elements

Table 5.6 Osculating orbital elements at Titania orbiter capture opportunity*

State	a	e	i	Ω	ω	ν
Before capture maneuver	4,336.08 km	0.664611	159.32°	154.47°	37.98°	3.21°
After capture maneuver	4,143.67 km	0.648818	159.11°	153.95°	40.60°	0.10°

* Titania-centric mean equatorial reference frame; node of 29 June 2035 at "midnight," the assumed epoch of the capture maneuver

included in Table 5.6 represent what would be elliptical orbits in the Titania-centric 2BP. In fact, both two-body orbits have an apoapse that is inside the sphere of influence, with radius calculated as $SOI = l^*(GM_T/GM_U)^{2/5}$ = 7,549 km, a rough approximation for the radius of the region in the vicinity of Titania where the Titania-centric 2BP may be considered a valid approximation in a patched-conic analysis [74]. However, quite notably, the 2BP does not predict the long-term behavior of the transit state (without the capture maneuver) in the CR3BP, where the S/C actually departs the vicinity of Titania. The immediate effect of the capture maneuver is to decrease both semimajor axis a as well as eccentricity e. That is, the maneuver results in an instantaneous orbit that possesses a lower two-body specific mechanical energy and which is also more circular at the instant after capture. Both states are very close to periapsis ($\nu = 0°$). Also note that both states have *retrograde* direction ($i > 90°$) with respect to the Titania-centric mean equatorial reference frame even though they have prograde direction with respect to Titania in both the *x-y-z* rotating frame and the *X-Y-Z* inertial frame of the CR3BP as defined in this investigation. The reason for this is that Titania's orbit about Uranus,

along with the rotational motion of Uranus itself, is retrograde with respect to the Titania-centric mean equatorial reference frame. This convention is based on Uranus's axial tilt (obliquity) of approximately 98° with respect to its orbit about the Sun. The "up" direction of Uranus's rotation axis (by the right-hand rule) actually has a component in the typical "down" direction of the solar system based on the average orbit normal of the eight planets.

To validate the key results in Design Example #7, the designed transit and capture states specified in Table 5.6 are transitioned to a higher-fidelity, ephemeris-based model using Satellite Tool Kit® (STK®) [112] (see Section 2.8.2). The simplifying assumptions of the CR3BP are replaced with a more realistic dynamical model for S/C motion in the Uranian system. Uranus and Titania are still treated as point masses in the gravity model, however, the orbit of Titania about Uranus is now modeled based on JPL ephemeris data [111], as are the orbits of the other four major Uranian moons: Miranda, Ariel, Umbriel, and Oberon. These additional moons are also treated as point masses in the gravity model. The five major moons are depicted in the STK® 3-D view in Figure 5.40 at the epoch of the capture maneuver. Note that, because of the convention described earlier, the near-equatorial and near-circular orbits of the moons have *clockwise* direction of motion in this view. Thus, from the perspective of Titania (displayed in pink) at the epoch of the capture maneuver, Umbriel is approaching inferior conjunction and Oberon is approaching opposition. Also included in the higher-fidelity model is the gravity from the Sun as well as the other gas giant planets: Jupiter, Saturn, and Neptune, with all orbits based on ephemeris data. Note that the total "system" gravitational parameter is used for Jupiter, Saturn, and Neptune. In addition, solar radiation pressure [74] is modeled, assuming a perfectly absorbing S/C with a cross-sectional area-to-mass ratio equal to 0.02 m^2/kg. Finally, to preserve the validity of the original capture maneuver cost ($\left|\overrightarrow{\Delta V}\right|$ = 11.6 m/s) calculation, the maneuver is still assumed to be instantaneous (impulsive).

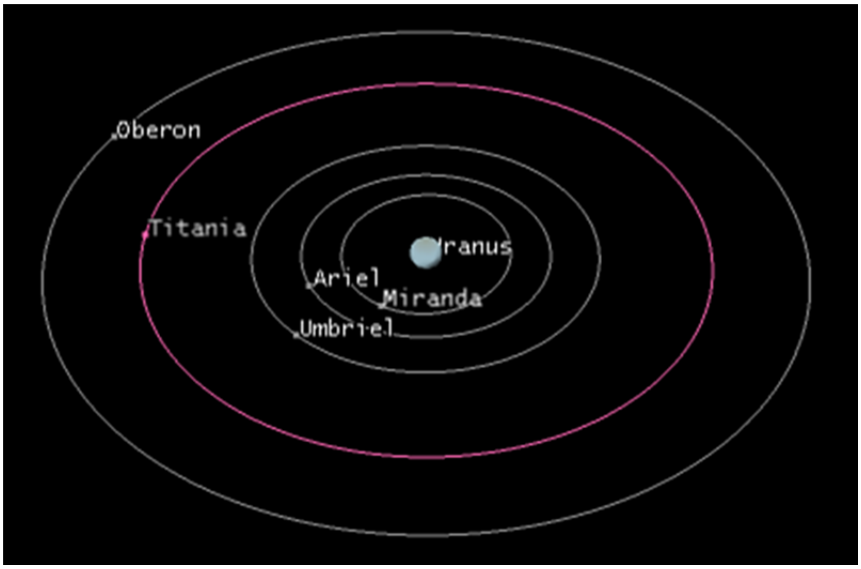

Figure 5.40. STK® 3-D view of the five major moons of Uranus in higher-fidelity model at capture maneuver epoch (clockwise orbital motion) [112]

The results of the transition to the higher-fidelity model are depicted in the STK® 3-D rotating view in Figure 5.41. In this view, Titania's orbit is represented in pink, as is its orbit normal vector, which is effectively the *z*-axis of a rotating frame centered at Titania. The rotating frame *x*-axis (cyan) always points away from Uranus, while the rotating frame *y*-axis is aligned with Titania's orbital velocity vector. In Figure 5.41(a), the S/C transit state is propagated both forward and backward in time from the capture maneuver epoch and depicted (in green) in rotating frame coordinates. A transit from outside to inside Titania's orbit is accomplished in roughly ten days, as predicted by the preliminary design in the CR3BP. Next, the capture state is propagated forward in time for almost fourteen days. Figure 5.41(b) indicates (in cyan) that the S/C approximately repeats its initial state in this rotating frame in roughly the time predicted by the 13.6-day period in the CR3BP. Just as in the CR3BP, the S/C appears to pass through eight periapses before returning to the first periapse after the approximate period. Finally, Figure 5.41(c) depicts the result of propagating the capture state forward in time for one year. Even though the capture orbit is not periodic, it appears tightly-bounded for at least one year subsequent to the capture maneuver, while retaining the approximate shape of the stable periodic orbit modeled in the CR3BP. Moreover, it neither escapes nor impacts

Titania during this time. Thus, the preliminary design for both the capture maneuver and the transit contingency option—accomplished in the simplified model of the CR3BP—is successfully validated by confirming the desired qualitative behavior in the higher-fidelity model. Also note that the capture orbit symmetries described earlier appear to be

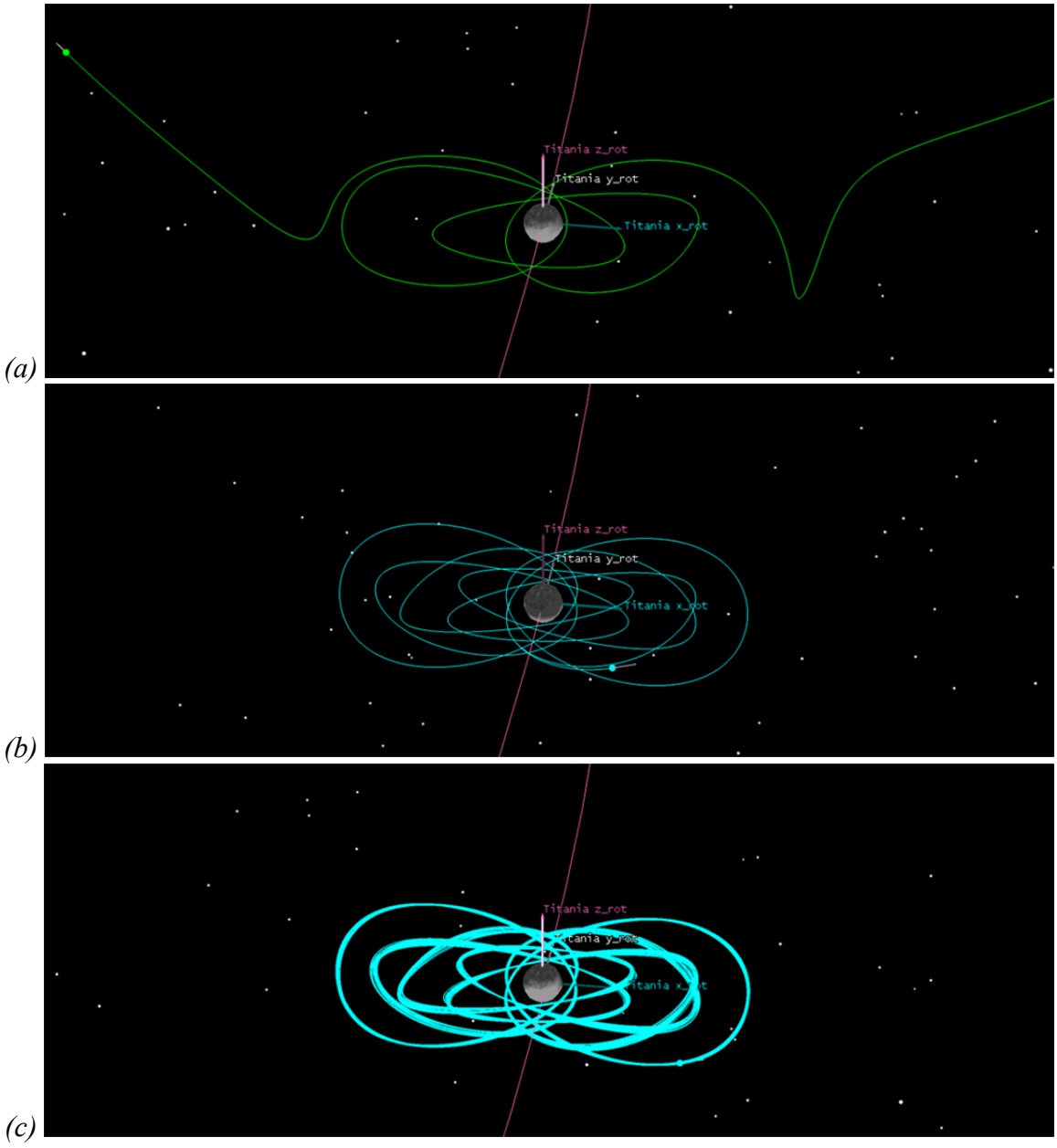

Figure 5.41. STK® 3-D view of Titania transit and capture design validation in higher-fidelity model; transit (*a*), capture for almost fourteen days (*b*), and capture for one year (*c*) [112]

roughly preserved even after transitioning to the higher-fidelity model. Such symmetries in the rotating view could be useful for a Titania orbiter because Titania's rotation is assumed to be synchronous with its orbit about Uranus. That is, the rotating view depicted in Figures 5.41 is also a Titania *body-fixed* view.

The last step in the design process for Design Example #7 is the consideration of a plausible mission scenario in which the designed Titania capture/transit path is the final phase. Recent studies [136, 137, 138, 139, 140] of potential Uranus orbiter missions assume a near-polar (e.g., 97.7°-inclination), highly-elliptical mission orbit about Uranus, a choice that is driven by primary science objectives. A high-inclination arrival at Uranus in the decade of the 2030s is enabled by Uranus's axial tilt (obliquity) of approximately 98° with respect to its roughly eighty-four-year orbit about the Sun. The resulting "seasonal" variation in the orientation of Uranus's equatorial plane with respect to the Sun is a key factor in determining available Earth launch windows and planetary gravity assist opportunities to achieve a desired arrival trajectory at Uranus. Furthermore, a critical trade-off exists such that shorter interplanetary cruise durations generally require higher Uranus orbital insertion $\left|\overrightarrow{\Delta V}\right|$ costs [138]. To achieve the arrival trajectory necessary for insertion into a near-polar orbit about Uranus, a single Earth gravity assist flyby is employed in the NASA Ice Giants Decadal Study [136], with launch in 2020 and arrival in 2033. An alternative Venus-Earth-Earth-Saturn gravity assist sequence is considered by Arridge et al. [140], with launch in 2021 and arrival at Uranus in 2037. Dankanich and McAdams [138] examine a wide variety of gravity assist options involving Earth, Venus, Mars, Jupiter and/or Saturn, with launches in 2018-2026 and Uranus arrivals in 2028-2036. Yet, none of these studies are directly applicable to the Titania orbiter scenario in Design Case #7, which requires a final approach to Titania with a low two-body hyperbolic excess velocity V_∞ on a path that is roughly in the plane of Titania's orbit (inclination $i > 179°$), i.e., roughly in Uranus's equatorial plane. Essentially, the condition required for the "energy" level depicted in Figure 5.27 to be practically available is that the S/C is already in a Uranus-centric orbit that enables a low-$\left|\overrightarrow{\Delta V}\right|$ rendezvous with Titania. Although flybys of the Uranian moons are included in the recent studies, the near-polar-inclination mission orbit assumed therein precludes an

equatorial approach to Titania or any other major moon. Furthermore, a direct insertion into a Titania capture orbit would be prohibitive, requiring approximately $\left|\overrightarrow{\Delta V}\right|$ = 5 km/s based on satellite tour information given by McAdams et al. [137].

An earlier Uranus mission study that is more directly applicable to Design Example #7 is provided by Heaton and Longuski [67], who investigate a near-equatorial-inclination, "Galileo-style" tour of the major Uranian moons with the end objective of inserting into a capture orbit around Ariel. That mission design scenario assumes a launch in 2008, followed by a Jupiter gravity assist (JGA) in 2009 and arrival at Uranus in 2018. For capture about Ariel to be practical in terms of $\left|\overrightarrow{\Delta V}\right|$, the necessary excess velocity V_∞ with respect to that moon is assumed in that study to be V_∞ < 1 km/s, which is achieved 3.4 years following Uranus arrival by means of a series of repeated flybys of all major moons except Miranda [67]. Although the specific interplanetary path and the tour of the Uranian moons given by Heaton and Longuski are not *perfectly* applicable to the scenario for Design Example #7 (a Titania orbiter capture in 2035), it does offer a suitable reference for developing a cursory description of a plausible modified scenario. Accordingly, various results and assumptions presented by Heaton and Longuski are applied to Design Example #7, while adjusting for the Titania orbiter mission requirements as well as the significant seasonal change in the orientation of Uranus's equatorial plane between 2018 and the 2030s.

To modify the JGA trajectory and Uranian system tour employed in the Ariel orbiter study [67] for Design Example #7, it is assumed that a launch in 2021, with an Earth-centric departure $V_\infty \cong$ 10 km/s, followed by a JGA in 2022, with a Jupiter-centric flyby $V_\infty \cong$ 11 km/s, allows for a feasible ten-year cruise to Uranus, arriving in 2031 with a Uranus-centric arrival V_∞ < 7.5 km/s. This assumption is based on the approximately fourteen-year cycle in the JGA launch window studied by Heaton and Longuski [67] as well the availability of JGA paths to Uranus in 2020-2022 [139]. Furthermore, a twelve-year Earth-Earth-Jupiter gravity assist sequence given by Dankanich and McAdams [138] appears consistent with the assumed ten-year JGA path to Uranus beginning in 2021 if a (higher-velocity) launch occurs instead of the 2021 Earth flyby. In the Ariel orbiter study,

the assumed maximum allowable cost of Uranus orbit insertion is $\left|\overrightarrow{\Delta V}\right|$ = 2.5 km/s, which corresponds to a Uranus arrival V_∞ = 7.5 km/s.

Given the JGA path to Uranus, it is next assumed that a suitable final approach to Titania is represented by the flyby event "34/Titania" in the Uranian tour "U00-01" designed by Heaton and Longuski [67]. This event occurs 448 days after the completion of an orbit inclination "crank down" in which nine flybys of Titania are exploited to change the S/C orbit inclination about Uranus to equatorial (a change of almost 14° over 261 days) [67]. The Titania-centered excess velocity V_∞ = 1.04 km/s at the "34/Titania" flyby is roughly consistent with the capture criterion for the Ariel orbiter given in the same study (V_∞ < 1 km/s). It is therefore assumed that the Titania orbiter capture maneuver plotted in Figure 5.36 can occur 448 days after a sufficient inclination "crank down." Unfortunately, however, significantly more change in inclination is expected to be required for Design Example #7 with a Uranus arrival in the 2030s. The orientation of Uranus's equatorial plane changes roughly 56° between 2018 and 2031. Heaton and Longuski indicate that this changing orientation results in increasingly less favorable Uranus insertion orbits after 2019. Moreover, favorable conditions similar to that of the 2008 launch window are not repeated until the launch window in 2050 [67]. As a worst-case estimate for Design Example #7, it is assumed that the total inclination "crank down" required would be 70° (14° from the Ariel orbiter study plus an additional 56° due to the seasonal change). Based on the Heaton and Longuski statement that a 20° "crank down" to a Uranus equatorial inclination requires roughly one year, it is assumed for Design Example #7 that a 40° change can be accomplished in two years using Titania flybys. The remaining 30° of required inclination change is assumed to be accomplished with a simple plane change maneuver implemented at apoapsis along the orbit before the beginning of the Titania-assisted "crank down" (before event "1/Titania") [67]. This maneuver requires roughly $\left|\overrightarrow{\Delta V}\right| \cong$ 300 m/s. The estimated time between the beginning of the "crank down" phase and Titania capture is 2 years + 448 days ≅ 3.2 years. However, this duration does not account for the delay between Uranus orbit insertion and the first opportunity to flyby Titania to begin the "crank down" phase (along with any delay required for other science objectives). For Design Example #7, a delay of 1.2 years

is assumed, which is the delay indicated in the Ariel orbiter study [67]. Therefore, the total time between Uranus arrival and Titania capture is assumed to be 4.4 years, implying a capture epoch in roughly 2035. The Titania capture maneuver epoch is assumed to be 29 June 2035, which is consistent with the JGA trajectory and Uranian system tour assumed for Design Example #7. Note that this date is also exactly two years after the Uranus arrival date in the NASA Ice Giants Decadal Study preliminary design [136]. The specific date selection is actually based on an arbitrary choice made earlier in the Design Example #7 design process.

To connect the assumed Uranian system tour with the final approach path to Titania depicted in Figure 5.36, it is assumed that a final approach maneuver is implemented along a Uranus-centric two-body ellipse based on the parameters of Heaton and Longuski event "34/Titania" [67]. The ellipse has a radius of periapse equal to 12.2 Uranus radii and a two-body period equal to 8.7 days, which is, in fact, roughly the same period as that of the primaries in the Uranus-Titania CR3BP. This Uranian tour ellipse is assumed to be in the *x*-*y* plane of the primaries (in the same plane as Titania's orbit about Uranus). The final approach to Titania is plotted in Figure 5.42 in the barycentric *x*-*y* rotating view and in Figure 5.43 in the Uranus-centric *X*-*Y* inertial view. The Uranus-centric two-body propagation (yellow) begins one two-body period of the tour ellipse before the final approach maneuver (ΔV_0). The propagation in the CR3BP begins after the final approach maneuver and continues along the capture/transit path (green) into the interior region of Uranus until fourteen days following the capture maneuver opportunity. The final approach maneuver, which is not claimed to be optimal, is "energy"-lowering and requires $\left|\overrightarrow{\Delta V}\right|$ = 974.4 m/s; it is implemented during the ascending portion of the two-body Uranian tour ellipse at a time equal to 7.6 days before the Titania capture maneuver opportunity. The maneuver location is selected to be the transit path's last crossing of the *x*-*y* plane ($z = 0$) before entry through the L_2 gateway.

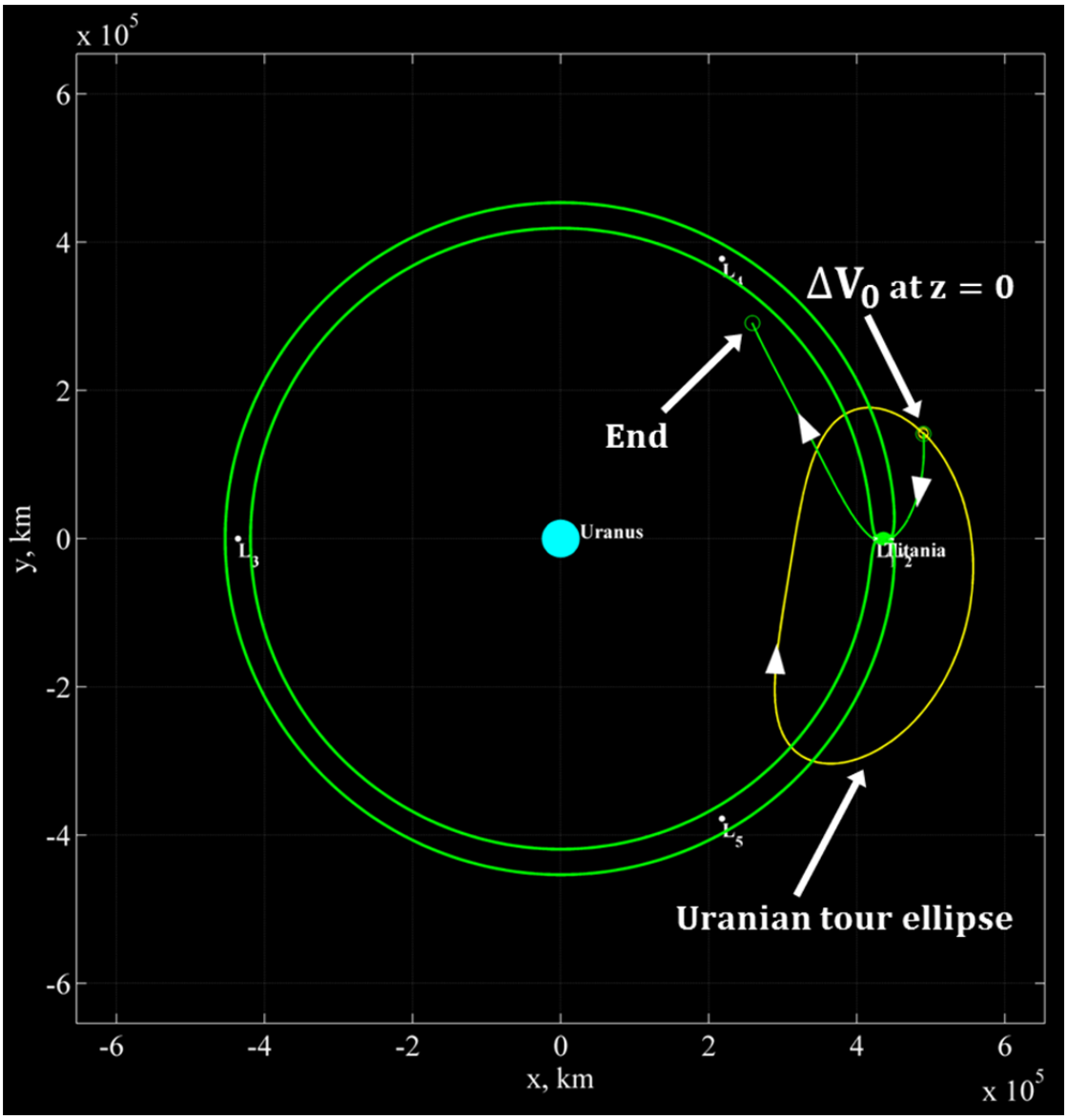

Figure 5.42. Rotating view of final approach maneuver; transfer between two-body Uranian tour ellipse and Titania transit path; before approach maneuver (yellow); after approach maneuver and continuing past capture opportunity (green)

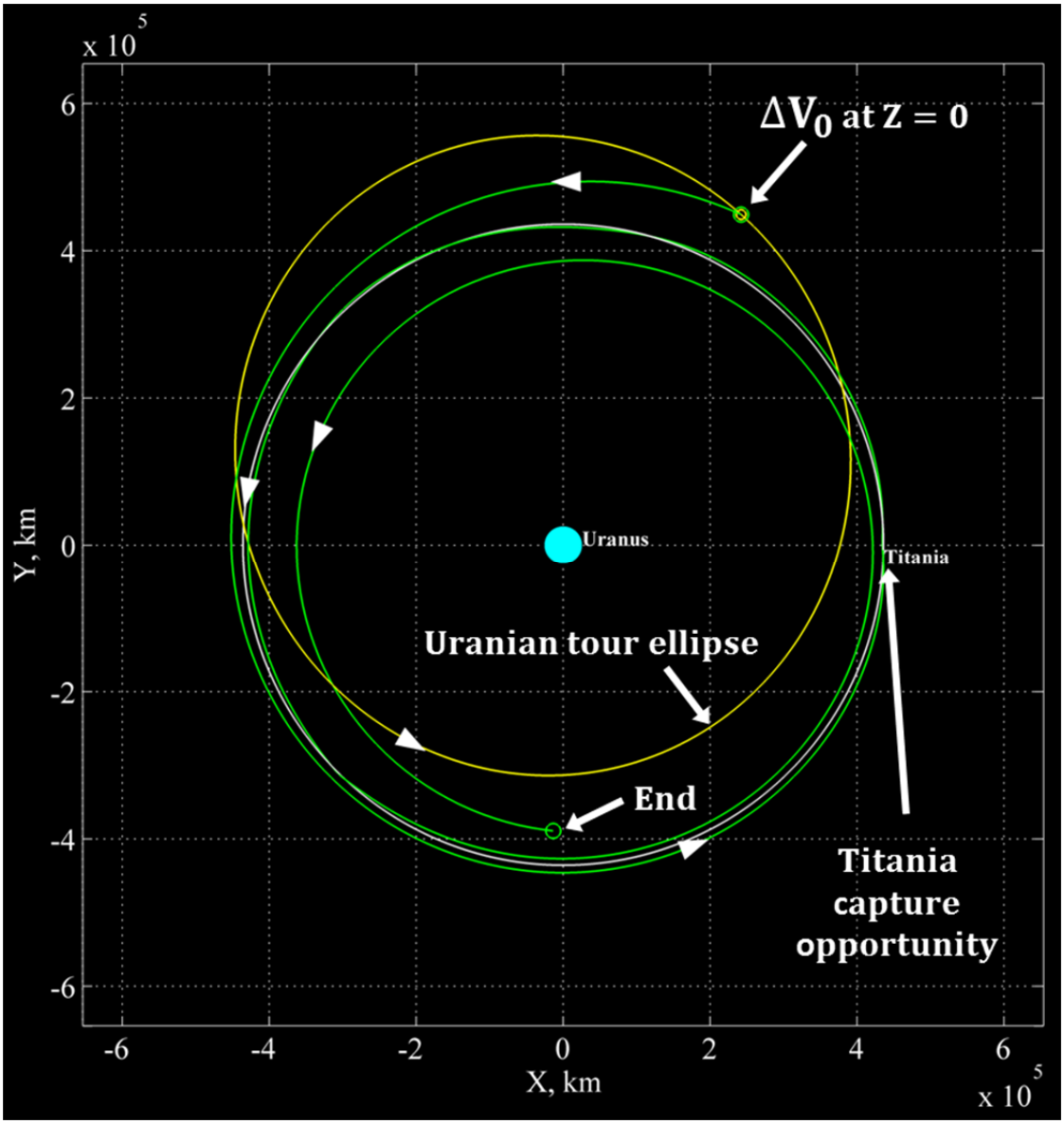

Figure 5.43. Inertial view of final approach maneuver; transfer between two-body Uranian tour ellipse and Titania transit path; before approach maneuver (yellow); after approach maneuver and continuing past capture opportunity (green)

The sequence of events in the assumed interplanetary trajectory and subsequent Uranian tour leading to Titania orbiter capture/transit in Design Example #7 are summarized in Table 5.7. Note that these assumptions—while grounded in a rough analysis based on the Ariel orbiter study [67] as well as the other sources mentioned—have *not* been verified in a realistic dynamical model. They serve only to describe a

rough idea of a plausible mission scenario fitting the precise Titania capture maneuver design accomplished in the CR3BP. The final approach maneuver and the Titania capture maneuver opportunity are the only events that have been rigorously modeled.

Table 5.7 Assumed mission scenario for Design Example #7

Event	Time	Characteristics
Launch	2021	$V_\infty \cong 10$ km/s
Jupiter flyby	2022	$V_\infty \cong 11$ km/s
Uranus arrival & orbit insertion maneuver	2031	$V_\infty < 7.5$ km/s $\lvert\overrightarrow{\Delta V}\rvert < 2.5$ km/s
Initial plane change maneuver	2032	$i = 110° \rightarrow 140°$ $\lvert\overrightarrow{\Delta V}\rvert \cong 300$ m/s
Titania-assisted "crank-down" phase	2032-2034	Repeated flybys of Titania $i = 140° \rightarrow 180°$
Uranian moon tour: energy reduction & Titania rendezvous phase	2034-2035	Repeated flybys of major Uranian moons to achieve Titania $V_\infty \cong 1$ km/s
Final Titania approach maneuver	21 June 2035	$\lvert\overrightarrow{\Delta V}\rvert = 974.4$ m/s
Titania capture maneuver opportunity	Capture 29 June 2035 or complete transit 6 July 2035	$\lvert\overrightarrow{\Delta V}\rvert = 11.6$ m/s for capture
Total until capture opportunity	14 years after launch	$\lvert\overrightarrow{\Delta V}\rvert < 3.8$ km/s after launch

Furthermore, the transit path along with the capture maneuver and capture orbit are the only elements of the scenario that been validated in a higher-fidelity model.

A comparison of the values in Table 5.7 with the Heaton and Longuski Ariel orbiter study [67] indicates that the requirements for the scenario in Design Example #7 are significantly more demanding. The time-of-flight from launch until the final moon capture (around either Titania or Ariel) is roughly one year longer in the current investigation. This is because the Titania orbiter mission requires a longer inclination "crank down" phase than in the Ariel orbiter study. To compare $\left|\overrightarrow{\Delta V}\right|$ requirements, it is necessary to estimate the Uranus orbit insertion cost as well as the Ariel capture maneuver cost implied in the Ariel orbiter study. Based on the Heaton and Longuski final Ariel excess velocity of V_∞ = 0.92 m/s, the minimum cost of a capture into a highly-elliptical two-body orbit about Ariel is determined to be $\left|\overrightarrow{\Delta V}\right|$ = 535 m/s, assuming an Ariel-centric gravitational parameter equal to GM_A = 86.48943821066345 km^3/s^2 and a minimum maneuver altitude of 50 km above Ariel's 581-km body radius. Furthermore, the Heaton and Longuski Uranus arrival excess velocity is V_∞ = 6.44 km/s, implying a minimum Uranus capture cost of $\left|\overrightarrow{\Delta V}\right|$ = 1.8 km/s, assuming a minimum maneuver radius of four Uranus radii (for ring clearance). These values indicate that the assumed total $\left|\overrightarrow{\Delta V}\right|$ requirement in Table 5.7 is 1.5 km/s larger than that in the Ariel orbiter study. However, it should be emphasized that the assumed orbital insertion cost listed in Table 5.7 is conservative and based on the *maximum allowable* cost ($\left|\overrightarrow{\Delta V}\right|$ = 2.5 km/s) given by Heaton and Longuski. Furthermore, the upper limit for the Ariel excess velocity is actually V_∞ = 1 km/s, implying that a capture maneuver requiring $\left|\overrightarrow{\Delta V}\right|$ = 605 m/s is acceptable. Adjusting for these facts, the scenario described for Design Example #7 is really only 700 m/s more costly in $\left|\overrightarrow{\Delta V}\right|$ as compared to what is considered practical by Heaton and Longuski [67]. That remaining increased cost is due to two factors: (1) the 30° plane change maneuver ($\left|\overrightarrow{\Delta V}\right|$ = 300 m/s), and (2) a penalty of roughly $\left|\overrightarrow{\Delta V}\right|$ = 500 m/s resulting from the fact that a large final approach maneuver is implemented outside of Titania's sphere of influence. For a Titania-centric excess velocity of V_∞ = 1 km/s, the minimum cost of a capture around Titania is only $\left|\overrightarrow{\Delta V}\right|$ = 505 m/s, assuming a minimum

maneuver altitude of 50 km. Interestingly, because of Titania's significantly larger mass—which reduces the capture costs assuming similar excess velocity V_∞ and maneuver radius—the Titania orbiter scenario would actually require roughly 100 km/s *less* $\left|\overrightarrow{\Delta V}\right|$ than the Ariel scenario if a traditional capture maneuver (e.g., at 50 km altitude) were employed and also if the extra 30° plane change maneuver were not required.

Given the high penalty (over a traditional capture nearer to Titania) associated with implementing the final approach maneuver depicted in Figure 5.42 and 5.43, it is appropriate to consider possible circumstances that might justify such a cost. The final approach maneuver in this scenario is implemented at more than 151,000 km distance from Titania, relatively far given that this value is twenty times the radius of Titania's sphere of influence and almost fifteen times its Hill radius. A circumstance which might require this is one where some type of navigation error results in a S/C missing a planned close approach to Titania, thus preventing a traditional capture maneuver within a severe time constraint. A similar situation could occur if a time-constrained S/C attempts to implement a planned (smaller) maneuver at an earlier phase of the approach to Titania but that maneuver fails to achieve the planned $\left|\overrightarrow{\Delta V}\right|$. An additional scenario where the large final approach maneuver may be justified is one where some type of Earth communication or data processing constraint, or perhaps even a mission science requirement, makes a significant capture maneuver close to Titania undesirable. Although these possibilities seem somewhat far-fetched, it is clear that considering the dynamics of the Uranus-Titania CR3BP enables the design of a precise Titania approach path beginning far outside Titania's sphere of influence without having to model two separate 2BPs under the patched-conic approximation.

Finally, an alternative Titania approach scenario is considered, which reduces the $\left|\overrightarrow{\Delta V}\right|$ of the final approach maneuver while still employing the CR3BP capture/transit path designed in Design Example #7. In this alternative scenario, only the final path to Titania is considered; therefore, the assumed interplanetary trajectory and Uranian tour described in Table 5.7 do not necessarily apply. The final approach maneuver is assumed to be implemented at the same position as in Figures 5.42 and 5.43, however, the approach path leading to that maneuver is now assumed to be a two-body (elliptical)

Hohmann transfer [106] between the 582,600-km radius of Oberon's orbit about Uranus and the 510,062-km radius of the assumed maneuver location. For simplicity, because both Titania's and Oberon's orbits are near-equatorial, the transfer is assumed to be in the *x*-*y* plane of the Uranus-Titania CR3BP primaries (in the same plane as Titania's orbit about Uranus). The alternative final approach is plotted in Figure 5.44 in the barycentric *x*-*y* rotating view and in Figure 5.45 in the Uranus-centric *X*-*Y* inertial view. The Uranus-centric two-body propagation (yellow) begins at the radius of Oberon's orbit 6.1 days prior to the final approach maneuver. As before, the propagation in the CR3BP (green) begins after the final approach maneuver and continues for 7.6 days until the capture maneuver opportunity and then into the interior region of Uranus until fourteen days following the capture maneuver opportunity. This alternative final approach maneuver, which is not claimed to be optimal, is now "energy"-raising and requires only $\left|\overrightarrow{\Delta V}\right|$ = 278.5 m/s. Furthermore, the S/C path in the Uranus-centric 2BP before the maneuver appears more consistent with the natural dynamics of the CR3BP path after the maneuver, especially in the inertial view in Figure 5.45, where the overall transit path is effectively a spiral from outside to inside Titania's orbit. Ignoring the assumed capture maneuver epoch in this scenario, if it is instead assumed that the orbital phasing between Titania and Oberon is such that Oberon is at the position labeled "Oberon departure" 13.7 days prior to the desired capture maneuver opportunity, then the required Oberon-centric excess velocity is a small V_∞ = 106.5 m/s. This value provides a possible—although rather stringent—flyby condition for the end of a Uranian system tour, where a slow Oberon flyby leads to the final approach path to Titania. Yet, a more practical scenario incorporating the Hohmann transfer path is one where a S/C already captured around Oberon in a highly-elliptical orbit implements a departure maneuver designed to insert it onto the Hohmann transfer approach path. Thus, an Oberon orbiter could also visit (and capture around) Titania. Assuming an Oberon-centric gravitational parameter equal to GM_O = 190.9467780172403 km^3/s^2 and a minimum maneuver altitude of 50 km above Oberon's 761-km body radius, the minimum Oberon departure cost is a small $\left|\overrightarrow{\Delta V}\right|$ = 8.2 m/s.

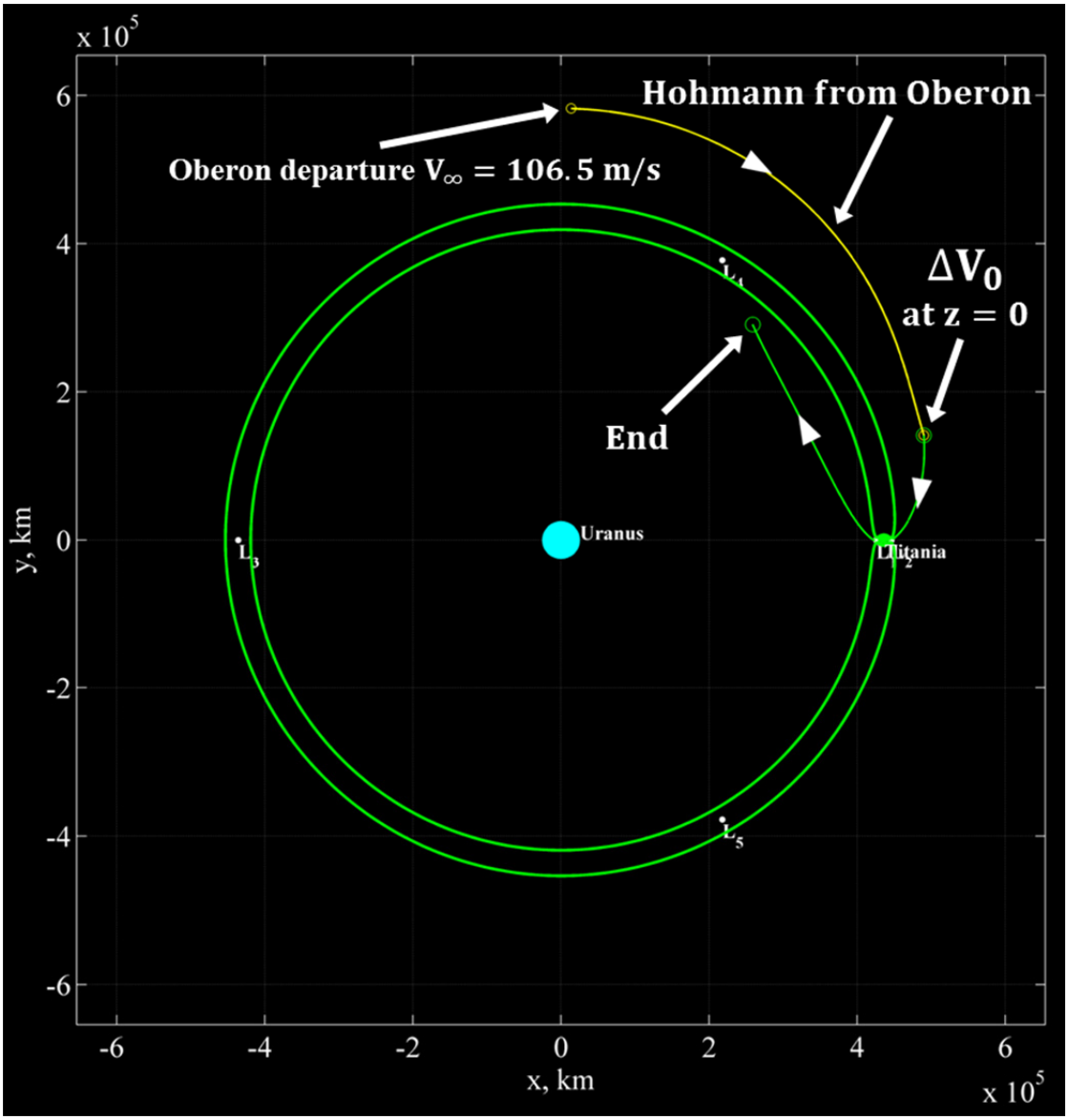

Figure 5.44. Rotating view of alternative final approach maneuver; transfer between two-body Oberon Hohmann transfer ellipse and Titania transit path; before approach maneuver (yellow); after approach maneuver and continuing past capture opportunity (green)

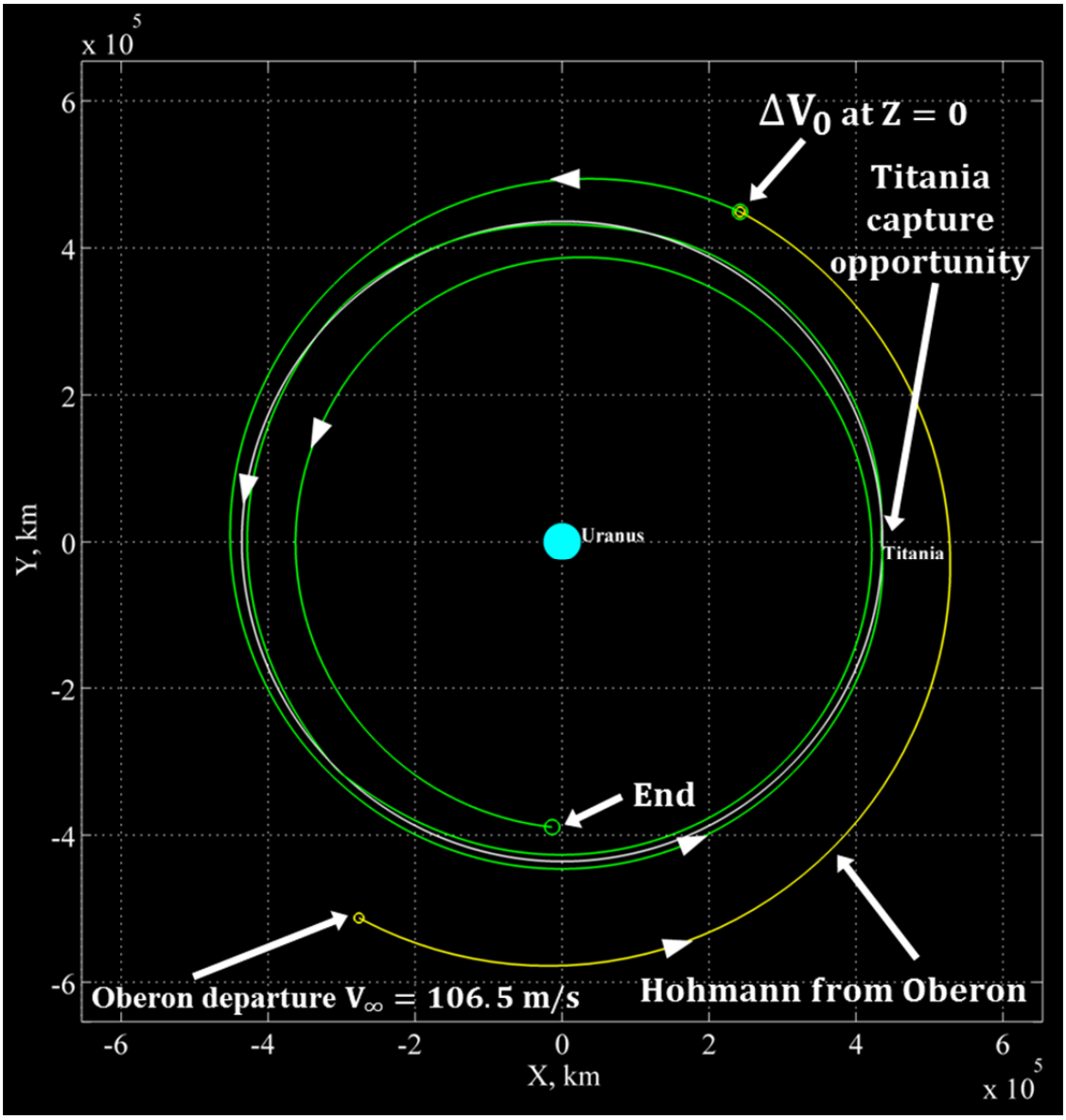

Figure 5.45. Inertial view of alternative final approach maneuver; transfer between two-body Oberon Hohmann transfer ellipse and Titania transit path; before approach maneuver (yellow); after approach maneuver and continuing past capture opportunity (green)

6. SUMMARY AND CONCLUSIONS

With no known, closed-form analytical solution to the CR3BP, it is difficult to obtain an appropriate reference solution for a S/C trajectory design objective in a multi-body dynamical environment. Moreover, chaotic regions of the CR3BP phase space make S/C motion—in some cases—effectively unpredictable over more than a brief span of time. Despite these obstacles, modeling orbits in the CR3BP can often expand the design options available to include trajectories—and low-cost maneuvers transferring between trajectories—that are not predicted/possible based on a purely two-body analysis. Yet, an added complexity exists in the spatial CR3BP as compared to the planar CR3BP. This complexity amounts to much more than simply the addition of a third direction of motion. Due to the differences between 2-DOF and 3-DOF systems, the spatial CR3BP exhibits behavior that is fundamentally more diverse and complex than in the planar CR3BP. Visual tools such as Poincaré maps, if they can be represented and interpreted, may provide valuable insight needed to overcome these complexities by reducing the view of the design space to one "slice" at a time. However, unlike the planar CR3BP, where a 2-D Poincaré map allows a map-based designer to view a "slice" of the S/C trajectory design space, the spatial CR3BP requires a 4-D map to achieve an analogous and equivalent view. Such a higher-D map presents a visualization challenge because it exists in a space consisting of more dimensions than the 3-D "real world" with which a human being is intuitively familiar. Further complicating matters is the fact that features on 4-D maps for the spatial CR3BP obey a fundamentally different topology than on 2-D maps. The challenges associated with representing a 4-D Poincaré map—and then utilizing it for S/C mission design—provide the motivation for the present investigation, which addresses the questions of how a 4-D map should be represented and

if it is possible/practical to employ such a higher-D representation to solve real-world trajectory design problems.

A novel approach to higher-D-map-based analysis and design in the spatial CR3BP is developed and successfully applied to a variety of 3-D S/C trajectory design scenarios. The design strategy is methodical and not restricted to any particular map formulation. To illustrate as much as possible of the "true" shape of 4-D Poincaré map features, all four map dimensions are represented in this analysis. This allows for a one-to-one mapping between a 6-D state in the full phase space and a 4-D point on a map, permitting full representation of higher-D map features and realization of some aspects of their form that might be lost when viewing merely their lower-D projections. Distinguished from typical methods of representing 4-D Poincaré maps in the CR3BP, which involve adding some type of arrow or line segment to a point (e.g., Paskowitz and Scheeres [2] and Haapala and Howell [3, 4, 5]), the design approach in the current effort includes the space-plus-color method for representing, interpreting, and manipulating 4-D Poincaré maps in an interactive, 3-D visual environment in which the fourth dimension is displayed using color. This method expands on the color and rotation method developed by Patsis and Zachilas [7], which has been successfully employed in studies related to stellar motion in a galaxy. The focus of the current investigation is on the practical tools and techniques that enable 4-D-map-based design in the dynamical environment of the CR3BP by overcoming challenges inherent in utilizing information displayed on higher-D maps. Especially challenging are the cases where a 4-D map is generated by many different trajectories.

The main contribution of this effort is the extension of 2-D-map-based CR3BP trajectory analysis and design strategies to higher dimensions. By representing, interpreting, and manipulating 4-D maps using the space-plus-color method in a visual environment, human insight is leveraged to initiate automated processes and expand the design options. Design results include S/C trajectory solutions of practical use. An additional analysis result is the correlation of the long-term variations in osculating eccentricity of a high-altitude Earth orbit perturbed by lunar gravity with the shape and evolution of the surface of a deformed 2-torus on a 4-D map. This concluding chapter

summarizes these contributions/results, with recommendations for future work presented in the final section.

6.1 Extending 2-D-Map-Based Design Strategies to Higher Dimensions

The present investigation develops and applies techniques for trajectory design using a "true" 4-D Poincaré map for the spatial CR3BP. The basic premise of this effort is that twenty-first-century visualization technology has advanced sufficiently such that the task of representing and interpreting higher-D maps may only be difficult—but not impossible. Two-dimensional-map-based design strategies useful in the planar CR3BP are successfully extended to the higher dimensions required for the spatial CR3BP. This is demonstrated though a variety of S/C mission design cases involving 3-D trajectories in the Earth-Moon, Sun-Earth, and Uranus-Titania CR3BP systems while utilizing several different 4-D Poincaré map formulations. Note that a map formulation that is practical for a given problem is a key element in a successful design strategy. The maps are used to visualize and gain insight into the design space for different types of astrodynamics problems in a multi-body environment.

Four examples of basic, 3-D trajectory design are initially presented, focusing on the creation of appropriate 4-D Poincaré maps and the use of those maps in an interactive visual environment to obtain trajectory design solutions through what are mainly visual processes. In Design Example #1, a process used by Craig Davis and Howell for S/C capture maneuver design in the planar CR3BP [34, 35] is successfully extended to the spatial CR3BP to design a 3-D capture maneuver in the vicinity of Titania in the Uranus-Titania CR3BP. In Design Example #2, a 3-D S/C "return-to-Earth" maneuver in the Earth-Moon spatial CR3BP is implemented based on an adjustment to create a potential intersection in the full 4-D space of a map, with a reasonable guess for the required adjustment determined by visual inspection. Design Example #3 provides an example involving the single location ambiguity of the space-plus-color method as applied to 4-D maps. Included is a strategy for overcoming this challenge through careful interpretation of map returns to design a 3-D S/C Earth transit maneuver in the Sun-Earth spatial CR3BP. Finally, Design Example #4 demonstrates the design of a 3-D S/C transfer

between orbits in the Earth-Moon spatial CR3BP based on 4-D manifold maps. Note that the first three basic design examples involve trajectory design in the context of different types of CR3BP libration point gateway dynamics in the vicinity of the smaller primary in various systems. In these examples, the resulting visual guess obtained from the Poincaré map is, in and of itself, a valid—but not claimed to be optimal—solution to the qualitative objective of the problem (e.g., capture, departure, or transit). On the other hand, Design Example #4 is an orbit transfer problem between two periodic LPOs; the estimate obtained visually from the 4-D map must be fed into an automated targeting process to achieve a precise—but still not claimed to be optimal—solution to the problem. For completeness, a locally-optimal transfer solution to this orbit transfer problem is also presented.

Four-dimensional-map-based design techniques are next demonstrated for three, advanced, real-world astrodynamics problems involving 3-D S/C trajectories, thus providing a validation of the design approach presented in this investigation. Reasonable guesses obtained visually from the map are exploited in follow-on, automated processes—i.e., targeting, optimization, and transitions to other dynamical models—to determine precise solutions that are of practical use for real-word trajectory design scenarios. These three advanced design examples involve more complex trajectory design tasks than the four basic examples. In Design Example #5, different 4-D maps are used for different phases of analysis/design for a HEO-to-LPO-to-LPO orbit transfer problem consisting of multiple 3-D trajectory legs in the Earth-Moon spatial CR3BP. In Design Example #6, a 4-D map is exploited to design an Earth-Moon spatial CR3BP 3-D transfer path between two GEO orbits (at two epochs) defined based on both a lower-fidelity (two-body) model as well as two higher-fidelity (ephemeris) reference states. Finally, in Design Example #7, a 4-D map is used to locate a stable periodic orbit in the vicinity of Titania in the Uranus-Titania spatial CR3BP; that orbit is then used as the basis for designing a Titania orbiter mission—with multiple contingencies—as the final phase of a plausible tour of the Uranian system.

Based on the results of the basic and advanced design examples, the key findings from this investigation are that higher-D-map-based design in the spatial CR3BP is

practical and that success is enabled by interactive tools and techniques in a visual environment. It is important to emphasize that, while this investigation focuses heavily on how tools and techniques in a visual environment enable the space-plus-color method of representing, interpreting, and manipulating 4-D Poincaré maps, most of the basic concepts presented in this dissertation are relevant to 4-D-map-based design utilizing any representation method. Furthermore, many aspects of the trajectory design strategy in this analysis—from generic display methods and filtering processes to the specific design approaches for different 4-D-map-based design examples—apply to higher-D-map-based design as a whole. Thus, this dissertation can be considered a report of an investigation into 4-D-map-based design (in the spatial CR3BP) accomplished using a visual environment, with many benefits, challenges, and lessons learned applicable to future investigations no matter how the four map dimensions are represented.

6.2 Representing, Interpreting, and Manipulating 4-D Maps Using the Space-Plus-Color Method in a Visual Environment

This investigation advances the understanding of effective strategies for orbit design in a multi-body dynamical environment. While there are many examples of Poincaré-map-based analysis and design in the planar CR3BP, there are fewer examples of map-based analysis and design in the spatial CR3BP, most of which employ some form of reduction or projection to fewer dimensions. Furthermore, methods of representing all four dimensions associated with Poincaré maps for design in the spatial CR3BP are even rarer and typically involve adding some type of arrow or line segment to a point associated with a given map return. Such methods suffer to various extents from the spatial scale limitation because they represent an extra dimension by augmenting a point in space with a higher-than-“zero”-dimensional object (see Section 3.1.1). To maximize the ability of a 4-D map representation to provide insight into all four map dimensions—even when greatly zoomed out—it is desirable to choose a method for representing the extra dimension that suffers the least from the spatial scale limitation. For trajectory design applications of Poincaré maps for the spatial CR3BP, the more a plot of map returns can be zoomed out while still allowing insight into all four map dimensions, the

more likely it is that a map-based designer can gain insight into the "global" view and the higher-D nature of the design space. While a particular method of representing an extra dimension on a map may allow visibility of all four dimensions when the view is sufficiently zoomed in to a region of interest, an important aspect of map-based design is the ability of a fully-zoomed-out map to provide visual cues that indicate what region of interest should be zoomed into in the first place. In other words, the power of the 4-D Poincaré map is most realized when all map dimensions are visible in the "big picture" and features of interest for design can be located without prior knowledge of the appropriate region to zoom.

In the current investigation, the purpose of representing all four dimensions is to visualize—as much as is possible—the "true," higher-D shape of features on a map. Consequently, three of the four map dimensions are displayed in a 3-D space, thus maximizing the number (three) of map coordinates that can be represented in a familiar and intuitive manner. Because there are no more spatial dimensions available—either in the physical, everyday world or in a 3-D visual environment—the extra, fourth dimension must be represented by some other characteristic associated with a given map point. The choice in the present investigation is the space-plus-color method, using the plotted color of a dot to represent the value of the extra coordinate. This method effectively preserves the "zero"-dimensionality of a dot and thereby avoids the spatial scale limitation suffered by other methods. That is not to say that the space-plus-color method is necessarily superior to other methods for all types of map-based design, nor is it free from its own unique limitations. What can be claimed is that the space-plus-color method, at a fundamental level, has the potential to maximize the ability of the human eye to discern all four dimensions on a 4-D Poincaré map consisting of many points even when zoomed out. Within this context, it is possible to distinguish the 4-D locations of each map point and also to define higher-D map regions. Moreover, patterns and symmetries are identified using a color scale—even amidst the clutter of many map points.

The space-plus-color method for representing, interpreting, and manipulating 4-D Poincaré maps in an interactive, 3-D visual environment expands on the color and rotation method developed by Patsis and Zachilas [7] (used for the study of motion in a

galaxy) by applying additional tools and techniques that enable 4-D-map-based design in the dynamical environment of the CR3BP. The focus herein is on the practical techniques needed to overcome challenges inherent in utilizing information displayed on higher-D maps, especially in the case where a map is generated by many different trajectories. Thus, an ancillary contribution of the current investigation is the extensive demonstration of an effective, color-based method for representing a 4-D Poincaré map in the context of design; the method seems well-suited to engineering applications in general.

In this investigation, successful higher-D-map-based trajectory design is enabled by a visual environment created in MATLAB®. Six-dimensional trajectory data sets and 4-D Poincaré map data sets are processed in MATLAB®, and results are normally first displayed and interpreted using MATLAB® plots. Often, interpretation of Poincaré map images is then supported by transferring certain visualizations to the Avizo® visual environment, which greatly facilitates the interpretation of higher-D map features. To perform map-based trajectory design using the space-plus-color method—often based on 4-D maps generated by many different trajectories—in addition to rotating and zooming an image in 3-D space, further manipulation of the image is accomplished. This additional manipulation is iterative in nature and includes: (1) interactively "zooming" in the color dimension in a manner similar to zooming in the spatial dimensions, (2) "filtering" out features that are obscuring the view based on the spatial and color coordinates as well as various other criteria, (3) exploring a map in stages with short versus long-term propagations, (4) associating and annotating map returns with information relevant to CR3BP trajectory design, and (5) interactively modifying the size(s) of plotted dots.

The space-plus-color method of representing 4-D Poincaré maps is not without its limitations. The most fundamental and significant limitation as compared to other methods happens to be a consequence of its greatest advantage over those other methods. While the use of color to represent an extra coordinate associated with a point in a 3-D space effectively preserves the "zero"-dimensionality of a dot and thereby avoids the spatial scale limitation suffered by other methods, this same aspect of the space-plus-

color method also leads to an ambiguity associated with plotting more than one point at the same location in the 3-D space but with different color coordinate values. This single location ambiguity must be recognized when generating and interpreting 4-D Poincaré maps for the spatial CR3BP. In practical, map-based trajectory design applications, the ambiguity is most often encountered in the case of a seeded, 4-D grid of initial conditions, where multiple points with a range of different color coordinate values are selected to have the same exact location in the 3-D map space. Careful and problem-dependent interpretation of the initial condition map returns displayed (as in Design Example #3) along with interactive filtering (as in Design Example #7) assist a map-based designer in overcoming the challenges associated with this limitation of the space-plus-color method.

Other limitations of using color to represent an extra dimension are the result of the sensitivities associated with viewing color. For example, a point with the same specified color can appear different on a computer screen when displayed in different visual environments, depending on factors such as the background color used and the size and shape of the dot chosen to represent a point. Such discrepancies with color do not normally detract from the ability to interpret the Poincaré map and accurately estimate the value of the color coordinate associated with a particular map point—as long as appropriate color scale limits are selected. Furthermore, a lesson learned from experimenting with various color schemes, with a range of observers, for this 4-D map display method is the fact that the full spectrum of color is better resolved against a black (or gray) map background. Though dark colors (like blue and purple) are more difficult to view against a black background, lighter colors (like cyan and yellow) are even more difficult to view against a white background. Also important are techniques for "zooming" and filtering in terms of the color dimension in order to properly estimate the value of the fourth coordinate on a 4-D map. Note that there is an ambiguity due to the color red representing both the lower and upper limits of the color scale employed in the current investigation. This ambiguity may be resolved by defining the color scale values such that the limits are large enough to have all possible fourth coordinate values uniquely associated with the "inner" colors on the scale (i.e., orange though magenta). In addition, order/structure in the color dimension of a 4-D Poincaré map for the spatial

CR3BP is often encountered; a "rainbow" spectrum of color on the map may be used to resolve the red color ambiguity.

Significant advantages of representing all four dimensions on 4-D maps (rather than simply 3-D projections) for the spatial CR3BP are evident from various examples in this investigation. In the analysis of the "doughnut" presented in Section 3.1.2, patterns in the color dimension aid in the interpretation of the topology of features on a 4-D map associated with quasi-periodic and periodic behavior. Similar insight is exploited for locating a stable, period-eight orbit from a map with 543,816 returns generated by 1,296 different trajectories in Design Example #7. Moreover, in Design Example #1, a comparison of two 4-D Poincaré maps reveals that capture trajectories generate periapsis returns in an isolated region around Titania and also include velocity angles (colors) indicating near-planar retrograde direction in the rotating frame. The velocity angle information would be missing from a 3-D projection view of the map. In Design Example #2, a "return-to-Earth" maneuver implemented based on all four dimensions of the map successfully achieves the design objective, while a maneuver based on only three of the dimensions does not. Similarly, in Design Example #3, an Earth transit maneuver based on all four dimensions of the map results in passage through the L_1 gateway within three months, while a maneuver based on a design process that ignores the fourth dimension is unsuccessful. Finally, as discussed in Section 3.2, it is demonstrated that two "side views" of a 4-D Poincaré map properly represented in a visual environment can display a total of four dimensions of information. Even in the cases where more than two "side views" of a map are displayed, this visual technique is useful (throughout this investigation) for interpreting the same map feature across multiple perspectives.

6.3 Leveraging Human Insight to Initiate Automated Processes and Expand the Design Options

Exploiting higher-D Poincaré maps for S/C orbit design in a multi-body environment requires a combination of visual and automated processes. Given the complex design space in the CR3BP—which is an effectively "unsolvable" dynamical problem—certain trajectory design steps cannot be completely automated. In a 2BP-focused design

procedure, conic arcs serve as reference solutions for the motion of a S/C in the vicinity of a central body, assuming any additional forces can be modeled as small perturbations on the nominal, conic path. However, with no known, closed-form analytical solution to the CR3BP, which contains chaotic regions in its phase space, it is far more difficult to obtain an appropriate reference solution for a given trajectory design objective. A "brute-force" search of the design space for a particular solution satisfying some criterion would not only be computationally inefficient but, more importantly, it would not likely result in sufficient understanding of the design space. This is particularly true in the chaotic regions of the CR3BP phase space, where the future state along a given trajectory is extremely sensitive to the initial condition. A small difference in either the position or velocity of a S/C could result in a vastly different future path. Understanding the "big picture" of a design space is critical when analyzing trade-offs between qualitatively different solutions and also in applying lessons learned from one design result to future design cases. The "big picture" view also provides an engineer the context to verify that a particular design result is valid and usable.

The Poincaré map itself is an effective visual tool for obtaining a reasonable initial guess for a design solution satisfying various qualitative criteria. Combined with other visual tools and techniques enabled by computer software, a 4-D map generated by trajectories in the spatial CR3BP leverages human cognitive capabilities by providing an estimate that may then be used to initiate a more precise, automated process, e.g., targeting, optimization, or the transition to other dynamical models. Thus, the overall map-based design procedure involves cooperation between uniquely-human intuition and the computational power of modern computers. For trajectory design in the spatial CR3BP using 4-D Poincaré maps—as represented using the space-plus-color method in this investigation—interactive visual processes are most useful for obtaining initial guesses that meet certain qualitative criteria, while automated processes are normally better-suited for tasks requiring quantitative precision and/or algorithmic repetition. In Design Examples #4, #5, #6, and #7, reasonable design estimates obtained visually from a 4-D Poincaré map are fed into follow-on, automated processes that lead to precise and/or locally-optimal solutions to the design objectives. For instance, in Design

Example #7, visual estimates based on 4-D map structures are fed into a multiple shooting process, which results in periodic solutions to within a satisfactory convergence criterion/tolerance.

In the case of optimization, once a precise (targeted) solution is available to initiate the optimization process, many of the assumptions that prove useful up until this step in the design process are no longer necessary and are removed so that a locally-optimal solution (in terms of total $\left|\overrightarrow{\Delta V}\right|$ of the transfer) can be determined with greater flexibility. In other words, while various simplifying assumptions such as the definition of a hyperplane and the "energy" level(s) associated with one or more 4-D Poincaré maps are useful for obtaining an initial estimate as well as a targeted solution using the map, these assumptions should not be requirements on the final solution. In general, the fewer constraints that are enforced on a design space, the more flexibility there is in reducing a cost function through optimization of the design variables within that space. This removal of assumptions/requirements in a later stage of the design process ultimately increases the power of higher-D-map-based trajectory design.

The second phase of Design Example #5 (see Section 5.1.2) provides a striking example of the concept that the 4-D Poincaré map and its associated interactive visual processes are most useful for obtaining initial guesses that meet certain qualitative criteria rather than for assessing quantitative metrics When two visually-obtained halo-to-butterfly LPO transfer options are compared based on the quantitative criterion of the total $\left|\overrightarrow{\Delta V}\right|$ of the estimate—while ignoring the qualitative information from the 4-D map concerning the natural dynamics of the LPOs—it seems as if the "northern" butterfly orbit transfer option is at least equal to, and even slightly superior to, the "southern" butterfly option. However, the "southern" option involves a transfer path that is more consistent with the natural dynamics of the two LPOs. Although the visually-obtained estimates and the targeted solutions for the two transfer options yield similar values of total $\left|\overrightarrow{\Delta V}\right|$, the associated optimized solution for the "northern" option is more than twice as costly as the "southern" option. The $\left|\overrightarrow{\Delta V}\right|$ comparison also demonstrates how optimization can play a critical role in the overall Poincaré-map-based design strategy. Also noteworthy in this design example is the fact that the design space for the

"southern" transfer option is obtained through reflection in two dimensions of the 4-D map (one spatial coordinate and the color coordinate). This reflection is accomplished entirely in the visual environment of the map, without having to calculate either the orbit itself or the stable manifold tube associated with the "southern" butterfly LPO.

An additional example of the power of the 4-D-map-based—and CR3BP-focused—design process is given in Design Example #6 for a scenario involving a transfer between two GEOs—with a large inclination difference—by means of a lunar flyby. A "kink" on a 4-D map provides a unique visual indication that the effect of the CR3BP dynamics—namely, the addition of the Moon's gravity—is to warp the flat orbit plane geometry of what are nominally equatorial and polar-inclination trajectories with respect to the Earth-centric 2BP. Moreover, this significant warping effect provides a visual cue that the GEO-to-GEO transfer $\left|\overrightarrow{\Delta V}\right|$ might be reduced by exploiting lunar gravity. Ultimately, the 4-D-map-based and CR3BP-focused design process, though requiring more time, achieves GEO-to-GEO transfer results (in this example) that are superior to those determined through a more traditional, 2BP-focused design process. The map-based process not only yields lower-$\left|\overrightarrow{\Delta V}\right|$ solutions for both a three-maneuver and a two-maneuver transfer, but it also is the only process that leads to a practical two-maneuver option. In fact, even when an additional 2BP-focused method is considered, the map-based process still compares favorably. While it can certainly not be claimed that such benefits would be achieved in all problems (the benefits of any design method are problem-dependent and sensitive to the assumptions made in each design scenario), what is clear is that the map-based process can expand the design options available for consideration. This expanded design space has the potential in other scenarios, just as in this particular scenario, to reveal lower-$\left|\overrightarrow{\Delta V}\right|$ solutions not predicted by 2BP-focused design methods. Moreover, since the CR3BP is used from the outset in the map-based design process, the estimates obtained from the Poincaré map are expected to be more accurate and more qualitatively similar to the precise CR3BP solutions than estimates based on the 2BP (a lower-fidelity model).

For each design example included in the present investigation, the total time required to successfully perform the entire design procedure is between several hours and roughly

one day, depending on the complexity of the design objective and/or the associated design space. Note that this total time is actually spread out over a few days in the development of each design case in the current effort. Seeding initial conditions and generating 4-D Poincaré maps requires anywhere from several minutes to a few hours. Filtering/interpretation using tools in the visual environment also requires between minutes and a few hours. Trajectory targeting requires anywhere from a few seconds to several minutes, while trajectory optimization requires anywhere from roughly one minute to several hours. Finally, transitioning a CR3BP solution to another dynamical model requires roughly minutes for transitioning to the 2BP and several hours for transitioning to the higher-fidelity dynamical model constructed in STK®. The times required for automated tasks performed in MATLAB® are specified in elapsed time (MATLAB® Version: 7.14.0.739 (R2012a); benchmark: 0.0600, 0.0637, 0.0741, 0.1641, 0.2727, 0.7146).

6.4 Spacecraft Trajectory Solutions of Practical Use

Results of design examples considered in the present investigation include several preliminary S/C trajectory solutions of potential practical use. The first is a transfer between a GTO-style, HEO trajectory and an LPO near the Moon (Design Example #5). Even though a practical Earth-centric orientation for the HEO is not a consideration in the HEO-to-LPO transfer design process, the inclination of 35.50° for the solution chosen from the 4-D map is roughly representative of that of a real-world GTO and well within the allowable limits of a KSC launch based on launch azimuth constraints. In the same design example, transfers between LPOs in the vicinity of the Moon are also determined. In Design Example #7, a transfer into a capture orbit around Uranus's moon Titania is designed. The capture is also validated in a realistic, higher-fidelity model using STK®. Furthermore, the preliminary capture orbit design is considered in the context of a plausible mission scenario in which the designed path is the final phase of a Uranian system tour of the type designed by Heaton and Longuski [67].

6.5 Correlating the Long-Term Variations in Osculating Eccentricity of a High-Altitude Earth Orbit Perturbed by Lunar Gravity with the Shape and Evolution of the Surface of a Deformed 2-Torus on a 4-D Map

The current investigation includes an analysis (see Section 3.1.2) correlating the long-term variations in instantaneous eccentricity of a high-altitude Earth orbit perturbed by lunar gravity with the shape and evolution of the surface of a deformed 2-torus on a 4-D map. Additional study is necessary to determine the extent to which the specific relationship, in this one example, is applicable in other cases. Yet, the association of perturbed, nominally two-body, Earth orbits with KAM tori is evident from investigations by Wiesel [69, 70] of low-altitude orbits perturbed by the Earth's non-spherical gravity field, i.e., the geopotential. Also, based on analyses using reference KAM tori that ignore lunar gravity, Bordner [119] and Hagen [120] both indicate that there may be value in incorporating/fitting lunar gravity into a reference KAM torus for Earth satellite motion. Although this topic is not the focus of the present investigation, the analysis in Section 3.1.2 suggests that the space-plus-color method—as applied to 4-D Poincaré maps displayed in a visual environment—could allow an intuitive means to explore relationships between Earth satellite perturbations and deformed KAM tori.

6.6 Recommendations for Future Work

This effort is not the first study related to orbit design in a multi-body dynamical environment using higher-D Poincaré maps, nor should it be the last. The following are ten recommendations for future investigators:

- *Implement the 4-D-Poincaré-map-based trajectory design approach developed in this investigation using more sophisticated visualization software tools*.

  In the current investigation, applying the space-plus-color method, visual filtering processes in the MATLAB® visual environment are accomplished by reprocessing/replotting the map image. On the other hand, in the Avizo® visual environment, filtering based on both the spatial and color coordinates of map returns, as well as the trajectory number, return counter, and propagation time

associated with returns, is accomplished in real time using the GUI; yet, other filtering tasks still require reprocessing/replotting the image. Moreover, follow-on, automated processes—i.e., targeting, optimization, and transitions to other dynamical models—are initiated (in MATLAB® scripts) outside the visual environment after obtaining a visual estimate from the 4-D map. Also, displays of trajectories in the configuration space of the spatial CR3BP are separate from the map displays. The software tools utilized do not include any capability to "point and click" on a 4-D map return and immediately investigate the 6-D CR3BP trajectory associated with that return or initiate any follow-on, automated processes.

To improve the interactivity of both visual and automated map-based design processes for future investigations, software tools like those developed by Schlei [125, 126], which interact directly with images in the Avizo® visual environment to initiate various numerical processes (and display their results), may prove useful. Such tools could greatly reduce the time required for a map-based designer to visually obtain estimates from the 4-D Poincaré map in more advanced implementations of the map-based design approach developed in this analysis. Furthermore, a more sophisticated visual environment enabled by such tools could allow for a map-based designer to quickly survey a wider variety of available trajectory design options based on multiple 4-D maps defined over a range of hyperplane locations and "energy" levels.

The ultimate goal might be for a map-based trajectory designer to be able to stand in a room filled with holographic images representing features on a 4-D Poincaré map. This could provide a completely immersive experience of the visual cues relevant to design. Through a combination of hand, head, and eye movements, the designer could explore the higher-D design space by zooming, rotating, or even "flying" through the surrounding image of the map. Similar hand/head/eye movements could be used to filter map returns based on their spatial or color coordinates or any other criteria, resulting in an unobscured view of a map region/structure of interest. Once the designer uses her intuition to

obtain a trajectory design estimate from the map by visual inspection, she might then seamlessly transition to a virtual reality perspective of the S/C orbit(s), which could allow her to initiate, and witness the results of, various follow-on, automated processes (e.g., targeting, optimization, and transitions to other dynamical models) in real time.

- *Study further the various "tori"/"doughnut" structures observed on 4-D Poincaré maps for the spatial CR3BP using the space-plus-color method and rigorously correlate their appearance with different types of dynamical "flow" relevant to trajectory design.*

  Improved understanding of Poincaré map features associated with various types of deformed KAM tori may lead to a systematic (and straightforward?) method of obtaining visual estimates for periodic and quasi-periodic orbits using a 4-D map for the spatial CR3BP in a manner that is analogous to the interpretation of "island" and "island chain" structures on 2-D maps for the planar CR3BP. Greater clarity may be achieved through a more in-depth comparison between structures observed on 4-D maps for the CR3BP and the various features analyzed using the color and rotation method [6, 7, 57, 58, 59, 60, 61]. In those studies related to stellar motion in a galaxy, the appearance of various types of "tori" and "tubes" are rigorously correlated with dynamical behavior, especially the stability/instability of nearby fixed points generated by periodic orbits. Further insight may be gained by correlating the spatial shape and color patterns of various "doughnut"-like features observed on the 4-D map with a rigorous numerical frequency analysis of the type accomplished by Bosanac [121] and Bosanac et al. [122] for 2-D maps generated in a modified version of the planar CR3BP.

  A study of various "tori" in the spatial CR3BP should examine a wide variety of quasi-periodic orbits, considering those associated with both stable and unstable periodic orbits, including the families of quasi-periodic variants of 3-D, periodic orbits in the vicinity of both the collinear and triangular libration points.

Perturbations on, as well as asymptotic manifold paths to/from, these trajectories should also be examined. Further investigation may reveal fundamental features—e.g., certain recurring spatial shapes or color patterns—on 4-D Poincaré maps that might illuminate the solution space for mission design. This effort should also consider the potential applications of 4-D map formulations that use variables/coordinates other than those already investigated herein.

Because the apparent shape of 4-D map structures generated by any given trajectory varies depending on the choice of map formulation—including which coordinate is represented by color—it may be useful to explore certain map features using multiple formulations of space versus color. That is, if a 4-D map is displayed by representing coordinates A, B, and C in 3-D space and coordinate D using color, that same map could also be examined by representing coordinates B, C, and D in 3-D space and coordinate A using color. Of course, there are two other possible combinations, with either B or C represented using color.

- *Investigate the possibility that the space-plus-color method might be adapted to allow the mixing of different colors of light on a 4-D Poincaré map display in a way that could highlight information relevant to trajectory design.*

  A more sophisticated approach to analyzing visible patterns in the color dimension of a 4-D map could be enabled by a projection method that allows the human eye to perceive the mixing of different-colored light associated with a given map region. For example, a region filled with many red as well as many blue map returns would appear magenta-colored to the map-based designer. This approach could allow map features with order/structure—often appearing with a smooth progression through a "rainbow" spectrum of color—to maintain their distinct appearance, while a chaotic, mixed-colored "cloud" of surrounding points might appear white due to the mixing of most/all colors. Of course, for this method to be useful, the apparent white regions of the map may have to be filtered out by the map-based designer so that they do not obscure other regions possessing apparent structure in color.

The mixing of different-colored light could also aid the process of obtaining an estimate for the "average" color value associated with a region of a 4-D map. For example, in map displays in the present investigation, a 3-D map space filled with both green and blue dots implies that a cyan dot in the same 3-D space would also be inside the boundaries of the associated 4-D map region. In the imagined, future approach where light is allowed to mix, this region might actually appear cyan-colored, allowing a direct, visual estimate for the color value of a point inside the 4-D map region.

- *Evaluate which "visual" 4-D-Poincaré-map-based design processes might be automated with computer vision and artificial intelligence.*

  In the current investigation, a distinction is made between the visual 4-D-map-based design steps, which leverage human cognitive capabilities (intuition based on visual cues) and the automated steps, which exploit the speed and numerical accuracy of computers. As human engineers design more capable computers, some "uniquely"-human insight might be encoded in 4-D-map-based design software. This technological advancement would not, however, make the current investigation irrelevant. It would simply mean that the visual processes described herein would shape the requirements for the "visual" computer algorithm. Furthermore, even if all "visual" design processes can someday be automated, a human engineer will likely still require insight gained from viewing displays of maps, if only for the purpose of understanding how to program the computer.

- *Explore the relationships between Earth satellite perturbations and deformed KAM tori using 4-D Poincaré maps displayed in a visual environment.*

  Additional study is necessary to determine the extent to which the specific relationship noticed in the current investigation—between the long-term variations in instantaneous eccentricity of a high-altitude Earth orbit perturbed by lunar gravity and the shape and evolution of the surface of a deformed 2-torus on a 4-D map—is applicable in other cases. Future investigations employing the

space-plus-color method may result in insight that enables the incorporation of lunar gravity into a reference KAM torus for Earth satellite motion, along the lines of previous research by Wiesel [69, 70] using reference tori that ignore lunar gravity.

- *Depict the evolution of 4-D Poincaré map features in the CR3BP as the "energy" level is varied.*

  Although examples are not presented in this dissertation, it appears from the current investigation that various structures on the 4-D map for the spatial CR3BP, in addition to "pointing" to various periodic behavior in their immediate vicinity on the same map—at the same value of "energy"—also "point" to related behavior at other "energy" levels. This is akin to the structure of "island chains" on 2-D maps for the planar CR3BP that often indicates the approximate map location of the bifurcation that formed the feature at a different "energy" level. Accordingly, representations of 4-D maps using the space-plus-color method may provide insight supporting bifurcation analysis in the spatial CR3BP.

- *Perform a comparative study of various methods for representing 4-D Poincaré maps in the spatial CR3BP.*

  The relative strengths and weaknesses of different methods for representing 4-D maps should be assessed in the context of different types of trajectory design problems in a multi-body environment. The most suitable method of representing a 4-D map will likely depend on the specific application. The space-plus-color-method could be compared to other methods such as the planar "glyph" visualizations utilized by Haapala and Howell [3, 4, 5] or the 3-D phase space sections employed by Richter [63] and Richter et al. [64].

- *Catalog different types of 3-D S/C capture orbits in the vicinity of the smaller primary for a variety of systems in the spatial CR3BP in terms of their appearance on a 4-D Poincaré map.*

  This effort would employ 4-D Poincaré maps in a similar manner as Craig Davis uses 2-D periapsis maps to identify 2-D capture orbits in the planar CR3BP [40]. The goal would be to classify various 3-D orbits in the vicinity of P_2 by correlating their behavior in the rotating and inertial frames with various regions on 4-D maps represented using the space-plus-color method. Such classifications could then support more sophisticated mission design.

- *Examine the characteristics of 4-D Poincaré map features that provide visual cues supporting trajectory optimization in the CR3BP.*

  In the present investigation, qualitative information from a 4-D map in one design example implies that a particular LPO-to-LPO transfer option is more consistent with the natural dynamics of the two LPOs than another possible option. Although the visually-obtained estimates and the targeted solutions for the two transfer options yield similar values of total $\left|\overrightarrow{\Delta V}\right|$, the associated optimized solution for the more consistent option is less than half as costly as the other option. Similar types of qualitative information may provide visual cues that allow a map-based designer to choose design estimates that lead to lower-$\left|\overrightarrow{\Delta V}\right|$ solutions after optimization. In addition, while the current investigation relies exclusively on local optimization procedures, future studies may identify 4-D map features indicating that a visual estimate is associated with a global optimum.

- *Apply the 4-D-Poincaré-map-based trajectory design approach developed in this investigation to other dynamical models.*

  Mission design in the spatial CR3BP is the subject of the present investigation. A 4-D Poincaré map allows a map-based designer to view a "slice" of the S/C trajectory design space. Yet, future studies may represent 4-D maps using the space-plus-color method for the purpose of design in other dynamical

environments. Analysis and design in the context of any time-invariant, 3-DOF system with one constant of the motion could similarly benefit from a one-to-one mapping between a 6-D state in the phase space and a 4-D point on a map. Furthermore, other types of dynamical models—even those with more than six dimensions in the phase space or more than four dimensions on a surface of section—may benefit from 4-D visualization. Perhaps the definition of a "map" will need to be relaxed to allow for displays of hyperplane crossings associated with trajectories without a constant of the motion. In addition, systems with more than four dimensions on a true surface of section might be represented using only a 4-D projection of the higher-than-4-D map.

Other S/C dynamical models worthy of exploration using 4-D views are: (1) multi-body environments with more than three bodies; (2) continuous-thrust or solar sail applications; (3) perturbations on Earth satellite two-body motion due to the geopotential, atmospheric drag, third-body (lunar/solar) gravity, or solar radiation pressure; and (4) formation flying involving more than one S/C. Additionally, 4-D visualization could be applied to models incorporating the attitude dynamics of a S/C.

Finally, the space-plus-color method of representing, interpreting, and manipulating a 4-D map may be applicable/useful in other engineering or scientific disciplines.

LIST OF REFERENCES

LIST OF REFERENCES

[1] Szebehely, V., *Theory of Orbits: The Restricted Problem of Three Bodies*, Academic Press, New York, 1967.

[2] Paskowitz, M. and Scheeres, D., "Robust Capture and Transfer Trajectories for Planetary Satellite Orbiters," *Journal of Guidance, Control, and Dynamics*, Vol. 29, No. 2, 2006, pp. 342-353.

[3] Haapala, A. and Howell, K., "Representations of Higher-Dimensional Poincaré Maps with Applications to Spacecraft Trajectory Design," IAF 63rd International Astronautical Congress, Naples, Italy, October 1-5, 2012.

[4] Haapala, A. and Howell, K., "Trajectory Design Strategies Applied to Temporary Comet Capture Including Poincaré Maps and Invariant Manifolds," *Celestial Mechanics and Dynamical Astronomy*, Vol. 116, No. 3, 2013, pp. 299-323.

[5] Haapala, A. and Howell, K., "Representations of Higher-Dimensional Poincaré Maps with Applications to Spacecraft Trajectory Design," 25 Nov. 2013, to appear in *Acta Astronautica* [online], URL: http://dx.doi.org/10.1016/j.actaastro.2013.11.019 [cited 28 Nov. 2013].

[6] Patsis, P. and Zachilas, L., "A Method for Visualizing the 4-Dimensional Space of Section in 3-D Hamiltonian Systems," *Hamiltonian Mechanics: Integrability and Chaotic Behavior*, Proceedings of the NATO Advanced Research Workshop on Hamiltonian Mechanics, Torun, Poland, 28 Jun. - 2 Jul. 1993, NATO Advanced Study Institute Series B: Physics, Vol. 331, Ed. Seimenis, J., Plenum Press, New York, 1994, pp. 399-403.

[7] Patsis, P. and Zachilas, L., "Using Color and Rotation for Visualizing Four-Dimensional Poincaré Cross-Sections with Applications to the Orbital Behavior of a Three-Dimensional Hamiltonian System," *International Journal of Bifurcation and Chaos*, Vol. 4, No. 6, 1994, pp. 1399–1424.

[8] Bate, R., Mueller, D., and White, J., *Fundamentals of Astrodynamics*, New York, Dover, 1971.

[9] Prussing, J. and Conway, B., *Orbital Mechanics*, Oxford University Press, Oxford, 1993.

[10] Wiesel, W., *Spaceflight Dynamics*, Second Edition, Irwin/McGraw-Hill, Boston, 1997.

[11] Tan, A., *Theory of Orbital Motion*, World Scientific, Hackensack, NJ, 2008.

[12] Murray, C. and Dermott, S., *Solar System Dynamics*, Cambridge University Press, New York, 1999.

[13] Roy, A., *Orbital Motion*, Second Edition, Adam Hilger, Bristol, England, UK, 1982.

[14] Wiesel, W., *Modern Astrodynamics*, Aphelion Press, Beavercreek, OH, 2003.

[15] Deprit, A. and Henrard, J., "Symmetric Doubly Asymptotic Orbits in the Restricted Three-Body Problem," *The Astronomical Journal*, Vol. 70, No. 4, 1965, pp. 271-274.

[16] Farquhar, R. and Kamel, A., "Quasi-Periodic Orbits About the Translunar Libration Point," *Celestial Mechanics*, Vol. 7, No.4, 1973, pp. 458-473.

[17] Richardson, D., "Halo Orbit Formulation for the ISEE-3 Mission," *Journal of Guidance and Control*, Vol. 3, No. 6, 1980, pp. 543-548.

[18] Howell, K., "Three-Dimensional, Periodic, 'Halo' Orbits," *Celestial Mechanics*, Vol. 32, No.1, 1984, pp. 53-71.

[19] Domingo, V., Fleck, B., and Poland, A., "The SOHO Mission: An Overview," *Solar Physics*, Vol. 162, Nos.1-2, 1995, pp. 1-37.

[20] Holmes, P., "Poincaré, Celestial Mechanics, Dynamics-Systems Theory and 'Chaos'," *Physics Reports*, Vol. 193, No. 3, 1990, pp. 137-163.

[21] Wiggins, S., *Introduction to Applied Nonlinear Dynamical Systems and Chaos*, Texts in Applied Mathematics, Vol. 2, Ed. John, F., Marsden, J., Sirovich, L., Golubitsky, M., and Jäger, W., Springer-Verlag, New York, 1990.

[22] Howell, K., Mains, D., and Barden, B., "Transfer Trajectories from Earth Parking Orbits to Sun-Earth Halo Orbits," *AAS/AIAA Spaceflight Mechanics Meeting 1994*, Proceedings of the 4th AAS/AIAA Spaceflight Mechanics Meeting, Cocoa Beach, FL, 14-16 Feb. 1994, *Advances in the Astronautical Sciences*, Vol. 87, Ed. Cochran, J., Edwards, C., Hoffman, S., and Holdaway R., Univelt, 1994, pp. 399-422.

[23] Howell, K., Barden, B., and Lo, M., "Application of Dynamical Systems Theory to Trajectory Design for a Libration Point Mission," *Journal of the Astronautical Sciences*, Vol. 45, No. 2, 1997, pp. 161-178.

[24] Lo, M, Williams, B., Bollman, W., Han, D., Hahn, Y., Bell, J., Hirst, E., Corwin, R., Hong, P., Howell, K., Barden, B., and Wilson, R., "Genesis Mission Design," AIAA/AAS Astrodynamics Specialist Conference and Exhibit, Boston, MA, 10-12 Aug. 1998.

[25] Folta, D., Woodard, M., Howell, K., Patterson, C., and Schlei, W., "Applications of Multi-Body Dynamical Environments: The ARTEMIS Transfer Trajectory Design," *Acta Astronautica*, Vol. 73, Apr.-May, 2012, pp. 237–249.

[26] Folta, D., Woodard, M., Pavlak, T., Haapala, A., and Howell, K., "Earth-Moon Libration Stationkeeping: Theory, Modeling, and Operations," Proceedings of the 1st AIAA/AAS Conference on Dynamics and Control of Space Systems, Porto, Portugal, 19-21 Mar. 2012. *Advances in the Astronautical Sciences*, Vol. 145, Part 1, Ed. Guerman A., Bainum, P., and Contant, J., Univelt, 2012, pp. 489-508.

[27] Folta, D., Pavlak, T., Haapala, A., Howell, K., and Woodard, M., "Earth-Moon Libration Point Orbit Stationkeeping: Theory, Modeling, and Operations," *Acta Astronautica*, Vol. 94, No. 1, 2014, pp. 421-433.

[28] Perko, L., *Differential Equations and Dynamical Systems*, Texts in Applied Mathematics, Vol. 7, Ed. John, F., Marsden, J., Sirovich, L., Golubitsky, M., and Jäger, W., Springer-Verlag, New York, 1991.

[29] Hénon, M., "Numerical Exploration of the Restricted Three-Body Problem," *The Theory of Orbits in the Solar System and in Stellar Systems*, Proceedings of International Astronomical Union Symposium No. 25, Thessaloniki, Greece, 17-22 Aug. 1964, Ed. Contopoulos, G., Academic Press, London, 1966, pp. 157-169.

[30] Jefferys, W., "An Atlas of Surfaces of Section for the Restricted Problem of Three Bodies," *Publications of the Department of Astronomy, The University of Texas at Austin*, Series II, Vol. 3, No. 6, Applied Mechanics Research Laboratory, AMRL 1034, 1971.

[31] Jefferys, W., "Stability Regions for Quasiperiodic Motion in the Restricted Problem of Three Bodies," *The Astronomical Journal*, Vol. 79, No. 6, 1974, pp. 710-721.

[32] Koon, W., Lo, M., Marsden, J., and Ross, S., "Shoot the Moon," *Spaceflight Mechanics 2000*, Proceedings of the AAS/AIAA Spaceflight Mechanics Meeting, Clearwater, FL, 23-26 Jan. 2000, *Advances in the Astronautical Sciences*, Vol. 105, Part 1, Ed. Kluever, C., Neta, B., Hall, C., and Hanson, J., Univelt, 2000, pp. 1017-1030.

[33] Villac, B. and Scheeres, D., "Escaping Trajectories in the Hill Three-Body Problem and Applications," *Journal of Guidance, Control, and Dynamics*, Vol. 26, No. 2, 2003, pp. 224–232.

[34] Craig Davis, D. and Howell, K., "Trajectory Evolution in the Multi-Body Problem with Applications in the Saturnian System," IAF 61st International Astronautical Congress, Prague, Czech Republic, 27 Sep.-1 Oct. 2010, pp. 1-13.

[35] Craig Davis, D. and Howell, K., "Trajectory Evolution in the Multi-Body Problem with Applications in the Saturnian System," *Acta Astronautica*, Vol. 69, Nos. 11-12, 2011, pp. 1038-1049.

[36] Craig Davis, D. and Howell, K., "Long-Term Evolution of Trajectories Near the Smaller Primary in the Restricted Problem," *Spaceflight Mechanics 2010*, Proceedings of the 20th AAS/AIAA Spaceflight Mechanics Meeting, San Diego, CA, 14-17 Feb. 2010, *Advances in the Astronautical Sciences*, Vol. 136, Ed. Mortari, D., Starchville, T., Trask, A., and Miller, J., Univelt, 2010.

[37] Vaquero M., *Poincaré Sections and Resonant Orbits in the Restricted Three-Body Problem*, M.S. Thesis, School of Aeronautics and Astronautics, Purdue University, West Lafayette, IN, 2010.

[38] Haapala, A., *Trajectory Design Using Periapse Maps and Invariant Manifolds*, M.S. Thesis, School of Aeronautics and Astronautics, Purdue University, West Lafayette, IN, 2010.

[39] Haapala, A. and Howell, K., "Trajectory Design Using Periapse Poincaré Maps and Invariant Manifolds," *Spaceflight Mechanics 2011*, Proceedings of the 21st AAS/AIAA Spaceflight Mechanics Meeting, New Orleans, LA, 13-17 Feb. 2011, *Advances in the Astronautical Sciences*, Vol. 140, Part 1, Ed. Jah, M., Guo, Y., Bowes, A., and Lai, P., Univelt, 2011, pp. 415-434.

[40] Craig Davis, D., *Multi-Body Trajectory Design Strategies Based on Periapsis Poincaré Maps*, Ph.D. Dissertation, School of Aeronautics and Astronautics, Purdue University, West Lafayette, IN, 2011.

[41] Vaquero, M. and Howell, K., "Poincaré Maps and Resonant Orbits in the Circular Restricted Three-Body Problem," *Astrodynamics 2011*, Proceedings of the AAS/AIAA Astrodynamics Specialist Conference, Girdwood, AK, 31 Jul. - 4 Aug. 2011, *Advances in the Astronautical Sciences*, Vol. 142, Ed. Schaub, H., Gunter, B., Russell, R., and Cerven, W., Univelt, 2012.

[42] Craig Davis, D. and Howell, K., "Characterization of Trajectories Near the Smaller Primary in Restricted Problem for Applications," *Journal of Guidance, Control, and Dynamics*, Vol. 35, No. 1, 2012, pp. 116-128.

[43] Howell, K., Craig Davis, D., and Haapala, A., "Application of Periapse Maps for the Design of Trajectories Near the Smaller Primary in Multi-Body Regimes," *Journal of Mathematical Problems in Engineering*, Vol. 2012, Article ID 351759.

[44] Froeschlé, C., "Numerical Study of Dynamical Systems with Three Degrees of Freedom: I. Graphical Displays of Four-Dimensional Sections," *Astronomy and Astrophysics*, Vol. 4, 1970, pp. 115-128.

[45] Gómez, G., Masdemont, J., and Simó, C., "Quasihalo Orbits Associated with Libration Points," *Journal of the Astronautical Sciences*, Vol. 46, No.2, 1998, pp. 135–176.

[46] Gómez, G., Koon, W., Lo, M., Marsden, J., Masdemont, J., and Ross, S., "Connecting Orbits and Invariant Manifolds in the Spatial Restricted Three-body Problem," *Nonlinearity*, Vol. 17, No. 5, 2004, pp. 1571-1606.

[47] Vaquero, M. and Howell, K., "Design of Transfers [*sic*] Trajectories Between Resonant Orbits in the Restricted Problem with Application to the Earth-Moon System," Proceedings of the 1st AIAA/AAS Conference on Dynamics and Control of Space Systems, Porto, Portugal, 19-21 Mar. 2012. *Advances in the Astronautical Sciences*, Vol. 145, Part 1, Ed. Guerman A., Bainum, P., and Contant, J., Univelt, 2012, pp. 469-488.

[48] Vaquero, M. and Howell, K., "Transfer Design Exploiting Resonant Orbits and Manifolds in the Saturn-Titan System," *Journal of Spacecraft and Rockets*, Vol. 50, No. 5, 2013, pp. 1069-1085.

[49] Vaquero, M., *Spacecraft Transfer Trajectory Design Exploiting Resonant Orbits in Multi-Body Environments*, Ph.D. Dissertation, School of Aeronautics and Astronautics, Purdue University, West Lafayette, IN, 2013.

[50] Froeschlé, C., "Numerical Study of a Four-Dimensional Mapping," *Astronomy and Astrophysics*, Vol. 16, 1972, pp. 172-189.

[51] Vrahatis, M., Bountis, T., and Kollmann, M., "On the Computation of Periodic Orbits and Invariant Surfaces of 4D-Symplectic Mappings," *Hamiltonian Systems with Three or More Degrees of Freedom*, Proceedings of the NATO Advanced Study Institute on Hamiltonian Systems with Three or More Degrees of Freedom, S'Agaro, Spain, 19-30 Jun. 1995, NATO Advanced Study Institute Series C: Mathematical and Physical Sciences, Vol. 533, Ed. Simó, C., Kluwer Academic Publishers, Dordrecht, The Netherlands, 1999, pp. 633-637.

[52] Vrahatis, M., Bountis, T., and Kollmann, M., "Periodic Orbits and Invariant Surfaces of 4D Nonlinear Mappings," *International Journal of Bifurcation and Chaos*, Vol. 6, No. 8, 1996, pp. 1425-1437.

[53] Vrahatis, M., Isliker, H., and Bountis, T., "Structure and Breakdown of Invariant Tori in a 4-D Mapping Model of Accelerator Dynamics," *International Journal of Bifurcation and Chaos*, Vol. 7, No. 12, 1997, pp. 2707-2722.

[54] Todesco E., "Analysis of Resonant Structures of a 4D Model of a Nonlinear Magnetic Lattice Through Resonant Normal Forms," *EPAC 94*, Proceedings of the Fourth European Particle Accelerator Conference, London, 27 Jun.-1 Jul. 1994, Ed. Suller, V. and Petit-Jean-Genaz, C., World Scientific, Singapore, 1995, pp. 914-916.

[55] Todesco, E., "Analysis of Resonant Structures of Four-Dimensional Symplectic Mappings, using Normal Forms," *Physical Review E,* Vol. 50, No. 6, 1994, pp. R4298-R4301.

[56] Gemmi, M. and Todesco, E., "Stability and Geometry of Third-Order Resonances in Four-Dimensional Symplectic Mappings," *Celestial Mechanics and Dynamical Astronomy*, Vol. 67, No. 3, 1997, pp. 181-204.

[57] Katsanikas, M. and Patsis, P., "The Structure of Invariant Tori in a 3D Galactic Potential," *International Journal of Bifurcation and Chaos*, Vol. 21, No. 2, 2011, pp. 467–496.

[58] Katsanikas, M., Patsis, P., and Contopoulos, G., "The Structure and Evolution of Confined Tori Near a Hamiltonian Hopf Bifurcation," *International Journal of Bifurcation and Chaos*, Vol. 21, No. 8, 2011, pp. 2321–2330.

[59] Katsanikas, M., Patsis, P., and Pinotsis, A., "Chains of Rotational Tori and Filamentary Structures Close to High Multiplicity Periodic Orbits in a 3D Galactic Potential," *International Journal of Bifurcation and Chaos*, Vol. 21, No. 8, 2011, pp. 2331–2342.

[60] Katsanikas, M., Patsis, P., and Contopoulos, G., "Instabilities and Stickiness in a 3D Rotating Galactic Potential," *International Journal of Bifurcation and Chaos*, Vol. 23, No. 2, 2013, pp. 1330005-1 – 1330005-30.

[61] Zachilas, L., Katsanikas, M., and Patsis, P., "The Structure of Phase Space Close to Fixed Points in a 4D Symplectic Map," *International Journal of Bifurcation and Chaos*, Vol. 23, No. 7, 2013, pp. 1330023-1 - 1330023-7.

[62] Contopoulos, G., Voglis, N., and Efthymiopoulos, C., "Order and Chaos in 3-D Systems," *Hamiltonian Systems with Three or More Degrees of Freedom*, Proceedings of the NATO Advanced Study Institute on Hamiltonian Systems with Three or More Degrees of Freedom, S'Agaro, Spain, 19-30 Jun. 1995, NATO Advanced Study Institute Series C: Mathematical and Physical Sciences, Vol. 533, Ed. Simó, C., Kluwer Academic Publishers, Dordrecht, The Netherlands, 1999, pp. 26-38.

[63] Richter, M., *Classical and Quantum Investigations of Four-Dimensional Maps with a Mixed Phase Space*, Ph.D. Dissertation, Technische Universität Dresden, 2012.

[64] Richter M., Lange, S., Bäcker, A., Ketzmerick, R., "Visualization and Comparison of Classical Structures and Quantum States of 4D Maps," arXiv:1307.6109v2, *arXiv.org* [online], 2013, URL: http://arxiv.org/abs/1307.6109 [cited 11 Nov. 2013].

[65] Sprott, J., *Strange Attractors: Creating Patterns in Chaos*, M&T Books, New York, 1993.

[66] Sprott, J., "Can a Monkey with a Computer Create Art?" *Nonlinear Dynamics, Psychology, and Life Sciences*, Vol. 8, No. 1, 2004, pp.103-114.

[67] Heaton, A. and Longuski, J., "Feasibility of a Galileo-Style Tour of the Uranian Satellites," *Journal of Spacecraft and Rockets*, Vol. 40, No. 4, 2003, pp. 591-596.

[68] Broer, H., "KAM Theory: The Legacy of Kolmogorov's 1954 Paper," *Bulletin of the American Mathematical Society*, Vol. 41, No. 4, 2004, pp. 507-521.

[69] Wiesel, W., "Earth Satellite Orbits as KAM Tori," *Journal of the Astronautical Sciences*, Vol. 56, No. 2, 2008, pp. 151–162.

[70] Wiesel, W., "Earth Satellite Perturbation Theories as Approximate KAM Tori," *Journal of the Astronautical Sciences*, Vol. 58, No. 2, 2011, pp. 153-165.

[71] MATLAB®, Version 7.14.0.739 (R2012a), The MathWorks, Inc., Natick, MA, 2012.

[72] Avizo®, Version 7.0.1, Visualization Sciences Group, SAS, Burlington, MA, 2012.

[73] Marchal, C., *The Three-Body Problem*, Studies in Astronautics, Vol. 4, Elsevier, Amsterdam, 1990.

[74] Vallado, D., *Fundamentals of Astrodynamics and Applications*, McGraw-Hill, New York, 1997.

[75] Shampine, L. and Reichelt, M., "The MATLAB ODE Suite," *SIAM Journal on Scientific Computing*, Vol. 18, No. 1, 1997, pp. 1-22.

[76] Meirovitch, L., *Methods of Analytical Dynamics*, McGraw-Hill, New York, 2003.

[77] Bruno, A., *The Restricted 3-Body Problem: Plane Periodic Orbits*, Trans. Erdi, B., De Gruyter Expositions in Mathematics Series, Vol. 17, Berlin, 1994.

[78] Howell, K, Marchand, B., and Lo, M., "Temporary Satellite Capture of Short-Period Jupiter Family Comets from the Perspective of Dynamical Systems," *Journal of the Astronautical Sciences*, Vol. 49, No. 4, 2001, pp. 539-557.

[79] Wawrzyniak, G., "biglabel.m," MATLAB® Script, AAE 699 Research, Multi-Body Dynamics Research Group, School of Aeronautics and Astronautics, Purdue University, West Lafayette, IN, 2011.

[80] Woodford, O., "export_fig.m," MATLAB® Script, 2012. *MATLAB® Central File Exchange* [online], URL: http://www.mathworks.com/matlabcentral/fileexchange/23629-exportfig [cited 16 Nov. 2013].

[81] Lindner, M., "arrow3d.m," MATLAB® Script, Bar-Ilan University, Israel, 2010, *MATLAB® Central File Exchange* [online], URL: http://www.mathworks.com/matlabcentral/fileexchange/28324-3d-arrow-plot/content/arrow3d.m [cited 16 Nov. 2013].

[82] Greenwood, D., *Classical Dynamics*, Dover, New York, 1997.

[83] Howell, K. and Campbell, E., "Three-Dimensional Periodic Solutions that Bifurcate from Halo Families in the Circular Restricted Three-Body Problem," *Spaceflight Mechanics 1999*, Proceedings of the AAS/AIAA Spaceflight Mechanics Meeting, Breckenridge, CO, 7-10 Feb. 1999, *Advances in the Astronautical Sciences*, Vol. 102, Part 2, Ed. Bishop, R., Mackison, D., Culp, R., and Evans, M., Univelt, 1999, pp. 891-910.

[84] Sicardy, B., "Stability of the Triangular Lagrange Points Beyond Gascheau's Value," *Celestial Mechanics and Dynamical Astronomy*, Vol. 107, No. 1-2, 2010, pp. 145-155.

[85] Lichtenberg, A. and Lieberman, M., *Regular and Chaotic Dynamics*, Second Edition, Applied Mathematical Sciences, Vol. 38, Ed. John, F., Marsden, J., and Sirovich, L., Springer-Verlag, New York, 1992.

[86] Hilborn, R., *Chaos and Nonlinear Dynamics: An Introduction for Scientists and Engineers*, Oxford University Press, Oxford, 1994.

[87] von Milczewski, J., Diercksen, G., and Uzer, T., "The Arnol'd Web in Atomic Physics," *Hamiltonian Systems with Three or More Degrees of Freedom*, Proceedings of the NATO Advanced Study Institute on Hamiltonian Systems with Three or More Degrees of Freedom, S'Agaro, Spain, 19-30 Jun. 1995, NATO Advanced Study Institute Series C: Mathematical and Physical Sciences, Vol. 533, Ed. Simó, C., Kluwer Academic Publishers, Dordrecht, The Netherlands, 1999, pp. 499-503.

[88] Wiggins, S., "Phase Space Geometry and Dynamics Associated with the 1:2:2 Resonance," *Hamiltonian Systems with Three or More Degrees of Freedom*, Proceedings of the NATO Advanced Study Institute on Hamiltonian Systems with Three or More Degrees of Freedom, S'Agaro, Spain, 19-30 Jun. 1995, NATO Advanced Study Institute Series C: Mathematical and Physical Sciences, Vol. 533, Ed. Simó, C., Kluwer Academic Publishers, Dordrecht, The Netherlands, 1999, pp. 254-269.

[89] Rasband, S., *Chaotic Dynamics of Nonlinear Systems*, John Wiley and Sons, New York, 1990.

[90] Eddy, J. and Lewis, K., "Visualization of Multidimensional Design and Optimization Data Using Cloud Visualization," Proceedings of DETC'02, American Society of Mechanical Engineers 2002 Design Engineering Technical Conferences and Computers and Information in Engineering Conference, Montreal, 29 Sep. – 2 Oct. 2002, DETC2002/DAC-34130.

[91] Wegman, E., "Hyperdimensional Data Analysis Using Parallel Coordinates," *Journal of the American Statistical Association*, Vol. 85, No. 411, 1990, pp. 664-675.

[92] Weaver, C., "Cross-Filtered Views for Multidimensional Visual Analysis," *IEEE Transactions on Visualization and Computer Graphics*, Vol. 16, No. 2, 2010, pp. 192-204.

[93] Chiu, P. and Bloebaum, C., "Hyper-Radial Visualization (HRV) Method with Range-Based Preferences for Multi-Objective Decision Making," *Structural and Multidisciplinary Optimization*, Vol. 40, No. 1, 2010, pp. 97–115.

[94] Zhang, X., Simpson, T., Frecker, M., and Lesieutre, G., "Supporting Knowledge Exploration and Discovery in Multi-Dimensional Data with Interactive Multiscale Visualisation," *Journal of Engineering Design*, Vol. 23, No. 1, 2012, pp. 23-47.

[95] Willcox, K. and Peraire, J., "Balanced Model Reduction via the Proper Orthogonal Decomposition," *AIAA Journal*, Vol. 40, No.11, 2002, pp. 2323-2330.

[96] Ribeiro, L., Sechi, A., and Biscaia E., "A New Technique of Model Order Reduction Based on Weighted Residuals in Discrete Domain," Proceedings of the 20th European Symposium on Computer Aided Process Engineering, Naples, Italy, 6-9 Jun. 2010, Ed. Pierucci, S. and Ferraris, G., Elsevier, 2010.

[97] Cochran, W., *Sampling Techniques*, Third Edition, John Wiley & Sons, New York, 1977.

[98] Levy, P. and Lemeshow, S., *Sampling of Populations: Methods and Applications*, Third Edition, John Wiley & Sons, New York, 1999.

[99] Box, G., Hunter, J., and Hunter, W., *Statistics for Experimenters*, Second Edition, John Wiley & Sons, Hoboken, NJ, 2005.

[100] Lanczos, C., *The Variational Principles of Mechanics*, Fourth Edition, Dover, New York, 1986.

[101] Longuski, J., Guzmán, J., and Prussing, J., *Optimal Control with Aerospace Applications*, Microcosm Press and Springer, El Segundo, CA, 2014.

[102] Byrd, R., Gilbert, J., and Nocedal, J., "A Trust Region Method Based on Interior Point Techniques for Nonlinear Programming," *Mathematical Programming*, Vol. 89, No. 1, 2000, pp. 149–185.

[103] Nocedal, J. and Wright, S., *Numerical Optimization*, Springer Series in Operations Research, Ed. Glynn, P. and Robinson, S., Springer, New York, 1999.

[104] Weinberg, S., *Gravitation and Cosmology: Principles and Applications of the General Theory of Relativity*, John Wiley & Sons, New York, 1972.

[105] Tavel, M., *Contemporary Physics and the Limits of Knowledge*, Rutgers University Press, Piscataway, NJ, 2002.

[106] Sellers, J., *Understanding Space: An Introduction to Astronautics*, Third Edition, Ed. Kirkpatrick, D., McGraw-Hill, New York, 2005.

[107] Wertz, J. and Larson, W., *Space Mission Analysis and Design*, Third Edition, Microcosm Press, Torrance, CA, 1999.

[108] King-Hele, D., *Satellite Orbits in an Atmosphere: Theory and Applications*, Blackie & Son Ltd., Glasgow, 1987.

[109] Geisel, C., *Navigation Solutions to Enable Space Superiority Through the Repeated Intercept Mission from Highly Elliptical Orbits*, M.S. Thesis, Air Force Institute of Technology, Wright-Patterson Air Force Base, OH, 2008.

[110] Chobotov, V., *Orbital Mechanics*, Third Edition, American Institute of Aeronautics and Astronautics, Inc., Reston, VA, 2002.

[111] Jet Propulsion Laboratory Solar System Dynamics Group, "JPL HORIZONS System web-interface," [online], URL: http://ssd.jpl.nasa.gov/?horizons [cited 14 Jul. 2012].

[112] Satellite Tool Kit® (STK®), Version 9.2.3, Analytical Graphics, Inc., Exton, PA, 2011.

[113] RUBIK'S CUBE®, Rubik's Brand Ltd., London, *rubiks.com* [online], URL: http:// www.rubiks.com [cited 5 Nov. 2013], Invented 1974.

[114] Irons, M., "Visualizing the Fourth Dimension Using Color," [online], URL: http://www.rdrop.com/~half/Creations/Puzzles/visualizing.4D/index.html [cited 4 Mar. 2011].

[115] Boccaletti, D. and Pucacco, G., *Theory of Orbits: Integrable Systems and Non-Perturbative Methods*, Vol. 1, Springer, Berlin, 1996.

[116] Duhamel, P. and Vetterli, M., "Fast Fourier Transforms: A Tutorial Review and a State of the Art," *Signal Processing*, Vol. 19, No. 4, 1990, pp. 259-299.

[117] Polthier, K., "Imaging Maths - Inside the Klein Bottle," [online], URL: http://plus.maths.org/content/imaging-maths-inside-klein-bottle [cited 17 Jun. 2011].

[118] Olikara, Z. and Howell, K., "Computation of Quasi-Periodic Invariant Tori in the Restricted Three-body Problem," *Spaceflight Mechanics 2010*, Proceedings of the 20th AAS/AIAA Spaceflight Mechanics Meeting, San Diego, CA, 14-17 Feb. 2010, *Advances in the Astronautical Sciences*, Vol. 136, Ed. Mortari, D., Starchville, T., Trask, A., and Miller, J., Univelt, 2010.

[119] Bordner, R., *Orbital Tori Construction Using Trajectory Following Spectral Methods*, Ph.D. Dissertation, Air Force Institute of Technology, Wright-Patterson Air Force Base, OH, 2010.

[120] Hagen, L., *Effects of Air Drag and Lunar Third-Body Pertubrations* [sic] *on Orbital Motion Near a Reference KAM Torus*, M.S. Thesis, Air Force Institute of Technology, Wright-Patterson Air Force Base, OH, 2011.

[121] Bosanac, N., *Exploring the Influence of a Three-Body Interaction Added to the Gravitational Potential Function in the Circular Restricted Three-Body Problem: A Numerical Frequency Analysis*, M.S. Thesis, School of Aeronautics and Astronautics, Purdue University, West Lafayette, IN, 2012.

[122] Bosanac, N., Howell, K., and Fischbach, E., "Exploring the Impact of a Three Body Interaction Added to the Gravitational Potential Function in the Circular Restricted Three-Body Problem," *Spaceflight Mechanics 2013*, Proceedings of the 23th AAS/AIAA Spaceflight Mechanics Meeting, Kauai, HI, 10-14 Feb. 2013, *Advances in the Astronautical Sciences*, Vol. 148, Ed. Tanygin, S., Park, R., Starchville, T., and Newman, L., Univelt, 2013, pp. 1829-1848.

[123] Geisel, C., 4-D-Map-Based CR3BP Design Software Suite, MATLAB® Scripts, AAE 699 Research, Multi-Body Dynamics Research Group, School of Aeronautics and Astronautics, Purdue University, West Lafayette, IN, 2011-2013.

[124] Schlei, W., "makePSIfile.m," MATLAB® Script, AAE 698 Research, Multi-Body Dynamics Research Group, School of Aeronautics and Astronautics, Purdue University, West Lafayette, IN, 2011.

[125] Schlei, W., *An Application of Visual Analytics to Spacecraft Trajectory Design*, M.S. Thesis, School of Aeronautics and Astronautics, Purdue University, West Lafayette, IN, 2011.

[126] Schlei, W. and Howell, K., "A Visual Analytics Approach to Preliminary Trajectory Design," 22nd AAS/AIAA Spaceflight Mechanics Meeting, Charleston, SC, 29 Jan.-2 Feb. 2012, pp. 1-20.

[127] "Constants," AAE 632 Handouts, School of Aeronautics and Astronautics, Purdue University, West Lafayette, IN, Fall 2010.

[128] Geisel, C., Presentations on 4-D-Map-Based Trajectory Design in the Spatial CR3BP, AAE 699 Research Presentations to Multi-Body Dynamics Research Group, School of Aeronautics and Astronautics, Purdue University, West Lafayette, IN, 4 Mar. 2011 - 11 Oct. 2013.

[129] Geisel, C., "Spacecraft Orbit Design in the Circular Restricted Three-Body Problem Using Higher-Dimensional Poincaré Maps," Ph.D. Preliminary Examination Prospectus, School of Aeronautics and Astronautics, Purdue University, West Lafayette, IN, 3 Aug. 2012.

[130] Hamilton, D. and Krivov, A., "Dynamics of Distant Moons of Asteroids," *Icarus*, Vol. 128, No.1, 1997, pp. 241-249.

[131] Grebow, D., *Generating Periodic Orbits in the Circular Restricted Three-Body Problem with Applications to Lunar South Pole Coverage*, M.S. Thesis, School of Aeronautics and Astronautics, Purdue University, West Lafayette, IN, 2006.

[132] Clark, S., "Satellite Refueling Testbed Completes Demo in Orbit," *Spaceflight Now*, [online], 25 Jan. 2013, URL: http://www.spaceflightnow.com/news/n1301/25rrm/#.UQQMpvJ5GIR [cited 17 Oct. 2013].

[133] Alessandro, A., "Japanese Vehicle Delivers New Hardware for NASA's Robotic Refueling Mission," *nasa.gov* [online], 2 Aug. 2013, URL: http://www.nasa.gov/content/goddard/japanese-vehicle-delivers-new-hardware-for-nasa-s-robotic-refueling-mission [cited 17 Oct. 2013].

[134] Humble, R., Henry, G., and Larson, W., *Space Propulsion Analysis and Design*, First Edition-Revised, McGraw-Hill, New York, 1995.

[135] Ocampo, C., "Trajectory Analysis for the Lunar Flyby Rescue of AsiaSat-3/HGS-1," *Annals of the New York Academy of Sciences*, Vol. 1065, Dec. 2005, pp. 232-253.

[136] Hubbard, W., "Ice Giants Decadal Study," Revision 6/3/2010, NASA Ice Giants Decadal Mission Study Final Report, SDO-12345, 2010.

[137] McAdams, J., Scott, C., Guo, Y., Dankanich, J., and Russell, R., "Conceptual Mission Design of a Polar Uranus Orbiter and Satellite Tour," *Spaceflight Mechanics 2011*, Proceedings of the 21st AAS/AIAA Spaceflight Mechanics Meeting, New Orleans, LA, 13-17 Feb. 2011, *Advances in the Astronautical Sciences*, Vol. 140, Part 1, Ed. Jah, M., Guo, Y., Bowes, A., and Lai, P., Univelt, 2011, pp. 1257-1270.

[138] Dankanich, J. and McAdams, J., "Interplanetary Electric Propulsion Uranus Mission Trades Supporting the Decadal Survey," *Spaceflight Mechanics 2011*, Proceedings of the 21st AAS/AIAA Spaceflight Mechanics Meeting, New Orleans, LA, 13-17 Feb. 2011, *Advances in the Astronautical Sciences*, Vol. 140, Part 1, Ed. Jah, M., Guo, Y., Bowes, A., and Lai, P., Univelt, 2011, pp. 1271-1290.

[139] Committee on the Planetary Science Decadal Survey, Space Studies Board, Division on Engineering and Physical Sciences, "Vision and Voyages for Planetary Science in the Decade 2013-2022," Prepublication Copy, National Research Council, The National Academies Press, Washington, DC, 2011.

[140] Arridge, C. et al., "Uranus Pathfinder: Exploring the Origins and Evolution of Ice Giant Planets," *Experimental Astronomy*, Vol. 33, No. 2, 2012, pp. 753-791.

VITA

VITA

Christopher D. Geisel graduated with a B.S. in Astronautical Engineering from the U.S. Air Force Academy in 2001. During an undergraduate internship, he worked as an orbital analyst for the Advanced Payload Design Team at NASA's Jet Propulsion Laboratory in Pasadena, California.

While stationed at the Air Force Research Laboratory Sensors Directorate in Rome, New York, he led the design of a sensor system for hypersonic vehicles. For his master's thesis at the Air Force Institute of Technology in Dayton, Ohio, he researched innovative, fuel-saving navigation solutions for on-orbit inspection of satellites, and he earned an M.S. in Astronautical Engineering in 2008. Next, at the Space and Missile Systems Center / Missile Defense Systems Group in El Segundo, California, he supervised development, integration, testing, and operator training for two satellites designed to track ballistic missiles. He is also a veteran of the wars in Iraq and Afghanistan where he mentored Iraqi and Afghan security forces.

He began his Ph.D. studies at Purdue University in the fall of 2010, while continuing to serve on active duty in the Air Force. Beginning in 2014, Major Geisel's next assignment is to join the faculty at the Air Force Institute of Technology's Department of Aeronautics and Astronautics.